Functionalization of Silicon substrates with Polyoxometalates

Kelly Trinh

Sorbonne Université

Ecole doctorale de Chimie Moléculaire de Paris Centre – ED 406

Institut Parisien de Chimie Moléculaire / Equipe Edifices polymétalliques

Institut des Nanosciences de Paris / Equipe Physico-chimie et dynamique des surfaces

Functionalization of Silicon substrates with Polyoxometalates

Par Kelly Trinh

Thèse de doctorat de Chimie

Dirigée par Anna Proust et Olivier Pluchery

Présentée et soutenue publiquement le 14 janvier 2022

Devant un jury composé de :

Thomas HUHN, Professeur	Université de Constance	Rapporteur
Talal MALLAH, Professeur	Université Paris Saclay	Rapporteur
Christophe PETIT, Professeur	Sorbonne Université	Examinateur
Kirill MONAKHOV, Directeur de recherche	Leibniz Institute of Surface Engineering	Examinateur
Irina IONICA, Maître de conférences	IMEP-LAHC/INPG	Examinatrice
Anna PROUST, Professeur	Sorbonne Université	Directrice de thèse
Olivier PLUCHERY, Professeur	Sorbonne Université	Co-directeur de thèse
Florence VOLATRON, Maître de conférences	Sorbonne Université	Co-encadrante

To my family

Let It

I have a rule about not thinking where I am or what comes next. I guess when you let go of the need to know, everything tends to fall into place. It is okay to dream, to allow your higher self to take care of the rest.
So, if something is calling you, answer. If it bursts out of your chest like a trapped bird set free, follow it. There is a mysterious pull that longs to take you exactly where you need to go. Let it.

- *Lang Leav*

Acknowledgements

The PhD project presented in this manuscript has been conducted at the Institut Parisien de Chimie Moléculaire (IPCM) in the E-POM (Edifices polymétalliques) group, and at the Institut des Nanosciences de Paris (INSP), in the PHYSUF (Physico-chimie et dynamique des surfaces) group, at Sorbonne Université (Paris, France).

I sincerely thank Pr. Thomas Huhn and Pr. Talal Mallah who kindly dedicated their time reviewing this manuscript. I would also like to thank Pr. Christophe Petit, Dr. Kirill Monakhov and Dr. Irina Ionica for being part of my thesis committee.

I would like to express my profound gratitude to my PhD advisors who were involved in this project and who gave me the chance to learn so much in these last 3-4 years. I sincerely thank Pr. Anna Proust who took the role of director with perfection since the beginning. Your knowledge in polyoxometalate chemistry was invaluable to me, and your scientific rigor was exactly what I was seeking from a research advisor. This encouraged me to work harder and harder and to always provide my best. Most of all, I was touched by your kindliness and your trust which created a pleasant stimulating and working atmosphere. I sincerely thank Dr. Florence Volatron for her kindness and her teaching during my first experiments in polyoxometalates synthesis and silicon substrates handling. I truly appreciated your ability to make everything becomes simple as well as your constant reactivity whenever I had issues during my experiments. To complete this dream team, I sincerely thank Pr. Olivier Pluchery for accompanying me along the physical experiments journey with which I was not familiar at all at the beginning. Your knowledge in physics and your help in the data processing were invaluable to me, and I was impressed by your undying optimism and calmness. These words are probably not enough to express how grateful I am to have collaborated with wonderful scientists and persons. Thank you to the three of you for all the discussions we had that always overcame the difficulties, for your open-mindedness and for the critical eyes you put on my results. Thank you for trusting me, for getting me back on the right track when doubts arose and for guiding me so well during these years.

This project actually saw the light of day four years ago when I had the opportunity to spend half of my final year internship in Dallas at the LSNM. In that way, I would like to acknowledge Pr. Yves Chabal and Dr. Milana Cherie Thomas who introduced me to the silicon substrates functionalization and who gave me precious advice when I was only a second year master's student. I am thankful to the Laboratory of Excellence in Multiscale Integrative Chemistry (Michem) which also provided a financial support for this internship.

I sincerely thank Dr. Irina Ionica and her padawan Miltiadis Alepidis for their warm welcome in Grenoble at IMEP-LAHC. Thank you Miltiadis for introducing me to the probe station and for your help during all the measurements. Thank you Irina for your kindness, for your time and your devotion in this collaboration and for making the electronics easier to understand. I was glad and honored to be the missing link between you and Olivier and I hope this is only the beginning of more fruitful ~~blabla~~ collaborations.

I sincerely thank Pr. Dominique Vuillaume and Dr. Stéphane Lenfant for their warm welcome in Lille at IEMN. It was an honor to complete the work of Maxime and Kevin, and I would like to thank you for introducing me to the electrical characterizations and for your time and help during the data processing.

The measurements carried out during the whole project were only possible thanks to the involvement of the following people. I sincerely thank Antoine Miche for carrying out all the XPS analyses. I would like to thank Sébastien Royer for your DIY skills on the FTIR spectrometer air dryer as well as on the UV-Vis-NIR spectrometer sample holder. I would like to thank Hervé Cruguel for the formation you gave me on AFM and KPFM with which I was not familiar at the beginning. Your presence during the last experiments was also precious to me. I would also like to thank Bruno Gallas for his help with the spectroscopic ellipsometer.

More globally, I would like to thank all the E-POM team members for the enjoyable atmosphere in the laboratory: Pierre, Guillaume, Valérie, Bernard, Geoffroy, Richard, Séverine and Sébastien. You also helped me at some point during the project, by giving me suggestions and with the discussions which pushed me to always go one step further in the reasoning for providing the best scientific answers.

I would like to thank all the fellow labmates I had the chance to meet throughout my journey in the E-POM team. Big shout out to my labmate and writing partner Raphaël who was always there to cheer me up. I sincerely thank you for the moments we spent together, for the laughing times and the relaxing (if not wood fire) atmosphere you created. I would like to thank Weixian for the supportive and scientific discussions, for your help and your enjoyable company during the "nothing-works"-experiments. I would like to thank Michele ("va bene!" is still written on the hood window), Xiaolei and Youssef. It was inspiring to learn from you and to share some aspects about Science, life and future. Thank you Cheriehan for the moments we shared in and out the laboratory. Thank you Kevin for your friendliness, your care and our late ARAM plays, of course. Thank you Ingrid for sharing your office with two writers and for the laughing times that brightened this writing process. Thank you Juba for the discussions we shared and Ludivine for your precious help during my very last experiments.

Though the experiments were mainly carried out in the E-POM group, I would like to thank the fellow labmates I had the chance to meet in the PHYSUF group. Special thanks to Ayoub, Angeline and Luis for the scientific discussions and their help during my experiments.

I would like to thank my other PhD student partners elsewhere for their support: Mylan T., Mylan L, Cécile and Dylan. More particularly, I would like to thank Yacine for your well-timed support during this project, the scientific discussions, and the ideas we shared at some point about life, work, passion and motivation. I would also like to give a special thank you to Mohammed for your friendship and support despite the distance and the time that passed, from when we were only innocent teens to PhD students.

I would like to thank my friends who contributed to the revitalizing moments out the laboratory which were essential to me: Marie, Nive, Laura, Nahidah, Sophie, Amira, Fabien, Stéphanie, Matthieu, Laurent, Sébastien.

I would especially like to thank Martial for his never-ending support, love and patience during these last years. You helped me to hold on, wipe away my doubts, motivated me during the hardest times and reassured me on my future projects. I love you so much.

Lastly, thank you Didi, Mom and Dad for being next to me, for your love and for giving me a warm and comforting environment at home to rest and relax. I love you so much.

Thank you all for taking part in my blossoming process.

Table of contents

Abbreviations

δ	Deformation mode
ν	Stretching mode
Ψ-MOSFET	Pseudo-metal-oxide-semiconductor field-effect transistor
AFM	Atomic force microscopy
APTES	(3-Aminopropyl)triethoxysilane
ATR	Attenuated total reflectance
BOX	Buried oxide
C-AFM	Conducting atomic force microscopy
CMOS	Complementary metal-oxide-semiconductor
COOSuc	Succinimidyl ester
CPD	Contact potential difference
CZ	Czochralski
DFT	Density functional theory
DMF	Dimethylformamide
DMSO	Dimethyl sulfoxide
EDC.HCl	*N*-(3-Dimethylaminopropyl)-*N′*-ethylcarbodiimide hydrochloride
FDSOI	Fully depleted silicon-on-insulator
FET	Field-effect transistor
FM-KPFM	Frequency modulation Kelvin probe force microscopy
FTIR	Fourier transform infrared
FZ	Float-zone
g_m	Transconductance
GOM	Grafted organic monolayer
HF	Hydrofluoric acid
HOMO	Highest occupied molecular orbital
HRS	High-resistance state
IC	Integrated circuit
I_D	Drain current
ITO	Indium-tin-oxide
IVCT	Intervalence charge transfer
KPFM	Kelvin probe force microscopy

$K^{W}_{Si}[(N{=}PPh_3)_2]$	$TBA_3[PW_{11}O_{39}\{O(SiC_2H_4N{=}PPh_3)_2\}]$
$K^{W}_{Si}[(N_3)_2]$	$TBA_3[PW_{11}O_{39}\{O(SiC_2H_4N_3)_2\}]$
$K^{W}_{Si}[(NH_2)_2]$	$TBA_3[PW_{11}O_{39}\{O(Si(C_6H_4)NH_2)_2\}]$
$K^{W}_{Si}[COOH]$	$TBA_{3.4}[PW_{11}O_{39}\{O(SiC_2H_4COOH_{0.8})_2\}]$
$K^{W}_{Sn}[COOH]$	$TBA_{4.4}[PW_{11}O_{39}\{Sn(C_6H_4)C{\equiv}C(C_6H_4)COOH_{0.6}\}]$
$K^{W}_{Sn}[NH_2]$	$TBA_4[PW_{11}O_{39}\{Sn(C_6H_4)C{\equiv}C(C_6H_4)NH_2\}]$
LBL	Layer-by-layer
LED	Light-emitting diode
LMCT	Ligand-to-metal charge transfer
LO	Longitudinal optic phonon mode of SiO_2
LRS	Low-resistance state
LUMO	Lowest unoccupied molecular orbital
ME	Molecular electronics
MES	4-Morpholineethanesulfonic acid
MOS	Metal-oxide-semiconductor
MOSFET	Metal-oxide-semiconductor field-effect transistor
NH_4F	Ammonium fluoride
NHS	*N*-hydroxysuccinimide
PDSOI	Partially depleted silicon-on-insulator
POM	Polyoxometalate
POM(0)	$(n\text{Bu}_4\text{N})_3[PMo^{VI}_{12}O_{40}]$
POM(I)	$(n\text{Bu}_4\text{N})_4[PMo^{VI}_{11}Mo^{V}O_{40}]$
POM(II)	$\text{Li}(n\text{Bu}_4\text{N})_4[PMo^{VI}_{10}Mo^{V}_{2}O_{40}]$
POM-vinyl	$TBA_3[PW_9O_{34}(OSiCH{=}CH_2)_3(SiCH{=}CH_2)]$
POM-allyl	$TBA_3[PW_9O_{34}(OSiCH_2CH{=}CH_2)_3(SiCH_2CH{=}CH_2)]$
POMOF	Polyoxometalate-based metal-organic framework
RCA1	H_2O : NH_4OH 27% : H_2O_2 30% (4:1:1) solution
RCA2	H_2O : HCl 27% : H_2O_2 30% (4:1:1) solution
RRAM	Resistive random-access memory
SAM	Self-assembled monolayer
SiCOOH	Si-$(CH_2)_{10}$-C(=O)-OH surface
SiCOOSuc	Si-$(CH_2)_{10}$-C(=O)-O-N($C_4H_4O_2$) surface
Siester	Si-$(CH_2)_{10}$-C(=O)-O-CH_2-CH_3 surface

SiH	Hydrogenated-silicon surface
$SiNH_2$	Si-$(CH_2)_{10}$-C(=O)-NH-CH_2-CH_2-NH_2 surface
$SiNMe_2$	Si-$(CH_2)_{10}$-C(=O)-NH-CH_2-CH_2-NMe_2 surface
SOI	Silicon-on-insulator
STM	Scanning tunneling microscopy
TBA	Tetrabutylammonium
$TBAPF_6$	Tetrabutylammonium hexafluorophosphate
TO	Transversal optic phonon mode of SiO_2
US	Ultrasonication
UV-Vis-NIR	UV-visible-near infrared
V_{BG}	Back gate voltage
V_{CPD}	Contact potential difference
V_{DC}	Direct current voltage
V_{FB}	Flat-band voltage
V_G	Gate voltage
V_{Th}	Threshold voltage
WF	Work function
XPS	X-ray photoelectron spectroscopy

Chapter I

An overview of the project

I. Introduction

This chapter aims at providing to the reader an overview of the project. Accordingly, description of polyoxometalates and their appealing (redox) properties for the project will be first given. The interest and advantages brought by immobilizing such molecules onto surface will be explained within the context of molecular electronics and miniaturization trend of electronic components for more than 70 years. In our case, the goal will be to study the photoreduction phenomenon of immobilized POMs onto Si surface, which will require to control POM/surface interface.

II. Polyoxometalates

II.1. Definition

Polyoxometalates (POMs) are anionic nanosized metal-oxo clusters formed by early transition metals in their highest oxidation state, such as W^{VI}, Mo^{VI} or V^{V}, that are linked together via oxo-ligands (O^{2-}).[1–4] Most of them are labeled $[X_xM_mO_y]^{n-}$, with the X heteroatom (P, Si…) and the M metal. The metal-oxygen octahedra (MO_6) can be gathered in different ways, resulting in various structures of POM anions as shown in Figure 1.[5]

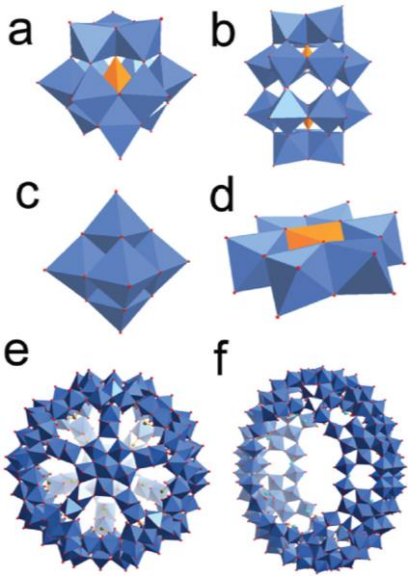

Figure 1 : A diversity of POM structures.[5] a) Keggin-type POM $[XM_{12}O_{40}]^{n-}$, b) Dawson-type POM $[X_2M_{18}O_{62}]^{n-}$, c) Lindqvist-type POM $[Mo_6O_{19}]^{2-}$, d) Anderson-type POM $[XM_6O_{24}]^{n-}$, e) $[Mo_{132}O_{372}(CH_3COO)_{30}(H_2O)_{72}]^{42-}$ ball shaped cluster and f) $[Mo_{154}O_{462}H_{14}(H_2O)_{70}]^{14-}$ Bielefeld wheel structure.

The project will more precisely focus on the Keggin-type POMs (Figure 1a), involving whether molybdenum (Mo^{6+}) or tungsten (W^{6+}) cations in our case, and later called polyoxomolybdates or polyoxotungstates, respectively. The POMs have been extensively studied starting from the mid-19th century, and their integration for POM-based materials has been more particularly explored since the 2000s.[6–10] POMs find their main applications in the field of catalysis, electronic materials and biology. Though the polyoxometalates as we know them were still unknown at that time, they were first obtained in 1826 by Berzelius. Through the reaction of phosphoric acid and ammonium molybdate, Berzelius indeed obtained a yellow precipitate (actually $(NH_4)_3[PMo_{12}O_{40}]$ salt) that turned blue (the reduced derivative).[1,3] On the other hand, polyoxotungstates were first obtained in 1864 by Marignac. However, the structure and composition of such compounds were still not well understood leading to studies over the 1900s-1920s period to characterize them. The structure of $H_3[PW_{12}O_{40}].6H_2O$ was finally solved by X-ray diffraction in 1933 by Keggin, who found that the POM structure involves corner-sharing but also edge-sharing WO_6 octahedra.

A Keggin-type POM is composed of a central XO_4 tetrahedron (X = P, Si…) surrounded by 12 MO_6 octahedra assembled in four edge-sharing $\{M_3O_{13}\}$ units. Starting from the α-Keggin, different Keggin isomers can be obtained by the rotation of one, two, three or all the four $\{M_3O_{13}\}$ units as depicted in Scheme 1.[11] The Keggin isomers display a diameter of approximately 1 nm.

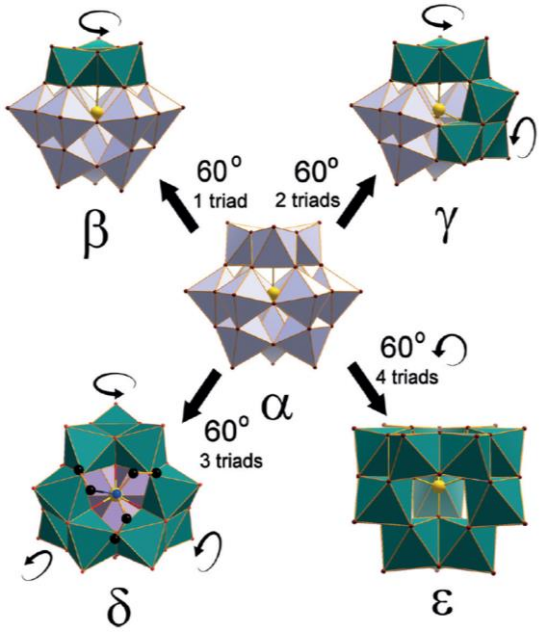

Scheme 1 : α-Keggin POM and the corresponding β-isomer, γ-isomer, δ-isomer and ε-isomer obtained by a 60° rotation of one, two, three or four $\{M_3O_{13}\}$ units.[11]

Our work will focus more precisely on the α-Keggin POM in which each $\{M_3O_{13}\}$ unit is linked to another one via corners. The α-Keggin structure will be discussed more in details in Chapter III. Briefly, the POM is constituted of oxygen atoms bounded to the central X heteroatom, M-O-M bridges and terminal M=O bonds.

II.2. Redox properties

Depending on whether there is one or two terminal M=O bonds in each octahedron, the POMs have been labeled by Pope "type I" or "type II", respectively.[1] Consequently, type I POMs are made of metal centers having a local C_{4v} symmetry, while the local symmetry is C_{2v} in type II POMs.[12] In our case, focus of our project will be given to type I POM because they are known to be easily and reversibly reduced unlike type II POM for which the reduction is more difficult and irreversible.[1,2]

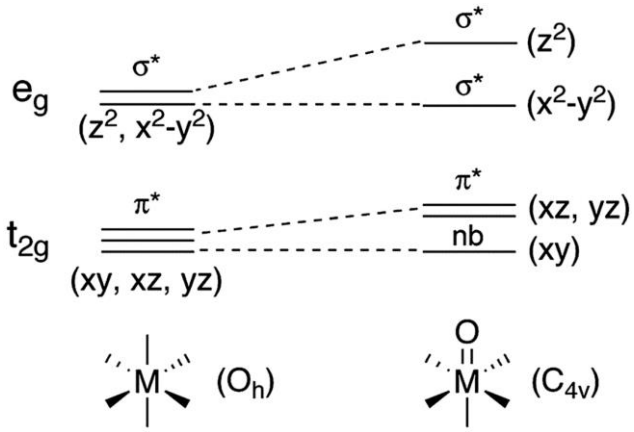

Figure 2 : Molecular orbital (MO) levels of one octahedron (O_h symmetry) on the left. In a POM, the octahedron is distorted leading to a d-orbitals splitting. The metal center in the resulting octahedron (right) displays a C_{4v} symmetry.[13,14]

To understand the reduction properties of the POMs, let us have a closer look at the d-orbitals of the metal centers of the POMs. Since the metal centers are in their highest oxidation state, their d orbitals are unoccupied (d^0). In a type I POM, there is one terminal oxygen atom (M=O) in each octahedron, shorter than the other M-O bonds, such that the octahedra are distorted. The metal centers thus display a C_{4v} symmetry in which the d-orbitals split into A_1 (z^2), B_1 (x^2-y^2), E (xz, yz) and B_2 (xy) (see Figure 2).[2,15] The d_{xy}-like orbital is nonbonding and can thus accept electron(s) without structural change in the coordinate bonds.

Density functional theory (DFT) calculations were made by Poblet and coll.[16,17] to investigate the bonding energies and the structures of several α-Keggin POMs. It has been shown that the

highest occupied molecular orbital (HOMO) of the POM, constituted with orbitals of the oxygen atoms, is well separated from the lowest unoccupied molecular orbital (LUMO), mainly constituted with the nonbonding orbitals of the metal centers described above, as shown in Figure 3. The LUMO of the POM is thus essentially nonbonding, meaning that it can receive one or several electrons reversibly without structural change. The electron accepted is delocalized over the metal centers of the POM. First, the gain of electrons leads to the formation of "heteropoly blues" or "molybdenum blues" (blue colored mixed-valence species).[1,2,18,19] Second, the presence of nonbonding orbitals indeed suggests the possibility for electron to be delocalized if the orbitals overlap. However, as the metals centers are not directly bonded, the electron delocalization is made possible by an indirect interaction through the nonbonding orbitals and suitable p-orbitals of the oxygen atoms.[12,20] Thus, the possibility to reduce successively the POMs is the reason why they are so called "electron reservoirs".

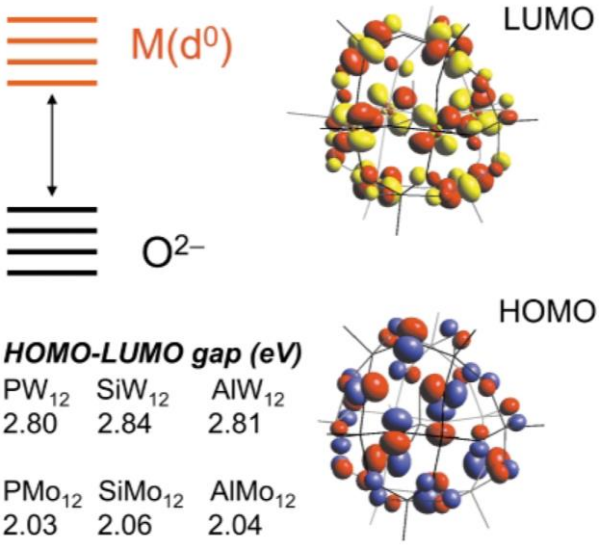

Figure 3 : Molecular orbital diagram of α-Keggin POM. The LUMO of the POM is mainly constituted with d-orbitals (nonbonding) of the metal centers while the HOMO is mainly composed of p-orbitals of the oxygen atoms. HOMO-LUMO gap of several α-Keggin POMs is also listed.[16]

For the project, we choose to study the α-$[PMo_{12}O_{40}]^{3-}$ POM. It can be isolated as a tetrabutylammonium (TBA) salt as reported by Sanchez *et al.*[21] leading to the $(n Bu_4N)_3$α-$[PMo_{12}O_{40}]$, or $(TBA)_3[PMo_{12}O_{40}]$, compound. The cyclic voltammogram of $[PMo_{12}O_{40}]^{3-}$ was recorded in acetonitrile and revealed the presence of three successive and reversible one-electron reduction waves as shown in Figure 4a.[22] Note that the half-wave potential $E_{1/2}$ of the first redox couple appear near the zero potential (at -170 mV vs Ag/0.01 M

Ag^+ CH_3CN), meaning that it does not require a lot of energy to reduce $[PMo_{12}O_{40}]^{3-}$, compared to the $[PW_{12}O_{40}]^{3-}$ counterpart exhibiting $E_{1/2}$ = -580 mV vs Ag/0.01 M Ag^+ CH_3CN for the first redox couple. Redox properties of the POMs can be modulated by the presence of cations.[22–24] For example, after addition of triflic acid, the monoelectronic reduction waves transformed into bielectronic reduction waves at higher potentials values (Figure 4b), suggesting the protonation of $[PMo^{VI}_{11}Mo^{V}O_{40}]^{4-}$. Similarly, addition of lithium perchlorate leads to the formation of a unique bielectronic reduction wave (Figure 4c) due to the strong association of $[PMo^{VI}_{10}Mo_2{}^{V}O_{40}]^{5-}$ with the Li^+ cation.

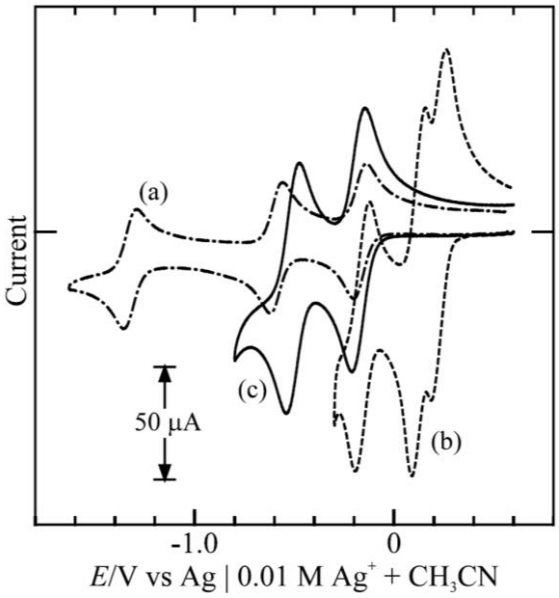

Figure 4 : Cyclic voltammograms of 0.50 mM $[PMo_{12}O_{40}]^{3-}$ in CH_3CN containing a) 0.1 M n-Bu_4NClO_4; b) (a)+5.0 mM CF_3SO_3H ; c) 0.1 M $LiClO_4$.[22]

The α-$[PMo_{12}O_{40}]^{3-}$ POM is an efficient electron reservoir. It has been studied by Awaga and coll.[25] for cluster batteries applications and particularly, the authors reported that the POM could accept up to 24 electrons, as initially demonstrated with $[H_2W_{12}O_{40}]^{6-}$ by Launay.[15] Note that the POM has also the ability to be chemically reduced in the presence of a reducing agent such as phenyllithium, leading to the formation of the one- and two-electrons reduced derivatives of $[PMo^{VI}_{12}O_{40}]^{3-}$, which are $[PMo^{VI}_{11}Mo^{V}O_{40}]^{4-}$ and $[PMo^{VI}_{10}Mo^{V}{}_2O_{40}]^{5-}$ respectively.[26]

The electron-acceptor character of POMs is thus an advantage for their integration in molecular electronics and especially memory devices applications. Let us now understand the context of the research development in this particular molecular electronics field.

III. From microelectronics to nanoelectronics and molecular electronics

The field of electronics was first marked by the development of vacuum tubes (or thermionic valve) in the beginning of the 20th century and their use in wireless radio communications.[27,28] The first diode was patented by Fleming in 1904 and was at that time made of two plates (an anode and a cathode) inside a glass tube. Thermoionic emission of electrons at the cathode by heating and subsequent external applied voltage at the anode allow the electrons to move from one plate to another under vacuum. Nowadays diode is an electronic semiconductor component allowing electrical current to flow in only one direction. Research has then followed to bring alternatives to vacuum tubes to improve the lifetime, to facilitate the fabrication process or to reduce the power consumption.[27,29]

The late 1940s-1950s marked the second key moment in the electronics field. The first transistor, called point-contact transistor, was invented at Bell Laboratories in 1947 and reported in 1948 by Bardeen and Brattain, in the group of Shockley.[30,31] A transistor (or transfer resistor) is a device constituted of three terminals, in which the resistance, and thus the current, between two terminals can be controlled by the third terminal.[32] The triode reported in 1948 and depicted in Figure 5 was made of three electrodes (an emitter, a collector and a base) on an *n*-type* germanium (Ge) substrate. An increase in output current at the collector (I_C) was observed when the emitter was positively forward biased, suggesting that holes flowed from the emitter to the collector, and that a thin inversion layer onto the surface was formed (as the substrate is *n*-type, it means that there is a layer, or region, at the semiconductor surface where majority carriers are holes instead of electrons). This rectifier (a two-terminal device that allows the current to flow in only one direction, characterized by a high conductance in one direction and a high resistance in the other direction)[32] operated as an amplifier (a device in which the output signal is greater than the input signal) when the two contacts (the emitter and the collector) were placed close enough.[30,31,33]

* *n*-type Ge means that a small quantity of donor-type atoms – or impurities – are inserted onto Ge such that the doped Ge now contains majority electrons charge carriers and minority holes charge carriers. On the contrary, *p*-type Ge are obtained after insertion of acceptor-type atoms onto Ge and contains holes as majority charge carriers and electrons as minority charge carriers

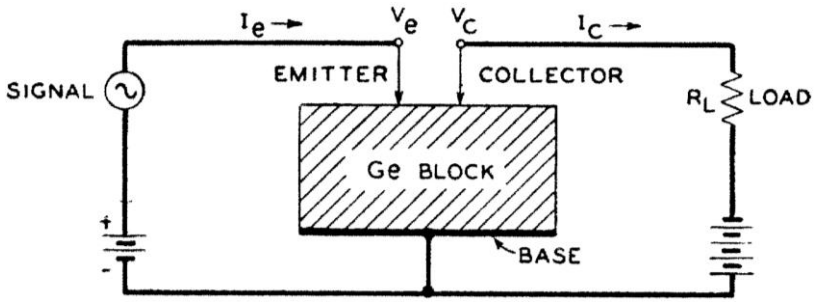

Figure 5 : The first transistor reported in 1948, called point-contact transistor at that time.[30]

Following the point-contact transistor, bipolar transistors (or bipolar junction transistors, BJT) based on *n*-*p*-*n* or *p*-*n*-*p* junctions were successively invented by Shockley *et al*. and the first BJT was reported in 1951.[34] With the development of new device architectures made of semiconductor materials, electronic circuits were made of electronic components (resistors, transistors, diodes, capacitors) connected together with wires on a circuit board in the 1950s. It is not until 1959 that the first planar transistor was invented by Jean Hoerni and obtained in the Si wafer plane unlike the conventional transistors that were raised from the Si plane.[35,36] The planarization discovery subsequently opened the way for circuit integration, developed by Noyce and Kilby, where the planar transistors were electrically connected on the same chip.[35,37] Another key advance was made in 1960 when the first Si/SiO_2 metal-oxide-semiconductor field-effect transistor (MOSFET) was reported by A. Kahng and M. M. Atalla,[38] although first patents with early MOSFET concepts were reported by Lilienfeld in 1926 and 1928.[36]

A MOSFET is a four-terminal device constituted by a substrate (or body), a source, a drain and a gate. Figure 6 represents the structure of a common *n*-channel MOSFET: the substrate is a *p*-type silicon substrate into which two heavily *n*-doped regions ("n^+" regions) called the source and the drain, are generally created by ion implantation.[32] On top of the substrate, a thermally grown SiO_2 layer serves as a dielectric. The metal contact on top of the oxide is called the gate and is made of heavily doped polysilicon or silicide/polysilicon mixture. The *n*-MOSFET works by applying a positive voltage to the gate, called gate voltage V_G. At a particular V_G called threshold voltage V_{Th}, the voltage is sufficient to create an inversion layer between the n^+-regions: the electrons of the substrate are attracted by the electric field generated such that an electron channel between the source and the drain appears (thus the name *n*-channel MOSFET or *n*-MOSFET, in contrary to *p*-MOSFET where a hole channel is formed between two p^+-regions). Current flows through the channel and is confined between the source and the drain thanks to the SiO_2 dielectric. The channel conductance is thus modulated by V_G. Another

bias can also be applied to the substrate backside (called substrate bias V_{BS}) to reduce V_G. The MOSFET is electrically isolated from another one in integrated circuits thanks to a thick oxide layer, called field oxide, that separates them. Complementary metal-oxide-semiconductor (CMOS) technology was further developed and involves the combination of both *p*- and *n*-channel MOS within the same transistor for the fabrication of logic circuits.

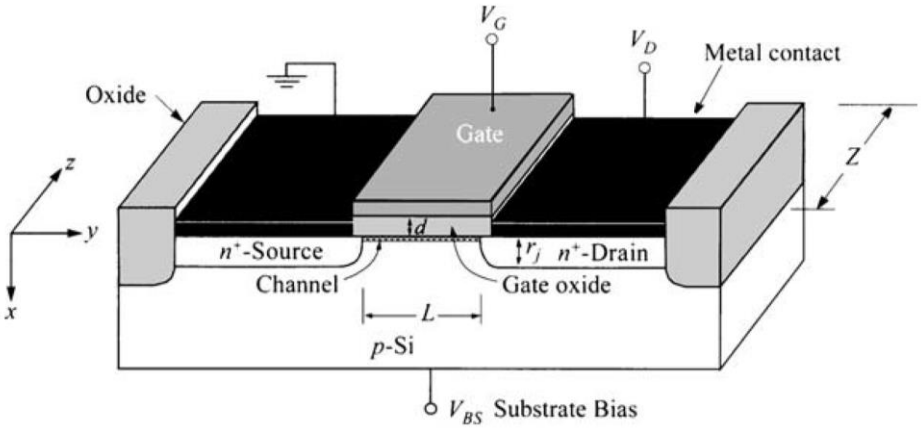

Figure 6 : Structure of an *n*-channel MOSFET.[32] L is the length of the channel, d is the thickness of the gate oxide, Z is the width of the channel, r_j is the depth of the junction.

The field of microelectronics thus started to flourish in the late 1950s. Microelectronics refers to the technology of electronic components integration onto a single chip, involving materials or structures development in the 0.1-100 µm range.[39,40] The number of components per integrated circuit (IC, or chip) started to increase following the discovery of planarization, MOSFET and CMOS. In 1961, an IC with 4 transistors was built, followed by the production of chips with 32 components in 1964, while ICs with 64 components were about to get released in 1965. In 1965, for the 35th anniversary edition of Electronics magazine, Gordon E. Moore (director of the Research and Development Laboratories of Fairchild Semiconductor at that time), was asked to predict the future of the semiconductor components industry over the next 10 years.[41] Based on the average factor of two increase in components per IC every year, Moore guessed that this doubling in ICs components will continue at least for the 10 following years, as shown in Figure 7. This became Moore's Law. According to Moore, the increase number of components per chip will reduce the cost per component. This effectively happens.

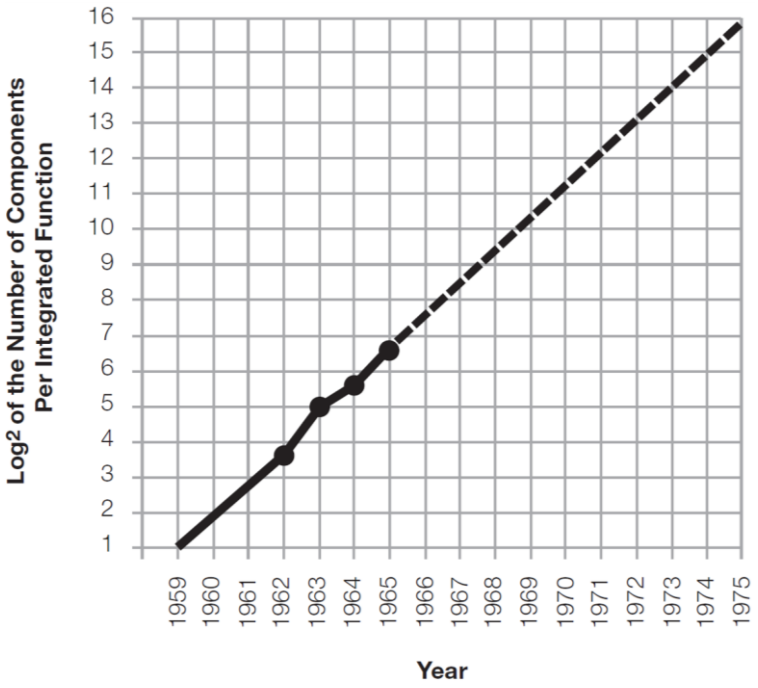

Figure 7 : Number of components per chip (logarithmic scale) over the years, from 1959 to 1965, and the evolution prediction over the 1965-1975 period.[41]

Based on the current device developments at his company and a possible slowing rate of the Moore's Law, Moore revised his prediction at the IEEE International Electron Devices Meeting in 1975. He suggested that the doubling trend in IC components will slow down and happen every two years instead of each year.[42] Over the years, Moore's prediction ended up being quite accurate, with a continuous increase in density of components on a chip, with cheaper components running faster and with lower power consumption. Moore's era faced the golden hours especially in the 1990s where approximately 10 million transistors could be put on a chip,[37] making possible the development of smaller devices such as computers, telephones and so on.

Microelectronics mutated into nanoelectronics in the early 2000s when the gate length, *i.e.* the distance between the source and the drain, was lower than 100 nm as depicted in Figure 8.[43] The development of the 130 nm technology node indeed involved transistors with a gate length of ~70 nm. However, with shorter gate length, leakage current phenomenon started to appear due to an easier moving of charge carriers within the components, leading to heat generation and loss of power issues.

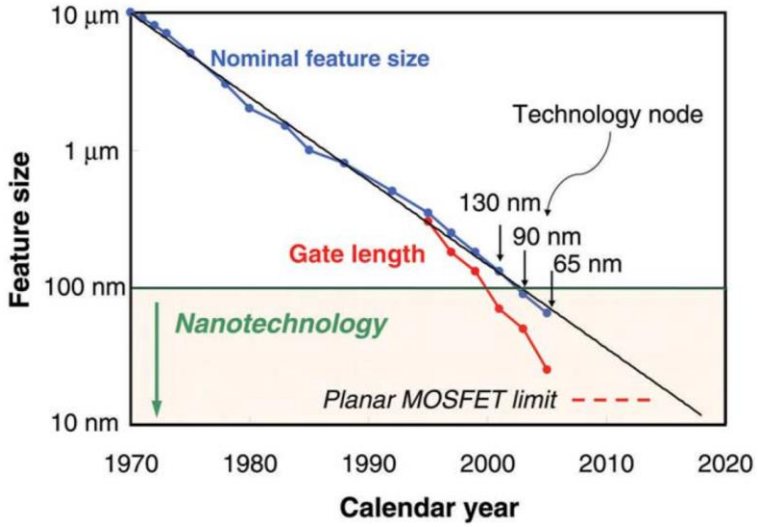

Figure 8 : Evolution of the logic technology node and gate length over the years.[43]

A power loss of ~20-30 W was for example observed in CMOS transistors for a power supply of 100 W.[43] This power loss can be explained by a thinner oxide layer as well as a smaller gate length (*i.e.* smaller channel). With thinner oxide layer, it is less efficient to confine the flow of electrons or holes in the channel. On the other hand, decreasing the gate length leads to an easier flowing of charge carriers even when the device is switched off. Indeed, when the channel was longer, the gate bias (gate-to-source bias) modulation was itself sufficient for allowing or not electrons to surpass the potential barrier at the source, as depicted in Figure 9a.[32] The drain bias (drain-to-source bias) had no influence on the potential barrier. However, with shorter channel, the potential barrier is now decreased by the drain bias (drain-to-source bias) because the drain is closer to the source (Figure 9b). This facilitates the injection of charge carriers to the extent that the flow of electrons can occur when the gate bias is lower than the threshold voltage. This phenomenon is called punch-through.

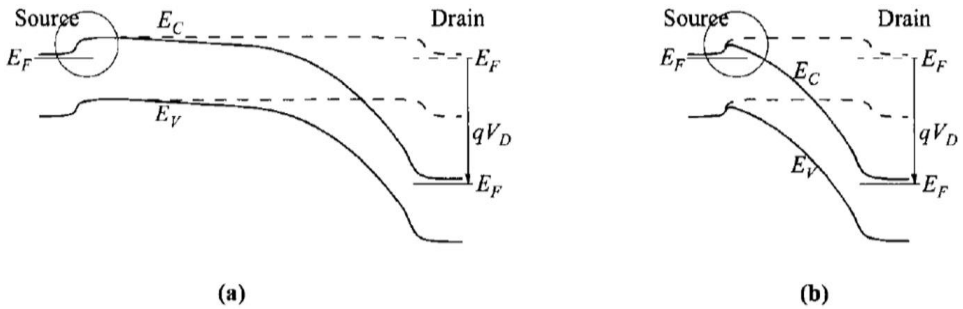

Figure 9 : Energy-band diagram from the source to the drain at the semiconductor surface of a MOSFET in the case when the channel is long (a) and short (b). The dashed lines represent the case when the drain bias equals zero, while the solid lines represent the case when the drain bias is positive.[32]

These perceptible and unavoidable physical limitations however did not sound the death knell of Moore's Law. Indeed, over the time, Moore's law has become a roadmap for semiconductor companies to stick to in order to be the more competitive ones in providing the best devices to the consumers, generation after generation. This subsequently led to higher consumer needs in terms of device performances and new needs for more sophisticated devices (mobile/smart/flexible devices for example).[44] Thus, despite the physical limitations encountered along with components shrinking, alternatives for CMOS scaling were still required and sought.

Accordingly, the increase in transistor clock speed (*i.e.* speed of executing instructions) was for example stopped in 2004, while multicore processors started to be developed.[45,46] Another alternative to pursue with CMOS scaling was to design other CMOS structures. CMOS structures involving "silicon-on-insulator" (SOI) substrates emerged. An SOI substrate is composed of a monocrystalline Si film on top of an insulator layer. Though the technology appeared in the 1960s, it is in the 1990s that it became more attractive thanks to a new fabrication process, called "SmartCut™", developed at CEA-Leti, in Grenoble (France), by Bruel. Soitec company was subsequently founded in 1992 with the aim to produce on an industrial scale SOI wafers based on the SmartCut™ process. The process, described in details in Chapter IV, can be viewed as an "atomic scalpel":[47] a thin layer of material is "cut" from the material and "transferred" to another substrate. This process was first developed on Si substrates and provides high quality of SOI substrates with ultra-thin layers and crystalline homogeneity. When developed on Si substrates, the SOI is composed of a thin layer of monocrystalline silicon on top of a thin buried oxide layer, called BOX, lying on a bulk silicon substrate. The BOX helps in confining the flow of electrons that moves from the source to the drain, thus reducing leakage currents, as depicted in Figure 10.

Figure 10 : Bulk MOS structure (left) versus fully depleted SOI (FD-SOI) structure (right). The electrons flowing from the source to the drain are confined in the channel region in the latter case thanks to the presence of the buried oxide layer (BOX).[48]

The Smart Cut™ fabrication process of the SOI wafers offers possible adjustments of the top silicon and the BOX thicknesses, leading to the formation of partially depleted SOI (PDSOI) or fully depleted SOI (FDSOI) wafers, the latter exhibiting thinner layers stacking. Moreover, a second gate can be connected to the bulk silicon so that the threshold voltage of the transistor can be modified, resulting in a better device control. The wafers production indeed started in 1999 with the inauguration of the first SOI production site and Soitec company became the world leader in SOI over time. Companies such as Samsung, STMicroelectronics or Sony are now working with SOI technology. In 2016 for example was released the Huami/Xiaomi Amazfit smartwatch equipped with a Sony GPS chip built on a FDSOI substrate.[49,50] The watch provided a battery life of ~35 hours (two to five times higher than the other smartwatches on the market) and consumed ~7 times less power than other GPS chips, fostering the development of SOI technology.

By entering the nanoelectronics, the size of the components obtained using the "top-down" approach started to be in the same order of magnitude as what was obtained in Molecular Electronics (ME) using the "bottom-up" approach. The top-down approach consists in obtaining smaller structures from the division of a larger bulk material, while in the bottom-up approach, the resulting structure is obtained from atomic or molecular building blocks.[51,52] In the field of ME, these building blocks are single molecule or an ensemble of molecules used to create functional electronic components.[52–57]

The field of ME emerged in the 1970s, more particularly with a report of Aviram and Ratner.[58] Through calculations, the authors indeed demonstrated the possibility to fabricate a single-molecule diode. More precisely, the organic molecule was constituted of a π-acceptor system (tetracyanoquinodimethane, TCNQ) and a π-donor system (tetrathiofulvalene, TTF), separated by a methylene bridge, "mimicking" a semiconductor-based diode in which a *p*-type region meets a *n*-type region. In this configuration, when an external bias is applied, the current preferentially flows in one preferential direction being the electrode → acceptor → donor → electrode pathway. Following this pioneer work, other studies involving single molecules emerged over the years, together with new characterization tools such as scanning tunneling microscopy (STM) and atomic force microscopy (AFM).[55,59] The groups of Reed and Tour reported in 1997 the fabrication of a single-molecule junction.[60] They contacted two gold electrodes functionalized with benzene-1,4-dithiol self-assembled monolayers (SAMs), using the mechanically controlled break junction (MCBJ) technique, and

were able to measure the conductance of the gold-sulfur-aryl-sulfur-gold junction, as shown in Figure 11.

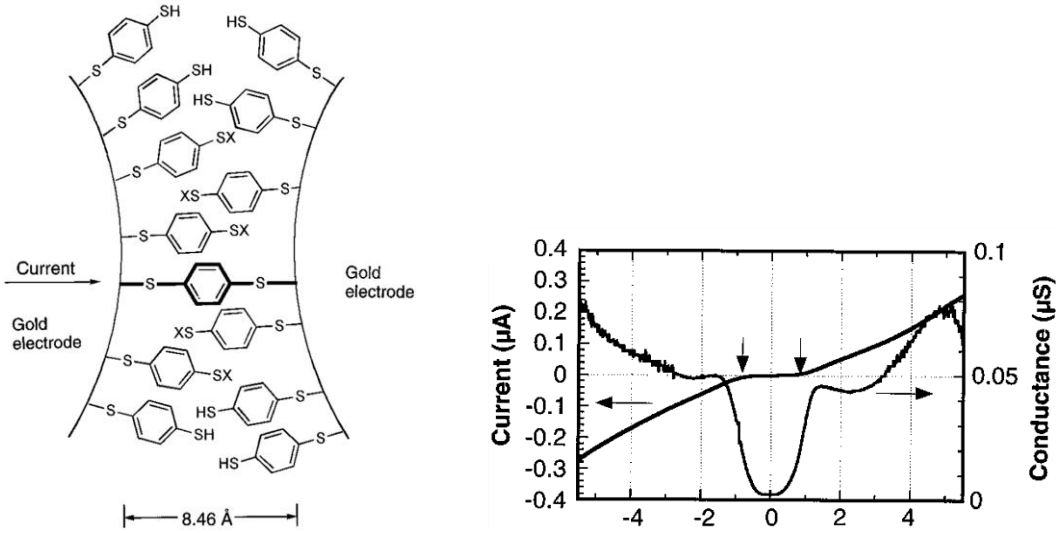

Figure 11 : Scheme of a benzene-1,4-dithiolate SAM between two gold electrodes formed by MCBJ (left). The thiolate is normally H-terminated after deposition; the X end groups can be either H or Au, with the Au potentially arising from a previous contact/retraction event. The typical I-V curve of the gold-sulfur-aryl-sulfur-gold junction (right) illustrating a gap of 0.7 V; and the first derivative conductance-voltage curve showing a steplike structure.[60]

This work actually constituted the first transport measurements through a symmetric single molecule junction and fostered other studies of molecules-based devices. The development of such devices, especially since the 2000s, constituted a way to compete with MOS structures obtained by conventional top-down approach. Indeed, the latter involves lithography and etching processes that were used for many years. However, the shrinking in electronics components size has pushed the industry to develop more sophisticated lithography techniques which in turn increased the fabrication costs. On the contrary, the bottom-up approach offers a large diversity of nanosized molecules that can be assembled at the nanometric scale with lower costs. Moreover, the interest comes from the added functionality that can provide the molecules. Their intrinsic properties can be "transferred" to the resulting molecule-based device which opens new routes for the design of multifunctional devices, diverse stimulus-responsive devices and so on, and thus constitutes a great advantage for extending Moore's Law. Molecular transistors, diodes, capacitors, insulators, or wires have been developed over the years, as particularly well described by Mathew and Fang.[56]

Nevertheless, the development of such devices requires intensive investigations on the selected molecules before they can effectively be employed in real-life devices.[61] Among the molecules studied, redox-active molecules provide interesting properties for information

storage applications due to their intrinsic redox properties, and especially for nonvolatile memory devices. Nonvolatile memory is a device in which the information is preserved within the device even when the latter is in its off state (e.g. flash drive, CD, DVD…). In the following, nonvolatile memory devices made of POMs will be described.

IV. Towards POM-based materials for molecular electronics

Redox-active molecules have been studied for charge storage applications due to their intrinsic redox properties.[61,62] Among them, type I POMs are particularly appealing, especially for their incorporation into nonvolatile memory devices. Not only do they exhibit several discrete redox states that can be reversibly accessible in a restricted range of potentials, but they are also robust and stable at high temperature which is required for the molecule in order to be compatible with CMOS manufacturing processes (up to ~400°C). The fact that they can be reduced reversibly without structural change suggests an apparent stability under device operation. Together with the large diversity of structures and redox properties, these POMs could thus serve as building blocks for molecular electronics. Though promising, integration of POM into devices still requires thorough studies to master POM immobilization onto surfaces and understanding of the POM/surface interaction.

Busche *et al*. were able to build a POM-based flash memory device by using the $[W_{18}O_{54}(SeO_3)_2]^{4-}$ Wells-Dawson POM.[63] The POM has a core-shell structure (see Figure 12) characterized by a $\{W_{18}O_{54}\}$ shell that can be reduced several times, while the two Se dopants located in the core of the POM can be oxidized (see the cyclic voltammogram in Figure 12). The authors investigated the properties of both the core and the shell for charge storage device.

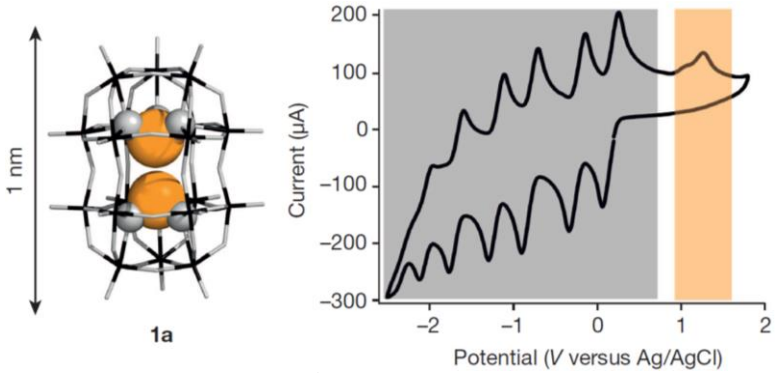

Figure 12: Structure of $[W_{18}O_{54}(SeO_3)_2]^{4-}$(left) and its cyclic voltammogram (right) obtained on glassy carbon electrode in 0.1 M TBAPF6 acetonitrile solution at a scan rate of 200 mV/s and a scanning range V of -2.5 V to 1.8 V against Ag/AgCl reference.[63]

POMs were immobilized by a dropcasting of POM solution around the Si nanowire channel covered with SiO_2 insulator, as depicted in Figure 13. The system obtained has a flash memory device configuration in which the POMs constitute the floating gate of the device.

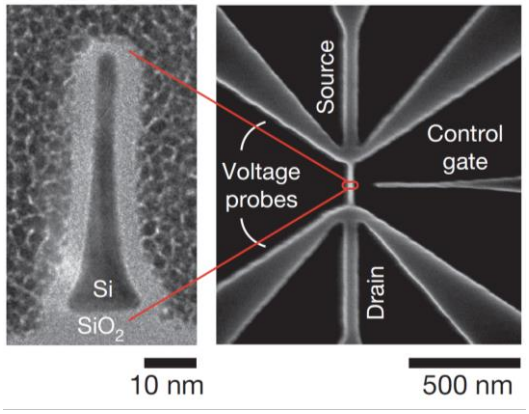

Figure 13 : Image of the flash memory device and the I-V curves obtained via an external bias applied to the control gate.[63]

Basically, a flash memory device configuration (or floating-gate memory cell) is similar to a MOSFET but having two gates instead of a unique one and which are called control gate and floating gate (see Figure 14). The floating gate lies on top of the bulk substrate (*i.e.* the Si nanowire in the current study) and is isolated inside a dielectric (here, SiO_2). Under an applied bias, electrons flow from the source to the drain and can be trapped within the floating-gate due to tunneling effect. The flash memory device is based on three operations: erase, program or write, and read. The negative charging of the floating-gate with electrons is called the programming or writing operation, while the release of electrons from the floating-gate to the substrate is called the erasing operation. Both operations are performed by modulation of the applied bias on the substrate and on the control gate. During the reading operation, a specific bias is applied to the control gate. When the floating-gate is empty, a current flows between the source and the drain (ON state of the device) and this corresponds to a logical "1". On the contrary, when the floating-gate is negatively charged, the device is on its OFF state and this corresponds to a logical "0". In the study, the floating-gate constituted of POMs act as charge storage centers.

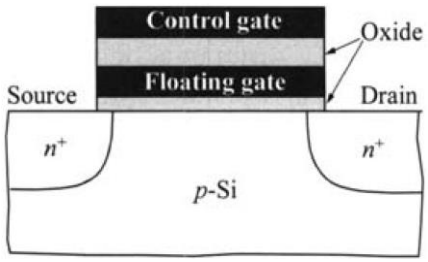

Figure 14 : Structure of a floating-gate memory cell.[32]

The drain current was measured as a function of the control gate bias and the I-V curves are shown in Figure 15. The authors found that by applying a negative external bias of -20 V to the control gate (blue curve), the threshold voltage increased due to the charging of POM, and the value goes back towards the initial one when the opposite external bias was applied (red curve), which corresponds to a discharging process. As described above, the charge and discharge processes correspond to the program and the erase operations of the device, respectively, that take place within 0.1 s and that can be repeated several times. A POM-based flash memory was thus obtained, though calculations suggest that faster operations could be obtained by lowering the POM concentration and by having a better POM distribution over the surface.

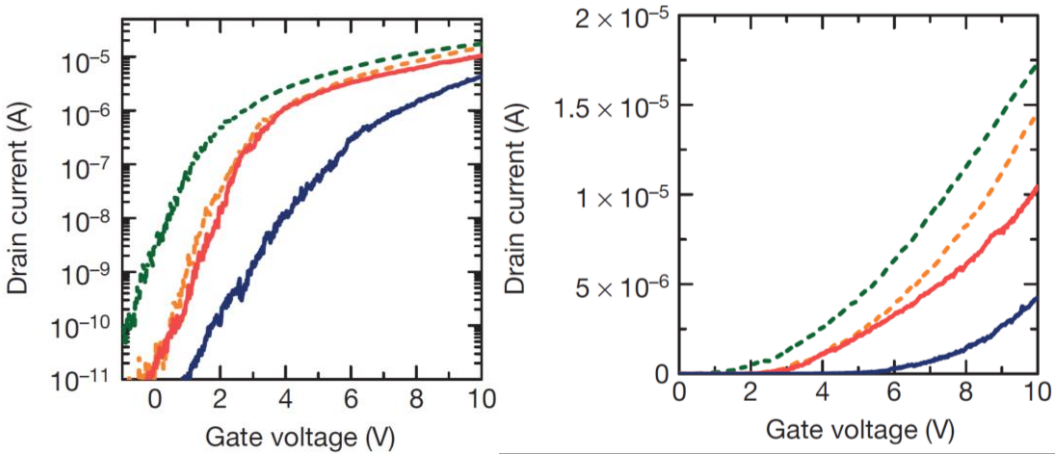

Figure 15 : Drain current versus gate voltage in a logarithmic (left) and linear (right) scale, for a source-drain voltage of 0.5 V, obtained before POM deposition (green curve), after POM deposition (orange), after a -20 V pulse (blue) and a +20 V pulse (red).[63]

Das and coll. have recently reported the fabrication of a POM-based resistive random-access memory (RRAM) device.[64] A RRAM device,[65] which is considered as a promising memory technology, is a two-terminal device constituted with a metal-insulator-metal structure. The RRAM operation is based on a resistance change in the insulator by applying an electric field between the two electrodes. The resistance can be alternatively switched between two states: the high-resistance state (HRS), corresponding to the OFF state, and the low-resistance state (LRS), corresponding to the ON state. The resistive switching from high to low constitutes the SET process (that can be viewed as a writing operation or as the storage of logical “1”), while the resistive switching from low to high corresponds to the RESET operation (erasing operation or storage of a logical “0”). The growth of conductive filaments (CFs) inside the insulator is responsible for the device switching from OFF to ON, and can be triggered by the displacement of metal ions or oxygen vacancies.

The authors have immobilized $[V_{10}O_{28}]^{6-}$ polyoxovanadate on top of an indium-tin-oxide (ITO)-coated glass substrate via spincoating, leading to a POM multilayer thickness of approximately 90 nm. After an annealing step at 70°C, they subsequently fabricated the Cr(10nm)/Au(80nm) contact pads via sputtering. For the measurements, the gold electrode act as the top contact while the ITO is the bottom electrode, as depicted in Figure 16. A first I-V curve was recorded by sweeping the bias from 0 to 3.0 V (black I-V curve in Figure 16). A sudden increase in current is spotted at 3.0 V and is attributed to the device switching to the LRS or the ON state (forming process). The latter remains even when the bias was swept back to zero. To switch the device back to the HRS, the bias was slowly swept again from 0 to 1.0 V (blue I-V curve in Figure 16), and a sudden decrease in current (thus higher resistance) is detected at 0.8 V (reset voltage). This corresponds to the LRS → HRS process (or RESET operation). A further applied bias of 1.2 V (set voltage) switched the device back to the LRS (red I-V curve in Figure 16) and is referred as the SET operation. During this measurement, the forming process allows the device to enter a resistive switching regime in which the resistance state can alternate from high to low.

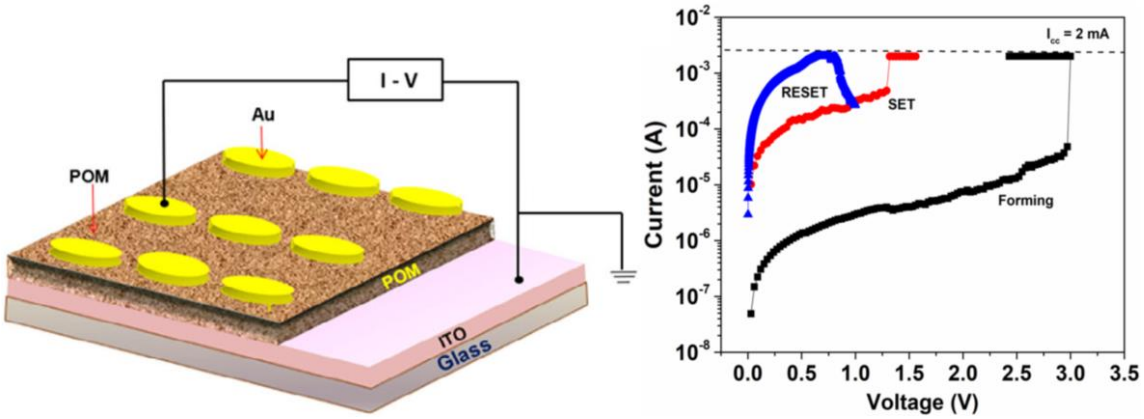

Figure 16: Structure of the RRAM device (left) and semi-log plot of I-V curve characteristics (right). The compliance current I_{cc} was set (at 2mA) to protect the device from high current when the device enters the ON state.[64]

A nonvolative memory device is obtained as the LRS and HRS remain when the applied voltage turned off. The LRS-HRS switching process could be repeated for more than 210 cycles with no degradation for the first ~35 minutes.

Authors have described the resistive switching process taking place in the device obtained (Scheme 2) and attributed the growth of conductive filaments to the presence of the POM that generates oxygen vacancies when reduced. The oxygen vacancies can indeed accumulate and migrate towards the top electrode as the external bias is increased (Scheme 2b-d). As they act as electron traps, the trapping nature of the oxygen vacancies is responsible for the switching

from HRS to LRS. The high current thus generated can lead to a Joule heating which can successively break the CF and drive the device back to the HRS (Scheme 2e-g). The POM-based RRAM device built thus takes advantage from the multiple redox states of the POM.

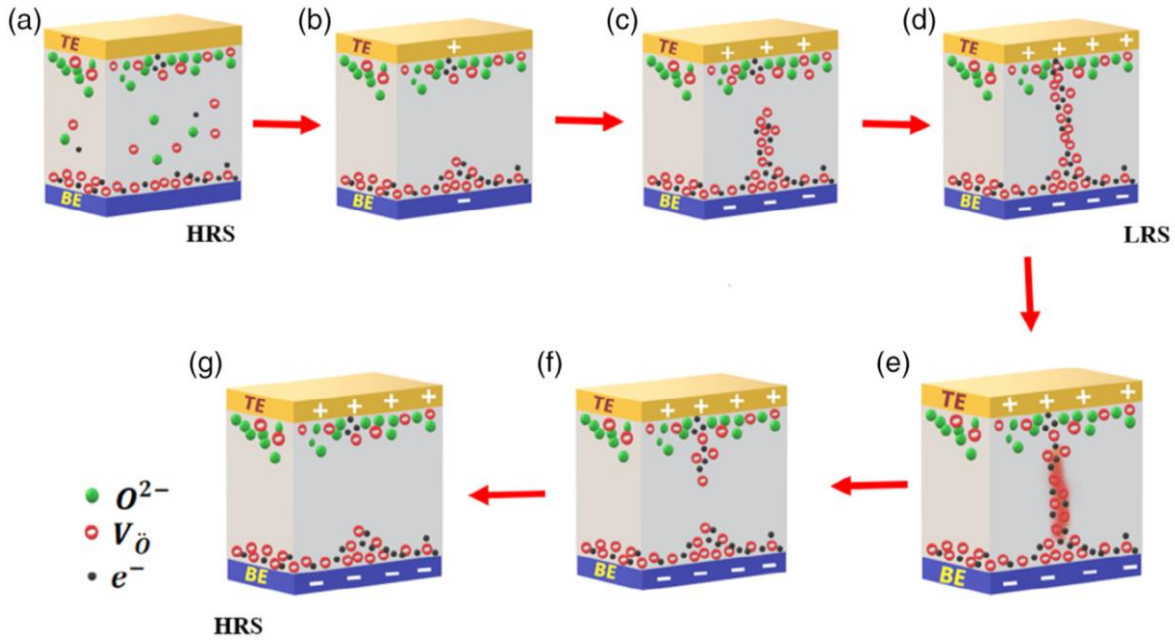

Scheme 2 : Illustrative diagrams showing the formation and rupture of CFs due to oxygen vacancies (red dots) migration between the bottom electrode (BE) and the top electrode (TE). a) The initial HRS when no bias is applied, and b,c) show gradual formation of CFs as the oxygen vacancies move towards the TE and accumulate with increase in bias. d) A full-grown CF between the TE and the BE, when the bias reaches the SET voltage. Device is in LRS (SET process). e-g) Rupture of the CF due to joule heating, driving the device back to HRS (RESET process).[64]

Finally, Chen and coll. have more recently reported the fabrication of a resistive switching device containing a polyoxometalate-based metal-organic framework (POMOF) made of $[\alpha\text{-}GeW_{12}O_{40}]^{4-}$ POMs in the metalloviologen cationic $[Co_2(bpdo)_4(H_2O)_6]_n^{4n+}$ cavities.[66] The POMs are anchored onto the cavities via C-H…O_{POM} hydrogen bonds (see Figure 17). The system has the advantage to resist against high temperature: a heating at 150°C subsequently leads to the removal of three water molecules while at the same time strengthening the H-bonds and providing a more condensed structure.

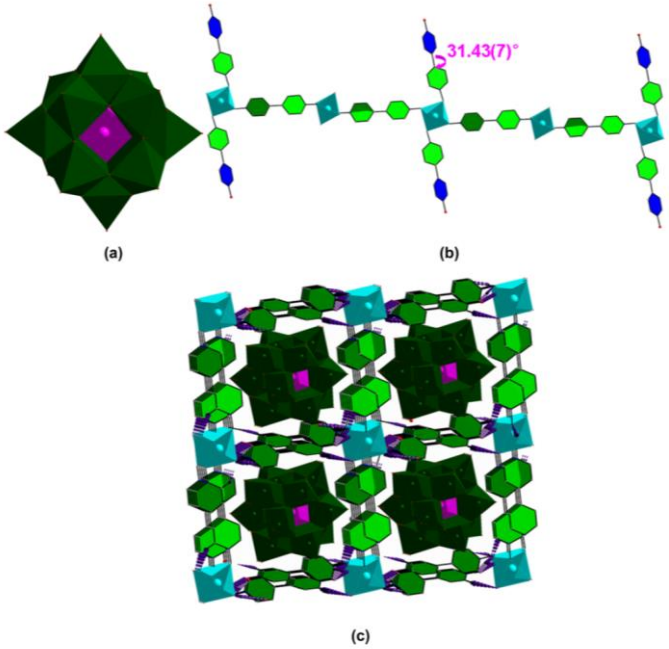

Figure 17 : a) Saturated $(\alpha\text{-}GeW_{12}O_{40})^{4-}$ POM anion; b) 1D $[Co_2(bpdo)_4(H_2O)_6]_n^{4n+}$ cationic chain; c) diagram of POM@MOF with hydrogen atoms without involving H-bonds being omitted for clarity.[66]

The POM deposition was, as for the previous study, carried out by a spincoating of POMOF dispersion in DMF onto ITO surface. The obtained substrate was subjected to an annealing step and electrical measurements were carried out on the ITO/POMOF/Ag configuration, with the ITO as the bottom electrode (see Figure 18, left). A typical current-voltage (I-V) curve obtained is shown in Figure 18 (right), where the bias was forward swept from -4 V to 4 V and reversed from 4 V to -4 V. The device enters the LRS when the voltage reached 1.4 V (SET voltage) as an abrupt current increase is detected. The current stays in the LRS when the bias is reversed back, until -3.6 V is reached: at this RESET voltage, the current suddenly drops and the device is in the HRS.

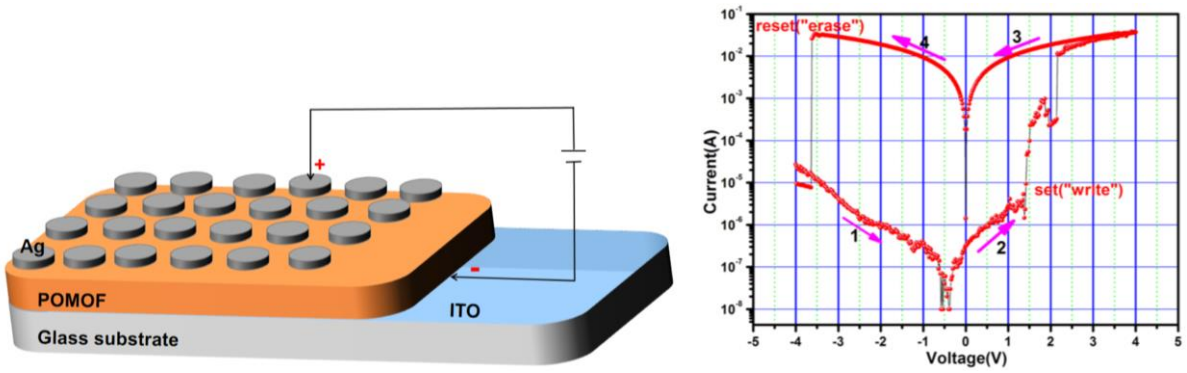

Figure 18 : Structure of the ITO/POMOF/Ag memory device (left) and I-V curve of the device with one cycle (right).[66]

The same measurements were carried out at 150°C. The cycle endurance of the system at room temperature and at 150°C is compared in Figure 19. The current measured when the device is in LRS (ON current) is nearly the same independently of the temperature over the cycles (black dots in Figure 19). The OFF current is also found to remain the same at room temperature and at 150°C (red dots in Figure 19). This suggests that the memory device can work at high temperature which is an important parameter sought for example for the integration of POM-based materials into electronic devices.

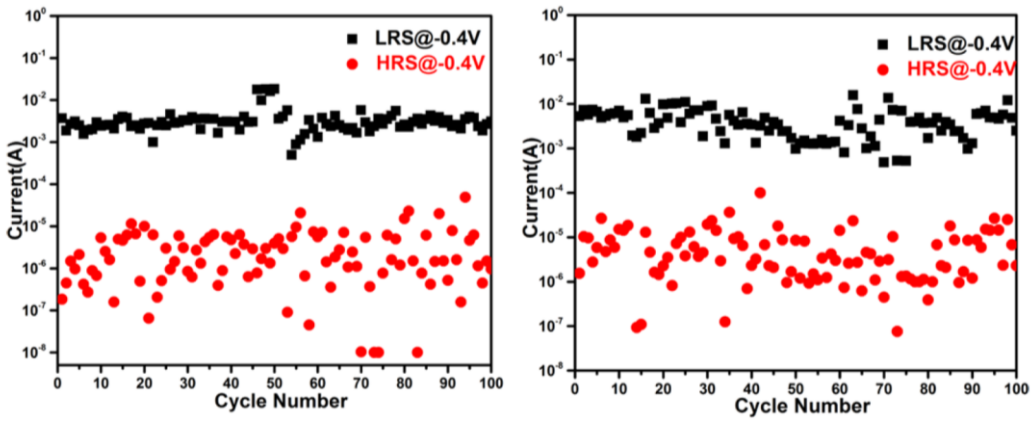

Figure 19 : Cycle endurance of the ITO/POMOF/Ag device at room temperature (left) and at 150°C (right), where the ON current is in black and the OFF current is in red.[66]

The resistive switching mechanism was explained by carrying out DFT calculations. The LUMO and HOMO of the POMOF were compared before and after the injection of two electrons. The HOMO is initially constituted with π orbitals from bpdo and only small contributions from the 2p orbitals of the POM Oc atoms. However, when the two electrons are added, the HOMO is mainly constituted with the 2p orbitals of the POM Ob and Oc atoms. It was thus found that the electrons were accepted by the POM with the help of metalloviologen, in agreement with the electron reservoir property of the POM.

Those examples demonstrate the benefits of POMs as building blocks for molecular memories applications such as flash-memory or RRAM devices. Our group has also been studying the immobilization of POMs (functionalized and non-functionalized) onto surfaces since several years. A particular attention has been given to the preparation of POM monolayer, unlike the aforementioned studies, which allows a better control on the POM/surface interaction, as will be described in Chapter III. The preparation of such monolayer constitutes a more accessible and easier step before considering the case of charge storage within a single

POM immobilized onto the surface. However, the electrical properties of the final POM monolayer-based material depend highly on the quality of the POM organization onto the surface, its stability and reproducibility. Previous results obtained in our group have encouraged us to tackle more complex studies on immobilized POMs. Indeed, $[PMo_{12}O_{40}]^{3-}$ has in solution the ability to be reduced in the presence of a reducing agent but also under UV irradiation, as will be detailed in Chapter III and Chapter IV. Being able to study and to probe this photoreduction process once the POM is immobilized onto the surface thus constitutes a new challenge and a step forward towards photoswitchable memory devices.

Our strategy was thus i) to prepare a well-organized, homogeneous and compact grafted organic monolayer (GOM) of alkyl chains on Si surface, bearing reactive functions ($\mathscr{F}$ = COOH, NH_3^+) as terminal groups, prior to ii) POM deposition either via electrostatic ($\mathscr{F}$ = NH_3^+) or covalent ($\mathscr{F}$ = COOH) interactions and finally iii) to investigate the POM redox state after UV irradiation by electrical measurements.

POMs can be immobilized onto a positively charged surface by electrostatic interactions, as will be discussed in Chapter III. Our group has for example reported the electrostatic deposition of $[H_7P_8W_{48}O_{184}]^{33-}$ onto 8-amino-1-octanethiol SAMs on gold surfaces,[67] while Wang *et al*. reported the immobilization of $[PMo_{12}O_{40}]^{3-}$ onto L-cysteine SAMs on gold surfaces.[68] Our strategy was first to prepare a GOM bearing terminal active functions onto hydrogenated-Si surface. Hydrogen-terminated silicon surface functionalization was extensively studied by the group of Chabal and seems to be a good ally for our project as the resulting GOMs were found to be stable, reproducible and efficient against surface oxidation.[69–71] Such a GOM was for example used by Seitz *et al*. in order to build a field-effect transistor (FET) biosensor.[72] As depicted in Scheme 3, SOI substrates are prepared in a way that only Si channels are functionalized with ester-terminated GOM while the other parts are functionalized with “inactive” methyl-terminated GOM. The ester functions are hydrolyzed before reaction with the ethylenediamine via a peptide coupling, leaving the surface locally NH_2/NH_3^+-terminated. This FET was used to selectively immobilize citrate-stabilized gold nanoparticles via electrostatic interactions, similarly as a biosensor that would selectively detects the desired analytes reacting on the active parts of the surface. This type of GOM was thus efficiently integrated within a device.

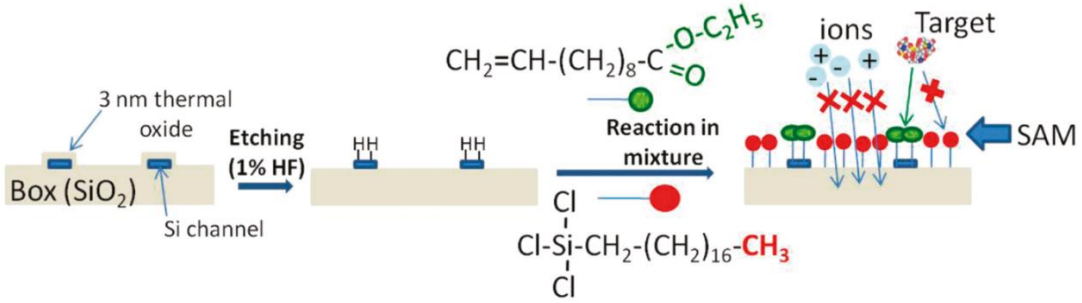

Scheme 3 : One-step selective functionalization of SOI surface with a mixture of ethyl 10-undecenoate containing 1% octadecyltrichlorosilane.[72]

To go further in the study of immobilized POM, we chose to focus on photoreducible POM. However, to the best of our knowledge, only a few reports of immobilized photoreducible POM can be found in the literature. Bubeck and coll.[73] have for example immobilized multilayers of polyoxotungstate $H_3PW_{12}O_{40}$ (PW) and graphene oxide (GO) on different kind of substrates (quartz, flexible PET, and silicon) into which layers of cationic polymers, poly(ethyleneimine) (PEI) and poly(allylamine hydrochloride) (PAH), were inserted to ensure electrostatic interactions between the POM and the graphene oxide as depicted in Scheme 4.

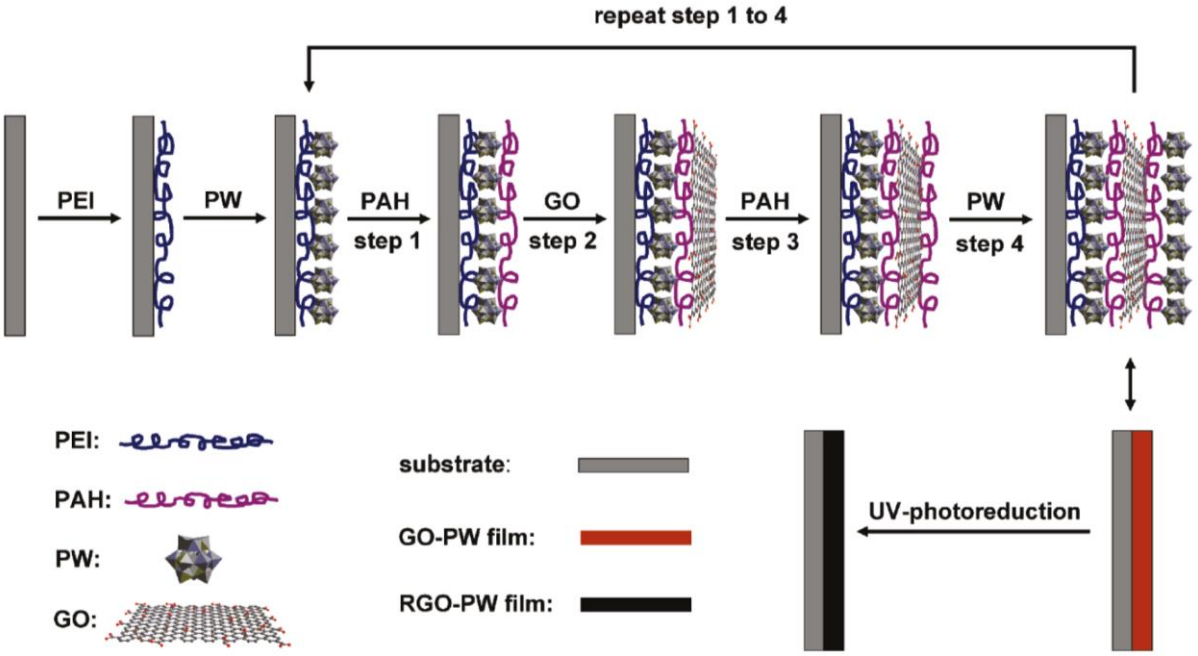

Scheme 4 : Functionalization procedure of rGO-PW multilayers films via layer-by-layer assembly followed by photoreduction of the GO to rGO.[73]

The idea was to photoreduce graphene oxide thanks to the presence of the POM, such that reduced graphene oxide becomes conducting. Indeed, when the POM is irradiated under UV irradiation, electron-hole pair is created due to the excitation of the charge transfer band from

the oxygen to the metal. Cationic polymer PAH gets oxidized by the holes generated under UV irradiation, while the remaining electrons are transferred to the GO sheets, resulting in reduced graphene oxide (rGO). During the photoreduction process, POM thus acts as photocatalyst and electron relay from the POM to the GO.

Thanks to the ability of graphene oxide to get reduced under UV irradiation with the presence of the POM, the authors used a photomask to locally reduce the graphene oxide nanosheets on Si surface, leading to rectangular (Figure 20A) and squared (Figure 20B) patterns of rGO. They spin-coated the resulting surface with a polymer blend of poly(3-hexylthiophene) (P3HT) and 1-(3-methoxycarbonyl)propyl-1-phenyl[6,6]C61 (PCBM) that improve the charge separation when employed in solar cells. Here, the polymer blend serves as photoswitching material while the rGO areas serve as microelectrodes for the photodetector. By periodically irradiating the resulting surface, a repeatable photocurrent response was obtained which is encouraging for exploiting more strenuously the POM photoreduction property.

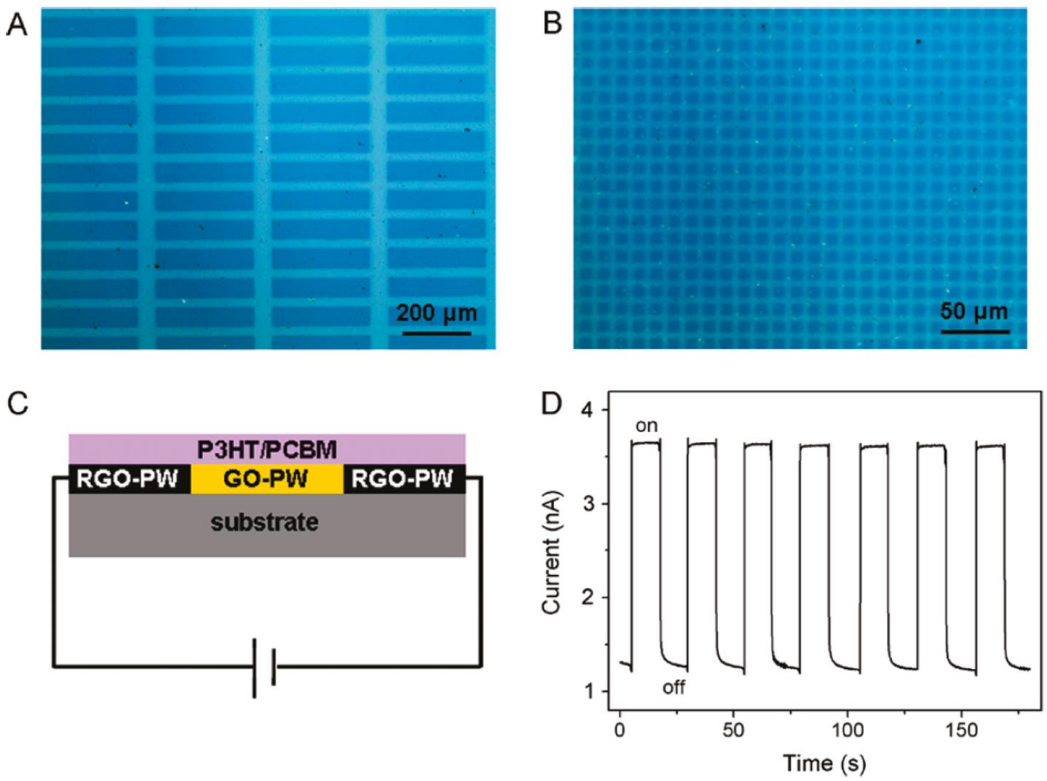

Figure 20 : A, B) Optical microscope images of oxidized Si surface functionalized with PEI/PW precursor film and $(PAH/GO/PAH/PW)_6$ multilayers obtained after 6 hours UV irradiation through a photomask. rGO is seen in dark blue color on the images; C) Structure of the photodetector device after spin-coating of P3HT/PCBM; D) Photocurrent response of the photodetector involving patterns in image A versus time at a bias voltage of 10 V and successive ON/OFF UV irradiation.[73]

V. Goal of the project

We have thus demonstrated that POMs, especially type I POMs, are promising redox-active molecules to be integrated into molecular electronics thanks to their redox properties. Accordingly, several examples have arisen from the literature during the last two decades, involving covalent/electrostatic immobilization of POM monolayers and POM multilayers onto various substrates, including silicon.

Research on immobilized POMs onto surface has been driven by the redox properties of POM witnessed in solution but also by the opportunity to possibly extend Moore's Law with molecular electronics and its bottom-up approach. Accordingly, Si substrate is the best one for direct integration of POMs into MOS technology, due to its massive use in micro/nanoelectronics and as Si technology has been widely studied. Previous work in the laboratory were promising for investigating POM monolayers onto Si surfaces and more complex photoactive POMs.

Thus, the first and main objective of the project will be to study the $[PMo_{12}O_{40}]^{3-}$ redox state once immobilized as monolayers onto functionalized Si surface. Being able to probe and understand the photoreduction process of immobilized POMs constitutes a step forward towards POM-based material for molecular electronics and will offer more prospects for their use in photoactive devices. As the organization of POMs onto surface was found to be crucial for the resulting electrical properties, emphasis will be given to the quality of the POM monolayer. The second objective is thus to master the POM immobilization onto surface and to have a better control and understanding on the POM/surface interaction.

The manuscript is divided into 3 successive chapters, constituting 3 prerequisite steps towards electrical solid state characterization of the POM monolayer in a transistor configuration, as depicted by Figure 21.

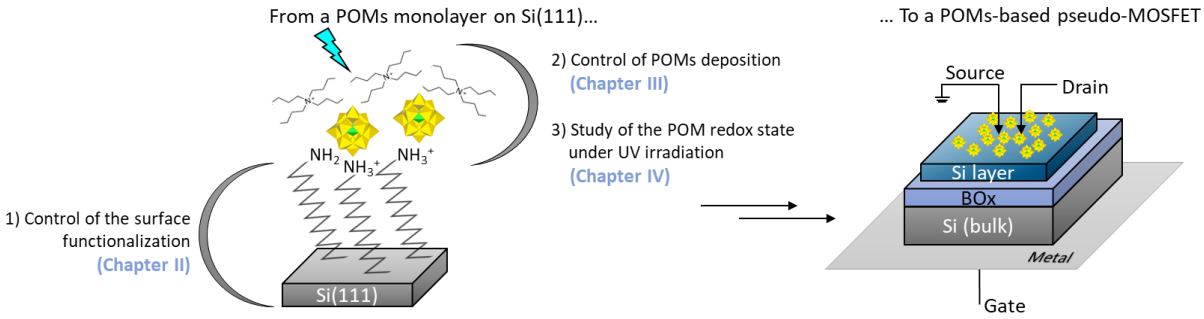

Figure 21 : Steps towards a POM-based transistor.

Chapter II will be dedicated to the functionalization of oxide-free hydrogenated-silicon surface with alkyl GOMs. The GOM will bear an active terminal group, firstly an ester function that will be subjected to further modifications. Finally, an NH_2/NH_3^+-terminated GOM will be obtained. The functionalization procedure will be presented on Si(111) and Si(100) surfaces, with highlights on the surface characterization techniques to achieve the best functionalization.

Chapter III will be dedicated to the $[PMo_{12}O_{40}]^{3-}$ POM deposition onto the functionalized Si surfaces prepared in Chapter II. The synthesis procedure of this POM and its corresponding reduced species will be described. During the course of the project, covalent grafting of POM hybrids have also been explored by taking advantage of the functionalized Si surface developed in Chapter II. Details on the tests and strategies using several POM hybrids will be given.

Chapter IV will finally be dedicated to the study of the photoreduction phenomenon of POM immobilized onto surfaces. To do so, $(TBA)_3[PMo_{12}O_{40}]$ and its reduced species will first be characterized as powders before moving to immobilized POM multilayers and monolayers characterization by means of ellipsometry, X-ray photoelectron spectroscopy (XPS) and UV-Visible-Near Infrared (UV-Vis-NIR) spectroscopy and Kelvin Probe Force Microscopy (KPFM). Finally, preliminary electrical measurements results on the POM-based transistor using SOI substrates and a probe station will be discussed. Insights on the photoreduction phenomenon will be provided as well.

VI. References

(1) Pope, M. T.; Müller, A. Polyoxometalate Chemistry: An Old Field with New Dimensions in Several Disciplines. *Angewandte Chemie International Edition in English* **1991**, *30* (1), 34–48.

(2) *Polyoxometalate Molecular Science*; Borrás-Almenar, J. J., Coronado, E., Müller, A., Pope, M., Eds.; Springer Netherlands: Dordrecht, 2003.

(3) Gouzerh, P.; Che, M. De Scheele et Berzelius à Müller : Les Polyoxométallates (POMs) Revisités et Le Chaînon Manquant Entre Les Approches « bottom up » et « top down » - L'Actualité Chimique. *L'Actualité Chimique* **2006**, *298*, 9–22.

(4) Gouzerh, P.; Proust, A. Main-Group Element, Organic, and Organometallic Derivatives of Polyoxometalates. *Chem. Rev.* **1998**, *98* (1), 77–112.

(5) Herrmann, S.; Ritchie, C.; Streb, C. Polyoxometalate – Conductive Polymer Composites for Energy Conversion, Energy Storage and Nanostructured Sensors. *Dalton Transactions* **2015**, *44* (16), 7092–7104.

(6) Song, Y.-F.; Tsunashima, R. Recent Advances on Polyoxometalate-Based Molecular and Composite Materials. *Chem. Soc. Rev.* **2012**, *41* (22), 7384–7402.

(7) Izzet, G.; Volatron, F.; Proust, A. Tailor–Made Covalent Organic-Inorganic Polyoxometalate Hybrids: Versatile Platforms for the Elaboration of Functional Molecular Architectures. *Chem. Rec.* **2017**, *17* (2), 250–266.

(8) Long, D.-L.; Cronin, L. Towards Polyoxometalate-Integrated Nanosystems. *Chem. Eur. J.* **2006**, *12* (14), 3698–3706.

(9) Coronado, E.; Gómez-García, C. J. Polyoxometalate-Based Molecular Materials. *Chem. Rev.* **1998**, *98* (1), 273–296.

(10) Cherevan, A. S.; Nandan, S. P.; Roger, I.; Liu, R.; Streb, C.; Eder, D. Polyoxometalates on Functional Substrates: Concepts, Synergies, and Future Perspectives. *Adv. Sci.* **2020**, *7* (8), 1903511.

(11) Sartzi, H.; Miras, H. N.; Vilà-Nadal, L.; Long, D.; Cronin, L. Trapping the δ Isomer of the Polyoxometalate-Based Keggin Cluster with a Tripodal Ligand. *Angew. Chem. Int. Ed.* **2015**, *54* (51), 15488–15492.

(12) Kazansky, L. P.; McGarvey, B. R. NMR and EPR Spectroscopies and Electron Density Distribution in Polyoxoanions. *Coordination Chemistry Reviews* **1999**, *188* (1), 157–210.

(13) Wasylenko, D. J.; Palmer, R. D.; Berlinguette, C. P. Homogeneous Water Oxidation Catalysts Containing a Single Metal Site. *Chem. Commun.* **2013**, *49* (3), 218–227.

(14) Betley, T. A.; Wu, Q.; Van Voorhis, T.; Nocera, D. G. Electronic Design Criteria for O−O Bond Formation via Metal−Oxo Complexes. *Inorg. Chem.* **2008**, *47* (6), 1849–1861.

(15) Launay, J. P. Réduction de l'ion métatungstate: stades élevés de réduction de $H_2W_{12}O_{40}^{6-}$, dérivés de l'ion $HW_{12}O_{40}^{7-}$ et discussion générale. *J. inorg. nucl. Chem.*, **1976**, *38* (4), 807–816.

(16) Poblet, J. M.; López, X.; Bo, C. Ab Initio and DFT Modelling of Complex Materials: Towards the Understanding of Electronic and Magnetic Properties of Polyoxometalates. *Chem. Soc. Rev.* **2003**, *32* (5), 297–308.

(17) Maestre, J. M.; Lopez, X.; Bo, C.; Poblet, J.-M.; Casañ-Pastor, N. Electronic and Magnetic Properties of α-Keggin Anions: A DFT Study of $[XM_{12}O_{40}]^{n-}$, (M = W, Mo; X=Al^{III}, Si^{IV}, P^{V}, Fe^{III}, Co^{II}, Co^{III}) and $[SiM_{11}VO_{40}]^{m-}$ (M = Mo and W). *Journal of the American Chemical Society* **2001**, *123* (16), 3749–3758.

(18) Pope, M. T.; Kortz, U. PolyoxometalatesUpdate Based on the Original Article by Michael T. Pope, *Encyclopedia of Inorganic Chemistry* © 2005, John Wiley & Sons, Ltd. In

Encyclopedia of Inorganic and Bioinorganic Chemistry; Scott, R. A., Ed.; John Wiley & Sons, Ltd: Chichester, UK, 2012.
(19) Sadakane, M.; Steckhan, E. Electrochemical Properties of Polyoxometalates as Electrocatalysts. *Chem. Rev.* **1998**, *98* (1), 219–238.
(20) King, R. B. Chemical Applications of Topology and Group Theory. 25. Electron Delocalization in Early-Transition-Metal Heteropoly- and Isopolyoxometalates. *Inorganic Chemistry* **1991**, *30* (23), 4437–4440.
(21) Sanchez, C.; Livage, J.; Launay, J. P.; Fournier, M.; Jeannin, Y. Electron Delocalization in Mixed-Valence Molybdenum Polyanions. *J. Am. Chem. Soc.* **1982**, *104* (11), 3194–3202.
(22) Himeno, S.; Takamoto, M. Difference in Voltammetric Properties between the Keggin-Type $[XW_{12}O_{40}]^{n-}$ and $[XMo_{12}O_{40}]^{n-}$ Complexes. *Journal of Electroanalytical Chemistry* **2002**, *528* (1–2), 170–174.
(23) Himeno, S.; Takamoto, M.; Santo, R.; Ichimura, A. Redox Properties and Basicity of Keggin-Type Polyoxometalate Complexes. *BCSJ* **2005**, *78* (1), 95–100.
(24) Maeda, K.; Himeno, S.; Osakai, T.; Saito, A.; Hori, T. A Voltammetric Study of Keggin-Type Heteropolymolybdate Anions. *Journal of Electroanalytical Chemistry* **1994**, *364* (1), 149–154.
(25) Wang, H.; Hamanaka, S.; Nishimoto, Y.; Irle, S.; Yokoyama, T.; Yoshikawa, H.; Awaga, K. In Operando X-Ray Absorption Fine Structure Studies of Polyoxometalate Molecular Cluster Batteries: Polyoxometalates as Electron Sponges. *J. Am. Chem. Soc.* **2012**, *134* (10), 4918–4924.
(26) Artero, V.; Proust, A. Reduction of the Phosphododecamolybdate Ion by Phosphonium Ylides and Phosphanes. *European Journal of Inorganic Chemistry* **2000**, No. 11, 2393–2400.
(27) Razavi, B. *Fundamentals of Microelectronics*, Preview ed.; John Wiley: Hoboken, N.J, 2006.
(28) Guarnieri, M. The Age of Vacuum Tubes: Early Devices and the Rise of Radio Communications [Historical]. *EEE Ind. Electron. Mag.* **2012**, *6* (1), 41–43.
(29) Han, J.-W.; Sub Oh, J.; Meyyappan, M. Vacuum Nanoelectronics: Back to the Future?—Gate Insulated Nanoscale Vacuum Channel Transistor. *Appl. Phys. Lett.* **2012**, *100* (21), 213505.
(30) Bardeen, J.; Brattain, W. H. The Transistor, A Semi-Conductor Triode. *Phys. Rev.* **1948**, *74* (2), 230–231.
(31) Shockley, W. The Path to the Conception of the Junction Transistor. *IEEE Trans. Electron Devices* **1976**, 23 (7), 597–620
(32) Sze, S. M.; Ng, K. K. *Physics of Semiconductor Devices*, 3. ed.; Wiley-Interscience: Hoboken, NJ, 2007.
(33) Hoddeson, L. The Discovery of the Point-Contact Transistor. *Historical Studies in the Physical Sciences* **1981**, *12* (1), 41–76.
(34) Shockley, W.; Sparks, M.; Teal, G. K. *p-n* Junction Transistors. *Phys. Rev.* **1951**, *83* (1), 151–162.
(35) Mack, C. The Multiple Lives of Moore's Law. *IEEE Spectr.* **2015**, *52* (4), 31–31.
(36) Sah, H.-T. Evolution of the MOS Transistor-From Conception to VLSI. *Proceedings of the IEEE* **1988**, 76 (10), 1280-1326
(37) Schaller, R. R. Moore's Law: Past, Present and Future. *IEEE Spectr.* **1997**, *34* (6), 52–59.
(38) Kahng, D. A Historical Perspective on the Development of MOS Transistors and Related Devices. *IEEE Trans. Electron Devices* **1976**, *23* (7), 655–657.

(39) *Nano- and Microtechnology from A-Z: From Nanosystems to Colloids and Interfaces*; Schramm, L. L., Ed.; Wiley-VCH Verlag GmbH & Co. KGaA: Weinheim, Germany, 2014.
(40) Ramsden, J. *Applied Nanotechnology: The Conversion of Research Results to Products*, 2. ed.; Micro & nano technologies series; Elsevier, William Andrew: Waltham, Mass., 2014.
(41) Moore, G. E. Cramming More Components Onto Integrated Circuits. *Proceedings of the IEEE* **1998**, *86* (1), 82–85.
(42) Moore, G. E. Progress in Digital Integrated Electronics. *International Electron Devices Meeting, IEEE* **1975**, 11–13
(43) Thompson, S. E.; Parthasarathy, S. Moore's Law: The Future of Si Microelectronics. *Materials Today* **2006**, *9* (6), 20–25.
(44) Wang, P.; Hu, M.; Wang, H.; Chen, Z.; Feng, Y.; Wang, J.; Ling, W.; Huang, Y. The Evolution of Flexible Electronics: From Nature, Beyond Nature, and To Nature. *Adv. Sci.* **2020**, *7* (20), 2001116.
(45) Geer, D. Chip Makers Turn to Multicore Processors. *Computer* **2005**, *38* (5), 11–13.
(46) Waldrop, M. M. The Chips Are down for Moore's Law. *Nature* **2016**, *530* (7589), 144–147.
(47) Innovation - Soitec https://www.soitec.com/en/company/innovation?__geom=%E2%9C%AA (accessed 2021 -11 -17).
(48) Learn More About FD-SOI - STMicroelectronics https://www.st.com/content/st_com/en/about/innovation---technology/FD-SOI/learn-more-about-fd-soi.html (accessed 2021 -11 -15).
(49) Big Win for FD-SOI: Sony GPS in Huami/Xiaomi Smartwatch (EETimes) https://soiconsortium.org/2016/10/26/big-win-for-fd-soi-sony-gps-in-huamixiaomi-smartwatch-eetimes/ (accessed 2021 -11 -17).
(50) EETimes - Sony-Inside Huami Watch: Is It Time for FD-SOI? *EETimes*, 2016.
(51) Teo, B. K.; Sun, X. H. From Top-Down to Bottom-Up to Hybrid Nanotechnologies: Road to Nanodevices. *J Clust Sci* **2006**, *17* (4), 529–540.
(52) Wielopolski, M. Introduction to Molecular Electronics. In *Testing Molecular Wires*; Springer: Berlin, Heidelberg, 2010; pp 3–8.
(53) Xiang, D.; Wang, X.; Jia, C.; Lee, T.; Guo, X. Molecular-Scale Electronics: From Concept to Function. *Chem. Rev.* **2016**, *116* (7), 4318–4440.
(54) Tour, J. M. Molecular Electronics. Synthesis and Testing of Components. *Acc. Chem. Res.* **2000**, *33* (11), 791–804.
(55) Cuevas, J. C.; Scheer, E. The birth of molecular electronics. In *Molecular Electronics: An Introduction to Theory and Experiment*, 2nd ed.; Reed, M., Ed.; World Scientific Series in Nanoscience and Nanotechnology; World Scientific, 2017; Vol. 1, pp 3–18.
(56) Mathew, P. T.; Fang, F. Advances in Molecular Electronics: A Brief Review. *Engineering* **2018**, *4* (6), 760–771.
(57) Choi, H.; Mody, C. C. M. The Long History of Molecular Electronics: Microelectronics Origins of Nanotechnology. *Soc Stud Sci* **2009**, *39* (1), 11–50.
(58) Aviram, A.; Ratner, M. A. Molecular Rectifiers. *Chemical Physics Letters* **1974**, *29* (2), 277–283.
(59) Ratner, M. A Brief History of Molecular Electronics. *Nature Nanotech* **2013**, *8* (6), 378–381.
(60) Reed, M. A.; Zhou, C.; Muller, C. J.; Burgin, T. P.; Tour, J. M. Conductance of a Molecular Junction. *Science* **1997**, *278* (5336), 252–254.

(61) Zhu, H.; Li, Q. Redox-Active Molecules for Novel Nonvolatile Memory Applications. In *Redox - Principles and Advanced Applications*; Khalid, M. A. A., Ed.; InTech, 2017.
(62) Fabre, B. Functionalization of Oxide-Free Silicon Surfaces with Redox-Active Assemblies. *Chem. Rev.* **2016**, *116* (8), 4808–4849.
(63) Busche, C.; Vilà-Nadal, L.; Yan, J.; Miras, H. N.; Long, D.-L.; Georgiev, V. P.; Asenov, A.; Pedersen, R. H.; Gadegaard, N.; Mirza, M. M.; Paul, D. J.; Poblet, J. M.; Cronin, L. Design and Fabrication of Memory Devices Based on Nanoscale Polyoxometalate Clusters. *Nature* **2014**, *515* (7528), 545–549.
(64) N. S., S.; Basu, N.; Cahay, M.; M. N., S.; Mal, S. S.; Das, P. P. Redox-Active Vanadium-Based Polyoxometalate as an Active Element in Resistive Switching Based Nonvolatile Molecular Memory. *Phys. Status Solidi A* **2020**, *217* (18), 2000306.
(65) Zahoor, F.; Azni Zulkifli, T. Z.; Khanday, F. A. Resistive Random Access Memory (RRAM): An Overview of Materials, Switching Mechanism, Performance, Multilevel Cell (mlc) Storage, Modeling, and Applications. *Nanoscale Res Lett* **2020**, *15* (1), 90.
(66) Chen, B.; Huang, Y.-R.; Song, K.-Y.; Lin, X.-L.; Li, H.-H.; Chen, Z.-R. Molecular Nonvolatile Memory Based on $[\alpha\text{-}GeW_{12}O_{40}]^{4-}$ /Metalloviologen Hybrids Can Work at High Temperature Monitored by Chromism. *Chem. Mater.* **2021**, *33* (6), 2178–2186.
(67) Dalla Francesca, K.; Lenfant, S.; Laurans, M.; Volatron, F.; Izzet, G.; Humblot, V.; Methivier, C.; Guerin, D.; Proust, A.; Vuillaume, D. Charge Transport through Redox Active $[H_7P_8W_{48}O_{184}]^{33-}$ Polyoxometalates Self-Assembled onto Gold Surfaces and Gold Nanodots. *Nanoscale* **2019**, *11* (4), 1863–1878.
(68) Wang, S.; Du, D. Preparation and Electrochemical Properties of Keggin-Type Phosphomolybdic Anions in Electrostaticly Linked l-Cysteine Self-Assembled Monolayers. *Sensors and Actuators B: Chemical* **2003**, *94* (3), 282–289.
(69) Seitz, O.; Dai, M.; Aguirre-Tostado, F. S.; Wallace, R. M.; Chabal, Y. J. Copper−Metal Deposition on Self Assembled Monolayer for Making Top Contacts in Molecular Electronic Devices. *Journal of the American Chemical Society* **2009**, *131* (50), 18159–18167.
(70) Aureau, D.; Varin, Y.; Roodenko, K.; Seitz, O.; Pluchery, O.; Chabal, Y. J. Controlled Deposition of Gold Nanoparticles on Well-Defined Organic Monolayer Grafted on Silicon Surfaces. *The Journal of Physical Chemistry C* **2010**, *114* (33), 14180–14186.
(71) Caillard, L.; Seitz, O.; Campbell, P. M.; Doherty, R. P.; Lamic-Humblot, A.-F.; Lacaze, E.; Chabal, Y. J.; Pluchery, O. Gold Nanoparticles on Oxide-Free Silicon–Molecule Interface for Single Electron Transport. *Langmuir* **2013**, *29* (16), 5066–5073.
(72) Seitz, O.; Fernandes, P. G.; Mahmud, G. A.; Wen, H.-C.; Stiegler, H. J.; Chapman, R. A.; Vogel, E. M.; Chabal, Y. J. One-Step Selective Chemistry for Silicon-on-Insulator Sensor Geometries. *Langmuir* **2011**, *27* (12), 7337–7340.
(73) Li, H.; Pang, S.; Wu, S.; Feng, X.; Müllen, K.; Bubeck, C. Layer-by-Layer Assembly and UV Photoreduction of Graphene–Polyoxometalate Composite Films for Electronics. *Journal of the American Chemical Society* **2011**, *133* (24), 9423–9429.

Chapter II

Organic monolayer formation on Si substrate: an initial platform for later POM deposition

I. Introduction

We have demonstrated in the previous chapter the interest of POM immobilization for molecular electronics applications. Keeping in mind our goal of studying the photoreduction properties of the later immobilized anionic Keggin POM $[PMo_{12}O_{40}]^{3-}$, the first focus of this manuscript will be given to the functionalization of silicon surfaces with positively charged terminal groups.

The choice of the silicon substrate will be first explained as well as the different strategies that can be found in the literature to functionalize silicon surfaces, and more precisely oxide-free silicon surfaces. Second part will highlight the experimental procedures, on Si(111) then on Si(100), constituted in several steps. Results will be presented and emphasize will be given on the strategies we had to develop to minimize the oxide growth during the experimental procedures.

I.1. Choice of silicon substrate

Silicon (Si) is the second most abundant element on Earth, where it is originally found as silicate minerals.[1] Together with its relatively cheap price, the quality of the silicon/silicon dioxide (Si/SiO_2) interface (thermally grown SiO_2 results in a low density of traps) and the easy process to get high purity wafers, Si has been considerably used in the microelectronics industry for more than 60 years.[2–5] The key advance was made back in 1960 when the first Si/SiO_2 MOSFET was reported by A. Kahng and M. M. Atalla.[6] The development of Si-based MOSFET was led by the fact that a stable oxide layer can grow on top of Si, which is not the case for example for other semiconductor material such as Germanium (Ge). Even though Ge provides higher hole and electron mobility than Si, germanium dioxide (GeO_2) is soluble in water and the Ge/GeO_2 interface is rougher than that of Si/SiO_2.[2,5,7–9]

Briefly, Si single-crystal (monocrystalline silicon) growth is mainly performed using either Czochralski (CZ) method or the floating-zone/float-zone (FZ) method.[10] Both processes are summarized in Scheme 1 and the successive steps are similar: polycrystalline silicon (polysilicon) is first melted followed by a seeding step and finally a single crystal Si growing step. In the CZ crystal growth process (Scheme 1b), the seed crystal is dipped in a polysilicon melt in a quartz crucible and gradually pulled off from the melt leading to the single-crystal growth. In the FZ crystal growth process (Scheme 1a), a heating ring creates a molten zone at

the tip of the polysilicon rod which fuses with a seed crystal. The latter is vertically moving down and allows the molten zone to travel along the polysilicon rod. Single-crystal Si ingot is thus obtained in both processes after solidification of the molten zone.

During the CZ growth process, the melt is in contact with a quartz crucible. The crucible surface is slowly dissolved through the reaction $SiO_2 + Si \rightarrow 2\ SiO$. Despite the evaporation of oxygen as SiO, some released oxygen atoms stay in the Si melt, leading to a final oxygen impurity concentration of ~10^{18} atoms/cm^3 in the CZ-Si crystal, approximately two orders of magnitude higher than that of FZ-Si crystals.[10,11] Indeed, external contact with crucible is avoided during the FZ growth process, which leads to a higher purity Si crystal. Note that CZ-Si crystals also contain one order of magnitude more carbon impurity than FZ-Si crystals, due to the starting polysilicon and the growth equipment made of graphite components.

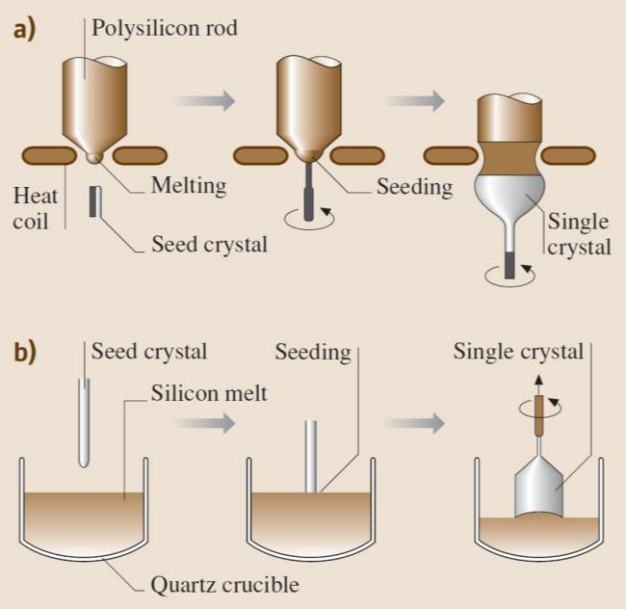

Scheme 1 : Si single-crystal growth process using a) floating-zone (FZ) method and b) Czochralski (CZ) method.[10]

Silicon crystallizes in a diamond structure: a face-centered cubic structure in which four over eight tetrahedral sites are occupied, resulting in one Si atom surrounded by four equidistant Si atoms (see Figure 1). Si wafers with different orientation planes can be purchased, the most common ones being the (100)-oriented silicon (later called **Si(100)**) and the (111)-oriented silicon (later called **Si(111)**) wafers. Surface Si atoms in the (100) plane have two dangling bonds (Figure 1b) while they only have one in the case of the (111) plane (Figure 1d).

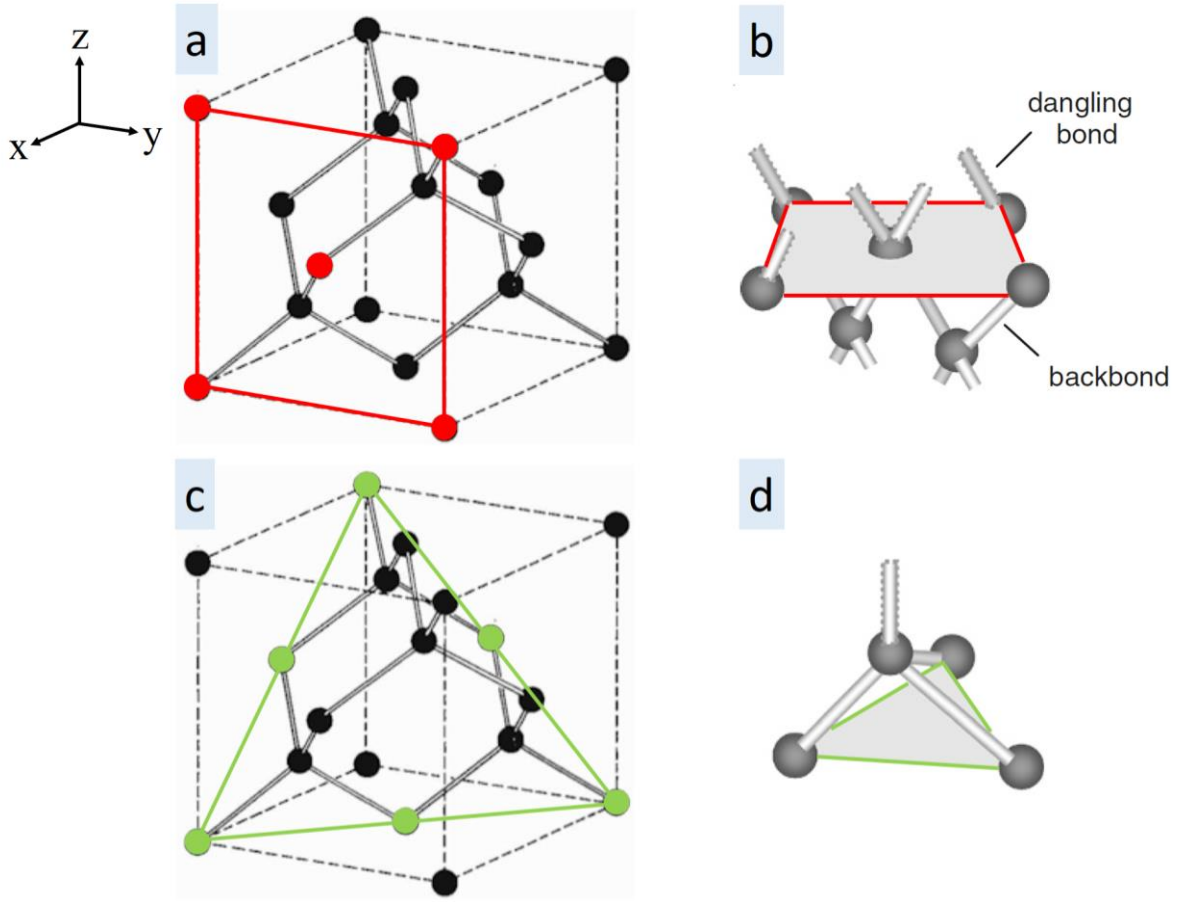

Figure 1 : Silicon crystal diamond structure and highlights on the (100) and (111) planes. (modified from ref. 12 and 13). a) the (100) plane is represented by the red lines and the in-plane Si atoms are colored in red, while c) the (111) plane is represented by the green lines and the in-plane Si atoms are colored in green. The configuration of Si-Si covalent bonds b) on the (100) plane (red) and d) on the (111) plane (green) is also shown.

Among the two Si planes, the (100) plane is more used in microelectronics. The first advantage is a practical one. As seen in Figure 1, the (100) plane is square while the (111) plane is triangular. Si wafer cleavage is easier to perform on Si(100) and more convenient square or rectangular Si dies are obtained.

As said previously, the Si/SiO_2 interface quality is important for MOSFET applications, but the interface is different whether Si(100) or Si(111) substrate is used, as studied by Ohmi *et al.*[14,15] The average $Si(111)/SiO_2$ and $Si(100)/SiO_2$ interface microroughness as a function of the oxide layer thickness was measured using AFM and results are depicted in Figure 2a. $Si(111)/SiO_2$ interface microroughness is higher than that of $Si(100)/SiO_2$ when oxide layer thickness is higher than 10 nm (in the case of field oxide) which gives another advantage to Si(100). When oxide is thinner, the interface microroughness is similar for both wafers. In terms of electrical properties, $Si(100)/SiO_2$ interface is still more reliable than $Si(111)/SiO_2$ with thinner oxide. The threshold voltage V_{Th} of *n*-MOSFET was measured as a function of the number of electrons

injected from the Si substrate into the gate oxide (Figure 2b). The V_{Th} shift is higher when Si(111) is used, which means that more electron traps are generated in the oxide during hot-electron injection than on Si(100). Interface trap density D_{it} at midgap was also measured on an Al/SiO_2/n-Si diode. Despite the same microroughness exhibited by both Si(111)/SiO_2 and Si(100)/SiO_2 interfaces for this study, the D_{it} of Si(100) was lower than that of Si(111), before and after annealing with forming gas (Figure 2c). Thus Si(100) is more appropriate and more reliable for MOSFET devices.

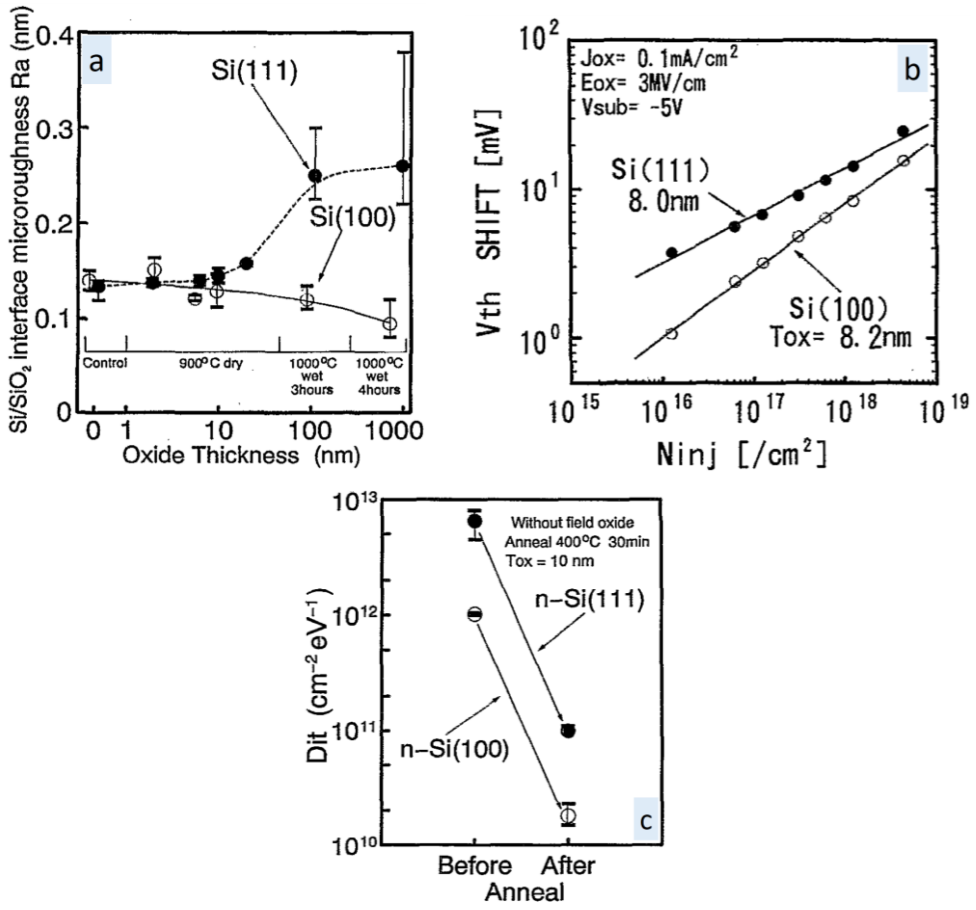

Figure 2 : Si/SiO_2 quality using Si(111) or Si(100) wafers.[14] a) Si(111)/SiO_2 and Si(100)/SiO_2 interface microroughness as a function of oxide thickness (dispersion is shown in vertical lines), b) threshold voltage (V_{th}) shift of *n*-MOSFET as a function of the number of injected electrons (N_{inj}). During hot-electron injection, the current density in the gate oxide J_{ox} was 0.1 mA/cm², the oxide field E_{ox} was 3 MV/cm and the substrate bias V_{sub} was -5 V, c) interface trap density D_{it} at midgap before and after forming gas annealing.

Even though the Si(100) substrate exhibits more advantages for microelectronics, the Si(111) substrate is more advantageous for chemical studies. Indeed, it is easier to obtain a hydrogen-passivated surface (later called "**SiH surface**") on Si(111) than on Si(100) surface and the resulting surface is smoother and more stable than a hydrogen-passivated Si(100) surface, as will be seen later.

I.2. SiO_2 surface versus SiH surface

Silicon has the ability to form a stable silicon oxide layer on top of it, which is not the case for other semiconductor materials. Research has been driven by the electrical quality of the Si/SiO_2 interface, especially for building Si-based electronic devices since the Si/SiO_2 interface contains a low density of interface trapped charges (or surface states),[16] *i.e.* negative or positive charges located at the Si/SiO_2 interface, when the oxide is grown thermally. On the contrary, a high density of surface states leads to the degradation of the MOSFET as charge transfer between the interface and the silicon can take place.[17]

Over the years, $Si\text{-}SiO_2$ based MOSFET was the more used technology where the silicon oxide layer played the role of the gate dielectric, but this technology reached the end. The oxide layer was used to confine the current flow, however with the downsizing of the transistors, the silicon dioxide has become thin enough for electrons to tunnel through the layer leading to current leakage phenomenon that degrades the device performance.[18] As discussed in Chapter I, the emergence of Molecular Electronics in the 1970s was appealing for the fabrication of functional devices at the nanometer level by the bottom-up approach. While Mann and Kuhn[19] performed the first conductivity measurements through cadmium salts of fatty acids monolayer sandwiched between metal electrodes in 1971, the first silicon/silicon dioxide modification was reported in the late 1970s and involved silane molecules. In 1978, Haller reported the grafting of aminopropylsilyl monolayer on SiO_2 surface in gas phase, by refluxing vapors of 3-aminopropyltriethoxysilane in toluene or xylene.[20] In 1980, another silanization of SiO_2 surface was reported by Sagiv who succeeded in grafting mixed monolayers containing n-octadecyltrichlorosilane.[21] Other functionalizations of SiO_2 surfaces using molecules such as phosphonates or carboxylates exist and are well reported.[22,23] However, the SiO_2 surface functionalization can lack of stability and reproducibility because of the variable hydroxyl group concentration on the surface. Also, the interfacial Si-O-Si bonds can be easily hydrolyzed under neutral pH conditions, leading to the creation of traps in the layer which further impacts the device properties.

Another approach consists in removing the SiO_2 layer and replacing it with a passivating organic monolayer. To do so, the surface needs to be first hydrogen passivated, as will be discussed hereinafter. In this context, the oxidation of silicon has to be avoided.

I.3. Si-C bond formation from hydrogenated silicon surfaces

The first functionalization of oxide-free surface was reported in 1993 by Chidsey and Linford in which alkyl monolayers were obtained via Si-C bonds formation.[24] The advantage of oxide free silicon functionalization lies in the stable bonding to Si, avoiding substrate oxidation. Several bond dissociation energies are reported in Table 1. The surface Si-C bond is strong with a bond dissociation energy of 369 kJ/mol, value supported in the literature,[25–27] and less polarized compared to the Si-O bond thus bringing kinetic and thermodynamic stability.[2]

element	self	H	C	O	F	Cl	Br	I
C	292−360	416		336	485	327	285	213
Si	210−250 (bulk) 310−340 (disilane) 105−126 (disilene)	323	369	368	582	391	310	234
Ge	190−210 (bulk) 256 (digermane)	290	255		465	356	276	213

Table 1 : Bond dissociation energies for various groups related to Group(IV) elements (kJ/mol).[2]

The removal of the oxide layer on Si is performed by an etching process involving in most cases fluoride containing solutions (HF, NH_4F). Indeed, Si-F bonds have a stronger bond dissociation energy than Si-O bonds (582 kJ/mol and 368 kJ/mol respectively), sufficient to break Si-O bonds. Silicon etching/hydrogenation is used in the semiconductor industry to create an oxide-free silicon surface that is stable only under inert atmosphere conditions. Through the detection of fluorine in XPS by Weinberger *et al.*,[28] the etching process of the substrate with HF was initially believed to form Si-F bonds as supported by the strength of these bonds (582 kJ/mol), almost twice higher than that of Si-H bonds.[29] This F-passivation was however abandoned over the years: XPS showed only traces of fluorine and a hydrogen-terminated surface was found to be actually formed using Fourier transform infrared (FTIR) spectroscopy.[30–32] Indeed, the Si-H bond stretching was obviously observed on Si(111) surface with the corresponding sharp band at 2083.7 cm^{-1} as shown in Figure 3a.[32]

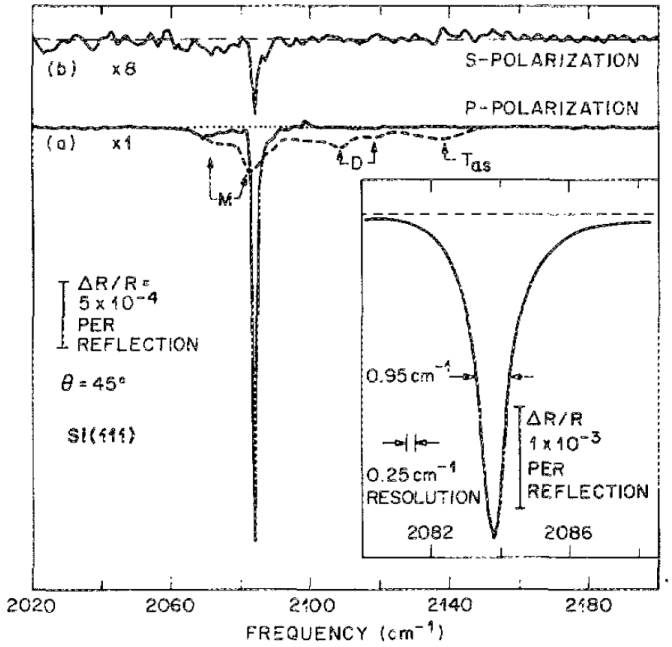

Figure 3 : Internal reflection spectra of HF-treated Si(111) surfaces : a) surface treated with pH modified buffered HF (pH = 9-10) (solid curve : resolution = 0.5 cm^{-1}) and with dilute HF (100:1 H_2O:HF) (dashed curve: resolution 1 cm^{-1}); b) s-polarization for surface treatment with pH modified buffered HF (pH = 9-10) (resolution = 2 cm-1). Inset: High-resolution spectrum of Si(111) surface treated with pH modified buffered HF (pH = 9-10).[32]

Using FTIR spectroscopy and through calculations, the mechanism of H-passivation was finally understood:[33,34] in the process described in Scheme 2 for Si(111) surface,[27] the terminal hydroxyl group is first removed as water molecule by HF, leaving the surface F-terminated. As fluorine exhibits a high electronegativity over Si, the Si-Si back bond is highly polarized in the direction $Si^{\delta-} - Si^{\delta+} - F^{\delta-}$, which weakens the Si-Si bond and promotes the insertion of HF molecule. As a result, the sublayer Si is hydrogenated. With the continuous insertion of HF molecules, the surface silicon atom is finally removed as SiF_4 molecule, leaving the sublayer Si atoms hydrogenated.

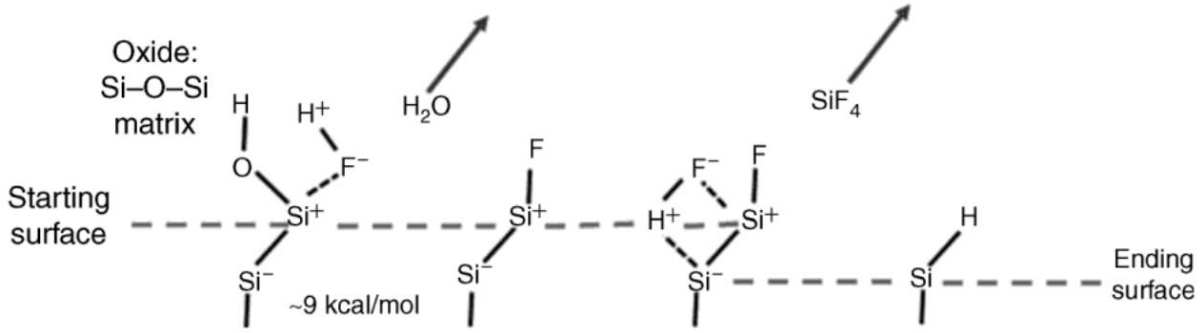

Scheme 2 : HF etching mechanism of Si(111) surface.[27]

Higashi *et al*. determined the best experimental conditions to get an atomically flat (111)SiH surface.[32] Using IR absorption spectroscopy, they noted that the concentration of HF solution had an impact on the Si-H stretching band. The latter has indeed a broaden full width at half maximum (FWHM) of (~30 cm^{-1}) when concentrated 49% HF solution was used, while it was narrower (~10 cm^{-1}) when etching was performed with diluted 1-10% HF solution,[31] as shown in Figure 3a (dashed curve). The broadening of the band is an evidence of surface inhomogeneity since it pointed out the formation of dihydrides, meaning that the etching process was not efficient enough to form exclusively monohydrides. As the pH shifted from 1 to 2 after dilution, they kept on studying the influence of the pH solution at which the etching process was performed. To do so, they used ammonium fluoride (NH_4F) as a buffering agent, and varied the pH from 0-5 to 5-12 by adding hydrochloric acid (HCl) or ammonium hydroxide (NH_4OH). They found that the Si-H stretching band becomes narrower for pH $\geq$ 5 and the FWHM was even measured at ~1 cm^{-1} for an etching solution of pH 9-10, as depicted in Figure 3a (solid curve).

The (111)SiH surface topography was analyzed by Hines and coll.[35–37] using Scanning Tunneling Microscopy (STM) and confirmed the dependence of surface morphology upon pH etching solution change. Not only is the Si-H stretching band broadened in IR spectroscopy when the etching process of the surface was performed at low pH (Figure 4a, inset), but the corresponding surface is also rough as supported by the STM image of the surface topography (Figure 4a). On the other hand, SiH surface prepared in high pH etchant solution shows a sharp band in the IR spectrum (Figure 4b, inset) and a flat surface in STM (Figure 4b) in which terraces are perfectly distinguishable.

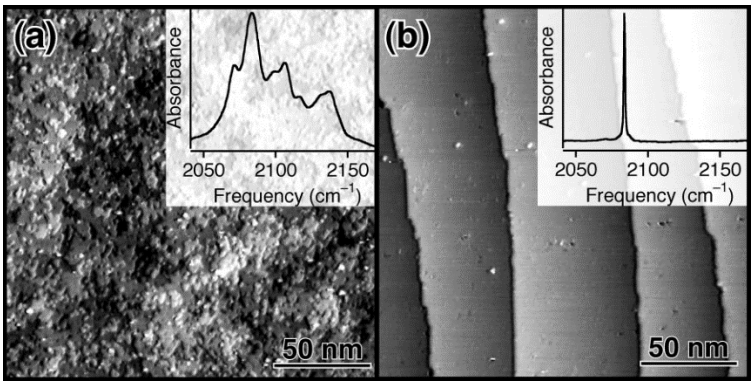

Figure 4: Comparison of Si-H stretching vibrational mode and STM images corresponding to Si(111) surface etched under different pH conditions: (a) low pH (≤5) HF/NH_4F mixture and (b) high pH (≥8) HF/NH_4F mixture.[35]

NH_4F is thus used for Si(111) etching and plays the role of an anisotropic etchant which "selectively attack(s) all surfaces except a specific crystallographic plane"[35] and will firstly attack the surface defects (kink, step...). Using kinetic Monte Carlo simulations (KMC), the defect sites were found to be at least 5000 times more reactive than the terrace sites, with the kink site (see Figure 5) being 10^7 times more reactive than the terrace site,[35] which supported the anisotropic effect of NH_4F etching.

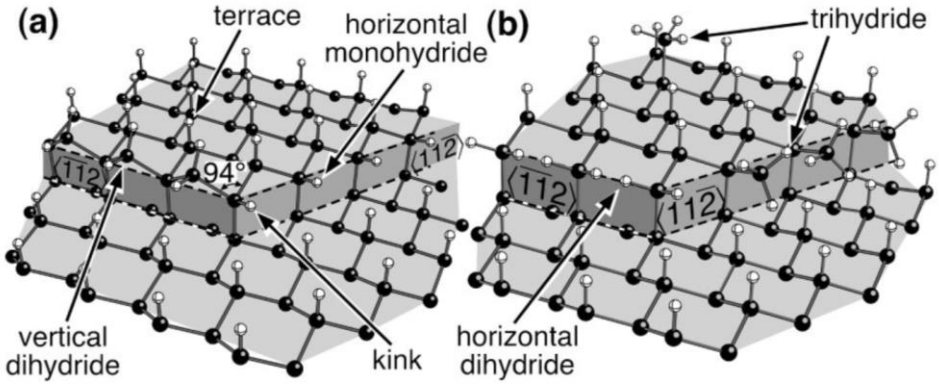

Figure 5 : Defect sites on Si surface.[35]

Then, different methods are available to create a Si-C link between the oxide-free silicon surface and the molecule of interest.

One of the most used strategies is the hydrosilylation reaction, reported for the first time in 1993 by Chidsey and Linford,[24] leading to the formation of Si-C-C-R or Si-C=C-R bond depending on whether 1-alkenes or 1-alkynes are used. The mechanism is depicted in Scheme 3 and was reported in 1999.[38] The process starts with the creation of a Si surface radical, which can be induced by the presence of a radical initiator through the decomposition of diacyl peroxides for example,[24,39] or by the Si-H bond homolytic cleavage (~3.5 eV) which can be induced by heat[40–44] (thermal hydrosilylation) or light[45–48] (photochemical hydrosilylation). The surface radical subsequently attacks the unsaturated bond of the 1-alkene specie (or 1-alkyne) and propagates along the surface, leaving a covalently grafted alkyl (or alkenyl) chains onto the silicon surface. The hydrosilylation can also be initiated in the presence of Lewis acid catalysts such as $AlEtCl_2$.[38]

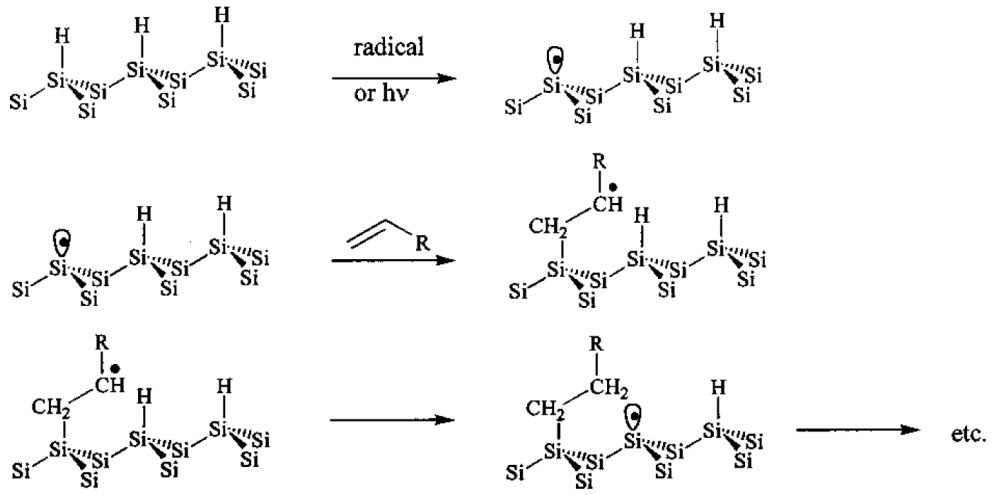

Scheme 3 : Hydrosilylation reaction mechanism of an alkene on hydrogenated-Si(111) surface.[38]

Thermal hydrosilylation has been reported for several applications, the monolayer of alkyl chain can be used for later gold nanoparticles deposition and subsequently Coulomb blockade measurements for example[40,43] and can be used for biosensors applications as well.[49] Photochemical hydrosilylation implies mild conditions which is also a way to have biocompatible systems.[46,47] However for the latter, studies have brought some doubt on the exact mechanism happening.[45,50] The first mechanism shown in Scheme 4a is similar to the one on Scheme 3, in which the energy brought by UV light is sufficient enough for Si-H bond homolysis. However, photons from UV light (generally 254 nm) have a higher energy than the Si work function meaning that an electron is removed from the material, leaving the surface positively charged where the π-electrons of the alkene can react as depicted in Scheme 4b.

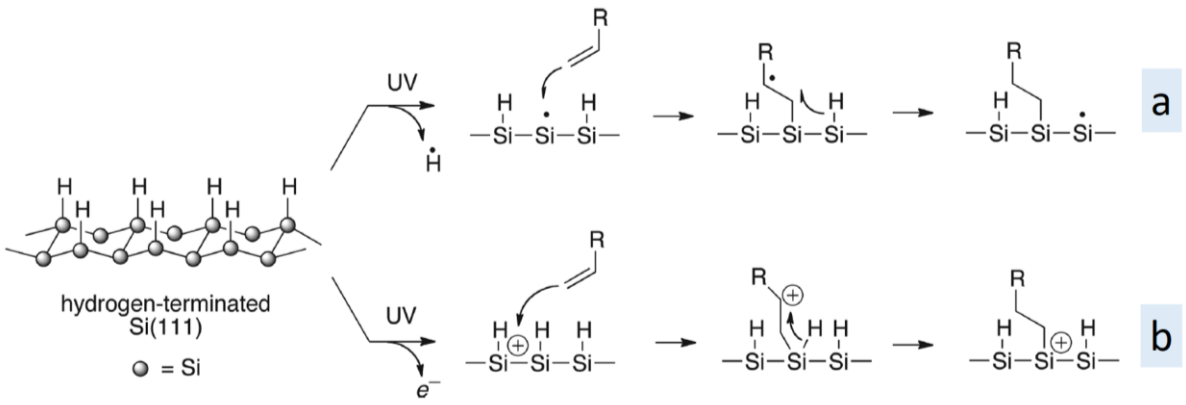

Scheme 4 : Possible UV-initiated hydrosilylation mechanisms of an alkene on a hydrogenated-Si(111) surface.[45]

Other covalent routes to functionalize the SiH surface exist but will not be studied in this project.[2,5,26,51] The possibilities are wide as depicted in Figure 6. For instance, the SiH surface can also react with aryldiazonium salts,[52,53] aldehydes or alcohols,[54,55] or organochalcogenides reagents such as thiols or thioethers.[56,57] Chlorination can also be performed on the SiH surface to obtain a Cl-terminated surface. As Cl group is a better leaving group, the resulting surface can further react with Grignard, organolithium, or sodium acetylides reagents.[58,59]

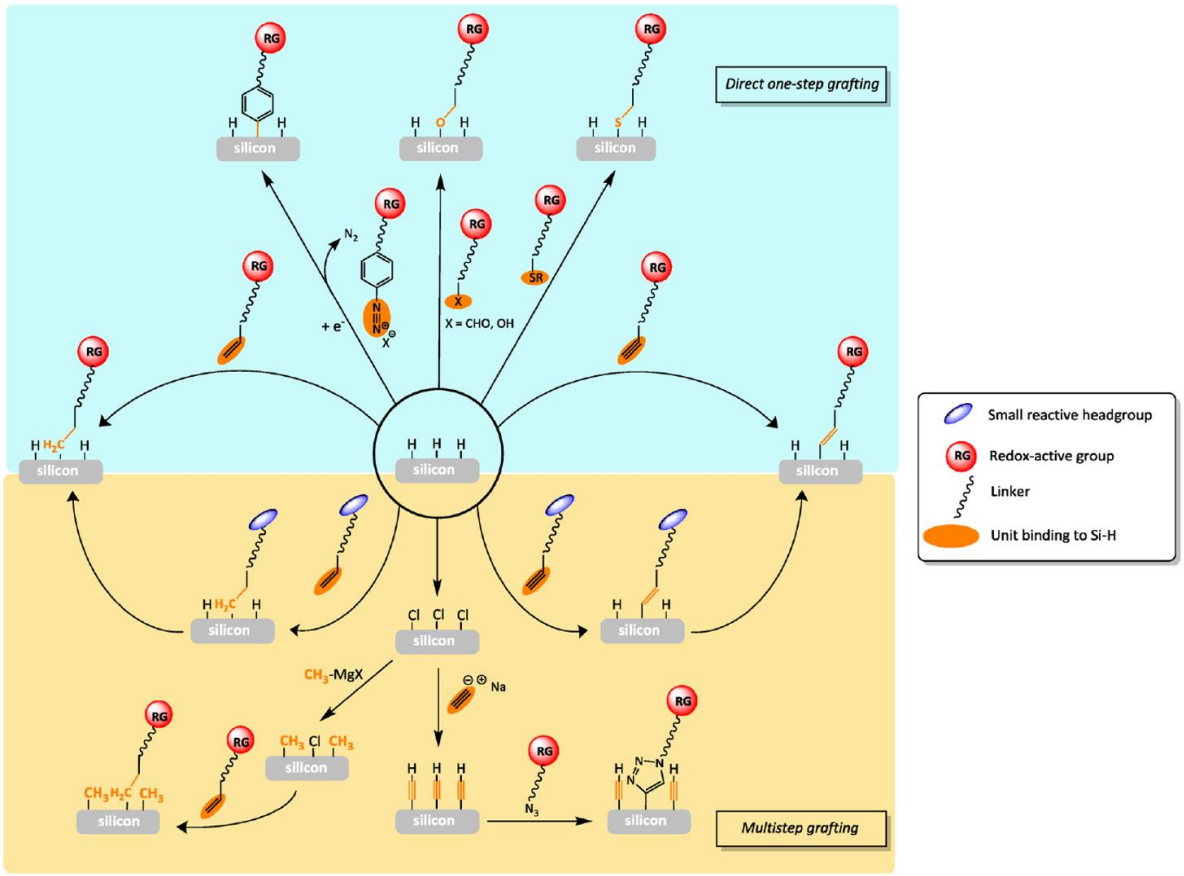

Figure 6 : Summary of covalent grafting possibilities of redox-active molecules on SiH surface.[26]

Etching and organic monolayer grafting can also be performed on Si(100) wafer and they involve similar mechanisms as for Si(111) wafer. The main difference lies in the surface morphology of both SiH surfaces: etching leaves the Si(100) dihydride-terminated while it leaves the Si(111) monohydride-terminated as shown in Figure 7.[60] This can further impact the coverage and stability of the monolayer that will be later grafted onto the SiH surface. The surface modification on (100)SiH is indeed expected to be less dense and homogeneous and more prone to oxidation than that on (111)SiH surface, due to the conformation of the Si-H bonds on the surface.

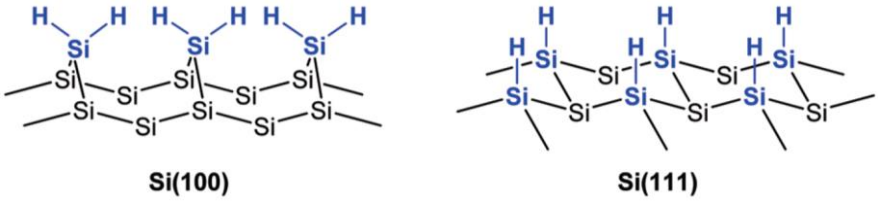

Figure 7 : Structure comparison between (100)SiH surface and (111)SiH surface obtained after etching.[60]

Silicon and especially oxide-free silicon surface thus seems to be an adapted starting material for grafting an ordered and homogenous organic monolayer that would serve as a good stable platform for the later POM monolayer deposition. The surface functionalization with organic monolayer was chosen for this purpose as it provides more stability and less defects than the multilayers, allowing us to have a better control on the functionalization. However, in order to have a reliable understanding of the immobilized POM photoreduction property, the organic monolayer grafting procedure needs to be reproducible. Among the strategies presented, thermal hydrosilylation with 1-alkene was envisioned in order to form dense monolayer of alkyl chains bearing head groups that can be post-modified. This strategy also constituted a way for us to protect the Si surface from oxidation during surface characterization in ambient atmosphere. In the following part, experimental procedure of organic monolayer grafting onto Si surface in the most possible reproducible way will be presented and the strategies adopted to avoid Si oxidation will be highlighted.

II. Experimental procedure

The functionalization procedure was first performed on Si(111) surface which has the advantage to form surface monohydride silicon, and is supposed to form a compact and homogeneous alkyl chain monolayer. As reproducibility is crucial for being able to study the photoreduction property of the POM, different parameters were explored to master the functionalization steps with the non-ideal conditions faced in the laboratory. However, having in mind the later immobilized POM electrical characterization, the same functionalization procedure was finally reproduced on SOI substrates introduced in Chapter I. Since fast characterization of the SOI-modified surface was not possible, as will be discussed in the following part, the idea was to develop the experimental procedure on Si(100) which constitutes

the superficial layer of the SOI substrate. Only then will it be possible to switch to SOI substrates and reproduce the same experimental procedure than on Si(100).
This section will start with the strategy adopted to follow the surface functionalization quality. After that, experimental procedure and results will be detailed first on Si(111) substrate then on Si(100) substrate.

II.1. Surface characterization by Fourier transform infrared (FTIR) spectroscopy: optimization of the parameters for FTIR spectra recording

FTIR spectroscopy is the characterization tool we used to detect the chemical bonds on the silicon substrate. The purpose of using the FTIR spectrometer was to probe the features on the functionalized Si surface, and thus to follow and evaluate the quality of the functionalization steps that will be described in the next part. A lot of IR spectra of functionalized silicon surface are reported in the literature and will give us some typical IR spectra references and band positions to stick with. The combination of ellipsometry measurements (see Appendix 1.1) and IR spectra recording have the advantage to be not so much time consuming to avoid possible oxidation of the substrate as much as possible and are easily available. Both tools were always used after each step to evaluate the quality of the surface modification.
In this section, the principle of FTIR spectroscopy will be first presented, then the IR spectra recording strategy used to follow the quality of the functionalization while avoiding formation of SiO_2 will be described.

Principle

The former IR spectrometers were dispersive ones: the sample was irradiated with different single wavelengths by light decomposition using prisms or gratings, and the signal was measured at each wavelength, leading to a slow acquisition and a low signal-to-noise ratio. These two drawbacks were overcome using a Fourier transform infrared (FTIR) spectrometer, in which the sample is irradiated at the same time with a polychromatic signal that covers the whole mid-IR region.

A FTIR spectrometer is composed of a source, a Michelson interferometer (which consists of a beamsplitter and two mirrors) and a detector. The IR beam originated from the source hits the beamsplitter where it gets split into two perpendicular beams: one is reflected towards the fixed mirror while the other one is transmitted through the beamsplitter to the

movable mirror, as shown in Figure 8. The movable mirror induces the transmitted split beam to be delayed, compared to the reflected split beam, creating an optical path difference (OPD). Back at the beamsplitter, the two split beams can thus interfere constructively or destructively depending on the position of the movable mirror and on the light wavelength.

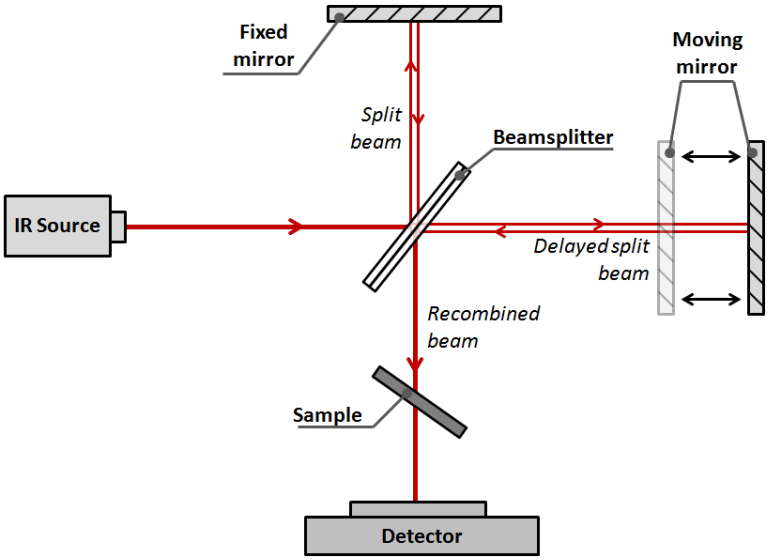

Figure 8: Components inside a FTIR spectrometer and IR beam path across each component.[61]

The recombined beam goes through the sample before reaching the detector. The detector output is an interferogram that shows the intensity of the resulting recombined beam as a function of the movable mirror position. The interferogram needs to be decoded using Fourier transform which finally provides a single channel spectrum displaying the measured intensity as a function of the wavenumber (in cm^{-1}).

In practice, to detect the chemical bonds of the surface, a reference is required. During two successive steps, for example step1 and step2, two single channel spectra are needed: one corresponding to the surface after step1 (called reference spectrum, see Figure 9a) and one corresponding to the surface after step2 (called modified sample spectrum, see Figure 9b). The two spectra are processed by calculating the "differential absorbance"* following the below equation:

$$\Delta \boldsymbol{A} = A_2 - A_1 = -\log_{10} T_2 + \log_{10} T_1 = -\log_{10} \frac{I_2}{I_0} + \log_{10} \frac{I_1}{I_0} = \boldsymbol{\log_{10} \frac{I_1}{I_2}}$$

*Note that the « differential absorbance » is still an absorbance. For an easier understanding of the spectra, we will use the terms "differential absorbance" and "differential spectrum" whenever two spectra are subtracted.

Where A_1, T_1 and A_2, T_2 are the absorbance and transmittance of the surface after step1 and step2 respectively. I_0 is the intensity of the IR beam without any sample, while I_1 and I_2 are the intensity of the IR beam passing through the surface after step1 and step2 respectively.

The resulting IR spectrum will thus show the differential absorbance as a function of the wavenumber. Figure 9c gives an example of a typical differential IR spectrum obtained using this process, which can be improved as will be detailed in the following.

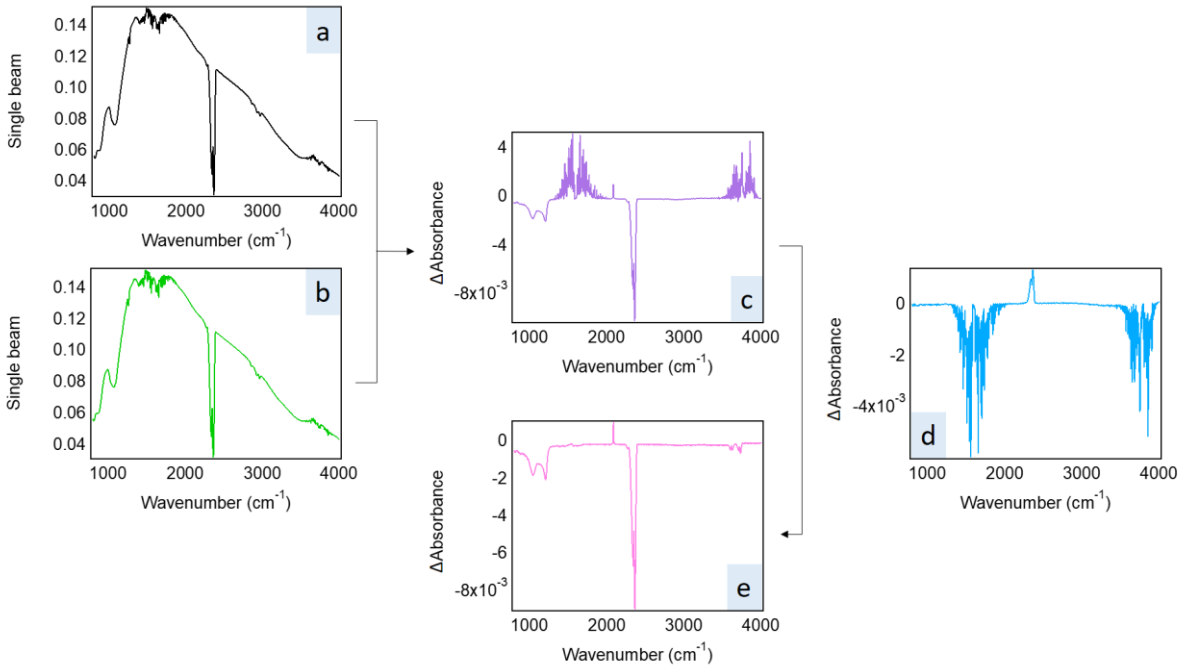

Figure 9 : Summary of the IR spectra processing. First, the single channel spectrum of the surface is recorded after step1 (a) and after step2 (b). The differential spectrum is calculated (c) and subsequently processed with a water vapor spectrum (d). After water vapor spectrum subtraction, the final differential spectrum is obtained (e) and further analyzed.

The transmittance of silicon substrate depends on its polishing and its resistivity. The substrates used during the project were grown FZ, lightly doped with a resistivity of 20-60 Ω.cm and double-side polished to maximize its transmittance which enables us to work with the FTIR spectrometer in transmission mode. To give a rough idea, using the air as background, the transmittance of the Si substrates was recorded for three different substrates: a double-side polished FZ-silicon, a single-side polished CZ-silicon and a single-side polished SOI substrate.[†] As shown in Figure 10, using the same parameters for the three recordings, FZ-Si double side

[†] The surface characteristics are the following :

a) Si(100) substrate from Sil'tronix, FZ, *n*-doped (Phosphorus), 20-60 Ω.cm, double side polished
b) Si(111) substrate from Sil'tronix, CZ, *n*-doped (Phosphorus), 0.1-1 Ω.cm, single side polished
c) SOI substrate from SOITEC, *p*-doped (Bore) bulk Si, 145 nm buried oxide, Si(100) film of 70 nm, single side polished

polished substrate is the most transparent to IR light. Its transmittance was measured at ~55%, approximately twice higher than that of the single side polished substrates (Figure 10b and c). FTIR spectroscopy will be used in the case of the functionalization study on the double-side polished Si(111) and Si(100) substrates, but as SOI substrate is twice more opaque than the two others, the goal was to master the functionalization procedure on the transparent substrates before using SOI substrates for which FTIR spectroscopy characterization is not suitable.

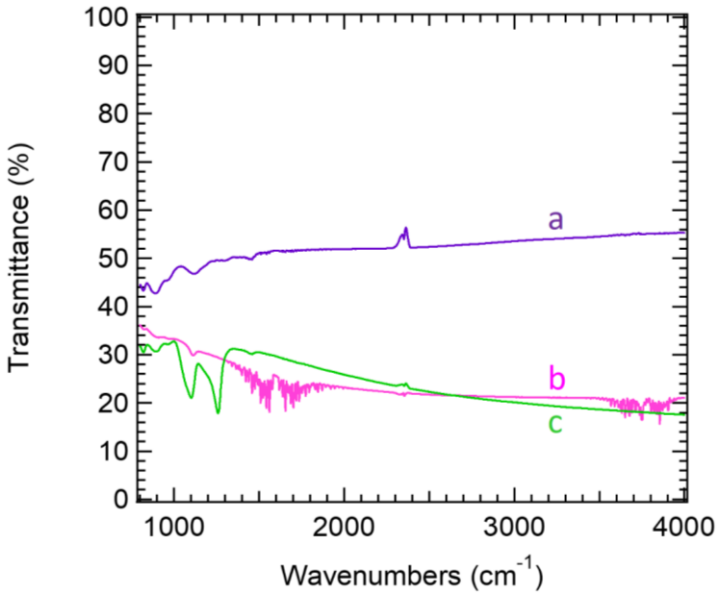

Figure 10 : Transmittance of a) FZ-Si double-side polished substrate, b) CZ-Si one-side polished substrate and c) SOI one side polished substrate. The background was recorded without sample.

To sum up, the idea was to obtain the differential absorbance spectrum after functionalization versus before functionalization to evaluate the quality of the functionalization step. As we wanted to probe fine modifications between two successive steps, we always recorded the spectrum of the surface before modification as a reference spectrum, instead of recording a background spectrum with no substrate.

In practice, a Bruker Tensor 27 FTIR spectrometer, equipped with a L-alanine doped triglycine sulfate (DLaTGS) thermodetector and KBr beam splitter, was used. The spectrometer is connected to a dryer (SDAT from Specken Drumag) that dries the compressed air before entering the spectrometer. The dryer does not remove the carbon dioxide but helps in reducing the atmospheric water vapor in the sample compartment.

All IR spectra were recorded in transmission mode at the Brewster angle of Si. At this particular Brewster angle, called polarization angle, set in our case at 70°, no reflection of the p-polarized component of light is observed. It is thus possible to detect modes parallel and perpendicular to the surface[62,63]. Finally, we worked with double side polished substrates to increase the transparency to IR light and also to strongly minimize the interferences that would have been created by the non-polished backside reflection.

Recording optimization

The procedure of spectra recording was inspired by the one used by Seitz *et al.*[41] Three spectra of the surface were recorded between 800 and 4000 cm^{-1} at a resolution of 4 cm^{-1} after each step of the surface modification. However, as our spectrometer was not installed inside an ultrahigh purity glovebox with O_2 and H_2O concentrations lower than 0.1 ppm, we needed to adapt the literature procedure in order to obtain good resolution spectra. Indeed, as shown in Figure 9c, differential absorbance spectrum displays intense bands corresponding to carbon dioxide (2300-2400 cm^{-1}) and atmospheric water vapor (1300-2000 cm^{-1}, 3500-3800 cm^{-1})[64], which could hide some surface features, especially in the range 1300-2000 cm^{-1} (C-H, C=O features). As our surfaces are sensitive to air, **we needed to find the best compromise between the spectra recording duration and the quality of the spectra**. We thus tried different possibilities, that will be discussed hereinafter.

Our first test was to determine the **number of scans**. One spectrum being a sum of a specific number of consecutive scans, an increase of the scans number will decrease the noise of the spectrum but will increase the acquisition time. As the Si surface will not be fully air-protected inside the sample chamber, we could not afford a too long acquisition time. Note that we are looking at surface features with relatively small intensities ranging from 10^{-4} to 10^{-3} in the differential spectrum, perfectly distinguishable when the spectrometer is inside a glovebox. In our case, we challenged ourselves to “mimic” the effect of a glovebox by obtaining an IR spectrum with a baseline as flat as possible.

Tests were thus performed with a number of scans ranging from 10 to 1000, with one spectrum being recorded every 10 secs to ~14 min respectively. The measurement consisted in recording a reference spectrum with X number of scans on Si/SiO_2 substrate and a sample spectrum with the same X number of scans on the same substrate and finally displaying the differential absorbance spectrum, which are shown in Figure 11.

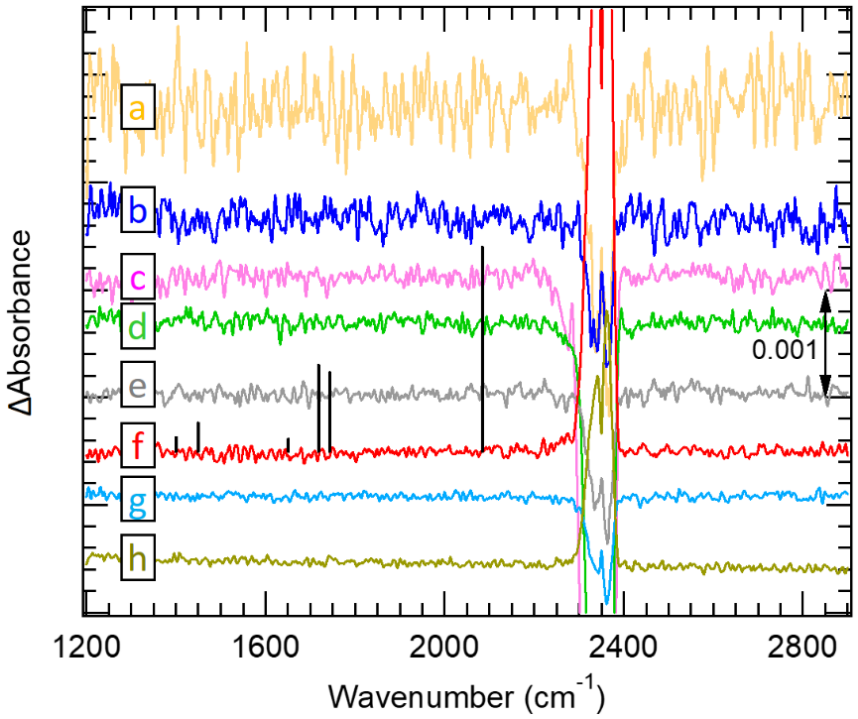

Figure 11: Differential spectrum obtained on a Si-SiO_2 substrate using a recording of a) 10 scans, b) 50 scans, c) 100 scans, d) 200 scans, e) 250 scans, f) 500 scans, g) 800 scans and h) 1000 scans. Expected intensities for some typical features of functionalized surface are represented in black.

To evaluate the flatness of the baseline, the latter between 1900 and 2100 cm^{-1} was analyzed for each measurement by calculating the standard deviation of Y values, denoted σ, using the following equation:

$$\sigma = \sqrt{\frac{1}{N}\sum_{i=0}^{N-1}(Y_i - \bar{Y})^2}$$

where N is the number of points and, Y_i the i^{th} value of Y, and $\bar{Y}$ the average of the Y values. The values are listed in Table 2. The IR absorption spectrum started to be satisfying with 100 scans where $\sigma = 5.7.10^{-5}$. Not a significant improvement of the spectrum baseline is observed when the number of scans is higher than 500, so we decided to keep this value that gives a standard deviation $\sigma = 2.5.10^{-5}$. This results in a spectrum recorded every **7 min**, which seems reasonable.

Number of scans	Standard deviation of Y values (1900-2100 cm^{-1})	Time per spectrum
10	$2.1.10^{-4}$	10 secs
50	$9.5.10^{-5}$	43 secs
100	$5.7.10^{-5}$	1min25
200	$5.1.10^{-5}$	2min47
250	$4.1.10^{-5}$	3min31
500	$2.5.10^{-5}$	**7 min**
800	$2.4.10^{-5}$	11min11
1000	$1.9.10^{-5}$	13min58

Table 2: Standard deviation of Y values calculated in the 1900-2100 cm^{-1} region of each differential spectrum recorded from 10 scans to 1000 scans.

Moreover, the intensities of the main absorption bands we expect to see on a differential spectrum of a functionalized Si versus oxide-free Si are displayed in Figure 11f, based on the intensities of similar functionalized surfaces reported in the literature[40,41] (for the assignment of these bands, see Appendix 7). Using a well purged glovebox, the intensities reported range from ~$1.0.10^{-4}$ to ~2.10^{-3}. **We thus have to keep in mind that some features will be hardly seen, at least when the spectrum will be referenced to the oxide-free Si surface, especially in the case of the NH_2-terminated Si surface.**[63]

After determining the optimal number of scans (500 scans, 7 minutes per spectrum) to obtain a relatively flat baseline, we needed **to adapt the purging time after substrate introduction** in the sample compartment. Indeed, as we are only working with differential spectra, there should not be a huge difference of atmospheric water vapor concentration before and after substrate introduction, otherwise the corresponding band in the differential spectrum will be too intense and will be difficult to suppress or not well enough suppressed. Thus the spectrometer needs to be purged in a defined time.

We thus wanted to determine the purging time after which the spectra will be recorded after sample positioning. To do so, we positioned a Si substrate on the sample holder (at t=0) and waited a purging time t_{purge} before recording one reference spectrum. After that, the compartment is opened for approximately 25 secs (it simulates the time needed for the sample removal and repositioning) without touching the substrate, and closed back again. Three

consecutive sample spectra are then recorded (starting at t_{purge} - 7 min), as sketched in Scheme 5, and referenced to the reference spectrum. At the end, three differential spectra are obtained for each t_{purge} value.

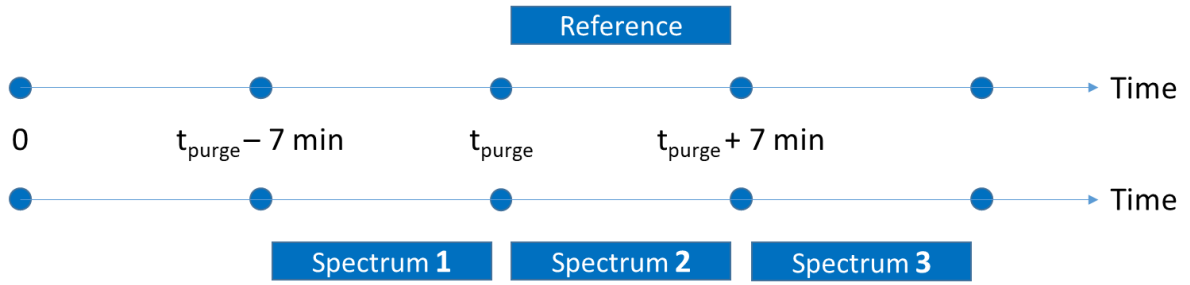

Scheme 5 : IR spectra recording procedure to determine the best purging time (t_{purge}) after introduction of the Si-SiO_2 substrate inside the FTIR spectrometer at t = 0. One reference spectrum is recorded at t = t_{purge}. After opening the sample chamber for 25 seconds, another round of spectra recording is carried out: three spectra are recorded, starting from t = t_{purge}- 7min.

We then extracted the value dY_{H2O} at 1560 cm^{-1} from each differential spectrum, which corresponds to the maximum intensity of the water vapor absorption band, and the values are reported in Table 3. Among each set of three differential spectra, the one that gives the lower dY_{H2O} value is shown in Figure 12.

t_{purge} (min)	dY_{H2O} at 1560 cm^{-1}		
	Spectrum1/reference	Spectrum2/reference	Spectrum3/reference
10	$2.4.10^{-2}$	$3.9.10^{-3}$	$2.7.10^{-3}$
15	$1.1.10^{-2}$	$1.8.10^{-3}$	$2.6.10^{-3}$
20	$4.6.10^{-3}$	$2.0.10^{-3}$	$1.5.10^{-4}$
25	$3.8.10^{-3}$	$6.8.10^{-4}$	$2.8.10^{-4}$
30	$2.3.10^{-3}$	$1.1.10^{-4}$	$4.0.10^{-4}$
35	$2.0.10^{-3}$	$1.3.10^{-4}$	$6.3.10^{-4}$
60	$2.2.10^{-4}$	$6.7.10^{-4}$	$1.1.10^{-3}$

Table 3 : Absorbance amplitude (absolute value) of the peak at 1560 cm^{-1} (dY_{H2O}) measured on the three differential spectra obtained for each purging time experiment (spectrum1/reference spectrum, spectrum2/reference spectrum and spectrum3/reference spectrum).

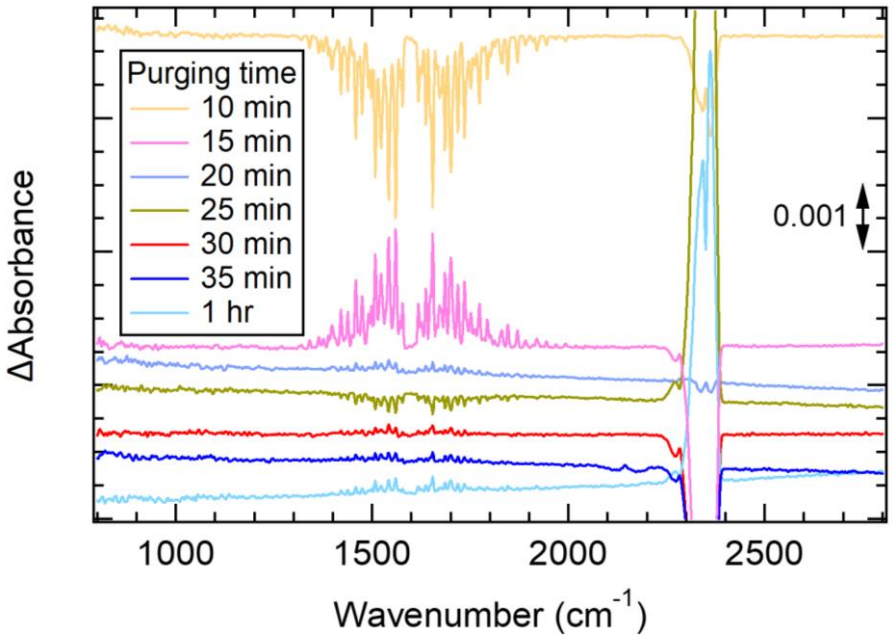

Figure 12 : Differential spectra obtained depending on the purging time after substrate positioning in the sample compartment of the FTIR spectrometer.

The best differential spectrum considering our compromise on the acquisition time was the one obtained with a t_{purge} = 20 min, where dY_{H2O} fell down at $1.5.10^{-4}$. Not a significant improvement of the value was obtained by increasing the purging time.

In the case of t_{purge} = 20 min, the best dY_{H2O} value was obtained when the last sample spectrum (spectrum 3 in Scheme 5) was recorded (*i.e.* at 27 minutes). We thus kept the procedure detailed in Scheme 5, but we added the recording of two more reference spectra to allow more spectra subtractions. Thus the recording procedure timing selected is summarized in Scheme 6: in practice, after substrate positioning in the sample compartment, three consecutive spectra will be recorded after a waiting time of 13 min.

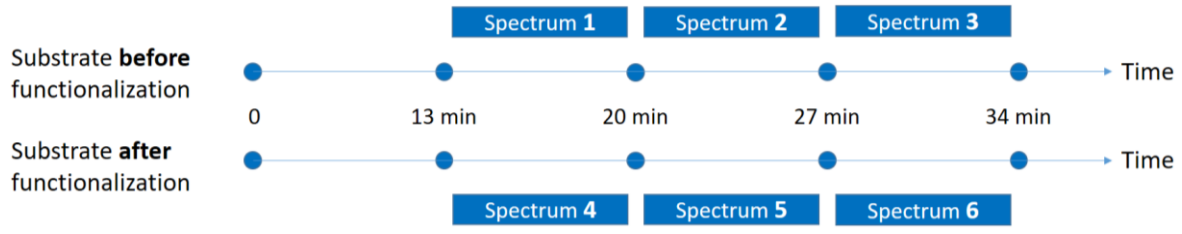

Scheme 6 : IR spectra recording procedure timing after introduction of the surface inside the FTIR spectrometer.

Note that the dY_{H2O} value can be decreased by operating a water vapor spectrum subtraction. To do so, after recording of the three reference spectra (Scheme 6), the spectrum 2 is referenced to the spectrum 1, and the spectrum 3 is referenced to the spectrum 2. Two water

vapor differential spectra are thus obtained showing more or less intense water vapor bands. Figure 9d gives an example of typical water vapor differential spectrum. These spectra are further used to remove the excess water vapor bands on the differential spectra, and a resulting spectrum is for example shown in Figure 9e.

Finally, an attempt to improve the purge system and to reduce the concentrations of H_2O and CO_2 inside the spectrometer was carried out using vapors from liquid nitrogen instead of a compressed air dryer. In both cases, the sample compartment was opened to insert the substrate and then closed. A set of 10 spectra was then recorded during one hour, with all the single channel spectra referenced to the last one. Spectra show that the purge with air dryer removes water molecules faster than using the vapors of liquid nitrogen system. As shown in Figure 13, the dY_{H2O} value at 1560 cm^{-1} decrease to ~10^{-2} in the first case while the value is at ~5.10^{-2} in the second case. Even though liquid nitrogen vapors purge removes H_2O but also CO_2 from the sample compartment, the purging time was not satisfying enough. Moreover, as the main features of the surface were expected to lie in the range 1200-2100 cm^{-1}, the band corresponding to $\nu_{CO_2}^{C=O}$ mode between 2300-2400 cm^{-1} (see Figure 9e) was not a real issue in the spectra analysis. The spectrometer might not be completely airtight, resulting in unavoidable remaining water molecules inside the sample compartment.

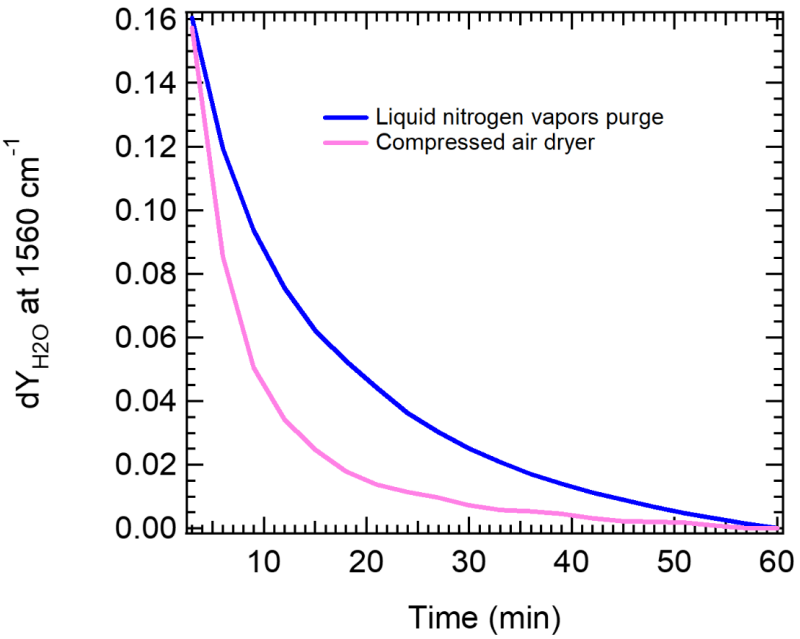

Figure 13: Variation of dY_{H2O} as a function of time, when the air dryer was used (pink) or when the liquid nitrogen vapors purging system was used (blue).

Last but not least, same repositioning of the substrate is crucial in order to obtain good quality IR spectra. The substrate needs to be positioned on the sample holder in the exact same place between the reference spectrum and the substrate spectrum, otherwise, the baseline will not be flat in the differential spectrum, making it more complicate to analyze and less accurate. Accordingly, a small blocking part was added to the sample holder.

Thereafter, the same notation will be used in all the differential spectra: **when the surface after step2 is referenced to the surface after step1**, it will be noted this way **Surface2/Surface1**. The resulting differential spectra will display positive and/or negative bands, depending on whether the band (so then the corresponding bond) appeared or disappeared after step 2. Examples will be given in the next section.

In this first section, parameters of IR spectra recording were optimized to record good quality IR spectra in a relatively short time. A flat baseline was obtained ($\sigma = 2.5.10^{-5}$), water vapor features on the differential spectrum were removed using water vapor differential spectra, and finally the compressed air dryer was found to be a suitable purging system to limit the contact of the surface with air, even though not completely suppressed since the spectrometer is not tight enough. Now that the FTIR spectroscopy characterization tool is optimized, surface functionalization can take place. In the following section, all IR bands assignment will be discussed and reported in Appendix 7. Surface functionalization will be first detailed on Si(111) prior to Si(100).

II.2. Si(111) functionalization

The functionalization procedure used on Si(111) substrate is shown in Scheme 7, and leads to the successive formation of a regrown oxide layer on the substrate ("**SiO_2**") and the oxide-free hydrogen-terminated Si surface ("**SiH**"). After that, the surface undergoes a thermal hydrosilylation with neat ethyl 10-undecenoate (the neat alkene, also called ethyl undecylenate), leading to the formation of the ester-terminated Si surface ("**Siester**"). The ester functions are hydrolyzed to form the carboxylic acid-terminated surface ("**SiCOOH**"). Finally, the carboxylic acid functions are activated by a coupling reagent before reaction with ethylenediamine. The amine-terminated Si surface ("**$SiNH_2$**") is finally obtained. The amine functions are basic (pKa RNH_3^+/RNH_2 ~10-11 in water) and are thus expected to get protonated when exposed to air, due to weak bonding of water molecules to the amine functions[65]. The whole and more detailed experimental procedure of each step is given in Appendix 5.2.

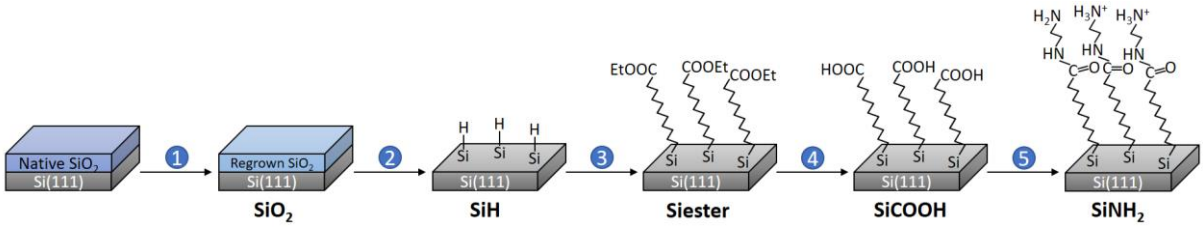

Scheme 7 : Functionalization procedure on Si(111) to successively obtain the regrown "SiO_2" surface, "SiH" surface, "Siester" surface, "SiCOOH" surface and "$SiNH_2$" surface.

The experimental procedure was first learned at the Laboratory for Surface and Nanostructure Modification (LSNM) at University of Texas at Dallas (UTD) during a final year internship back in 2018, in Pr. Yves Jean Chabal's team. Through his expertise on hydrogenated Si surfaces and their chemical functionalization, and with the help of Dr. Milana Cherie Thomas, the goal was to discover and to assimilate the experimental procedure to obtain NH_2-terminated Si surfaces, to finally export the technique back in Paris for further POM deposition.

At Dallas, the hydrosilylation was carried out using a Schlenk line and the IR spectra were recorded in a continuously N_2-purged glovebox after each step to follow the functionalization. The IR and XPS spectra showed the expected surface features with only a very low concentration of SiO_2 (see Appendix 2.1). No ellipsometry measurements were carried out though, as the cleaning and functionalization were considered as routine experiments. Back

in France, the same experimental procedure was reproduced but with the FTIR spectrometer apparatus described previously. However, it did not give the same results.

One of the very first experiments gave the successive differential spectra represented in Figure 14. In the SiH/SiO_2 spectrum (red curve), the band at 2084 cm^{-1} corresponding to the Si-H stretching mode (ν^{Si-H}) appeared positively meaning that it has been formed during the hydrogenation. In the meantime, bands at 1041 and 1215 cm^{-1} corresponding to the SiO_2 transversal optical (TO) and longitudinal optical (LO) phonon modes respectively, appeared as negative bands, meaning that the oxide layer was removed. Note that no oxidation is visible during the spectra recording. However, after hydrosilylation, even though $\nu_{ester}^{C=O}$ and C-H vibration modes are observed at 1741 cm^{-1} and 2800-3000 cm^{-1} in the Siester/SiH spectrum (blue curve), oxide growth can also be witnessed by the positive bands at 1041 and 1193 cm^{-1}. The band at 1193 cm^{-1} can indeed be attributed to the Si-O-C vibration mode of Si-O-CH_2-groups. Improvement of the different steps of the procedure will be detailed hereinafter.

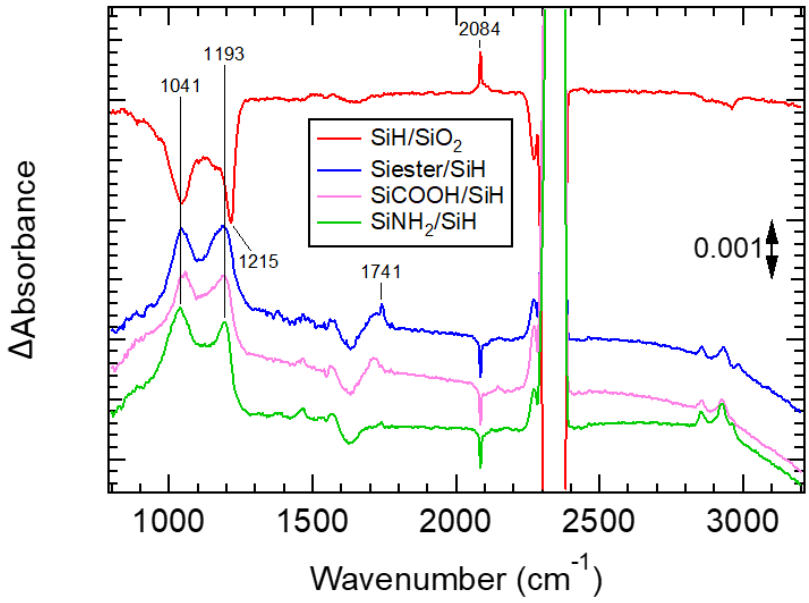

Figure 14 : One of the very first differential spectra obtained back in France. The SiH surface is referenced to the SiO_2 surface, the Siester, SiCOOH and $SiNH_2$ surfaces are referenced to the SiH surface.

As we did not know where the functionalization messed up, we went through an investigation to understand what happened after each step with the experimental conditions that we faced in Paris. Indeed, the FTIR spectrometer was not as well purged as in Dallas as discussed previously, and it was also not installed in the same laboratory as the one where chemical functionalizations were carried out: several round trips (2-3 min each) were made after each step when FTIR spectrometer was needed. Moreover, the neat alkene used for the

hydrosilylation step was not stored in a continuously purged glove box as the bottle in Dallas. These were the main differences between experiments carried out in Dallas and in France.

The goal of using FTIR spectroscopy and ellipsometry was to follow the functionalization but in our case it was also a way to find the parameters to change and readjust the experimental procedure. After that, the idea was to free ourselves from doing it so often as we lose ~45 min each time (including the round trips). Moreover, we have to keep in mind that the final functionalization for electrical measurements will be carried out on SOI substrate for which no IR spectra will be recorded.
Modifications of the initial experimental procedure will now be detailed for Si(111).

II.2.a. Etching

Step #1 : Substrate cleaning and oxide regrowth

The substrate cleaning begins with a degreasing step involving sonication baths in dichloromethane, acetone and methanol to remove grease and residual silicon slivers from the substrate due to handling and cleaving. The substrate is then subjected to the "RCA Standard Clean" procedure developed by Kern and Puotinen[66] at Radio Corporation of America (RCA) laboratories in the late 1960's in which the substrate is successively immersed in RCA1 solution (basic piranha solution) and RCA2 solution (acidic piranha solution). The purpose of these solutions is to remove organic contaminants and metal ions from the surface. After that, the substrate is subjected to etching with HF solution followed by an immersion in RCA1 to regrow the oxide layer. The regrown chemical oxide layer will help the SiO_2 reference in FTIR spectrum to be more controlled and more reproducible.

Histograms of the thicknesses measured for the regrown oxide layer are depicted in Figure 15 whether beakers or glass tubes are used for the cleaning process. Note that different Si substrates were used during the project and were purchased from Neyco and Sil'tronix. We began with Neyco substrates for which the oxide regrowth step was similar than the one used in Dallas, *i.e.* involving the immersion of the substrate in a 20-25% HF solution for 1 minute,[67] before switching to Sil'tronix substrate for which the oxide regrowth step involved the immersion of the substrate in a 10% HF solution for 30 seconds.[61] The change in wafer supplier and HF bath will be discussed later. For the very first experiments, beakers were used for the RCA clean, meaning that one face of the silicon surface obviously touches the bottom of the

beaker. This actually led to thickness inhomogeneity between the two faces of the substrate with an oxide layer thickness measured between 1.2 and 3.3 nm as shown in the orange histogram of Figure 15. Using glass tubes for substrate cleaning reduced the standard deviation of the thickness values as both faces of the substrate are not touching the glass wall. Ellipsometry showed a lower dispersion of values (from 1.0 to 1.3 nm approximately) as depicted by the green and purple histograms of Figure 15 and in most cases, the thickness of the regrown oxide layer was measured equal to 1.2 nm.

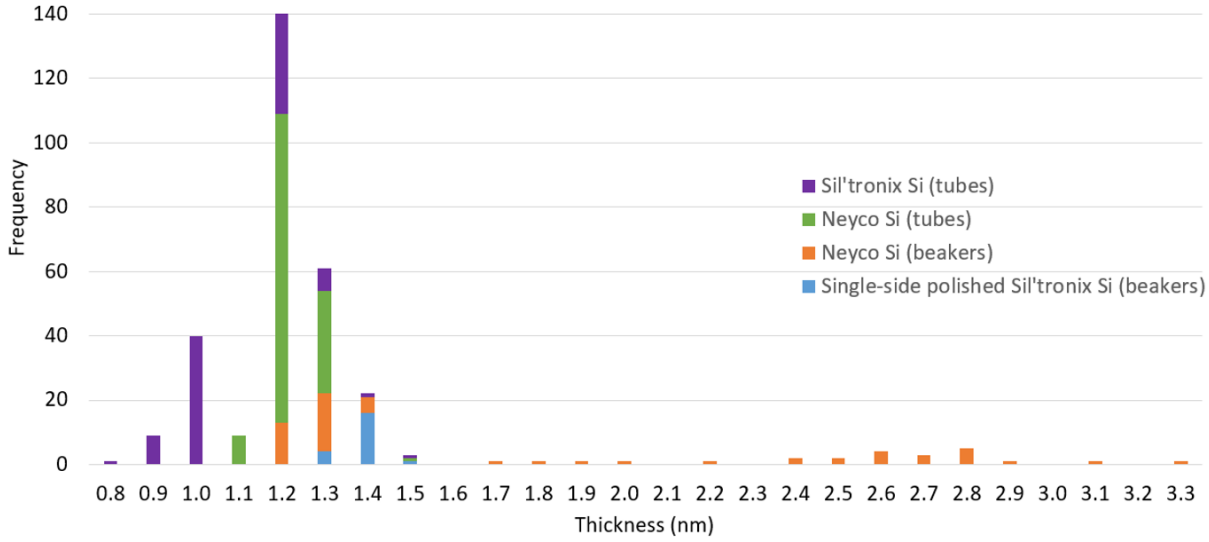

Figure 15 : Histograms of thicknesses measured for the regrown oxide layer when using beakers for substrate cleaning (orange and blue histograms) or glass tubes (purple and green histograms).

Step #1 : Hydrogenation

The experimental procedure used in Dallas was found to be unsatisfying back in Paris and was consequently subjected to some readjustments. The aim of this step was to leave the surface hydrogen-terminated prior to reaction with the neat alkene. As we are not working under inert atmosphere during this whole step, the fight against oxidation was made our first priority. First because it can affect the electronic properties of the final device. Second because the POM features on the IR spectrum are found to be in the same region than that of the oxide (1000-1200 cm^{-1}).

The procedure learnt in Dallas involved a 15 minutes immersion of the substrate in the 40% NH_4F solution. However, using the AFM optical microscope, circular features were

observed on the treated surface as shown in Figure 16. They seemed engraved onto the Si surface which was confirmed using a Scan asyst AFM tip: a sharp boundary of 100-150 nm depth was measured on the edge of the circle. This results in a rough surface that is likely to be oxidized.

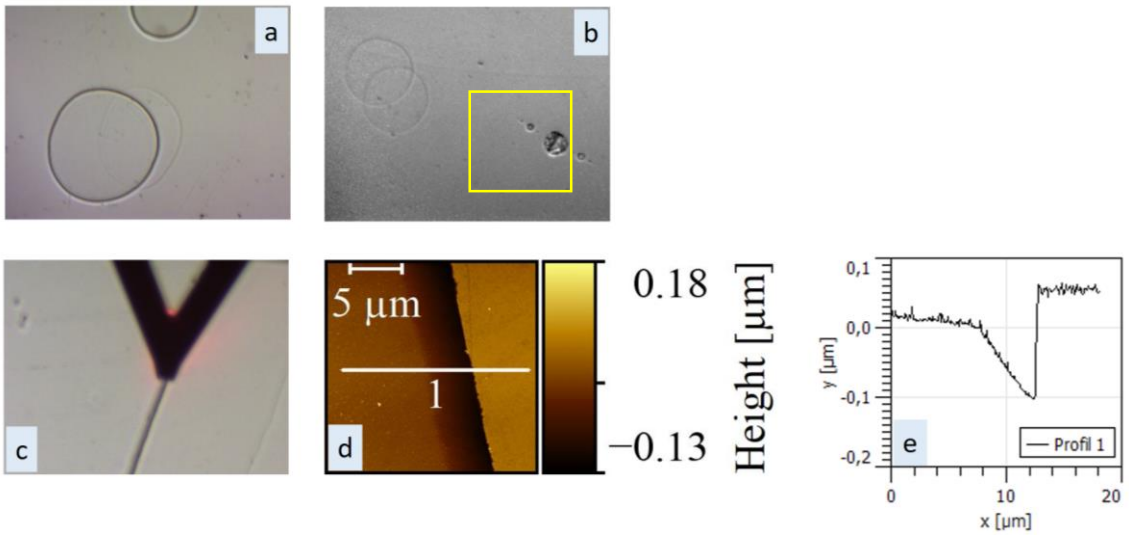

Figure 16 : Evidence provided by AFM of previously formed H_2 bubbles on the surface during hydrogenation. Pictures a, b and c show the optical images of different area of the surface. AFM image (d) is obtained at the circle edge of picture (c). The profile is traced and shown in picture (e).

These circular features were studied by Aldinger *et al*[68]. The hydrogenation mechanism is shown in Scheme 8. The first step involves the Si-H bond oxidation at a kink sites by water molecule with a release of H_2 bubble, followed by the formation of Si-F bonds. Due to the polarization of the $Si^{\delta-} - Si^{\delta+} - F^{\delta-}$ backbond, insertion of water molecules subsequently leads to the formation of Si-H bonds at the $Si^{\delta-}$ site, with release of $SiF_3(OH)$. If the H_2 bubbles are not removed, they develop on the surface during substrate immersion in NH_4F and can be visible by the naked eye.

$$\equiv Si - H + OH^- + H_2O \rightarrow \equiv Si - OH + H_2 + OH^- \ (Oxidation)$$
$$[\equiv Si]_3Si - OH + 3HF + H_2O \rightarrow 3[\equiv Si - H] + SiF_3OH \ \ (Etching)$$

Scheme 8 : NH_4F etching mechanism.[5,68]

Different mechanisms can be suggested on the fate of these bubbles. The bubbles grow and can create mounds and pillars as depicted on Scheme 9 depending on how continuous the growing is. By having a look at the profile of the circle edge on AFM image (Figure 16e), it looks like this is what happened in our case. The left part of the circle edge is lower in height than the

right part. The 15 minutes of hydrogenation seems long enough for H_2 bubbles to grow, thus creating localized "protection" against etching. Here, the uncompleted hydrogenation of the surface as well as the circular features seen on the AFM image result in a roughened surface prone to oxidation. The presence of unremoved SiO_2 islands can lead to an inhomogeneous functionalization of the SiH surface with organic molecules.

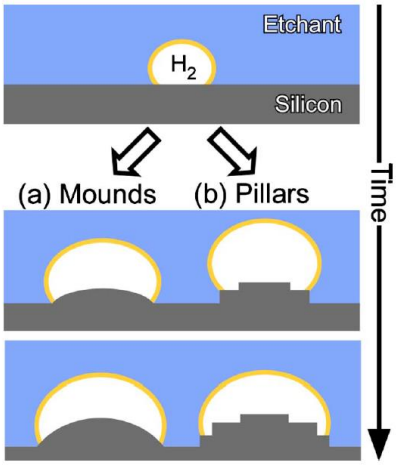

Scheme 9 : Formation of mounds and pillars structures during silicon etching.[68]

Other phenomena can happen, including coalescence of the H_2 bubbles as shown in Scheme 10. In that case after coalescence, the bigger H_2 bubble is exposed to the etchant solution, coalescence leads to formation of small droplets that favor the creation of micro pits on the surface. The symmetric circular features on the right side of Figure 16b (in the yellow square), suggests that coalescence has indeed taken place at this position.

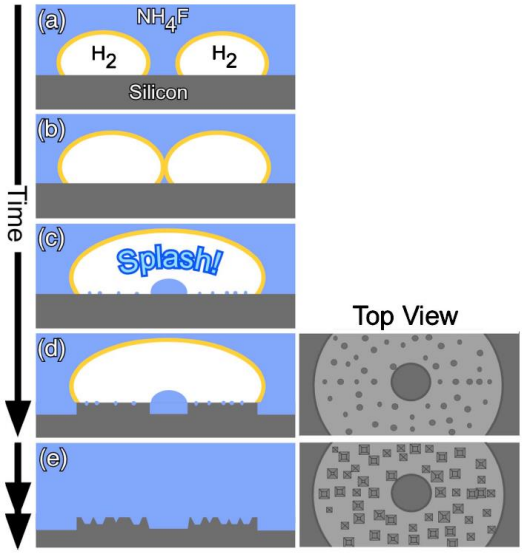

Scheme 10 : Circular etch pits formation by successive H_2 bubbles coalescence and disappearance.[68]

Due to the surface roughening observed in AFM images by the 15 minutes immersion of the substrate in 40% NH_4F solution, the immersion time was subsequently reduced to 2min30 as previously reported.[43]

Moreover, the storage of the substrate inside a Ar-purged or N_2-purged vial between the round trips between the Chemistry laboratory and the FTIR spectrometer was found to be the best solution to restrain the formation of oxide. However, reactions with moisture/water adsorbates are not completely avoidable.[69] Thus, another bath of the substrate in a 40% NH_4F solution for 1 minute followed by a quick rinse with H_2O and drying under N_2 gas was performed back in the Chemistry laboratory, right before hydrosilylation. Note that, as the reference spectrum of the SiH surface was recorded before this second bath, the Siester/SiH differential spectrum obtained in Figure 17 can not be quantitative in determining the percentage of Si-H bonds that have reacted with the neat alkene.

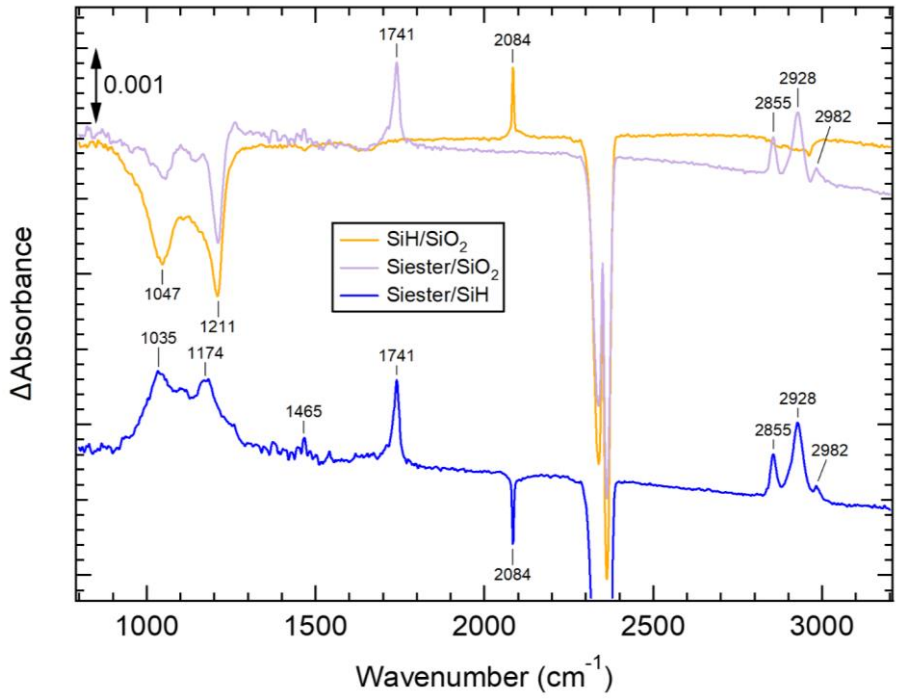

Figure 17 : Differential spectra of the SiH and Siester surfaces obtained when the immersion in NH_4F was reduced from 15 minutes to 2min30.

Using a reduced immersion time in NH_4F solution has improved the IR differential spectra. As seen on the Siester/SiH spectrum, oxide has still been formed after hydrosilylation as suggested by the Si-O-C bond vibration at 1174 cm^{-1} and the increase in both TO and LO phonon modes of SiO_2 at 1035 and 1211 cm^{-1}, respectively. However, the area of the oxide band has decreased compared to the Siester/SiH spectrum (Figure 14) when the surface was immersed for 15 minutes in NH_4F solution.

The surface was then studied by AFM in which circular features were less present on the surface but not completely suppressed (Figure 18a). A circular feature was found on the surface, and exhibits only a ~6 nm boundary, way lower than that of the one in Figure 16.

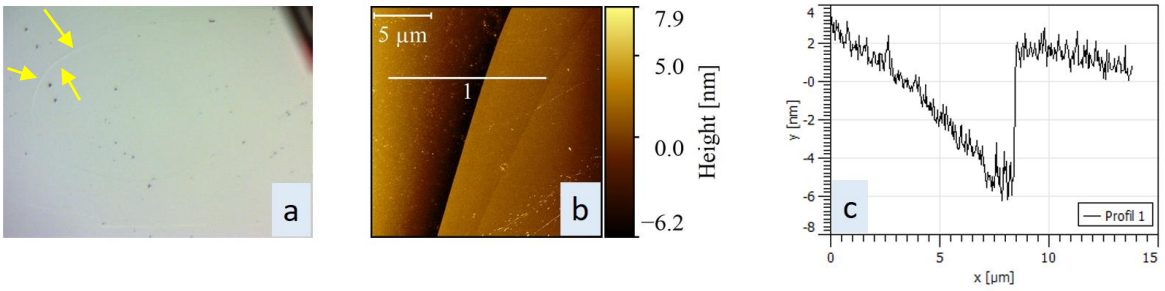

Figure 18 : Investigation on possible traces of H2 bubbles when the hydrogenation duration is reduced to 2min30, using AFM. An engraved feature is discernable on the optical image (a). A further look with AFM image (b) confirmed the engravement measured here at 7-10 nm deep on the profile (c).

As the reduced immersion time in NH_4F solution was found to reduce the roughening of the surface, we decided to keep on using the 2min30 immersion. Now that the SiH surface is formed, it is ready to react with the 1-alkene.

II.2.b. Hydrosilylation

The first hydrosilylation procedure used in Dallas involved performing it overnight at 200°C under a continuous flow of N_2. However, back in Paris, the same procedure was found to form oxide as suggested by ellipsometry measurements that gave thicknesses higher than 2.0 nm, as well as in the differential IR spectra in which bands around 1000-1200 cm^{-1} are obviously seen after hydrosilylation and attributed to oxide (Figure 14). As the results were not satisfying, we needed to play with different parameters in order to find the ones that would give thicknesses compliant with the alkene molecule, as well as limited oxidation on the IR spectra. The 1-alkene chosen was ethyl undecylenate having a theoretical total length of 1.78 nm.[70,71] Once grafted on the surface, the thickness of the organic monolayer was expected to be in the range 1.6-1.7 nm[40,43] indicating a tilt angle of 30-23° to the surface normal.

As the previous study on etching parameters was carried out at the same time, the initial hydrosilylation procedure used involved substrate that has been immersed in two baths of NH_4F solution: a 15 minutes bath right before IR spectra recording and a 2 minutes bath right before hydrosilylation due to the round trip to the Chemistry laboratory. First tests were performed

using Si wafers purchased from Neyco (FZ, double-side polished, 0.1-10 Ω.cm, *n*-doped). However, reproducibility issues occurred: specially, thicknesses obtained after hydrosilylation were higher than 2.0 nm. Different parameters were thus investigated to try to figure out the reproducibility issue: the cleaning after hydrosilylation, the commercial alkene solution, the etching/hydrogenation process, wafer suppliers and the hydrosilylation duration were studied and will be discussed below.

Cleaning after hydrosilylation

After an overnight hydrosilylation (~14h30-16h), the sample was rinsed with ethyl acetate and immersed in boiling dichloromethane for a few seconds. After a dry with N_2 gas, the thicknesses of the organic layer were measured. All hydrosilylation performed using this procedure led to higher thicknesses than the expected one, ranging from 1.9 to 4.6 nm as depicted by the brown histogram in Figure 19. Sonication baths in ethyl acetate and dichloromethane were thus added to remove the physisorbed species,[42] and seemed to be efficient to decrease the thicknesses or the organic layer, now ranging from 1.7 to 3.2 nm as depicted by the green histogram of Figure 19. The resulting thicknesses after sonication baths support the covalent Si-C link.

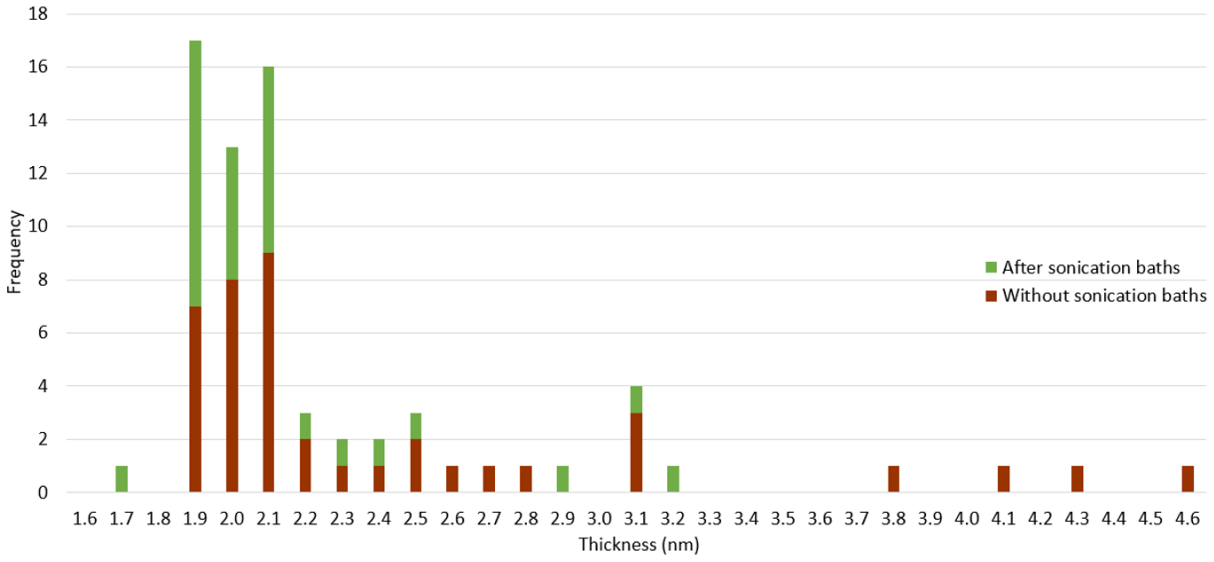

Figure 19 : Histograms of the thicknesses of the organic layer (ester-terminated) measured by ellipsometry after an overnight hydrosilylation. Brown histogram shows the values obtained after hydrosilylation after a simple rinse with ethyl acetate and immersion in boiling dichloromethane. Green histogram shows the values obtained when sonication baths in ethyl acetate and dichloromethane (5-10 minutes each) are added.

Neat alkene

As it seemed that the best results were obtained with a freshly opened commercial bottle of ethyl 10-undecenoate, we believed that the problem could be due to the neat alkene. The latter was indeed kept inside a N_2-purged glove box in Dallas, while it was kept in our case in a non-continuously N_2-purged glove box. An attempt to distill the neat alkene was thus performed under vacuum as the alkene exhibits a boiling point at 258-259°C. The alkene was successfully distilled under vacuum at 130°C before use. After several freeze-pump-thaw cycles, the alkene was allowed to react with an SiH surface. After an overnight hydrosilylation, the Siester spectrum was referenced to the SiH spectrum and the differential spectrum (Figure 20) exhibited a lower oxide increase in the range 1000-1300 cm^{-1}. All the differential spectra Siester/SiH obtained when performing hydrosilylation with a distilled alkene showed a reduced oxide formation, leading us to distill the commercial alkene everytime before use.

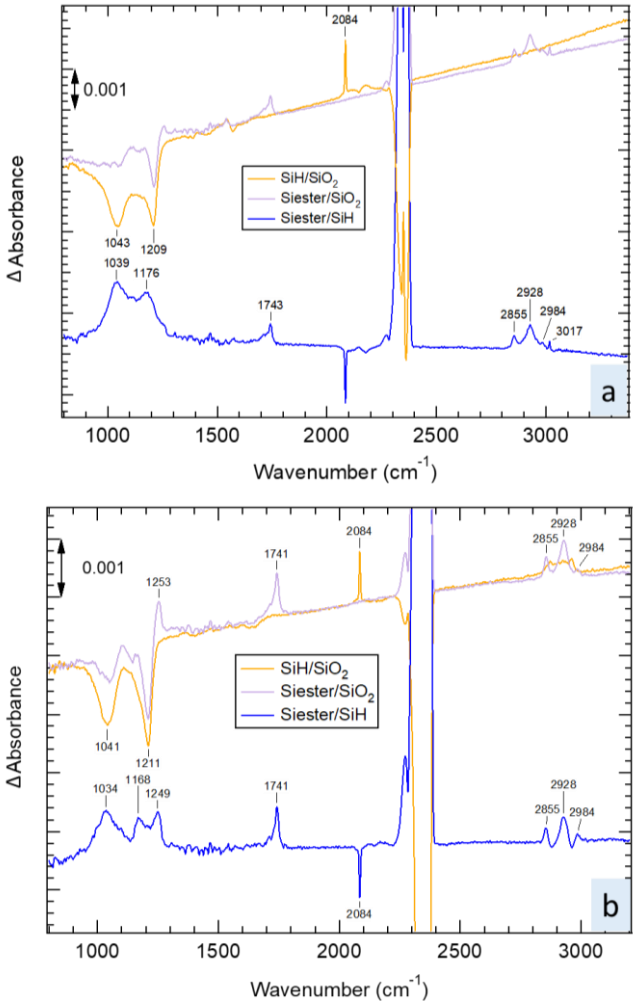

Figure 20 : Differential spectra obtained a) without and b) with distillation of the neat alkene. Oxide formation during hydrosilylation is found to be reduced when alkene is distilled before use.

The parameters modifications did not lead to satisfying enough results: only small improvement in the oxide limitation was done using distilled alkene. The thicknesses measured on the Siester surfaces were in most cases, to not say all, higher than the expected values. The functionalization was hardly reproducible and not homogeneous on both sides of the substrates which could impact the IR spectra. The difference in homogeneity between both sides lead us to re-evaluate the quality of the Si wafer. We thus decided to change the wafer supplier. Si(111) wafer from Sil'tronix were thus purchased with the same properties: FZ, double sides polished, lightly *n*-doped (20-60 Ω.cm), more widely used in the literature. At the same time, the regrown oxide procedure was slightly modified and performed after an immersion of the substrate in a 10% HF solution for ~30 seconds, instead of using a ~25% HF solution for 1 minute.

Hydrosilylation duration

The first test with the Sil'tronix wafer involved an overnight hydrosilylation with a SiH surface, hydrogenated by a 2min30 immersion in 40% NH_4F as the latter was better in reducing the formation of circular features on the surface due to H_2 bubbles. The second 1 minute bath was also kept right before hydrosilylation. As the neat alkene was freshly opened, no distillation of the alkene was performed before use. However, a ~4.0 nm on both sides was measured after hydrosilylation. The thicknesses did not decrease with the ultrasonic bath and the oxide formation is clearly seen on the IR differential spectrum reported in Figure 21 with the appeareance of a band at 1041 cm^{-1} and 1182 cm^{-1} and 1220 cm^{-1}. For a better comparison between the following tests, the differential IR spectrum were baseline-corrected using a polynomial fit.

The hydrosilylation duration was thus modified. As we wanted to compare different hydrosilylation durations, no distillation of the alkene was performed as in the first test. The SiH surface was thus immersed inside the degassed ethyl undecylenate for approximately 2 hours instead of almost 16 hours. The oxide formation seems to be restrained as supported by the thicknesses measured: ~2.5 nm on both sides. A ~2.2 nm on both sides was measured after a 1 hour hydrosilylation. The hydrosilylation duration was decreased to 25 minutes and a ~1.9 nm thickness was measured on both sides. We can observe that the increase in the bands at 1041 cm^{-1}, 1182 cm^{-1} and 1220 cm^{-1} tends to be restrained as the hydrosilylation duration decreases.

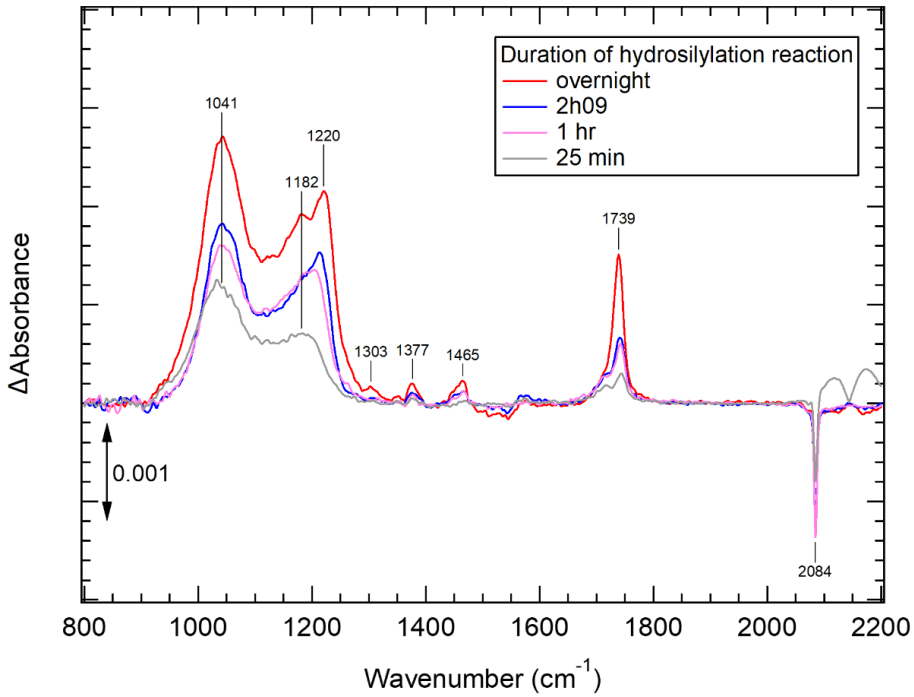

Figure 21 : Siester/SiH differential spectra obtained on Sil'tronix Si surface after an overnight, 2h09, 1 hour and 25 minutes hydrosilylation in a 1-alkene not distilled before use (all baselines were corrected with a polynomial function for clearer comparison and the « raw » spectra are shown in Appendix 2.2).

As the distillation of the commercial alkene was found to restrain the oxide formation on the previously used Neyco wafer, a hydrosilylation was performed for 20 minutes on Sil'tronix substrate with a distilled alkene. The baseline-corrected differential IR spectrum is shown in Figure 22 and the bands between 1000 and 1200 cm^{-1} are obviously lower in intensity than the ones using non-distilled alkene meaning that no or at least less oxide has been formed during hydrosilylation. Ellipsometry measurements also supported this observation. Without distillation of the alkene, the average thickness of resulting organic monolayer is measured at 1.9 (±0.2) nm, while it is measured at 1.7 (±0.1) nm when alkene is distilled. The 1.7 nm thickness is in good agreement with the expected value and is homogeneous on the different areas of the surface. It suggests a tilt angle of the alkyl chains of 23°.

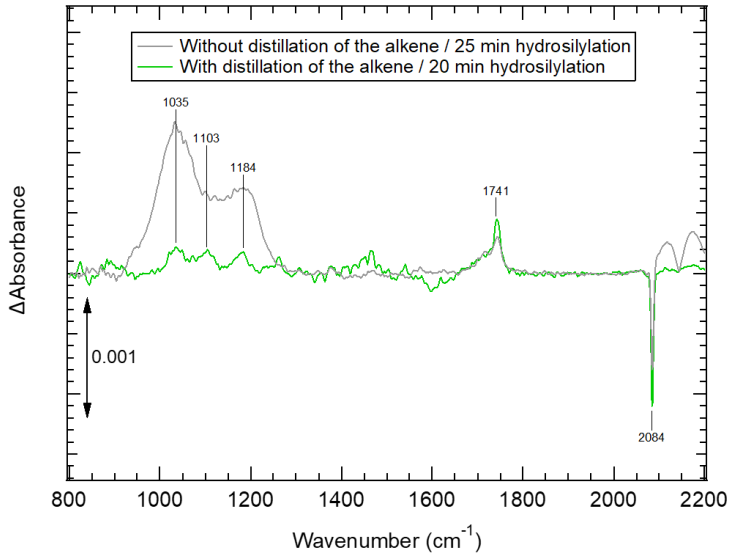

Figure 22 : Siester/SiH differential spectra obtained after 20-25 minutes hydrosilylation reaction using a 1-alkene used as receive in one case, and distilled under vacuum before use in the other case (both baselines were corrected with a polynomial function for clearer comparison and the « raw » spectra are shown in Appendix 2.2).

It was quite surprising at first sight as the hydrosilylation reported in the literature are performed in longer time (4h to overnight). However, with the IR spectra combined with ellipsometry measurements, the best results were obtained with a reduced hydrosilylation duration of ~20 minutes. Thicknesses of the ester-terminated monolayer on Sil'tronix substrates are reported in Figure 23. Even though thicknesses higher than 1.7 nm were obtained in some cases, most of the values measured lied in the range 1.2-1.7 nm, *i.e.* the alkyl chains are tilted from 50° to 23° with respect to the normal of the surface.

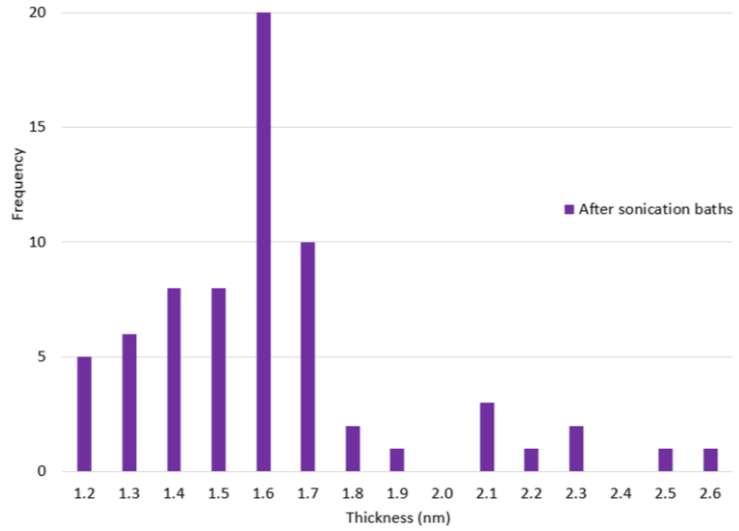

Figure 23 : Histogram of the thicknesses of the organic layer (ester-terminated) measured by ellipsometry after a ~20 minutes hydrosilylation and sonication baths in ethyl acetate and dichloromethane (5-10min each).

Several parameters were changed from the initial procedure learnt in Dallas. To summarize, the alkene was always distilled prior to use. The Neyco wafers did not gave the expected thickness of the organic layer and the thicknesses were not homogeneous so we changed the supplier and other tests were carried out on Sil'tronix wafers which overcome the inhomogeneity issue. Finally, the hydrosilylation duration was reduced to 20 minutes.

II.2.c. Post-functionalization

Ester functions hydrolysis

The procedure learnt in Dallas for the post-modification of the Siester surface was kept. After hydrolysis of the ester functions, a decrease of 0.2-0.3 nm was expected, corresponding to a loss of the ester functions of the alkyl chains. Thicknesses of the COOH-terminated organic monolayer are shown in Figure 24, and compared to the previously obtained ester-terminated organic monolayer. In our case, a decrease of 0.1 to 0.4 nm was measured.

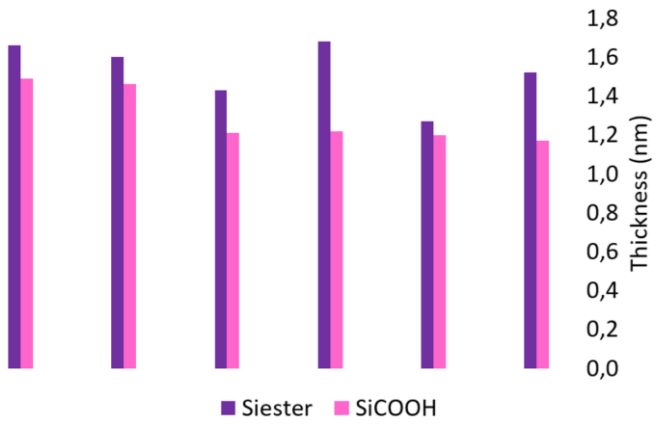

Figure 24 : Histogram of average organic monolayer thicknesses on both sides of the surface, after hydrosilylation and sonication baths (purple), and after hydrolysis (pink), for six different sets of experiments.

The loss of the ester functions was confirmed by FTIR spectroscopy. The differential spectra SiCOOH/Siester always gave the same feature, *i.e.* a band increase at 1718 cm^{-1} corresponding to the C=O stretching of the carboxylic acid, and a band decrease at 1743 cm^{-1} corresponding to the C=O stretching of the ester functions, as shown in Figure 25. The band decrease around 2984 cm^{-1} corresponding to the CH_3 of the ester function and the increase of the band at 1413 cm^{-1} which appear due to the C-O stretching and O-H deformation[41,43,72,73] also go the right way in letting us conclude that this step worked quite well without formation of oxide.

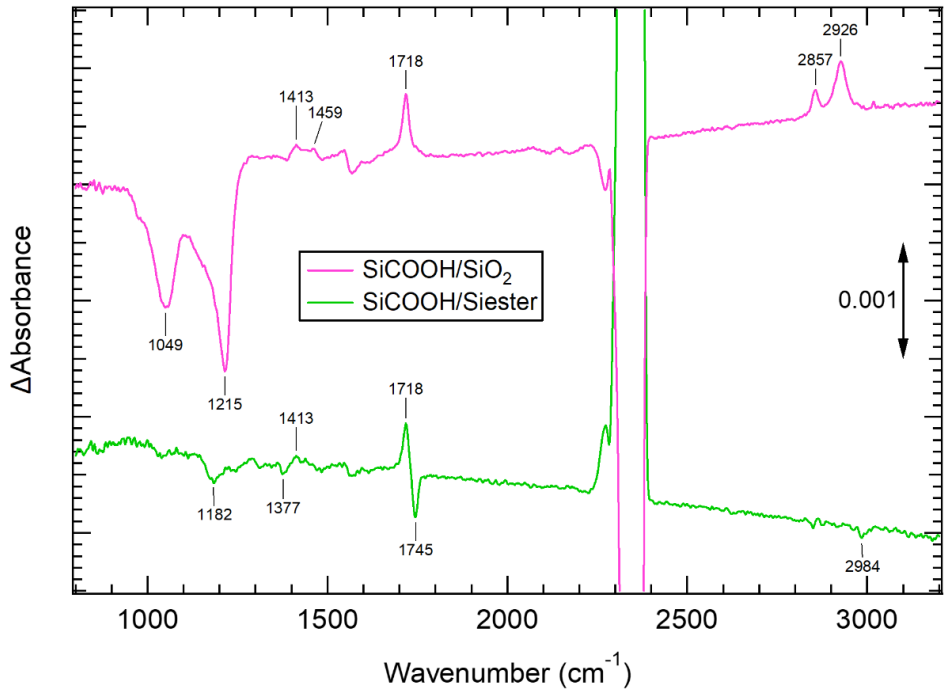

Figure 25 : SiCOOH differential spectra obtained after ester functions hydrolysis.

Peptide coupling

The procedure learnt in Dallas for this last step was also kept and was inspired by previous reports of Chabal's group.[61,74,75] It involves the immersion of the freshly COOH-terminated surface in a *N*-(3-Dimethylaminopropyl)-*N'*-ethylcarbodiimide hydrochloride/4-Morpholineethanesulfonic acid (EDC.HCl/MES) buffer solution at pH=6 before addition of ethylenediamine. The resulting differential spectra are shown in Figure 26. On the $SiNH_2$/SiCOOH differential spectrum (in red), the disappearance of the band corresponding to $\nu_{COOH}^{C=O}$ at 1720 cm^{-1} is clearly visible, suggesting the loss of the carboxylic acid functions. On the other hand, less intense bands appeared at ~1643 cm^{-1} and ~1560 cm^{-1} and have been attributed to an amide link.[40] The band at 1643 cm^{-1} can be attributed to $\nu_{amide\ I}^{C=O}$. The amide I function exhibits indeed a strongest band corresponding to the C=O stretching mode. The assignment of the band at 1560 cm^{-1} is less obvious and probably does not correspond to the amide I function. Instead, it could be attributed to δ_{sc}^{N-H} of a primary amine. This band was more specifically found at 1570 cm^{-1} in several reports in the case of an APTES SAM,[65,76] and the spectrum of the ethylenediamine (see Appendix 2.3) displays a strong band at 1595 cm^{-1}.

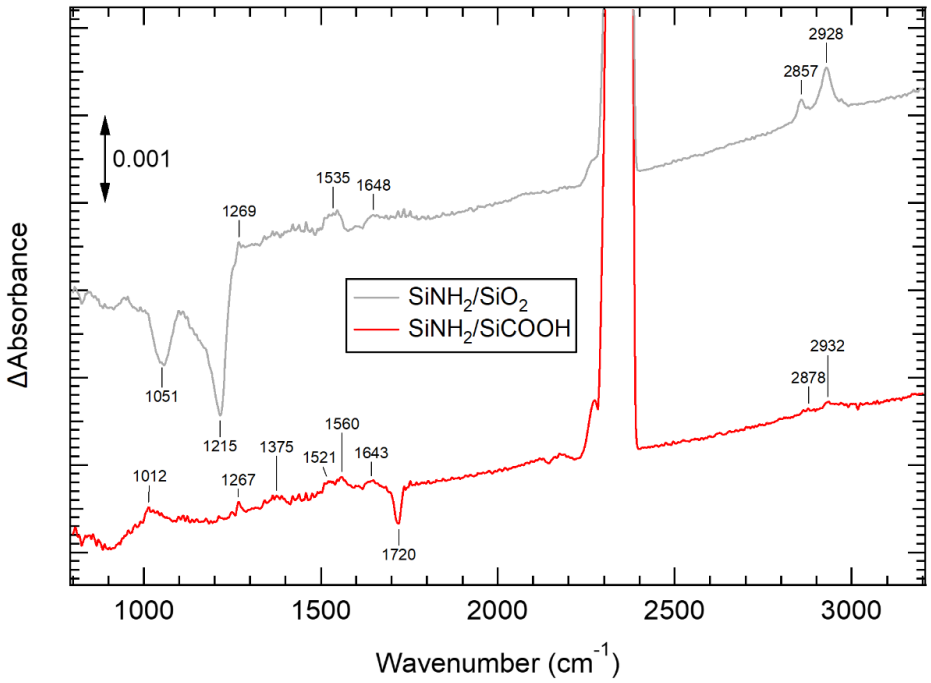

Figure 26 : $SiNH_2$ differential spectra obtained after reaction of the activated COOH surface with ethylenediamine.

The length of the grafted NH_2-terminated alkyl chain on Si(111) surface is expected to be ~1.8 nm if the chain is held perpendicularly to the surface.[70,77] With the tilt angle of 23°-30° (value from the expected ester-terminated alkyl chain on Si(111)), the thickness of the organic monolayer is expected to lie in the range 1.5-1.7 nm. Figure 27 depicts the average thicknesses measured after reaction with EDC.HCl and ethylenediamine (grey histogram) which effectively lie in the range 1.5-1.8 nm except for one value for which the thickness was 2.0 nm.

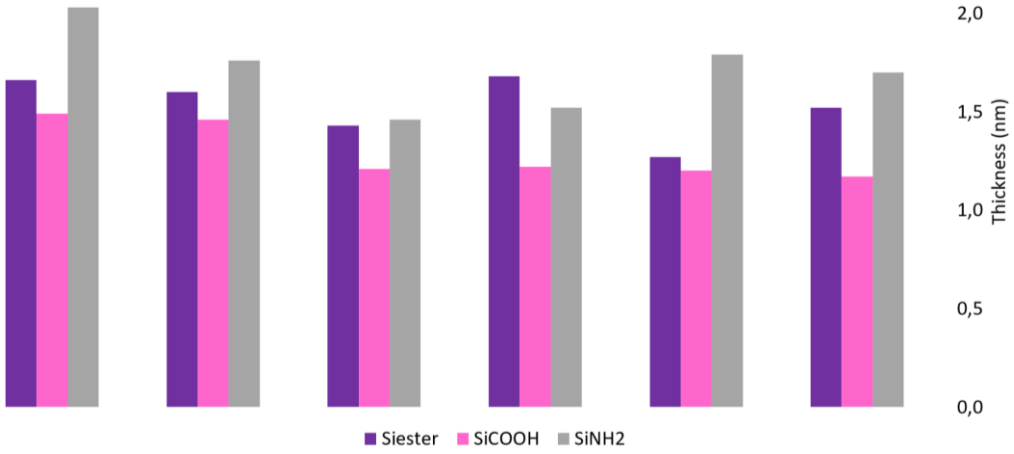

Figure 27 : Histogram of average organic monolayer thicknesses on both sides of the surface, after hydrosilylation and sonication baths (purple), and after hydrolysis (pink), and after reaction with the diamine (grey) for six different sets of experiments.

After determining the best experimental procedure parameters thanks to the combination of FTIR spectroscopy and ellipsometry to get at the end, in our conditions, a satisfying $SiNH_2$

surface, a final experiment was performed with the parameters selected for each step. The typical spectra obtained for Siester, SiCOOH and $SiNH_2$ surface are referenced to the SiH surface in Figure 28 (the corrected-baseline differential spectra are shown in Appendix 2.2). It is worth noting that the peptide coupling step is probably not quantitative. Indeed, some carboxylic acid functions still remain after this last step, as attested by the band at 1724 cm^{-1} in the $SiNH_2$/SiH spectrum (pink curve), corresponding to $\nu_{COOH}^{C=O}$.

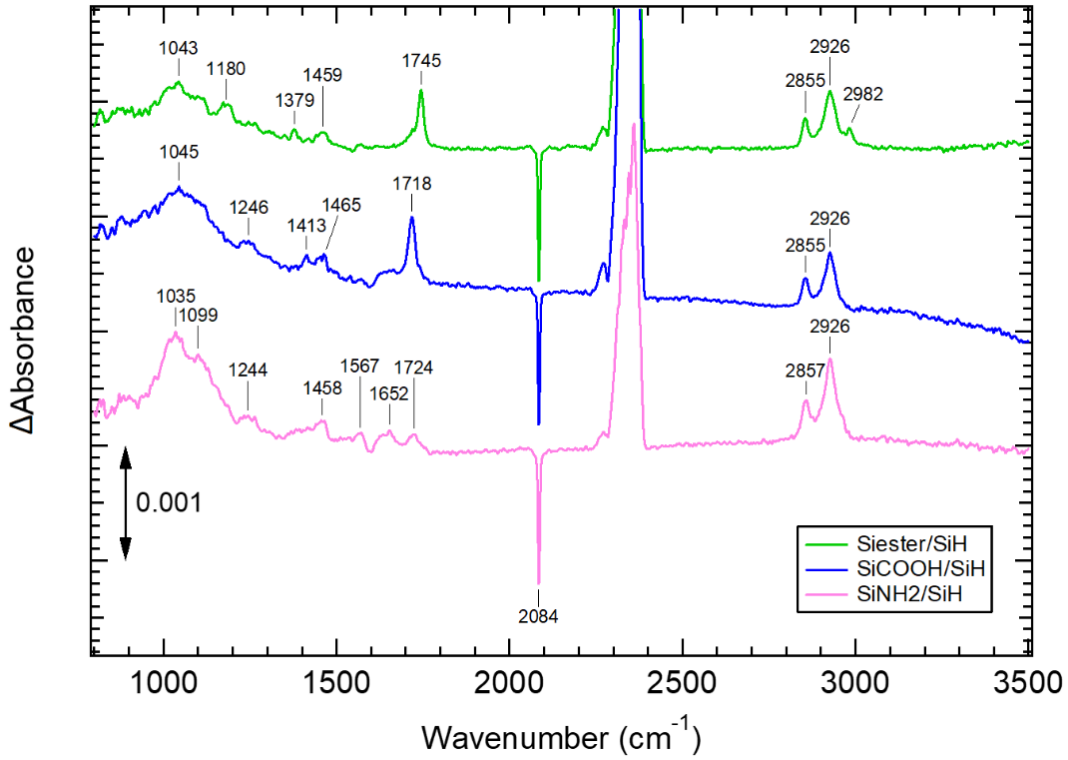

Figure 28 : Typical differential spectra obtained for Siester, SiCOOH and $SiNH_2$ surfaces with the optimized parameters selected for each surface modification step.

The Si(111) surface functionalization was thus readjusted from the original procedure learnt in Dallas. Hydrogenation and hydrosilylation duration were both decreased, to 2min30 and 20 minutes respectively. The hydrosilylation was performed with distilled alkene solution. No improvement of the hydrolysis and formation of NH_2-terminated surface procedures had to be found. Finally, we were able to functionalize Si(111) surface in a reproducible way.

II.3. Si(100) functionalization

For the study of the Si(100) procedure, wafers were purchased from Sil'tronix with the same specifications: FZ, double sides polished, lightly *n*-doped (Ph, 20-60 Ω.cm). An overview of the whole functionalization procedure on Si(100) substrates is given in Scheme 11, and the detailed procedure is described in Appendix 5.3.

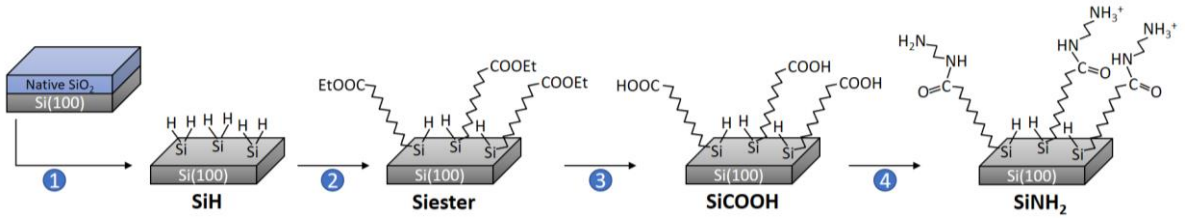

Scheme 11 : Functionalization procedure on Si(100) to successively obtain the "SiH" surface, "Siester" surface, "SiCOOH" surface and "$SiNH_2$" surface.

II.3.a. Etching

The etching procedure of Si(100) surface differs from the one of Si(111) surface. Stability of the H-Si(100) bond was studied using different etching procedures. We have to keep in mind that the Si(100) substrate serves as a test platform to help us determine the best parameters to further reproduce the procedure on SOI substrate, as we can not follow the surface modification quality on SOI substrate, the latter being not transparent to IR light. For the etching procedure, no NH_4F solution was used. Indeed, it is an anisotropic etchant that will preferentially attack the planes other than the (111) plane, resulting in a rougher Si(100) surface.[32,78,79] Only HF will be used for the etching process on Si(100) surface.

After cleaving, the substrates were degreased using the same procedure as for Si(111) substrate. Keeping in mind that the substrate immersion time in HF bath has to be low to avoid damaging of the SOI substrate, five cleaning/etching procedures were subsequently studied: i) ~50 min in H_2SO_4:H_2O_2 (3:1 v/v) followed by a 1 minute 24.5% HF bath,[49] ii) usual RCA1/RCA2 cleaning (15 minutes in each solution) followed by a 1 minute 24.5% HF bath, iii) RCA1/RCA2 cleaning followed by a 10 seconds 10% HF bath, iv) RCA1/RCA2 cleaning followed by a 5 seconds 10% HF bath, v) RCA1/RCA2 cleaning followed by a 5 seconds 5% HF bath.

Figure 29 depicts the differential spectrum of the SiH surface obtained following the etching procedure ii referenced to the Si-SiO_2 surface spectrum. The bands at 1047 and 1213 cm^{-1}

appear as negative bands as oxide was removed. The feature between 2000 and 2200 cm^{-1}, however different from the sharp band of the monohydride Si-H, is characteristic of an HF-treated Si(100) substrate. Indeed, a broad band is observed. Three bands can be distinguished at 2086, 2113 and 2139 cm^{-1} corresponding of a mixture of Si-H vibrations of strained and unstrained Si dihydrides[80–82]. The same broad band is obtained for all the etching procedures studied.

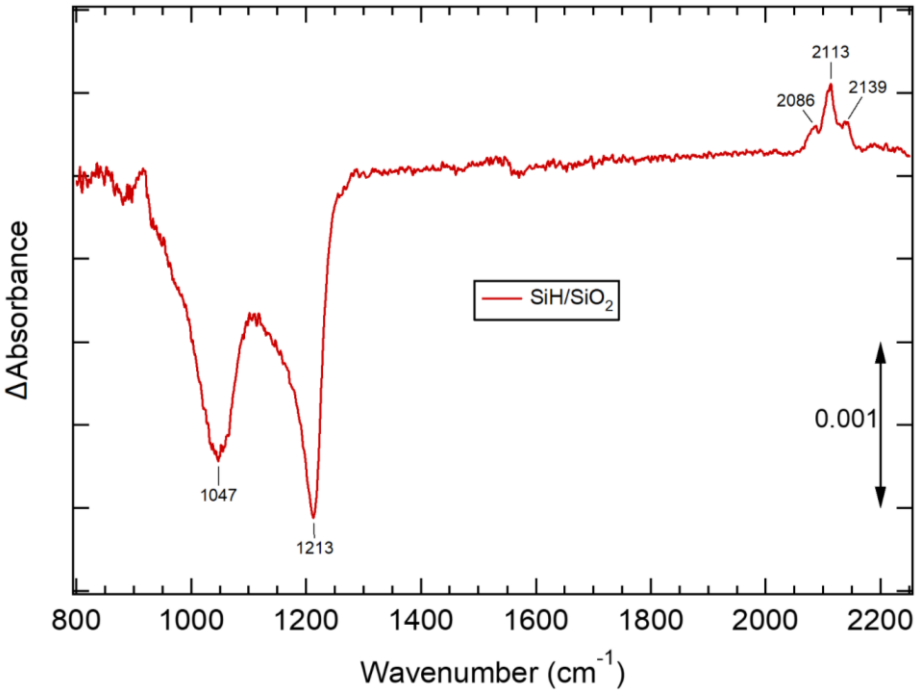

Figure 29 : SiH/SiO_2 differential spectrum using Si(100) surface.

The Si-H stability was studied as follows: after cleaning of the surface, three spectra of the SiO_2 surface were recorded. The etching procedure was then performed and other spectra were recorded and successively referenced to the SiO_2 surface spectrum. The area of the broad Si-H band was measured for each differential spectrum and the values are reported in Figure 30. At first sight, all the measured area of the Si-H broad band decreased in a similar fashion with time. The first etching procedure involving H_2SO_4/H_2O_2 cleaning was inspired by Seitz *et al.*[49] Using the similar etching procedure in 24.5% HF but switching the cleaning process with the usual RCA1-RCA2 clean provides higher Si-H band area, as depicted by the orange dots.

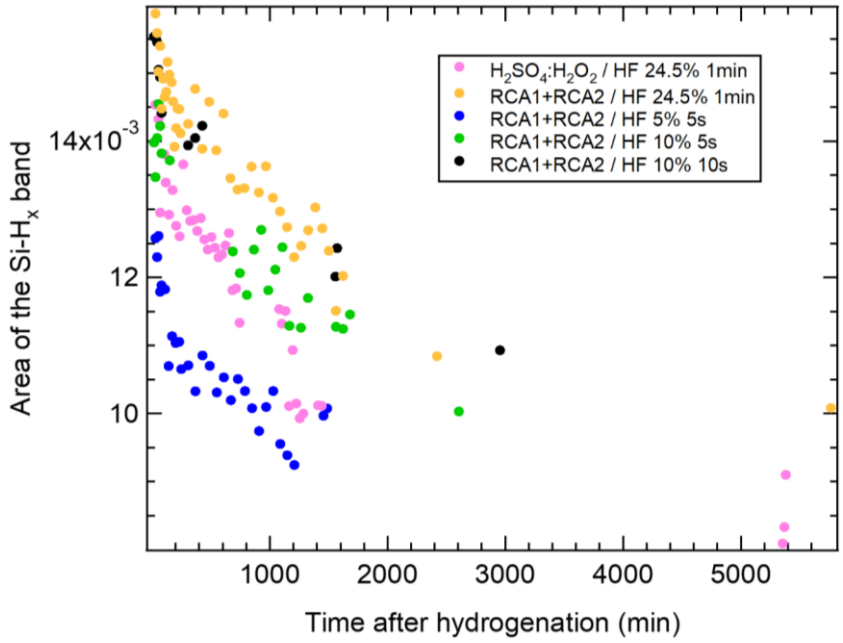

Figure 30 : Area of the Si-H_x band measured over time on the SiH/SiO_2 differential spectra.

We thus observe that the 24.5% HF for 1 minute was the best procedure. However, to avoid damaging of the buried oxide of the SOI substrate, the concentration of the HF solution has to be lower.

Tests were thus performed using a 5% and 10% HF bath. For a substrate immersion of 5 seconds, the 10% HF bath led to a higher Si-H_2 density than that using the 5% HF bath. The immersion time was increased to 10 seconds with the 10% HF bath and results obtained were rather comparable with the etching in 24.5% HF bath. **The etching procedure consisting in an immersion of the substrate in a 10% HF solution for 10 seconds was thus kept as a SOI-compatible etching procedure.**

II.3.b. Hydrosilylation

The hydrosilylation process on H-Si(100) was carried out first using the best etching procedure involving a 24.5% HF bath. The same hydrosilylation procedure as on H-Si(111) was reproduced, involving the incubation of the substrate in a distilled and degassed alkene solution for 20 min at 200°C. However, the thickness of the layer grafted onto the surface was measured to be 2.1 nm, higher than the expected value. Moreover, as shown in Figure 31, a positive broad band appear in the differential spectrum Siester/SiH in the 1000-1300 cm^{-1} region, suggesting oxide formation.

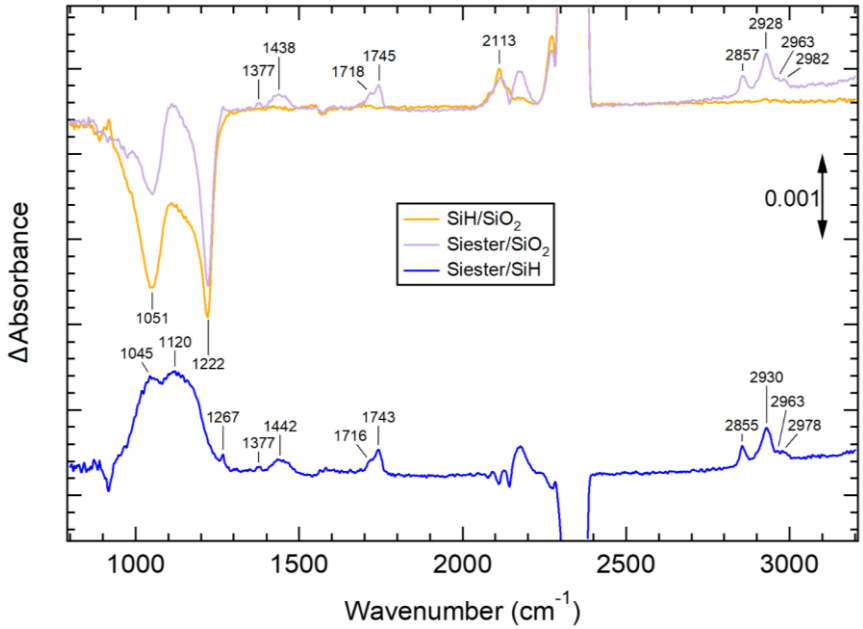

Figure 31 : SiH and Siester differential spectra obtained on Si(100) surface using the same hydrosilylation procedure as the one of Si(111).

The temperature was thus decreased to 150°C and another hydrosilylation was performed for 20 minutes. A 1.5-1.6 nm thickness was measured on both sides, and a final thickness of 1.4 nm was obtained after sonication baths in ethyl acetate and dichloromethane. The broad band in the differential spectrum in Figure 32 after hydrosilylation is still present but with a lower intensity.

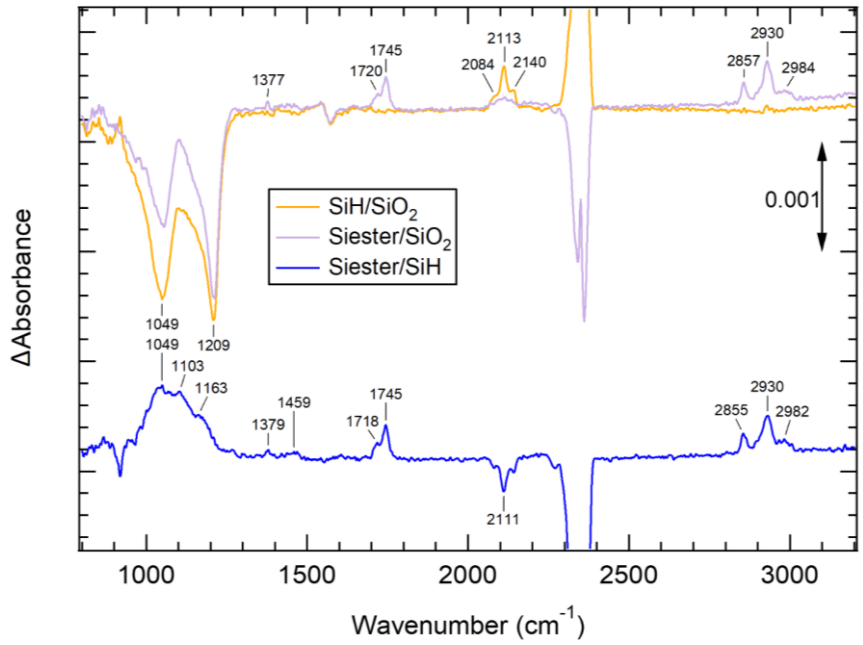

Figure 32 : SiH and Siester differential spectra obtained on Si(100) surface using the same hydrosilylation procedure as for the Si(111) surface but here the temperature was decreased from 200°C to 150°C.

The hydrosilylation on a Si-H obtained with a 1-minute immersion in a 24.5% HF solution did not gave satisfying results to use them as a reference. Nevertheless, the decrease of oil bath temperature for the hydrosilylation was found to give better results both in IR and ellipsometry and was thus kept for the further experiments.

The procedure involving a 10 seconds 10% HF bath was then tested. To improve the results, two HF baths were used, similar to the two NH_4F baths used before functionalization of Si(111): the Si(100) substrate was immersed 10 seconds in a 10% HF solution prior to the SiH surface spectra recording, and was immersed once again right before hydrosilylation. The organic layer was measured to be 1.4-1.5 nm thick after hydrosilylation. The differential spectrum obtained is shown in Figure 33 still depicts a positive broad band in the range 1000-1300 cm^{-1} but with a lower intensity.

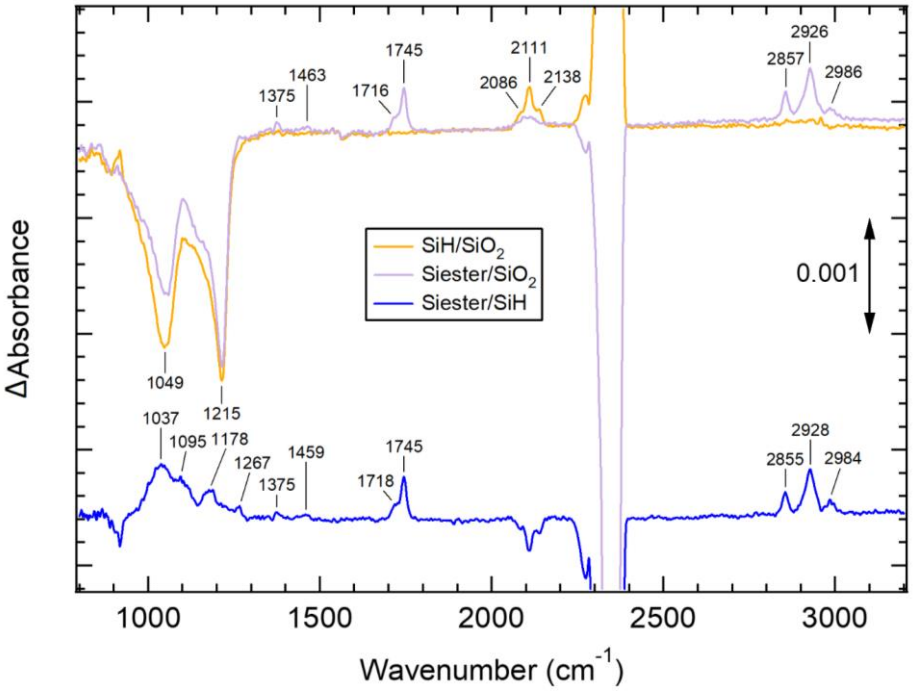

Figure 33 : SiH and Siester differential spectra obtained on Si(100) surface using the hydrosilylation 150°C 20 min, but with a total of 2 HF baths 10% 10s before hydrosilylation.

To improve the results and avoid oxidation growth, other experiments were performed but they turned out to be hardly reproducible. As the oxide formation was found, not surprisingly, more difficult to avoid, this hydrosilylation procedure involving two 10% HF baths was found to be the best one.

Before switching to SOI substrates, we wanted to free ourselves from recording IR spectra as the latter would not anyway be performed on SOI substrates. We thus performed a

hydrosilylation using a (100)SiH surface prepared in only **one bath of 10% HF for 10s**, similarly to the procedure that will be reproduced on SOI substrates. After etching, the substrate was quickly introduced in the distilled and degassed alkene solution for 20 minutes at 150°C. As we faced an ellipsometer breakdown, the surface was analyzed after hydrosilylation by X-ray photoelectron spectroscopy (XPS) and the spectra of the Si 2p and C 1s regions are shown in the Figure 34.

A low quantity of oxide has been formed after hydrosilylation as depicted by the presence of a broad peak at 102.0-104.0 eV even if the substrate was given to XPS analysis as fast as possible. A peak between 289.0 and 290.0 eV in the C 1s region is observed and corresponds to the ester function[40]. However, the intensity is quite low leading us to wonder if the hydrosilylation duration was long enough to allow the grafting of the ester-terminated alkyl chains.

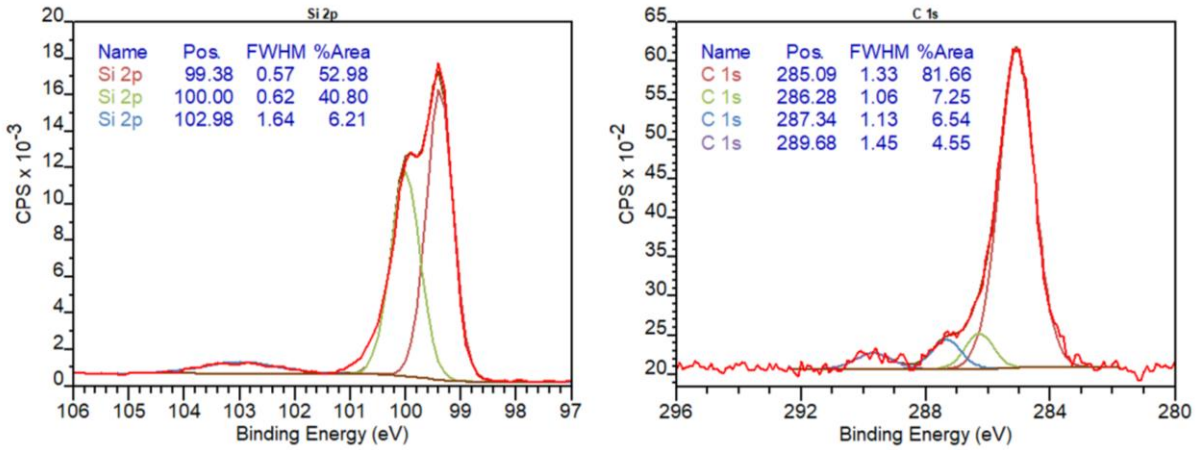

Figure 34 : XPS spectra (Si 2p and C 1s regions) after a 20 minutes hydrosilylation reaction at 150°C.

Another hydrosilylation was thus performed on another (100)SiH surface. The cleaning and etching steps were the same as on the previous substrate, but the incubation of the SiH surface was increased up to 1 hour, still at 150°C. The resulting Siester surface was analyzed by XPS and spectra of the Si 2p and C 1s regions are shown in Figure 35. While the Si 2p region is similar to the previous substrate, the C 1s region exhibits one difference as the peak between 289.0 and 290.0 eV has a higher intensity. Since the C 1s region was improved without oxidation of the substrate, the hydrosilylation duration was thus modified and the parameters selected are the following: an immersion of the substrate in 1-alkene for 1 hour at 150°C.

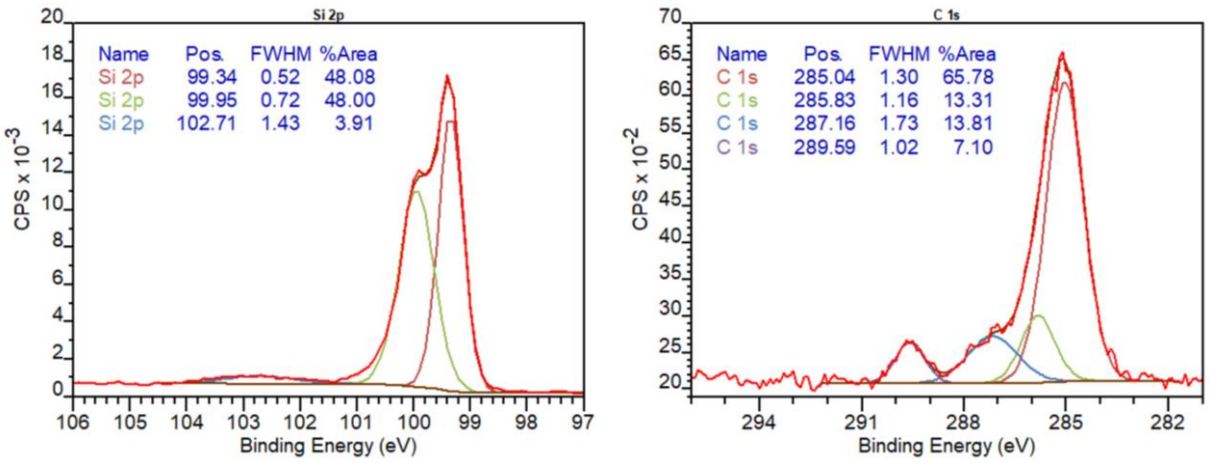

Figure 35 : XPS spectra (Si 2p and C 1s regions) after a 1 hour hydrosilylation reaction at 150°C.

To have as much information as possible despite the ellipsometer breakdown, different hydrosilylation procedures were tested before switching to SOI substrates and the resulting differential IR Siester/SiO_2 spectra are shown in Figure 36.

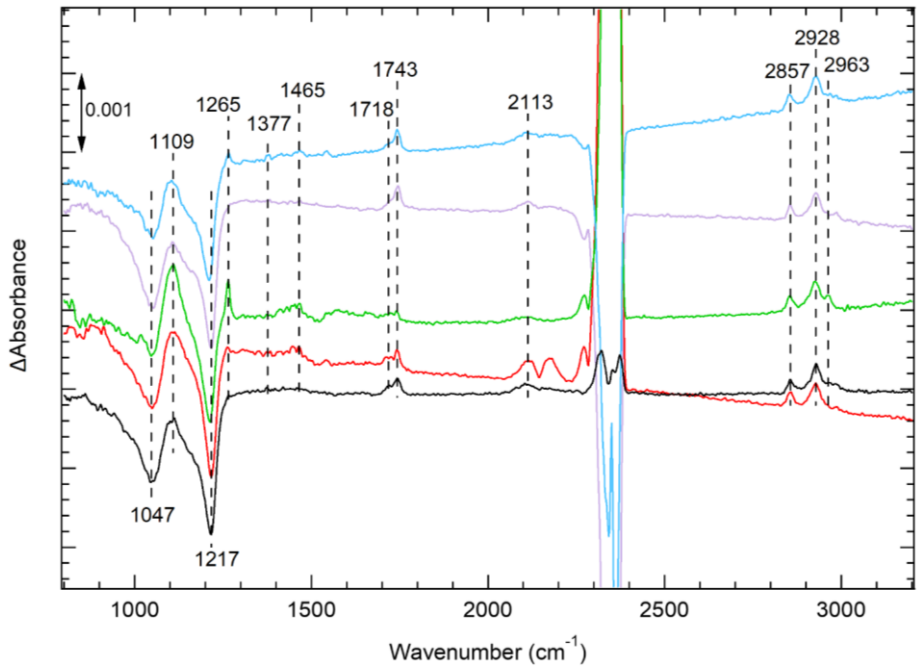

Figure 36: Siester/SiO_2 differential spectra obtained using different hydrosilylation procedures. The etching procedure involved a unique substrate immersion in 10% HF 10 seconds for the blue, purple, green and red curves, while the immersion time was increased to 30 seconds in the case of the black curve. Hydrosilylation parameters were the following: 20 minutes at 150°C (blue and black curves), 1 hour at 150°C (purple curve), 2 hours at 150°C (green cruve) and 1 hour at 170°C (red curve).

We first wanted to compare the incubation time at 150°C by FTIR spectroscopy: three hydrosilylations were performed for 20 minutes, 1 hour and 2 hours on a freshly prepared (100)SiH surface obtained after an unique 10% HF bath for 10 seconds. As the reference spectrum is SiO_2 and no SiH, the oxidation of the surface can be guessed by the shape of the negative Si-O-Si band. Indeed, if oxide has been formed during hydrosilylation, it will be seen by the growth of band(s) in the 1000-1300 cm^{-1} region. In our case, a band around 1110 cm^{-1} appeared in some experiments and could be attributed to Si-O-C or Si-O-Si vibrations. This band is actually clearly seen in the differential spectrum of the surface that was immersed in the alkene solution for 2 hours (green curve) and appear positive. The same band reaches almost the baseline level in the case of the surface that has been immersed in the alkene solution for 20 min (blue curve) while it stays below it in the case of an immersion for 1 hour (purple curve) which is counterintuitive. We can suppose that in the case of a 20 minutes hydrosilylation, the resulting organic layer obtained is not enough organized leading to a faster reoxidation.
The 1 hour immersion time was then kept and another hydrosilylation was performed at 170°C. Apparently more oxide was formed as suggests by the differential IR spectrum of the corresponding surface (red curve): the band at 1100 cm^{-1} reaches the baseline level.
As the incubation of the surface for 1 hour at 150°C was found to be the best one among the hydrosilylation procedures that were tested and regarding the XPS analysis, a last attempt was carried out using a 1 hour hydrosilylation but with an (100)SiH surface that was prepared in a 10% HF bath for 30 seconds instead of 10 seconds. The idea was to “simulate” the two 10% HF baths that gave the firsts good results. The resulting Siester/SiO_2 spectrum is shown in black and is quite comparable with the spectrum obtained using an HF bath of 10 seconds (purple curve), but the oxide growth still seems to be more restrained in the second case. Moreover, the HF-etching bath at 10% for 30 seconds might be inclined to damage the buried oxide of the SOI substrate.

Unfortunately, due to a lack of time, no more energy was put to figure out a better procedure. **The 1 hour incubation at 150°C was thus kept for the post-modification of the surface and for the SOI functionalization procedure.**

II.3.c. Post-functionalization

Ester functions hydrolysis

The experimental procedure was not changed compared to the one used on Si(111) substrates. However, as the Si(100) is more prone to get oxidized, more care was taken during the substrate incubation in the different solutions. The solutions were degassed before use and an Ar-bubbling was kept during the incubation of the substrate and typical differential spectra are shown in Figure 37. Despite the care we added with the Ar-bubbling, oxide could not be avoided and all the resulting differential spectra SiCOOH/Siester show an increase in the bands at 1020-1060 cm^{-1} and 1100-1200 cm^{-1} after hydrolysis. Note that the differential spectra after hydrolysis were obtained with substrates that have been subjected to a 20 minutes hydrosilylation at 150°C. The thicknesses of the Siester and SiCOOH surfaces prepared in these conditions are shown in Figure 38. A 0.1 nm decrease in thickness is found for all sets of experiment after ester functions hydrolysis, except for the last one, which also suggests oxide growth as the theoretical decrease in thickness is expected to be ~0.2 nm. As we faced off a breakdown of the ellipsometer, no thicknesses of the SiCOOH surface were measured when hydrosilylation involved the previously selected 1 hour incubation at 150°C.

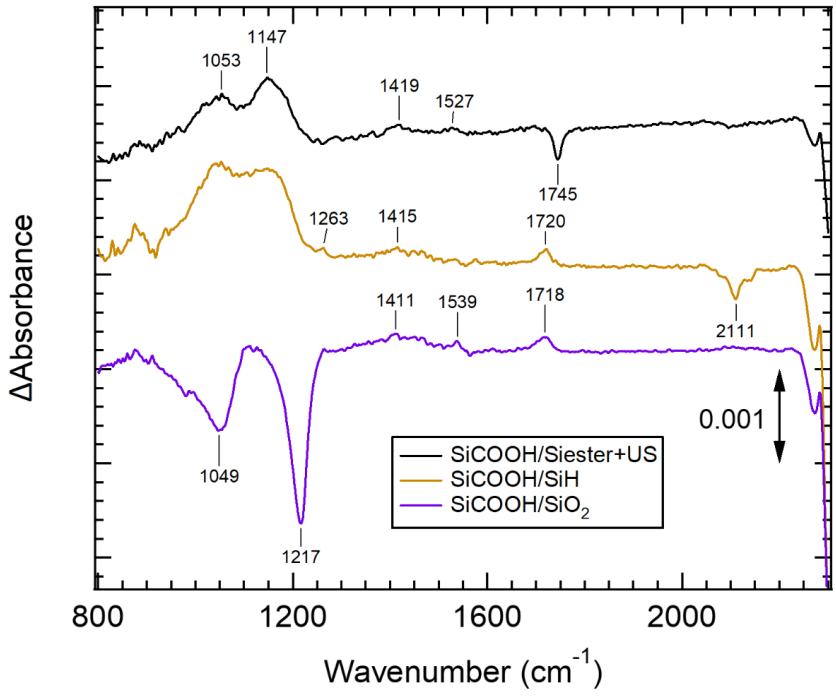

Figure 37 : SiCOOH differential spectra obtained using the same hydrolysis procedure as the one used on Si(111) surfaces, here with degassed solvents and aqueous solution.

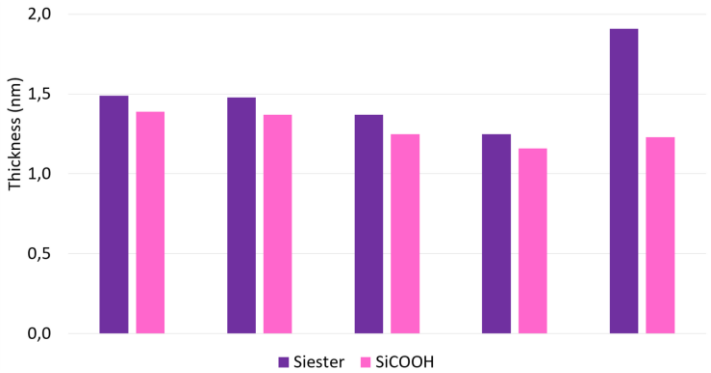

Figure 38 : Histograms of average organic monolayer thicknesses on both sides of the surface, after hydrosilylation and sonication baths (purple), and after hydrolysis (pink), for five different sets of experiments. For these sets, etching was performed using two 10% HF baths (10 seconds each) and a 20 minutes hydrosilylation at 150°C.

Peptide coupling

Again, the same procedure used on Si(111) substrate was reproduced on Si(100) substrate, involving the COOH-terminated substrate immersion in EDC.HCl/MES prior to addition of ethylenediamine to the solution. However, the first test on COOH-terminated Si(100) surface using the aforementioned procedure give rise to a higher quantity of oxide on the surface as shown in the differential spectra on Figure 39. The bands at 1030 and 1197 cm^{-1} are growing during this final step and the resulting $SiNH_2/SiH$ differential spectrum shows a high quantity of oxide that was formed during the overall functionalization procedure. This quantity of oxide was not that high in the case of Si(111), most likely because the latter was better protected with a more compact alkyl chain.

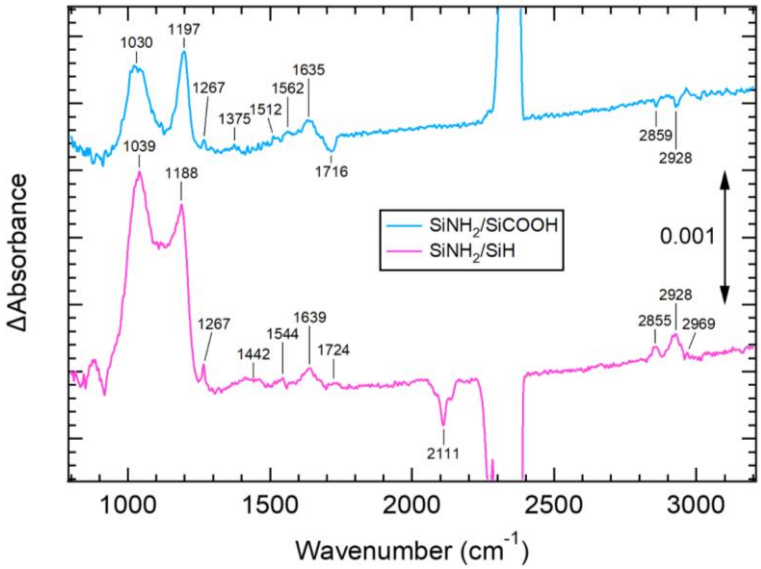

Figure 39 : $SiNH_2$ differential spectra obtained using the same procedure as the one on Si(111) surface.

Another procedure was tested and involved the use of EDC.HCl/*N*-hydroxysuccinimide (NHS) to activate the COOH functions before coupling with the ethylenediamine, as described by Seitz *et al.*[49] The reaction pathway is depicted in Scheme 12 and the formation of succinimidyl ester is expected.

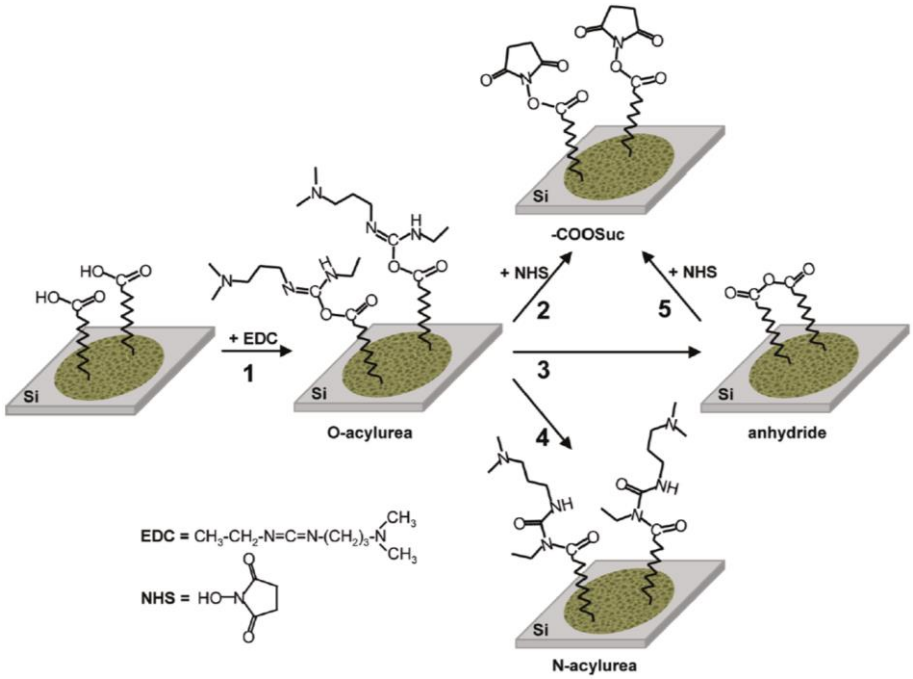

Scheme 12 : SiCOOH surface activation with EDC/NHS. Reaction with EDC (reaction 1) leads to the formation of O-acylurea. Various paths (reactions 2-5) can happen after addition of NHS leading to succinimidyl ester, anhydride or N-acylurea formation.[83] Note that in the case of a peptide coupling with EDC.HCl/NHS, the O-acylurea and N-acylurea compounds are $HN^{+}Me_2$,Cl^{-}-terminated.

The activation step of the carboxylic acid groups worked quite well as suggested by the three positive bands at 1735, 1789 and 1820 cm^{-1} that appear after this step in the differential spectrum as depicted in Figure 40 (green curve), which can be respectively attributed to the $\nu_{asym}^{C=O}$ and $\nu_{sym}^{C=O}$ of the suc-cycle and to the $\nu^{C=O}$ of the suc-ester carbonyl. The thickness of the layer increased from ~1.4 nm after hydrolysis to ~1.7 nm after the COOH activation step which supports the succinimidyl ester formation.

After the reaction with ethylenediamine, the three bands disappeared meaning that they have reacted. However, the oxide quantity formed is quite similar with the procedure involving EDC.HCl/MES.

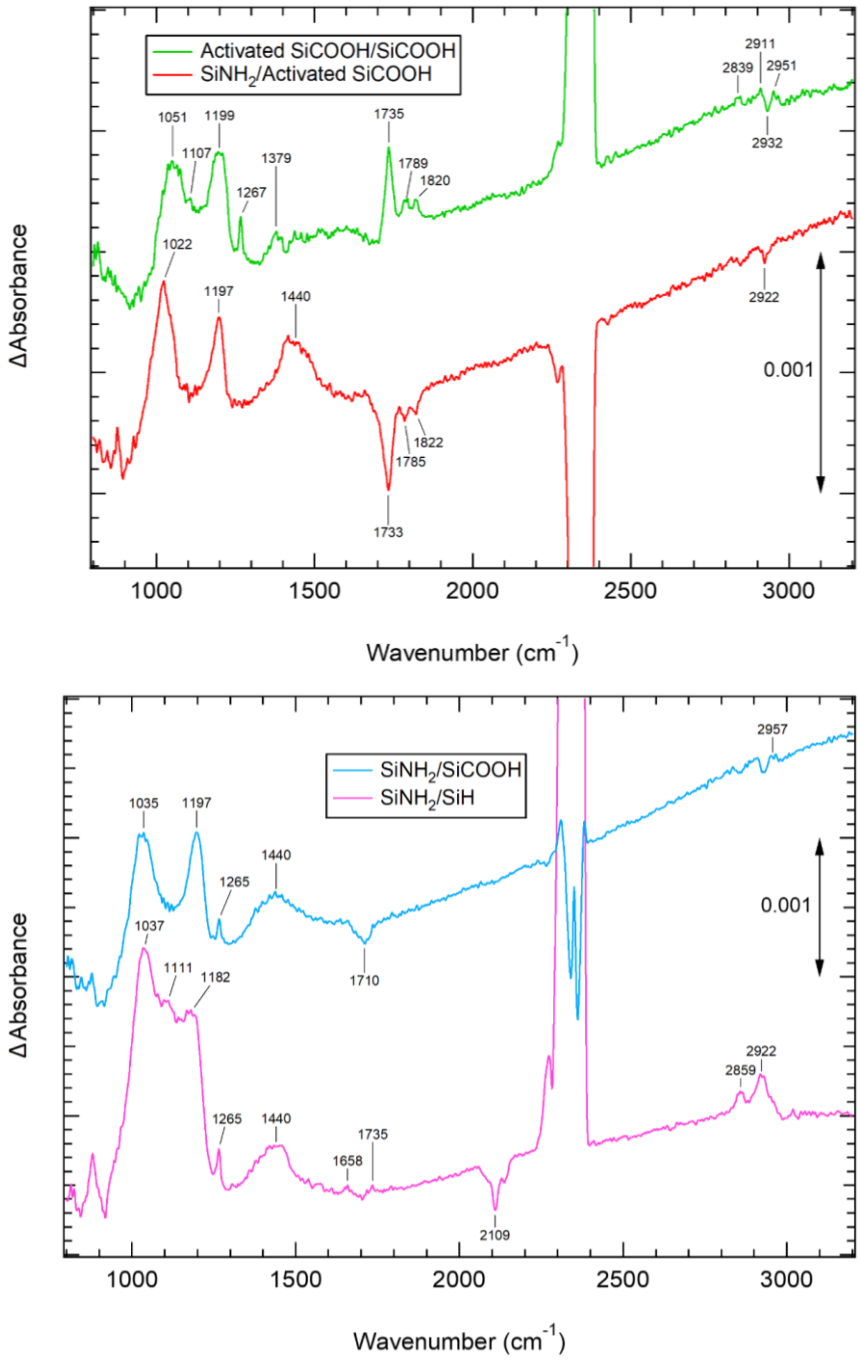

Figure 40 : Activated SiCOOH surface and $SiNH_2$ differential spectra obtained using the EDC.HCl/NHS procedure.

Another procedure was envisioned to get rid of the use of water during the peptide coupling step. The idea was to change the coupling reagent and involved the use of isobutyl chloroformate in the presence of triethylamine and was inspired by previous work by M. Laurans.[84] The advantage is that degassed organic solvent is used which purpose was to avoid too much water during the peptide coupling process. However, Et_3NHCl salt is formed at the end and stays onto the surface. A water rinse was required to remove it and the differential

spectra are shown in Figure 41. The oxide quantity at the end of the overall procedure is similar to what we obtained with the two previous methods involving EDC.HCl/MES and EDC.HCl/NHS.

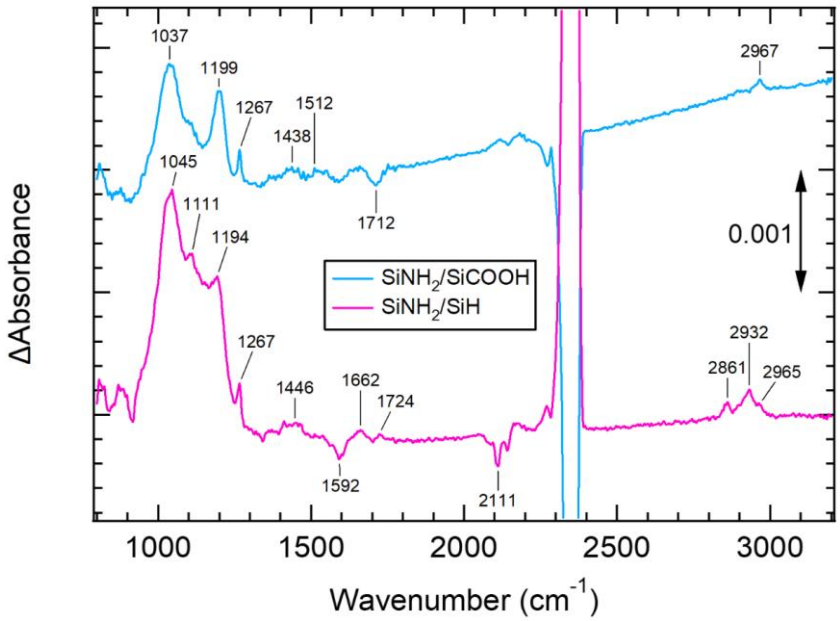

Figure 41 : $SiNH_2$ differential spectra obtained using isobutyl chloroformate during the modification step.

In summary, the procedure of grafting organic monolayer on Si(100) was slightly modified compared to the one on Si(111). Two main challenges were faced, the first one involving more care during the procedure as the etching of Si(100) leads to the formation of dihydride instead of monohydride, which impacts the homogeneity of the layer meaning: the organic monolayer is less compact and the surface is thus more prone to be oxidized than a (111)SiH surface. And second, the procedure needs to be compatible with further experiments on SOI substrate: the etching should not be too long otherwise it can damage the buried oxide layer of the SOI substrate and subsequently lead to an unusable substrate for electrical measurements.

Finally, the experimental conditions kept for SOI substrates are the following: etching of the substrate in a unique 10% HF solution for 10 seconds, hydrosilylation for 1 hour at 150°C, hydrolysis with degassed solutions and amine formation using the EDC.HCl/NHS/ethylenediamine procedure.

Despite the several tests performed, oxidation was found unavoidable. As we faced ellipsometer breakdown and lack of time, no more energy could be put to optimize the functionalization procedure.

III. Conclusion

Experimental procedures were described for both Si(111) and Si(100), with combined use of FTIR spectroscopy and ellipsometry measurements as surface characterization tools. We are thus able to correctly functionalize Si substrates with a NH_2-terminated organic monolayer. The monolayer is found to be well organized and really passivating in the case of Si(111) substrate, while being more sensitive to unavoidable reoxidation in the case of Si(100).

These NH_2 groups at the root of surface ammonium groups are useful to further immobilize photoreducible POMs. However, not all the amine is protonated in reality. As we will see in the next chapter, a low quantity of terminated NH_3^+ groups are present on the surface. One reason could be the low quantity of amine groups. Indeed, the high packing of COOH functions could result in a too strong affinity between them due to hydrogen bonds, leading to the inactivity of the COOH groups to react with EDC.HCl and ethylenediamine.[85] It thus could have been of great use to try to functionalize the oxide-free Si substrate with mix chains monolayer in order to increase the distance between two neighbors COOH groups.

Thinking of applications in molecular electronics, it could have also been interesting to shorten the alkyl chain monolayer in order to reduce the distance between the POM and the substrate, leading to an improvement of the electronic transport.[51] First tests were performed back in Dallas, but were not satisfying. As we wanted the most stable monolayer, we thus decided to focus on the C11 alkyl chains to optimize the functionalization procedure.

Although not perfectly perfect, the NH_2/NH_3^+ Si surfaces obtained on both Si(111) and Si(100) are now ready to electrostatically welcome the POM as will be discussed in the following chapter.

IV. References

(1) Skinner, B. J. Earth Resources. *Proc. Natl. Acad. Sci. USA.* **1979**, *76*(9), 4212–4217.
(2) Buriak, J. M. Organometallic Chemistry on Silicon and Germanium Surfaces. *Chemical Reviews* **2002**, *102* (5), 1271–1308.
(3) Segal, M. Learning from silicon. *Nature*. **2012**, *483*, S43–S44.
(4) Schulz, M. The End of the Road for Silicon? *Nature* **1999**, *399*, 729–730.
(5) DeBenedetti, W. J. I.; Chabal, Y. J. Functionalization of Oxide-Free Silicon Surfaces. *Journal of Vacuum Science & Technology A* **2013**, *31* (5), 050826.
(6) Kahng, D. A Historical Perspective on the Development of MOS Transistors and Related Devices. *IEEE Trans. Electron Devices* **1976**, *23* (7), 655–657.
(7) Sze, S. M.; Ng, K. K. *Physics of Semiconductor Devices*, 3. ed.; Wiley-Interscience: Hoboken, NJ, 2007.
(8) Shang, H.; Frank, M. M.; Gusev, E. P.; Chu, J. O.; Bedell, S. W.; Guarini, K. W.; Ieong, M. Germanium Channel MOSFETs: Opportunities and Challenges. *IBM J. Res. & Dev.* **2006**, *50* (4.5), 377–386.
(9) Tsetseris, L.; Pantelides, S. T. Morphology and Defect Properties of the Ge–GeO_2 Interface. *Appl. Phys. Lett.* **2009**, *95* (26), 262107.
(10) Shiruma, F. Single-Crystal Silicon: Growth and Properties. In *Springer Handbook of Electronic and Photonic Materials*; Kasap, S., Capper, P., Eds.; Springer, Boston, MA, 2006.
(11) Sumino, K.; Harada, H.; Yonenaga, I. The Origin of the Difference in the Mechanical Strengths of Czochralski-Grown Silicon and Float-Zone-Grown Silicon. *Japanese Journal of Applied Physics* **1980**, *19* (1), L49–L52.
(12) Yu, B.; Qian, L. Effect of Crystal Plane Orientation on the Friction-Induced Nanofabrication on Monocrystalline Silicon. *Nanoscale Research Letters* **2013**, 8, 137.
(13) Chegg.com https://www.chegg.com/homework-help/questions-and-answers/problem-1-diamond-cubic-structure-silicon-diamond-structure-shown-figure--answer-following-q27966869 (accessed 2021 -11 -18).
(14) Ohmi, T.; Matsumoto, K.; Nakamura, K.; Makihara, K.; Takano, J.; Yamamoto, K. Influence of Silicon Wafer Surface Orientation on Very Thin Oxide Quality. *Appl. Phys. Lett.* **1993**, *62* (4), 405–407.
(15) Nakamura, K.; Ohmi, K.; Yamamoto, K.; Makihara, K.; Ohmi, T. Silicon Wafer Orientation Dependence of Metal Oxide Semiconductor Device Reliability. *Jpn. J. Appl. Phys.* **1994**, *33* (Part 1, No. 1B), 500–504.
(16) Deal, B. E. Standardized Terminology for Oxide Charges Associated with Thermally Oxidized Silicon. *IEEE transactions on electron devices* **1980**, 27(3), 606–608.
(17) Cheng, Y. C. Electronic States at the Silicon-Silicon Dioxide Interface. *Progress in Surface Science* **1977**, *8* (5), 181–218.
(18) Wickenden, D. K. Semiconductor Devices: Moore Marches On. *Johns Hopkins APL Technical Digest* **2008**, *28* (1), 30–39.
(19) Mann, B.; Kuhn, H. Tunneling through Fatty Acid Salt Monolayers. *Journal of Applied Physics* **1971**, *42* (11), 4398–4405.
(20) Haller, I. Covalently Attached Organic Monolayers on Semiconductor Surfaces. *J. Am. Chem. Soc.* **1978**, *100* (26), 8050–8055.
(21) Sagiv, J. Organized Monolayers by Adsorption. 1. Formation and Structure of Oleophobic Mixed Monolayers on Solid Surfaces. *J. Am. Chem. Soc.* **1980**, *102* (1), 92–98.

(22) Onclin, S.; Ravoo, B. J.; Reinhoudt, D. N. Engineering Silicon Oxide Surfaces Using Self-Assembled Monolayers. *Angewandte Chemie International Edition* **2005**, *44* (39), 6282–6304.
(23) Pujari, S. P.; Scheres, L.; Marcelis, A. T. M.; Zuilhof, H. Covalent Surface Modification of Oxide Surfaces. *Angew. Chem. Int. Ed.* **2014**, *53* (25), 6322–6356.
(24) Linford, M. R.; Chidsey, C. E. D. Alkyl Monolayers Covalently Bonded to Silicon Surfaces. *Journal of the American Chemical Society* **1993**, *115* (26), 12631–12632.
(25) McCreery, R. L.; Bergren, A. J. Progress with Molecular Electronic Junctions: Meeting Experimental Challenges in Design and Fabrication. *Adv. Mater.* **2009**, *21* (43), 4303–4322.
(26) Fabre, B. Functionalization of Oxide-Free Silicon Surfaces with Redox-Active Assemblies. *Chem. Rev.* **2016**, *116* (8), 4808–4849.
(27) Aureau, D.; Chabal, Y. J. Formation of Organic Monolayers Through Wet Chemistry. In *Functionalization of Semiconductor Surfaces*; Tao, F. F., Bernasek, S. L., Eds.; John Wiley & Sons, Inc.: Hoboken, NJ, USA, 2012; pp 301–337.
(28) Weinberger, B. R.; Peterson, G. G.; Eschrich, T. C.; Krasinski, H. A. Surface Chemistry of HF Passivated Silicon: X-ray Photoelectron and Ion Scattering Spectroscopy Results. *Journal of Applied Physics* **1986**, *60* (9), 3232–3234.
(29) Walsh, R. Bond Dissociation Energy Values in Silicon-Containing Compounds and Some of Their Implications. *Acc. Chem. Res.* **1981**, *14* (8), 246–252.
(30) Yablonovitch, E.; Allara, D. L.; Chang, C. C.; Gmitter, T.; Bright, T. B. Unusually Low Surface-Recombination Velocity on Silicon and Germanium Surfaces. *Phys. Rev. Lett.* **1986**, *57* (2), 249–252.
(31) Burrows, V. A.; Chabal, Y. J.; Higashi, G. S.; Raghavachari, K.; Christman, S. B. Infrared Spectroscopy of Si(111) Surfaces after HF Treatment: Hydrogen Termination and Surface Morphology. *Appl. Phys. Lett.* **1988**, *53* (11), 998–1000.
(32) Higashi, G. S.; Chabal, Y. J.; Trucks, G. W.; Raghavachari, K. Ideal Hydrogen Termination of the Si (111) Surface. *Applied Physics Letters* **1990**, *56* (7), 656–658.
(33) Ubara, H.; Imura, T.; Hiraki, A. Formation of Si-H Bonds on the Surface of Microcrystalline Silicon Covered with SiO_x by HF Treatment. *Solid State Communications* **1984**, *50* (7), 673–675.
(34) Trucks, G. W.; Raghavachari, K.; Higashi, G. S.; Chabal, Y. J. Mechanism of HF Etching of Silicon Surfaces: A Theoretical Understanding of Hydrogen Passivation. *Physical Review Letters* **1990**, *65* (4), 504–507.
(35) Hines, M. A. In Search of Perfection : Understanding the Highly Defect-Selective Chemistry of Anisotropic Etching. *Annual Review of Physical Chemistry* **2003**, *54* (1), 29–56.
(36) Huang, Y.-C.; Flidr, J.; Newton, T. A.; Hines, M. A. Effects of Dynamic Step-Step Repulsion and Autocatalysis on the Morphology of Etched Si(111) Surfaces. *Phys. Rev. Lett.* **1998**, *80* (20), 4462–4465.
(37) Newton, T. A.; Boiani, J. A.; Hines, M. A. The Correlation between Surface Morphology and Spectral Lineshape: A Re-Examination of the H–Si(111) Stretch Vibration. *Surface Science* **1999**, *430* (1–3), 67–79.
(38) Boukherroub, R.; Morin, S.; Bensebaa, F.; Wayner, D. D. M. New Synthetic Routes to Alkyl Monolayers on the Si(111) Surface. *Langmuir* **1999**, *15* (11), 3831–3835.
(39) Linford, M. R.; Fenter, P.; Eisenberger, P. M.; Chidsey, C. E. D. Alkyl Monolayers on Silicon Prepared from 1-Alkenes and Hydrogen-Terminated Silicon. *J. Am. Chem. Soc.* **1995**, *117* (11), 3145–3155.

(40) Aureau, D.; Varin, Y.; Roodenko, K.; Seitz, O.; Pluchery, O.; Chabal, Y. J. Controlled Deposition of Gold Nanoparticles on Well-Defined Organic Monolayer Grafted on Silicon Surfaces. *The Journal of Physical Chemistry C* **2010**, *114* (33), 14180–14186.
(41) Seitz, O.; Dai, M.; Aguirre-Tostado, F. S.; Wallace, R. M.; Chabal, Y. J. Copper−Metal Deposition on Self Assembled Monolayer for Making Top Contacts in Molecular Electronic Devices. *Journal of the American Chemical Society* **2009**, *131* (50), 18159–18167.
(42) Seitz, O.; Vilan, A.; Cohen, H.; Hwang, J.; Haeming, M.; Schoell, A.; Umbach, E.; Kahn, A.; Cahen, D. Doping Molecular Monolayers: Effects on Electrical Transport Through Alkyl Chains on Silicon: Doping Molecular Monolayers. *Advanced Functional Materials* **2008**, *18* (14), 2102–2113.
(43) Caillard, L.; Seitz, O.; Campbell, P. M.; Doherty, R. P.; Lamic-Humblot, A.-F.; Lacaze, E.; Chabal, Y. J.; Pluchery, O. Gold Nanoparticles on Oxide-Free Silicon–Molecule Interface for Single Electron Transport. *Langmuir* **2013**, *29* (16), 5066–5073.
(44) Rück-Braun, K.; Petersen, M. Å.; Michalik, F.; Hebert, A.; Przyrembel, D.; Weber, C.; Ahmed, S. A.; Kowarik, S.; Weinelt, M. Formation of Carboxy- and Amide-Terminated Alkyl Monolayers on Silicon(111) Investigated by ATR-FTIR, XPS, and X-Ray Scattering: Construction of Photoswitchable Surfaces. *Langmuir* **2013**, *29* (37), 11758–11769.
(45) Huck, L. A.; Buriak, J. M. UV-Initiated Hydrosilylation on Hydrogen-Terminated Silicon (111): Rate Coefficient Increase of Two Orders of Magnitude in the Presence of Aromatic Electron Acceptors. *Langmuir* **2012**, *28* (47), 16285–16293.
(46) Sun, Q.-Y.; Smet, L. C. P. M. de; Lagen, B. van; Wright, A.; Zuilhof, H.; Sudhölter, E. J. R. Covalently Attached Monolayers on Hydrogen-Terminated Si(100): Extremely Mild Attachment by Visible Light. *Angewandte Chemie International Edition* **2004**, *43* (11), 1352–1355.
(47) Langner, A.; Panarello, A.; Rivillon, S.; Vassylyev, O.; Khinast, J. G.; Chabal, Y. J. Controlled Silicon Surface Functionalization by Alkene Hydrosilylation. *J. Am. Chem. Soc.* **2005**, *127* (37), 12798–12799.
(48) Yang, M.; Teeuwen, R. L. M.; Giesbers, M.; Baggerman, J.; Arafat, A.; de Wolf, F. A.; van Hest, J. C. M.; Zuilhof, H. One-Step Photochemical Attachment of NHS-Terminated Monolayers onto Silicon Surfaces and Subsequent Functionalization. *Langmuir* **2008**, *24* (15), 7931–7938.
(49) Seitz, O.; Fernandes, P. G.; Mahmud, G. A.; Wen, H.-C.; Stiegler, H. J.; Chapman, R. A.; Vogel, E. M.; Chabal, Y. J. One-Step Selective Chemistry for Silicon-on-Insulator Sensor Geometries. *Langmuir* **2011**, *27* (12), 7337–7340.
(50) Wang, X.; Ruther, R. E.; Streifer, J. A.; Hamers, R. J. UV-Induced Grafting of Alkenes to Silicon Surfaces: Photoemission versus Excitons. *J. Am. Chem. Soc.* **2010**, *132* (12), 4048–4049.
(51) Veerbeek, J.; Huskens, J. Applications of Monolayer-Functionalized H-Terminated Silicon Surfaces: A Review. *Small Methods* **2017**, *1* (4), 1700072.
(52) Volatron, F.; Noël, J.-M.; Rinfray, C.; Decorse, P.; Combellas, C.; Kanoufi, F.; Proust, A. Electron Transfer Properties of a Monolayer of Hybrid Polyoxometalates on Silicon. *J. Mater. Chem. C* **2015**, *3* (24), 6266–6275.
(53) He, T.; He, J.; Lu, M.; Chen, B.; Pang, H.; Reus, W. F.; Nolte, W. M.; Nackashi, D. P.; Franzon, P. D.; Tour, J. M. Controlled Modulation of Conductance in Silicon Devices by Molecular Monolayers. *J. Am. Chem. Soc.* **2006**, *128* (45), 14537–14541.
(54) Effenberger, F.; Götz, G.; Bidlingmaier, B.; Wezstein, M. Photoactivated Preparation and Patterning of Self-Assembled Monolayers with 1-Alkenes and Aldehydes on Silicon Hydride Surfaces. *Angew. Chem. Int. Ed.* **1998**, *37* (18), 2462–2464.

(55) Hacker, C. A.; Anderson, K. A.; Richter, L. J.; Richter, C. A. Comparison of Si−O−C Interfacial Bonding of Alcohols and Aldehydes on Si(111) Formed from Dilute Solution with Ultraviolet Irradiation. *Langmuir* **2005**, *21* (3), 882–889.
(56) Hu, M.; Liu, F.; Buriak, J. M. Expanding the Repertoire of Molecular Linkages to Silicon: Si–S, Si–Se, and Si–Te Bonds. *ACS Appl. Mater. Interfaces* **2016**, *8* (17), 11091–11099.
(57) Buriak, J. M.; Sikder, M. D. H. From Molecules to Surfaces: Radical-Based Mechanisms of Si–S and Si–Se Bond Formation on Silicon. *J. Am. Chem. Soc.* **2015**, *137* (30), 9730–9738.
(58) Bansal, A.; Li, X.; Yi, S. I.; Weinberg, W. H.; Lewis, N. S. Spectroscopic Studies of the Modification of Crystalline Si(111) Surfaces with Covalently-Attached Alkyl Chains Using a Chlorination/Alkylation Method. *J. Phys. Chem. B* **2001**, *105* (42), 10266–10277.
(59) Ciampi, S.; Harper, J. B.; Gooding, J. J. Wet Chemical Routes to the Assembly of Organic Monolayers on Silicon Surfaces via the Formation of Si–C Bonds: Surface Preparation, Passivation and Functionalization. *Chem. Soc. Rev.* **2010**, *39* (6), 2158–2183.
(60) Fabre, B. Ferrocene-Terminated Monolayers Covalently Bound to Hydrogen-Terminated Silicon Surfaces. Toward the Development of Charge Storage and Communication Devices. *Acc. Chem. Res.* **2010**, *43* (12), 1509–1518.
(61) Caillard, L. Grafted Organic Monolayer for Single Electron Transport and for Quantum Dots Solar Cells. Dissertation, The University of Texas at Dallas and Université Pierre et Marie Curie, **2014**.
(62) Webb, L. J.; Rivillon, S.; Michalak, D. J.; Chabal, Y. J.; Lewis, N. S. Transmission Infrared Spectroscopy of Methyl- and Ethyl-Terminated Silicon(111) Surfaces. *J. Phys. Chem. B* **2006**, *110* (14), 7349–7356.
(63) *Biointerface Characterization by Advanced IR Spectroscopy*; Pradier, C.M.; Chabal, Y.J., Eds.; Elsevier: Oxford, 2011.
(64) Chalmers, J. M. Mid-Infrared Spectroscopy: Anomalies, Artifacts and Common Errors. In *Handbook of Vibrational Spectroscopy*; Chalmers, J. M., Griffiths, P. R., Eds.; John Wiley & Sons, Ltd: Chichester, UK, 2006; Vol. 3.
(65) Pasternack, R. M.; Rivillon Amy, S.; Chabal, Y. J. Attachment of 3-(Aminopropyl)Triethoxysilane on Silicon Oxide Surfaces: Dependence on Solution Temperature. *Langmuir* **2008**, *24* (22), 12963–12971.
(66) Kern, W. The Evolution of Silicon Wafer Cleaning Technology. *Journal of The Electrochemical Society* **1990**, *137* (6), 1887–1892.
(67) Thomas, M. C. Aqueous-Derived Thin Films and Their Interfacial Interactions with Semiconductor Surfaces: A Spectroscopic Study. Dissertation, The University of Texas at Dallas, **2018**.
(68) Aldinger, B. S.; Gupta, A.; Clark, I. T.; Hines, M. A. The Same Etchant Produces Both Near-Atomically Flat and Microfaceted Si(100) Surfaces: The Effects of Gas Evolution on Etch Morphology. *Journal of Applied Physics* **2010**, *107* (10), 103520.
(69) Angermann, H.; Henrion, W.; Rebien, M.; Röseler, A. Wet-Chemical Preparation and Spectroscopic Characterization of Si Interfaces. *Applied Surface Science* **2004**, *235* (3), 322–339.
(70) Allen, F. H.; Watson, D. G.; Brammer, L.; Orpen, A. G.; Taylor, R. Typical Interatomic Distances: Organic Compounds. In *International Tables for Crystallography*; Prince, E., Ed.; Fuess, H., Hahn, Th., Wondratschek, H., Müller, U., Shmueli, U., Prince, E., Authier, A., Kopský, V., Litvin, D. B., Rossmann, M. G., Arnold, E., Hall, S., McMahon, B., Series Eds.; International Tables for Crystallography; International Union of Crystallography: Chester, England, 2006; Vol. C, pp 790–811.
(71) Schweizer, W. B.; Dunitz, J. D. Structural Characteristics of the Carboxylic Ester Group. *Helv. Chim. Acta* **1982**, *65* (5), 1547–1554.

(72) Jiang, X.; Ataka, K.; Heberle, J. Influence of the Molecular Structure of Carboxyl-Terminated Self-Assembled Monolayer on the Electron Transfer of Cytochrome c Adsorbed on an Au Electrode: In Situ Observation by Surface-Enhanced Infrared Absorption Spectroscopy. *J. Phys. Chem. C* **2008**, *112* (3), 813–819.
(73) Sun, L.; Crooks, R. M.; Ricco, A. J. Molecular Interactions between Organized, Surface-Confined Monolayers and Vapor-Phase Probe Molecules. 5. Acid-Base Interactions. *Langmuir* **1993**, *9* (7), 1775–1780.
(74) Nguyen, H. M.; Seitz, O.; Aureau, D.; Sra, A.; Nijem, N.; Gartstein, Yu. N.; Chabal, Y. J.; Malko, A. V. Spectroscopic Evidence for Nonradiative Energy Transfer between Colloidal CdSe/ZnS Nanocrystals and Functionalized Silicon Substrates. *Appl. Phys. Lett.* **2011**, *98* (16), 161904.
(75) Nguyen, H. M.; Seitz, O.; Peng, W.; Gartstein, Y. N.; Chabal, Y. J.; Malko, A. V. Efficient Radiative and Nonradiative Energy Transfer from Proximal CdSe/ZnS Nanocrystals into Silicon Nanomembranes. *ACS Nano* **2012**, *6* (6), 5574–5582.
(76) Aissaoui, N.; Bergaoui, L.; Landoulsi, J.; Lambert, J.-F.; Boujday, S. Silane Layers on Silicon Surfaces: Mechanism of Interaction, Stability, and Influence on Protein Adsorption. *Langmuir* **2012**, *28* (1), 656–665.
(77) Winkler, F. K.; Dunitz, J. D. The Non-Planar Amide Group. *Journal of Molecular Biology* **1971**, *59* (1), 169–182.
(78) *Physics and Technology of Amorphous-Crystalline Heterostructure Silicon Solar Cells*; van Sark, W. G. J. H. M., Korte, L., Roca, F., Eds.; Engineering Materials; Springer: Berlin, Heidelberg, 2012.
(79) Drucker, J.; Bandari, A.; Burrows, V. V. Si(100) Surface Corrosion by NH_4F Studied Using High Spatial Resolution Secondary Electron Imaging in a UHV - STEM. *MRS Proc.* **1993**, *315*, 479–484.
(80) Hines, M. A.; Faggin, M. F.; Gupta, A.; Aldinger, B. S.; Bao, K. Self-Propagating Reaction Produces Near-Ideal Functionalization of Si(100) and Flat Surfaces. *J. Phys. Chem. C* **2012**, *116* (35), 18920–18929.
(81) Peng, W.; DeBenedetti, W. J. I.; Kim, S.; Hines, M. A.; Chabal, Y. J. Lowering the Density of Electronic Defects on Organic-Functionalized Si(100) Surfaces. *Appl. Phys. Lett.* **2014**, *104* (24), 241601.
(82) Clark, I. T.; Aldinger, B. S.; Gupta, A.; Hines, M. A. Aqueous Etching Produces Si(100) Surfaces of Near-Atomic Flatness: Strain Minimization Does Not Predict Surface Morphology. *J. Phys. Chem. C* **2010**, *114* (1), 423–428.
(83) Sam, S.; Touahir, L.; Salvador Andresa, J.; Allongue, P.; Chazalviel, J.-N.; Gouget-Laemmel, A. C.; Henry de Villeneuve, C.; Moraillon, A.; Ozanam, F.; Gabouze, N.; Djebbar, S. Semiquantitative Study of the EDC/NHS Activation of Acid Terminal Groups at Modified Porous Silicon Surfaces. *Langmuir* **2010**, *26* (2), 809–814.
(84) Laurans, M. Synthèse d'hybrides de Polyoxométallates: Greffage Contrôlé Sur Électrodes Pour l'étude de Jonctions Moléculaires. Thèse Sorbonne Université, **2018**.
(85) Böcking, T.; Kilian, K. A.; Gaus, K.; Gooding, J. J. Modifying Porous Silicon with Self-Assembled Monolayers for Biomedical Applications: The Influence of Surface Coverage on Stability and Biomolecule Coupling. *Adv. Funct. Mater.* **2008**, *18* (23), 3827–3833.

Chapter III

POM immobilization onto Si substrates : controlling the POM/substrate interaction as a first step towards electrical transport measurements

I. Introduction

We have demonstrated the benefits of POMs immobilization onto surfaces for memory devices in Chapter I. However, the stability of the resulting functionalized surfaces and the POM/substrate interaction understanding are required for a larger POM integration in molecular electronics.

This Chapter will aim at exploring the different strategies for the deposition of POMs onto surfaces. After an overview of the existing methods, details will be first given on the $(TBA)_3[PMo_{12}O_{40}]$ POM and its reduced derivatives synthesis followed by their subsequent immobilization as monolayer onto the previously obtained $SiNH_2$ surfaces. The electrostatic route, easier to implement, was also chosen to keep the intrinsic properties of the POM. However, the covalent route is appealing in order to obtain more robust systems with a better control of the POM/surface interaction. Several attempts of covalent POM hybrids grafting onto Si surfaces were thus carried out and described in the third section. Specially, the direct grafting of POM hybrids bearing terminal COOH functions onto oxidized Si surface was achieved and electrical measurements were performed, which will be highlighted in the last section.

II. Strategies for POM immobilization onto surface: an overview

With the large diversity of POM structures that have been synthesized over the years, it is easy to conceive numerous ways to immobilize POM on a surface, as depicted in Figure 1.[1] As the POMs are anionic species, they can interact with the surface via electrostatic interactions.[2,3] They can also be immobilized via a covalent anchor[4,5] or via supramolecular interactions (hydrogen bonds, π-stacking), which requires a former functionalization of POMs. More details will be given below. Depending on the application, the host substrate can vary, from nanoparticles[6,7] to 3D matrices, to flat surfaces. In an experimental point of view, the POM adsorption/grafting onto the surface can be achieved by several means including simple dropcasting, dipcoating, layer-by-layer and so on. Many reviews can be found but we will particularly focus on the POM-based materials interest for molecular electronics.[1,8–12]

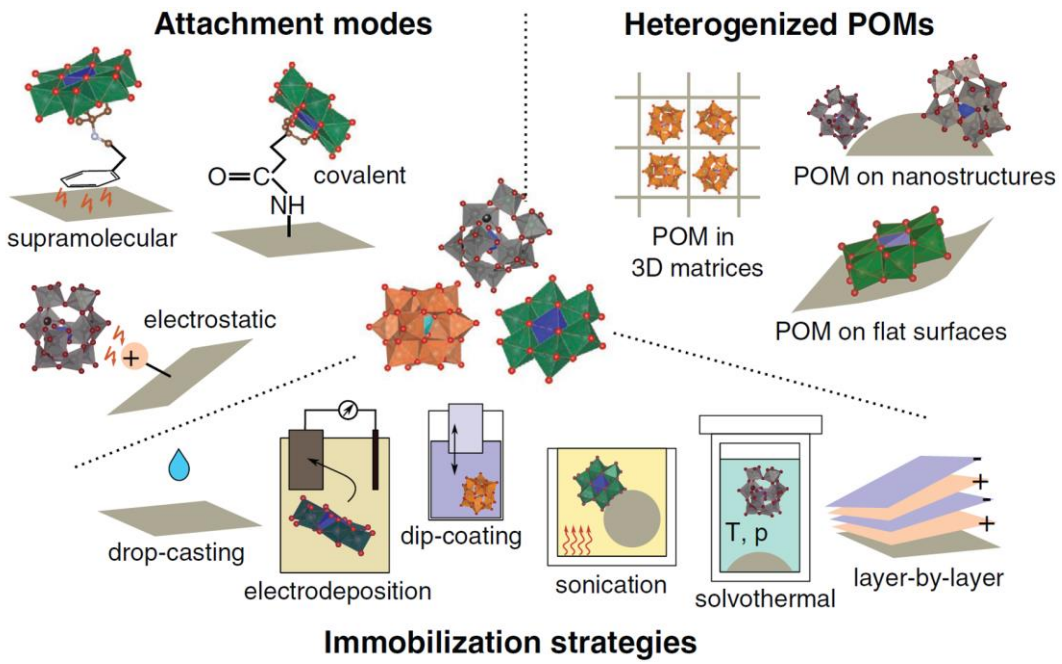

Figure 1 : Strategies for POM immobilization onto surfaces highlighting the possible attachment modes, substrates and immobilization methods.[1]

Some POM depositions have already been introduced in Chapter I and were performed by dropcasting and spincoating. These immobilization methods are easy to implement and thus the electrical characterization of the resulting surface is more easily attainable. This section will highlight the case of the electrostatic and the covalent POM/surface interaction, the two routes that were actually explored within the framework of this project.

II.1. Electrostatic route

The electrostatic route is easy to implement: when the POMs are dissolved, the anionic cluster can interact with positively charged species. We have for example described in Chapter I the layer-by-layer (LBL) assembly of graphene oxide nanosheets and $H_3PW_{12}O_{40}$ POMs involving electrostatic interactions with cationic polymers. These positive charges can also be provided by terminal functions of a SAM on a substrate.

Balliou *et al.* effectively built a POM-based memory cell in which $[PW_{12}O_{40}]^{3-}$ are immobilized by a LBL process, via electrostatic interactions onto an APTES SAM grafted onto Si-SiO_2 surfaces.[2] The POM layer (P) is capped with an isopentylamine (IPA) monolayer. As sketched in Figure 2, three devices, labeled P-Ox, Ox-P and Ox-P-Ox, were studied. In the three devices, a tantalum oxide Ta_2O_5 (Ox) is present and was chosen as a dielectric to reduce leakage currents in the devices. It is whether grown on top of the molecular assembly (P-Ox), or prior to the self-assembly of the molecules (Ox-P), or both (Ox-P-Ox), and an Al electrode serves as a top gate.

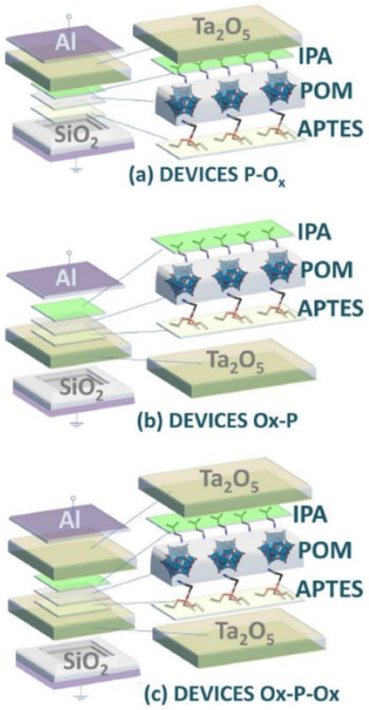

Figure 2 : Schematics of the fabricated stacks. In panel (a), Ta_2O_5 is grown on POM molecules self-assembled on the active region; Ta_2O_5 is directly grown on SiO_2 in panel (b) and the molecules are post-assembled on top; in panel (c), a passivated POM layer is sandwiched between two Ta_2O_5 films.[2]

The memory cells performances were first studied using an incremental-step-pulse programming (ISPP) procedure, to study the programming speed of the devices. It consists in applying increasingly a voltage pulse on the gate (programming step) in increments of 1 V, from 0 to 20 V. For each device, two sets of measurements were performed, involving whether a pulse duration of 100 ms or 100 µs (programming speed). ΔV_{FB} was measured throughout the experiment, and corresponds to the flat-band voltage between two successive voltage pulses (the flat-band voltage is the gate bias at which the flat-band condition is achieved, that is to say there is no supplementary charge at the semiconductor/insulator interface compared to the doping). The results are shown in Figure 3 (left). The authors attributed an increase in V_{FB} to electrons trapping which occurs within the POM framework and on the molecule/oxide interfaces of the device. The Ox-P and P-Ox devices display a higher ΔV_{FB} than the Ox-P-Ox device at fast pulse duration (100 µs), suggesting a better charge trapping. However, at lower programming speed (100 ms), the charge trapping of the Ox-P-Ox device is enhanced compared to the Ox-P and P-Ox counterparts, resulting is a larger memory window.

The charge retention was subsequently studied on the three devices by selecting the parameters (voltage pulse and programming speed) for which the charge trapping was enhanced. After a specific single pulse of 100 ms or 100 µs, the ΔV_{FB} was measured over the time. The results are shown in Figure 3 (right). Globally, the three cells display a significant retention time as they maintain their charge until ~10^4 seconds.

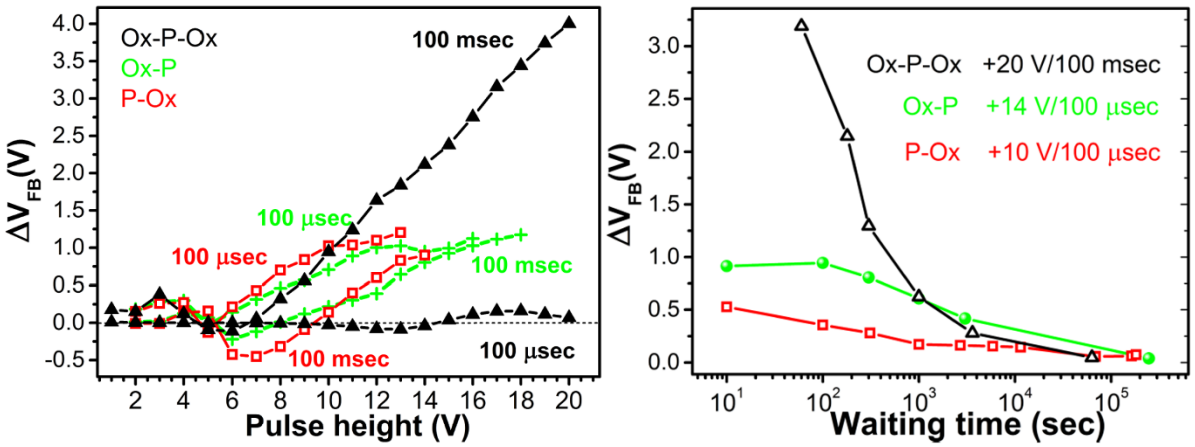

Figure 3: Left) Programming windows for the Ox-P-Ox, Ox-P and P-Ox cells obtained using the ISPP procedure. A pulse duration of 100 ms and 100 µs were studied for each device. Right) charge retention characteristics of the three cells programmed via single pulses.[2]

The electrostatic deposition was also explored in our group. Dalla Francesca *et al.* indeed reported the electrostatic immobilization of large $[H_7P_8W_{48}O_{184}]^{33-}$ POMs onto 8-amino-1-octanethiol (AOT) SAMs on gold surfaces, by a simple dipcoating of the substrates

into a POM solution.[3] POM monolayers were obtained, which was confirmed by ellipsometry, XPS, polarized modulated reflection absorption infrared spectroscopy (PM-RAIRS) and AFM. The first electrical measurements on this POM were carried out by conducting atomic force microscopy (C-AFM), as depicted in Figure 4a. In this configuration, an external bias was applied to the gold substrate, while the C-AFM tip was grounded. A forward and reverse voltage sweep was applied, from -1.5 to 1.5 V, and the current was measured. A total of ~300 I-V curves was obtained and plotted in a 2D current histogram in Figure 4b. The I-V curves were then processed to investigate the energetics of the Au-AOT//POM//C-AFM tip molecular junction. Specially, the POM LUMO was calculated with the help of three methods: the Simmons model, the transition voltage spectroscopy (TVS) method and the molecular model.

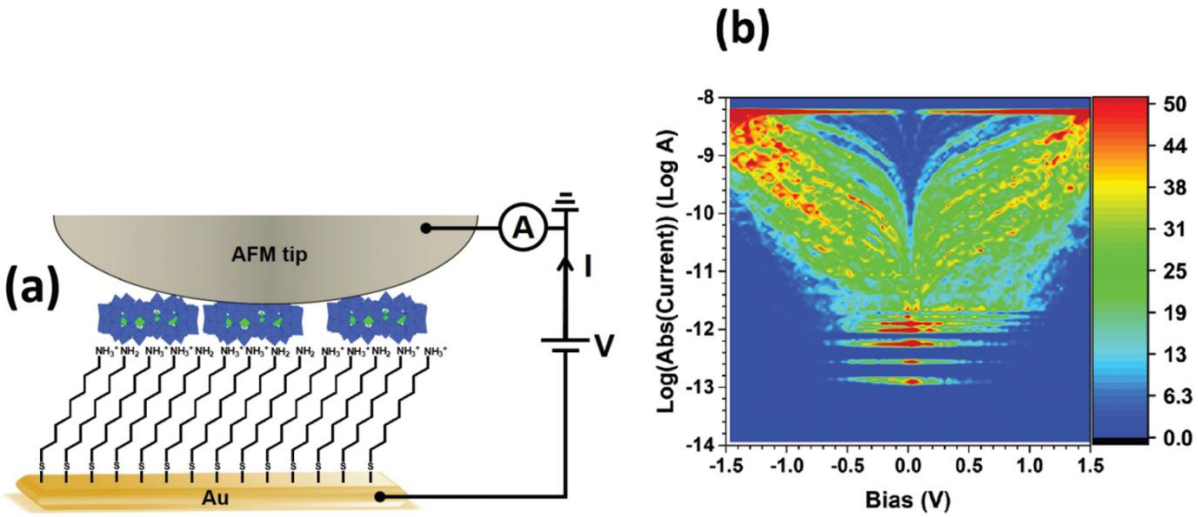

Figure 4 : a) Scheme of the electronic transport characterization by C-AFM of the $[H_7P_8W_{48}O_{184}]^{33-}$ electrostatically deposited onto a gold surface functionalized with an AOT SAM; b) 2D current histogram of 300 I-V curves measured at several locations on the SAM.[3]

The electrostatic route thus offers the advantage of an easy POM deposition with a direct access to the existing POMs. However, care should be taken to make sure that the POM deposition is homogeneous, especially if a POM-based material is studied for electronics applications. An alternative to improve the POM deposition can be envisioned by a covalent anchoring between the POM and the substrate, as will be discussed in the following.

II.2. Covalent route

The covalent grafting of POM onto surfaces allows a better control of the POM/surface interaction. However, the preparation of such surfaces is time consuming and somehow more challenging since it requires a functionalization of the POMs with an anchor prior to the reaction with the selected surface. Only few examples of such POM hybrids covalently grafted onto surfaces are found in the literature and will be spotlighted hereinafter.

Our group has been extensively working on the functionalization of POMs since the 2000s.[13–15] Starting with a Keggin or Dawson POM hybrid bearing a remote iodoaryl function, a diversity of POM hybrids functionalized with an organic tether has been obtained, as sketched in Scheme 1.[15] Covalent grafting of such POM hybrids onto a surface can thus be considered if the terminal functions of the organic tether react with the surface terminal functions, paving the way for POM-based materials especially for catalysis, charge storage or information processing.

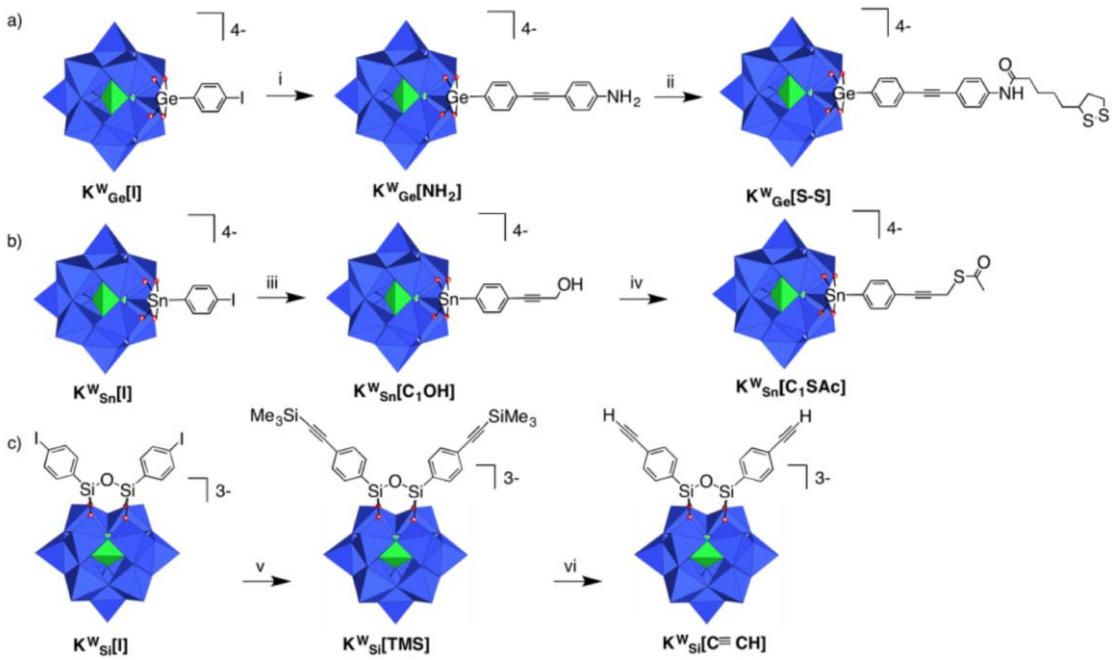

Scheme 1 : Two-step post-functionalization of iodoaryl-terminated hybrid platforms.[15] i) $[PdCl_2(PPh_3)_2]$, CuI, TEA, DMF, 4-ethynylaniline; ii) C_4H_9OCOCl, TEA, thioctic acid, MeCN; iii) $[PdCl_2(PPh_3)_2]$, CuI, TEA, propargyl alcool, DMF; iv) thioacetic acid, diisopropyl azodicarboxylate, PPh_3, DMF/THF; v) $[PdCl_2(PPh_3)_2]$, CuI, TEA, trimethylsilylacetylene; vi) $AgNO_3$, MeCN/MeOH/H_2O.

Accordingly, Keggin-type POM hybrid $[PW_{11}O_{39}\{Ge(p\text{-}C_6H_4\text{-}C{\equiv}C\text{-}C_6H_4\text{-}N_2^+)\}]^{3-}$ ($K_{Ge}[N_2^+]$) was successfully synthesized by Rinfray *et al.* as tetrabutylammonium (TBA) salt

and bears a terminal diazonium function that reacts easily onto surfaces.[16] $K_{Ge}[N_2^+]$ was subsequently immobilized as monolayer onto glassy carbon, and finally onto Si surface more recently by Volatron *et al.*, through a process depicted in Scheme 2.[17]

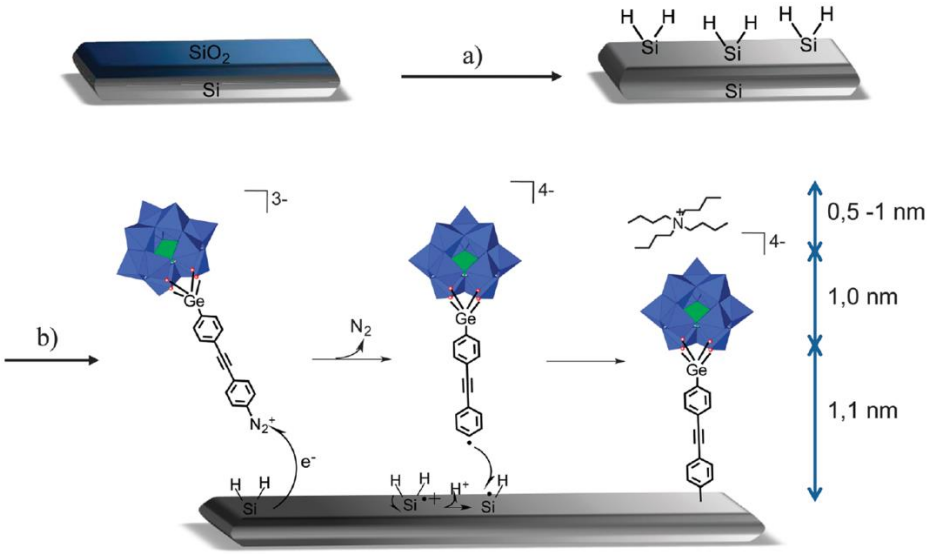

Scheme 2 : Chemical procedure steps and mechanism of spontaneous covalent grafting of diazonium post-functionalized POMs on a silicon surface. (a) H_2SO_4/H_2O_2 (2:1), HF_{aq} 10%; (b) POM-N_2^+, ACN.[17]

In the two cases, the vertical electron transfer between the POM and the surface was studied by cyclic voltammetry and results showed that the electron transfer rate constant k_{ETvert} was dependent on the substrate. It indeed decreased from 800 s^{-1} to 5 ± 0.5 s^{-1} when moving from glassy carbon to Si substrate. The presence of low quantity of SiO_2 at the Si surface could be responsible of the slowing of the electron transfer, and could be avoided with the use of a protective self-assembled monolayer prior to POM immobilization for example. On the other hand, the POM monolayer on Si surface was studied by scanning electrochemical microscopy (SECM), as depicted in Scheme 3.[17]

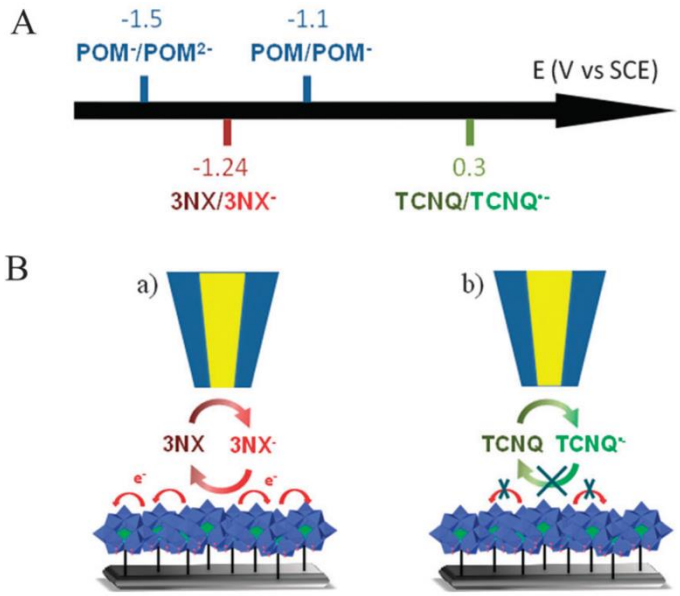

Scheme 3 : (A) Redox mediators/layers and their corresponding potentials evaluated in DMF solution containing 0.1 M $TBABF_4$. (B) Principle of SECM measurements on a POM layer in the case of (a) a conducting layer (b) an insulating layer.[17]

Basically, a platinum ultramicroelectrode (UME) approaches the POM containing substrate in solution. The presence of the 3-*ortho*-nitroxylene redox mediator in solution leads to the reduction of the POM. The regeneration of the redox mediator at the tip was observed on the SECM approach curves, meaning that the POM layer is conducting and that a POM-to-POM lateral electron transfer takes place. This electron transfer was by the way improved when working with a well-organized POM monolayer. By recording successive approach curves at the same spot of the surface, a negative charge accumulation in the POM monolayer was witnessed and the latter can actually be discharged by using an oxidative agent that displays a higher redox potential than the POM. Those results were thus encouraging for further studies of immobilized POMs layers at the solid-solid interface. Particularly, they strengthen the potential of POMs for molecular memories. However, this requires a well-organized and dense monolayer of POMs as well as a mastering in the control of the POM/surface interaction.

POM monolayer grafted onto oxide-free Si was thus recently studied in solid state by Laurans *et al.*[4] Two POM hybrids $[PM_{11}O_{39}\{Sn(C_6H_4)C{\equiv}C(C_6H_4)N_2^+\}]^{3-}$ bearing a diazonium function remote were synthesized, involving whether M=molybdenum atoms or M=tungsten atoms (Figure 5a). In solution, polyoxomolybdates are more easily reduced than the polyoxotungstates. After POM grafting, silicon-molecules-metal (SMM) junction was obtained using a mercury (Hg) drop as a top electrode (Figure 5a). Current-voltage (I-V) curves were recorded by applying an external bias to the Hg drop (Figure 5b), and processed with the

Simmons model in order to extract the tunnel energy barrier of the POM monolayer ϕ_{POM}, *i.e.* the energy required to move an electron from the Fermi level of the Si to the LUMO level of the POM. Histograms of all ϕ_{POM} extracted revealed an average ϕ_{POM} = 1.6 eV for the polyoxomolybdate monolayer and an average ϕ_{POM} = 1.8 eV for the polyoxotungstate monolayer, which indeed matches the trend observed in solution: an easier POM reduction suggests a lower LUMO level, thus a lower ϕ_{POM}. The molecular signature of the POM was thus successfully identifiable in solid-state using a SMM junction configuration. Results were thus promising to go deeper in solid-state POM monolayer characterization.

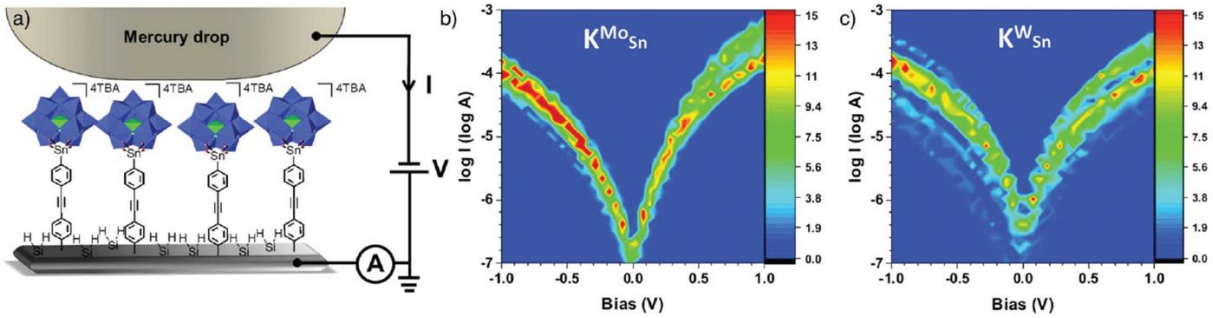

Figure 5: a) Scheme of the molecular layer grafted on a Si substrate and the SMM junction Si-K^{W}_{Sn}//Hg. b) 2D current histogram of 75 I–V curves measured for K^{Mo}_{Sn} and (c) K^{W}_{Sn} monolayers chemically grafted on a highly doped (degenerated) *n*-type ⟨100⟩ silicon substrates (resistivity of ~1–5.10^{-3} Ω cm). Voltage was applied on the mercury and Si substrate was grounded.[4]

Another example of grafted POM monolayer was reported by Tour and coll.[18] The authors grafted four different monolayers of molecules onto hydrogenated-Si surfaces and subsequently studied those systems in a MOSFET configuration (Figure 6a). The molecules studied were the following: a Lindqvist-type POM hybrid bearing a terminal diazonium function, and three other molecules more or less π-electron donor/acceptor depending on their terminal groups (Figure 6b). By applying an external bias V_G at the back contact, the drain current I_D was measured before and after monolayer grafting (Figure 6c). As the studied POM is a strong π-electron acceptor, it has been shown that the drain current increased in the case of a POM monolayer grafting for a given V_G applied in the four cases. The possibility to modulate the conductance thanks to the presence of the POM is thus encouraging for the incorporation of other POMs in a transistor configuration.

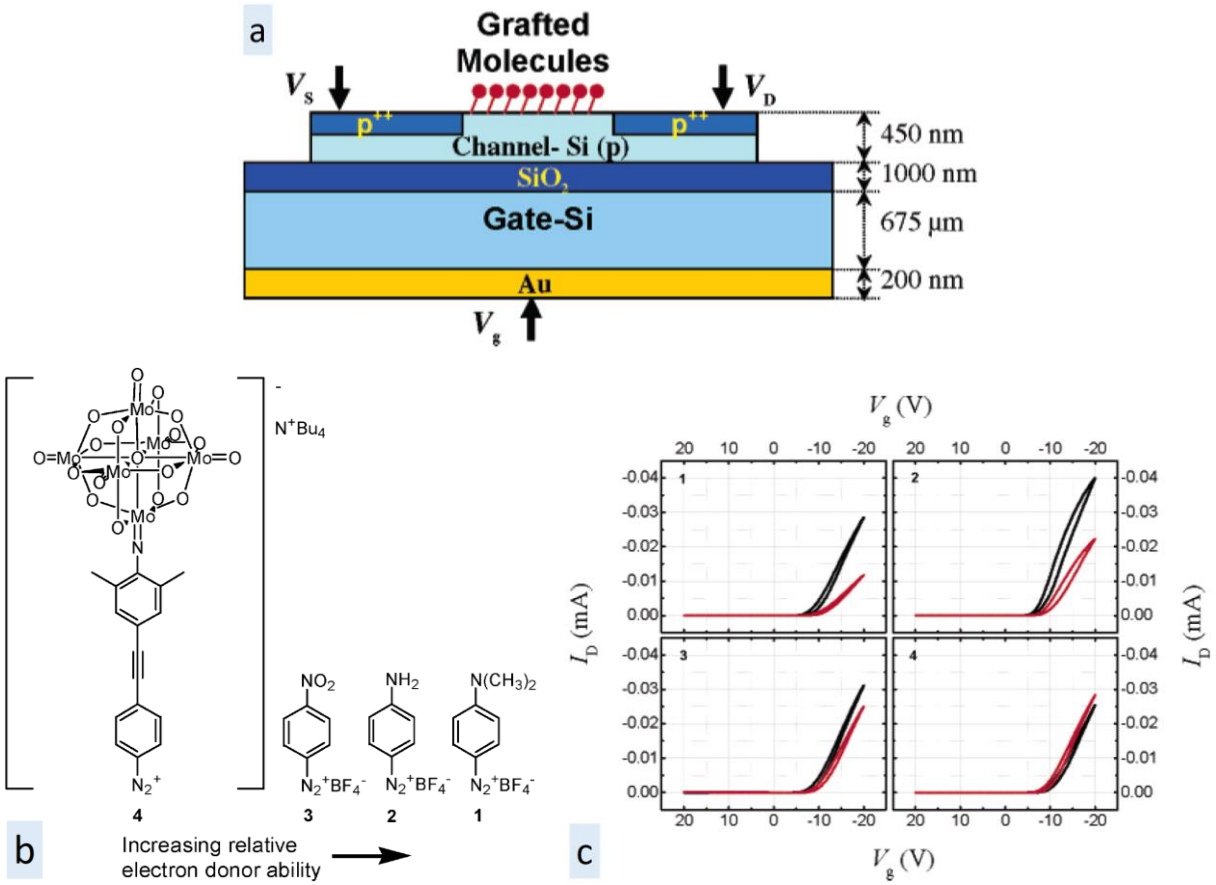

Figure 6 : Study of the channel conductance of a SOI substrate functionalized with several molecules.[18] a) The MOSFET configuration for this study; b) the four molecules studied, ranging from the strongest π-electron donor (1) to the strongest π-electron acceptor (4); and c) Drain current (I_D) as a function of the back gate voltage V_G obtained before (black) and after (red) each molecular monolayer grafting.

Several POM-based devices were thus introduced in this section and the POM immobilization onto a surface can be achieved using a variety of POMs and strategies. The electrostatic route and the covalent route were exemplified. Though the covalent route offers a more robust system and a more controlled POM/surface interaction, the targeted material is not easy to reach, as it requires the mastering in the POM hybrid synthesis in a first step. The POM immobilization procedures developed in Chapter I (dropcasting and spincoating) and the electrostatic depositions described in this section are easy to carry out. The electrostatic route is thus a simple way to immobilize POMs as it offers more choice on the substrates and on the POM.

In the following sections, the electrostatic and covalent routes will be explored as depicted in Figure 7, with the former constituting the core of the project. POM hybrids bearing one or several terminal amine, iminophosphorane, alkene or carboxylic acid functions will also be studied.

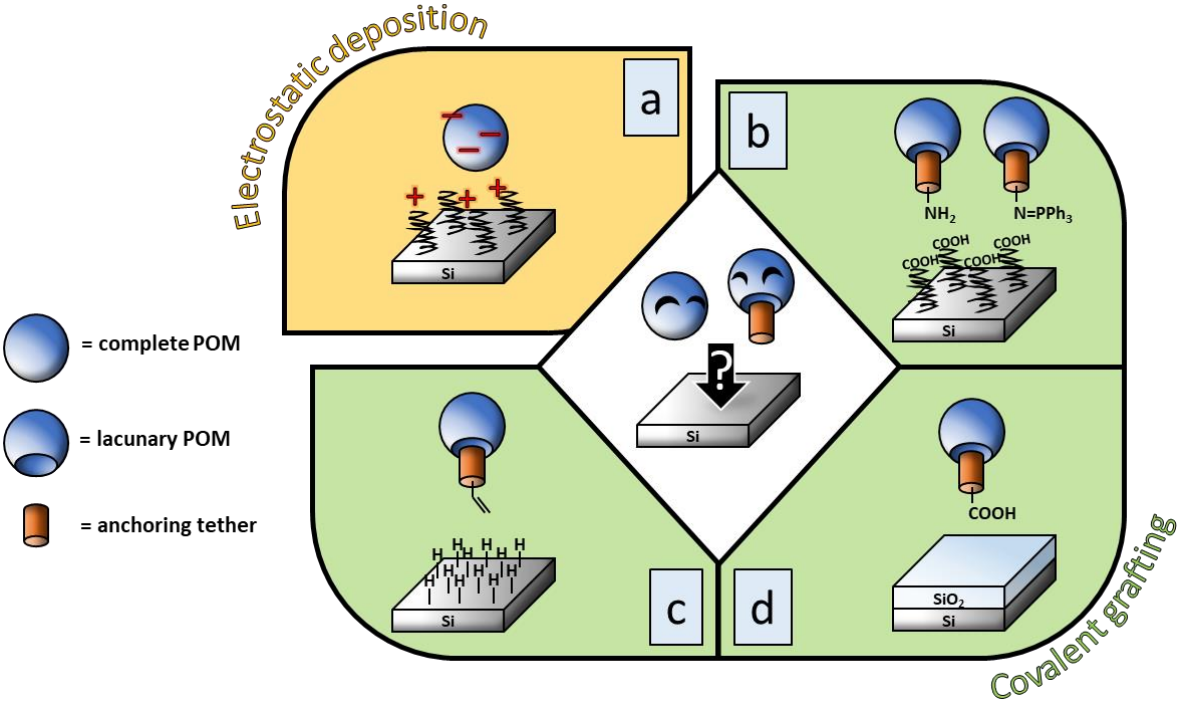

Figure 7 : Strategies of POM immobilization onto Si surface. The electrostatic route (yellow) is the main route of the project with a) the deposition of $[PMo_{12}O_{40}]^{3-}$ onto NH_2/NH_3^+-terminated GOM on Si surfaces. The covalent grafting (green) was envisioned b) on SiCOOH, c) on SiH and d) on SiO_2 surface with POM hybrids bearing different reactive terminal groups (amine or iminophosphorane, alkene, or carboxylic acid functions, respectively).

III. Electrostatic deposition of POMs onto functionalized Si surface

To achieve our project goal on studying the photoreduction phenomenon of immobilized $[PMo_{12}O_{40}]^{3-}$ onto functionalized Si surface, the POM synthesis will be first described before taking a closer look at the adsorption procedure.

III.1. $[PMo_{12}O_{40}]^{3-}$, $[PMo_{12}O_{40}]^{4-}$ and $[PMo_{12}O_{40}]^{5-}$ syntheses

The α-Keggin $(n\text{Bu}_4\text{N})_3[PMo^{VI}_{12}O_{40}]$ POM was synthesized following a well described procedure reported by Sanchez *et al.*[19] and the POM will be labeled **POM(0)** to make it simpler and shown in Figure 8. POM(0) corresponds to the POM in its oxidized state and has the ability to be reduced in solution through the addition of a reducing agent. The one electron reduced compound $(n\text{Bu}_4\text{N})_4[PMo^{VI}_{11}Mo^{V}O_{40}]$ and the two electrons reduced compound $Li(n\text{Bu}_4\text{N})_4[PMo^{VI}_{10}Mo^{V}_{2}O_{40}]$ can be synthesized and they will be labeled **POM(I)** and **POM(II)**, respectively, again to make it simpler. The detailed experimental procedures for the POMs syntheses are given in Appendix 6.1, Appendix 6.2 and Appendix 6.3.

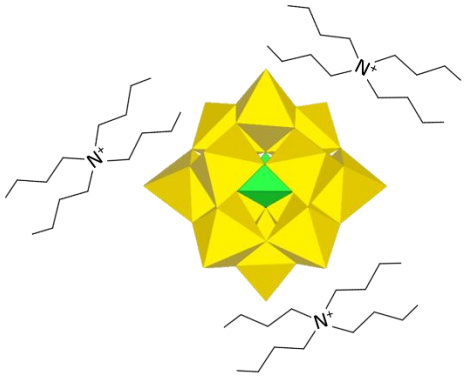

Figure 8 : Representation of the α-Keggin $(n\text{Bu}_4\text{N})_3[PMo^{VI}_{12}O_{40}]$, labeled POM(0).

The synthesized POM is first characterized by ^{31}P and ^{1}H NMR. A singlet at $\delta \approx -3.3$ ppm appears in the ^{31}P NMR spectrum but is accompanied with other signals with rather low intensities that are attributed to impurities. Nevertheless, the recrystallization of the POM powder in acetone[19] is efficient to remove them and the resulting recrystallized POM exhibits a unique singlet at -3.3 ppm, as shown in Figure 9. POM(0) is stored in a glass vial in the dark, in ambient atmosphere. The powder color can turn from yellow to green over time which suggests the formation of reduced species (yellow oxidized species + blue reduced

species = green color), but this happens very slowly by the naked eye. ^{31}P NMR spectrum was always recorded before POM deposition onto surface to make sure that there is only a unique singlet.

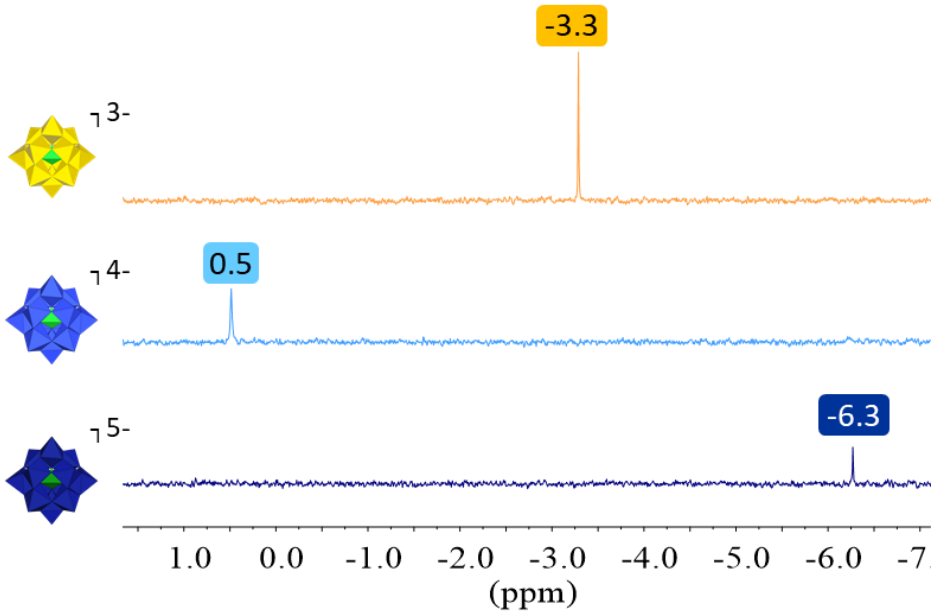

Figure 9 : ^{31}P NMR spectrum of POM(0), POM(I) and POM(II), from top to bottom, recorded in CD_3CN.

The syntheses of both POM(I) and POM(II) have been reported by Artero and Proust,[20] but the procedure used were slightly modified and simplified by M. Mattera (post-doctoral research assistant in the E-POM group). Basically, phenyllithium was added to a POM(0) solution in acetonitrile and the reaction was followed by ^{31}P NMR of the reaction mixture. The addition of phenyllithium was accompanied with a color change, from yellow to green-blue to dark-blue. The more phenyllithium is added, the more the POM gets reduced, leading to the formation of POM(I) and subsequently to the formation of POM(II). As reported by Artero and Proust,[20] a shift in the singlet is also observed in the ^{31}P NMR. POM(I) is characterized by a singlet at 0.5 ppm while POM(II) exhibits a singlet at -6.3 ppm, as shown in Figure 9. Both POMs were stored in the glove box in the dark as there are prone to oxidation when stored in ambient atmosphere.

The POMs can also be characterized by infrared (IR) spectroscopy using KBr pellets. The IR spectrum of POM(0) was recorded and the bands observed are in good agreement with the POM structure.[19–21] In the α-Keggin structure, different types of oxygen atoms can be differentiated as depicted in Figure 10.[22] 4 oxygen atoms are bounded to the central X heteroatom and generally labeled O_a. 24 bridging M-O-M oxygen atoms can be found: 12 of

them are corner-sharing oxygen atoms between two $\{M_3O_{13}\}$ units and labeled O_b, while the 12 others are edge-sharing oxygen atoms inside a $\{M_3O_{13}\}$ unit and labeled O_c. Finally, the 12 terminal oxygen atoms involved in M=O bonds are labeled O_d.

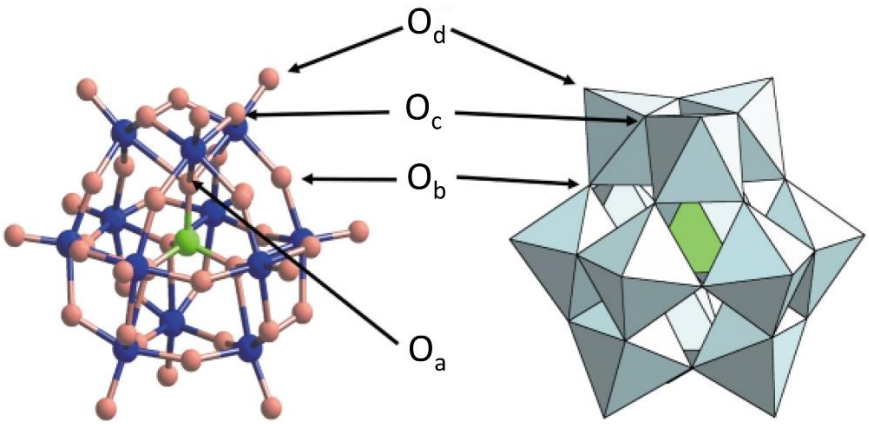

Figure 10: Ball and stick (left) and polyhedral (right) representation of an α-$[XM_{12}O_{40}]^{n-}$ anion. Legend for the ball and stick representation: X (green), M (blue) and O (red). (For a more convenient IR bands assignment, the figure was modified from the original version in ref. 22)

In the IR spectrum, the region between 800 and 1100 cm^{-1} depicted in Figure 11 contains features from the oxo-ligands. The oxygen atom linked to the central P heteroatom of the POM (P-O_a) results in a band at 1063 cm^{-1}. Bridging oxo-ligands between two Mo atoms results in a band at 880 cm^{-1} and 806 cm^{-1}, attributed to Mo-O_b-Mo bridge and Mo-O_c-Mo bridge, respectively. Finally, Mo=O_d bonds result in two bands at 967 and 956 cm^{-1}. We can also note the presence of the bands at 1381 and 1473 cm^{-1} on one hand, and between 2850-3000 cm^{-1} region on the other hand, corresponding to the C-H deformation and stretching of the TBA cations, respectively.

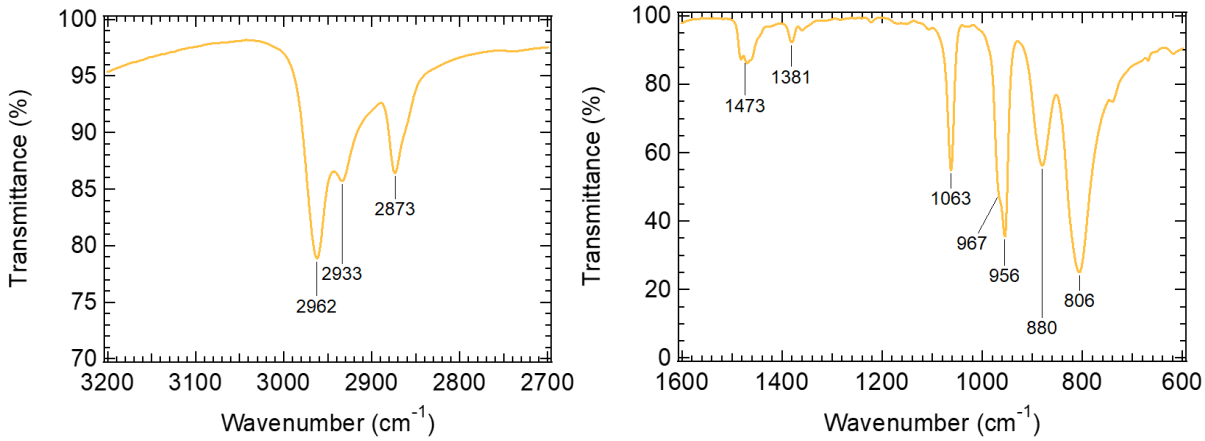

Figure 11 : IR spectrum of $(TBA)_3[PMo_{12}O_{40}]$ (POM(0)) highlighting the 2700-3200 cm^{-1} and the 600-1600 cm^{-1} regions.

III.2. POMs adsorption onto $SiNH_2$ surfaces

As POMs are anionic species, an electrostatic interaction with the surface NH_3^+ functions is expected. After the sample preparation, the $SiNH_2$ surface is inevitably exposed to air (for the rinsing step, ellipsometry measurements, FTIR spectra recording), leading to a weak bonding between the amine NH_2 functions and the water molecules present in air.[23] This subsequently leads to the protonation of the amine to ammonium functions due to their basicity (pKa RNH_3^+/RNH_2 ~10-11 in water, for a non-grafted amine).

After the synthesis of POM(0), adsorption was performed first onto (111)$SiNH_2$ surface by a simple dipcoating of the substrate into a 10^{-3} M POM solution in acetonitrile, which proved to be efficient in the case of an electrostatic immobilization of $[H_7P_8W_{48}O_{184}]^{33-}$ POM onto NH_3^+-terminated alkyl SAM on Au substrate.[3] The resulting surface was routinely characterized by ellipsometry, which was preferred for the rapidity of the measurements over FTIR spectroscopy (also the POM features can be hidden by the SiO_2 region in the IR spectrum). Ellipsometry has been proved to be an efficient and reliable technique in previous studies.[4,17] POM(0) has an approximate diameter of 1.0 nm. It is surrounded by TBA cations that can add 0.5 to 1.0 nm to the total thickness of the POM layer depending on the butyl chains arrangement. The POM can be approximated as a sphere with a diameter of 1.5-2.0 nm. As the occupied volume fraction of a 2D assembling of spheres represents only 60 %,[24] this suggests that a POM monolayer should have a thickness ranging from 0.9 to 1.2 nm. However, from the few sets of values measured by ellipsometry depicted in Figure 12, the POM(0) layer thickness was found below this theoretical thickness range, between 0.3 and 0.6 nm, corresponding to a submonolayer rather than a monolayer of POM(0). Interestingly, POM(I) and POM(II) layers were thicker (POM(II) layer is thicker than POM(I) layer) for the same POM deposition procedure, suggesting a better POM immobilization probably due to the less negative total charge of both POMs, POM(II) being more attracted to the $SiNH_2$ surface. From the thickness measurements, the POM(I) layer thickness is reaching the low end of the theoretical thickness range and the POM(II) layer is globally within the range. Globally, POM(I) and POM(II) monolayers were obtained.

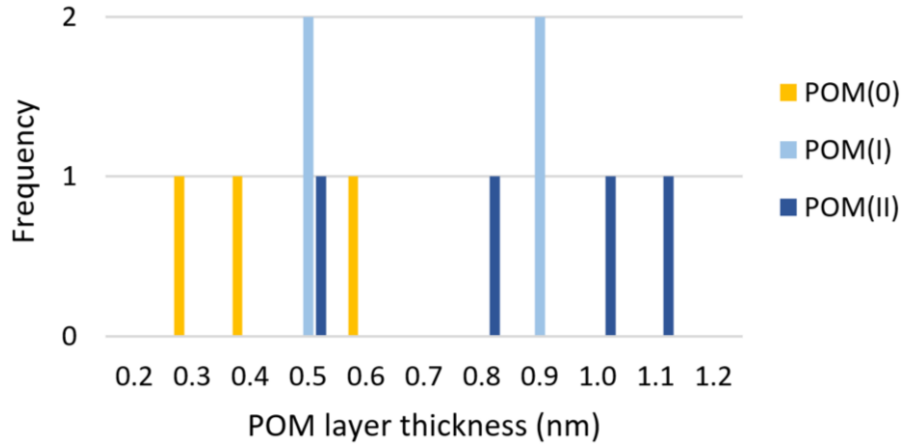

Figure 12 : Histogram of the average thickness of POM(0) (yellow), POM(I) (light blue) and POM(II) (dark blue) layers measured on (111)$SiNH_2$ surfaces.

To improve the deposition of POM(0), we tried to increase the quantity of NH_3^+ groups on the surface. XPS analysis on the N 1s region of $SiNH_2$ surfaces resulted in the presence of two photopeaks at around 402.4 and 400.5 eV, as depicted in Figure 13, corresponding on one hand to nitrogen atoms from the NH_3^+ functions, and on the other hand nitrogen atoms from amide and possibly remaining amine groups.[25,26] XPS analysis performed 3 months after obtaining $SiNH_2$ surface revealed the presence of 22 % of NH_3^+ functions versus 78 % of amide/amine functions after peak deconvolution (Figure 13a). Note that for a freshly prepared sample, the same concentration of NH_3^+ was found (~20 %). We first tried to increase the number of NH_3^+ functions in order to maximize the chance for POM(0) electrostatic immobilization. Accordingly, the $SiNH_2$ surface obtained after the last "peptide coupling" step of the Si functionalization procedure was immersed in a 0.1 M HCl solution for 2 minutes. Without any rinsing with water, the substrate was dried under a stream of N_2 gas. The resulting sample was analyzed by XPS from which a decrease in the quantity of NH_3^+ functions was actually observed (Figure 13b). The same sample was immersed again in acidic medium, this time in a 1.0 M HCl solution for 5 minutes. Again, the substrate was not rinsed with water but it was rinsed with the same 1.0 M HCl solution prior to drying with N_2 gas. The quantity of NH_3^+ decreased again and a final concentration of 11% was deduced from the XPS spectrum in the N 1s region (Figure 13c). An attempt to maximize the NH_3^+ functions on the surface via methylation of the NH_2-terminal groups was performed, following a procedure reported by Fleury *et al.*[27] The $SiNH_2$ substrate was immersed overnight in a solution containing 1.0 mL iodomethane and 5.0 mL dichloromethane. The resulting substrate was rinsed with dichloromethane and ethanol and finally dried under a stream of N_2 gas. However, no increase in the concentration of methylated amine groups was observed.

Thus, it seems that there is a maximum amount of NH_3^+ groups of ~20 % (without any treatment), though XPS analysis of $SiNH_2$ surfaces was not systematically performed. This difficulty to protonate the terminal amine groups could be explained by a lower apparent surface pKa value of the RNH_3^+/RNH_2 couple. Indeed, it has been reported that a NH_2-terminated SAM grafted onto gold electrode has a lower apparent surface pKa than the pKa of 10-11 observed in water. Interestingly, the apparent surface pKa decreased even more when the chain length increases, and this was attributed to an increase in electrostatic repulsions between the terminal NH_3^+ groups.[28] The concentration of NH_3^+ groups observed in the XPS spectrum thus corresponds to the concentration of the amine groups at the acid-base equilibrium.

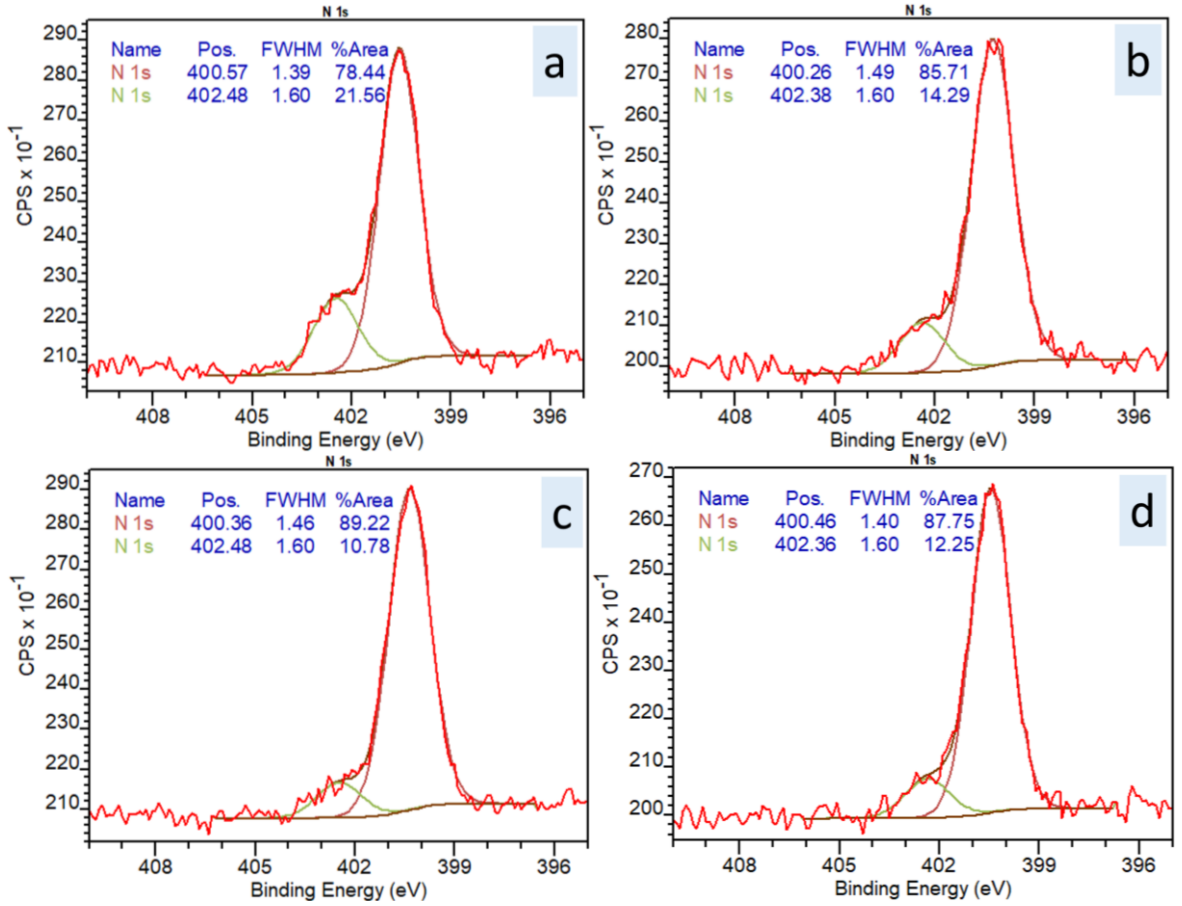

Figure 13 : XPS spectrum in the N1s region of a) $SiNH_2$ surface obtained after the last peptide coupling step of the functionalization procedure; b) the same $SiNH_2$ surface after immersion in 0.1 M HCl solution for 2 minutes; c) the same $SiNH_2$ surface after immersion in 1.0 M HCl solution for 5 minutes and d) the same $SiNH_2$ surface after methylation attempt in iodomethane solution.

Also based from the functionalization procedure reported by Fleury *et al*,[27] an attempt to functionalize SiCOOH with *N*,*N*-dimethylethylenediamine instead of ethylenediamine was performed. This will result in a surface terminated with dimethylamine functions (labeled **SiNMe$_2$** surface). Indeed, the authors reported a 35% higher surface coverage of $[SiW_{12}O_{40}]^{4-}$ when using terminated methylated instead of protonated amine groups. To do so, the SiCOOH substrate was immersed ~5 minutes in a 5.0 mL solution containing EDC (0.8 mg/mL) and dichloromethane. After addition of 0.5 mL of *N*,*N*-dimethylethylenediamine to the solution, the substrate was left overnight in the solution at room temperature under argon. After rinsing with dichloromethane, acetone and ethanol, and drying with N_2 gas, an increase of 0.3 nm was measured by ellipsometer, compared with the SiCOOH before peptide coupling. The SiNMe$_2$/SiCOOH differential spectrum (Figure 14, left) also supports the grafting as the $\nu_{amide\ I}^{C=O}$ at 1654 cm^{-1} is observed. At this stage, the same concentration of ~22% of protonated dimethyleamine functions was measured by XPS, as depicted in Figure 14 (right).

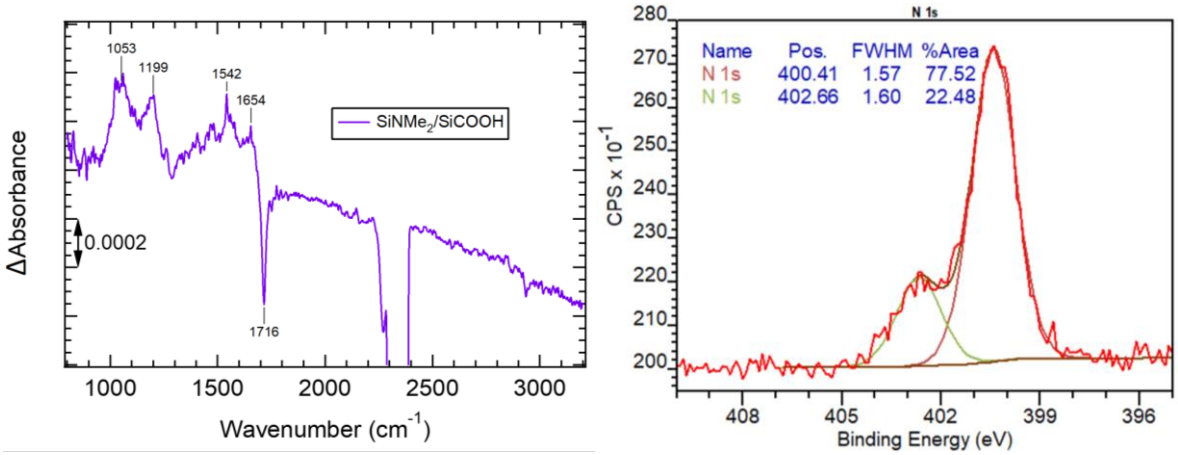

Figure 14 : SiNMe$_2$/SiCOOH differential spectrum (left) and XPS spectrum in the N 1s region of the SiNMe$_2$ surface (right).

The SiNMe$_2$ sample was thus subjected to a methylation with iodomethane as previously described, followed by XPS analysis. The N 1s region shown in Figure 15 reveals an increase of ~5% in the NMe_3^+ groups concentration on the surface. However, after POM(0) deposition, only an increase of 0.1 nm was measured, lower than what was obtained with the SiNH$_2$ surface not subjected to acidic medium or methylation.

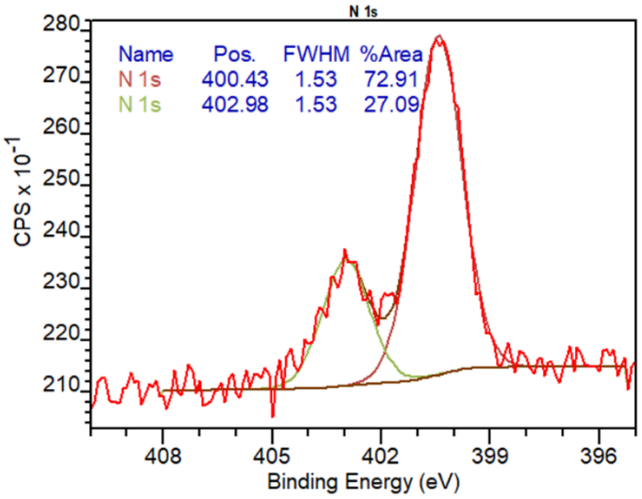

Figure 15 : XPS spectrum in the N 1s region of the $SiNMe_2$ surface after methylation with iodomethane.

In conclusion, a protonated amine groups concentration of ~20-25% was calculated by XPS on the $SiNH_2$ surfaces analyzed. We decided to keep the $SiNH_2$ surface as it is, which is sufficient enough to get a monolayer of POM(I) and POM(II), while POM(0) submonolayer is systematically obtained. The characterization of those (sub)monolayers were carried out and will be described in the next chapter.

IV. POM hybrids grafting onto Si surfaces: an exploration

Though not constituting the main goal of the project, the POM grafting onto functionalized Si surfaces via a covalent linkage was explored. The covalent grafting of POMs has the advantage, over the electrostatic route, to allow a better control on the POM/surface interaction while at the same time improving the stability of the assembling. Note that more time was spent on the optimization of the $SiNH_2$ functionalization procedure (Chapter II) and on the POM photoreduction study (Chapter IV), thus not a lot a statistics pop out from the several grafting attempts that will be described hereinafter. The two-step grafting (*i.e.* functionalizing the Si surface prior to POM hybrid immobilization) and the direct grafting of POM (*i.e.* directly onto an unfunctionalized surface) will be detailed. These two parts will remain only qualitative and clearly requires more investigation for more reliability and POM/surface interaction understanding. A final POM grafting example onto SiO_2 surface with a more complete set of characterization including electrical measurements will be described.

IV.1. Grafting of POM hybrids onto SiCOOH surfaces

Previous work in our group has investigated the interaction between the activated form of $TBA_4[PW_{11}O_{39}\{Sn(C_6H_4)C{\equiv}C(C_6H_4)(COOH)\}]$ and a SAM of 8-amino-1-octanethiol on gold surface.[26] However, a preferential electrostatic interaction between the NH_3^+ functions and the inorganic core of the POM was observed.[26] Yet, the covalent grafting was achieved by reversing the system, that is to say using a COOH-activated Au surface and an NH_2-terminated POM.

Here, the covalent grafting of POM hybrids will be explored by taking advantage from our previously prepared SiCOOH surface but also from the POM functionalization developed in the group. For this two-step grafting process, we set our choice first on POM hybrids bearing one or two terminal NH_2 functions, which are $TBA_4[PW_{11}O_{39}\{Sn(C_6H_4)C{\equiv}C(C_6H_4)NH_2\}]$ (later labeled $\mathbf{K^W_{Sn}[NH_2]}$) and $TBA_3[PW_{11}O_{39}\{O(Si(C_6H_4)NH_2)_2\}]$ (later labeled $\mathbf{K^W_{Si}[(NH_2)_2]}$), respectively (see Figure 16). Both POMs were chosen to extend the peptide coupling of the ethylenediamine molecule used to prepare $SiNH_2$ surfaces. Their grafting procedures will be described and are summarized in Appendix 5.7. We also tried to synthesize $TBA_3[PW_{11}O_{39}\{O(SiC_2H_4N{=}PPh_3)_2\}]$ POM (later called $\mathbf{K^W_{Si}[(N{=}PPh_3)_2]}$), bearing iminophosphorane functions that are aimed to be highly reactive towards COOH functions, which is an alternative to the common peptide coupling. Insights on the synthesis procedure will be provided.

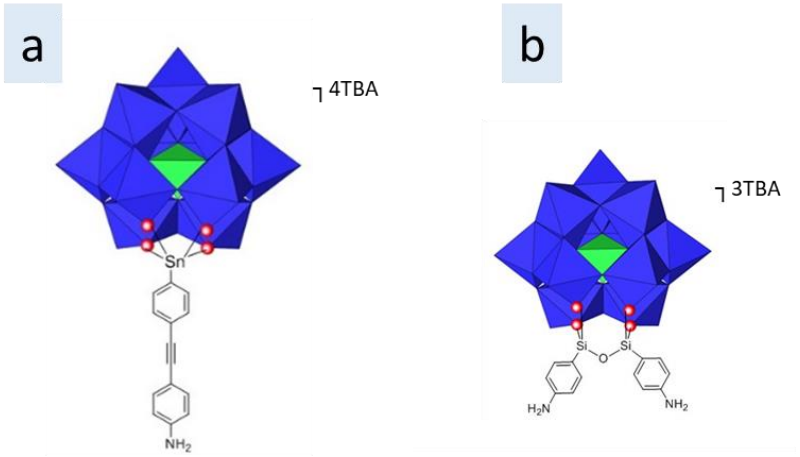

Figure 16 : Structure of a) $K^W_{Sn}[NH_2]$ and b) $K^W_{Si}[(NH_2)_2]$.

IV.1.a. $K^{W}_{Sn}[NH_2]$ onto activated SiCOOH surface

The $K^{W}_{Sn}[NH_2]$ POM synthesis was reported by M. Laurans.[26] Though not totally reproducible, a successful grafting of the POM onto a COOH-terminated SAM on gold surface (obtained from a 8-mercaptooctanoic acid solution) was achieved. The POM was prepared following the synthesis described in Appendix 6.5. As this covalent route was explored during the first year of the research project, the functionalization procedure on Si surfaces was not yet optimized: the SiCOOH surface preparation involved a 15 min hydrogenation in NH_4F and an overnight hydrosilylation, followed by the ester functions hydrolysis. Except for these two parameters, the surface functionalization procedure remained unchanged from the procedure described in Appendix 5.2. In order to react with the amine function of the POM, the SiCOOH surface has to be activated via the formation of reactive succinimidyl ester terminal groups (later called **SiCOOSuc** surface). To do so, the SiCOOH surface was immersed in a EDC.HCl/NHS solution (30/60 mM) in water for 1h15-1h30 under a static flow of argon. It was subsequently rinsed with water, subjected to a sonication bath in water, rinsed again with water and dried under a stream of N_2 gas. The resulting activated SiCOOH substrate was immersed in a $K^{W}_{Sn}[NH_2]$ POM solution in acetronitrile (10^{-3} M) under a static flow of argon for 72 hours. The resulting substrate was first rinsed with a flow of acetonitrile and dried under N_2 gas for a first set of ellipsometry measurements. It was then thoroughly rinsed with acetonitrile and subjected to 3-4 sonication baths in acetonitrile, including one with $TBAPF_6$ (0.1 M) to remove all the physisorbed species. The organic tether of $K^{W}_{Sn}[NH_2]$ has a length of 1.3 nm. Together with the inorganic core (~1.0 nm) and the TBA cations (0.5-1.0 nm), a thickness of the $K^{W}_{Sn}[NH_2]$ layer is expected to range from 2.8 to 3.3 nm if the POM is grafted vertically. Due to the arrangement of the terminal COOH functions, a tilt of the grafted POM is conceivable, though no exact value was calculated. Considering a reasonable tilt of 30-50°, the thickness of the POM layer could range from approximately 2.0 to 2.7 nm. Two attempts of grafting of $K^{W}_{Sn}[NH_2]$ on activated SiCOOH surface were performed.

Due to an issue with the compressed air dryer of the FTIR spectrometer, the first attempt was carried out on a single side polished Si surface and the functionalization procedure was followed by ellipsometry only. The second attempt was carried out with a double side polished Si surface, after the repairs of the air dryer allowing ellipsometry measurements and IR spectra recording. The average thicknesses measured after each step of the functionalization procedure for both attempts are reported in Table 1.

Layer thickness (nm)	*Attempt #1*	*Attempt #2*
Regrown oxide	1.4	1.3
Siester	1.6	2.1
Siester after sonication baths	1.6	1.8
SiCOOH	1.4	1.7
Activated SiCOOH	1.6	1.9
$K^{W}_{Sn}[NH_2]$ layer only	2.3	1.6
$K^{W}_{Sn}[NH_2]$ layer only after sonication baths	1.2	1.2

Table 1 : Average layer thickness (in nm) measured by ellipsometry after each step of the functionalization procedure from the oxide regrown to the $K^{W}_{Sn}[NH_2]$ grafting step.

From the oxide regrowth step to the activation of the SiCOOH surface, the thicknesses are in good agreement with the expected values, except for the Siester surface on the second attempt that is a little bit thicker (1.8 nm), probably due to the formation of oxide during the hydrosilylation reaction as observed in the Siester/SiH spectrum by the growth of bands at 1041 and 1182 cm^{-1} corresponding to the TO mode of SiO_2 and $\delta^{CH_2}_{rocking}$ of $SiO\text{-}CH_2\text{-}$ groups (Figure 17a, blue curve). Globally, a ~2.0 nm POM layer was measured right after the first rinse with acetonitrile. However, it decreased throughout the sonication baths and the resulting POM layer exhibited an average thickness of only 1.2 nm, lower than the targeted 2.0-2.7 nm range.

The spectrum of $K^{W}_{Sn}[NH_2]$ layer recorded after sonication baths was referenced to the spectrum of SiCOOH, labeled $K^{W}_{Sn}[NH_2]$/SiCOOH and shown in Figure 17b. No amide bond around 1650 cm^{-1} can be distinguished from the spectrum, suggesting at first sight that the covalent grafting of the POM onto the SiCOOSuc surface failed. The substrate activation and incubation for 72 hours in the POM solution followed by sonication baths obviously led to the formation of oxide with the growth of bands at 1039 and 1211 cm^{-1}. The band at 1743 cm^{-1} could correspond to the $\nu^{C=O}_{COOSuc}$ asymmetric stretch of the remaining succinimidyl ester.[29,30] The region around 1500-1600 cm^{-1} is not very clear. It looks, from the shape of the curve in this region in the Siester/SiH and SiCOOH/SiH spectra, that the single channel spectra subtractions (together with the water vapor spectrum subtraction) were not good enough, probably due to a bad repositioning of the substrate on the sample holder. The band arisen at 1571 cm^{-1} in the $K^{W}_{Sn}[NH_2]$/SiCOOH is thus probably not characteristic of the $K^{W}_{Sn}[NH_2]$-containing surface.

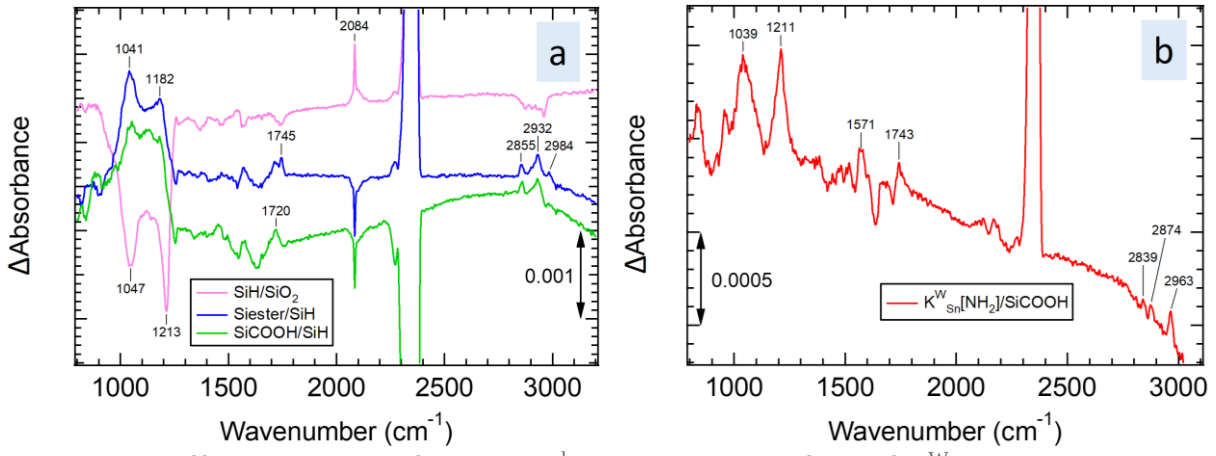

Figure 17 : Differential spectra from the 2nd attempt in the grafting of $K^{W}_{Sn}[NH_2]$ on activated SiCOOH surface. a) The SiH surface is referenced to the SiO_2 surface, while both Siester and SiCOOH surfaces are referenced to the SiH surface; b) spectrum of the $K^{W}_{Sn}[NH_2]$ layer after sonication baths referenced to the SiCOOH surface.

Though only two attempts were performed, the grafting of $K^{W}_{Sn}[NH_2]$ was not very conclusive according to the results obtained both by ellipsometry and FTIR spectroscopy.

IV.1.b. $K^{W}_{Si}[(NH_2)_2]$ onto activated SiCOOH surface

As the grafting of $K^{W}_{Sn}[NH_2]$ onto SiCOOSuc surface was not satisfying, we turned to the $K^{W}_{Si}[(NH_2)_2]$ polyoxotungstate exhibiting two terminal NH_2 functions instead of one, which could increase the chance of POM grafting. The $K^{W}_{Si}[(NH_2)_2]$ POM synthesis was reported by Proust and coll.,[31] and successfully grafted onto a succinimidyl ester terminated SAM on gold surface.[30] Three grafting attempts were carried out using a batch of POM kindly provided by M. Martin (post-doctoral research assistant in the E-POM group). The activation of the COOH-terminated GOM and the POM grafting step were the same as described above in the section IV.I.a. The organic tether of $K^{W}_{Si}[(NH_2)_2]$ has an approximative length of 0.5 nm while the inorganic core and TBA cations have a thickness of ~1.0 nm and 0.5-1.0 nm, respectively. The thickness of the $K^{W}_{Si}[(NH_2)_2]$ layer is thus expected to range between 2.0 and 2.5 nm.

The average thicknesses measured during the SiCOOH surface modification are reported in Table 2 for the three grafting attempts. The differential spectra obtained throughout the surface modification are depicted in Figure 18a, Figure 18b and Figure 18c corresponding to the differential spectra obtained during the first, second and third attempt, respectively. Note that the "$K^{W}_{Si}[(NH_2)_2]$" written in the legend of each set of spectra refers to the spectrum of the SiCOOSuc surface in presence of $K^{W}_{Si}[(NH_2)_2]$ POMs.

Layer thickness (nm)	Attempt #1	Attempt #2	Attempt #3
SiCOOH	2.0	1.9	2.1
Activated SiCOOH	2.2	2.3	2.3
$K^{W}_{Si}[(NH_2)_2]$ layer only	2.1	1.0	1.2
$K^{W}_{Si}[(NH_2)_2]$ layer only after sonication baths	0.9	0.6	x

Table 2 : Average layer thickness (in nm) measured by ellipsometry after each step of the functionalization procedure from the ester functions hydrolysis to the $K^{W}_{Si}[(NH_2)_2]$ grafting step

We can first exclude the results obtained from the second attempt. Indeed, as observed on the differential spectrum $K^{W}_{Si}[(NH_2)_2]$/SiH in Figure 18b, a band arose at 1737 cm^{-1} after the POM grafting attempt and is attributed to the asymmetric $\nu^{C=O}_{COOSuc}$ of the succinimidyl ester functions. Apparently, the latter did not react with the NH_2 functions of the POM as no amide bond around 1650 cm^{-1} is observed. Moreover, a 1.0 nm thickness was observed after the POM grafting attempt which decreased throughout the sonication baths and reached a final 0.6 nm thickness.

The first and third attempt were more successful. During the first attempt, a satisfying POM thickness of 2.1 nm was obtained after a simple rinsing with acetonitrile. The spectrum of the resulting surface was referenced to the SiH spectrum and depicted in red in Figure 18a. A band at 1739 cm^{-1} ($\nu^{C=O}_{COOSuc}$) is still observed but with a lower intensity than for the second attempt. Instead, a band at 1658 cm^{-1} is detected and can be attributed to $\nu^{C=O}_{amide\ I}$, suggesting a covalent grafting of the POM onto the SiCOOSuc surface. A band at 964 cm^{-1} is detected as well, and can be attributed to the $W{=}O_d$ bond of the inorganic core of the POM hybrid. It is by the way the more intense band on the IR spectrum of the POM powder recorded on a KBr pellet (see Appendix 3.1). Successive ultrasonication (US) baths decreased twice the POM layer thickness, but the bands at 1658 and 964 cm^{-1} can still be guessed in the $K^{W}_{Si}[(NH_2)_2]$+US/SiH differential spectrum (green curve in Figure 18a).

For the third attempt, a thickness of 1.2 nm of the POM layer was achieved after a thorough rinse with acetonitrile, close to the thickness obtained in the first attempt after thorough sonication baths. Because of this thickness lower than the expected one, no added sonication baths were performed. Interestingly, the bands at 1658 and 964 cm^{-1} were also detected in the $K^{W}_{Si}[(NH_2)_2]$/SiH spectrum, shown in red in Figure 18c, with similar intensities than the $K^{W}_{Si}[(NH_2)_2]$/SiH spectrum of the first attempt (red curve in Figure 18a). Due to the presence of the band at 1658 cm^{-1}, it looks like the POM is attached to the surface via covalent

linkage. Note also the bands at 1577 cm^{-1} and 1604 cm^{-1} which are clearly distinguished after POM deposition and can be attributed to the C=C stretching mode of the aromatic cycles and the N-H deformation mode of the amine groups of the POM, respectively. These two bands are indeed observed in the IR spectrum of the POM and appeared shifted at 1599 cm^{-1} and 1623 cm^{-1} respectively (see Appendix 3.1). The presence of the latter on the spectrum after POM deposition suggests that not all the amine groups of the POM have reacted to the surface.

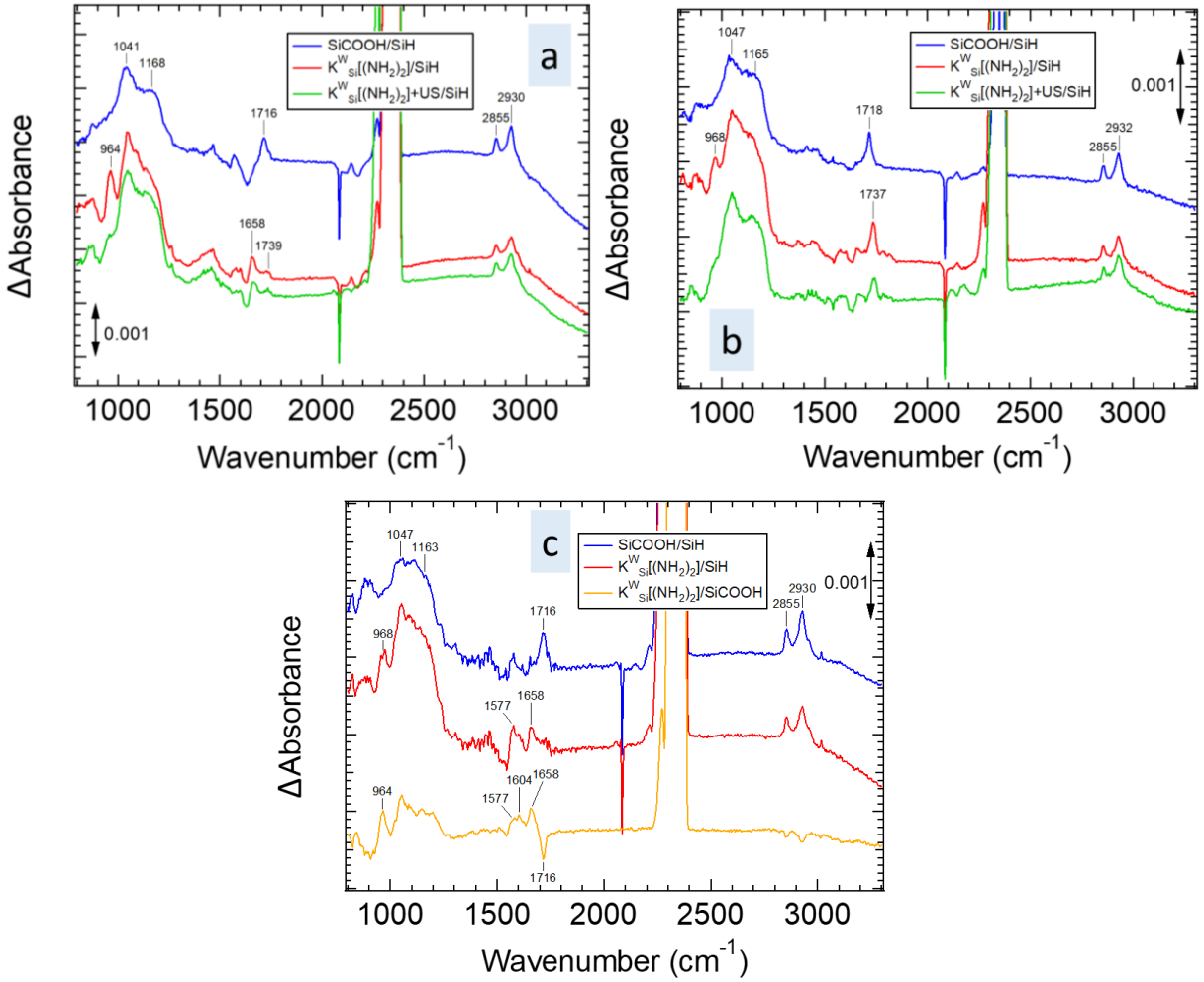

Figure 18 : Differential spectra from the first (a), second (b) and third (c) attempt in the grafting of $K^{W}_{Si}[(NH_2)_2]$ on activated SiCOOH surface. The SiCOOH spectrum is referenced to the SiH spectrum (blue), the spectrum of the $K^{W}_{Si}[(NH_2)_2]$ containing surface after an acetonitrile rinsing (red) and after ultrasonication (US) baths (green) is referenced to the SiH spectrum.

Among the three attempts, two gave similar results with a $K^{W}_{Si}[(NH_2)_2]$-containing surface exhibiting a POM layer of ~1.0 nm, twice lower than what we expected, which could bring some doubt on the amount of POMs immobilized on the surface. More experiments need to be carried out for more statistics, together with other characterization tools to support the POM covalent anchoring and their arrangement on the surface. The $K^{W}_{Si}[(NH_2)_2]$ grafting was at least more successful than the $K^{W}_{Sn}[NH_2]$ grafting.

IV.1.c. An attempt for $K^{W}_{Si}[(N=PPh_3)_2]$ synthesis

An attempt to synthesize $K^{W}_{Si}[(N=PPh_3)_2]$ POM bearing two iminophosphorane groups was performed as another way to graft POM onto an activated SiCOOH. Iminophosphorane groups have indeed been used to form amide bonds,[32–34] via a Staudinger ligation used a lot in chemical biology.[35] The synthesis of $K^{W}_{Si}[(N=PPh_3)_2]$ was investigated by the reaction between an "azido-POM" $TBA_3[PW_{11}O_{39}\{O(SiC_2H_4N_3)_2\}]$, labeled **$K^{W}_{Si}[(N_3)_2]$**, bearing two azide functions, with triphenylphosphine (PPh_3) under anhydrous conditions (Scheme 4). Care should be taken since the iminophosphorane functions can undergo a hydrolysis in the presence of water molecules, leading to the formation of amine functions and triphenylphosphine oxide ($O=PPh_3$).

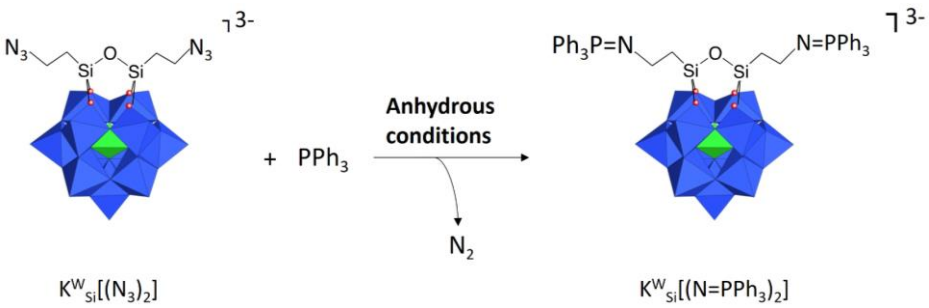

Scheme 4 : Synthesis of $K^{W}_{Si}[(N=PPh_3)_2]$ POM.

The $K^{W}_{Si}[(N_3)_2]$ POM powder was kindly provided by W. Wang (PhD student in the E-POM group) with the help of procedures developed by N. Kostopoulos (intern in the group). The first attempt involved the use of 1 equivalent of POM for 2 equivalents of PPh_3 and anhydrous DMF as solvent (bought on molecular sieves) which was degassed prior to the reaction. The reaction was performed under argon at room temperature. Precipitation of a fraction of the reaction mixture by addition of diethylether (Et_2O) and centrifugations were performed to monitor the reaction. The resulting white powder was analyzed by NMR, together with IR spectroscopy via KBr pellets.

From the ^{1}H NMR spectra shown in Figure 19a, the starting POM, $K^{W}_{Si}[(N_3)_2]$, exhibits signals at ~1.0, 1.3, 1.6 and 3.2 ppm corresponding to the TBA cations, as well as signals at ~1.2 and 3.5 ppm corresponding to the CH_2 groups of the organic tethers. As the reaction proceeds, a broad signal increases in the aromatic proton region around 7.8 ppm, corresponding to the protons of the phenyl groups.

On the ^{31}P NMR spectra (Figure 19b), the starting POM displays an intense signal at -13.2 ppm. Throughout the reaction, this signal evolves: after 24 hours of reaction, the signal

is not present anymore. Instead, a new couple of signals appears after 48 hours of reaction, at -12.9 and -12.5 ppm, suggesting that the POM evolves into several species as the reaction proceeds. Another signal is also growing throughout the reaction at 37.1 ppm. ^{31}P NMR spectra of PPh_3 and $O{=}PPh_3$ are shown in Appendix 3.2 and Appendix 3.3, and they are characterized by a signal at approximately -6.2 ppm and 26.0 ppm, respectively. Since PPh_3 and $O{=}PPh_3$ are soluble in Et_2O, the signal depicted at 37.1 ppm can thus be attributed to a new specie.[36]

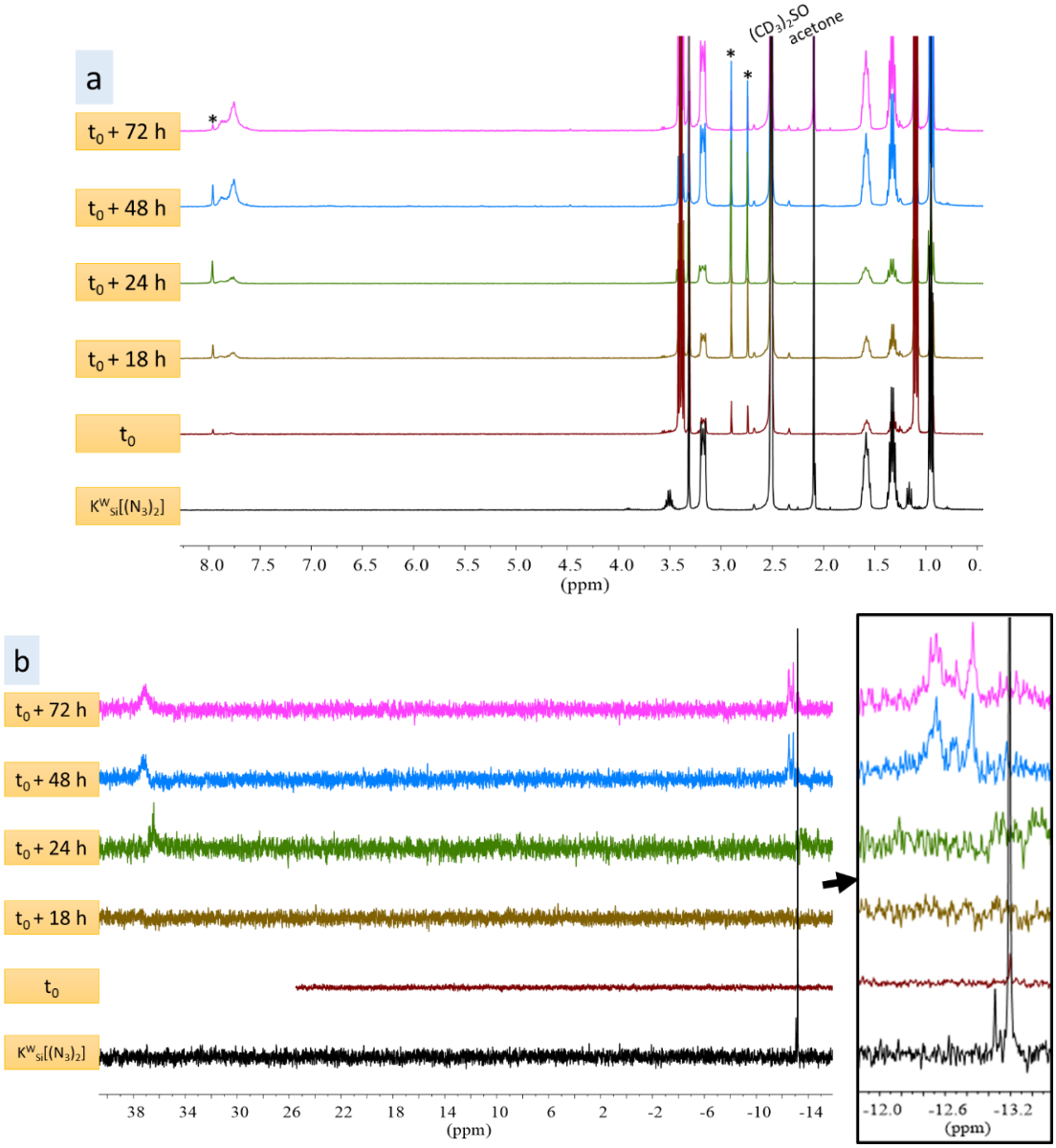

Figure 19 : a) ^{1}H and b) ^{31}P NMR spectra of the powder obtained after precipitation of a fraction of the reaction mixture with Et_2O, at the start of the reaction, after 18, 24, 48 and 72 hours. (* = DMF; the inset is an enlargement of the region between -12.0 and -14.0 ppm). The NMR spectra of the $K^W_{Si}[(N_3)_2]$ POM are also shown (black). All NMR spectra were recorded in deuterated DMSO (DMSO-d_6).

IR spectra of the powders obtained after the several precipitations of the reaction mixture were recorded for supplementary information and they are shown in Figure 20. The main changes in the IR spectrum between the starting POM and the final product lie in the 1200-2200 cm^{-1} region. The starting POM exhibits bands at 2086 and 2122 cm^{-1} correspond to the asymetric N_3 stretching mode, together with bands at 1381 and 1483 cm^{-1} corresponding to δ^{C-H} of the C-H groups in the TBA cations. As the reaction proceeds, the spectra of the powder obtained are characterized by an strong band at 1667 cm^{-1} corresponding to $\nu^{C=O}_{amide\ I}$ of DMF. On the other hand, a band at 1440 cm^{-1} appears and could be attributed to the P=N stretching.[37] However, the bands corresponding to the N_3 stretching mode are still present, suggesting an incomplete reaction of the azido functions.

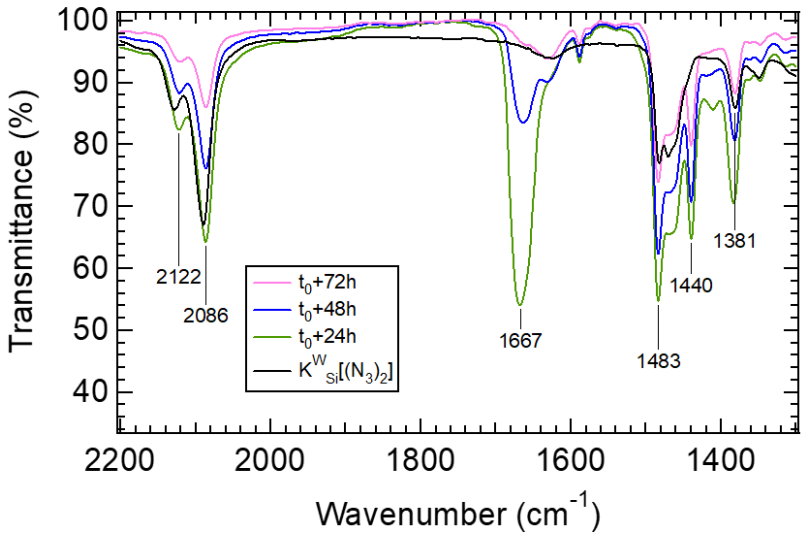

Figure 20 : IR spectra of the powder obtained by precipitation of the reaction mixture, after 24h (green), 48h (blue) and 72h (pink) of reaction. The IR spectrum of the starting $K^{W}_{Si}[(N_3)_2]$ POM is also shown (black).

In order to have a better conversion of the azido groups, other tests were performed. Increasing the temperature reaction to 60°C was worse, since the ^{31}P NMR spectra of the reaction mixture after ~20 hours of reaction revealed a signal at ~26.0 ppm corresponding to the $O=PPh_3$. The procedure was thus kept at room temperature, but the quantity of PPh_3 was raised to 10 equivalents. The reaction was followed by ^{1}H and ^{31}P NMR directly from fractions of the reaction mixture (without precipitation this time), and the spectra are shown in Figure 21. The same signal around 37.1 ppm appears, as previously, in the ^{31}P NMR spectrum (Figure 21b). Again, the signal of the starting POM at -13.1 ppm evolves throughout the reaction and faster than in the experimental procedure involving less equivalents of PPh_3. After 41 hours of reaction, the signal is seen at -12.3 ppm and looks unique compared to the previous experiment

(see inset of Figure 19b). Note also that no formation of $O=PPh_3$ specie was witnessed by ^{31}P NMR of the reaction mixture fractions for the 45 hours of reaction (Figure 21b).

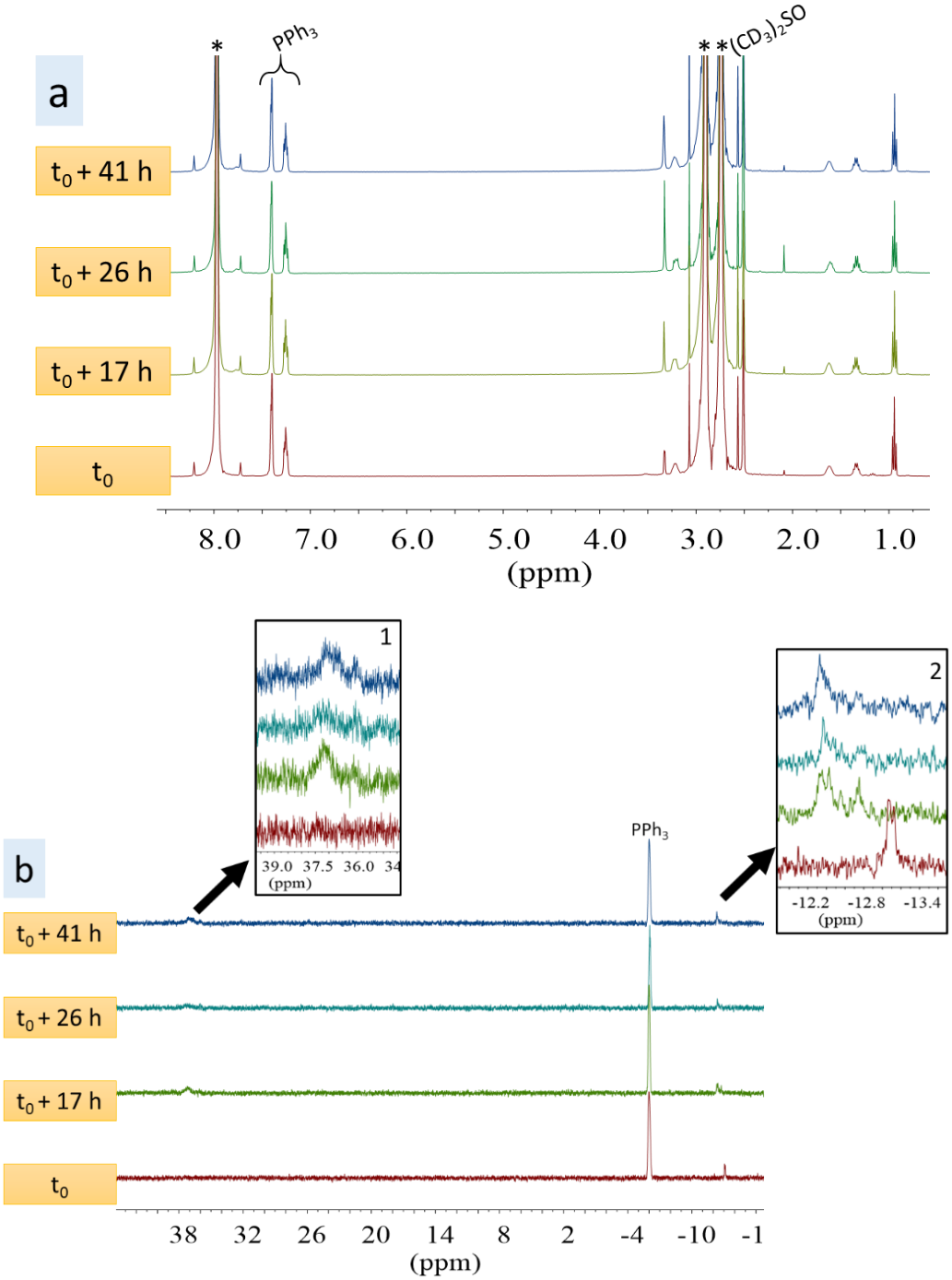

Figure 21 : a) ^{1}H and b) ^{31}P NMR spectra of a fraction of the reaction mixture (without precipitation) at the start, after 17h, after 26h and after 41h of reaction. (* = DMF; inset 1 is the enlargement of the 34.0-39.0 ppm region, inset 2 is the enlargement of the region between -12.0 and -14.0 ppm). The reaction is performed in DMF with 10 equivalents of PPh_3 and the spectra are recorded with DMSO-d_6.

After precipitation of a fraction of the reaction mixture, the IR spectrum of the crude was recorded and is shown in Figure 22 (blue curve). The band at 2086 cm^{-1} is still there, suggesting that some N_3 groups remain.

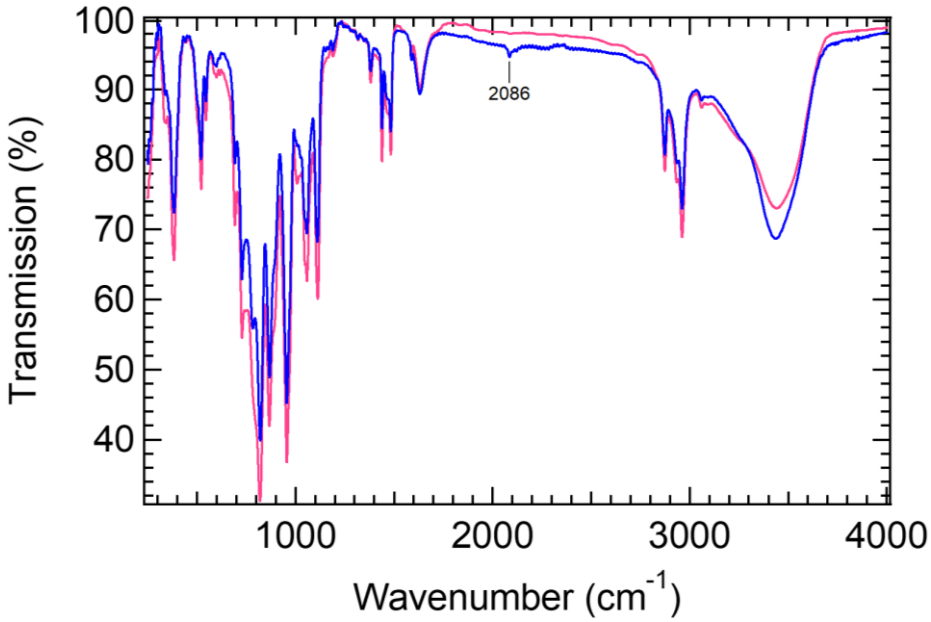

Figure 22 : IR spectrum of the precipitate obtained after the reaction with 10 equivalents of PPh_3 at room temperature in DMF (blue curve) and acetonitrile (pink curve).

The reaction solvent was finally changed to acetonitrile, as we suspected a degradation of the POM in DMF, still with the 10 equivalents of PPh_3. The reaction was again followed by ^{1}H and ^{31}P NMR of fractions of the reaction mixture and the spectra are shown in Figure 23. The use of acetonitrile allows us to see a growth in a signal between 7.7 and 7.9 ppm in the aromatic proton region, as shown in Figure 23a, clearly distinguishable from the protons of PPh_3 molecules at 7.3 and 7.4 ppm. This deshielding supports the formation of $N{=}PPh_3$ bonding. The ^{31}P NMR spectrum (Figure 23b) also displays a signal at ~38.0 ppm suggesting the formation of a new specie. Also, the unique signal of the POM at -12.9 ppm at the beginning completely disappeared and a new unique signal is observed at -12.2 ppm (see inset of Figure 23b) after 17h of reaction. The use of acetonitrile led practically to the same results. After 72 hours of reaction the precipitate was isolated and its IR spectrum is shown in Figure 22 (pink curve). The band at 2086 cm^{-1} corresponding to the N_3 stretching, has completely vanished (note that it could be due to the longer time reaction rather than the change of solvent).

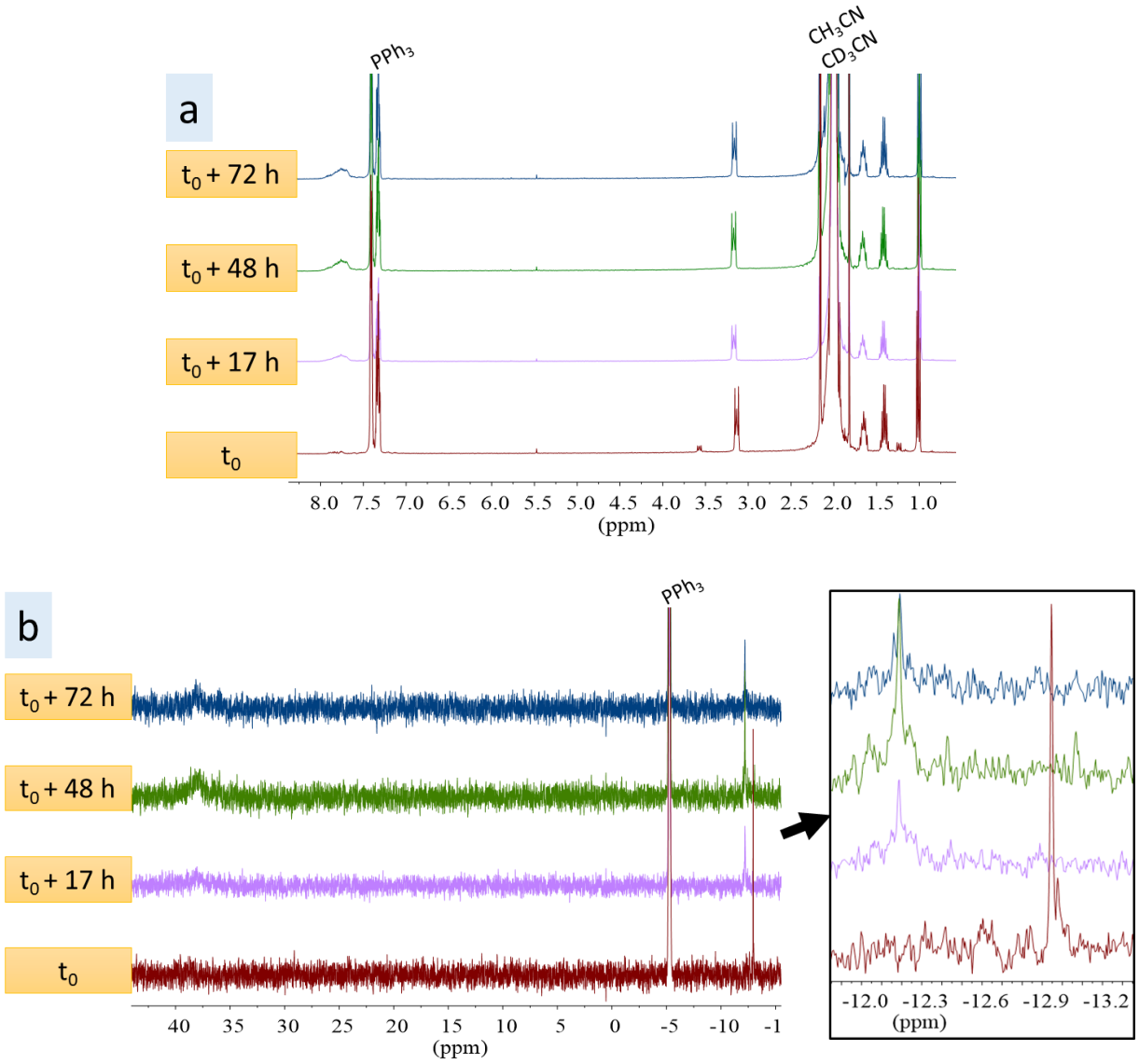

Figure 23 : a) ^{1}H and b) ^{31}P NMR spectra of fractions of the reaction mixture (without precipitation), at the start, after 17h, after 48h and after 72h of reaction. (inset in (b) is the enlargement of the region between -12.0 and -13.2 ppm. The reaction is performed in acetonitrile with 10 equivalents of PPh_3 and the spectra are recorded with CD_3CN.

To summarize, the reactivity of $K^{W}_{Si}[(N_3)_2]$ towards PPh_3 in search of $K^{W}_{Si}[(N{=}PPh_3)_2]$ was investigated. Preliminary results obtained with the help of NMR and IR spectroscopy are encouraging. While the ^{31}P NMR spectra suggest the formation of a new specie with the growth of a signal at ~37.0-38.0 ppm and the modification of the unique signal of the starting POM, the IR spectra confirmed the reactivity of the azido groups throughout the reaction. However, further characterizations are needed to confirm or not the formation of $K^{W}_{Si}[(N{=}PPh_3)_2]$. Doubts still remain as we expected the product to be much more sensitive to water, while in our case no formation of triphenylphosphine oxide was witnessed during the syntheses.

IV.2. Direct grafting of POM hybrids onto SiH surfaces via hydrosilylation

Attempts in grafting POM hybrids bearing a terminal alkene function directly onto (111)SiH surface via hydrosilylation were performed. The idea was to shorten the distance between the POM (inorganic core) and the substrate which could possibly improve the vertical electron tunneling transport between the POM and the substrate, while at the same time allowing a covalent anchor of the POM for a more robust system. We thus focused on two POMs which are $TBA_3[PW_9O_{34}(OSiCH{=}CH_2)_3(SiCH{=}CH_2)]$ (later labeled **POM-vinyl**) and $TBA_3[PW_9O_{34}(OSiCH_2CH{=}CH_2)_3(SiCH_2CH{=}CH_2)]$ (later labeled **POM-allyl**). They have been studied by N. Joo[38] and LM. Perkins,[39] helped with reports from Niu *et al.*[40,41] particularly. These POMs have four short organic arms and each of them is terminated with an alkene function. They are obtained via the reaction of the trivacant polyoxotungstate $[PW_9O_{34}]^{9-}$ with trichlorovinylsilane ($CH_2{=}CHSiCl_3$) or allyltrichlorosilane ($CH_2{=}CH\text{-}CH_2SiCl_3$). The trivacant specie was kindly provided by T.Zhang (PhD student in the E-POM group). More details about their synthesis is given in Appendix 6.6 and Appendix 6.7, following the procedures reported by N. Joo.[38]

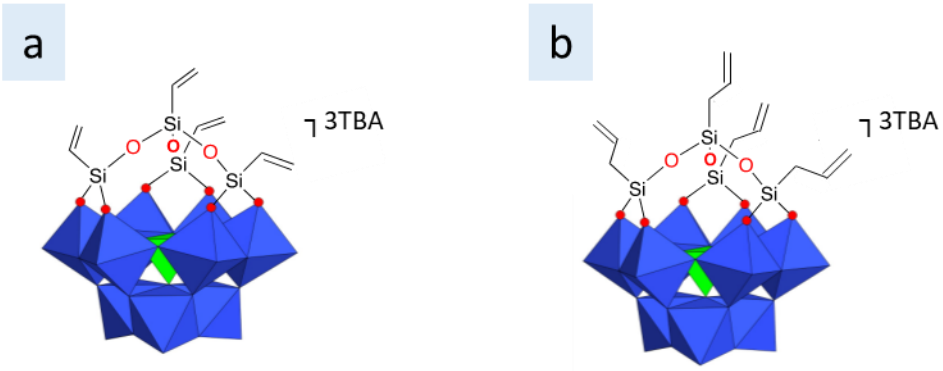

Figure 24 : Structure of a) POM-vinyl and b) POM-allyl.

The first question was how to perform the hydrosilylation reaction? In Chapter II, the neat alkene used was a liquid and a “simple” thermal hydrosilylation was performed below its boiling point (bp = 258-259 °C). Here the POM-vinyl and POM-allyl are powders. To perform a “wet (thermal) hydrosilylation” as in Chapter II, generally at 150-200°C for Si-H bonds to break,[42,43] the POM has to be soluble in an appropriate solvent that has a sufficient high boiling point. POM-vinyl and POM-allyl were isolated as tetrabutylammonium salts which restrain the choice of solvent. The POMs are soluble in aprotic polar solvents such as acetone, acetonitrile, DMF or DMSO, exhibiting a boiling point of 56°C, 82°C, 153°C and 189 °C respectively. Acetone and acetonitrile can be ruled out for their low boiling point. DMF is probably more

preferred over DMSO thanks to its lower water content but not the ideal one because it degrades and decomposes at temperatures lower than its boiling point, leading to the formation of dimethylamine and carbon monoxide.

The first strategy was to follow the procedure reported by N. Joo[38] (see Appendix 5.8) that we will call "dry hydrosilylation" (contrary to "wet hydrosilylation"). Basically, the freshly prepared (111)SiH substrate is placed in a flat-bottomed Schlenk tube, under argon atmosphere. Spatulas of POM powders are added little by little in a way to cover the whole face of the SiH surface facing upwards. The POM covering is only judged by the naked eye and the reproducibility in POM covering can thus be questioned. The Schlenk tube is then placed in an oil bath at 200°C.

The second strategy is the "photochemical hydrosilylation" discussed in Chapter II. This requires the immersion of the (111)SiH substrate in a POM solution under argon atmosphere prior to UV irradiation of the whole at 254 nm using a UV pen lamp. It requires also the use of a quartz vessel in order to allow the UV light to reach the substrate,[44] the UV light at 254 nm having a higher transmittance through a quartz material than a glass material. However, as we did not have any quartz vessel, another procedure was chosen inspired by the one reported by Huck and Buriak.[45] They indeed brought small volumes of alkene onto an SiH surface and subsequently covered the SiH sample with a Suprasil quartz disc. Then, they irradiated the covered substrate with an UV pen lamp at 254 nm, 15 cm far from the sample. The purpose of the quartz disc cover is to have a homogeneous coverage of alkene solution over the experiment. It tends to keep a homogeneous concentration of alkene despite its evaporation and tends to keep a wet surface as the Si-C bonds are formed. Similarly, drops of POM solution are brought to our (111)SiH surface lying on top of a cleaned quartz disc (rather than on a bench). It is subsequently covered with another cleaned quartz disc, as depicted in Figure 25. The UV pen lamp is held horizontally at ~5 cm far from the sample and the experiment is carried out in a dark box as a protection against UV radiation, under a glove box purged with nitrogen.

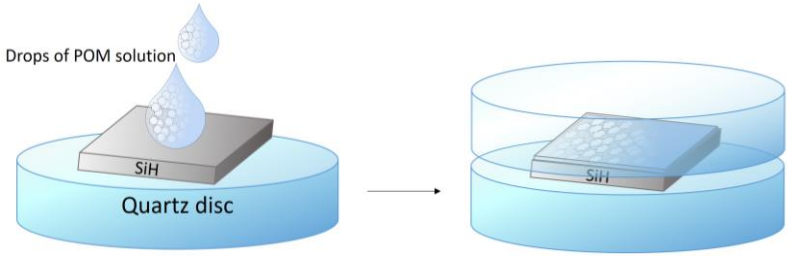

Figure 25 : Photochemical hydrosilylation procedure for the grafting of POM-allyl onto (111)SiH surface.

Due to the larger quantity of POM-allyl over POM-vinyl powder, the grafting attempts were carried using the former to have enough of powder to compare between the thermal and photochemical hydrosilylation routes. The ^{31}P NMR spectra of both compounds remain the same almost two years and a half after their synthesis (see Appendix 6.6 and Appendix 6.7).

The (111)SiH surface was prepared as described in Appendix 5.2 without recording SiH spectra. The dry hydrosilylation was first tested. A total of three attempts were performed, involving a dry hydrosilylation at 200°C, for 20 minutes, 1 hour and 2 hours. The surface after hydrosilylation will be labeled **SiPOMallyl**. IR spectra of the SiO_2 surface were the only ones recorded before hydrosilylation to have the fresher SiH surface prior to hydrosilylation and the differential spectra obtained for the three attempts are shown in Figure 26.

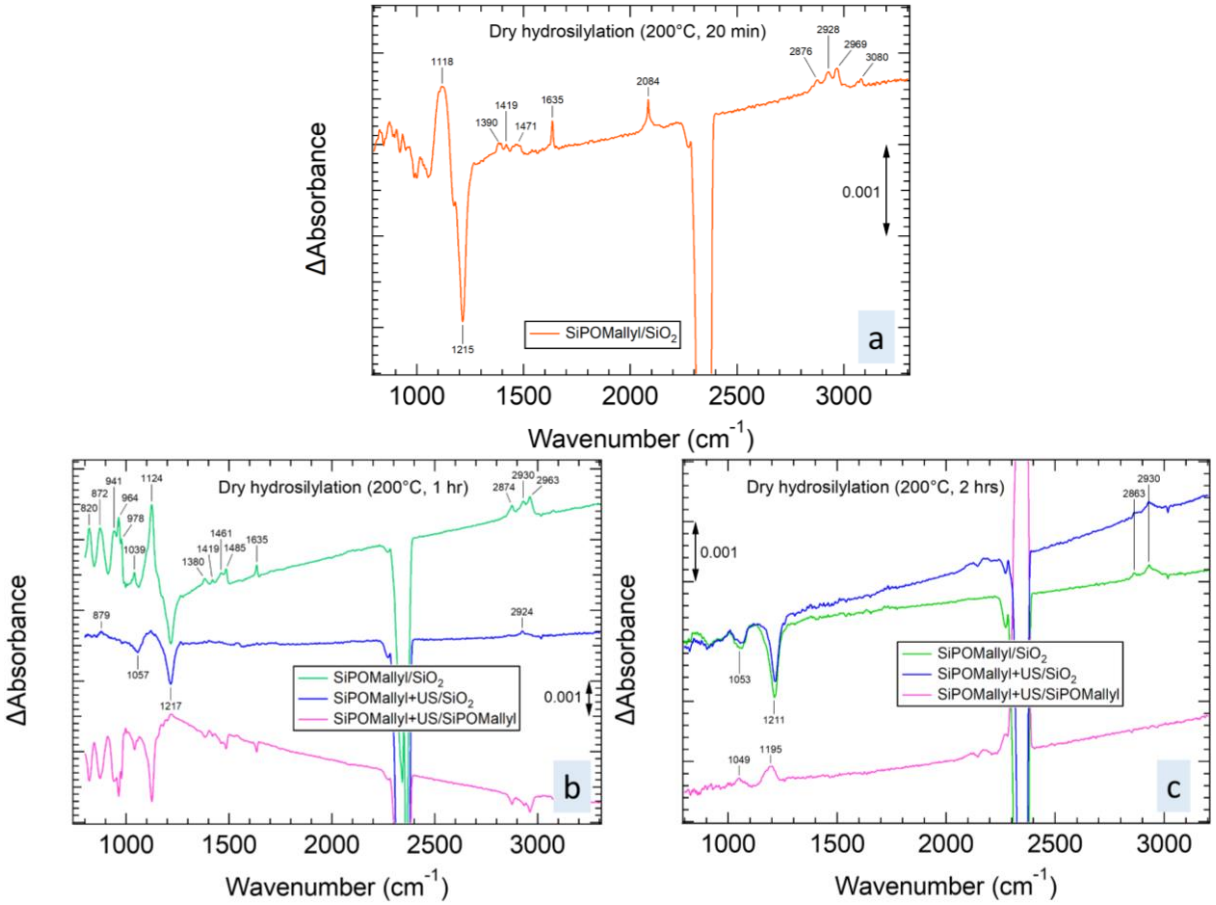

Figure 26 : Differential spectra obtained after the dry hydrosilylation procedure of POM-allyl onto (111)SiH surface at 200°C, for a) 20 minutes, b) 1 hour and c) 2 hours.

In the case where the dry hydrosilylation lasted 20 minutes, the SiPOMallyl was rinsed with acetonitrile and its spectrum was referenced to the SiO_2 surface before hydrosilylation (Figure 26a). The band at 2084 cm^{-1}, corresponding to the stretching of Si-H bonds, is spotlighted because it is a first evidence to know whether the Si-H bonds have indeed reacted during the

hydrosilylation. As the band is clearly visible on the SiPOMallyl/SiO_2 differential spectrum, we can deduce that not all SiH have reacted throughout the experiment. Features at ~1120 cm^{-1}, in the 1300-1700 cm^{-1} and 2800-3100 cm^{-1} are detected as well on the IR of the POM-allyl powder (see Appendix 6.7). The band at 1118 cm^{-1} can be attributed to the Si-O stretching mode of Si-O-Si groups in the POM. The 1215 cm^{-1} corresponds to the LO mode of SiO_2. The bands at 1390 and 1470 cm^{-1} on one hand, and at 1419 cm^{-1} on the other hand, corresponds to the C-H deformation of the methylene groups in the TBA cations and in the organic arm of the POM, respectively, while the 2800-3100 cm^{-1} region is related to their C-H stretching modes. Finally, the alkene C=C stretching mode of the POM is witnessed at 1635 cm^{-1}. The presence of those POM features suggest that POMs remain on the surface but they did not (entirely) grafted onto the (111)SiH surface.

The dry hydrosilylation procedure duration was thus increased to allow more time for Si-H bonds to react. The second attempt involved a 1 hour dry hydrosilylation and the differential spectra obtained are shown in Figure 26b. After a similar rinsing step with acetonitrile, the same features are met again in the SiPOMallyl/SiO_2 spectrum (green), but this time without any Si-H band suggesting that all the Si-H bonds have reacted. The bands below 1000 cm^{-1} are also more distinguishable than previously. We can notably detect the $\upsilon_{asym}^{P-O_a}$ vibration at 1039 cm^{-1}, the $\upsilon_{asym}^{W=O_d}$ at 941, 964, and 978 cm^{-1}, and the $\upsilon_{asym}^{W-O_b-W}$ at 820 and 872 cm^{-1},[41] suggesting a higher quantity of physisorbed and grafted POM at first sight. The substrate was subjected to four sonication baths (5 minutes each), similarly as N. Joo's procedure,[38] with acetonitrile rinse after each sonication bath. The resulting surface was dried with N_2 gas and its spectrum was referenced to the SiO_2 spectrum (blue curve) and to the surface right before sonication baths (pink curve). Clearly, all the POM features almost disappeared throughout ultrasonication (US). However, bands at 879 and 2924 cm^{-1} can be guessed in the SiPOMallyl+US/SiO_2 spectrum, which suggest that there are still some POM attached to the surface. The bands at 1057 and 1217 cm^{-1} corresponds to the SiO_2 TO and LO phonon modes, respectively, and are attributed to the SiO_2 surface and not to the Si-O-Si groups present in the POM. The fact that these bands are still negative seems to indicate that the surface did not get oxidized, or at least not too much, through the hydrosilylation process and sonication baths.

Finally, the last dry hydrosilylation attempt was carried out for 2 hours, still at 200°C, and the differential spectra obtained during the process are shown in Figure 26c. The SiPOMallyl/SiO_2 spectrum is similar to the SiPOMallyl+US/SiO_2 spectrum obtained previously for a 1 hour dry hydrosilylation: no band corresponding to the ν^{Si-H} and the $\nu^{C=C}$

vibrations are seen, but the bands corresponding to $\upsilon_{asym}^{W-O_b-W}$ and ν^{C-H} of the POM are distinguishable. Sonication baths led to an increase in the band at 1049 and 1195 cm^{-1} in the SiPOMallyl+US/SiPOMallyl spectrum, corresponding to the TO and LO phonon modes of SiO_2, suggesting a reoxidation of the surface. This is not unexpected as the POM-allyl can be viewed as a quadrapod that does not allow a homogeneous coverage of the whole surface, leaving space where Si-H bonds are not protected and prone to oxidation.

To check if POMs are indeed present on the surface, XPS analysis were performed on the POM-allyl powder and on the SiPOMallyl obtained after this 2 hours-dry hydrosilylation and sonication baths. A summary of the XPS spectra features is given in Table 3 (in comparison with the photochemical hydrosilylation that will be discussed in the next case).

Let us first have a look on the XPS spectra of the POM-allyl powder, shown in Figure 27. First, the Si 2p peak can be decomposed into three contributions. The main component at 102.3 eV can be attributed to silicon atoms bounded to carbon atoms, and the components at 103.8 eV and 105.8 eV to silicon atoms bounded to oxygen atoms. In the O 1s region, contributions of W-O/W=O and Si-O are found at 530.9 and 532.2 eV, respectively. The component at 534.1 eV could be due to residual water. In the C1s region, the peak decomposition suggests a contribution from the C-C and C=C bonds of the organic tether of the POM at 284.8 eV, and a contribution at 286.2 eV corresponding to carbon atoms bounded to the nitrogen atom of the TBA cations. An apparent contamination involving oxidized carbon atoms can be deduced by the component at 288.2 eV. The W 4f region is characterized by photopeaks at 35.9 and 38.4 eV corresponding to W(VI) 4f (7/2) and (5/2) core levels, respectively,[26] together with the peak at 41.4 eV that can be attributed to W 5p (3/2).[46] However, W(V) is also guessed by the peaks et 34.9 eV and 37.7 eV, corresponding to W(V) 4f (7/2) and (5/2), respectively,[47] suggesting a POM reduction. A concentration of 93% of W^{6+} and 7% of W^{5+} is calculated. Unfortunately, no XPS analysis was performed right after the POM synthesis to evaluate the possible POM reduction or contamination over the years. The N 1s region is surprisingly constituted with two photopeaks with a main peak at 402.2 eV corresponding to the nitrogen atom of the TBA cations. However, the origin of the peak at 405.0 eV is unclear. To summarize, the photopeaks expected for the POM-allyl powder were observed, though accompanied with features suggesting a partial reduction of the POM as well as the presence of contamination.

The XPS spectra of the SiPOMallyl surface were recorded and shown in Figure 28. The Si 2p region is characterized by the typical photopeaks of the Si(111) substrate at 99.3 and 99.9 eV, accompanied with a peak at 103.1 eV that corresponds to the SiO_2 present on the surface. The Si-O contribution from the POM can not be distinguished and is maybe hidden by the contribution of the SiO_2 on the surface. The same observation is attributable to the unique photopeak in the O 1s region at 532.5 eV: the contribution from SiO_2 of the surface and Si-O bonds from the POM can not be differentiate in the resulting SiPOMallyl surface. We thus focus on the other photopeaks. First, no contributions from W-O/W=O is observed around 530.9 eV in the O 1s region. This is quite surprising since the contributions from W(VI) 4f (7/2) and (5/2) are witnessed in the W 4f region at 35.9 and 38.1 eV, respectively, with low intensities. Also surprising was the lack of peak in the N 1s region, where the contribution from the nitrogen of the TBA cations was expected. This casts doubt on the attribution of the peak at 286.8 eV in the C 1s region which we attributed to the $C\text{-}N^+$ contributions in the POM-allyl powder analysis. Thus, it seems that only a very low amount of POM have been immobilized on the surface.

Since some of the photopeak of the POM powder are missing on the XPS spectra of the SiPOMallyl surface prepared by dry hydrosilylation, doubts remain on the effective immobilization of the POM onto the surface. It seems that the amount of immobilized POMs on the surface is very low, which is also supported by the IR spectra. Moreover, the experimental procedure leaves a lot to be desired. We thus turned to the photochemical hydrosilylation.

Region	Assignment	**POM-allyl** (powder)	**SiPOMallyl** after dry hydrosilylation (200°C, 2 hrs)	**SiPOMallyl** after photochemical hydrosilylation	
				15 min UV	5 min UV
W 4f	W(V) $4f_{7/2}$	34.9	x	x	x
	W(VI) $4f_{7/2}$	35.9	35.9	36.1	36.2
	W(V) $4f_{5/2}$	37.7	x	x	x
	W(VI) $4f_{5/2}$	38.4	38.1	38.3	38.3
	W(VI) $5p_{3/2}$	41.4	x	41.9	41.8
Si 2p	Si in the Si(111) substrate	x	99.3	99.4	99.4
		x	99.9	99.9	99.9
	Si-O-C, Si-O	102.3	103.1	103.3	103.3
		103.8			
	Silicate ?	105.8	x	x	x
P 2p	$P-O_a$	134.3	~135	~135	Not recorded
P 2s		Not recorded	Not recorded	Not recorded	~185
C 1s	C-C and C=C in the organic arm	284.8	285.1	285.1	285.1
	$C-N^+$ in the TBA cation	286.2	(286.8)	286.8	286.5
	C-O ?	288.2	289.1	288.8	289.1
N 1s	N^+ of TBA of the POM on the surface	x	x	400.3	400.3
	N^+ of TBA	402.2	x	402.2	402.2
	?	405.0	x	x	x
O 1s	W=O, W-O	530.9	x	531.0	531.0
	Si-O-Si	532.2	532.5	532.6	532.7
	Residual H_2O	534.1	x	x	x

Table 3 : Comparison of the XPS spectra features of the POM-allyl powder, the SiPOMallyl surface obtained after dry hydrosilylation (200°C, 2 hours), the SiPOMallyl surface after photochemical hydrosilylation with an UV irradiation for 15 minutes and 5 minutes. The XPS analysis was performed after the sonication baths. The XPS spectra of the powder were calibrated with the C 1s at 284.8 eV, while the XPS spectra of the SiPOMallyl surfaces were calibrated with the Si $2p_{3/2}$ peak at 99.4 eV.

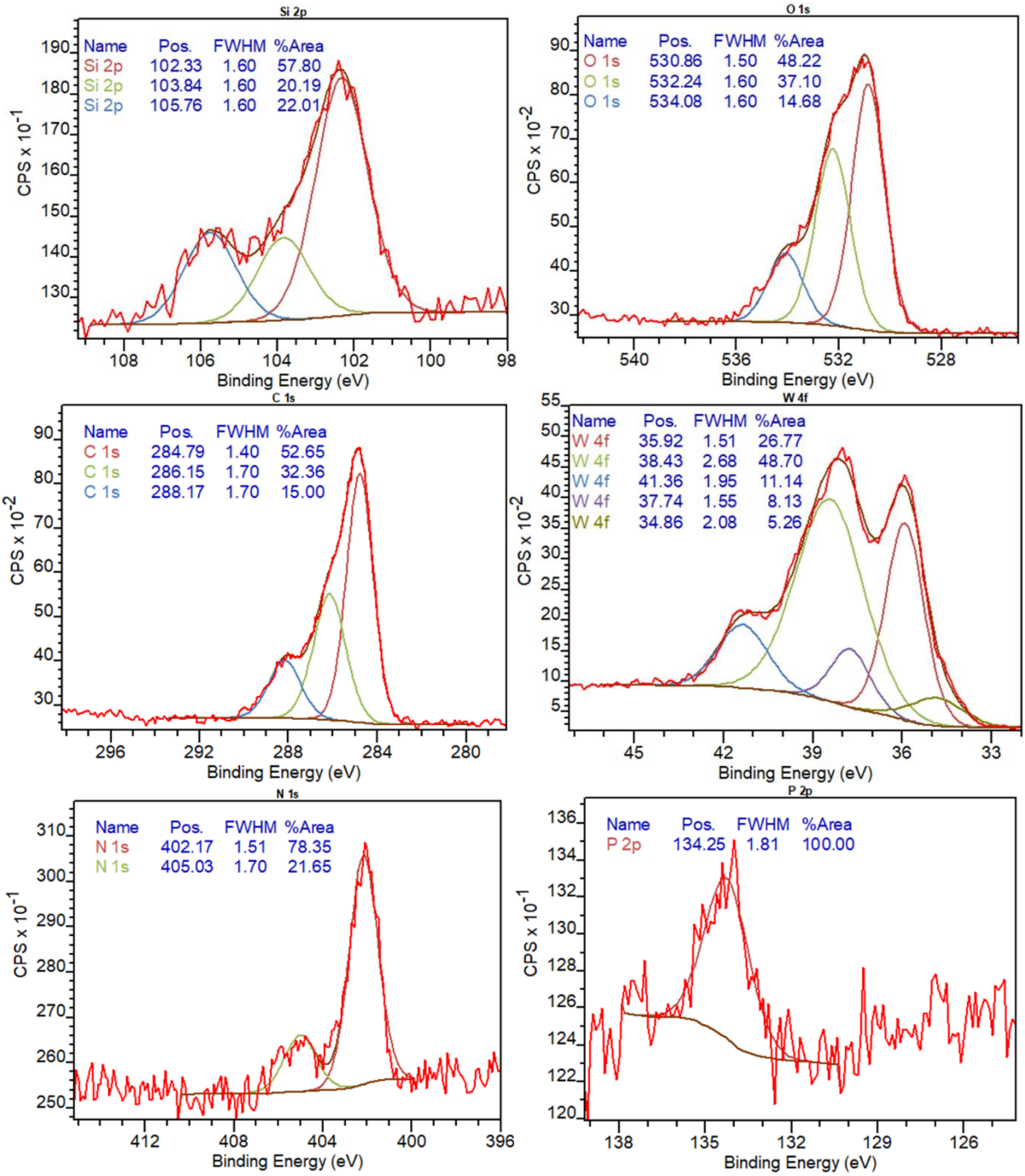

Figure 27 : XPS spectra of the Si 2p, O 1s, C 1s, W 4f, N 1s and P 2p regions of the POM-allyl powder, obtained two years and a half after their synthesis (calibrated with the C1s peak at 284.8 eV).

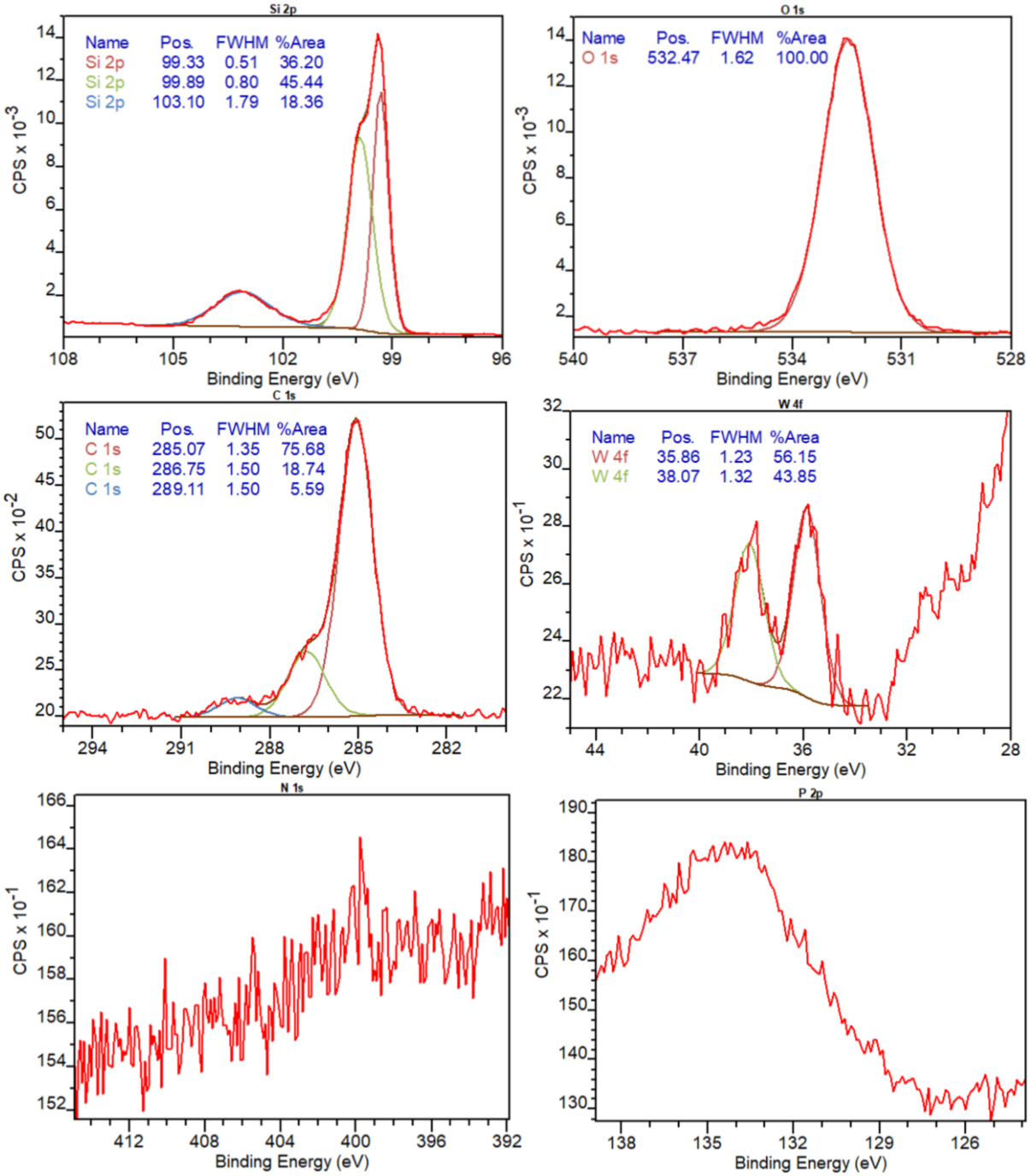

Figure 28 : XPS spectra of the Si 2p, O 1s, C 1s, W 4f, N 1s and P 2p regions of the SiPOMallyl obtained after a dry hydrosilylation at 200°C for 2 hours and after rinse and sonication baths.

Two attempts of photochemical hydrosilylation were performed, involving a 15 minutes UV irradiation in the first case and a 5 minutes irradiation in the second case. The differential spectra are shown in Figure 29a and Figure 29b, respectively. Although the band at 2084 cm^{-1}, corresponding to the Si-H stretching mode remains on the SiPOMallyl/SiO_2 spectra (green curves), features corresponding to the POM-allyl are distinguished. Some alkene functions remain as suggested by the $\nu^{C=C}$ band at 1660 cm^{-1}, while the C-H deformation and stretching

of the organic arm and TBA cations around 1400-1500 cm^{-1} and 2800-3000 cm^{-1} respectively, are observed. The bands at 849 and 964 cm^{-1}, corresponding to $\upsilon_{asym}^{W-O_b-W}$ and $\upsilon_{asym}^{W=O_d}$ respectively, are also observed in the SiPOMallyl surface after 15 minutes of UV irradiation (Figure 29a). In the case of the spectra corresponding to the SiPOMallyl surface prepared after 5 minutes of UV irradiation, the baseline is not flat and does not allow a reliable band assignment. After ultrasonication baths, some features corresponding to the POM disappeared. When referenced to the SiO_2 surface (blue curves), the spectrum of the SiPOMallyl surface prepared by a 15 minutes UV irradiation still exhibits positive bands corresponding to the POM (Figure 29a) while these bands are hardly visible on the spectrum of the SiPOMallyl surface prepared by a 5 minutes UV irradiation (Figure 29b). Thus from the IR spectra, the 15 minutes photochemical hydrosilylation seems better than the 5 minutes procedure in providing a higher amount of POM on the surface.

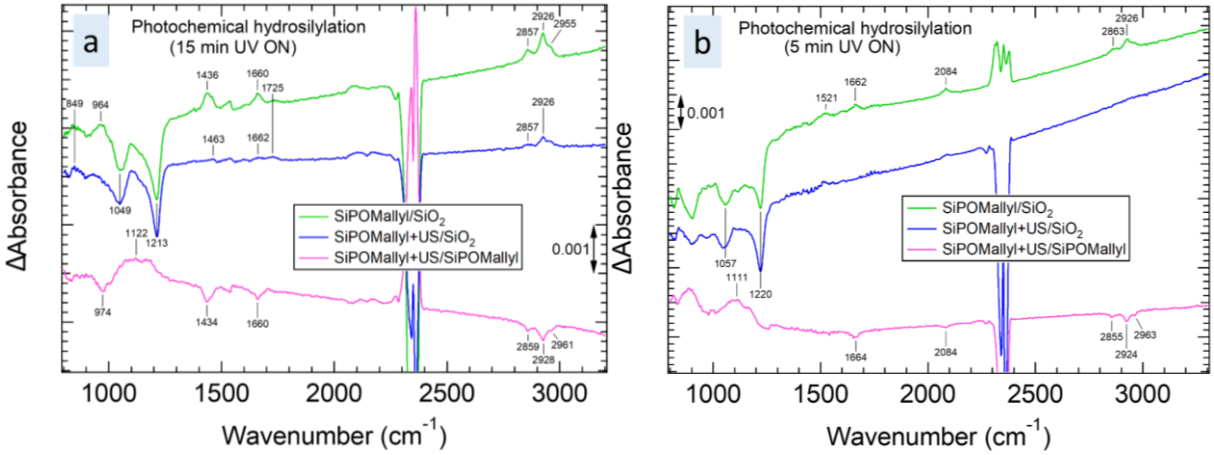

Figure 29 : Differential spectra obtained after a a) 15 minutes and b) 5 minutes photochemical hydrosilylation.

XPS analysis was then carried out on both substrates, and the spectra obtained were quite similar from one to another (see Table 3). They are depicted in Figure 30 for the 15 minutes photochemical hydrosilylation and in Figure 31 for the 5 minutes photochemical hydrosilylation. Unlike the dry hydrosilylation, the presence of POM on the surface is undoubted. The doublet in the W 4f region is observed, as well as the peak at 531.0 eV in the O 1s region, though in low concentration (7-10%), corresponding to W=O and W-O. Here, the TBA cation signature is witnessed by the peaks at 400.3 and 402.2 eV in the N 1s region, corresponding to the TBA nitrogen atom once the POM is grafted onto the surface and to the TBA nitrogen atoms of physisorbed POMs, respectively, as studied by M. Laurans.[26] The XPS analysis thus seems to indicate a better grafting of POM via the photochemical procedure.

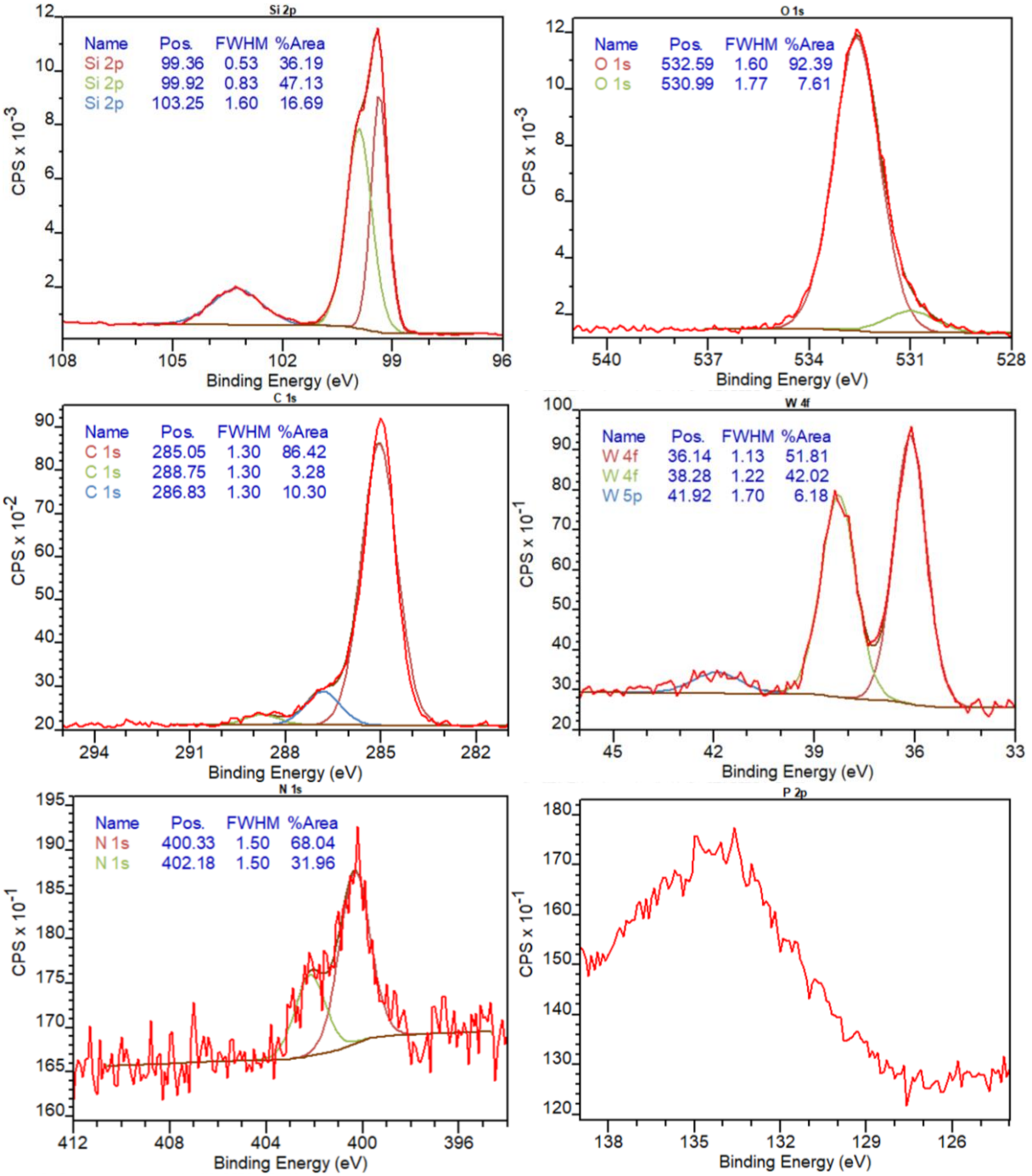

Figure 30 : : XPS spectra of the Si 2p, O 1s, C 1s, W 4f, N 1s and P 2p regions of the SiPOMallyl obtained after a 15 minutes photochemical hydrosilylation and after rinse and sonication baths.

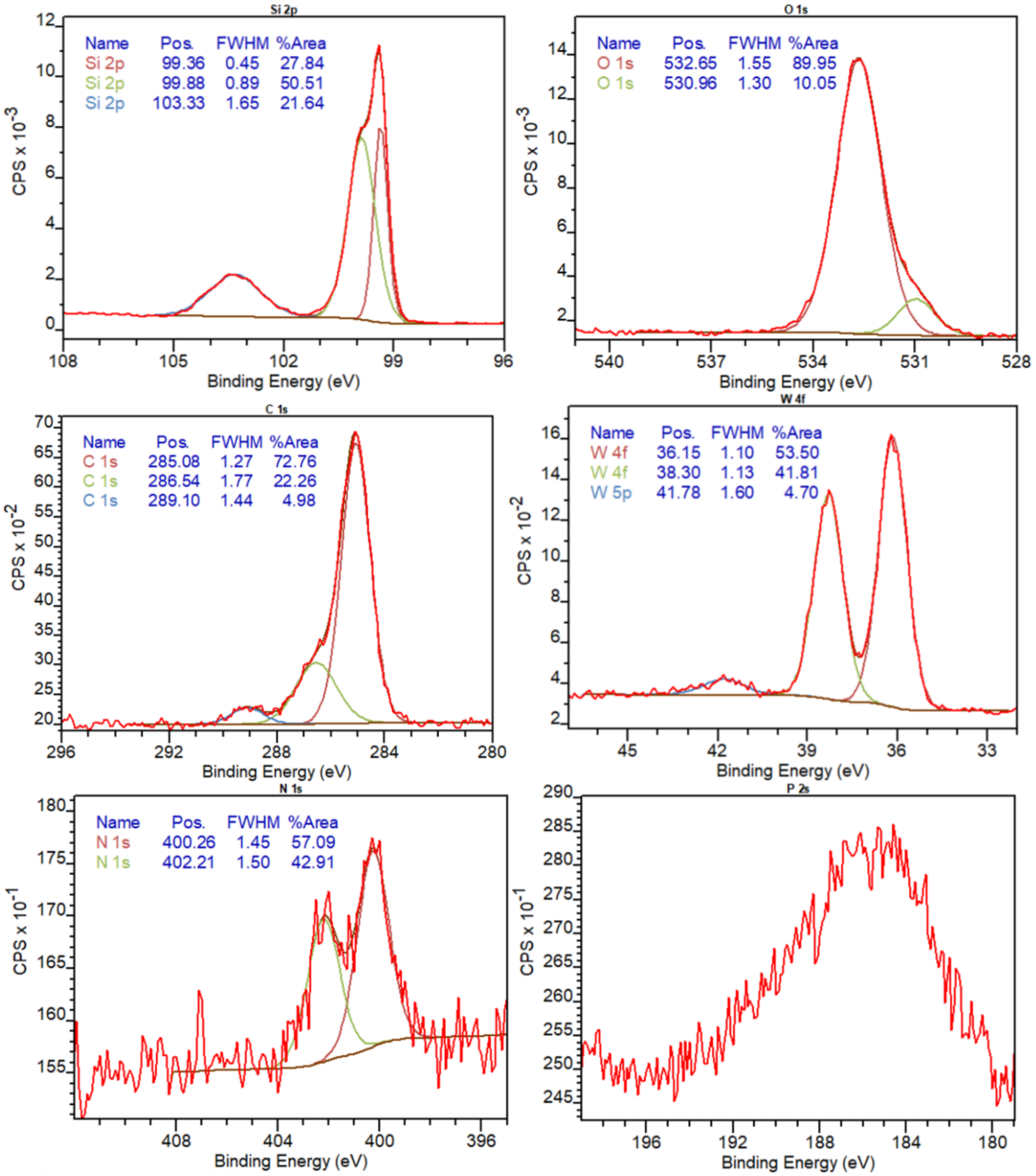

Figure 31 : XPS spectra of the Si 2p, O 1s, C 1s, W 4f, N 1s and P 2s regions of the SiPOMallyl obtained after a 5 minutes photochemical hydrosilylation and after rinse and sonication baths.

In the case of the SiPOMallyl surface prepared by a 5 minutes UV irradiation and after ultrasonication baths, the results from the IR spectra seem in contradiction with the XPS spectra. Indeed, the former suggests a lack of POM on the surface while the XPS revealed all the expected photopeaks of a grafted POM. Since the XPS characterization tool is more precise in probing the composition of the surface, we believe that POM-allyl are effectively present on the surface. The lack of POM features in the IR spectrum could be discussed in terms of POM nature/amount. The POM has indeed a short organic arm thus the area of the bands

corresponding to the C-H vibrations is expected to be lower. Caillard *et al*. have for example reported a decrease of the ν^{C-H} band area when moving from a Si surface functionalized with ethyl 10-undecenoate ("SiC_{11}") to a Si surface functionalized with ethyl 6-heptenoate ("SiC_7").[48,49] In terms of band intensities, a decrease from 8.10^{-4} to 2.10^{-4} was observed. In our case, only a three carbon atoms chain develops if the POM-allyl is indeed grafted onto the surface. This suggests that the intensity of the band corresponding to ν^{C-H} from the organic arm of the POM should be very low with an order of magnitude of 10^{-5} in terms of band intensity, thus nearly imperceptible in the SiPOMallyl IR spectra. The fact that neither the contributions of ν^{C-H} from the TBA cations are observed could suggest a low quantity of grafted POM on the surface.

Finally, ellipsometry measurements were carried out on a spectroscopic ellipsometer (see Appendix 1.1), different from the one used in Chapter II because of the breakdown. A Si/SiO_2 model was used in order to have a very rough idea on the POM layer thickness, since the SiO_2 and POM layers have quite similar refractive indexes. The thickness was measured after hydrosilylation on two spots of each surface and reported in Table 4. The organic tether of the POM has a length of approximately 0.3 nm. Together with the inorganic core and the TBA cations, a thickness of 1.8-2.3 nm of the POM-allyl layer is targeted. From the IR spectra and XPS analyses, we can not exclude the formation of oxide during the hydrosilylation which can slightly increase the thickness measured. Based on our results, this theoretical thickness range is practically reached after the sonication of the SiPOMallyl substrates. Though the thickness values are not 100% reliable, the unchanged or decreased thicknesses measured in the case of the dry or photochemical hydrosilylation, are in agreement with the IR spectra where the nonremoval (dry hydrosilylation, 2 hours) or removal (photochemical hydrosilylation) of physisorbed species after sonication baths was deduced. From the XPS analyses, better results are obtained via photochemical hydrosilylation. For the 15 minutes procedure, the POM-allyl layer has an average thickness of 2.3 nm (high-end of the theoretical thickness range) after sonication, while for the 5 minutes procedure, a thickness of 1.6 nm (low-end of the theoretical thickness range) is measured after sonication and is homogeneous. Thus, the 5 minutes UV irradiation suggests a more homogeneous POM deposition than the 15 minutes procedure.

Surface	Dry hydrosilylation (200°C, 2 hrs)	Photochemical hydrosilylation	
		15 minutes	5 minutes
POM-allyl layer*	1.7 / 1.6	2.8 / 5.7	2.5 / 2.4
POM-allyl layer after US*	1.7 / 1.6	2.7 / 1.8	1.6 / 1.6

Table 4 : Thicknesses (in nm) of the POM-allyl layer measured on two areas of the SiPOMallyl surface obtained after hydrosilylation (dry and photochemical) and after sonication baths. (*the thicknesses include oxide that was formed during the hydrosilylation).

To summarize, POM-allyl grafting onto Si-H was explored through a dry and a photochemical hydrosilylation, but the experiments have to be repeated for more statistics. From an experimental point of view and from the surface characterizations, the photochemical hydrosilylation provides a better POM deposition than the dry hydrosilylation. More precisely, the 5 minutes UV irradiation provides a more homogeneous POM deposition than the 15 minutes procedure, though only two areas of the surface were analyzed. Another experiment is needed at least for better IR spectra with a flatter baseline and to confirm or not the inconsistency between IR and XPS spectra.

There are still some doubts, especially with the 2 hours dry hydrosilylation process since some crucial peaks corresponding to the POM are missing in the XPS spectra, but visible in the ones involving photochemical hydrosilylation. It would have been also interesting to try a wet thermal hydrosilylation despite the non-ideal conditions discussed at the beginning of this section. We can for example consider the use of anhydrous DMSO or a mixing of solvent that would allow the dissolution of POM while avoiding the evaporation of the solution. Cation exchange can also be envisioned with the use of tetrahexylammonium (THA) bromide for example to extend the aliphatic chain of the cation. In that way, it opens the choice of solvent and the resulting THA-POM can for example be soluble in anisole exhibiting a boiling point at 153.8°C.

Another direct grafting process was carried out with COOH-terminated POM but on SiO_2 surface this time, with more reliable results, as will be discussed hereinafter

V. Electrical measurements of POM monolayer on Si/SiO_2: the case of COOH-terminated POM grafting

From the previous studies in our group described in the beginning of this chapter, the results obtained were promising for further solid state electrical characterization of POM monolayers grafted onto surfaces.

Here, the purpose was to compare two other POM hybrids, this time having the same $\{PW_{11}O_{39}\}$ framework but differing by their organic tether and their total charge. Accordingly, $TBA_{4.4}[PW_{11}O_{39}\{Sn(C_6H_4)C{\equiv}C(C_6H_4)COOH_{0.6}\}]$ (labeled $\mathbf{K^{W}_{Sn}[COOH]}$) and $TBA_{3.4}[PW_{11}O_{39}\{O(SiC_2H_4COOH_{0.8})_2\}]$ (labeled $\mathbf{K^{W}_{Si}[COOH]}$) were successfully synthesized by M. Laurans (Figure 32a) and grafted onto oxidized Si surface.[26,50] Preliminary solid state characterizations through SMM junctions were performed by K. Dalla Francesca (post-doctoral research assistant in the E-POM group), in collaboration with D. Vuillaume and S. Lenfant from Institute for Electronics, Microelectronics and Nanotechnology (IEMN) in Lille (France), similarly as for the previous study. In the frame of this thesis, further electrical measurements and data processing were performed for more reliable results and the POM anchoring onto the surface, which is not commonly studied, was probed by taking advantage of the FTIR spectroscopy tool, as will be discussed hereinafter. These combined results were published in in a recent article.[50]

First, $K^{W}_{Sn}[COOH]$ was synthesized by Sonogashira coupling on the hybrid iodoaryl-terminated POM platform while the synthesis of $K^{W}_{Si}[COOH]$ involves the condensation of carboxyethylsilanetriol on the monolacular $K_7[PW_{11}O_{39}]$ POM. The structure of the POMs is shown in Figure 32a, while the cyclic voltammograms (CV) of both POMs recorded in a 10^{-3} M solution in acetonitrile with 0.1 M terabutylammonium hexafluorophosphate ($TBAPF_6$) are depicted in Figure 32b. The CV were recorded at a scan rate of 100 $mV.s^{-1}$ and three reversible one-electron reduction waves are observed in both cases. The first one-electron reduction wave appears at $E_{1/2}$ = -1.01 V/SCE and $E_{1/2}$ = -0.38 V/SCE for $K^{W}_{Sn}[COOH]$ and $K^{W}_{Si}[COOH]$ respectively. It is closer to the zero potential in the latter case, meaning that $K^{W}_{Si}[COOH]$ is more easily reduced that $K^{W}_{Sn}[COOH]$, which can be guessed by the lower total charge exhibiting by the POM. The LUMO position of both POMs can be calculated using the following formula:

$$E_{LUMO} = -\left(E_{1/2} + E_{SCE/SHE}\right) - 4.4$$

With $E_{SCE/SHE}$ = 0.24 eV. The LUMO position was calculated at **-3.6 eV** and **-4.2 eV** for K^{W}_{Sn}[COOH] and K^{W}_{Si}[COOH] respectively.

Following the POM solution characterization, UV-Visible spectra were recorded in solution and a band at 265 nm was observed in both cases. DFT calculations confirmed that the band corresponds to a charge transfer between the oxygen atoms lone pairs and the d orbitals of the tungsten centers. They revealed that the lowest unoccupied molecular orbital (LUMO) of both POM hybrids is constituted in majority of the d orbitals of the metal centers without contributions from the organic arm. The LUMO of K^{W}_{Sn}[COOH] and K^{W}_{Si}[COOH] were calculated at **-3.3 eV** and **-3.9 eV**, respectively.

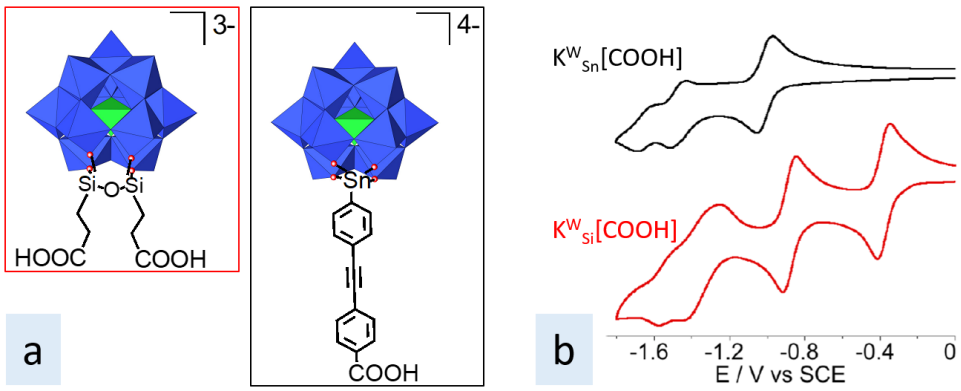

Figure 32 : a) K^{W}_{Si}[COOH] and K^{W}_{Sn}[COOH] hybrid POM structures ; b) cyclic voltammograms of K^{W}_{Si}[COOH] (red) and K^{W}_{Sn}[COOH] (black) recorded in a 10^{-3} M POM solution in acetonitrile with $TBAPF_6$ 0.1 M, at a scan rate of 100 $mV.s^{-1}$. Modified from ref. 50.

The grafting of those POM hybrids onto oxidized Si surface was then carried out by immersion of the freshly prepared Si-SiO_2 substrate in the corresponding POM solution in acetonitrile for 24 hours under solvent reflux. The resulting sample is rinsed and subjected to multiple sonication baths in acetonitrile and acetonitrile containing $TBAPF_6$ to ensure all the physisorbed species are removed. The thickness of the POM layer was followed during the sonication baths and in most cases, monolayers of POM were successfully obtained despite the harsh rinsing conditions, which is a first indication of covalent grafting. Homogeneous POM monolayers are achieved as confirmed by AFM, while the POM monolayer composition probed by XPS was in good agreement with the expectations.[26,50]

The interaction between the carboxylic acid COOH functions of the POMs and the SiO_2 surface was studied using FTIR spectroscopy with an optimization of both measurements and substrate handling learned from Chapter II. IR spectra on multilayers (obtained by a dropcasting of POM solution onto the Si-SiO_2 surface) and monolayers on Si-SiO_2 surfaces were recorded

in transmission mode. As depicted in Figure 33, those POM hybrids can interact with SiO_2 surface via hydrogen bonds (involving the integrity of the COOH functions) or via covalent interaction (involving the presence of carboxylate groups and/or the presence of ester functions). Focus has thus been given to the 1300-1800 cm^{-1} region.

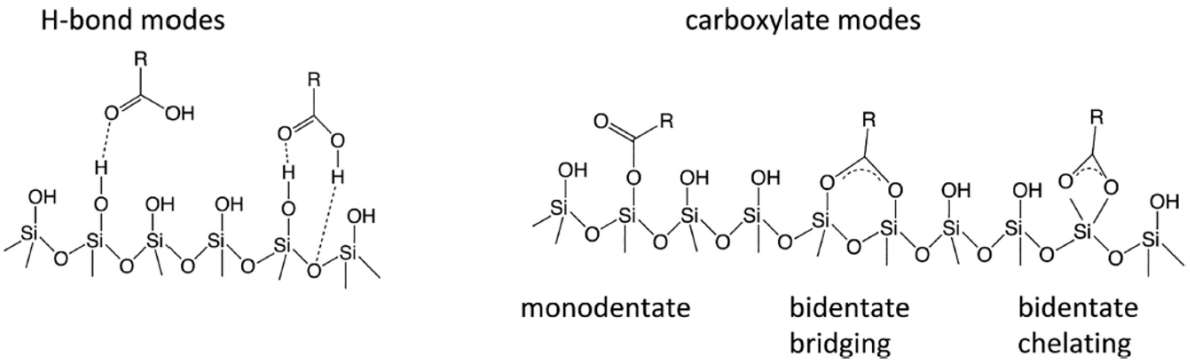

Figure 33 : Possible binding modes of COOH (left) and COO^- groups (right) onto SiO_2 surface.[50,51]

IR spectra of the modified Si-SiO_2 surface after a dropcasting of K^W_{Sn}[COOH] and K^W_{Si}[COOH] were recorded and the resulting differential spectra (referenced to the SiO_2 surface spectrum) are shown in Figure 34a and Figure 34b respectively. Both POM multilayers are characterized by the presence carboxylic acid groups ($\nu^{C=O}_{COOH}$ at 1704 cm^{-1} in K^W_{Sn}[COOH]/SiO_2 ; at 1710 cm^{-1} in K^W_{Si}[COOH]/SiO_2) and carboxylate groups ($\nu^{CO_2^-}_{asym}$ at 1548 and 1602 cm^{-1} for K^W_{Sn}[COOH] and K^W_{Si}[COOH] respectively). Differential spectra were then recorded in the case of POM monolayers and depicted in Figure 34c. When immobilized as monolayers, the carboxylate groups of the POMs are still observed in both cases: the band corresponding to $\nu^{CO_2^-}_{asym}$ can be found at 1548 and 1571 cm^{-1} for K^W_{Sn}[COOH] monolayer and K^W_{Si}[COOH] monolayer respectively, while the band corresponding to $\nu^{CO_2^-}_{sym}$ appears at 1390 and 1421 cm^{-1}. The band corresponding to $\nu^{C=O}_{COOH}$ can be guessed at 1700 and 1718 cm^{-1} for K^W_{Sn}[COOH] and K^W_{Si}[COOH] monolayer respectively, though its intensity is lower than that of the carboxylate bands as shown by the blue and red spectra in Figure 34c obtained after sonication baths. IR spectra do not seem to suggest a linkage of the COOH-terminated POM via the formation of ester functions due to the absence of $\nu^{C=O}_{ester}$, but rather suggest a covalent anchoring mode of the POM to the surface by carboxylate groups, more likely via a bidentate binding mode. The presence of COOH groups depicted in the IR spectra does not reject some interaction involving hydrogen bonds.

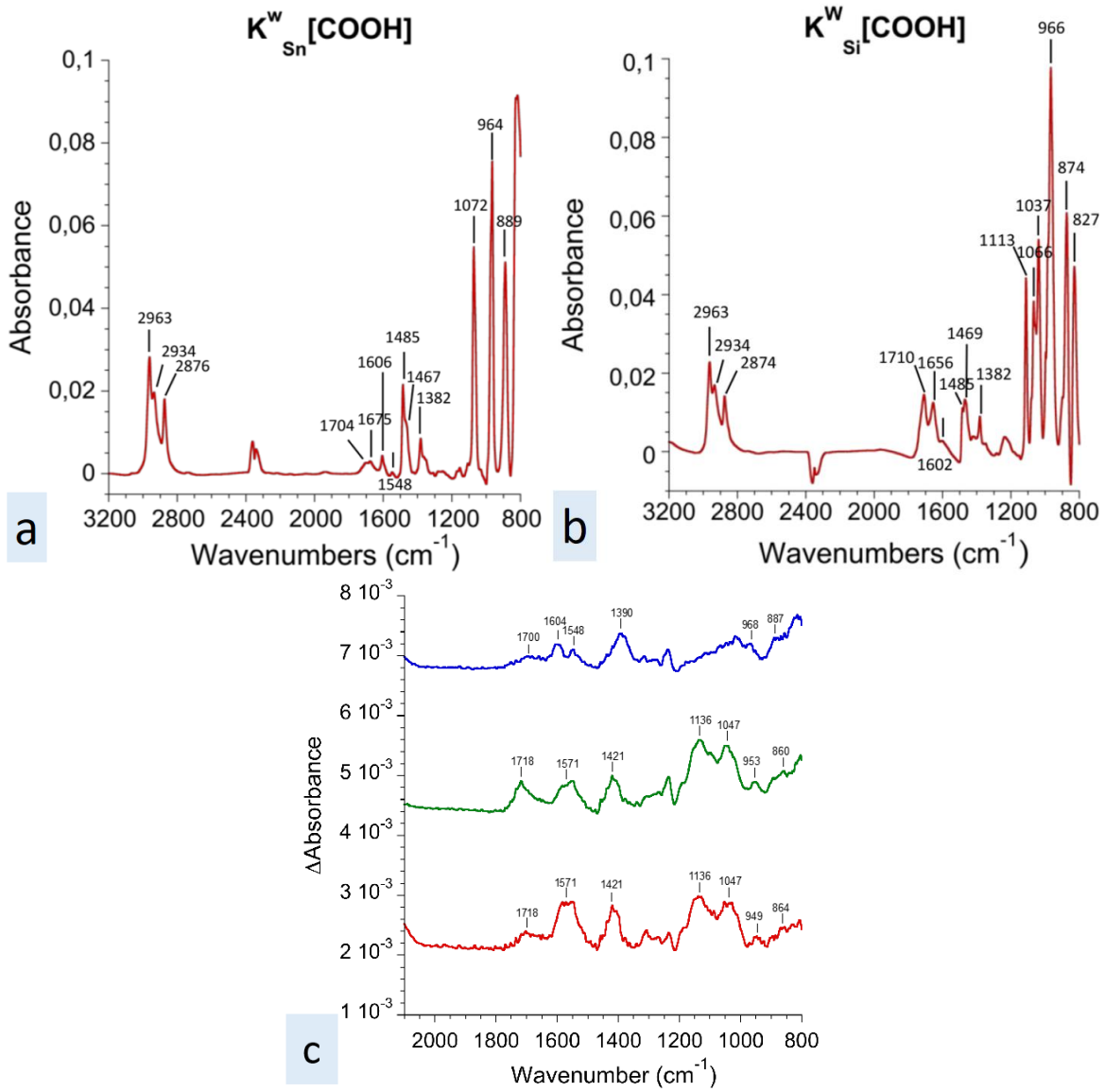

Figure 34 : Differential absorbance spectrum of a) K^{W}_{Sn}[COOH] multilayer on SiO_2 surface; b) K^{W}_{Si}[COOH] multilayer on SiO_2 surface; c) POM monolayer of K^{W}_{Sn}[COOH] (blue curve) and K^{W}_{Si}[COOH] (green cruve) on SiO_2 surface. The latter has been subjected to an added treatment by ultrasonication resulting in the red curve. (Modified from ref. 50)

Electrical measurements on the POM monolayers was thus carried out using the SMM junction configuration, as shown in Figure 35. K^{W}_{Sn}[COOH] and K^{W}_{Si}[COOH] monolayer on Si-SiO_2 surface were studied, as well as a Si/SiO_2 reference surface. A mercury drop was brought into contact to the POM-containing Si surface under a glove box purged with N_2 atmosphere. Photos of the drop contact were taken thanks to a camera positioned close to the substrate. An approximate contact area between the drop and the surface was further determined by photos processing using ImageJ software. An external voltage was applied to the Hg drop acting as a top electrode and the substrate was grounded through an ammeter allowing current measurements.

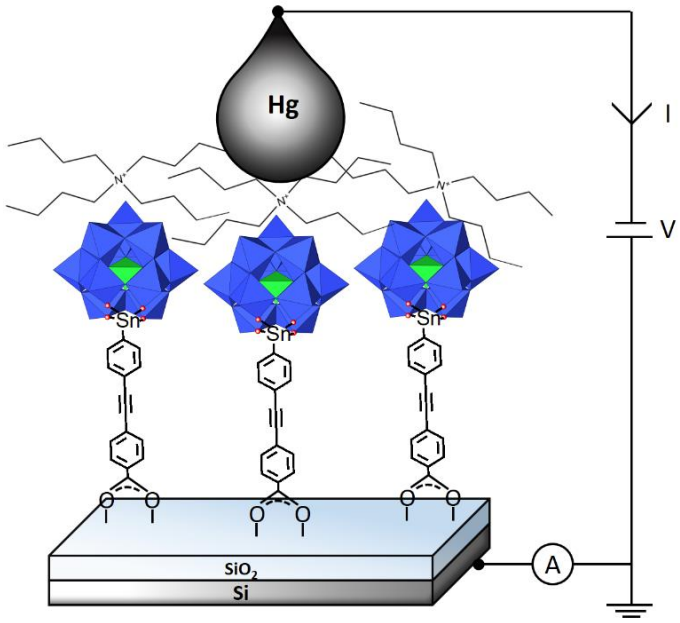

Figure 35 : Principle of the electrical measurements on the K^{W}_{Sn}[COOH] monolayer on the SiO_2 surface.

The voltage was swept from -1.0 to 1.0 V (forward and reverse) several times at the same location on the surface and the current is measured. A total of 5 to 10 drops were contacted on each substrate. After recording the I-V curves, the current density J was calculated knowing the contact area of the drop on the surface. Current density – voltage (J-V) curves were then obtained and depicted in Figure 36, together with log(J) histograms calculated from the current density at 1.0 V. A first observation is that the three samples have clearly different signature.

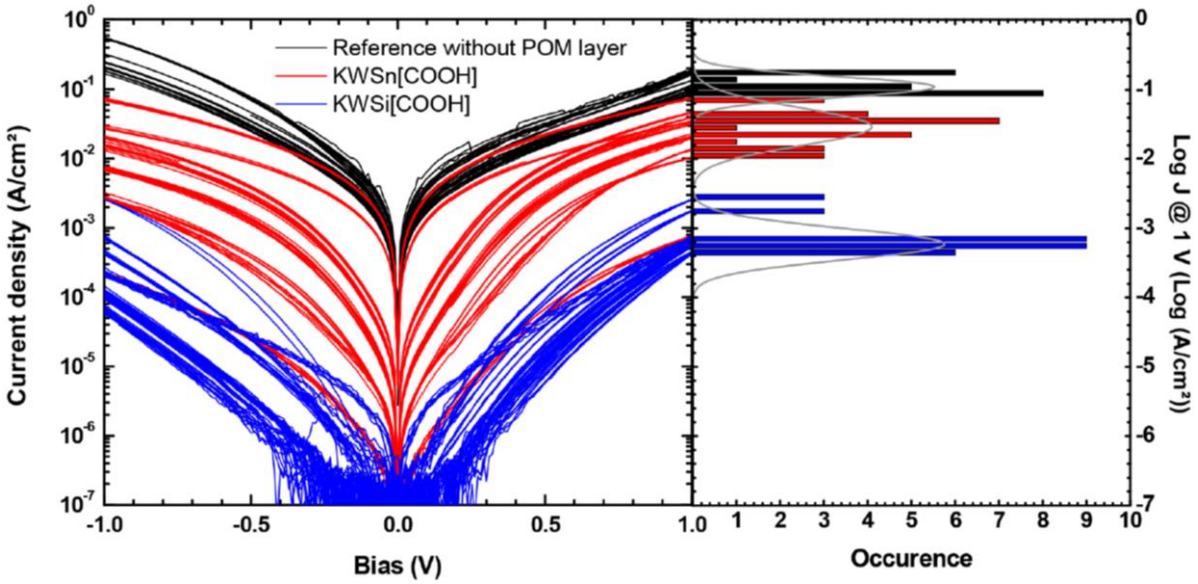

Figure 36 : J-V curves measured on the Si-SiO_2 reference surface (black), K^{W}_{Sn}[COOH] monolayer (red) and K^{W}_{Si}[COOH] monolayer (blue) on Si/SiO_2 surface. Current density histograms at 1.0 V fitted by a log-normal distribution are shown on the right.[50]

J-V curves are then processed with a Simmons model that is used for metal-insulator-metal junctions. It is a tunneling model describing an electron transfer through a rectangular energy barrier via tunnel effect. In our case, the silicon substrate is heavily *n*-doped, Schottky contact is avoided and we can approximate the silicon substrate as a metal. We more specifically used a modified Simmons model that includes a nonideality shape factor α (unitless) in the equation (Equation 1):

$$J = \left(\frac{e}{4\pi^2\hbar d^2}\right)\left\{\left(\Phi - \frac{eV}{2}\right) * exp\left[-\frac{2(2m)^{1/2}}{\hbar}\alpha\left(\Phi - \frac{eV}{2}\right)^{1/2} d\right] - \left(\Phi + \frac{eV}{2}\right) * exp\left[-\frac{2(2m)^{1/2}}{\hbar}\alpha\left(\Phi + \frac{eV}{2}\right)^{1/2} d\right]\right\}$$

Equation 1 : Modified Simmons model equation for a tunnel barrier in a metal-insulator-metal junction, with : J the current density, e the electron charge, m the bare electron mass, $\hbar$ the reduced Planck constant, d the barrier width corresponding to the thickness of the native oxide and POM monolayer measured by ellipsometry, Φ the effective barrier height, V the applied bias, α the shape factor.

The shape factor takes into consideration a poorly defined electron effective mass in molecular junction, as well as a deviation from the ideal rectangular energy barrier in molecular junctions and/or a more complex barrier. The insulating part of our junction is indeed more complex as it is constituted with the SiO_2 layer, the organic spacer and the inorganic core of the POM. Thus, when α equals 1, the electron effective mass equals the bare electron mass and the energy barrier is rectangular.

Using Equation 1, it was possible to extract the effective barrier height Φ of the POM. In the case of the Si-SiO_2 sample, the effective barrier height extracted is directly equal to the barrier height of the SiO_2 layer, labeled Φ_{ox}, as depicted in Figure 37. From the J-V curves, an average effective barrier height of Φ_{ox} = 1.91 ± 0.13 eV was extracted. In the case of POM-containing samples, the effective barrier height Φ takes into account the total length of the layers on top of the silicon substrate. An average effective barrier height of 1.75 ± 0.12 eV and 1.39 ± 0.23 eV was measured for K^W_{Sn}[COOH] and K^W_{Si}[COOH] monolayer, respectively. Despite a higher effective barrier height displaying by the K^W_{Sn}[COOH] sample, the latter provides higher currents than the K^W_{Si}[COOH] counterpart. This can be explained by the lower shape factor measured for K^W_{Sn}[COOH] monolayer. Indeed, the dominant term in Equation 1 is $\exp(-\alpha\Phi^{1/2}d)$, with $\alpha\Phi^{1/2}d$ lower for the K^W_{Sn}[COOH] sample (~2.3) than for the K^W_{Si}[COOH] sample (~3.1).

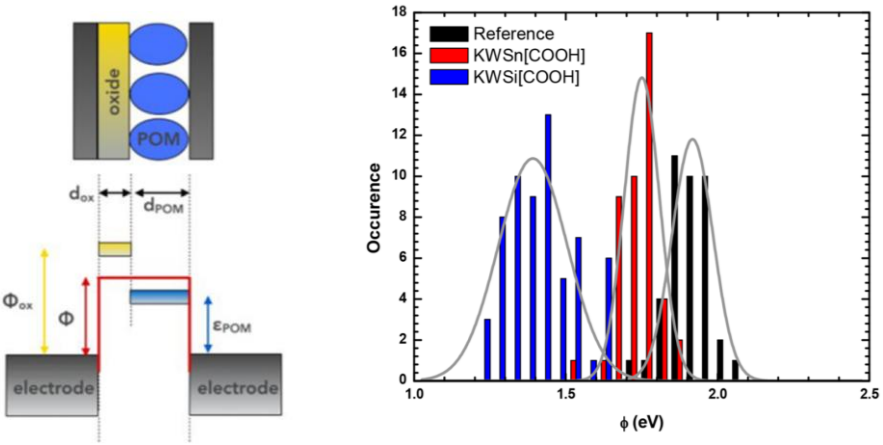

Figure 37 : Junction energy diagram where the LUMO of the oxide and the POM are depicted in yellow and blue rectangles respectively (left), and histograms of the effective barrier height Φ for K^{W}_{Sn}[COOH], K^{W}_{Si}[COOH] monolayers and the reference bare Si/SiO_2 sample.[50]

As the POMs are electron acceptors and as their effective tunnel barrier are measured lower than that of the oxide, the LUMO of the POMs should be lower than that of the oxide. The staircase tunnel barrier of our molecular junction is thus characterized by Equation 2 in the Wentzel-Kramers-Brilloin (WKB) approximation. The barrier height of the POM, ε_{POM}, which corresponds to the energy difference between the Fermi level of the electrodes and the LUMO of the POM, can thus be extracted.

$$\sqrt{\Phi}(d_{ox} + d_{POM}) = \sqrt{\Phi_{ox}}d_{ox} + \sqrt{\varepsilon_{POM}}d_{POM}$$

Equation 2: Equation describing the staircase tunnel barrier of our junction with the WKB approximation, with: d_{ox} and d_{POM} the averaged thickness of the native SiO_2 and POM monolayer respectively

An ε_{POM} value of 1.7 eV and 1.1 eV for K^{W}_{Sn}[COOH] and K^{W}_{Si}[COOH] monolayer, respectively, was found. Assuming that the Fermi level of the highly doped silicon substrate lies at -4.1 eV, we estimated a LUMO position of **-2.4 eV** and **-3.0 eV** for K^{W}_{Sn}[COOH] and K^{W}_{Si}[COOH] monolayer, respectively.

The LUMO position of the two POMs obtained from the cyclic voltammograms, the DFT calculations and the I-V curves processing are summarized in Figure 38. In the three cases, the LUMO of the of the K^{W}_{Sn}[COOH] lies higher in energy than the LUMO of the K^{W}_{Si}[COOH], which was expected due to the higher total charge of K^{W}_{Sn}[COOH]. Interestingly, a difference in energy of 0.6 eV between the two LUMO positions was systematically found. Laurans *et al*. have previously focused on the $K^{W}_{Sn}[N_2^{+}]$ POM grafted tonto SiH surface as discussed in the beginning of the chapter,[4] where a practically similar ε_{POM} than K^{W}_{Sn}[COOH] was found. This means that the electronic properties of the Si|POM|Hg

molecular junction are driven by the LUMO of the POMs (constituted with a majority of d-orbitals with no contributions from the organic arm from the DFT calculations), rather than the π-orbitals or the terminal group of the organic tether.

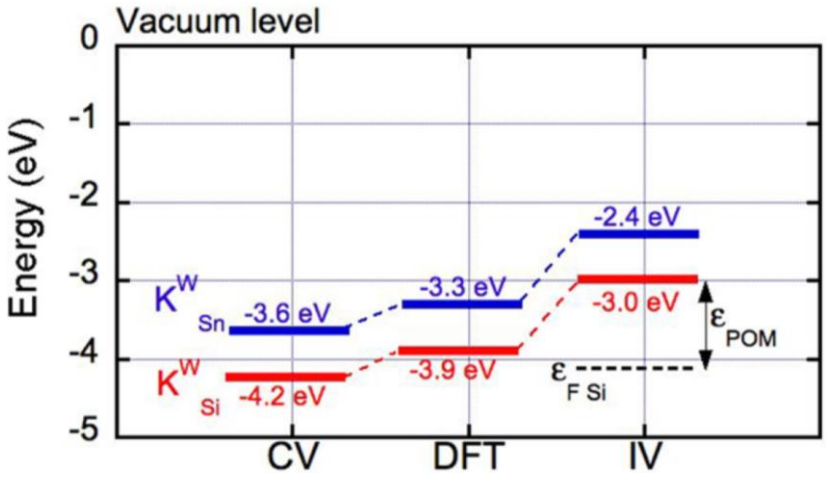

Figure 38 : LUMO energy positions of the K^{W}_{Sn}[COOH] (blue) and K^{W}_{Si}[COOH] POM (red) with respect to the vacuum level. The DFT position is given by the first empty d orbital of the POMs. The CV position is calculated from the first reduction waves. The IV position is obtained from the ε_{POM} value considering the n^{+} doped silicon Fermi energy at -4.1 eV.

Covalently attached K^{W}_{Sn}[COOH] and K^{W}_{Si}[COOH] POM onto Si-SiO_2 surface were thus achieved as supported by the combined use of characterization techniques. While XPS, AFM and ellipsometry measurements were previously done, we added the FTIR spectroscopy characterization as a supplementary tool to investigate the POM/surface interaction. The difference in LUMO energy positions between these two POMs is maintained in solution as well as in solid state. This study thus goes one step further towards the POM/substrate interaction understanding in relation with the electronic properties of the resulting material.

VI. Conclusion

Electrostatically and covalently POM immobilization onto Si surface have been explored during the project. In both cases, the objective was to obtain POM monolayers that are found more reliable for electrical measurements unlike POM multilayers.

The electrostatic route constitutes the main goal of the project. POM(0) has indeed the ability to be reduced under UV in the presence of a reducing agent and the goal is to probe this photoreduction phenomenon once the POM is immobilized as monolayers onto functionalized

Si surface. Accordingly, POM(0) and its one- and two-electron reduced derivatives were synthesized and immobilized onto $SiNH_2$ surface via a substrate dipcoating in the corresponding POM solution. POM(0) was immobilized as submonolayer with POM(I) and POM(II) were immobilized as monolayers. Attempts to increase the 20-25% concentration of NH_3^+ groups on the $SiNH_2$ surface, and thus the POM(0) deposition, were performed. However, no improvement was achieved. XPS analysis on the resulting surface after POM dipcoating indeed support the presence of POM on the surface as will be discussed in the following chapter. The next step is to probe the redox state of the immobilized POM (sub)monolayers and to study the photoreduction phenomenon prior to electrical measurements.

The covalent route was explored in using several POM hybrids and Si substrates. The two-step grafting constitutes a way to extend the peptide coupling with other species. To do so, the first study involved the interaction between SiCOOH surface and NH_2-terminated POMs where a covalent grafting was obtained by increasing the NH_2 functions at the end of the POM. An attempt for the synthesis of a POM bearing $N{=}PPh_3$ functions was then envisioned but results were not sufficient enough to give the exact nature of the POM.

The one-step grafting was finally studied. The immobilization of POM-allyl onto SiH surfaces suggests a better POM grafting when a photochemical hydrosilylation is carried out. However, more experimental data are needed on a freshly prepared POM-allyl to confirm or not the inconsistency between IR and XPS spectra. On the other hand, the covalent grafting of $K^W{}_{Sn}$[COOH] and $K^W{}_{Si}$[COOH] on Si/SiO_2 surface provides insights in the electrical properties of the POM in solid state in relation to the nature of the POM and to the POM/substrate interaction.

Going back to the goal of the project, the features of POM(0), POM(I) and POM(II) monolayers will be provided in the following chapter. The photoreduction phenomenon will be successively studied by means of several characterization tools. Electrical characterization of a POM-based SOI material in a transistor configuration will be performed and preliminary results discussed.

VII. References

(1) Cherevan, A. S.; Nandan, S. P.; Roger, I.; Liu, R.; Streb, C.; Eder, D. Polyoxometalates on Functional Substrates: Concepts, Synergies, and Future Perspectives. *Adv. Sci.* **2020**, *7* (8), 1903511.

(2) Balliou, A.; Papadimitropoulos, G.; Skoulatakis, G.; Kennou, S.; Davazoglou, D.; Gardelis, S.; Glezos, N. Low-Dimensional Polyoxometalate Molecules/Tantalum Oxide Hybrids for Non-Volatile Capacitive Memories. *ACS Appl. Mater. Interfaces* **2016**, *8* (11), 7212–7220.

(3) Dalla Francesca, K.; Lenfant, S.; Laurans, M.; Volatron, F.; Izzet, G.; Humblot, V.; Methivier, C.; Guerin, D.; Proust, A.; Vuillaume, D. Charge Transport through Redox Active $[H_7P_8W_{48}O_{184}]^{33-}$ Polyoxometalates Self-Assembled onto Gold Surfaces and Gold Nanodots. *Nanoscale* **2019**, *11* (4), 1863–1878.

(4) Laurans, M.; Dalla Francesca, K.; Volatron, F.; Izzet, G.; Guerin, D.; Vuillaume, D.; Lenfant, S.; Proust, A. Molecular Signature of Polyoxometalates in Electron Transport of Silicon-Based Molecular Junctions. *Nanoscale* **2018**, *10* (36), 17156–17165.

(5) Lu, M.; Nolte, W. M.; He, T.; Corley, D. A.; Tour, J. M. Direct Covalent Grafting of Polyoxometalates onto Si Surfaces. *Chem. Mater.* **2009**, *21* (3), 442–446.

(6) Wang, Y.; Weinstock, I. A. Polyoxometalate-Decorated Nanoparticles. *Chem. Soc. Rev.* **2012**, *41* (22), 7479–7496.

(7) Mayer, C. R.; Neveu, S.; Cabuil, V. A Nanoscale Hybrid System Based on Gold Nanoparticles and Heteropolyanions. *Angewandte Chemie International Edition* **2002**, *41* (3), 501–503.

(8) Song, Y.-F.; Tsunashima, R. Recent Advances on Polyoxometalate-Based Molecular and Composite Materials. *Chemical Society Reviews* **2012**, *41* (22), 7384–7402.

(9) Moors, M.; Warneke, J.; López, X.; de Graaf, C.; Abel, B.; Monakhov, K. Yu. Insights from Adsorption and Electron Modification Studies of Polyoxometalates on Surfaces for Molecular Memory Applications. *Acc. Chem. Res.* **2021**, *54* (17), 3377–3389.

(10) Chen, X.; Zhou, Y.; Roy, V. A. L.; Han, S. Evolutionary Metal Oxide Clusters for Novel Applications: Toward High-Density Data Storage in Nonvolatile Memories. *Adv. Mater.* **2018**, *30* (3), 1703950.

(11) Long, D.-L.; Cronin, L. Towards Polyoxometalate-Integrated Nanosystems. *Chem. Eur. J.* **2006**, *12* (14), 3698–3706.

(12) *Polyoxometalate Molecular Science*; Borrás-Almenar, J. J., Coronado, E., Müller, A., Pope, M., Eds.; Springer Netherlands: Dordrecht, 2003.

(13) Proust, A.; Thouvenot, R.; Gouzerh, P. Functionalization of Polyoxometalates: Towards Advanced Applications in Catalysis and Materials Science. *Chem. Commun.* **2008**, No. 16, 1837–1852.

(14) Proust, A.; Matt, B.; Villanneau, R.; Guillemot, G.; Gouzerh, P.; Izzet, G. Functionalization and Post-Functionalization: A Step towards Polyoxometalate-Based Materials. *Chemical Society Reviews* **2012**, *41* (22), 7605–7622.

(15) Izzet, G.; Volatron, F.; Proust, A. Tailor–Made Covalent Organic-Inorganic Polyoxometalate Hybrids: Versatile Platforms for the Elaboration of Functional Molecular Architectures. *Chem. Rec.* **2017**, *17* (2), 250–266.

(16) Rinfray, C.; Izzet, G.; Pinson, J.; Gam Derouich, S.; Ganem, J.-J.; Combellas, C.; Kanoufi, F.; Proust, A. Electrografting of Diazonium-Functionalized Polyoxometalates: Synthesis, Immobilisation and Electron-Transfer Characterisation from Glassy Carbon. *Chem. Eur. J.* **2013**, *19* (41), 13838–13846.

(17) Volatron, F.; Noël, J.-M.; Rinfray, C.; Decorse, P.; Combellas, C.; Kanoufi, F.; Proust, A. Electron Transfer Properties of a Monolayer of Hybrid Polyoxometalates on Silicon. *Journal of Materials Chemistry C* **2015**, *3* (24), 6266–6275.
(18) He, T.; He, J.; Lu, M.; Chen, B.; Pang, H.; Reus, W. F.; Nolte, W. M.; Nackashi, D. P.; Franzon, P. D.; Tour, J. M. Controlled Modulation of Conductance in Silicon Devices by Molecular Monolayers. *J. Am. Chem. Soc.* **2006**, *128* (45), 14537–14541.
(19) Sanchez, C.; Livage, J.; Launay, J. P.; Fournier, M.; Jeannin, Y. Electron Delocalization in Mixed-Valence Molybdenum Polyanions. *J. Am. Chem. Soc.* **1982**, *104* (11), 3194–3202.
(20) Artero, V.; Proust, A. Reduction of the Phosphododecamolybdate Ion by Phosphonium Ylides and Phosphanes. *European Journal of Inorganic Chemistry* **2000**, No. 11, 2393–2400.
(21) Rocchiccioli-Deltcheff, C.; Fournier, M.; Franck, R.; Thouvenot, R. Vibrational Investigations of Polyoxometalates. 2. Evidence for Anion-Anion Interactions in Molybdenum(VI) and Tungsten(VI) Compounds Related to the Keggin Structure. *Inorg. Chem.* **1983**, *22* (2), 207–216.
(22) Poblet, J. M.; López, X.; Bo, C. *Ab initio* and DFT Modelling of Complex Materials: Towards the Understanding of Electronic and Magnetic Properties of Polyoxometalates. *Chem. Soc. Rev.* **2003**, *32* (5), 297–308.
(23) Pasternack, R. M.; Rivillon Amy, S.; Chabal, Y. J. Attachment of 3-(Aminopropyl)Triethoxysilane on Silicon Oxide Surfaces: Dependence on Solution Temperature. *Langmuir* **2008**, *24* (22), 12963–12971.
(24) Kurth, D. G.; Volkmer, D.; Ruttorf, M.; Richter, B.; Müller, A. Ultrathin Composite Films Incorporating the Nanoporous Isopolyoxomolybdate "Keplerate" $(NH_4)_{42}[Mo_{132}O_{372}(CH_3COO)_{30}(H_2O)_{72}]$. *Chem. Mater.* **2000**, *12* (10), 2829–2831.
(25) Graf, N.; Yegen, E.; Gross, T.; Lippitz, A.; Weigel, W.; Krakert, S.; Terfort, A.; Unger, W. E. S. XPS and NEXAFS Studies of Aliphatic and Aromatic Amine Species on Functionalized Surfaces. *Surface Science* **2009**, *603* (18), 2849–2860.
(26) Laurans, M. Synthèse d'hybrides de Polyoxométallates: Greffage Contrôlé Sur Électrodes Pour l'étude de Jonctions Moléculaires. Thèse Sorbonne Université 2018.
(27) Fleury, B.; Billon, M.; Duclairoir, F.; Dubois, L.; Fanton, A.; Bidan, G. Electrostatic Immobilization of Polyoxometallates on Silicon: X-Ray Photoelectron Spectroscopy and Electrochemical Studies. *Thin Solid Films* **2011**, *519* (11), 3732–3738.
(28) Marmisollé, W. A.; Capdevila, D. A.; de la Llave, E.; Williams, F. J.; Murgida, D. H. Self-Assembled Monolayers of NH_2-Terminated Thiolates: Order, pKa, and Specific Adsorption. *Langmuir* **2013**, *29* (17), 5351–5359.
(29) Sam, S.; Touahir, L.; Salvador Andresa, J.; Allongue, P.; Chazalviel, J.-N.; Gouget-Laemmel, A. C.; Henry de Villeneuve, C.; Moraillon, A.; Ozanam, F.; Gabouze, N.; Djebbar, S. Semiquantitative Study of the EDC/NHS Activation of Acid Terminal Groups at Modified Porous Silicon Surfaces. *Langmuir* **2010**, *26* (2), 809–814.
(30) Mercier, D.; Boujday, S.; Annabi, C.; Villanneau, R.; Pradier, C.-M.; Proust, A. Bifunctional Polyoxometalates for Planar Gold Surface Nanostructuration and Protein Immobilization. *J. Phys. Chem. C* **2012**, *116* (24), 13217–13224.
(31) Matt, B.; Renaudineau, S.; Chamoreau, L.-M.; Afonso, C.; Izzet, G.; Proust, A. Hybrid Polyoxometalates: Keggin and Dawson Silyl Derivatives as Versatile Platforms. *J. Org. Chem.* **2011**, *76* (9), 3107–3112.
(32) Kosiova, I.; Janicova, A.; Kois, P. Synthesis of Coumarin or Ferrocene Labeled Nucleosides via Staudinger Ligation. *Beilstein J. Org. Chem.* **2006**, *2* (23).

(33) Burés, J.; Martín, M.; Urpí, F.; Vilarrasa, J. Catalytic Staudinger—Vilarrasa Reaction for the Direct Ligation of Carboxylic Acids and Azides. *J. Org. Chem.* **2009**, *74* (5), 2203–2206.
(34) Hong, S. Y.; Tobias, G.; Ballesteros, B.; El Oualid, F.; Errey, J. C.; Doores, K. J.; Kirkland, A. I.; Nellist, P. D.; Green, M. L. H.; Davis, B. G. Atomic-Scale Detection of Organic Molecules Coupled to Single-Walled Carbon Nanotubes. *J. Am. Chem. Soc.* **2007**, *129* (36), 10966–10967.
(35) Bednarek, C.; Wehl, I.; Jung, N.; Schepers, U.; Bräse, S. The Staudinger Ligation. *Chem. Rev.* **2020**, *120* (10), 4301–4354.
(36) Cheisson, T.; Mazaud, L.; Auffrant, A. Ruthenium Complexes Featuring Cooperative Phosphine–Pyridine–Iminophosphorane (PNN) Ligands: Synthesis, Reactivity and Catalytic Activity. *Dalton Trans.* **2018**, *47* (41), 14521–14530.
(37) Socrates, G. *Infrared and Raman Characteristic Group Frequencies: Tables and Charts*, 3. ed.; Wiley: Chichester, 2001.
(38) Joo, N. New functionalized polyoxometalates (POMs) for molecular memory devices compatible with a CMOS processing. Thèse Laboratoire LETI, **2010**.
(39) Perkins, L. Organic-inorganic hybrid materials: new functionalised polyoxotungstates. Dissertation, The University of Birmingham, **2009**.
(40) Niu, J.; Li, M.; Wang, J. Organosilyl Derivatives of Trivacant Tungstophosphate of General Formula α-A-$[PW_9O_{34}(RSiO)_3(RSi)]^{3-}$. *Journal of Organometallic Chemistry* **2003**, *675* (1–2), 84–90.
(41) Niu, J.; Zhao, J.; Wang, J.; Li, M. An Organosilyl Derivative of Trivacant Tungstophosphate. Synthesis, Characterization and Crystal Structure Determination of α-A-$[NBu^n_4]_3[PW_9O_{34}(C_2H_5SiO)_3(C_2H_5Si)]$. *Journal of Molecular Structure* **2003**, *655* (2), 243–250.
(42) Vilan, A.; Yaffe, O.; Biller, A.; Salomon, A.; Kahn, A.; Cahen, D. Molecules on Si: Electronics with Chemistry. *Advanced Materials* **2010**, *22* (2), 140–159.
(43) Aureau, D.; Chabal, Y. J. Formation of Organic Monolayers Through Wet Chemistry. In *Functionalization of Semiconductor Surfaces*; Tao, F. F., Bernasek, S. L., Eds.; John Wiley & Sons, Inc.: Hoboken, NJ, USA, 2012; pp 301–337.
(44) Khung, Y. L.; Ngalim, S. H.; Scaccabarozi, A.; Narducci, D. Thermal and UV Hydrosilylation of Alcohol-Based Bifunctional Alkynes on Si (111) Surfaces: How Surface Radicals Influence Surface Bond Formation. *Sci Rep* **2015**, *5* (1), 11299.
(45) Huck, L. A.; Buriak, J. M. UV-Initiated Hydrosilylation on Hydrogen-Terminated Silicon (111): Rate Coefficient Increase of Two Orders of Magnitude in the Presence of Aromatic Electron Acceptors. *Langmuir* **2012**, *28* (47), 16285–16293.
(46) Bouvard, O.; Krammer, A.; Schüler, A. *In Situ* Core-Level and Valence-Band Photoelectron Spectroscopy of Reactively Sputtered Tungsten Oxide Films: *In Situ* XPS and UPS Study of Reactively Sputtered Tungsten Oxide Films. *Surf. Interface Anal.* **2016**, *48* (7), 660–663.
(47) Bourdin, M.; Mjejri, I.; Rougier, A.; Labrugère, C.; Cardinal, T.; Messaddeq, Y.; Gaudon, M. Nano-Particles (NPs) of WO_3-Type Compounds by Polyol Route with Enhanced Electrochromic Properties. *Journal of Alloys and Compounds* **2020**, *823*, 153690.
(48) Caillard, L. Grafted Organic Monolayer for Single Electron Transport and for Quantum Dots Solar Cells. Dissertation, The University of Texas at Dallas and Université Pierre et Marie Curie, **2014**.
(49) Caillard, L.; Seitz, O.; Campbell, P. M.; Doherty, R. P.; Lamic-Humblot, A.-F.; Lacaze, E.; Chabal, Y. J.; Pluchery, O. Gold Nanoparticles on Oxide-Free Silicon–Molecule Interface for Single Electron Transport. *Langmuir* **2013**, *29* (16), 5066–5073.

(50) Laurans, M.; Trinh, K.; Dalla Francesca, K.; Izzet, G.; Alves, S.; Derat, E.; Humblot, V.; Pluchery, O.; Vuillaume, D.; Lenfant, S.; Volatron, F.; Proust, A. Covalent Grafting of Polyoxometalate Hybrids onto Flat Silicon/Silicon Oxide: Insights from POMs Layers on Oxides. *ACS Appl. Mater. Interfaces* **2020**, *12* (42), 48109–48123.
(51) Pujari, S. P.; Scheres, L.; Marcelis, A. T. M.; Zuilhof, H. Covalent Surface Modification of Oxide Surfaces. *Angew. Chem. Int. Ed.* **2014**, *53* (25), 6322–6356.

Chapter IV

Characterization of immobilized POMs on surfaces to probe the photoreduction phenomenon

I. Introduction

Several native and hybrid POMs were immobilized on functionalized and unfunctionalized Si surface, electrostatically or covalently as discussed in the previous chapter. As we want to study the POM photoreduction, this chapter will be exclusively dedicated to the study of POM(0), POM(I) and POM(II) previously synthesized. We are now going deeper to the core of the project: the goal is to probe and understand the photoreduction of these POMs once immobilized on surface using several characterization techniques.

An introduction will first be given with some examples involving photo-active and redox-active molecules and emphasis will be given to their interests for microelectronics applications. Our approach with the photoreducible POMs will then be described. The second part of this chapter will be dedicated to the characterization of the synthesized POM(0), POM(I) and POM(II) powders. The strategy was to work step by step and it was indeed important to make sure that the three POMs could be discriminated from each other before immobilizing them on surfaces and studying the phororeduction phenomenon. After POM immobilization as monolayer (and multilayer) onto surfaces, optical and electrical characterization of the resulting POM-containing surfaces will be finally performed in the last two sections. Results will be described and insights on the immobilized POM photoreduction mechanism will be provided.

I.1. State of the art

As discussed in Chapter II, molecular electronics opens new ways of extending Si technology by adding functionalities in devices at a molecular level. This can be achieved using external stimuli-responsive molecules for example. Under stimulus application, the resulting system can exhibit a change of color, conformation, physical properties… In electronic devices, these stimuli-responsive molecules are appealing when molecular conductance can be switched, leading to a modulation of the device performance that can be useful for charge storage and information processing applications.

Among the external stimuli such as temperature, electric/magnetic field or light irradiation, the latter is particularly interesting when combining silicon substrates with photoresponsive molecules due to the possible tuning of the electronic properties of Si substrate under light irradiation, giving more possibilities of device designs.[1,2] A few examples of immobilized photoresponsive molecules on Si surface will now be described, with a focus on photoswitchable molecules and redox-active molecules.

A photoswitchable molecule is a molecule that is subjected to a conformation change upon light irradiation at a specific wavelength, and the molecule can go back to its initial state (reversible process) upon light irradiation at a different wavelength or upon thermal activation. The more commonly used photoswitchable molecules are shown in Figure 1.[2] Among them, azobenzene[2–4] and diarylethene[2,5–8] derivatives were immobilized onto surfaces and examples below will only deal with silicon surfaces.

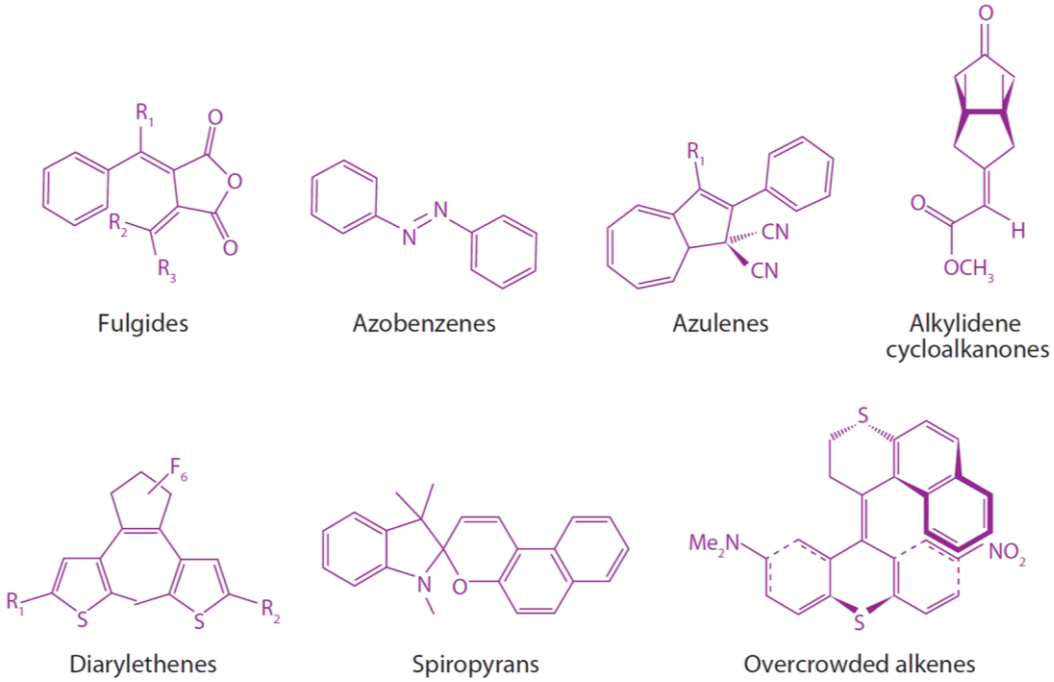

Figure 1 : More commonly used photoswitchable molecules.[2]

Wen *et al.* used an azobenzene derivative, the 4-nitro-4'-*N*,*N*-di(2-hydroxy propyl)aminoazobenzene (NHPA), and successfully grafted it onto Si(111) surfaces via Si-O bonds, leading to the formation of NHPA monolayer.[3] As shown in Figure 2a, the azobenzene derivative undergoes a fast conformation change upon UV irradiation at λ = 365 nm for 30 seconds, switching from the more thermodynamically stable trans isomer to the cis isomer. The process can be reversed by irradiation with visible light (at λ = 450 nm), again for 30 seconds, or by heating. The trans-cis isomerization of NHPA upon light irradiation was demonstrated using attenuated total reflectance (ATR) FTIR spectroscopy, contact angle measurements as well as AFM. The electrical properties were then studied using STM which measures the tunneling current between a metallic tip and the surface. I-V characteristics were thus be obtained and are depicted in Figure 2b. The I-V curve of the surface containing NHPA in the trans form is shown in blue (curve A), while the one of the surface containing NHPA in the cis form is shown in red (curve B). The change from the trans isomer to the cis isomer leads

to a decrease in the tunneling current for a same applied bias, which can be attributed to a height decrease induced by the cis isomer. The tunneling current modification can be reproducibly repeated for 10 cycles.

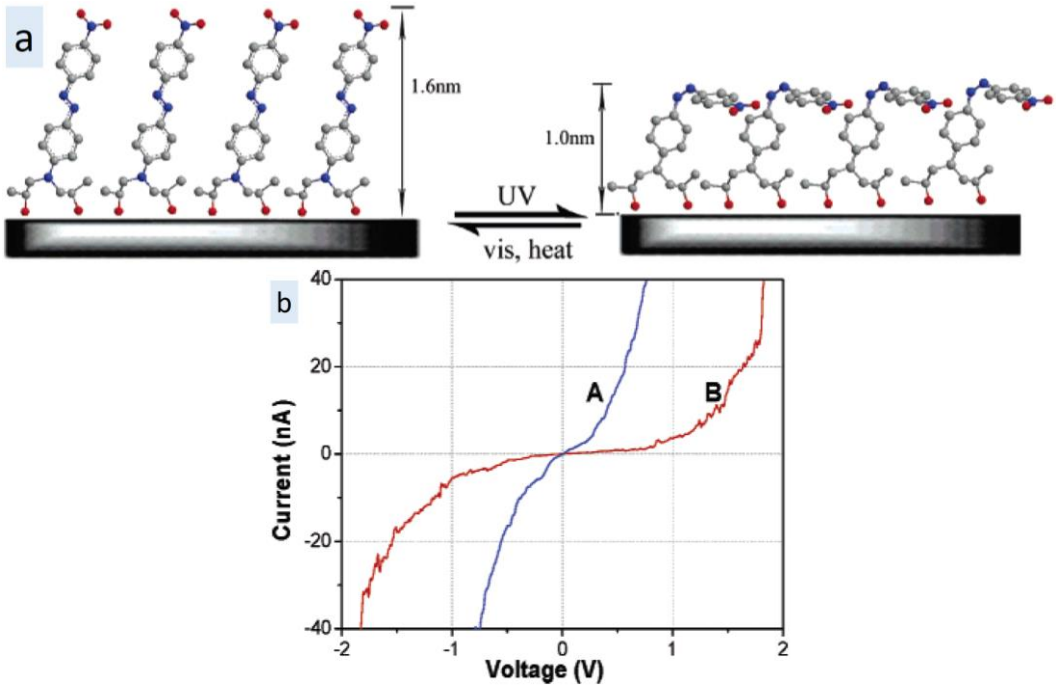

Figure 2 : a) NHPA monolayer trans (on the left) and cis (on the right) conformation change depending on the external stimulus. Carbon atoms are represented in grey, oxygen atoms in red, nitrogen atoms in blue. The hydrogen atoms are not represented. b) Current-voltage characteristics obtained by applying a changeable voltage on (A) trans form and (B) cis form of an NHPA monolayer on Si(111) surface. The tip used is an electrochemical-etched tungsten tip. The I-V curves are average curves from five different experimental locations on the surface. Tunneling conditions: V_{bias} = 0.15 V, I_t = 0.05 nA, scan rate: 1000 V/s.[3]

Using photoswitchable diarylethene derivatives, the two isomers obtained during the photoswitching process are both thermally stable. Nishihara and coll.[5] have synthesized an opened-ring diarylethene molecule bearing a terminal alkyne function. As depicted in Figure 3, the colorless opened-ring isomer (called 1o) is subjected to a conformation and color change under UV irradiation at λ = 313 nm, leading to the formation of the deep blue closed-ring isomer (1c). The process is reversed by irradiating 1c with visible light at λ = 578 nm. The bonds are π-conjugated on a wider region in 1c than in 1o.

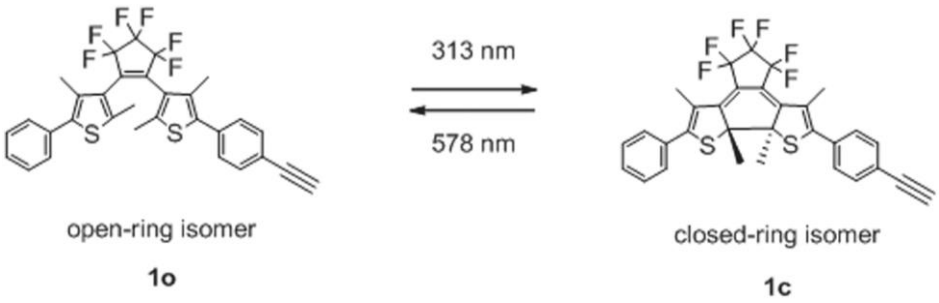

Figure 3 : Photoisomerization between the opened-ring isomer (1c) and the closed-ring isomer (1c).[5]

In order to take advantage of this photoswitching effect observed in solution, the opened-ring isomer synthesized was grafted onto (111)SiH surface via thermal hydrosilylation. The formation of opened-ring isomer monolayer was confirmed by a combination of water contact angle measurements and AFM. The electrical properties were then studied using the contact mode C-AFM. I-V curves were thus obtained on the opened-ring isomer monolayer grafted onto Si surface (1o-Si) and on the closed-ring isomer counterpart (1c-Si) (Figure 4). After UV irradiation of 1o-Si at λ = 313 nm for 30 minutes, the I-V curve of the resulting 1c-Si SAM exhibits a higher current, thus a better conductance: the opened-ring isomer can be assimilated to an OFF state of the system (lower conductance), while the closed-ring isomer can be assimilated to the ON state of the system (better conductance).

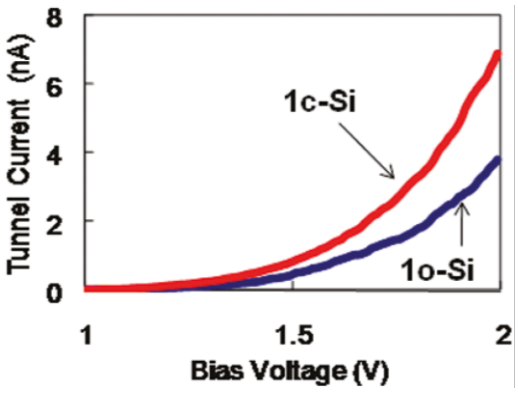

Figure 4 : Current-voltage (I-V) curves of freshly prepared 1o-Si SAM (blue curve) and after UV irradiation measured by C-AFM.[5]

UV light – Visible light irradiation cycles were then carried out with C-AFM on the 1o-Si surface. For a tip bias of 2 V, reversible modulation of the current was possible as depicted in Figure 5. The increase in current due to UV light and its decrease upon visible light irradiation were repeated with the same variation amplitude over the irradiation cycles. The stable covalent link between the isomer and the Si surface provided by the π-conjugation is responsible both for the reversible switching effect and for the stability of the current variation amplitude over

repeated light irradiation cycles. This system can thus find its application in optoelectronics devices.

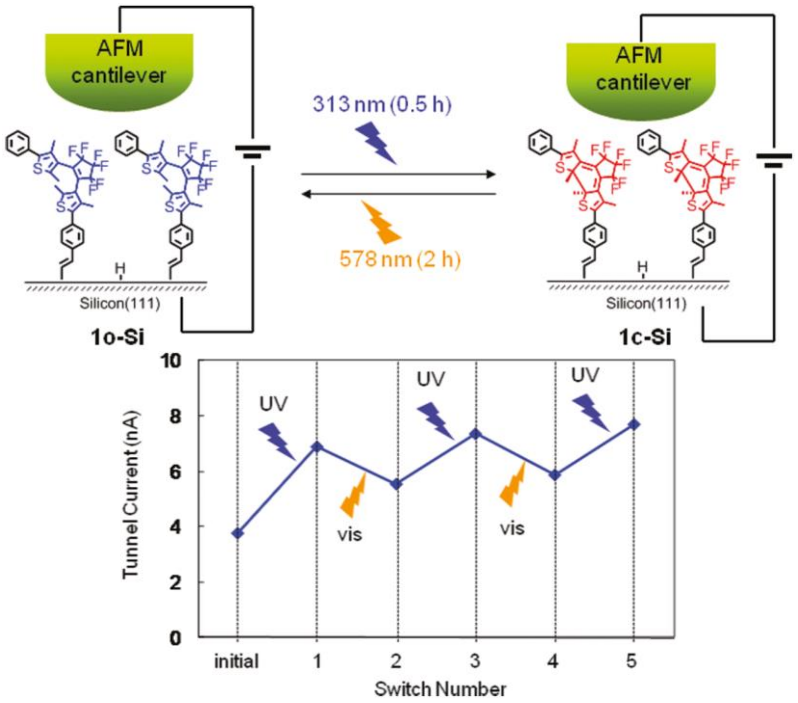

Figure 5 : Current variations of the 1o-Si and 1c-Si obtained by c-AFM with repeated irradiation cycles alternating UV light and visible light irradiations.[5]

Redox active molecules are molecules displaying different charged states depending on the applied bias. When an oxidizing voltage is applied, the redox active molecule loses electrons that will return back to the molecule by the application of a reducing voltage.[9] The intrinsic property of redox active molecules makes them good candidates for memory and information processing applications.

Among the redox active molecules, ferrocene (Fc) exhibits two stable redox states in solution that are neutral Fc and oxidized ferrocenium Fc^{+}, and Fc derivatives have been immobilized onto surfaces.[1,10–14] For example, Decker and coll.[11] have grafted vinylferrocene onto Si(100)H surfaces as a (sub)monolayer via photochemical hydrosilylation (Figure 6).

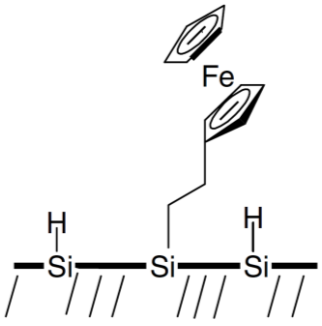

Figure 6 : Vinylferrocene grafted onto SiH surface.[11]

Capacitance measurements on the functionalized surface were carried out in 0.1 M tetraethylammonium perchlorate (NEt_4ClO_4) in dry acetonitrile. The resulting capacitance vs potential (C-E) characteristics is showed in Figure 7. For low potential ranging from -0.1 V and 0.4 V, a maximum capacitance density of ~100 µF.cm^{-2} was measured, approximately two orders of magnitude higher than that of an SiH electrode and one order of magnitude higher than in dynamic random access memory (DRAM) storage cells of less than 1 µm².[1] Ferrocene-based devices can thus find their applications in charge storage devices. However, the stability of such ferrocene-based surfaces under elevated temperature has to be studied in order to support the typical memory device fabrication temperature at ~400°C.

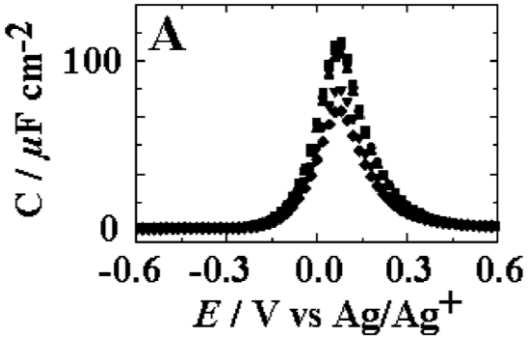

Figure 7: Capacitance-potential (C-E) curves of VFC grafted onto *p*-Si(100) electrode in CH_3CN/0.1 M NEt_4ClO_4 solution, measured at different frequencies: 25 Hz (squares), 50 Hz (circles), 100 Hz (upside triangle), 500 Hz (downside triangle) and 1000 Hz (rhombuses).[10]

Among the redox-active molecules, POMs are attractive compounds since they display multiple and reversible redox states as well as conformation and thermal stability making them advantageous for the design of high charge storage devices. Moreover, some POMs are photo-active as well, which gives more opportunities in device conception. A simulation study from Georgiev and coll.[15] was performed on POM-based device for application as flash memory cell. $[W_{18}O_{54}(SO_3)_2]^{4-}$ POM was studied and can be reduced to the corresponding one- and two-electrons reduced species, $[W_{18}O_{54}(SO_3)_2]^{5-}$ and $[W_{18}O_{54}(SO_3)_2]^{6-}$ respectively. The performance of the POM-based device was evaluated both in bulk and fully-depleted silicon-on-insulator (FDSOI) flash cell configuration. In the study, the floating-gate consists of POMs that act as charge storage centers (Figure 8). From the calculations, the threshold voltage V_{Th} can be modulated by the redox state of the POM. More specially, an increase in V_{Th} was observed as the POM is more reduced, which is encouraging for the electrical characterization of our system (see section IV.2). Also, the FDSOI structure allows smaller V_{Th} than using a bulk system, leading to a lower power consumption device, which also praises the use of SOI substrates in our study.

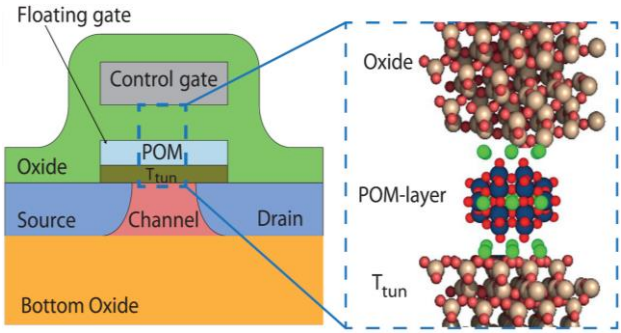

Figure 8 : FDSOI floating-gate memory cell using POM layer as the floating-gate. T_{tun} corresponds to the tunneling oxide thickness of 4.5 nm. On the right, tungsten atoms are represented in blue, oxygen in red, silicon in brown, and the surrounding counter cations in green.[15]

Photo-active and redox-active molecules thus display appealing properties in solution. Examples of some of their immobilization onto Si surface proved to be efficient designs when it comes to electrical properties modulation. As described in this opening part, the combination of such molecules with robust and widely used Si technology allows new device conceptions for optoelectronics, memory devices or information processing applications. The immobilization of photo- or redox-active molecules onto surface however remains a key challenge since thermal stability, quality of the functionalization and the electrical properties repeatability over time need to be taken into account for their integration in microelectronics.

The system developed in the course of this project involves the immobilization of photoreducible $[PMo_{12}O_{40}]^{3-}$ POM, both photo-active and redox-active, onto functionalized Si surface, and is thus a promising system considering the previous stated examples. After POM deposition, the resulting surface will be subjected to several characterizations to study the photoreduction property of the immobilized POM, as will be discussed in the following sections.

I.2. Our approach

The prospect is to build a POM-based material that could benefit from the POM photoreduction property. More specifically, we aim at fabricating a POM-based MOSFET using SOI wafer. In this particular configuration, the current (I_{DS}, drain-to-source current) in the conductive channel is adjusted with the potential applied at the gate. This gate can be either a conventional metallic backgate or charged molecules such as POMs (see Figure 9). This molecular gate is the original focus of our work and the POMs are immobilized on the **top surface**. Indeed, when the POMs are reduced by UV, they tend to acquire a negative charge which in turn induces a depletion zone and reduce the conductive channel as shown on Figure 9. This is the prototype of a phototransistor based on POM photoreduction.

In order to verify this working principle, we are going to probe the top interface with the Kelvin Probe Force Microscopy (KPFM) which is sensitive to the electrostatic charges on the top surface. This will be developed in section IV.I. On the other hand, we access the modulation of the current I_{DS} with the probe station measurements which will be explained in section IV.2. We will compare these two ways of measuring the electrostatic effect of the POMs and discuss how the **buried interface** affects the conductive channel.

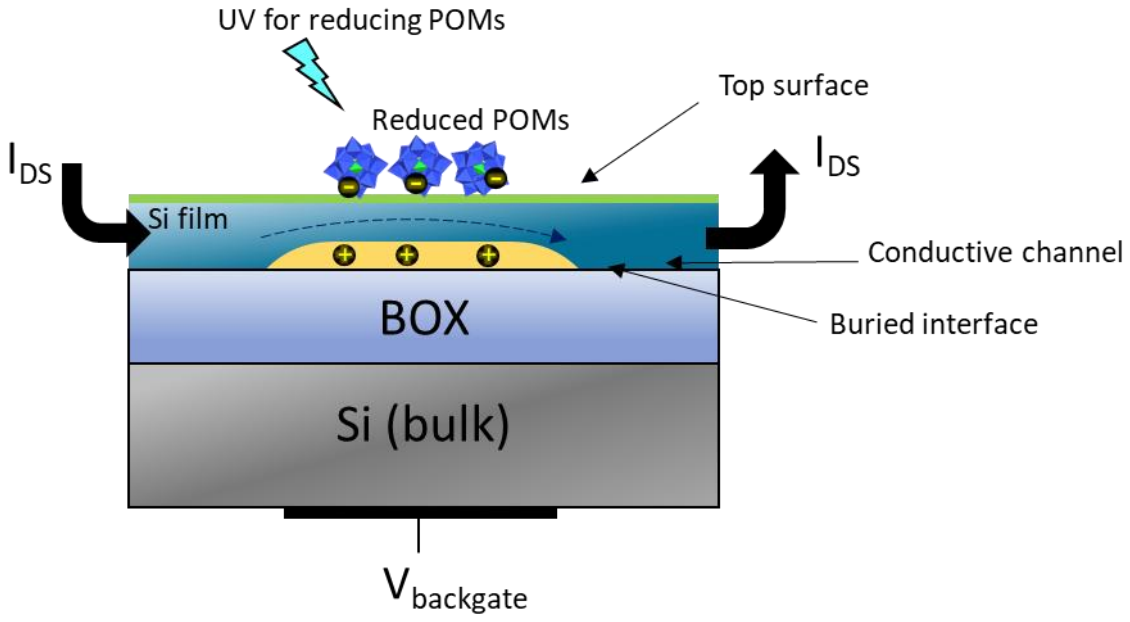

Figure 9 : The working principle of our POM-based pseudo-MOSFET. The conductive channel is squeezed by the charges brought by the POM, which is triggered by the UV light.

II. POM(0), POM(I) and POM(II) characterization as bulk powders

POM(0), POM(I) and POM(II) were successfully synthesized as described in Chapter III. The distinction between the three POMs is crucial in order to understand the photoreduction property. Indeed, as we will work on very thin POM (sub)monolayers (less than 1.0 nm), the stability is unknown and it could be more difficult to probe the photoreduction phenomenon. We first investigated the POMs in their more stable bulk form (powders) in order to get some references for the later immobilized POMs characterization onto surface, and to have as much tools as possible to distinguish between the three POMs. The first difference between them is their color: POM(0) is yellow, POM(I) is blue, and POM(II) exhibits a dark blue color. Also, their ^{31}P NMR spectrum is different from a POM to another: the unique signal is shifted depending on the POM, as shown in Chapter III. Differentiation can also be made using UV-Visible-Near infrared (UV-Vis-NIR) spectroscopy and XPS, as will be discussed hereinafter.

II.1. UV-Vis-NIR spectroscopy characterization

POM solutions were prepared in acetonitrile (concentration of 10^{-5}-10^{-4} mol.L^{-1}) and absorption spectra were recorded between 200 and 1200 nm using a Cary 5000 UV-Vis-NIR spectrophotometer (Agilent) and a 1 cm quartz cuvette. For an easier comparison between the three POMs, the molar attenuation coefficient (ε) was calculated and the ε=f(λ) spectra are shown in Figure 10. The resulting absorption spectra are composed of three main features: at ~220 nm, at ~315 nm and in the region 400-1200 nm.

The α isomer Keggin-type POM is composed of four kinds of oxygen atoms (O_a, O_b, O_c and Od) as discussed in Chapter III. The absorption bands at ~220 nm and ~315 nm (Figure 10a and Figure 10b) exhibit a high ε of ~85000 and ~20000 L.mol^{-1}.cm^{-1} respectively and are both attributed to ligand-to-metal charge transfer (LMCT).[16–19] More specifically, the band at ~220 nm in the three spectra is attributed to O_d → Mo charge transfer while the one at ~315 nm is attributed to $O_{b,c}$ → Mo charge transfer. Indeed, as the molybdenum centers have a d^0 electron configuration while the oxo (O^{2-}) ligand is electron-rich, the charge transfers imply the promotion of an electron from the bonding HOMO of the oxygen atoms to the empty antibonding LUMO of the molybdenum atoms under UV light absorption.

The main difference between POM(0), POM(I) and POM(II) lies in the 500-1200 nm region where an intervalence charge transfer (IVCT) absorption band is only observed for the reduced POMs. The maximum absorption bands are depicted in Figure 10c, with ε_{811} = 1265 L.mol^{-1}.cm^{-1} in the case of POM(I) and ε_{707} = 3068 L.mol^{-1}.cm^{-1} in the case of POM(II). These broad absorption bands correspond to an electron charge transfer from Mo at the oxidation state +5 (Mo(V)) to Mo at the oxidation state +6 (Mo(VI)): Mo(V)-O$_{b,c}$-Mo(VI) → Mo(VI)-O$_{b,c}$-Mo(V).[16,18,20–22] Indeed, the reduced POMs have an electron in the d orbitals (d^1 electron) that is delocalized within the POM due to orbitals overlapping. Under visible light activation, the electron hopping between Mo(V) and Mo(VI) results in an IVCT band. Note also that another small contribution can be guessed in POM(II) absorption spectrum at 504 nm where ε_{504} = 2275 L.mol^{-1}.cm^{-1} and could be attributed to d-d transitions or IVCT.

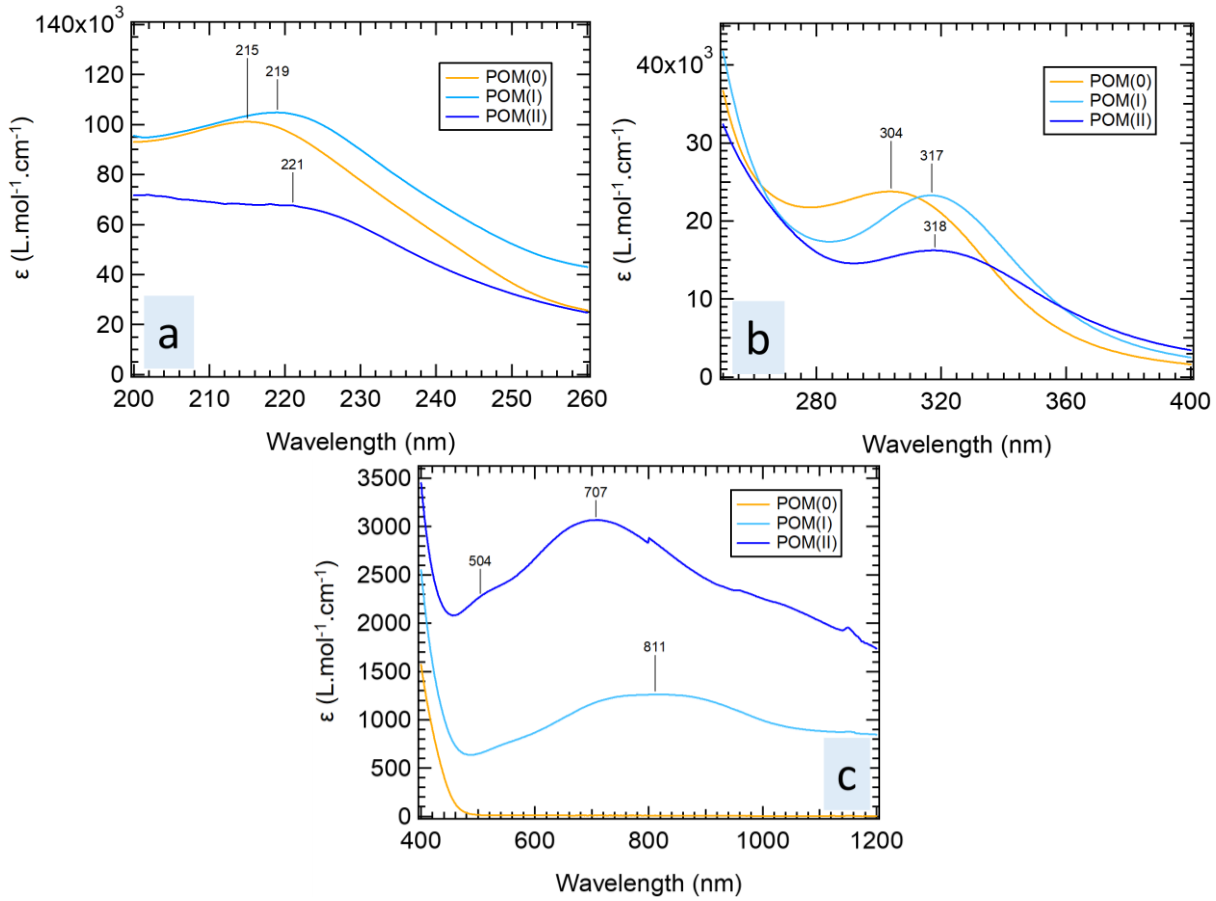

Figure 10 : ε=f(λ) absorption spectra of POM(0), POM(I) and POM(II) in solution in acetonitrile in the 200-260 nm range (a), 250-400 nm range (b) and 400-1200 nm range (c). Notice that the values of ε vary of a factor of ~100 in the various wavelength range. This is why the spectra were cut into three ranges.

Thus the distinction between the oxidized POM(0) and its corresponding electron reduced species POM(I) and POM(II) is clearly visible using UV-Vis-NIR spectroscopy.

II.2. XPS characterization

Freshly prepared POMs powders were analyzed by XPS to complete the set of characterizations. Focus was given to the Mo 3d region where the difference between the three POMs can be found. In this region, the proportion between Mo(VI) and Mo(V) is different depending on the POM.

The spectra are shown in Figure 11. For all the POMs, photopeaks corresponding to Mo(VI) 3d (3/2) and (5/2) are found around 236.2 and 233.1 eV respectively and appear as a doublet. After decomposition of the signal, contributions of Mo(V) 3d (3/2) and (5/2) are found around 235.1 eV and 232.0 eV respectively.

In the case of POM(0) (Figure 11a), contributions from Mo(V) were unexpected since the 12 Mo atoms in POM(0) are supposed to be exclusively fully oxidized Mo(VI) atoms ($[PMo^{VI}_{12}O_{40}]^{3-}$). The Mo(VI)/Mo(V) ratios for 3d (3/2) and 3d (5/2) were calculated and gave $\frac{Mo(VI)_{3/2}}{Mo(V)_{3/2}} \approx 14.98$ and $\frac{Mo(VI)_{5/2}}{Mo(V)_{5/2}} \approx 10.46$. The average Mo(VI)/Mo(V) ratio was 12.72. As the POM was freshly prepared, we thus attributed the presence of Mo(V) to a reduction of the POM during the measurement by the X-ray beam. Thus over the 12 Mo atoms, there are 11.1 Mo(VI) and 0.9 Mo(V) atoms.

In the case of POM(I), contributions of Mo(V) 3d (3/2) and (5/2) are found at 234.8 eV and 231.6 eV respectively after decomposition of the signal (Figure 11b). The Mo(VI)/Mo(V) ratios for 3d (3/2) and 3d (5/2) were calculated and gave $\frac{Mo(VI)_{3/2}}{Mo(V)_{3/2}} \approx 7.66$ and $\frac{Mo(VI)_{5/2}}{Mo(V)_{5/2}} \approx 8.02$. POM(I) is theoretically constituted with 1 reduced Mo(V) atom and 11 oxidized Mo(VI) atoms ($[PMo^{VI}_{11}Mo^{V}O_{40}]^{4-}$), We found a satisfying average Mo(VI)/Mo(V) ratio of 7.84, though lower than the ratio of 11 expected. As the reduction of Mo(VI) during XPS measurement seems to occur, the lower ratio could be attributed to the presence of a small excess of reduced Mo atoms. Thus over the 12 Mo atoms, there are 10.6 Mo(VI) and 1.4 Mo(V) atoms.

In the case of POM(II), contributions of Mo(V) 3d (3/2) and (5/2) are found at 234.8 eV and 231.7 eV respectively after decomposition of the signal (Figure 11c). The Mo(VI)/Mo(V) ratios for 3d (3/2) and 3d (5/2) were calculated and gave $\frac{Mo(VI)_{3/2}}{Mo(V)_{3/2}} \approx 3.72$ and $\frac{Mo(VI)_{5/2}}{Mo(V)_{5/2}} \approx 4.34$. POM(II) is theoretically constituted with 2 Mo(V) atoms and 10 Mo(VI) atoms ($[PMo^{VI}_{10}Mo^{V}_{2}O_{40}]^{5-}$). A satisfying average Mo(VI)/Mo(V) ratio of 4.03 was obtained, again lower than the ratio (of 5) expected. Thus, over the 12 Mo atoms of POM(II), 9.6 are Mo(VI) and 2.4 are Mo(V).

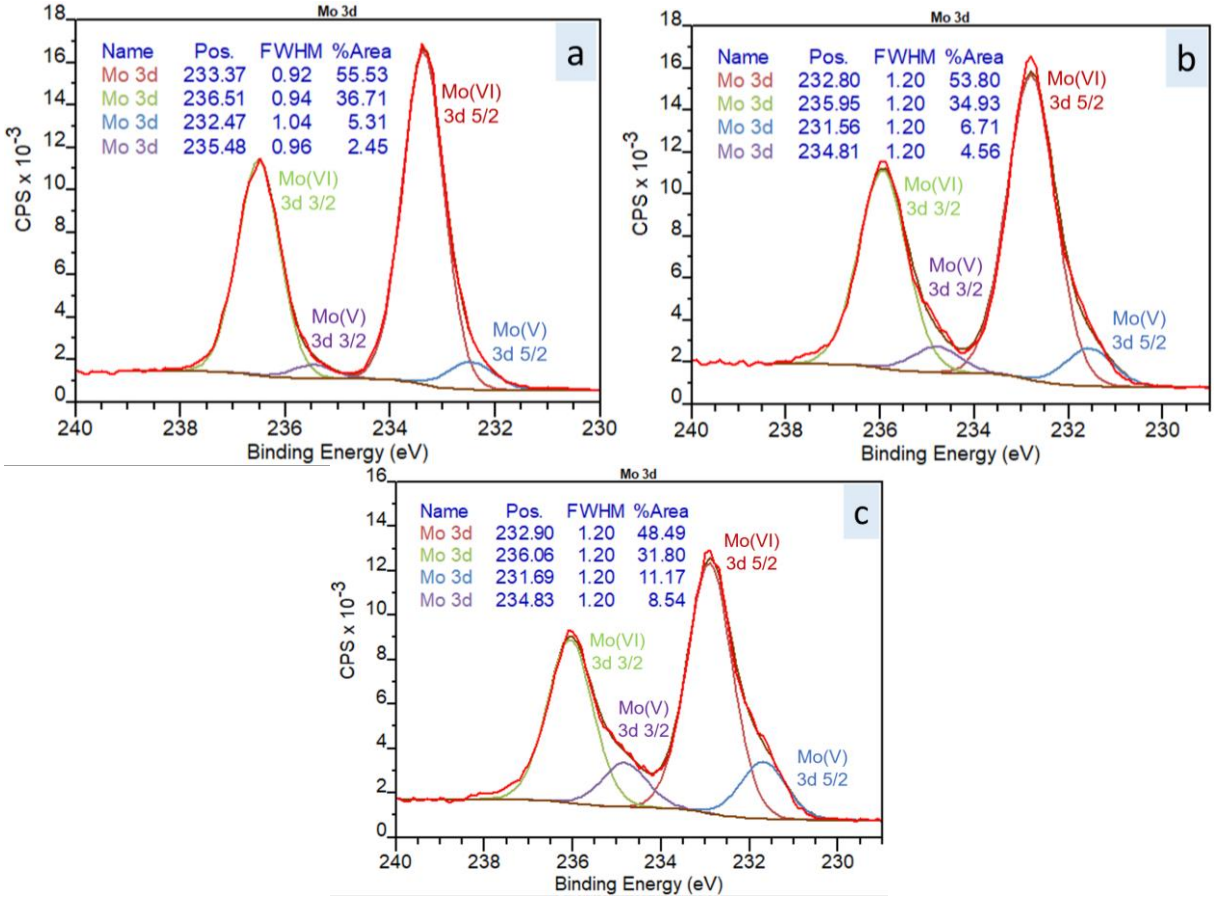

Figure 11 : XPS spectrum in the Mo 3d region of a) POM(0), b) POM(I) and c) POM(II) powders.

Note that the space in-between the two Mo(VI) photopeaks at ~234.5 eV is different depending on the POM. The more the POM is reduced, the more the space between the photopeaks intersection and the baseline is wide.

The distinction between POM(0), POM(I) and POM(II) is thus possible, as demonstrated by the different signatures exhibited by the three POMs on the absorption spectra and on the Mo 3d region XPS spectra when working with POM powders freshly synthesized. This observation is encouraging for probing the redox state of the three POMs once they will be immobilized onto the functionalized Si surface.

III. Immobilized POM(0), POM(I) and POM(II) characterization

The POMs powders obtained can thus be immobilized on $SiNH_2$ surfaces, as previously discussed in Chapter III, and the resulting thin POMs (sub)monolayers are then subjected to characterization. The purpose was to be able to differentiate POM(0), POM(I) and POM(II) monolayer, and then to irradiate POM(0) monolayer to know whether it gets reduced to POM(I) or POM(II) depending on the signature obtained using the characterization tools. This section will thus be dedicated to the characterization of POMs monolayers using XPS and UV-Vis-NIR spectroscopy that proved to be efficient in differentiating POM powders.

III.1. XPS characterization

As the previous XPS characterization on POM powders was found to be efficient in differentiating the POMs, we therefore try the same procedure on the freshly prepared POM monolayers onto $SiNH_2$ surfaces.

A (111)$SiNH_2$ substrate was prepared in two days using the procedure described in Appendix 5.2. The thickness of the resulting organic monolayer was measured by ellipsometry and was found in the range 1.5-1.6 cm. The functionalized substrate was subsequently cleaved into three pieces using a diamond tip scriber. Each piece was quickly rinsed with water and dried under a stream of N_2. The three pieces were stored in three different vials in the dark and purged with Ar. The day after, POM(0), POM(I) and POM(II) monolayers were prepared by a simple dipcoating in POM solutions in acetonitrile under the glove box. To avoid any POM monolayer reduction prior to XPS analyses, the thicknesses of each POM monolayer were measured after XPS analyses. The freshly prepared POM monolayer-containing substrates were thus purged with Ar right after their exit from the glove box and kept in the dark by covering the vials with foil. The substrates were then brought for XPS analyses and results were obtained a few hours later. Again, the focus is given here on the Mo 3d region and the corresponding XPS spectra of the $SiNH_2$-POM(0), $SiNH_2$-POM(I) and $SiNH_2$-POM(II) surfaces are shown in Figure 12. An approximate thickness of 0.4 nm, 0.5 nm and 1.1 nm were measured after XPS analyses for the POM(0) monolayer, POM(I) monolayer and POM(II) monolayer, respectively.

As expected, no contribution of Mo(V) was found in the Mo 3d region of POM(0) monolayer and deconvolution only reveal contributions from Mo(VI) as depicted in Figure 12a. However, the same observation is made for POM(I) monolayer (Figure 12b) and POM(II) monolayer (Figure 12c), where contributions of Mo(V) were expected. As those contributions

are missing, it means that POM(I) and POM(II) monolayers probably got reoxidized before XPS analysis.

The only difference between the three XPS spectra can be spotted at ~235 eV, between the curve and the baseline. At this location, the more the POM is reduced, the more the space between the curve and the baseline increases. While the difference between the XPS spectrum of POM(0) monolayer and POM(I) monolayer is not obvious, the XPS spectrum of POM(II) monolayer exhibits a higher space between the curve and the baseline at ~235 eV than the two other spectra. However, this difference is not precise enough to have a quantitative estimation of the redox state of the POM. Moreover, the XPS spectra of the POM monolayers exhibit more noise than the POM powders counterparts (Figure 11), which also suggests that the density of POM on surface is possibly not sufficient for probing Mo(V) contributions, which are expected to be 11 and 5 times lower than the Mo(VI) contributions.

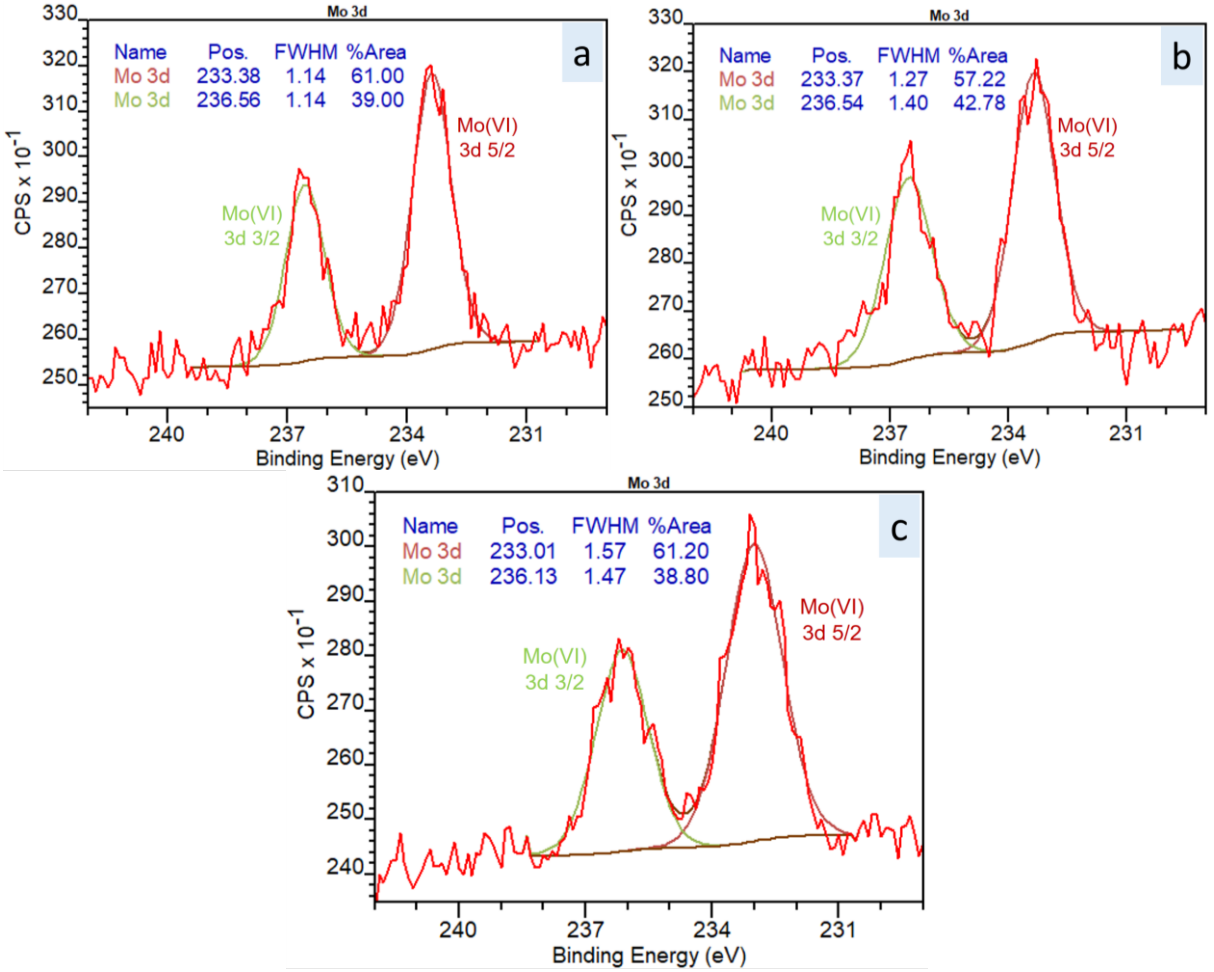

Figure 12 : XPS spectrum in the Mo 3d region of a) POM(0) monolayer, b) POM(I) monolayer and c) POM(II) monolayer on $SiNH_2$ substrates.

Despite all the care taken to avoid contact of the substrate with air prior to XPS analyses and the care taken to provide the most freshly prepared POM monolayer, difference between the three POM monolayers is hardly visible using XPS characterization. This is probably due to a reoxidation of the POM monolayer prior to analysis and/or a lack of POM density on the surface. In all cases, XPS does not seem to be appropriate to analyze the redox state of the immobilized POM monolayers, and results suggest that POM monolayers are less stable than their POM powders counterparts. We then turned to the UV-Vis-NIR spectroscopy that proved to be efficient to distinguish the three POM powders.

III.2. UV-Vis-NIR spectroscopy characterization

The immobilized POMs are analyzed using a JASCO V-750 spectrophotometer. Our lightly doped Si has the particularity to be transparent to IR light but opaque to UV light. Thus, the characterization of POM monolayer on Si substrates required to work in reflection mode. Results will be first presented but as they are not reliable, POMs multilayers were prepared on quartz substrates which allows us to work in the common transmission mode, and the results will be presented in the second part.

III.2.a. Absorbance spectra of POM layer on Si substrates recorded in reflection mode

The spectrophotometer was equipped with the UV-Vis VeeMAX variable angle specular reflectance accessory, shown in Figure 13. By positioning a substrate on the top of the accessory, downwards (Figure 13a), the light beam coming from the right part of the accessory is reflected inside the accessory onto the several mirrors. After hitting the sample surface, the beam is reflected off towards the exit aperture on the left side with the help of mirrors (Figure 13b). This accessory allows adjusting the reflection angle onto the sample surface, from 20 to 80°.

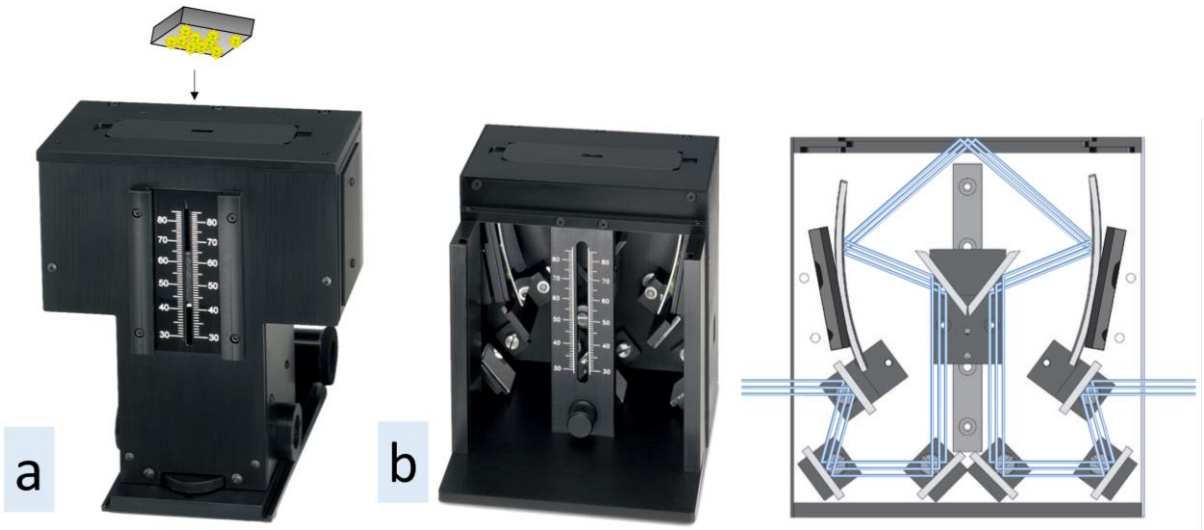

Figure 13 : a) UV-Vis VeeMAX variable angle specular reflectance accessory and b) the inside part with an optical geometry schematic of the accessory.

The aim of using this accessory was the characterization of the POM monolayer onto $SiNH_2$ surface. However, to the best of our knowledge, no POM containing surface has been characterized using the reflection mode of the spectrophotometer. Therefore, it was necessary to optimize the parameters for better quality spectra. As the preparation of POM monolayers is time consuming, we decided first to immobilize the POMs onto Si-SiO_2 surface as multilayers, to also make sure that spectra could be obtained. It is crucial to be able to position the sample always at the exact same place in order to have more reproducible spectra subtractions. We added a small blocking part on the sample holder so that our silicon pieces were always analyzed at the same place with an accuracy of a few µm. The spectra were recorded at ~45°. Three pieces of Si(111) substrates were degreased and cleaned with RCA solutions. The surface spectrum was then recorded for each substrate (reference spectrum). POM(0), POM(I) and POM(II) were then immobilized onto each surface by a dropcasting performed under glove box. The modified surface spectrum was then recorded and referenced to the reference spectrum. The spectra obtained after 1 drop of POM solution added onto the surface are shown in Figure 14 and they were recorded in absorbance for an easier comparison with the previous absorbance spectra.

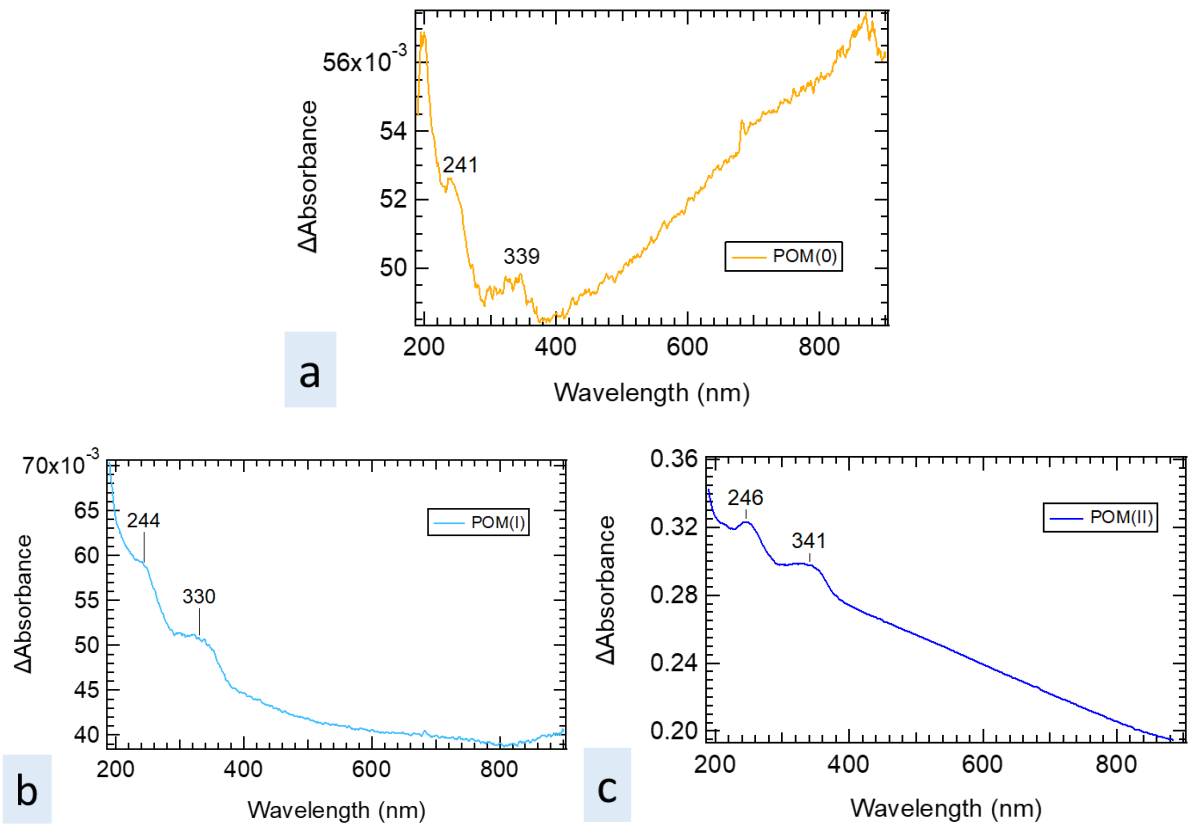

Figure 14 : Absorbance spectrum of a) POM(0) multilayer, b) POM(I) multilayer and c) POM(II) multilayer immobilized on Si(111)-SiO_2 surfaces obtained after the addition of 1 drop of POM solution onto the surface, recorded in reflection mode. The reference spectrum is the surface spectrum obtained before POM deposition

In all the absorbance spectra, a band at ~245 nm is observed and another one at ~335 nm is observed for POM(I) and POM(II) multilayers. The bands are in the range of the LMCT bands observed in POM solution. However, critical points in crystalline Si are also expected at ~365 and ~288 nm (3.4 and 4.3 eV respectively) and correspond to interband transitions in the Si due to the excess carriers recombination.[23–25] Moreover, the IVCT band can not be distinguished: the band is lower in intensity than the LMCT bands and the latter have already a low intensity on the spectra. Thus, the differentiation between the three POMs can not be made at this stage. 4 more drops of POM solution were subsequently added on the same surfaces and the resulting absorbance spectra are shown in Figure 15. The difference between the oxidized POM and the reduced POMs seems to be more visible. A band at ~800 nm is indeed present on both POM(I) and POM(II) multilayers spectra, as depicted by the black arrows on the spectra, while missing in the POM(0) spectrum. This band can be attributed to IVCT and its intensity could be related to the density of the POM coverage on the surface, higher in the case of the POM(II).

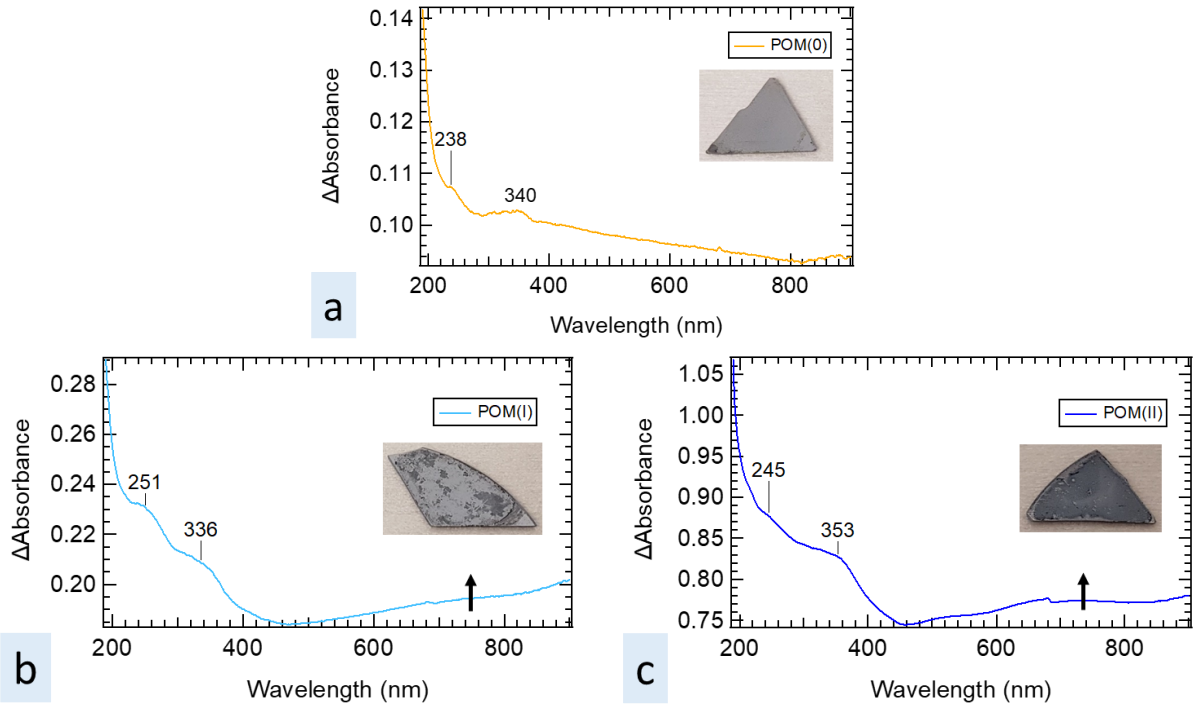

Figure 15 : Absorbance spectrum of a) POM(0) multilayer, b) POM(I) multilayer and c) POM(II) multilayer immobilized on Si(111)-SiO_2 surfaces obtained after a total of 5 drops of POM solution added to the surface, recorded in reflection mode. The reference spectrum is the surface spectrum obtained before POM deposition. The corresponding aspect of the resulting surfaces are also shown.

As a POM monolayer prepared by dipcoating of an $SiNH_2$ substrate is expected to have a lower density coverage than the corresponding multilayer prepared by dropcasting, a lower quality of spectrum compared to the ones in Figure 14 and Figure 15 was expected. Nevertheless, in order to have a rough idea of the spectrum on POM monolayer, a POM(0) monolayer was immobilized by dipcoating on an Si(100)NH_2 surface that was prepared almost 9 months before. The initial $SiNH_2$ surface was referenced to itself at the beginning (Figure 16, red curve). After dipcoating, the $SiNH_2$-POM(0) surface spectrum was recorded and referenced to the $SiNH_2$ surface spectrum (Figure 16, orange curve). Finally, after 10 minutes of UV irradiation, the spectrum of the resulting surface was recorded and again, referenced to the $SiNH_2$ surface spectrum (Figure 16, green curve). Several spectra were actually recorded after each step but the spectra shown in Figure 16 are the best ones obtained (*i.e.*, with the lowest shift in absorbance compared to the baseline). The UV lamp used for the experiment is a low-pressure mercury (Hg) gaseous discharge Pen-Ray lamp (90-0012-01 model), purchased from Analytik Jena US (formerly UVP Ultra-Violet Products), which emits light with a primary energy at 254 nm.

The $SiNH_2$ and $SiNH_2$-POM(0) spectra seem to only differ in absorbance shift and no apparent band is observed after POM deposition. The UV irradiation process required to remove the $SiNH_2$-POM(0) substrate from the accessory to be able to irradiate the POM layer. Although a shift of absorbance of $1\text{-}5.10^{-3}$ (up to 10.10^{-3} in the worst case) may occur due to an imperfect sample repositioning, we can clearly distinguish a negative feature at 822 nm after 10 minutes of UV irradiation. This could be the IVCT band expected after reducing POM(0).

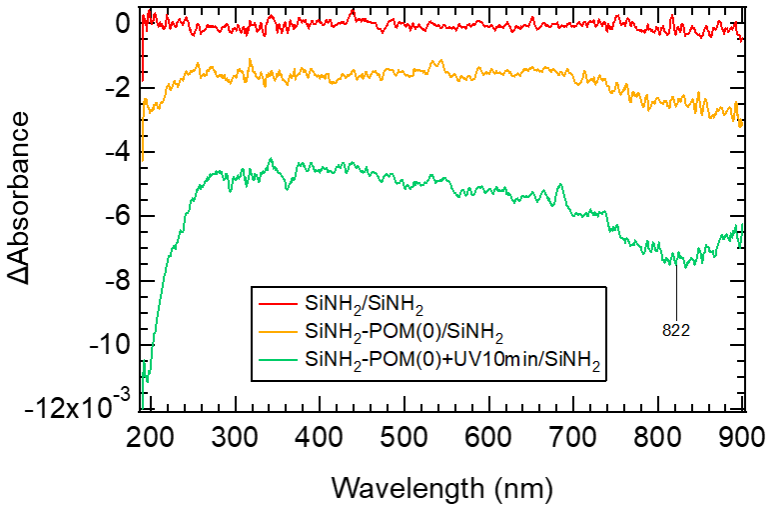

Figure 16 : Absorbance spectrum (in absorbance units) of the $SiNH_2$ surface (red curve), $SiNH_2$-POM(0) surface (orange curve) and $SiNH_2$-POM(0) surface after 10 minutes UV irradiation at λ = 254 nm with an Hg lamp (green curve), recorded in reflection mode. In all cases, the reference spectrum is the $SiNH_2$ surface spectrum.

As the characterization of the immobilized POM onto Si surfaces was not obvious using the UV-Vis-NIR spectrophotometer in reflection mode and laborious because of the substrate positioning, we thus turned to the more common transmission mode. As the Si substrate can not be used in this mode, multilayers of POM were instead prepared onto quartz substrates.

III.2.b. Transmission mode for POM multilayer on quartz substrates

POM(0), POM(I) and POM(II) multilayers were prepared on quartz substrates via a dropcasting of the corresponding POM solution. The quartz substrates were first rinsed with and sonicated in acetonitrile, followed by a degreasing and cleaning step similar to the one on Si substrates. As the quartz discs are larger than the Si substrates, more drops were added onto them under a glove box. 10 to 15 drops of POM(0) solution are added onto the quartz surface, while only 5 drops of POM(I) and POM(II) are added. The number of drops was determined

through trial-and-error experiments and we tried to have comparable spectra between each POM-containing surface.

The spectra were recorded in the range 190-900 nm, in transmission mode. The experiment started with a spectrum recording of the cleaned quartz substrate, and the resulting spectrum is called "reference spectrum". After POM immobilization, another spectrum was recorded and processed with the reference spectrum, resulting in a differential spectrum of the immobilized POM onto surface. These absorbance spectra obtained for POM(0), POM(I) and POM(II) multilayers are shown in Figure 17.

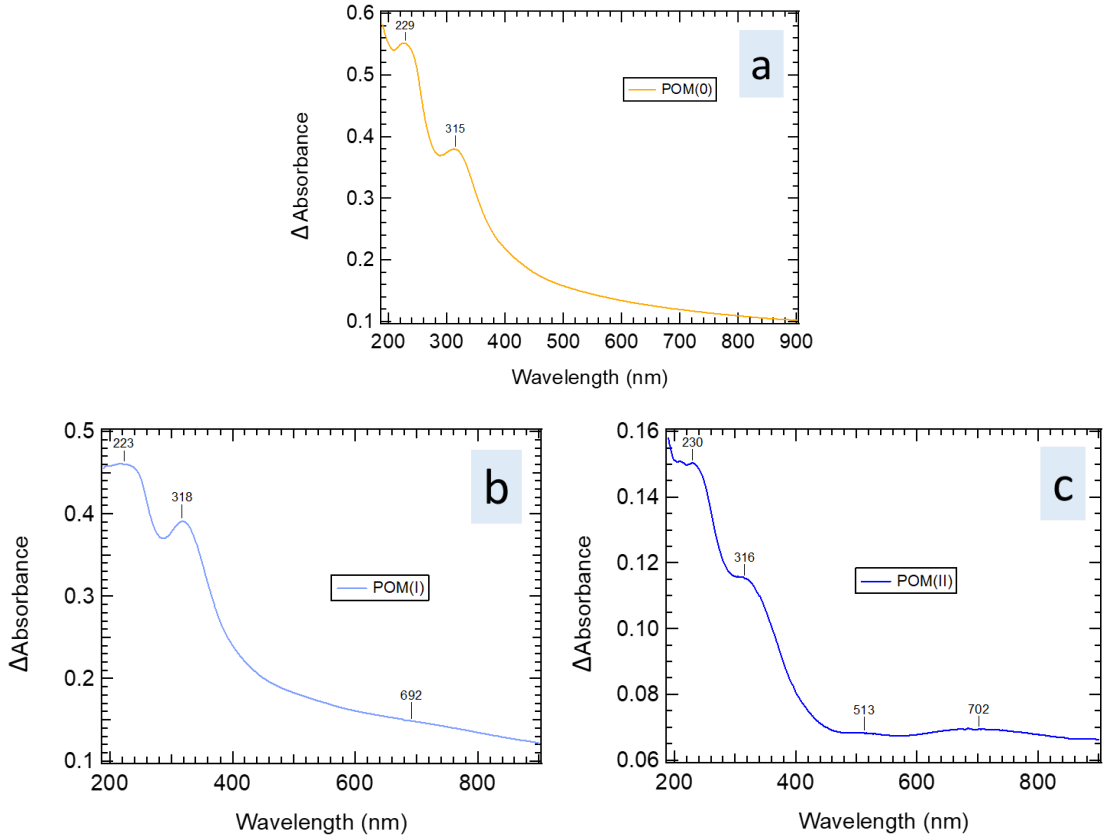

Figure 17 : Absorbance spectrum of a) POM(0) multilayer, b) POM(I) multilayer and c) POM(II) multilayer on quartz substrates. For each case, the reference spectrum is the spectrum of the quartz surface before POM deposition.

While leaving the quartz substrate at the same position (to avoid possible variations due to sample repositioning), the UV pen lamp was brought near the substrate face where POM were immobilized (at ~3-4 cm). After each 5 minutes UV irradiation cycle, the UV pen lamp was removed from the sample compartment and a spectrum was recorded. The UV irradiation stopped when a total of 20 or 30 minutes irradiation was reached (depending on the experiment). After the lamp was definitely removed from the compartment, several spectra were recorded to follow the absorption bands variation, 30 to 50 minutes after the UV irradiation stopped. The

spectra of the POM(0), POM(I) and POM(II) multilayers-containing surfaces before, under and after UV irradiation are referenced to their corresponding initial quartz surface spectrum and will respectively be called **POM(0)/quartz**, **POM(I)/quartz** and **POM(II)/quartz**. The resulting differential spectra obtained over the experiment are shown in Figure 18.

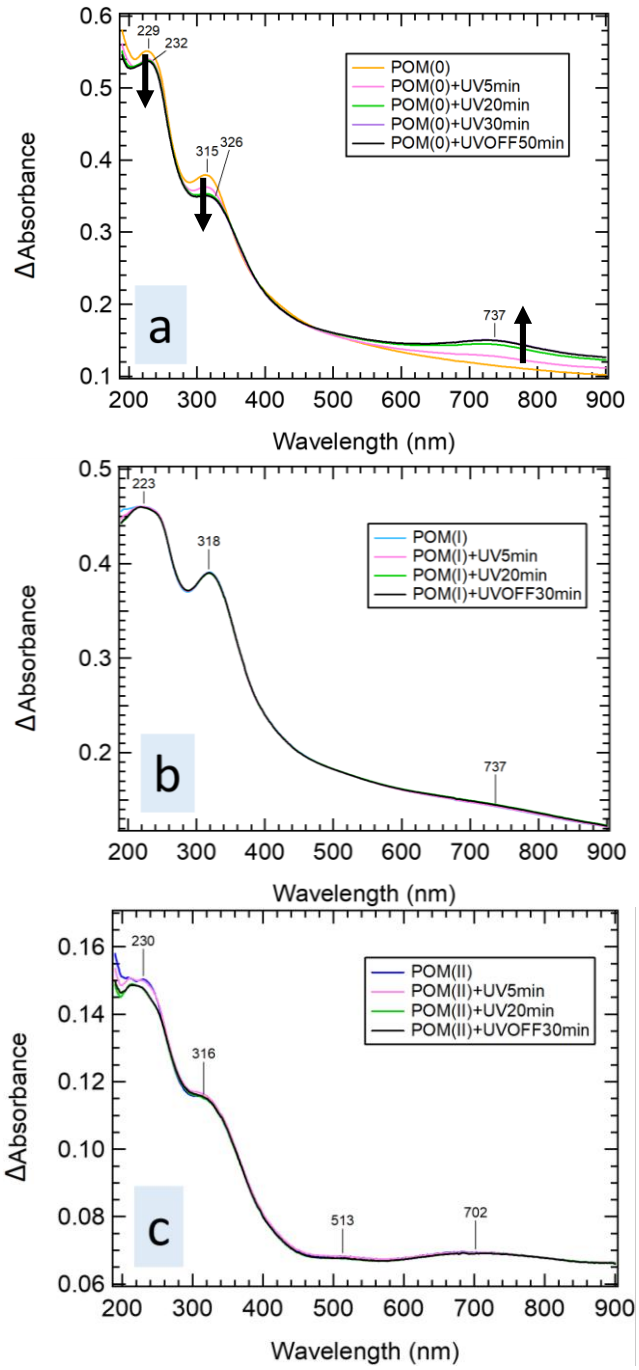

Figure 18 : a) POM(0)/quartz spectra, b) POM(I)/quartz spectra and c) POM(II)/quartz spectra obtained during the experiment. Arrows in Figure 18a shows the LMCT and IVCT bands variation during UV irradiation.

First, POM multilayers immobilized on quartz surfaces exhibit similar absorption spectra compared to the ones obtained with POMs in solution. POM(0)/quartz spectrum (Figure

17a) exhibits absorption bands at 229 nm and 315 nm due to O→M LMCT. The same bands are observed on POM(I)/quartz spectrum (Figure 17b) at 223 nm and 318 nm, as well as on POM(II)/quartz spectrum (Figure 17c) at 230 nm and 316 nm. Absorption band due to IVCT can be guessed at ~737 nm in POM(I)/quartz spectrum and at ~702 nm in POM(II)/quartz spectrum.

Under UV irradiation, an absorption band is clearly growing at ~737 nm on the POM(0)/quartz spectrum suggesting that the immobilized POM(0) is getting reduced, which is also supported by the decrease in intensity of the two LMCT bands.[21,26] When looking closer at the POM(I)/quartz spectra, a slight growth of the IVCT band (Figure 19a) and slight decrease in LMCT bands are observed, suggesting a slight reduction of the POM(I). On the other case, when looking closer at the POM(II)/quartz spectra, the IVCT band is subjected to a decrease (Figure 19b), which suggests a reoxidation of the POM(II) due to UV irradiation.

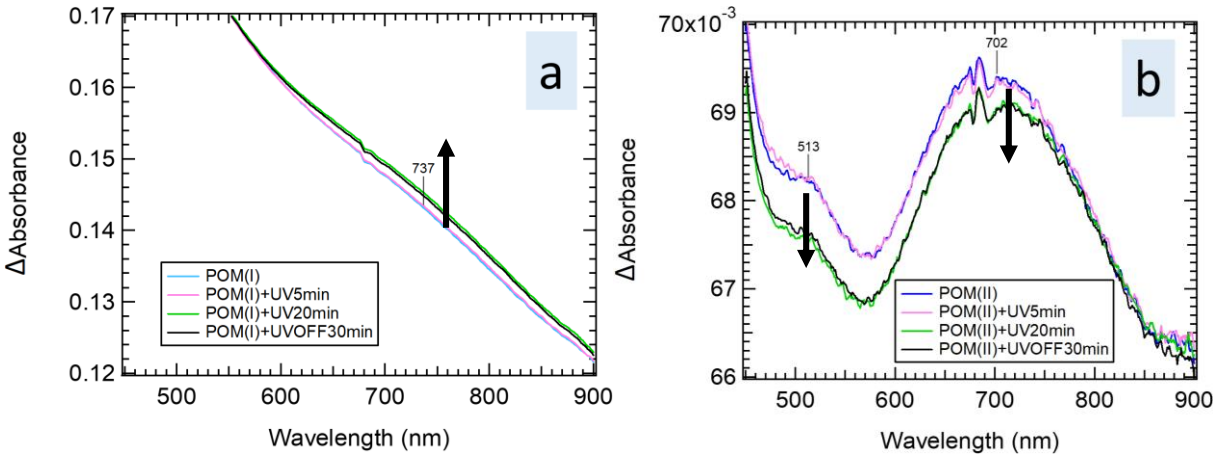

Figure 19: A closer look on the 450-900 nm region of a) POM(I)/quartz spectra and b) POM(II)/quartz spectra obtained over during the measurement. The growth or decrease of the IVCT band are highlighted by arrows.

50 minutes after the lamp was switched off, the POM(0)/quartz spectrum remain unchanged compared to the spectrum recorded after 30 minutes UV irradiation, suggesting that the irradiated POM(0) multilayer is stable. Note that the color of the irradiated surface area changed from yellow to blue as shown in Figure 20a. The blue color still remains five days after the experiment (Figure 20b) and even longer (not showed). 30 minutes after the lamp was switched off, POM(I)/quartz spectrum is only slightly modified: the IVCT band slowly and slightly decreases again, while LMCT bands remain almost unchanged. The behavior of IVCT band suggest a reoxidation of the irradiated POM(I) after the lamp is off. Finally, no change occurs on the POM(II)/quartz spectrum after the lamp was switched off.

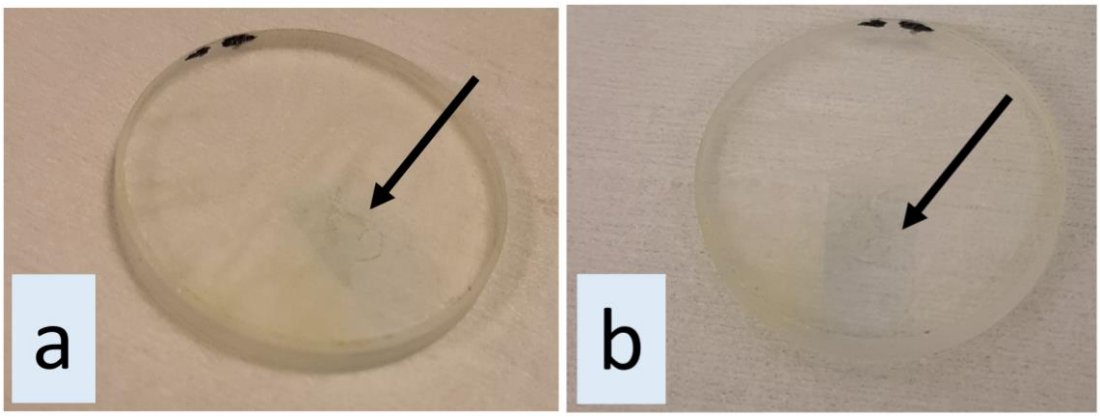

Figure 20 : a) UV-irradiation of the immobilized POM(0) multilayer leads to a color change from yellow to blue on the area indicated by the arrow. b) Picture of the same surface taken 5 days after the end of the experiment still shows a blue colored area

Since photoreduction seems to occur under UV irradiation of POM(0) multilayer on quartz substrate, doubts arose on the real mechanism since no apparent electron is present for the POM reduction.

In the case of $SiNH_2$ surface, the NH_2/NH_3^+-terminated organic monolayer can provide a proton to the POM for its photoreduction. As depicted by Scheme 5, due to the O→Mo LMCT generated by UV irradiation, a proton transfer from the NH_3^+ groups to a bridging oxygen atom is expected. The non-bonding electrons of the NH_3^+ group thus interact with the hole created by the O→Mo LMCT process, leading to the formation of a charge-transfer complex.[16,21,27]

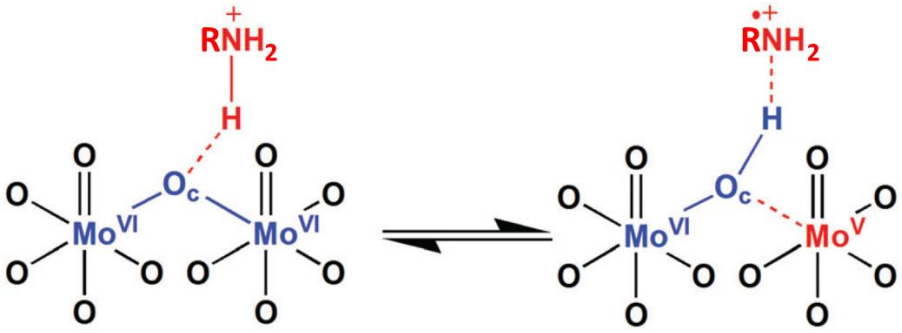

Scheme 5 : Photoreduction mechanism of POM(0) onto $SiNH_2$ surface. (Modified from ref. 21).

Here, in the case of POM multilayers onto quartz substrate, there is no more reducing species. The first hypothesis was that traces of solvent could play the role of the reducing agent. Thus, another experiment using the spectrophotometer was carried out using, this time, a POM(0) powder that was dried prior to its deposition onto quartz substrate to remove traces of solvent. The POM drying process was carried out using a Buchi GKR-51 titration drying oven: POM(0) was introduced in a Schlenk tube which was subsequently inserted inside the glass tube of the oven and heated at 120°C for 3 hours under vacuum. After the POM solution preparation under

the glove box, 10 drops were added to the cleaned quartz substrate. The spectrum of the surface was recorded before and after POM deposition, under and after UV irradiation. The resulting differential spectra are shown in Figure 21, where all surface spectra were referenced to the quartz surface spectrum. Under UV irradiation, a growth of an absorption band is still spotted at 737 nm, due to IVCT, and remain unchanged after the UV lamp is switched off. Despite the POM(0) drying, a reduction of POM(0) on the surface is still observed under UV irradiation. For the moment, the origin of the electron for the POMs reduction is not clear. Note that, as the spectra recording was performed under ambient atmosphere, unavoidable contact of immobilized POM with water molecules occurred during the measurement. Further investigation is needed to definitively figure out the mechanism of the POMs photoreduction.

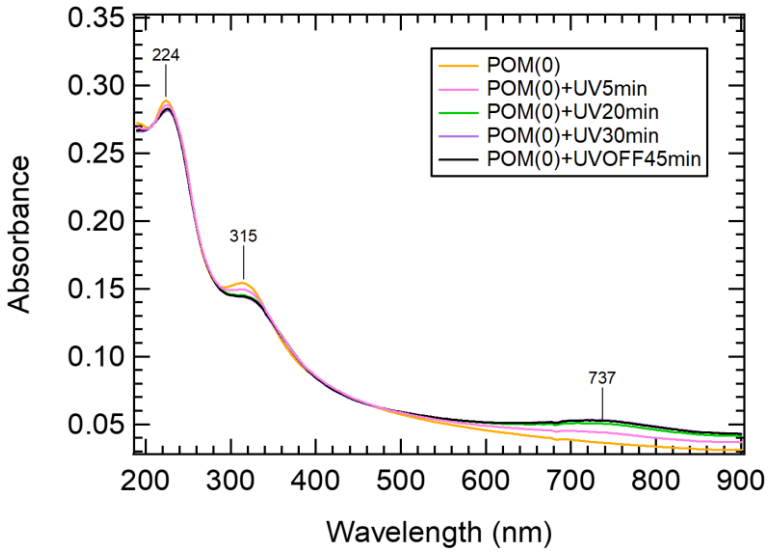

Figure 21 : POM(0)/quartz differential spectra before, under and after UV irradiation. The POM(0) used in this experiment was dried under vacuum at 120°C for 3 hours.

Reliable results of POM monolayer characterization when working with UV-Vis-NIR spectroscopy on reflection mode were hardly obtained. POM multilayers were thus analyzed on quartz substrates in order to work with the more convenient transmission mode. After deposition, POM(I) and POM(II) are distinguishable from POM(0) due to the IVCT band exhibited on the UV-Vis-NIR spectra. In the case of POM(0), the main feature lies in the evolution of the spectrum under UV irradiation: the IVCT band obviously grows under UV irradiation, which is not the case for POM(I) and POM(II) multilayers, suggesting that POM(0) multilayer is more prone to get reduced under UV light than the two other reduced multilayers. It was however surprising to observed a POM(0) multilayer photoreduction since no electron is apparently provided by the quartz substrate. Traces of solvent were thus suspected to play the role of the reducing agent. However, despite a drying of the POM(0) prior to the dropcasting,

a photoreduction of the POM(0) multilayer was still observed. Doubts thus arose about the real mechanism actually occurring during UV-light irradiation and further investigations are required.

Going back to the POM monolayers, another surface characterization tool was needed.

IV. Electrical characterization of POM-modified interfaces

As the XPS measurements were not satisfying in giving precise evidence of a photoreduction phenomenon on $SiNH_2$-POM surfaces and giving the difficulties encountered by using the reflection mode in UV-Vis-NIR spectroscopy measurements on modified Si surfaces, the need of a characterization tool that allows us to do "*in situ* UV irradiation" (*i.e.* being able to analyze the surface while irradiating it) appeared necessary. This section will thus be dedicated to the electrical characterization of POM monolayers, as well as multilayers, using the Kelvin Probe Force Microscopy (KPFM) and the probe station. Also, with the aim of building a POM-based phototransistor (Figure 9), these two characterization tools could provide insights on the local change occurring on the top surface under UV irradiation, but also on the current modulation at the buried interface of the device.

IV.1. KPFM measurements

In its working principle, KPFM is aimed at measuring the local surface charge. This ability to tune the charges by photo-reducing the POM is precisely the core of the devices we aim at fabricating. KPFM will therefore be essential to ensure POMs are working like intended. A presentation of the KPFM apparatus and principle will first be given, followed by the results obtained on POM monolayers and multilayers.

IV.1.a. KPFM principle

KPFM is a characterization tool used to study the electrical properties, and more precisely the surface potential of metals and semiconductors. This technique allows the calculation of the surface work function (WF) as will be described hereinafter. Definition of work function and other electronic levels characteristic of semiconductor materials are given in Appendix 4.1 for a clearer understanding. KPFM provides topography image as well as a surface potential image of the scanned surface and the apparatus is shown in Figure 22.

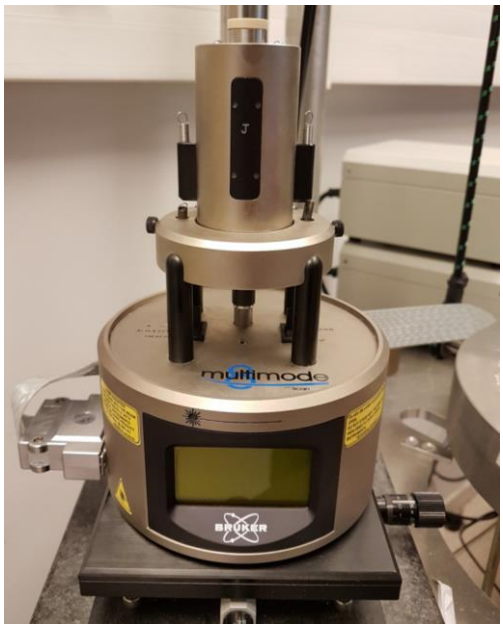

Figure 22 : Bruker Multimode 8 AFM, equipped with the KPFM module.

During the measurement, the selected surface area is mapped from top to down or from down to top using a tip positioned at the end of a cantilever, similarly to the AFM. The topography image obtained using KPFM is similar as using AFM and is thus obtained based on electrostatic interactions between the tip (cantilever) and the surface of the sample. The sample is positioned on a piezoelectric tube, allowing the surface scan along the x-, y- and z-axis. A laser beam is focused on the backside of the cantilever and reflected off to the center of a four-quadrant photodetector (sensor). During the surface mapping, attractive or repulsive forces between the tip and the surface change the cantilever deflection. In the most conventional operation, the cantilever is driven into oscillation close to its resonance frequency. The software maintains a constant oscillation amplitude. When a tip comes closer to the surface, the Van der Waals interaction modifies the resonance frequency and the software acts on the piezoelectric tube and take the tip slightly away. This is the “tapping” mode. Scanning over the surface allows recording the topography with a typical resolution of 5 nm laterally and 0.1 nm vertically.

In our case, surfaces were more precisely analyzed using the PeakForce KPFM™ mode of Bruker, which is a combination of the PeakForce™ mode and frequency modulation KPFM (FM-KPFM) mode. PeakForce KPFM™ mode is depicted in Figure 23 and operates in a dual-pass mode: during the scanning along each line of the surface area selected, the tip first works in PeakForce™ mode to provide the topography image. The tip then rises at a height defined by the user and traces the line backwards while operating in FM-KPFM mode.

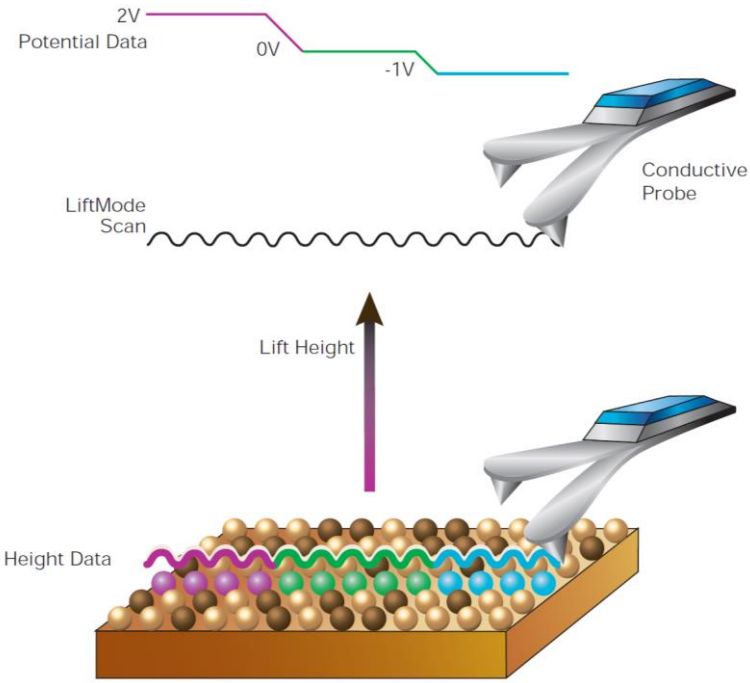

Figure 23 : PeakForce KPFM™ operation mode.[28]

PeakForce™ mode corresponds to a mode operation where the cantilever oscillates below its resonance frequency (off-resonance tapping mode), and where the peak force, *i.e.* the maximum force between the tip and the surface of the sample, is maintained constant and down to 10 pN during the surface mapping.[29,30] The tip intermittently and gently taps the surface. FM-KPFM is based on the FM mode (non-contact mode) of AFM. During the surface scanning, attractive and repulsive forces modify the distance between the tip and the surface sample, which result in a frequency change of the tip oscillation in the case of FM-AFM as depicted in Figure 24.[31] As the tip oscillation frequency is related to the electrostatic force gradient between the tip and the sample, the latter is detected by FM-KPFM.

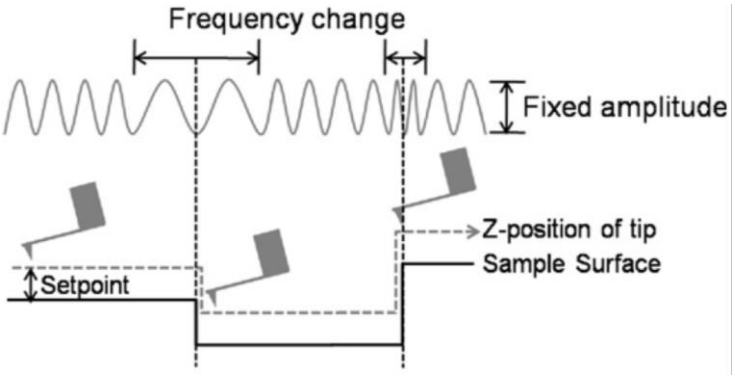

Figure 24 : FM-AFM operation mode.[31]

Figure 25 represents the electronic energy diagram of the sample and the tip.[31] ϕ_s and ϕ_t are the work function of the sample and the tip, respectively. The work function is the minimum energy required to remove an electron from the Fermi level E_f to the vacuum (E_{VAC}), just outside the surface material. E_{fs} and E_{ft} are the Fermi level of the sample and the tip, respectively. In the first case (Figure 25a), the distance d between the tip and the sample is large enough so that there is no electrical contact between the materials. Then the tip approaches the surface until it is close enough for electrostatic forces to play a role. Electrons will equilibrate through the KPFM electrical circuits so that they flow from the material with the lower work function to the one with a higher work function, until their Fermi levels are aligned. An equilibrium of charges is set and a contact potential difference (CPD or V_{CPD}) is thus created between the two materials (Figure 25b). An external direct current voltage (V_{DC}) is thus applied to nullify the CPD (Figure 25c) which is measured during the experiment.

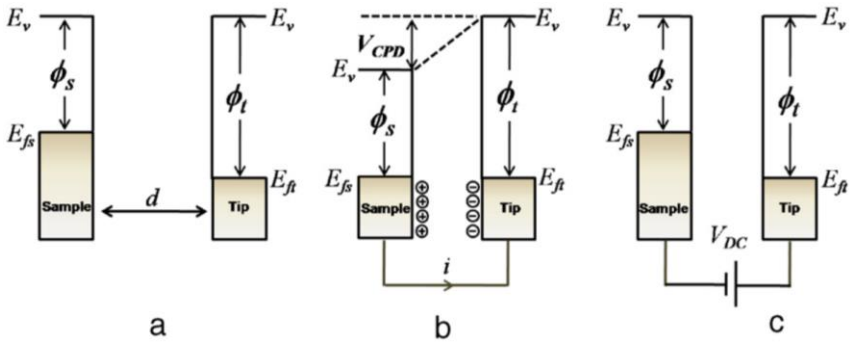

Figure 25 : Electronic energy diagram of the tip and the sample a) when the tip and sample are far from each other by a distance d without electrical contact, b) when the tip and sample are in electrical contact and c) when an external bias V_{DC} is applied to nullify the CPD.[31]

During the experiments, V_{DC} is applied to the sample, which gives the following equation (1):

$$V_{CPD} = -V_{DC} = \frac{\phi_{sample} - \phi_{tip}}{|e|} \qquad \text{Equation 1}$$

with e = 1.602*10^{-19} C. According to Equation 1, the surface work function ϕ_{sample} can be calculated using a commercial reference substrate in order to calibrate the tip prior to surface mapping by using Equation 2.

$$\phi_{tip} = \phi_{sample} - |e|.V_{CPD} \qquad \text{Equation 2}$$

To do so, a reference substrate from Bruker (PFKPFM-SMPL) is used. The sample is made by lithography and consists in Al and Au films onto an *n*-doped Si substrate, as shown in Figure 26a.[32] The contacts are created using a conductive silver paste. By scanning along the Al/Si/Au, using a commercial cantilever (see below) a potential image can be obtained with a corresponding staircase potential profile due to the different materials (Figure 26b). Among the

three materials, Al is the most stable one, less sensitive to humidity variations. As the KPFM experiment is performed under ambient atmosphere, a native oxide layer lies on top of the Al.[33] The work function of the corresponding Al/Al_2O_3 surface is 3.9 eV. According to the profile in Figure 26b, the potential of Al surface corresponds to $V_{CPD,Al}$ = -1.050 V. As ϕ_{sample} = 3.9 eV, the work function of the tip is measured to be 4.95 eV.

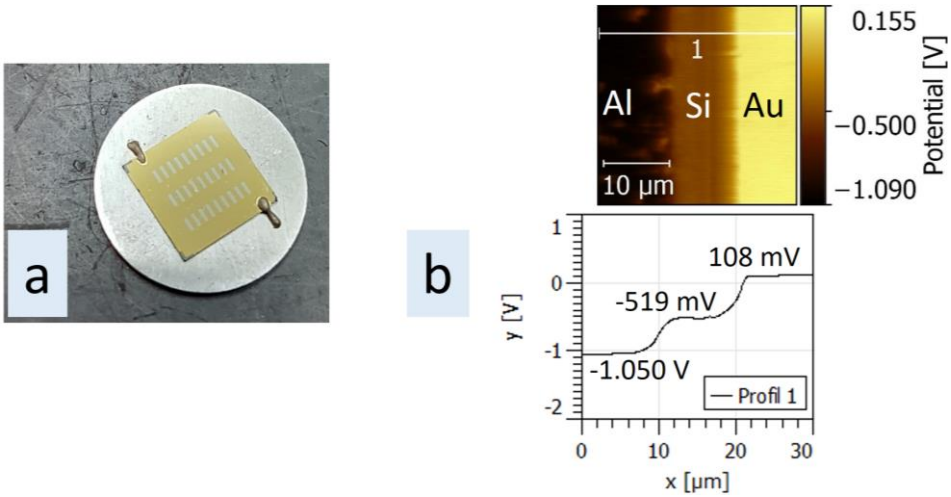

Figure 26: a) PFKPFM-SMPL Bruker standard KPFM sample, patterned with Al, Si and Au strips. b) the surface potential image at the interfaces Al/Si/Au and the staircase potential profile along the line 1.

During the measurements involving *in situ* UV irradiation, variations of V_{CPD} will be measured by KPFM. Equation 1 thus provides Equation 3:

$$\Delta V_{CPD} = V_{CPD,2} - V_{CPD,1} = \frac{\phi_{sample,2} - \phi_{sample,1}}{|e|} = \frac{\Delta\phi}{|e|} \qquad \text{Equation 3}$$

Therefore, an increase of V_{CPD} corresponds to an increase to the work function and vice versa for a decrease of V_{CPD}.

In practice, the sample to be analyzed is mounted onto a sample holder shown in Figure 27a. The sample holder consists of a magnetic metallic disc where a standard silicon substrate sits on top of it. A small metallic wire (stainless steel) ensures the contact and presses the sample mounted on top of the standard silicon substrate (Figure 27b).

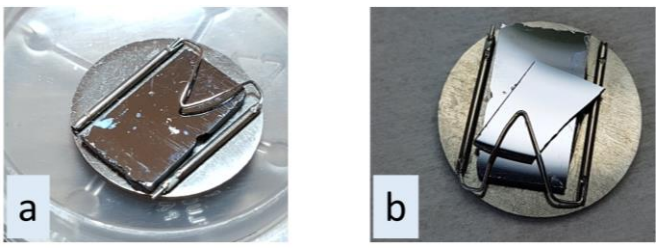

Figure 27 : a) KPFM sample holder and b) sample mounted onto the KPFM sample holder.

The tips used for KPFM measurements are SCM-PIT-V2 probes from Bruker, which are made of silicon and covered with a Pt-Ir conductive coating and display the following parameters: cantilever resonance frequency f_0 = 75 kHz, cantilever spring constant k = 3 N/m, tip radius of 25 nm. During the POM-containing surface scanning, the lift scan height was set at 60 nm.

IV.1.b. POM monolayer

Surface functionalization was carried out on *n*-type Si(111) surface following the procedure described in Chapter II (see Appendix 5.2). The functionalization was followed by both ellipsometry and FTIR spectroscopy and was satisfying. The IR spectra are shown in Figure 28 of Chapter II. The resulting $SiNH_2$ substrate was immediately cleaved into four pieces using a diamond tip scriber. All of them were rinsed with water, dried under a stream of nitrogen gas, stored in vials and purged with Ar. KPFM measurements were performed as fast as possible on those pieces coming from the same initial functionalized substrate.

Prior to any POM deposition, all $SiNH_2$ surfaces were analyzed by KPFM in order to have the initial work function of each surface. The experiment consisted in following the surface work function variation after POM(0), POM(I) and POM(II) deposition, as well as under/after UV irradiation of the POM monolayer. Thus, POM(0), POM(I) and POM(II) monolayer were immobilized on three of the four $SiNH_2$ pieces. The resulting surface are called **$SiNH_2$-POM(0)**, **$SiNH_2$-POM(I)** and **$SiNH_2$-POM(II)**, respectively. The last $SiNH_2$ piece was left without POM and was only irradiated under UV irradiation with the same Hg lamp previously used (λ = 254 nm). This reference surface serves as a way to make sure that the effect we could detect under UV irradiation actually comes from the POM and not from the $SiNH_2$ substrate. In order to calculate the surface work function, the tip was calibrated before and after the sample analysis with the reference Al/Si/Au substrate as described previously. In this way, it also helped in following eventual issues arisen from the tip if the work function of the tip had to undergo a huge variation before and after the sample analysis. The experiment was done under ambient air. During the KPFM measurements, the UV lamp was held vertically at approximately 5 cm far from the substrate, as shown in Figure 28. Thus, surface potential variation was measured before and after POM deposition, under 15 minutes of UV irradiation, and 20-40 minutes after the UV lamp was switched off.

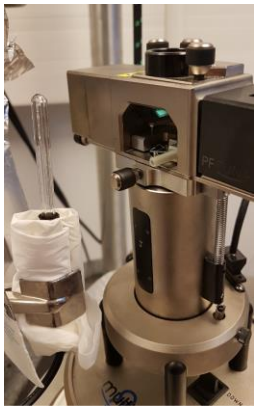

Figure 28 : *In situ* UV irradiation KPFM measurements.

Surface potential variations over the experiment are shown in Figure 29. For a clearer comparison between the four functionalized Si pieces, all the initial surface work functions are calculated via the measured V_{CPD} and are adjusted to exhibit the same work function value (shown in red in Figure 29). POMs were then immobilized on the surfaces by a dipcoating of the substrates in POM(0), POM(I) and POM(II) solution. Surfaces were analyzed by ellipsometry which revealed thicknesses of 0.6 nm, 0.9 nm and 1.0 nm for the POM(0) monolayer, POM(I) monolayer and POM(II) monolayer, respectively. The surfaces work functions calculated during the experiment are reported in Appendix 4.2.

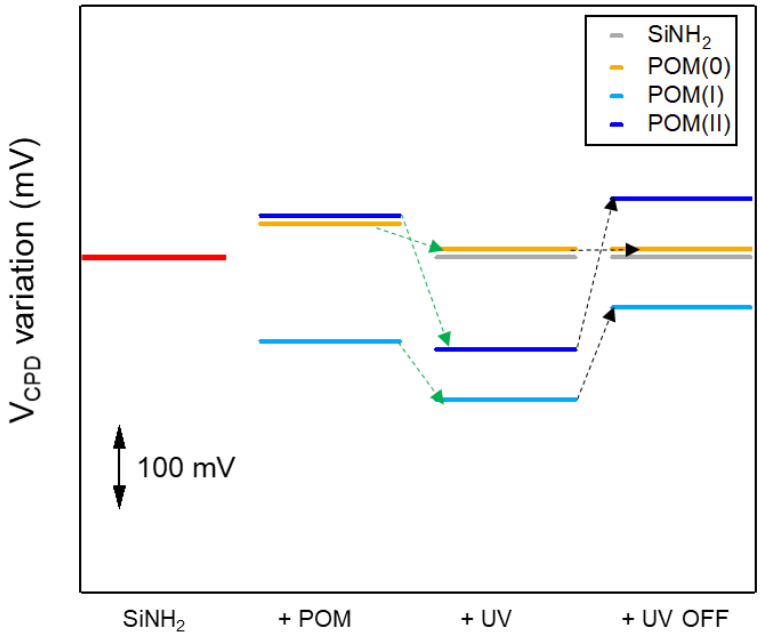

Figure 29 : Surface potential variations of POM monolayers on $SiNH_2$ surfaces over the KPFM measurement, after POM deposition, after 15 minutes of UV irradiation, and 20-40 minutes after the UV lamp has been switched off. The green arrows indicate the surface potential variation under UV irradiation, while the black ones indicate the surface potential variation after UV irradiation stops.

All initial work functions of the $SiNH_2$ surfaces were in the range 4.10-4.30 eV. The first observation is the surface potential variation induced by POM immobilization on $SiNH_2$ surfaces. An increase of 40 mV, 50 mV and a decrease of 100 mV were approximately measured for POM(0), POM(II) and POM(I) monolayer, respectively.

Under UV irradiation, a decrease in V_{CPD} of 30 mV, 70 mV and 160 mV was measured for POM(0), POM(I) and POM(II) monolayer, respectively. Note that besides this set of experiments, all the other $SiNH_2$-POM surfaces studied by KPFM were also subjected to a decrease in V_{CPD} under UV irradiation. It is thus reasonable to assume that a decrease in V_{CPD} is related to a reduction of the immobilized POM on surface. At this point, without looking at the variation amplitude, it looks like POM(0) is reduced to POM(I) and that POM(I) is reduced to POM(II) under UV irradiation. The photoreduction mechanism is supposed to be similar to the one depicted in Scheme 5 and should occur due to the presence of NH_3^+ groups on the organic monolayer.

Once the UV lamp was switched off, all surface potentials tend to go back to their initial value in 20-40 minutes, except for $SiNH_2$-POM(0) surface for which V_{CPD} did not vary after UV irradiation. Again, without looking at the variation amplitude, it looks like the POM(0) monolayer that has been reduced under UV irradiation stays in its reduced state after the UV lamp is switched off. Similarly, it looks like the POM(I) monolayer is getting reoxidized after the lamp is switched off.

The surface potential variation of POM(II) monolayer is less clear. The increase in V_{CPD} after its deposition on $SiNH_2$ surface suggests that it was reoxidized before UV irradiation. The surface potential variation under and after UV irradiation are similar to the ones obtained on $SiNH_2$-POM(I) surfaces. Two other KPFM measurements on $SiNH_2$-POM(II) surface led to a different result: in one case, V_{CPD} increased after POM(II) deposition, but the UV irradiation led to a decrease of only 10 mV; on the second case, V_{CPD} decreased after POM(II) deposition and follows the same variation as $SiNH_2$-POM(I), *i.e.* a decrease under UV irradiation and an increase after UV light is switched off. These different results suggest a lower stability of POM(II) monolayer than the two other counterparts and a less reliable surface potential variation.

As the POM(0) is in its oxidation state, it is expected to be more prone to photoreduction than the two corresponding reduced species, meaning that the surface potential amplitude variation of $SiNH_2$-POM(0) surface under UV irradiation was expected to be the largest one among the three POM-containing surfaces studied. Since it is not the case, the low CPD

variation could be originated from the low coverage of POM(0) on the $SiNH_2$ surface. Indeed, $SiNH_2$-POM(0) surface exhibits the lowest POM layer thickness among the three monolayers. Thus, we decided to compare the results obtained here, with POM multilayers on Si-SiO_2 substrates. This could also give more reliable results in that thicker POM multilayers are more stable than the corresponding monolayers, similarly to XPS results on POM powders vs POM monolayers where a possible reoxidation of POM(I) and POM(II) monolayer prior to XPS analysis could take place.

IV.1.c. POM multilayer

POM(0), POM(I) and POM(II) multilayers were thus prepared by a dropcasting of POM(0), POM(I) and POM(II) solution, respectively, on *n*-type Si(111)-SiO_2 substrates. The resulting substrates will respectively be called **Si-SiO_2-POM(0)**, **Si-SiO_2-POM(I)** and **Si-SiO_2-POM(II)** substrates. Here the substrates were only subjected to a degreasing step and a cleaning step in RCA solutions. One **Si-SiO_2** surface, that served as a reference surface, was left without POM and was only irradiated with UV light.

Similarly to the study of POM monolayers with KPFM, the surface potential variation was followed before and after POM deposition, under and after UV irradiation using the same Hg lamp and *in situ* UV irradiation setup. The surfaces work functions during the experiment were calculated by calibrating the tip with the same reference substrate from Bruker. The work function variations during the KPFM measurements are depicted in Figure 30. Again, the initial Si-SiO_2 surfaces work functions are calculated via the measured V_{CPD} and are adjusted to exhibit the same work function value (in red in Figure 30).

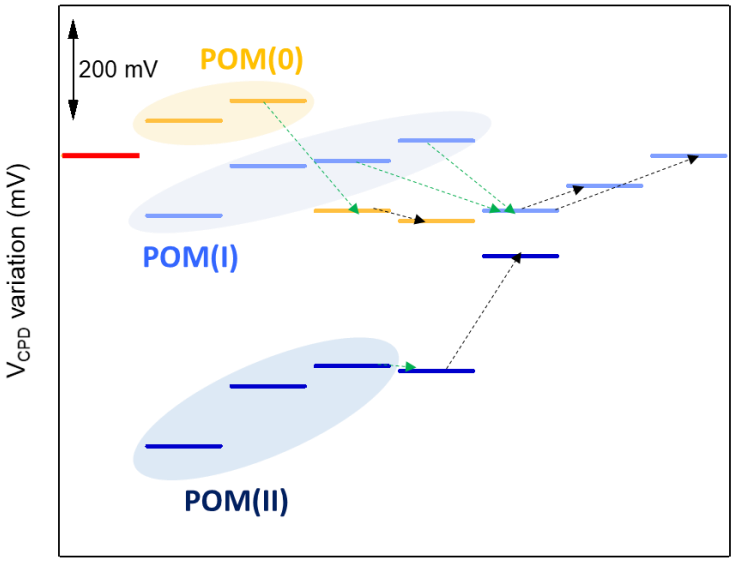

Figure 30 : Surface potential variation of POM multilayers on Si-SiO_2 surfaces over the KPFM experiment. The ellipsoid colored regions represent the surface potential measured on the POM aggregates after POM deposition. The green arrows indicate the surface potential variation under UV irradiation, while the black ones indicate the surface potential variation after UV irradiation stops.

The initial work functions of the Si-SiO_2 surfaces lied in the range 4.2-4.5 eV. After POM deposition (one drop of 1.0 mM POM solution on each Si-SiO_2 surfaces), thicknesses of the POM layers were measured by ellipsometry. A thickness of ~4.2 nm was measured for

POM(0) multilayer but the thicknesses of POM(I) and POM(II) multilayers were too high for them to be reliable (more than 50 nm, exceeding the ellipsometer precision). Aggregates of POMs were observed of the surface topography images shown in Figure 31. Note that only two 5 µm * 5 µm surface areas were selected for each POM-containing surface for the UV *in situ* irradiation measurement. Si-SiO_2-POM(0) surface exhibits 250-400 nm high round-shape aggregates that are 1.5-3.0 µm wide (Figure 31a). The low thickness measured on ellipsometry could be due to a lower coverage of POM on the surface, which can be guessed by comparing the aggregates with the ones observed on Si-SiO_2-POM(I) and Si-SiO_2-POM(II) surfaces. Indeed, 40-100 nm high aggregates are seen on Si-SiO_2-POM(I) surface (Figure 31b). The aggregates are larger than the POM(0) aggregates since they cover a larger area of the 5 µm * 5 µm image. POM(II) aggregates are even larger and wider than POM(0) and POM(I) aggregates, with a height of 200 to 600 nm (Figure 31c).

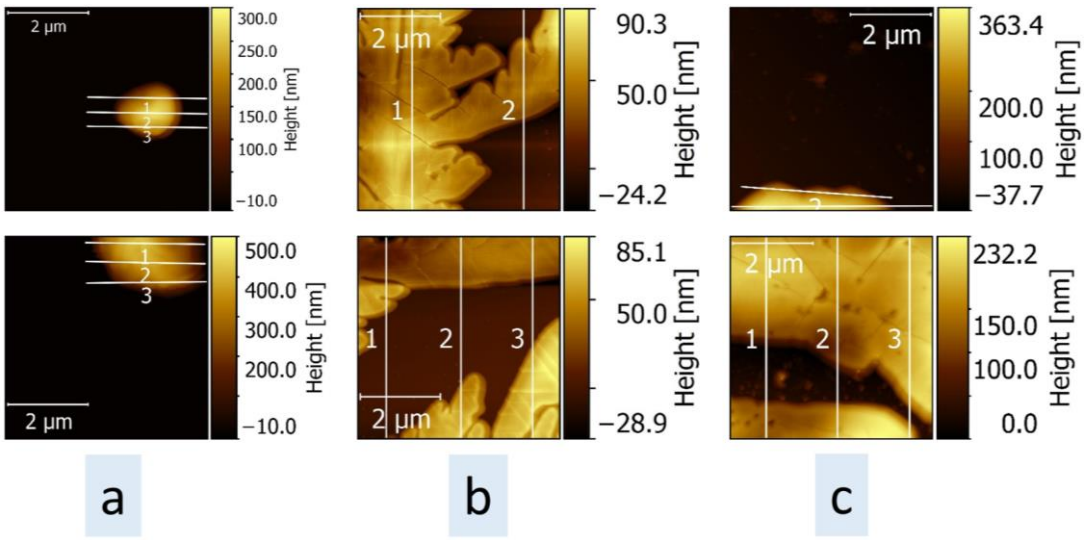

Figure 31 : Topography images of a) Si-SiO_2-POM(0), b) Si-SiO_2-POM(I) and c) Si-SiO_2-POM(II) surfaces obtained by KPFM in the AFM mode.

Each surface exhibits a surface potential change on the aggregates location, as depicted in Figure 32. In order to follow more precisely the modifications under UV irradiation, two different values were measured on each surface potential image and will be called $V_{CPD,agg}$ and $V_{CPD,surface}$. $V_{CPD,agg}$ corresponds to the average surface potential obtained on the apparent aggregate using the mask tool of Gwyddion software. On the other hand, $V_{CPD,surface}$ refers to the average V_{CPD} obtained on the "surface" where no apparent POM aggregate is spotted. The $V_{CPD,agg}$ and $V_{CPD,surface}$ of all surfaces are reported in Appendix 4.3. Figure 30 actually represents the $V_{CPD,agg}$ of Si-SiO_2-POM(0), Si-SiO_2-POM(I) and Si-SiO_2-POM(II) surfaces

during the experiment and are respectively called **$V_{CPD,agg-POM(0)}$**, **$V_{CPD,agg-POM(I)}$** and **$V_{CPD,agg-POM(II)}$**.

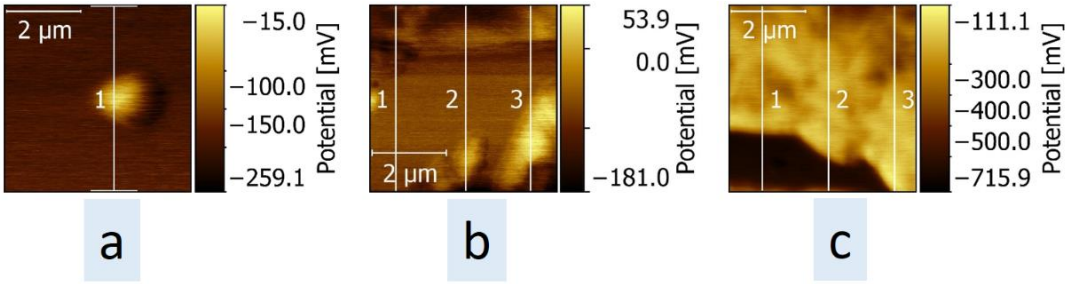

Figure 32 : a) Si-SiO_2-POM(0), b) Si-SiO_2-POM(I) and c) Si-SiO_2-POM(II) surface potential obtained by KPFM.

The colored ellipsoidal areas in Figure 30 represent the $V_{CPD,agg}$ before UV irradiation. When immobilized as multilayers, POM deposition has a higher effect on the surface potential than the corresponding POM monolayers. Indeed, the two aggregates of POM(0) exhibit a $V_{CPD,agg}$ increase of 120 mV and 160 mV. An increase in V_{CPD} was also observed on the $SiNH_2$-POM(0) surface, though the variation here is larger and can be attributed to a larger coverage of POM on the surface. On the other hand, POM(I) and POM(II) multilayers lead to a decrease in $V_{CPD,agg}$. Four aggregates can be observed on the Si-SiO_2-POM(I) surface: they exhibit a decrease in V_{CPD} of 140 mV, 40 mV and 30 mV, except on the last aggregate scanned where V_{CPD} increased of 10 mV. The $V_{CPD,agg-POM(I)}$ increase over the scanning can suggest a POM(I) reoxidation, prior to UV irradiation. In the case of Si-SiO_2-POM(II) surface, $V_{CPD,agg}$ variation induced by the presence of the POM(II) is even larger: a decrease of 550 mV, 430 mV and 390 mV are measured on three aggregates. Again, the increase in $V_{CPD,agg-POM(II)}$ over the scanning can suggest a possible reoxidation of POM(II). Globally, $V_{CPD,agg-POM(0)} > V_{CPD,agg-POM(I)} > V_{CPD,agg-POM(II)}$. This supports the previous observation on POM monolayer-containing surfaces: a decrease in V_{CPD} is attributed to a POM reduction on the surface.

Note that $V_{CPD,surface}$ is slightly modified after POM(0) deposition (30-70 mV, lower than the CPD variation amplitude induced by the aggregates) while it is subjected to a larger variation when more reduced POM are immobilized (see Appendix 4.3). From the topography images, the more the POM is reduced the more the POM coverage on the surface is high, meaning that the presence of small POM aggregates (especially POM(II) and POM(I)) on what we previously called “surface” (area where no apparent POM is present) is not to be excluded. This results in an inaccurate estimation of $V_{CPD,surface}$.

Contrary to the $SiNH_2$ reference surface, the reference Si-SiO_2 surface undergone a surface potential decrease of 110 mV and 120 mV during the first and second UV irradiation cycle (15 minutes each), respectively (see Appendix 4.3). This decrease can be attributed to the generation of negative surface charges due to the UV lamp that brought enough energy to create an electron hole pair in the substrate. More details on the mechanism will be given in section IV.2 involving SOI substrates. As the promotion of electron to the surface is facilitated by the UV lamp, the surface work function is subsequently lowered. The V_{CPD} decrease under UV irradiation of Si-SiO_2 surface was slightly pursued after UV lamp was switched off: a decrease of 20 mV and 30 mV was measured at the end of the first and second UV irradiation cycle, respectively. Note that when looking at the $V_{CPD,surface}$ modification on POM multilayer, the decrease under UV irradiation is a little bit higher than the 110 mV and 120 mV decrease observed on Si-SiO_2 surface: $V_{CPD,surface}$ is subjected to a decrease of 140 mV and 160 mV on Si-SiO_2-POM(0) and Si-SiO_2-POM(I) surface, respectively. This could be due to the "surface" contamination with POM leading to an inaccurate $V_{CPD,surface}$ value as discussed above. Again, $V_{CPD,surface}$ decrease was pursued after UV lamp was turned off. No $V_{CPD,surface}$ of Si-SiO_2-POM(II) was measured during the 15 minutes of UV irradiation as the aggregate was bigger, but the final $V_{CPD,surface}$ (1h20 after the lamp is turned off) exhibits a decrease of 200 mV with respect to the initial $V_{CPD,surface}$ before UV irradiation.

Under 15 minutes UV irradiation, $V_{CPD,agg}$ on the last scanned POM aggregates were measured: $V_{CPD,agg,POM(0)}$ and $V_{CPD,agg,POM(I)}$ decrease while $V_{CPD,agg,POM(II)}$ does not vary. According to the previous assumption, this suggests that both POM(0) and POM(I) are getting reduced under UV irradiation while POM(II) does not get more reduced. In the case of Si-SiO_2-POM(0), the aggregate exhibit a decrease of 220 mV. If the effect of the "surface" is subtracted (a $V_{CPD,surface}$ decrease of 140 mV), a decrease of 80 mV due to the POM is still observed. By looking at Figure 30, $V_{CPD,agg,POM(0)}$ under UV irradiation falls in the range of the V_{CPD} values of POM(I) aggregates (before UV irradiation), which supports the reduction of POM(0) into POM(I). In the case of POM(I), a decrease of 100 mV and 140 mV is observed on two aggregates, under UV irradiation, and both V_{CPD} reach the same value. However, both $V_{CPD,agg}$ fall in the range of the $V_{CPD,agg,POM(I)}$ initially measured (before UV irradiation), and is more precisely comparable to the $V_{CPD,agg}$ of the first POM(I) aggregate. This could suggest a partial reoxidation of POM(I) aggregates prior to UV irradiation, and an overall reduction of the POM aggregates to POM(I) aggregates under UV irradiation.

$V_{CPD,surface}$ and $V_{CPD,agg}$ were then followed after UV irradiation and the values reported in Appendix 4.3 and Figure 30 correspond to the values measured 1h20 up to 2h after the UV

lamp was switched off. In the case of Si-SiO_2-POM(0) surface, $V_{CPD,agg}$ only decreased of 20 mV. This decrease is low compared to the amplitude variation undergone by $V_{CPD,surface}$ after UV irradiation (a decrease of 90 mV in 15 minutes). Thus, $V_{CPD,agg,POM(0)}$ is almost unchanged after UV irradiation, suggesting that the resulting POM monolayer is stable. In the case of Si-SiO_2-POM(I) surface, $V_{CPD,agg}$ values slowly increase (+50 mV and +110 mV) towards the initial values before UV irradiation and can correspond to a reoxidation of the POM(I) aggregates. Finally, in the case of Si-SiO_2-POM(II) surface, the $V_{CPD,agg}$ increases after the lamp is switched off (+230 mV) and tends to reach $V_{CPD,agg,POM(I)}$. Again, it looks like POM(II) aggregates are getting reoxidized after UV irradiation.

Thus, as $V_{CPD,surface}$ variation and $V_{CPD,agg}$ variation are different during the experiment, the effect due to the presence of POM can be extracted using KPFM characterization tool. Even though the $\Delta\phi_{tip}$ calculated are larger than on the KPFM experiment involving POM monolayer, the $V_{CPD,agg}$ measured right after POM depositions is still significant. The larger $\Delta\phi_{tip}$ on the POM multilayer experiment could be attributed to the inhomogeneity of the surface due to POM deposition by dropcasting and a possible tip contamination as the POMs aggregates are scanned.

IV.1.d. Insights on the top surface modification with the presence of POM

From the KPFM measurements described above, the deposition of POM either on the $SiNH_2$ surface or the Si-SiO_2 surface affects the surface work function. The work function modification is known to be dependent on the surface dipoles induced by molecular deposition. Heimel *et al*. studied the correlation between the electrostatics of thin films and their molecular structure.[34] More precisely, the orientation of molecules on a surface, and subsequently the surface dipoles, was found to significantly affect the ionization energy and electron affinity of the corresponding thin film.

V_{CPD}, which is the variable measured by KPFM, is in fact the potential energy of an electron in electrostatic interaction with the surface. Let us call $V(\vec{r})$ the potential created by the surface at point $\vec{r}$, this potential energy writes:

$$E = -eV(\vec{r})$$

Let us consider the case of an isolated charge q on a surface depicted in Figure 33, the potential is:

$$V = \frac{1}{4\pi\varepsilon_0}\frac{q}{r}$$

Where ε_0 is the vacuum permittivity and r the distance between the charge and the tip.

Thus, when scanning along the x axis at a lift scan height of 50 nm, the presence of a negative isolated charge induces a local increase in potential. Similarly, a positive isolated charge induces a decrease in potential.

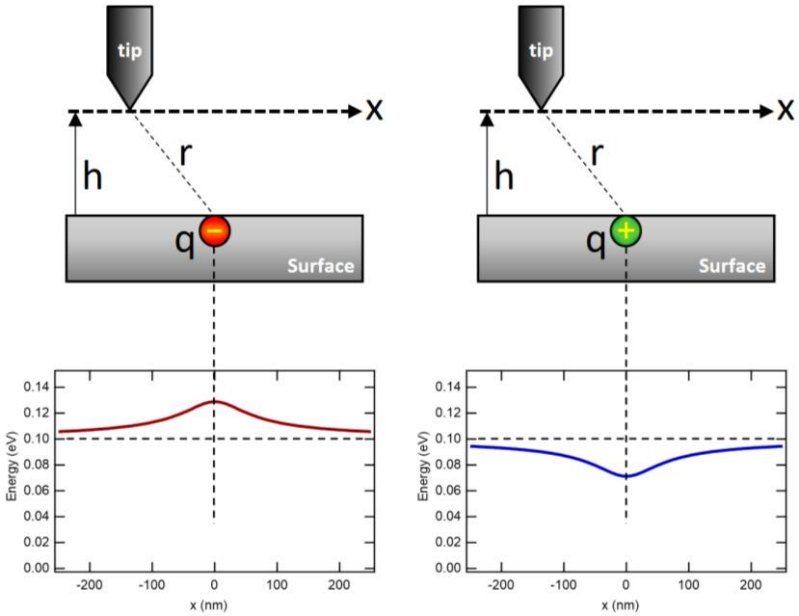

Figure 33 : Potential energy of an electron (opposite of the work function) measured by the KPFM tip along the x axis whether a negative (left) or positive (right) isolated charge ($q = \pm e$) is present on the surface. The lift scan height (h) is 50 nm.

From this electrostatics consideration, the effect of a single dipole or a dipole layer on a surface can be understood. In the case of a single dipole isolated on a surface, the small variation induced by the presence of that dipole is negligible on the overall surface potential as depicted on Figure 34 for a single outward dipole.

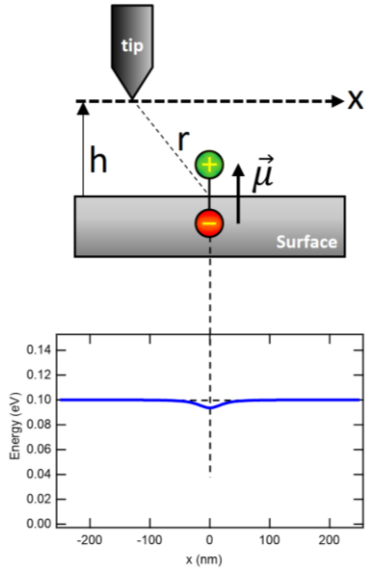

Figure 34 : Surface potential variation measured by KPFM, considering a single outward dipole on a surface

In the same review, Heimel *et al*. simulated a 2D layer of dipoles represented on the left part of Figure 35. The potential energy of an electron through this layer in a perpendicular plane cutting is plotted on the right part of Figure 35. We can clearly observe that the positive side of the dipole induces a lowering of the electron potential energy. On the other hand, the negative side of the dipole leads to an increase in energy. This shift in electron potential energy is thus characteristic of the presence of a dipole layer.

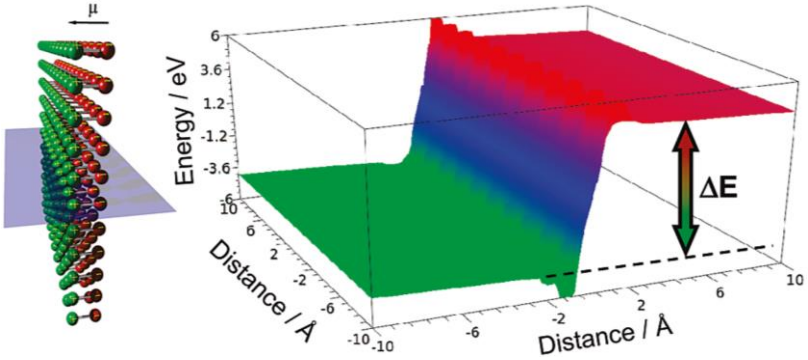

Figure 35 : Electrostatic potential energy for electrons in a plane cutting through a layer of discrete dipoles (±1/10 of the elementary charge separated by 2 Å) that are laterally spaced by 2 Å on a square grid. The magnitude of the potential-energy step in indicated by ΔE).

To make it clear, when the molecules assembly exhibits an inward dipole on the surface (Figure 36a), the overall surface potential, will significantly increase at this location relatively to the case of a naked surface. The opposite variation is observed for surfaces with outward dipoles (Figure 36b). These effects are clearly measured by the KPFM.

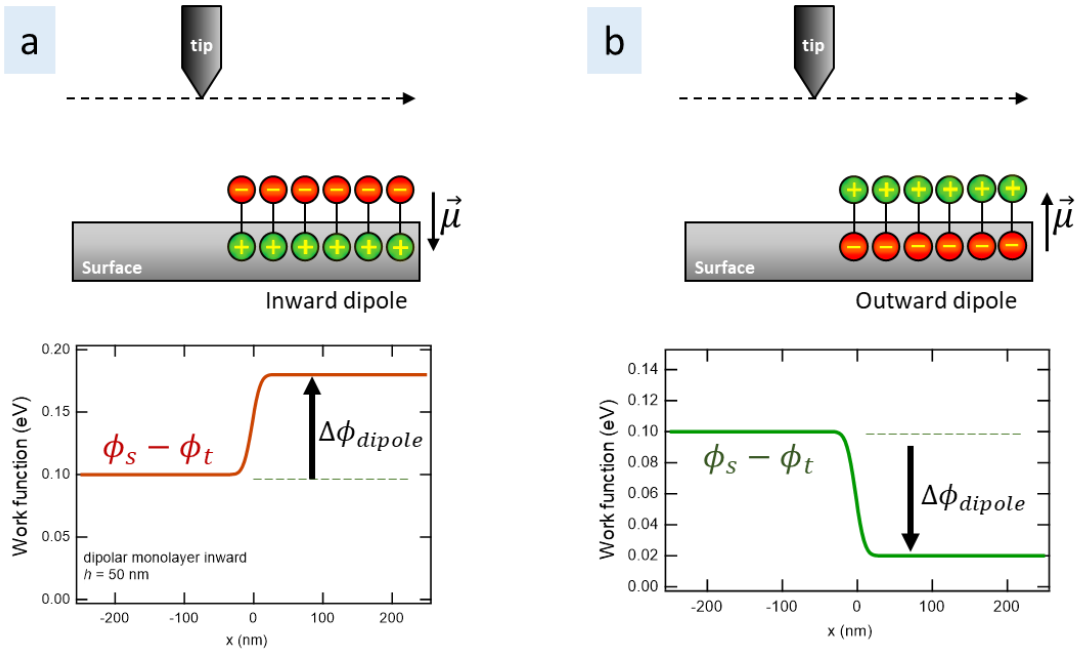

Figure 36 : Work function variation measured by KPFM on a surface constituted with an assembly of molecules displaying whether a) an inward dipole or b) an outward dipole.

The work function variation $\Delta\phi_{dipole}$ at the surface for a monolayer of dipoles of absolute value μ and each one occupying an area A is characterized by the Helmholtz equation:[34]

$$\Delta\phi_{dipole} = -\frac{\mu}{\varepsilon_0 A}$$

Application to the POM monolayer

Let us first focus on the POM monolayer on $SiNH_2$ surfaces. In this case, the work function variations calculated from the V_{CPD} variations during the KPFM measurements are reported in Table 1. The latter must be read line by line, from left to right. We have reported a V_{CPD} increase of 40 mV after POM(0) deposition. From the Helmholtz equation reported above, this corresponds to a positive $\Delta\phi_{dipole}$ and the dipole stands inward on the surface. After UV irradiation of the POM(0) monolayer, a V_{CPD} decrease of 30 mV was measured, and we know that the POM(0) reduces to POM(I). By doing the same irradiation on a POM(I) monolayer, a V_{CPD} decrease of 70 mV was measured. The $\Delta\phi_{dipole}$ are then calculated: The POM(0) monolayer is characterized by $\Delta\phi_{dipole} = \mathbf{+40\ meV}$; the POM(I) monolayer is characterized by $\Delta\phi_{dipole} = +40 - 30 = \mathbf{10\ meV}$; finally, the POM(II) monolayer is characterized by $\Delta\phi_{dipole} = +40 - 30 - 70 = \mathbf{-60\ meV}$ and the resulting molecular dipole now stands outward on the surface. This is depicted in Figure 37.

	Si	POM(0)	+UV =POM(I)	+UV =POM(II)
Variation of WF induced by surface dipole	0	+40 meV	-30 meV	-70 meV
$\Delta\phi_{dipole}$	0	+40 meV	+10 meV	-60 meV
Value of the WF	4.10 eV	4.14 eV	4.11 eV	4.04 eV

Table 1 : Summary of the KPFM results for the POM monolayers on $SiNH_2$ surfaces. The $\Delta\phi_{dipole}$ corresponds to the variation of V_{CPD} following the sequences: deposition of POM(0), then UV irradiation that leads to POM(I), then UV irradiation that leads to POM(II).

Going through POM(0) to POM(I) to POM(II), the more the POM accepts electrons, the more it is reduced. To preserve the charge neutrality, the TBA cations rearranged themselves around the POM. These KPFM measurements show that these cations tend to globally lie on top of the POM. From POM(0) to POM(II), the dipole moment is expected to gradually

reorients from inward to outward, as shown by Figure 37 (from $\overrightarrow{\mu_{(0)}}$ to $\overrightarrow{\mu_{(I)}}$ to $\overrightarrow{\mu_{(II)}}$). The resulting dipole effectively measured by KPFM follows this reorientation from inward to outward.

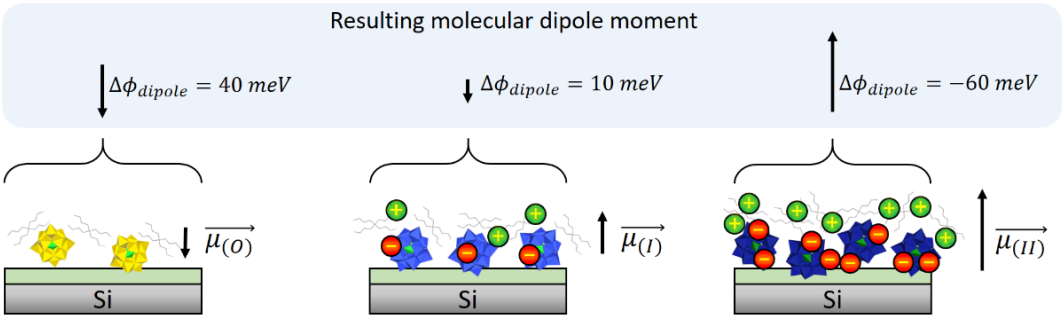

Figure 37 : $SiNH_2$-POM(0), $SiNH_2$-POM(I) and $SiNH_2$-POM(II) surface with their expected dipole $\overrightarrow{\mu_{(0)}}$, $\overrightarrow{\mu_{(I)}}$, $\overrightarrow{\mu_{(II)}}$ versus the effective dipole measured by KPFM

The same trend is observed in the case of POM multilayers on Si-SiO_2 surfaces and the values calculated are summarized in Table 2. In this case, the variations of $\Delta\phi_{dipole}$ are much larger probably due to the larger density of the molecules on the surface. Again, the resulting molecular dipoles reorients from inward to outward.

	Si	POM(0)	+UV =POM(I)	+UV =POM(II)
Variation of WF induced by surface dipole	0	+140 meV	-220 meV	-120 meV
$\Delta\phi_{dipole}$	0	+140 meV	-80 meV	-200 meV
Value of the WF	4.40 eV	4.54 eV	4.32 eV	4.20 eV

Table 2 : Summary of the KPFM results for the POM multilayers on Si-SiO_2 surfaces. The $\Delta\phi_{dipole}$ corresponds to the V_{CPD} following the sequences: deposition of POM(0), then UV irradiation that leads to POM(I), then UV irradiation that leads to POM(II).

To summarize, KPFM measurements were thus performed both on POM monolayers and multilayers and results show that POM deposition has an impact on the surface work function, and more precisely a V_{CPD} decrease, thus a work function decrease, can be attributed to a reduction of POM on the surface. Immobilized POM(0) apparently reduces to POM(I) irreversibly under UV irradiation, while immobilized POM(II) is hardly more reduced under UV irradiation. Some doubts remain on the case of the immobilized POM(I) under UV irradiation. Indeed, when the POM(I) are immobilized as monolayers, the large V_{CPD} variation

under UV irradiation (the largest among the three POMs) suggests a reduction of the POM. However, when immobilized as multilayers, V_{CPD} variation reveals a partial reoxidation of the POM after deposition and the subsequent UV irradiation leads to an overall reduction to POM(I).

These work function variations are due to the molecular surface dipoles of the POMs and ultimately to a delicate charge reorganization within these structures when they are photoreduced. The impact of photoreduction is clearly demonstrated since work function changes of several 50-200 meV are detected for a given monolayer/multilayer when irradiated. The WF changes are not just due to different surface coverages when adsorbing POM(0), POM(I) or POM(II). There is a clear charge motion induced by light, which is essential for our application. More precisely, the negative dipole induced by depositing POM(0) on the surface ($SiNH_2$ and Si-SiO_2) indicates an increase of positive charges at the substrate/POM interface. Upon UV light irradiation, the negative dipole turns more and more positive, and it is explained by charge reorganizations that are due to the accumulation to negative charges at the substrate/POM interface. Meanwhile positive charges insure the electroneutrality on the outmost POM surface. This increase of negative charges closer to the conductive channel will be essential driving modulation of the current in the field-effect transistor that will be presented in the following section

.

IV.2. Probe station measurements: investigating the global electrical response of the POMs

Electrical measurements on silicon-on-insulator (SOI) substrates were carried out at IMEP-LAHC in Grenoble (France), in collaboration with Dr. Irina Ionica and Miltiadis Alepidis. This last part of Chapter IV will be divided into 5 parts: first, more details on SOI substrate will be given, followed by the description of the probe station apparatus and pseudo-MOSFET electrical characterization principle. Results on POM(0), POM(I) and POM(II) monolayers and multilayers will be then presented with a particular emphasis on the effect of the UV light on the substrates.

IV.2.a. SOI substrate and probe station principle

History and motivation

SOI substrates, as the name suggests, are composed of a Si monocrystalline film on top of an insulator layer. The SOI technology appeared back in the 1960-1970 and development of SOI materials was made since the 1980s. The context of the development of these substrates was the countdown of the Si technology limits with the observation of parasitic effects of the bulk Si induced by the downsizing of the components. SOI substrates were considered as a way to extend the Si technology, with appealing properties such as their insensitivity against ionizing radiation and their ability to enhance device performances while reducing power consumption. Indeed, the reduction of leakage current by the presence of the insulator layer helps in reducing the power loss and on the other hand, microprocessors involving SOI substrates operate faster than their bulk Si counterparts for the same supply voltage.[35–37] However, the inherent structure of SOI substrate constituted a challenge for the fabrication process since no deposition of monocrystalline Si film on a substrate were known at that time.[36]

The first successfully fabricated SOI material with commercial use was the silicon-on-sapphire (SOS) reported for the first time in 1964 by Manasevit and Simpson.[35,38] It involved the heteroepitaxial growth of a thin Si film on a bulk sapphire substrate (Al_2O_3). Thanks to its radiation robustness, SOS substrate was mainly developed for military and aerospace markets but the high cost led to the development of other SOI substrates.[36,39] Other fabrication techniques thus emerged and the SOI industry was dominated by the Separation by Implanted

Oxygen (SIMOX) technology from 1985 to 1995,[35,36,39] and currently by the worldwide SmartCut™ technology. The first one implies internal oxidation while the second one is based on wafer bonding. Wafer bonding technology comes from the visible phenomenon that two cleaned wafers are attracted and adhere to each other once put into contact, due to Van der Waals forces: they "bond" together. The wafers need to be annealed in a further step to strengthen the interfacial bonds.

The SmartCut™ technology[35,40,41] was created by Michel Bruel from LETI (CEA Grenoble) and is used by the market leader SOITEC company for producing worldwide SOI substrates. The SmartCut™ process is depicted in Figure 38 and involves the use of two Si wafers: wafer A (the later top Si film) and wafer B (the final Si bulk). The process starts with the thermal oxidation of the wafer A (step 2 in Figure 38), followed by hydrogen implantation that creates microcavities parallel along the surface plane (step 3). The oxide layer will become the later buried oxide (BOX) layer. After both substrates cleaning, the hydrophilic surfaces A and B are put into contact creating interfacial hydrogen bonds (step 4). The resulting wafer is annealed. At 400-600°C, the pressure of H_2 molecules increases, leading to the growth of the microcavities inside wafer A and to a subsequent horizontal crack. Wafer A thus splits along the microcavities (step 5) and the resulting SOI substrate displays microroughness. At ~1100°C (step 6), the bonds are strengthened by the formation of Si-O-Si interface bonds between wafer A and B. Finally, the resulting SOI substrate (modified wafer B) is polished and the leftover wafer A can be reused in the process. The SOI substrates obtained by the SmartCut™ process are of high quality, with uniform Si film and BOX layers. The thickness of these two layers can also be adjusted depending on the use.

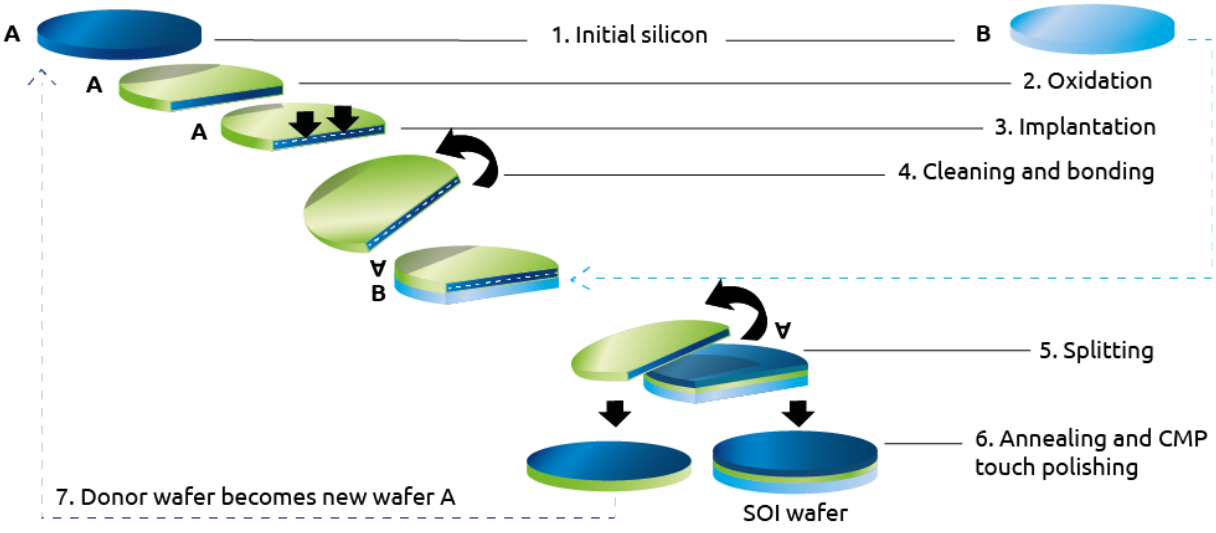

Figure 38 : SmartCut™ technology process.[42]

For our project, the SOI substrates are particularly appealing for studying the redox state of the immobilized POM since the electrical measurements on SOI substrates are known to be sensitive to the surface charge.

The electrical response of the device are for example dependent on the surface states[23] located at the interface between the Si film and top oxide layer that covers it due to the dangling bonds present at this interface. The Ψ-MOSFET characteristics are more sensitive to the nature of the surface when the Si film is thinner: the surface states are closer to the channel (at the Si film/BOX interface) and the surface-to-channel coupling is enhanced. On the other hand, Hamaide *et al*. found a dependence of the Ψ-MOSFET characteristics with the surface charge density by comparing passivated and non-passivated SOI substrates.[43] Similarly, adding charges on the top surface can also impact the electrical results. Ionica *et al*. reported the immobilization of gold nanoparticles on functionalized SOI samples with APTES.[44] The SOI characteristics were modified after the grafting of APTES terminated with positively charges, as well as after deposition of negatively charged gold nanoparticles, and were found to be dependent on the density of gold nanoparticles. Functionalizing SOI substrates with POMs displaying different redox states could thus provide insights on the effect of the immobilized POM redox states on the SOI conductance and open routes for new applications that could take advantage of the POM photoreduction property

.

Presentation of the probe station

Following our approach on the fabrication of a POM-based phototransistor, we aim at measuring the conductive channel and we need to evaluate I_{DS}, as sketched in Figure 9. Two probes, acting as source and drain, will be contacted onto the top surface. The electrical measurements of the functionalized SOI substrates (see below) were carried out at IMEP-LAHC laboratory (Grenoble, France) using a Jandel probe station (Figure 39a) connected to an Agilent B1500A Semiconductor device analyzer (Figure 39b). The probe station is composed of four controlled pressure probes made of tungsten carbide (Figure 39c), separated by 1 mm from one to another. The diameter of the probes apex is 40 µm. The "pressure" p can be adjusted from 0 g to 100 g. The improper name "pressure" corresponds to the force that the probes apply on the SOI and that has a direct impact on the quality of the contact and the measurements. A higher pressure value corresponds to a higher force and therefore a better contact. However, depending on the thickness of the Si film and the BOX, a

too large pressure can damage the structure and the BOX under that mesa will become leaky.[45,46] The probe station has a dark lid which allows us to perform experiments in the dark (Figure 39d).

The setup is shown in Figure 39e: the source and the drain are obtained by simply applying two probes on the top Si film thus avoiding further lithography steps. This configuration, called "pseudo-MOSFET" (Ψ-MOSFET) or point-contact transistor, serves as a simple characterization technique to control the quality of SOI wafer before CMOS processing.[47,48] The SOI substrate is placed on a metallic chuck and maintained still thanks to a vacuum system. The metallic chuck plays the role of a back gate since the top Si film is grounded. In this configuration, the BOX acts as the gate dielectric. A back gate voltage V_{BG} applied to the Si substrate will induce the formation of a channel between source and drain where the drain current I_D is measured (Figure 39f). The aim of Ψ-MOSFET technique is thus to record several $I_D=f(V_{BG})$, later called **I_D-V_{BG} curves**, in order to extract parameters such as carriers mobility or the threshold voltage (V_{Th}) and flat-band voltage (V_{FB}) that will be discussed in the next part.[48,49]

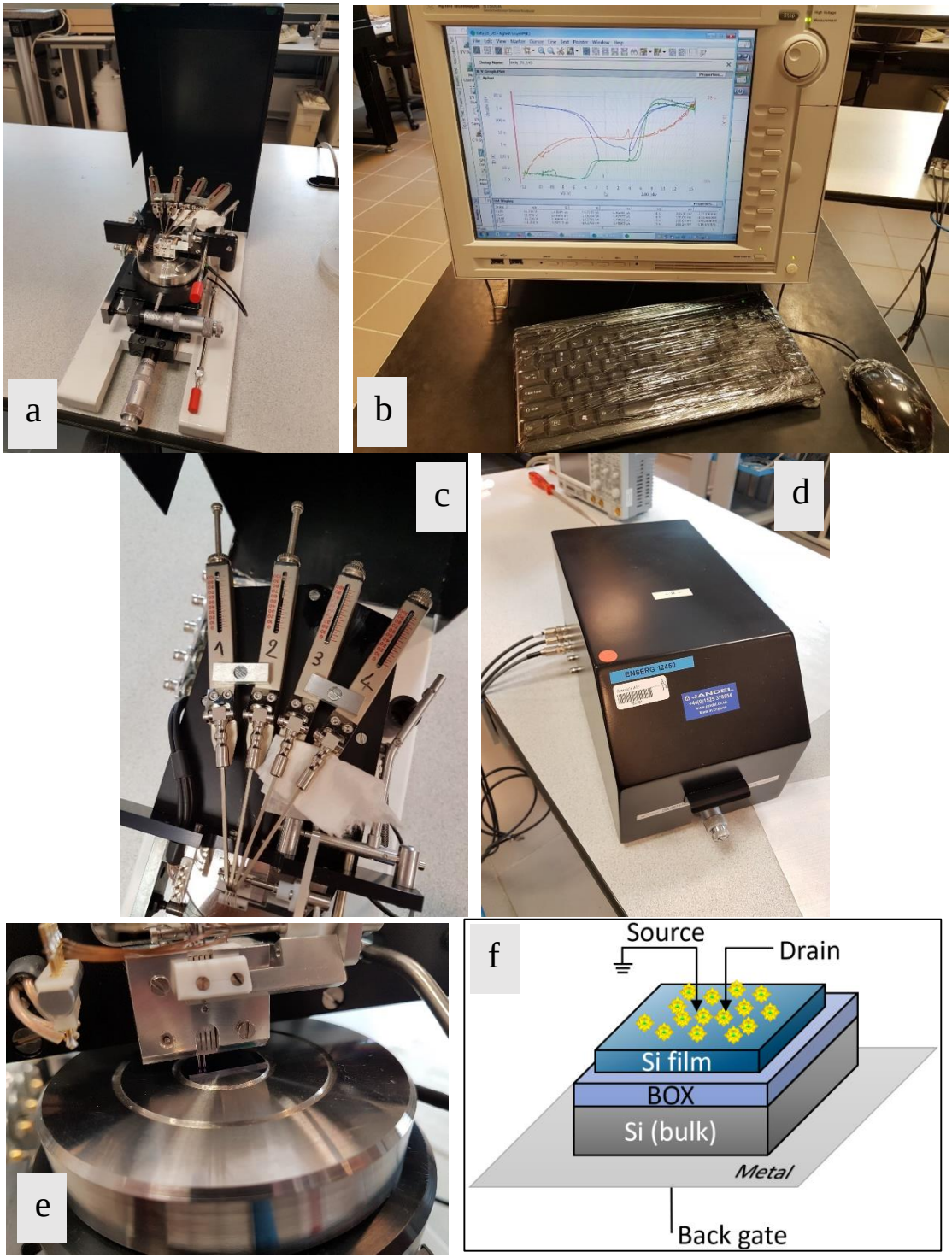

Figure 39 : Probe station for pseudo-MOSFET electrical characterization on POM-containing SOI substrates. The probe station (a) is connected to a semiconductor device analyzer (b). The probe station is composed of four probes (c) and a lid (d). The source and drain are obtained directly by applying the probes on the surface (e) and drain current can be measured by applying a back gate bias (f) through the metallic chuck.

As we wanted to study the effect of UV light, the *in situ* UV measurements were performed with the probe station lid closed and the UV pen lamp was simply positioned under the probe station lid with some tape, as shown in Figure 40. The UV pen lamp is the same Hg

lamp used for UV-Vis-NIR spectroscopy and KPFM *in situ* measurements, emitting light with a primary energy at 254 nm.

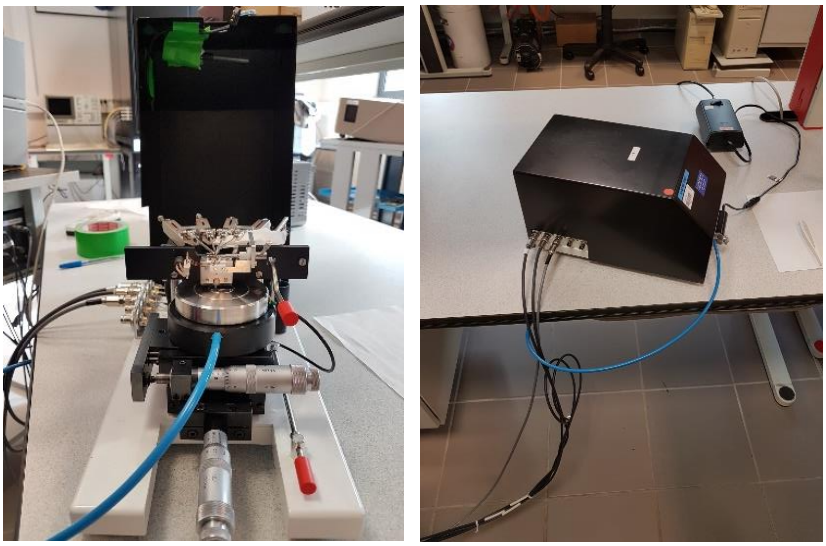

Figure 40 : *In situ* UV measurements setup configuration

To sum up, the SOI substrates offer advantages for the fabrication of low power consumption devices (for example automobile, Internet of Things, smartphones). On the other hand, the Ψ-MOSFET configuration is easy to implement for electrical measurements, as it does not require any lithography steps for the contacts fabrication. The sensitivity of the SOI substrates for the surface charge is thus promising for the study of the immobilized POMs redox state in correlation with the electrical response of the device.

IV.2.b. Pseudo-MOSFET electrical measurements

This section is a tutorial about the electrical measurements with the pseudo-MOSFET where we describe how to extract the key parameters such as threshold voltage and flat-band voltage based on the probe station measurements. Our original results will be presented in sections IV.2.c and IV.2.d.

Presentation of pseudo-MOSFET electrical measurements and parameters extraction procedure

Another advantage of the Ψ-MOSFET configuration with the two probes as source and drain is that the conduction of both holes and electrons can be monitored with the same device by simply recording I_D-V_{BG} curves, which is not the case for a conventional MOSFET where

either holes or electrons can be studied depending on whether it is an *p*-MOSFET or *n*-MOSFET (respectively).

POMs-based SOI substrates were thus analyzed using the probe station and the Ψ-MOSFET configuration. The aim was to understand how the immobilized POMs affect the SOI conductance depending on their redox states. Two kind of experiments were carried out: the SOI conductance modulation 1) by biasing the Si substrate with V_{BG} and 2) by UV irradiation of the POM layer at fixed V_{BG} over time. Before detailing the results obtained in the next part, a description of the electrical measurements and the parameters extraction procedure will be given.

•Conduction channel/ transfer characteristics

Depending on whether V_{BG} is negative or positive, a channel of holes or electrons will be induced respectively at the Si film/BOX interface of the SOI substrate. To understand the two mechanisms, we need to keep in mind that in our case, both the bulk Si substrate and the top Si film are lightly *p*-doped, meaning that the majority carriers in these semiconductor materials are holes.

When V_{BG} is negative, in the range -15 V → 0 V (Figure 41a), the free holes in the *p*-Si substrate are attracted to the back gate. As a result, as V_{BG} gets more negative, the BOX/bulk *p*-Si interface gets depleted of holes (depletion region) and eventually an inversion layer with electrons will be induced at this interface. The BOX can be viewed as a capacitor, with a positive armature and the other negative. Indeed, when a negative charge develops at one armature (here the BOX/bulk *p*-Si interface), a positive charge is generated on the other side of the dielectric (at the Si film/BOX interface) to maintain the charge neutrality.[50] A hole channel thus develops at the Si film/BOX interface due to the electric field.

Using the same analysis, when V_{BG} is positive, in the range 0 V → 15 V (Figure 41b), an excess of holes accumulates at the BOX/bulk *p*-Si interface (accumulation region). An electron channel develops on the other side of the capacitor, at the Si film/BOX interface (inversion layer) due to the electric field and the holes are evacuated to the probes.

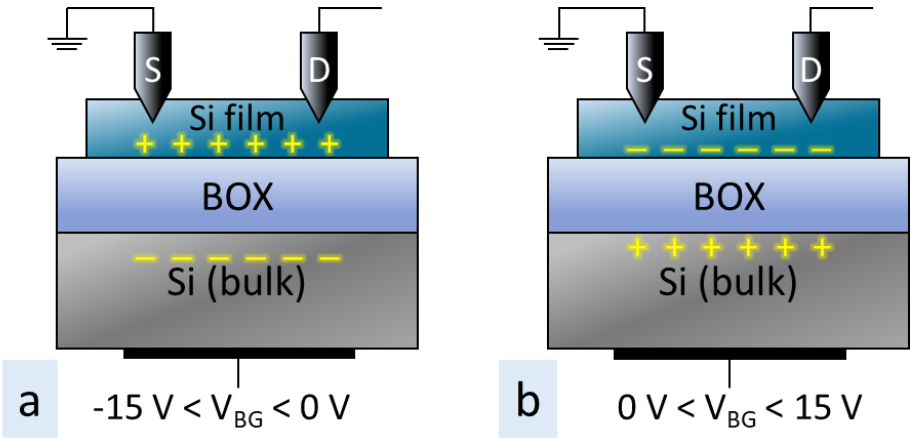

Figure 41 : Generation of a holes (a) and electrons (b) conduction channel at the Si film/BOX interface by a back gate biasing of the SOI substrate. Both Si film and Si substrate are *p*-type semiconductors (lightly doped).

By biasing the SOI substrate with a back gate voltage V_{BG}, transfer curves, or transfer characteristics, that is to say $I_D=f(V_{BG})$, can thus be obtained. A typical I_D-V_{BG} curve is shown in Figure 42. Before examining the regions 1, 2, 3 and 4, let us first define the flat-band voltage V_{FB} and the threshold voltage V_{TH} that can be extracted from the analysis of the I_D-V_{BG} curves.

The flat-band voltage V_{FB} is the gate bias (not necessarily V_{BG} = 0) at which the flat-band condition is achieved, that is to say there is no supplementary charge at the Si film/BOX interface compared to the doping. It can be viewed as a threshold voltage for the generation of a channel of holes: a V_{BG} lower the V_{FB} induces a band bending favorable to holes accumulation.

The threshold voltage V_{Th}, or turn-on voltage,[51] is "the gate bias beyond flat-band just starting to induce an inversion charge sheet".[23] In other words, in the case of a *p*-doped top Si film, it is the minimum voltage at which an electrons channel starts to appear at the interface Si film/BOX between the source and the drain. For transistors, the threshold voltage is a good indicator of device performances.

Thus, the top Si film is depleted of free carriers when $V_{FB} < V_{BG} < V_{Th}$. When $V_G < V_{FB}$, a conduction channel of holes is formed at the top Si film/BOX interface while a conduction channel of electrons is formed for $V_G > V_{Th}$.

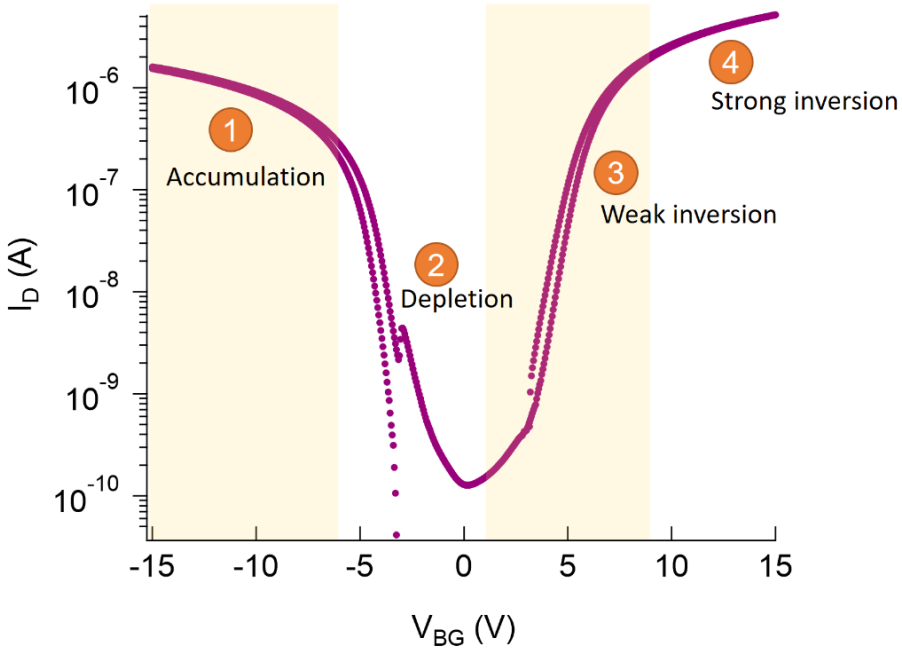

Figure 42 : Typical I_D-V_{BG} transfer curve (semi-logarithmic plot) obtained from a SOI substrate degreased and cleaned with RCA1/RCA2 solutions, for V_D = 0.1 V. The back gate voltage was double swept from -15 to 15 V and backwards.

In the region 1 of the I_D-V_{BG} curve f Figure 42, high I_D current is obtained and corresponds to the holes accumulation regime as discussed previously. When the back gate bias increases, the holes start to leave the Si film/BOX interface, such that a depletion region is generated and is characterized by a drop in the drain current (region 2). As V_{BG} becomes positive and higher than V_{Th}, electrons start to be injected at the Si film/BOX interface leading to the increase in drain current. The region 3 corresponds to a weak and moderate inversion region where the density of the minority electron carriers is still lower than the density of majority carriers (*i.e.* dopants) in the Si film. When the density of the minority electron carriers becomes higher, the strong inversion regime (region 4) is reached.[52,53]

•Extraction of parameters/Ohmic contact/output characteristics: I_D-V_D

In order to obtain a reliable parameter extraction, the contacts between Ψ-MOSFET probes and the top Si film need to be ohmic.[45] An ohmic contact (unlike a Schottky contact) is a metal-semiconductor contact exhibiting "a negligible junction resistance relative to the total resistance of the semiconductor device".[23] In other words, it is a contact where current can enter and exit the semiconductor without a significant decrease in the voltage. This linear dependence of I_D to V_D is obtained at low V_D (linear regime) in an ideal MOS, as shown in Figure 43a.[23,52] In a classical Ψ-MOSFET, the contacts turn ohmic when a sufficient pressure is applied on the probes.[46] In our case, for a pressure of 100 g applied on the probes, the I_D-V_D curves are indeed

linear at low V_D as depicted in Figure 43b for a few V_{BG}. For the experiments which will be detailed in the next parts, V_D was set at 100 mV.

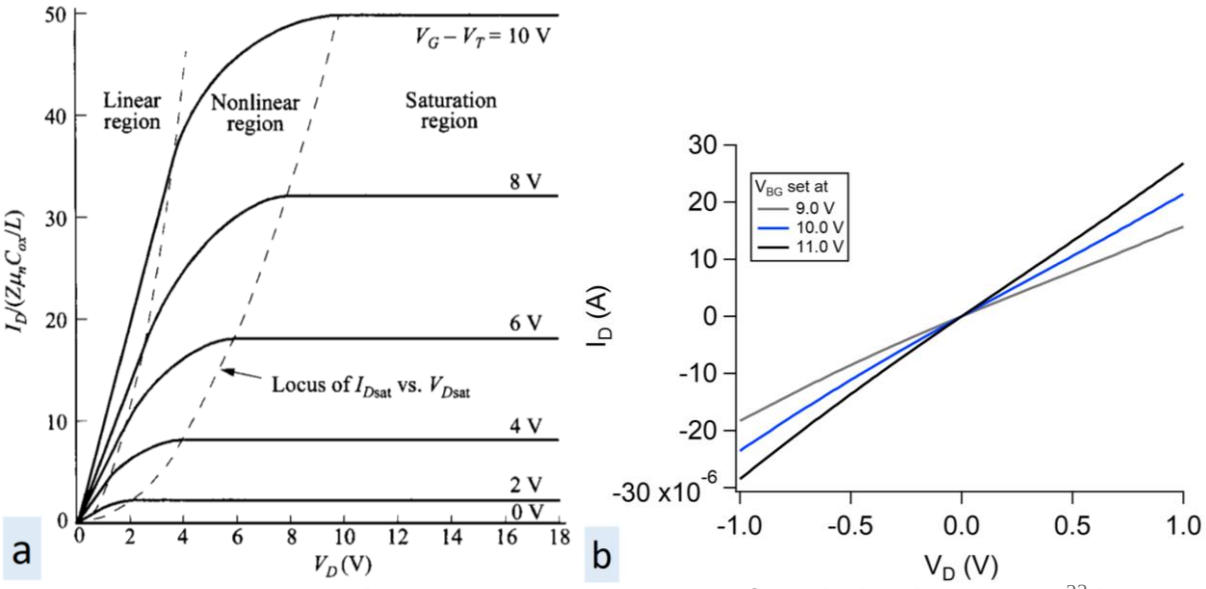

Figure 43: a) Basic output characteristics (I_D-V_D curve) of an idealized MOSFET.[23] b) I_D-V_D curves measured on the bare SOI sample at V_{BG} set at fixed value.

The extraction of V_{Th} and V_{FB} is found to be interesting to compare the POM-based SOI substrates with and without UV irradiation. Indeed, negative charge on surface is expected to shift V_{Th} (and V_{FB}) to higher values. In the case when V_{BG} is positive, the negative charge on surface can be viewed as a supplementary negative gate bias (by the top) meaning that the backgate voltage needed to turn on the channel of electrons (V_{Th}) should be higher to compensate the contribution from the surface. On the contrary, when V_{BG} is negative, the formation of holes channel is facilitated by negative charges from the top so the V_{FB} increases. Similar to the KPFM measurements where a decrease in CPD was attributed to the reduction of the POM on the surface, here the idea is to probe the photoreduction of the POMs by a shift of V_{Th} and V_{FB} to higher values.

The parameters extraction method allowing to obtain V_{Th} and V_{FB} values was developed by Ghibaudo.[54] It involves the study of the I_D-V_G and g_m-V_G curves, shown in Figure 44, in the strong inversion regime, where g_m is the transconductance (transfer conductance) defined as $g_m = \partial I_D / \partial V_{BG}$. The transconductance measures the variation of output current induced by a variation of input voltage. Unlike former methods for V_{Th} extraction, the one developed by Ghibaudo provides a more reliable V_{Th} in the way that it is independent of the source and drain parasitic series resistances and channel mobility degradation.

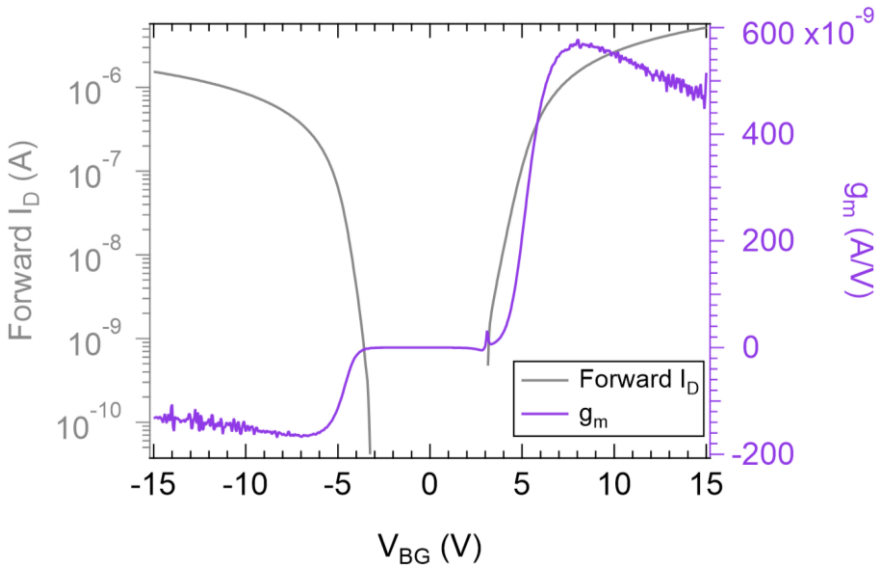

Figure 44 : I_D-V_{BG} and g_m-V_{BG} curves.

Here, the extraction of V_{Th} and V_{FB} requires three steps. For low V_D (linear regime), the drain current is modeled as follows:

$$I_D = \frac{W*C_{ox}}{L} * \frac{\mu_0}{[1+\theta(V_{BG}-V_{Th})]} * (V_{BG} - V_{Th}) * V_D \qquad \text{Equation 4}$$

W and L are the effective channel width and length respectively. C_{ox} is the gate oxide capacitance, μ_0 is the low field mobility, θ is the mobility reduction coefficient, V_{BG} is the gate voltage, V_{Th} is the threshold voltage, and V_D is the drain voltage. At negative backgate voltage, conduction occurs with holes and the relevant parameter is V_{FB} which is obtained by the same formula by replacing V_{Th} by V_{FB} in this equation and the following ones (below).

In Ψ-MOSFET, the W/L ratio is replaced by a geometrical factor f_g that was estimated to be equal to ~0.75.[49,55] As electrons and holes channels can be both studied in the same device with a single I_D-V_{BG} curve, both V_{Th} and V_{FB} can be extracted from a single measurement.

Using Eq. 1, the transconductance g_m can be derived as follows:

$$g_m = \frac{dI_D}{dV_{BG}} = \frac{W}{L} C_{ox} \frac{\mu_0}{[1+\theta(V_{BG}-V_{Th})]^2} * V_D \qquad \text{Equation 5}$$

In order to simplify the parameter extraction, the idea is to linearize the dependence with V_{BG}. More precisely, we can remove the mobility reduction coefficient which is dependent to the back gate voltage by using the following "$Y_{function}$":

$$Y_{function} = \frac{I_D}{\sqrt{g_m}} = \sqrt{\frac{W}{L} C_{ox} \mu_0 V_D} * (V_{BG} - V_{Th}) \qquad \text{Equation 6}$$

By plotting $Y_{function}$=f(V_{BG}) the extraction of both V_{FB} and V_{Th} is possible by an extrapolation of the linear fit to the x-axis in the accumulation and inversion regimes respectively, as depicted in Figure 45.

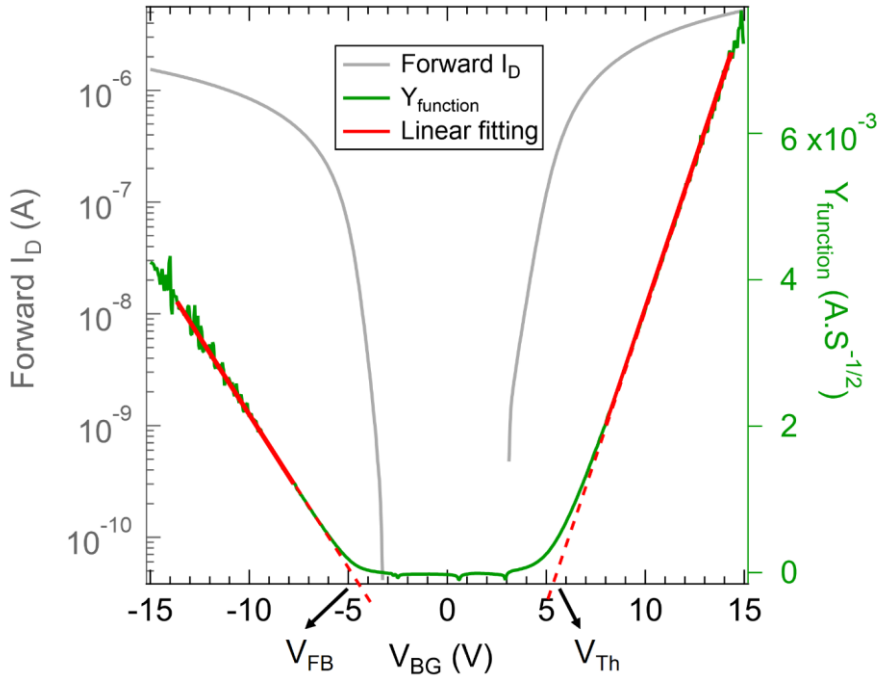

Figure 45 : Extraction of V_{FB} and V_{Th} by extrapolation of the linear parts of the $Y_{function}$.

Using the different I_D-V_{BG} and g_m-V_{BG} curves manipulations, the "$Y_{function}$ method" will thus be used in our case to extract V_{FB} and V_{Th} for all the modified SOI substrates. In the following part, results on the SOI conductance modulation by V_{BG} or UV irradiation will be detailed. The effect of POMs is supposed to modify the electrostatic effect of the back gate. Therefore, we expect that the whole characteristics is shifted when the charge state of the POM is modified. We will focus on the values of V_{Th} and V_{FB} as key parameters for measuring the impact of the POM layers.

SOI sample and their functionalization

For our project, Dr. Irina Ionica and Miltiadis Alepidis provided us a piece of SOI wafer with squared patterns. It is actually a piece of SOI wafer from Soitec that was subjected to a supplementary lithography and reactive ion etching steps to create Si film islands (SOI mesas) with a size of 5 mm² x 5 mm². The squares are separated from each other by a 2 mm buried oxide width, where Si film was actually removed, as seen on the left of Figure 46. Indeed, if defects are present on the edge of an unpatterned SOI substrates and if leakage currents between the Si film and the bulk Si are present, that would affect the electrical response of the whole substrate. Here, if leakage current through the buried oxide is present only under a specific mesa, it will only affect the latter. The Si islands thus give more reliable results than using a

piece of unpatterned SOI substrate by isolating the possible leakage current issues.[35] The top Si "film" and the BOX have a respective thickness of 70 nm and 145 nm. Both the top Si film and the bulk Si substrate are lightly *p*-doped (Bore) with a dopant concentration of ~10^{15} cm^{-3}. The received piece of wafer was cleaved prior to any chemical treatment using a diamond wire saw on the 2 mm oxide lines to obtain seven pieces (see Figure 46). Different functionalizations were performed on the seven pieces during the week prior to the electrical measurements. The functionalized substrates were stored in Ar-purged vials for at least 2 days in the dark and were subsequently and carefully carried to Grenoble.

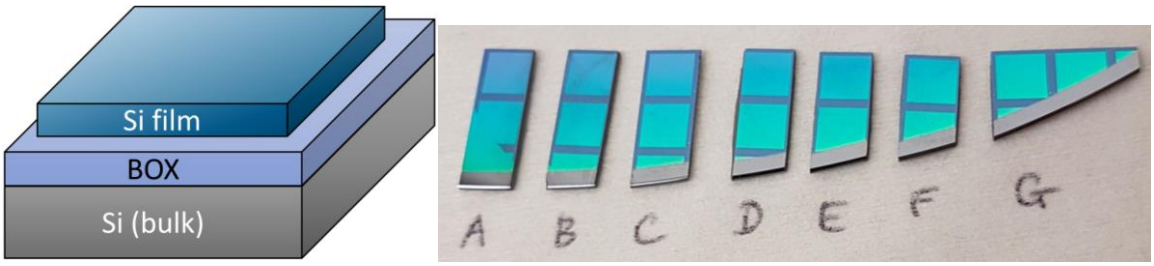

Figure 46 : SOI mesa (on the left) and piece of patterned SOI substrate after cleaving with a diamond wire saw (on the right). The squared shape surfaces are the superficial Si(100) film with a thickness of 70 nm and the BOX thickness is equal to 145 nm.

As we were limited by the number of SOI substrates and by the time, we chose to prepare only the most relevant surfaces. The SOI samples functionalization procedure is shown in Figure 47 and was detailed in Chapter II. As POM(II) was found to be the less useful for the photoreduction property study, as shown by the previous KPFM and UV-Vis-NIR measurements, we decided to prepare only POM(0) and POM(I) monolayer, later called **SOI-NH_2-POM(0)** (sample D on Figure 46) and **SOI-NH_2-POM(I)** (sample C) respectively. POM(0) and POM(I) monolayer were prepared by a simple dipcoating of the NH_2-terminated SOI substrate in the corresponding POM solutions in acetonitrile. Since the substrates were not analyzed right after their functionalization and can lack of stability, multilayers of POM(0), POM(I) and POM(II) were also prepared on oxidized SOI substrates. They will be later called **SOI-SiO_2-POM(0)** (sample F), **SOI-SiO_2-POM(I)** (sample E) and **SOI-SiO_2-POM(II)** (sample G) respectively. They have the advantage of a better stability over the POM monolayers which could give a more reliable photoreduction signature. Finally, **SOI-SiO_2** (sample A) and **SOI-ester** (sample B) substrates were prepared and were used as reference substrates for POM multilayer and POM monolayer respectively. Note also that a few electrical measurements were carried out on an unmodified SOI substrate, later called **bare SOI**. It differs from the SOI-SiO_2

substrate on which degreasing with organic solvents and cleaning with RCA1/RCA2 solutions were performed (same procedure as for the Si(100) wafer cleaning).

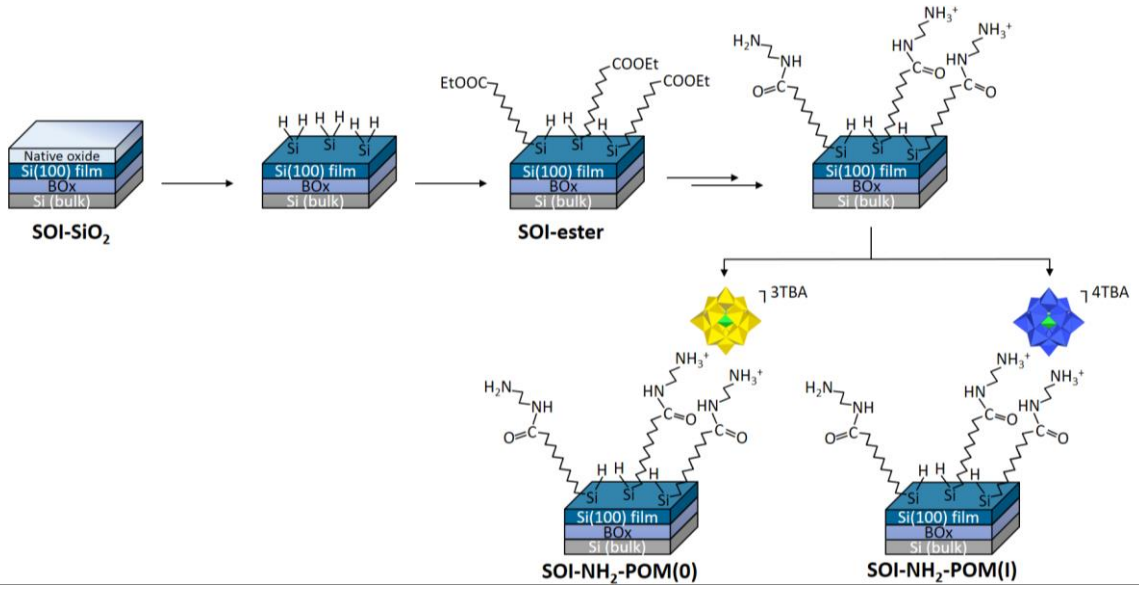

Figure 47 : SOI substrate functionalization procedure. The SOI-SiO_2 substrate is subjected to a similar procedure developed on Si(100) substrates, leading to the formation of SOI-ester substrate. After hydrolysis of the ester functions, activation of the COOH functions and reaction with ethylenediamine, the NH_2-terminated SOI substrate is subjected to a dipcoating in POM solution to finally give SOI-NH_2-POM(0) and SOI-NH_2-POM(I) substrates.

IV.2.c. SOI conductance modulation by the presence of the POM

The first objective was to modulate the conductance of the POM-based SOI substrates by a back gate voltage. V_{BG} was swept from -15 V to 15 or 20 V (forward and reverse bias) and the drain current between the source and the drain was measured for the seven pieces of modified SOI substrates. As we wanted to study the photoreduction effect, several curves were obtained for each substrate, before UV irradiation, during ~10-15 minutes of UV irradiation, and after UV irradiation. Note that the references substrates (**SOI-SiO_2**, **SOI-ester**) were subjected to the same experiments to be able to separate the effect of the POM layer.

I_D-V_{BG} curves were successfully recorded and shown in Appendix 4.4, except for the SOI-ester sample which was unusable. Indeed, due to an experimental issue during the functionalization procedure, the oxidized substrate was etched twice in 10% HF solution prior to hydrosilylation (instead of once), which probably damaged the BOX resulting in current leakage through the substrate (see details in Appendix 4.4).

Nevertheless, for all experiments including the reference SOI-SiO_2 substrate, the UV light seemed to have an effect since it induced a shift in the I_D-V_{BG} curve, as highlighted in Figure 48.

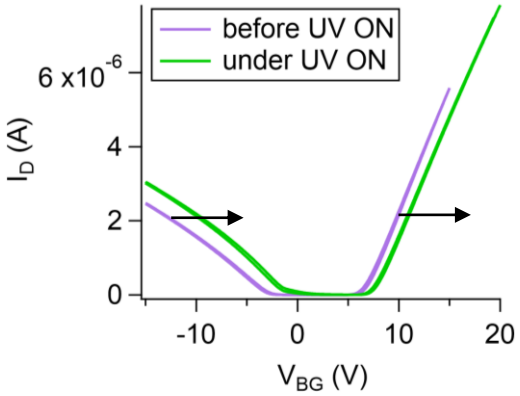

Figure 48 : I_D-V_{BG} curve (linear scale) of the SOI-SiO_2-POM(I) device measured before and under UV irradiation.

All V_{FB} and V_{Th} were thus extracted using the $Y_{function}$ method described previously. As the extraction was performed 5 times for each V_{FB} and for each V_{Th} of each device, an average V_{FB} and an average V_{Th} were calculated and are reported in Table 3 (in V).

Substrate	Before UV irradiation		Under and after 10-15 min UV irradiation		10-30 min after UV OFF		After 1, 2 or 3 days	
	V_{FB}	V_{Th}	V_{FB}	V_{Th}	V_{FB}	V_{Th}	V_{FB}	V_{Th}
Bare SOI	-1.6 to -2.2	3.8 to 3.9	x	x	x	x	x	x
SOI-SiO_2	-5.3	5.9	-2.9	7.2	-4.0	6.3	-4.9	5.5
SOI-SiO_2-POM(0)	-3.1	6.8	-1.0	7.8	-1.9	7.5	-3.0	6.4
SOI-SiO_2-POM(I)	-4.9	6.3	-3.0	7.4	-3.4	7.1	x	x
SOI-SiO_2-POM(II)	-4.5	6.1	-2.1	7.8	-2.1	7.8	x	x
SOI-NH_2-POM(0)	-2.8	6.2	-2.0	6.5	-2.7	5.7	-2.9	5.0
SOI-NH_2-POM(I)	-2.8	5.9	-2.3	6.2	-2.8	6.2	-1.3	7.5

Table 3 : Average V_{FB} and V_{Th} (in V) extracted using the $Y_{function}$ method on the I_D-V_{BG} curves obtained.

For an easier comparison between the different substrates, a "corrected threshold voltage" (ΔV_{Th}) and a "corrected flat-band voltage" (ΔV_{FB}) are calculated for each device. They are defined as: $\Delta V_{Th} = V_{Th} - V_{Th,initial}$ and $\Delta V_{FB} = V_{FB} - V_{FB,initial}$ respectively (similarly to the

KPFM measurements, the purpose is to equalize all the values obtained at the beginning before the experiment starts). In the equations, V_{Th} and V_{FB} are the threshold and flat-band voltage extracted from the I_D-V_{BG} curves, while $V_{Th,initial}$ and $V_{FB,initial}$ are the threshold and flat-band voltage extracted from the I_D-V_{BG} curve recorded at the beginning, before UV irradiation. The ΔV_{FB} and ΔV_{Th} variations during the experiment (UV ON then UV OFF) are shown in Figure 49 for the POM multilayers and the SOI-SiO_2 substrate, and in Appendix 4.5 for the POM(0) and POM(I) monolayers. On each figure, the ΔV_{FB} and ΔV_{Th} calculated at the beginning, before UV irradiation, are represented by a red closed circle. Again, as for the previous characterization techniques, the colors correspond to the surface feature: orange for the POM(0)-containing SOI substrates, light blue for the POM(I)-containing SOI substrates, dark blue for the POM(II)-containing SOI substrates, and grey for the SOI-SIO_2 sample. For each variation curve, the UV light is switched on at t = 0 s. The dark closed circles correspond to the parameters extraction obtained right after the UV lamp was switched OFF. As the extraction of V_{FB} and V_{Th} parameters is made "manually" by choosing two points in the linear part of the $Y_{function}$, the standard deviation is also shown in both Figure 49 and Appendix 4.5 and was obtained by repeating each parameter extraction five times. In some cases, I_D-V_{BG} curves were recorded a few days after the end of the experiment and the corresponding V_{FB} and V_{Th} were extracted and also reported.

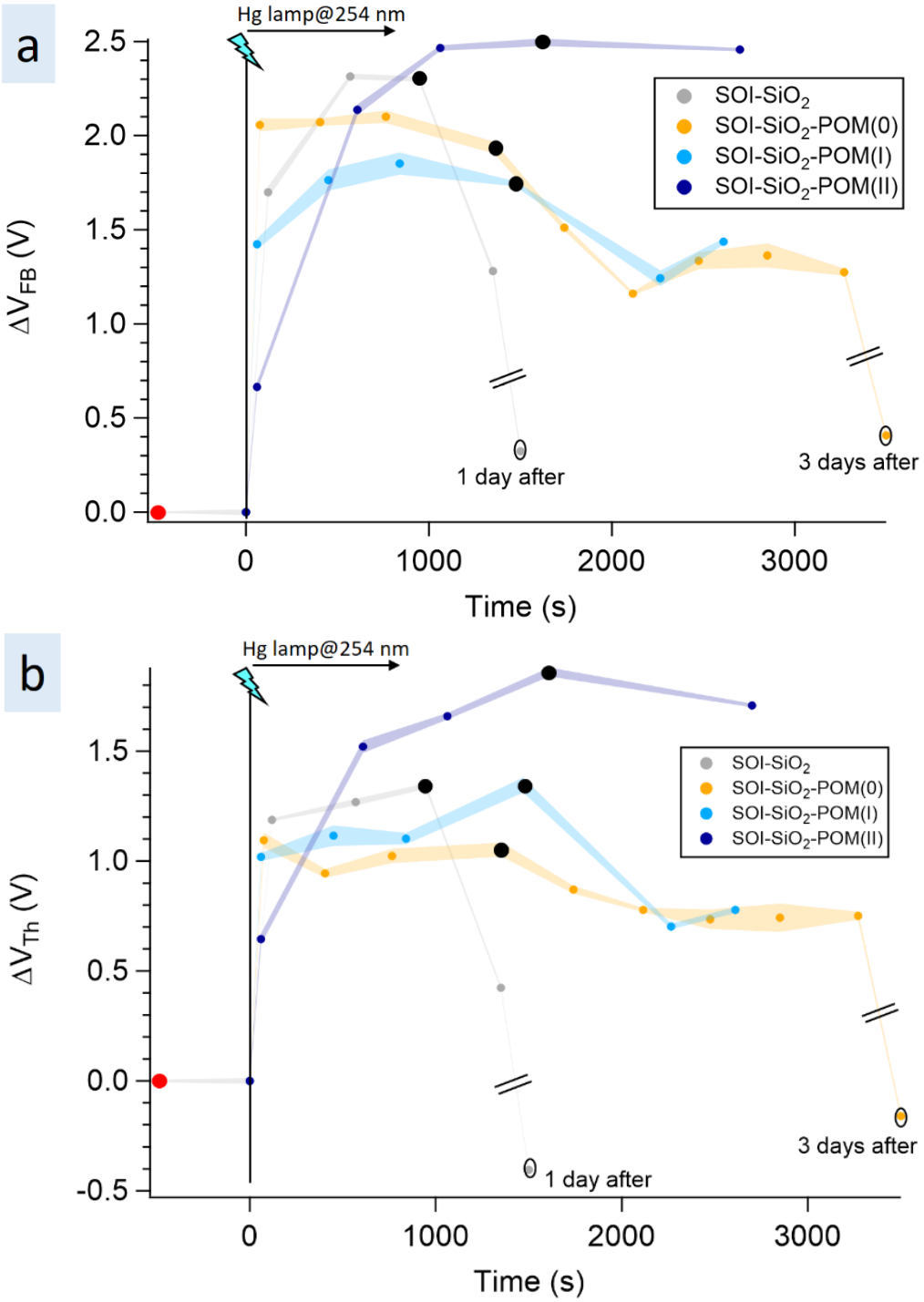

Figure 49 : a) ΔV_{FB} variation and b) ΔV_{Th} variation during the experiment in the case of SOI-SiO_2 substrates, with and without POMs. The red closed circle corresponds to the extracted parameters before UV irradiation. The Hg lamp (λ=254 nm) is switched on at t=0 s and several I_D-V_{BG} curves are recorded during 10-15 minutes. The black closed circles correspond to the extracted parameters right after the UV lamp is switched off and last I_D-V_{BG} curves are recorded.

Globally, the trend in V_{FB} and V_{Th} variation (and thus ΔV_{FB} and ΔV_{Th} variation) is the same for all the SOI substrates under ~10-15 minutes UV irradiation: V_{FB} and V_{Th} both

increased under UV irradiation. The UV light has a higher effect on the POM multilayer-containing device and on the SOI-SiO_2 than on the POM monolayer-containing devices.

The V_{FB} and V_{Th} variations are quite significant under UV irradiation: for example, in the case of SOI-SiO_2-POM(0) device, a 2.0 V increase in V_{FB} and a 1.0 V increase in V_{Th} were measured. The same trend is observed in the other POM multilayer-containing samples. After the lamp was switched off, V_{FB} and V_{Th} decreased again, except for the SOI-SiO_2-POM(II) device. The decrease was pursued as confirmed by V_{FB} and V_{Th} measured after one and three days for SOI-SiO_2 and SOI-SiO_2-POM(0) substrates respectively. The almost parallel evolution in V_{FB} and V_{Th}, is what is expected when a backgate voltage is applied to the device.

However, the reference SOI-SiO_2 substrate also reacts the same way under UV irradiation (increase in ΔV_{FB} and ΔV_{Th} under UV irradiation and subsequent decrease after the irradiation stops), making it difficult to extract the effect on SOI conductance brought by the POMs. The results obtained here were quite surprising since the UV light effect on Si substrates was negligible during the KPFM measurements. Contrary to the KPFM measurements where the top surface was scanned, the focus during the probe station measurements is given to the channel located at the buried interface because this is where the space charge region (*i.e.* depletion zone that can turn into inversion or accumulation) builds up. As the UV light induces a significant modification of V_{Th} and V_{FB} for the substrates with and without POMs, it appeared necessary to understand more precisely what is happening in the buried interface under UV irradiation.

A mechanism of the effect of UV irradiation on Si substrate was proposed by Katayama and Shimura[56] inspired by the work of Caplan *et al.*[57] and shown in Figure 50. This mechanism can be applied to the Si/SiO_2 interfaces of the SOI substrate. Si has a bandgap energy of ~1.1 eV, while our Hg lamp emits light at a wavelength of λ = 254 nm ≈ 4.9 eV, almost five times higher than the Si bandgap. The energy brought to the substrate is thus sufficient to generate electron-hole pairs in the Si. The authors emphasized the importance of interface states present at the Si/SiO_2 interface that exhibit recombination times different for holes and electrons. In our case, the UV irradiation seems to boost the conductivity which can be ascribed to the increase of hole population in the space charge region. The exact mechanism taking place at the interfaces is not really clear but some possibilities can be discussed.

In the two reports mentioned above, the UV light irradiation induces the formation of negative charges on the surface. The oxygen molecules adsorbed on the oxidized Si surface was found to attract the electron generated by UV irradiation, leading to the formation of O_2^-

species.[57] On the other hand, the Si-OH groups on the surface also attract the generated electron following the reaction:[58,59]

$$(\equiv Si - OH) + e^- \rightarrow (\equiv Si - O)^- + H$$

The mechanism proposed by Katayama and Shimura highlights the Si/SiO_2 interface (Figure 50a) where surface states can be found. These fast states are carrier traps that act as recombination centers. On the other hand, slow states are located in the top oxide, near the interface with the top Si film. They are donor-type state meaning that they are neutral when occupied by electrons, while positively charged when empty. After the generation of electron-hole pairs, the electrons neutralize some positively-charged emptied slow states but also lead to the formation of O_2^- centers (Figure 50b). Once the UV lamp is switched off, the oxygen molecules release electrons that travel back to the top SiO_2/top Si film interface due to the electric field created (Figure 50c). Thus, negative surface charges slowly disappear.

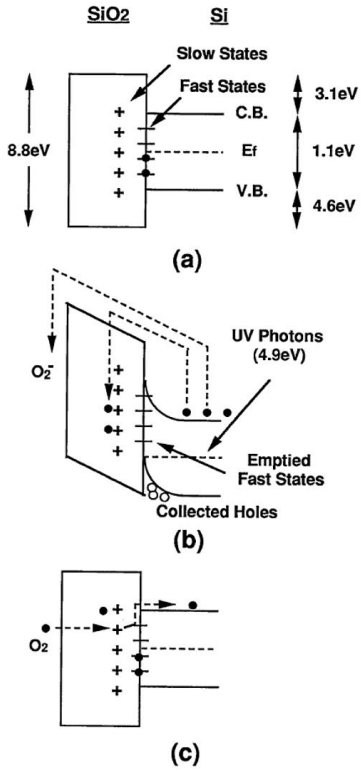

Figure 50 : Mechanism of negative surface charge formation on Si/SiO_2 substrate. The band diagrams correspond to a) the equilibrium state, b) under UV irradiation and c) after UV irradiation when the UV light is turned off.[56]

This mechanism taking place at the Si/SiO_2 interface could explain why the V_{Th} and V_{FB} variations are higher in the case of the POM multilayers. Indeed, the latter were obtained on SOI-SiO_2 surfaces, unlike the POM monolayers immobilized on SOI-NH_2 surfaces which are supposed to be oxide-free. The UV light provided by the Hg lamp is thus affecting the interfaces of the SOI sample. It was also found that the UV irradiation of MOS capacitor increases the

density of the surface states.[59,60] From our measurements, the disruption of the buried interface by the UV irradiation with the Hg lamp seems to have a larger effect on the channel than does the top surface functionalization.

Going back to the study of SOI-SiO_2 devices with and without POM multilayers, the difference between the four substrates can be spotted in the region of Figure 49 after the lamp is switched off (starting from the black closed circle of each curve). A decrease of 0.8 V and 1.0 V in ΔV_{FB} and ΔV_{Th} respectively (thus V_{FB} and V_{Th}) is measured in approximately 7 minutes for the SOI-SiO_2 substrate, while a smaller decrease of approximately 0.6 V and 0.2 V in V_{FB} and V_{Th} respectively is measured in approximately 20-30 minutes for SOI--SiO_2-POM(0) and SOI-SiO_2-POM(I) substrates. For SOI-SiO_2 and SOI-SiO_2-POM(0), the decrease is pursued after several days towards the initial V_{FB} and V_{Th} values (before UV irradiation). This "remanence" effect could be attributed to the presence of POMs on the surface and their electron acceptor nature. Indeed, the longer and smaller decrease in V_{FB} and V_{Th} compared to the reference substrate suggests that the negative surface charge created by UV light take more time to travel back to the Si once the UV lamps is switched off.

Transfer characteristics were thus obtained for all substrates except the SOI-ester substrate using the probe station. All substrates were found to be photoresponsive. In the case of the POM monolayers, the effect of the UV light irradiation is less obvious because of the non-parallel variation of V_{Th} and V_{FB}. In the case of the POM multilayers, the effect of the POM is probably hidden by the effect of the SOI substrate itself under UV irradiation at 254 nm. This first set of measurements revealed a significant effect of the Hg lamp that disturb the Si/SiO_2 interfaces in the devices and notably the buried interface close to the conduction channel. Based on our results, this buried interface disturbance has a larger impact on the device electrical response than the nature of the top surface.

The POM monolayers are subjected to lower V_{Th} and V_{FB} variations under UV irradiation, probably because the surface contains less silicon oxide than the SOI-SiO_2 surfaces, thus less Si/SiO_2 interfaces disturbance. Another set of measurements involving the conductance modulation by UV irradiation was subsequently performed and will be detailed hereinafter. We expect to see the signature of the POMs similarly to the KPFM measurements on POM monolayer on $SiNH_2$ surfaces.

IV.2.d. POM-based SOI samples: conductance modulation by UV irradiation

The next step was to consider the POM layer as a top gate and to use its photoreduction property (thus UV irradiation) to modulate the SOI conductance. Thus, V_{BG} was set at fixed value and only I_D was measured as a function of time. During the experiment, after stabilization, the substrate was irradiated during ~20 minutes with UV light. Each experiment lasted 50 minutes. In this section, only POM monolayers-containing substrates were studied in order to clarify the effect of the POM monolayer, as well as the SOI-SiO_2 and bare SOI substrates. Prior to the real time measurements of the Ψ-MOSFET response, a few I_D-V_{BG} curves were recorded to have an estimation of the V_{FB} and V_{Th}. The back gate bias for the real time response experiments was thus chosen as follows: for each substrate, experiment was carried out at $V_{BG} < V_{FB}$ in the accumulation regime, at V_{BG} in the weak inversion regime, and at V_{BG} in the strong inversion regime of the I_D-V_{BG} curves. The purpose was to look at the different regimes and see where the effect of the POM could be higher than the effect of the substrate itself. The I_D=f(time) recorded in the accumulation regime is for example shown in Figure 51. The Ψ-MOSFET response obtained in weak and strong inversion regime are shown in Appendix 4.6.

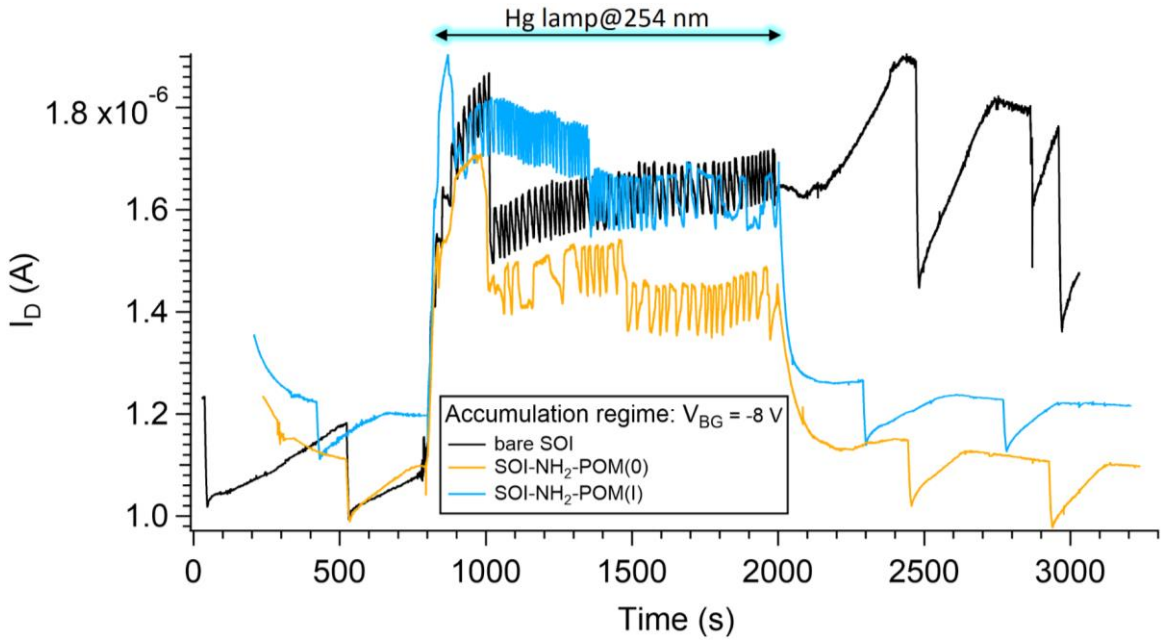

Figure 51 : I_D=f(time) at V_{BG} = -8 V (in the accumulation regime of the Ψ-MOSFET) for bare SOI, SOI-NH_2-POM(0) and SOI-NH_2-POM(I) substrates. The UV lamp was switched on at 810 s, 600 s and 620 s respectively, and switched off at 2000 s, 1780 s and 1800 s respectively.

As for the previous I_D-V_{BG} experiments, the effect of POM is again not obvious to understand. In all cases, the UV lamp has an effect on the drain current behavior: under UV irradiation, oscillations in drain current are observed and they seem related to the UV pen lamp itself as they are also observed on the reference substrates. The oscillations are characterized by variable periods from a substrate to another: approximately 10 to 20 s for the SOI-NH_2-POM(I) under UV irradiation, ~20 s for bare SOI sample and ~30 s for the SOI-NH2-POM(0) sample. The small drops in drain current before and after UV irradiation are probably artefacts. They occur quite periodically, approximately every 8 minutes. Right after UV lamp was switched on, a jump in drain current was observed in most cases and could be related to the generation of carriers. After UV irradiation, after the lamp was switched off, the drain current returned quite instantly to the initial value for POM monolayer-containing substrates. Again, the bare SOI reference sample is affected by UV irradiation (as well as the SOI-SiO_2 sample, see Appendix 4.6). Note that the SOI-ester would have served as a better reference substrate to possibly extract the effect of the POM under UV irradiation.

When looking at the drain current variation at V_{BG} = -8 V (Figure 51), UV light increases the drain current of the SOI-NH_2-POM(0) and SOI-NH_2-POM(I) substrates. This can be an evidence of POM photoreduction. Indeed, we have seen previously that UV irradiation leads to the reduction of POM on the surface, meaning that the POM are getting more electrons under UV irradiation. The negative surface charges lead to an easier holes channel formation, as they act as a supplementary top negative gate bias. The same increase of drain current is observed on the bare SOI substrate, and can be attributed to the formation of negative surface charges (O_2^-) as discussed previously which also act as a negative gate bias.

Thus, the SOI conductance modulation seems to be possible by UV irradiation of the POM monolayer, especially with a back gate bias in the accumulation or strong inversion regime of the Ψ-MOSFET. However, quantitative results were not obtained due to the missing SOI-ester piece. Moreover, the effect of the UV lamp on the reference substrates (bare SOI, SOI-SiO_2 substrate) is significant and should be removed in order to have a better control on the SOI conductance modulation. In the following part, we will discuss more in details the UV light source and try to understand how it can affect the electrical response of the SOI device. KPFM measurements will be carried out on SOI-SiO_2 substrates to make sure that the issue indeed comes from the UV light and not from the SOI substrates.

IV.2.e. UV effect on substrate: Hg lamp vs. Light-Emitting Diode (LED)

From the Ψ-MOSFET characterization results, the effect of the SOI substrate under UV irradiation is hard to isolate from the effect brought by the POMs. The culprit seems to be the Hg lamp used for the sets of measurements generating probably too much photons. This section will aim at clarify the effect of the UV irradiation: how much can the UV lamp promote carriers in the surface states at the Si film/BOX interface? As will be discussed below, the alternative is to use a less energetic source of UV, such as a LED. Comparisons between these two UV light sources applied on SOI substrates will be given through the use of KPFM as a diagnosis tool.

As shown previously, photons with λ = 254 nm are emitted and have a sufficient energy to induce the formation of negative surface charges. Moreover, a typical UV low pressure mercury lamp emission spectrum shown in Figure 52 reveals that other wavelengths are emitted, even though in minority.[61]

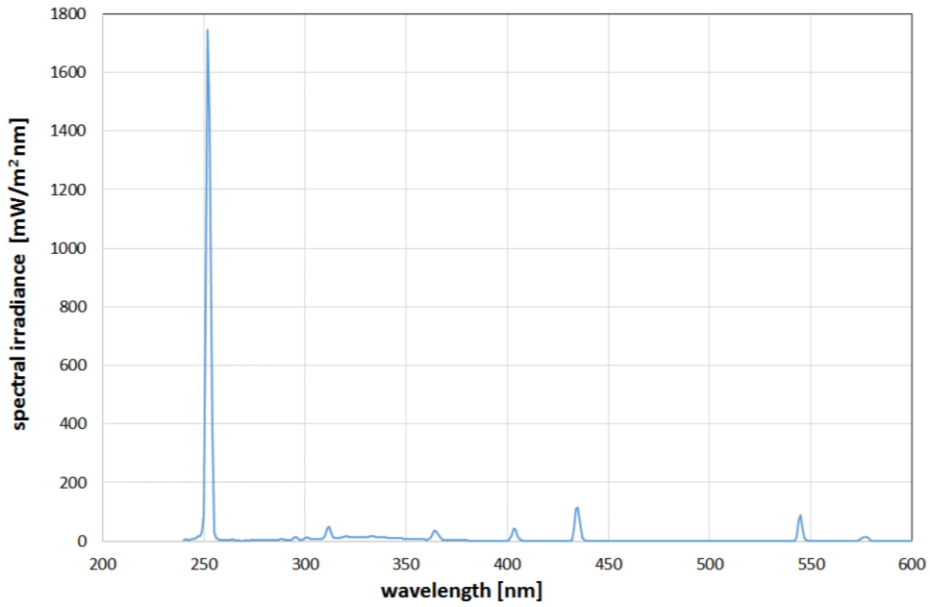

Figure 52 : Emission spectrum of a low pressure mercury vapor lamp.[61]

To investigate the impact of the UV lamp, calculations were made and reported in Table 4, based on the wavelengths of the lamp spectral power and on the light absorption coefficient and penetration depth in silicon.[62] Basically, it shows that the wavelength λ = 254 nm is the main one emitted from the UV lamp, and has a small transmission coefficient of $2.5*10^{-6}$, which is satisfying. On the contrary, other wavelengths such as λ = 405 nm, 546 nm and 578 nm represent only a low proportion of the emitted wavelengths, yet exhibit a 10^6 higher

transmission coefficient of 1, compared to λ = 254 nm. Some of the emitted wavelengths are thus transmitted through the Si/oxide interfaces in the SOI substrate. When looking at the number of photons reaching the buried interface, the effect of the Hg lamp is straightforward. The proportion of photons at 405 or 546 nm reaching the interface is 1000 to 2000 times higher than that of photons at 254 nm. The light penetration depth inside the POM layer was estimated to be ~5.0 mm, however the POM has a size of ~1.0 nm, therefore the UV light reaches the Si bulk in all cases.

Wavelength (nm)	**Spectral power (%)**	**Transmission coefficient of Si film (thickness = 70 nm)**	**Number of photons reaching the buried interface**
254	100	$2.5*10^{-6}$	100
310	2.7	$1.0*10^{-4}$	~1
365	2.2	$1.4*10^{-3}$	1232
405	2.5	1	1000000
434	6.5	0.17	442000
546	5.1	1	2040000
578	0.9	1	360000

Table 4 : Spectral power and transmission coefficient of Si film of the different wavelengths emitted by the UV lamp

From this calculations, it is easy to understand that this Hg lamp is not appropriate for our study in which we want to modulate the conductive channel by affecting only the top surface. As sketched in Figure 53, the 254 nm wavelength is sufficient to reduce the POM(0) to POM(I). However, the 405 nm wavelength emitted by the Hg impacts the buried interface of the SOI substrate by creating surface states (beige crosses) acting as recombination centers for the carriers generated by UV irradiation.

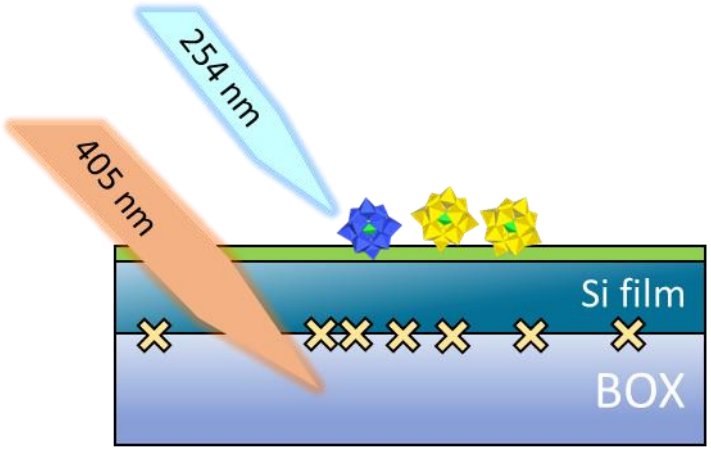

Figure 53 : Impact of the Hg lamp at the top surface and at the buried interface of an SOI substrate functionalized with POM(0). While the 254 nm wavelength emitted by the Hg lamp reduces POM(0) to POM(I) at the top surface, the 405 nm wavelength penetrates the substrate and creates surface states (beige crosses) at the buried interface.

The strategy was thus to suppress the undesirable effect brought by the minority wavelengths emitted from the Hg lamp. To do so, we decided to use an LED at 285 nm (~4.4 eV) in order to have a monochromatic radiation. It also gave the advantage of power modulation, which was not the case with the UV pen lamp. As we wanted to make sure that the LED was appropriate for the study of POM on SOI wafer, trials using KPFM were performed first before considering reproducing Ψ-MOSFET characterization. As the previously used KPFM faced a breakdown, another KPFM was used for the following experiments (Park Systems NX20 AFM) but was less stable due to an issue with the electronics. Nevertheless, some trends were extracted. Tests were done on SOI substrates (without mesas) degreased and cleaned with piranha solutions (RCA1 and RCA2), and are similar to the SOI-SiO_2 substrate characterized in the Ψ-MOSFET configuration.

As no KPFM measurements were performed on SOI substrates before the following experiments, the first test involved the UV irradiation of the SOI substrate with the Hg pen lamp, and the distance between the sample and the lamp was subsequently varied. The tip was not calibrated and the V_{CPD} measured are reported in Table 5. The SOI surface is scanned on the same area from experiment no. 1 to no. 5 (in this order). For each experiment:

- The distance between the UV pen lamp and the sample ($d_{lamp\text{-}sample}$) was modified
- The V_{CPD} was measured 1) at the beginning when UV lamp was OFF (for ~2 min); 2) during 2min15 UV irradiation and 3) for the last ~2 min of the scan when the lamp was OFF
- The V_{CPD} difference after UV irradiation vs before UV irradiation is calculated (ΔV_{CPD})

Exp. no.	$d_{lamp-sample}$	1) UV OFF	2) UV ON	3) UV OFF	ΔV_{CPD} (2-1)
1	5 cm	590 mV	690 mV	810 mV	+100 mV
2	2 cm	860 mV	700 mV	920 mV	-160 mV
3	3 cm	770 mV	550 mV	840 mV	-220 mV
4	5 cm	890 mV	500 mV	920 mV	-390 mV
5	4 cm	910 mV	500 mV	870 mV	-410 mV

Table 5 : V_{CPD} of SOI-SiO_2 substrate (without mesa) before, under and after UV irradiation. The distance between the lamp and the sample is varied from an experiment to another. The V_{CPD} difference after irradiation vs. before irradiation (ΔV_{CPD}) is also calculated.

Apart from experiment no.1, all V_{CPD} of SOI surface decreased under UV irradiation. The more the surface was exposed to UV light (from experiment no. 1 to 5), the more ΔV_{CPD} became higher (up to 400 mV variation). This seems independent of the distance between the lamp and the sample. Indeed, in experiment no. 1 and 4, $d_{lamp-sample}$ = 5 cm in both cases, while ΔV_{CPD} is different from one to another (see Figure 54). The large variation in V_{CPD} under UV irradiation confirms the significant effect of the Hg lamp on SOI-SiO_2 substrate observed in the Ψ-MOSFET characterization. The Hg lamp generates surface states in the SOI that affect the electrical response for a long period of time.

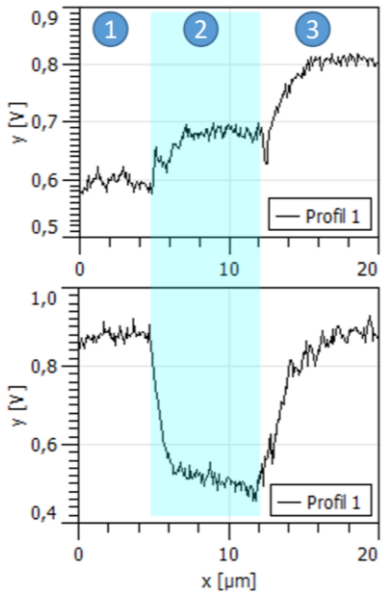

Figure 54 : V_{CPD} variation 1) before UV irradiation, 2) under UV irradiation and 3) after UV irradiation using the Hg lamp at 254 nm. The profile on the top corresponds to the V_{CPD} variation during experiment no. 1, while the profile on the bottom corresponds to the V_{CPD} variation during experiment no. 4. In both cases, $d_{lamp-sample}$ = 5 cm.

On the contrary, no effect, or at least only a lower effect, of the LED was observed on the SOI-SiO_2 substrate compared to the UV pen lamp as depicted in Figure 55.

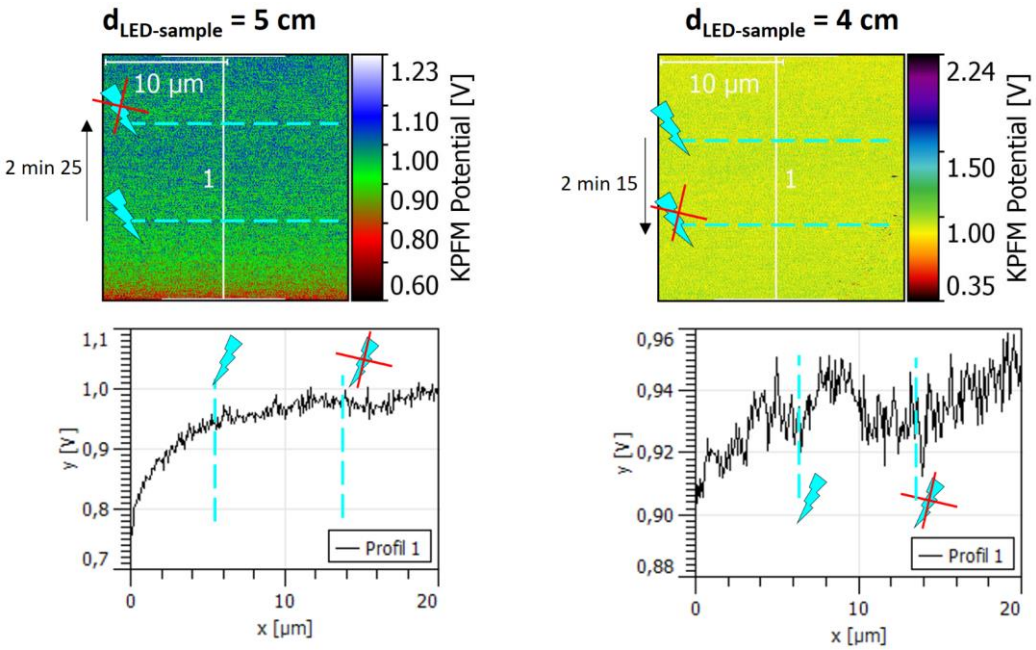

Figure 55 : V_{CPD} images (top) and corresponding profiles (bottom) of SOI-SiO_2 substrate (without mesa). On the left, the LED is at 5 cm far from the sample and the image scan goes from the bottom to the top, while on the right, $d_{LED\text{-}sample}$ = 4 cm and the image scan goes from the top to the bottom.

Now that the effect of the SOI substrate due to UV irradiation seems to be solved by the use of the LED, the next step was to immobilize POM(0) on top of it. After POM immobilization, the surface was scanned using KPFM and aggregates were observed. As for the previous KPFM measurements on Si substrates, here the V_{CPD} was averaged on the aggregates and called $V_{CPD,agg}$, while the V_{CPD} on the surface without apparent POM aggregate is called $V_{CPD,surface}$. The surface was subsequently irradiated with the LED and the UV pen lamp and the V_{CPD} variations were measured and listed in Table 6.

Experiment	$V_{CPD,agg\#1}$	$V_{CPD,agg\#2}$	$V_{CPD,surface}$
1) before UV irradiation	-191 mV	-127 mV	20 mV
2) under UV irradiation (~10 min) using the LED at d = 4 cm	-239 mV	-152 mV	46 mV
3) under UV irradiation (~4 min) using the UV pen lamp at d = 3 cm	132 mV	130 mV	211 mV
4) 5 min scan after the UV pen lamp is switched off	257 mV	254 mV	347 mV

Table 6 : V_{CPD} variation of SOI-SiO_2-POM(0) substrate (without mesa) under UV irradiation using the LED and the UV pen lamp.

Using the LED at a distance of 4 cm from the sample, the surface was scanned but the KPFM was not stable enough and the surface potential image revealed a lot of noise. Under 10 minutes irradiation with the LED at 285 nm, a decrease of 48 and 25 mV was measured on the aggregates, while the V_{CPD} of the surface increased of 26 mV. Thus, the irradiation with the LED led to a decrease in $V_{CPD,agg}$ which was shown to be associated with a POM reduction on the surface as discussed in the previous section with the KPFM measurements on Si-NH_2-POM substrates. However, irradiating the surface with the Hg lamp during 4 minutes had a higher impact on both $V_{CPD,agg}$ and $V_{CPD,surface}$. Indeed, an increase of 371 and 282 mV was measured on the aggregates and an increase of 165 mV was measured on the surface without POM. 5 minutes after the UV pen lamp was switched off, both $V_{CPD,agg}$ and $V_{CPD,surface}$ increased. Even though the effect on V_{CPD} is higher when using the UV pen lamp, the reliability of these results was not satisfying.

As a way lower effect of LED was observed on the $V_{CPD,agg}$ variation compared to the Hg lamp, we wanted to make sure that the LED was powerful enough to reduce the POM. Using a powermeter, a huge difference in effective power was actually observed whether the Hg lamp or the LED is used. The effective power as a function of the distance between the lamp/LED and the sample is shown in Appendix 4.7. At 2.5 cm far from the sample, the UV pen lamp (P_{eff} = 2.805 mW) is ~23 times more powerful than the LED (P_{eff} = 119.5 µW). In order to have a more reliable comparison between these two UV sources, we increased the power of the LED by using a lens between the LED and the sample such that a beam is focused on the substrate, as shown in Figure 56. Using the lens, a maximum effective power of approximately 200 µW was collected by the sample. For the next experiment detailed below, the Hg lamp was moved away at 10 cm far from the sample, for which the effective power was 383 µW, in the same order of magnitude as the power of the LED.

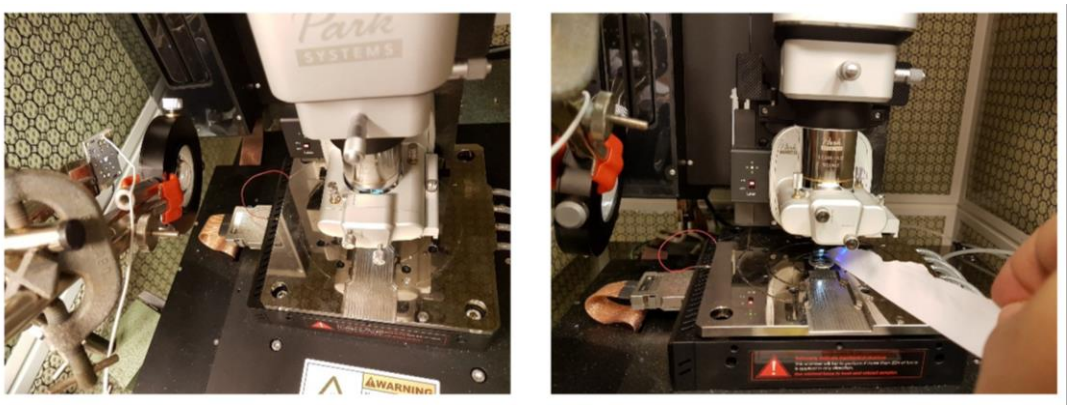

Figure 56 : KPFM measurement setup with the LED and an added lens between the LED and the sample.

An area of the sample was thus scanned with KPFM and topography image reveals an aggregate as depicted in Figure 57. After 45 minutes of irradiation with the LED and the lens, a decrease of ~30 mV in both $V_{CPD,surface}$ and $V_{CPD,agg}$ was observed, similarly to the previous experiment without lens. However, when using the UV pen lamp, a decrease of ~1.9 V was measured for both $V_{CPD,surface}$ and $V_{CPD,agg}$. This huge variation in V_{CPD} was never observed in the previous KPFM measurements involving functionalized Si substrates and supports the observation from the probe station measurements: the effect of the POM is hidden by the Hg lamp.

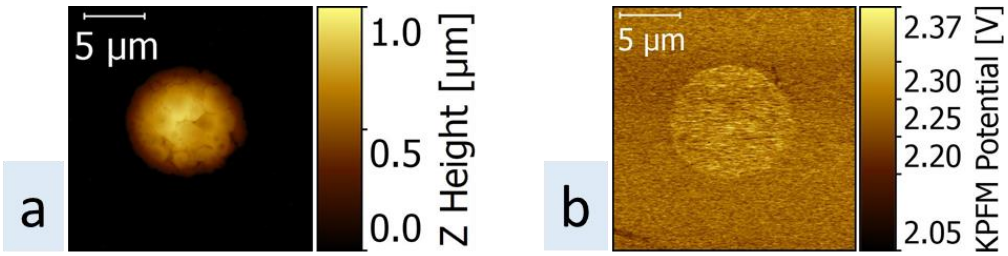

Figure 57 : a) Topography image and the corresponding b) surface potential image recorded on SOI-SiO_2-POM(0) surface.

Thus, KPFM results on SOI-SiO_2 substrates were consistent with the Ψ-MOSFET measurements. The Hg lamp is too powerful and generates too many charges on the Si/SiO_2 interfaces of the SOI substrate with and without POM, that impact the measurements on both KPFM and probe station.

In summary, measurements on immobilized POM on SOI substrates were thus performed using a probe station with the Ψ-MOSFET configuration. The purpose was to

modulate the SOI conductance by the POMs. Globally, UV irradiation leads to the photoreduction of POM(0) and thus more electrons are present on the surface and act as a negative gate bias from the top of the SOI substrate. When the back gate voltage is negative, the negative top gate has a coupling effect which improves the channel conduction. On the other hand, a positive back gate voltage and a negative top gate is supposed to lower the channel conduction. Thus, two ways to modulate the POM-based SOI samples conductance were envisioned: by a back gate bias or by UV light irradiation.

In the first case, I_D-V_{BG} curves were recorded by varying the backgate voltage and the corresponding V_{Th} and V_{FB} were extracted. In the case of the POM multilayer on SOI-SiO_2 surfaces, a parallel increase of V_{Th} and V_{FB} was observed under UV irradiation, which was not the case for the POM monolayer samples. Unfortunately, the unfunctionalized SOI substrate was also sensitive to UV light. The electrical response of the SOI-SiO_2 device, being similar to the electrical response of the SOI-SiO_2-POM devices under UV irradiation, let us conclude that the surface states generated at the buried interface (closer to the channel) have more impact on the conduction channel than the POM adsorbed at the top surface (farther from the channel).

In the second case, using the POM layer as a top gate gave encouraging results. With a fixed V_{BG} in the accumulation or strong inversion regime of the Ψ-MOSFET, the drain current was increased or decreased respectively under UV irradiation for both SOI-NH_2-POM(0) and SOI-NH_2-POM(I) substrates. However, doubts remain on the exact signature of the POM since the SOI-ester reference substrate was missing.

The significant effect of the Hg lamp on the SOI substrates was confirmed by supplementary KPFM measurements. Indeed, the UV irradiation of SOI-SiO_2 sample with the Hg lamp induces variations of the surface potential of 100-400 mV. The UV light coming from the Hg lamp thus affects the electrical response of the substrate (the surface potential in KPFM and the drain current in a Ψ-MOSFET configuration). To suppress the effect of the Hg lamp on SOI-SiO_2 substrate, a monochromatic and less powerful LED at 285 nm was used. Preliminary KPFM results using an LED were encouraging since they revealed only a slight surface potential variation. However, due to a lack of time, whether or not the LED is powerful enough to reduce the POM remains unanswered. Other measurements are required to know whether the LED is a good candidate for POM-based SOI devices conductance modulation.

V. Conclusion

Being able to differentiate POM(0), POM(I) and POM(II) as bulk powders by the means of surface characterization tools was considered as a prerequisite before studying the photoreduction phenomenon of immobilized POM onto Si surface. As bulk powders, POM(0), POM(I) and POM(II) are clearly distinguished from one to another as attested by UV-Vis-NIR spectroscopy and XPS.

The photoreduction of the POM(0) is identified by UV-Vis-NIR spectroscopy with a clear increase of the intervalence charge transfer (IVCT) band at ~800 nm for POM(I) and ~700 nm for POM(II). This band uptake was clearly detected on the POMs in the form of powders and only very discretely when deposited on silicon (reflection geometry) or on quartz (transmission geometry).

XPS was also able to identify the oxidation states of the 12 molybdenum atoms of our POMs. POM(0) is expected to include 12 Mo atoms in their oxidized state Mo(VI): they were detected with XPS, along with a small proportion of Mo(V) probably due to the reduction induced by the X-ray beam. Actually for the POM(0) powder, the XPS shows that there are about 11.1 Mo(VI) atoms for 0.9 Mo(V) atoms. Moreover, XPS shows that POM(I) and POM(II) exhibit an increasing proportion of Mo atoms in their reduced state Mo(V): over the 12 Mo atoms of a POM, there are 1.4 Mo(V) atoms in POM(I) and 2.4 Mo(V) atoms in POM(II). However, their differentiation once immobilized onto $SiNH_2$ surfaces was harder than expected. For this reason, we used characterization tools that allow a real-time surface characterization under UV irradiation.

KPFM measurements were thus performed on $SiNH_2$-POM surfaces (POM monolayer), as well as on Si-SiO_2-POM surfaces (POM multilayer). A decrease in V_{CPD}, thus in surface work function was attributed to a POM reduction on the surface. Accordingly, immobilized POM(0) photoreduction was detected and seemed to be irreversible, while no photoreduction of immobilized POM(II) was observed. Some doubts remain on the case of the immobilized POM(I) under UV irradiation: as monolayers, the large V_{CPD} variation under UV irradiation (the largest among the three POMs) suggests a reduction of the POM, but as multilayers, V_{CPD} variation reveals a partial reoxidation of the POM after deposition and an overall reduction to POM(I) under UV irradiation. Actually, KPFM shows that the negative dipole induced by depositing POM(0) on the surface ($SiNH_2$ and Si-SiO_2) is linked to an increase of positive charges at the substrate/POM interface. Upon UV light irradiation, the negative dipole turns

more and more positive due to the accumulation of negative charges at the substrate/POM interface. Meanwhile positive charges insure the electroneutrality on the outmost POM surface.

In the course of the immobilized POM photoreduction understanding, doubts arose on the real photoreduction mechanism taking place. The apparent photoreduction observed on POM monolayer by KPFM could be due to the NH_3^+ groups brought by the organic monolayer. However, in the case of POM(0) multilayers on quartz substrates, a photoreduction is observed even when traces of solvent were removed prior to POM deposition. No electron is apparently provided by the substrate and the photoreduction mechanism remains unclear. More investigations are required. Note also that both KPFM and UV-Vis-NIR spectroscopy measurements were performed in ambient atmosphere. KPFM measurements could for example be performed under N_2 atmosphere to improve our results.[33] This could protect the POM from reoxidation prior to UV irradiation.

Electrical measurements on a Ψ-MOSFET configuration using functionalized SOI substrates were then carried out. The purpose was to modulate the device conductance by means of an applied V_{BG} bias or an irradiation of the POM layer with UV light (Hg lamp). While the SOI-ester substrate was missing for a complete understanding of the effect of POM monolayer on the electrical properties, the effect of the SOI-SiO_2-POM devices under UV irradiation was hidden by the effect of the SOI-SiO_2 substrate itself. The UV irradiation with the Hg lamp induces negative surface charges but most of all surface states at the buried interface which affects the conduction channel, such that the effect of the POM at the top surface is negligible. After the probe station measurements in Grenoble, the use of a monochromatic LED instead of a low pressure Hg lamp was studied on SOI substrates with the KPFM as a diagnosis tool. Preliminary results show only a slight surface potential variation under UV irradiation with the LED compared to the Hg lamp. These results are promising for the POM-based SOI devices conductance modulation with the LED, on condition that the POM can effectively be reduced by the LED.

To complete our study, another set of probe station measurements is worth to try especially with an SOI-ester sample. The study of Katayama and Shimura[56] is encouraging since it reveals that UV light irradiation has no effect on the minority carrier lifetime of HF-treated Si wafers, unlike oxidized Si wafers. The UV irradiation on the SOI-ester device is thus expected to have no/lower effect on the conductance than the SOI-SiO_2 substrate.

The functionalization of SOI substrate also needs to be optimized. No XPS characterizations were for example performed.

Finally, it could be interesting to immobilize non photoresponsive molecules on top of the organic monolayer in order to be sure that the effect observed is due to the presence of the POM and not to the presence of a molecule. Indeed, Tour and coll.[63] grafted photoresponsive and non photoresponsive molecules on SOI wafers. V_{Th} variation under successive UV and visible light irradiation was compared between the different substrates prepared. They found that even the non photoresponsive molecule was actually sensitive to UV irradiation and that the observed photoeffects were more related to the molecular grafting than to the molecule itself.

VI. References

(1) Fabre, B. Functionalization of Oxide-Free Silicon Surfaces with Redox-Active Assemblies. *Chem. Rev.* **2016**, *116* (8), 4808–4849.

(2) Browne, W. R.; Feringa, B. L. Light Switching of Molecules on Surfaces. *Annu. Rev. Phys. Chem.* **2009**, *60* (1), 407–428.

(3) Wen, Y.; Yi, W.; Meng, L.; Feng, M.; Jiang, G.; Yuan, W.; Zhang, Y.; Gao, H.; Jiang, L.; Song, Y. Photochemical-Controlled Switching Based on Azobenzene Monolayer Modified Silicon (111) Surface. *J. Phys. Chem. B* **2005**, *109* (30), 14465–14468.

(4) Heinemann, N.; Grunau, J.; Leißner, T.; Andreyev, O.; Kuhn, S.; Jung, U.; Zargarani, D.; Herges, R.; Magnussen, O.; Bauer, M. Reversible Switching in Self-Assembled Monolayers of Azobenzene Thiolates on Au (111) Probed by Threshold Photoemission. *Chemical Physics* **2012**, *402*, 22–28.

(5) Uchida, K.; Yamanoi, Y.; Yonezawa, T.; Nishihara, H. Reversible On/Off Conductance Switching of Single Diarylethene Immobilized on a Silicon Surface. *J. Am. Chem. Soc.* **2011**, *133* (24), 9239–9241.

(6) Kim, D.; Jeong, H.; Lee, H.; Hwang, W.-T.; Wolf, J.; Scheer, E.; Huhn, T.; Jeong, H.; Lee, T. Flexible Molecular-Scale Electronic Devices Composed of Diarylethene Photoswitching Molecules. *Adv. Mater.* **2014**, *26* (23), 3968-3973.

(7) Kim, Y.; Hellmuth, T. J.; Sysoiev, D.; Pauly, F.; Pietsch, T.; Wolf, J.; Erbe, A.; Huhn, T.; Groth, U.; Steiner, U. E.; Scheer, E. Charge Transport Characteristics of Diarylethene Photoswitching Single-Molecule Junctions. *Nano Lett.* **2012**, *12* (7), 3736–3742.

(8) Hnid, I.; Frath, D.; Lafolet, F.; Sun, X.; Lacroix, J.-C. Highly Efficient Photoswitch in Diarylethene-Based Molecular Junctions. *J. Am. Chem. Soc.* **2020**, *142* (17), 7732–7736.

(9) Zhu, H.; Li, Q. Redox-Active Molecules for Novel Nonvolatile Memory Applications. In *Redox - Principles and Advanced Applications*; Khalid, M. A. A., Ed.; InTech, 2017.

(10) Fabre, B. Ferrocene-Terminated Monolayers Covalently Bound to Hydrogen-Terminated Silicon Surfaces. Toward the Development of Charge Storage and Communication Devices. *Acc. Chem. Res.* **2010**, *43* (12), 1509–1518.

(11) Dalchiele, E. A.; Aurora, A.; Bernardini, G.; Cattaruzza, F.; Flamini, A.; Pallavicini, P.; Zanoni, R.; Decker, F. XPS and Electrochemical Studies of Ferrocene Derivatives Anchored on *n*- and *p*-Si(100) by Si–O or Si–C Bonds. *Journal of Electroanalytical Chemistry* **2005**, *579* (1), 133–142.

(12) Fontanesi, C.; Como, E. D.; Vanossi, D.; Montecchi, M.; Cannio, M.; Mondal, P. C.; Giurlani, W.; Innocenti, M.; Pasquali, L. Redox-Active Ferrocene Grafted on H-Terminated Si(111): Electrochemical Characterization of the Charge Transport Mechanism and Dynamics. *Sci Rep* **2019**, *9* (1), 8735.

(13) Li, Q.; Mathur, G.; Homsi, M.; Surthi, S.; Misra, V.; Malinovskii, V.; Schweikart, K.-H.; Yu, L.; Lindsey, J. S.; Liu, Z.; Dabke, R. B.; Yasseri, A.; Bocian, D. F.; Kuhr, W. G. Capacitance and Conductance Characterization of Ferrocene-Containing Self-Assembled Monolayers on Silicon Surfaces for Memory Applications. *Appl. Phys. Lett.* **2002**, *81* (8), 1494–1496.

(14) Ichii, T.; Nanjo, S.; Murase, K.; Sugimura, H. Reversible Potential Change of Ferrocenylthiol Monolayers Induced by Atomic Force Microscopy. *Jpn. J. Appl. Phys.* **2009**, *48* (8), 08JB15.

(15) Georgiev, V. P.; Amoroso, S. M.; Ali, T. M.; Vila-Nadal, L.; Busche, C.; Cronin, L.; Asenov, A. Comparison Between Bulk and FDSOI POM Flash Cell: A Multiscale Simulation Study. *IEEE Transactions on Electron Devices* **2015**, *62* (2), 680–684.

(16) Yamase, T. Photo- and Electrochromism of Polyoxometalates and Related Materials. *Chem. Rev.* **1998**, *98* (1), 307–326.
(17) Streb, C. New Trends in Polyoxometalate Photoredox Chemistry: From Photosensitisation to Water Oxidation Catalysis. *Dalton Trans.* **2012**, *41* (6), 1651–1659.
(18) Sun, H.-R.; Zhang, S.-Y.; Xu, J.-Q.; Yang, G.-Y.; Shi, T.-S. Electrochemical and In-Situ UV-Visible-near-IR and FTIR Spectroelectrochemical Characterisation of the Mixed-Valence Heteropolyanion $PMo_{12}O_{40}^{n-}$ (n=4, 5, 6, 7) in Aprotic Media. *Journal of Electroanalytical Chemistry* **1998**, *455* (1–2), 57–68.
(19) Xiao, P.; Dumur, F.; Tehfe, M.-A.; Graff, B.; Fouassier, J. P.; Gigmes, D.; Lalevée, J. Keggin-Type Polyoxometalate ($[PMo_{12}O_{40}]^{3-}$) in Radical Initiating Systems: Application to Radical and Cationic Photopolymerization Reactions. *Macromolecular Chemistry and Physics* **2013**, *214* (15), 1749–1755.
(20) Sanchez, C.; Livage, J.; Launay, J. P.; Fournier, M.; Jeannin, Y. Electron Delocalization in Mixed-Valence Molybdenum Polyanions. *J. Am. Chem. Soc.* **1982**, *104* (11), 3194–3202.
(21) Douvas, A. M.; Tsikritzis, D.; Tselios, C.; Haider, A.; Mougharbel, A. S.; Kortz, U.; Hiskia, A.; Coutsolelos, A. G.; Palilis, L. C.; Vasilopoulou, M.; Kennou, S.; Argitis, P. Multi-Electron Reduction of Wells–Dawson Polyoxometalate Films onto Metallic, Semiconducting and Dielectric Substrates. *Phys. Chem. Chem. Phys.* **2019**, *21* (1), 427–437.
(22) Ku, Z. J.; Jin, S. R.; Zhou, H. B. Synthesis and Characterization of Two Charge-Transfer Salts Based on Keggin-Type Polyoxometalates and Morpholinebiguanide. *Russ J Coord Chem* **2009**, *35* (3), 195–199.
(23) Sze, S. M.; Ng, K. K. *Physics of Semiconductor Devices*, 3. ed.; Wiley-Interscience: Hoboken, NJ, 2007.
(24) Borensztein, Y.; Prévot, G.; Masson, L. Large Differences in the Optical Properties of a Single Layer of Si on Ag(110) Compared to Silicene. *Phys. Rev. B* **2014**, *89* (24), 245410.
(25) Aspnes, D. E.; Studna, A. A. Dielectric Functions and Optical Parameters of Si, Ge, GaP, GaAs, GaSb, InP, InAs, and InSb from 1.5 to 6.0 eV. *Phys. Rev. B* **1983**, *27* (2), 985–1009.
(26) Papaconstantinou, E.; Pope, M. T. Heteropoly Blues. V. Electronic Spectra of One- to Six-Electron Blues of 18-Metallodiphosphate Anions. *Inorg. Chem.* **1970**, *9* (3), 667–669.
(27) Yamase, T. Photoredox Chemistry of Polyoxometalates as a Photocatalyst. *Catalysis Surveys from Asia* **2003**, *7* (4), 203–217.
(28) Bruker AFM Probes. Innovation with Integrity. 2013.
(29) Kaemmer, S. B. Introduction to Bruker's ScanAsyst and PeakForce Tapping AFM Technology. Application Note 133; Bruker, 2011.
(30) PeakForce Tapping Brochure. How AFM Should Be; Bruker.
(31) Melitz, W.; Shen, J.; Kummel, A. C.; Lee, S. Kelvin Probe Force Microscopy and Its Application. *Surface Science Reports* **2011**, *66* (1), 1–27.
(32) Li, C.; Minne, S.; Hu, Y.; Ma, J.; He, J.; Mittel, H.; Kelly, V.; Erina, N.; Guo, S.; Mueller, T. PeakForce Kelvin Probe Force Microscopy. Application Note 140; Bruker, 2013.
(33) Bossard-Giannesini, L. Mesures et modélisation du travail de sortie de nanoparticules d'or fonctionnalisées et supportées. Thèse Sorbonne Université, **2018**.
(34) Heimel, G.; Salzmann, I.; Duhm, S.; Koch, N. Design of Organic Semiconductors from Molecular Electrostatics. *Chem. Mater.* **2011**, *23* (3), 359–377.
(35) Cristoloveanu, S.; Balestra, F. Technologie silicium sur isolant (SOI). *Techniques de l'Ingénieur, traité Electronique* **2013**, *E2*, 380.
(36) Celler, G. K.; Cristoloveanu, S. Frontiers of Silicon-on-Insulator. *Journal of Applied Physics* **2003**, *93* (9), 4955–4978.

(37) Dutertre, J.-M.; Beroulle, V.; Candelier, P.; Faber, L.-B.; Flottes, M.-L.; Gendrier, P.; Hely, D.; Leveugle, R.; Maistri, P.; Natale, G. D.; Papadimitriou, A.; Rouzeyre, B. The Case of Using CMOS FD-SOI Rather than CMOS Bulk to Harden ICs against Laser Attacks. In *2018 IEEE 24th International Symposium on On-Line Testing And Robust System Design (IOLTS)*; IEEE: Platja d'Aro, 2018; pp 214–219.
(38) Manasevit, H. M.; Simpson, W. I. Single-Crystal Silicon on a Sapphire Substrate. *Journal of Applied Physics* **1964**, *35* (4), 1349–1351.
(39) Colinge, J.-P. *Silicon-on-Insulator Technology: Materials to VLSI*; Springer US: Boston, MA, 2004.
(40) Bruel, M.; Aspar, B.; Auberton-Hervé, A.-J. Smart-Cut: A New Silicon On Insulator Material Technology Based on Hydrogen Implantation and Wafer Bonding. *Jpn. J. Appl. Phys.* **1997**, *36* (Part 1, No. 3B), 1636–1641.
(41) Aspar, B.; Bruel, M.; Moriceau, H.; Maleville, C.; Poumeyrol, T.; Papon, A. M.; Claverie, A.; Benassayag, G.; Auberton-Hervé, A. J.; Barge, T. Basic Mechanisms Involved in the Smart-Cut® Process. *Microelectronic Engineering* **1997**, *36* (1–4), 233–240.
(42) Smart Cut™ - Soitec https://www.soitec.com/en/products/smart-cut?__geom=%E2%9C%AA (accessed 2021 -11 -27).
(43) Hamaide, G.; Allibert, F.; Hovel, H.; Cristoloveanu, S. Impact of Free-Surface Passivation on Silicon on Insulator Buried Interface Properties by Pseudotransistor Characterization. *Journal of Applied Physics* **2007**, *101* (11), 114513.
(44) Ionica, I.; El Hajj Diab, A.; Cristoloveanu, S. Gold Nanoparticles Detection Using Intrinsic SOI-Based Sensor. In *2011 11th IEEE International Conference on Nanotechnology*; IEEE: Portland, OR, USA, 2011; pp 38–43.
(45) Ionica, I.; Savin, I.; Van Den Daele, W.; Nguyen, T.; Mescot, X.; Cristoloveanu, S. Characterization of Silicon-on-Insulator Films with Pseudo-Metal-Oxide-Semiconductor Field-Effect Transistor: Correlation between Contact Pressure, Crater Morphology, and Series Resistance. *Appl. Phys. Lett.* **2009**, *94* (1), 012111.
(46) Benea, L.; Cerba, T.; Bawedin, M.; Delacour, C.; Cristoloveanu, S.; Ionica, I. Nanoindentation Effects on the Electrical Caracterization in Ψ-MOSFET Configuration. *2018 Joint International EUROSOI Workshop and International Conference on Ultimate Integration on Silicon (EUROSOI-ULIS)*; IEEE: Granada, Spain, 2018.
(47) Cristoloveanu, S.; Williams, S. Point-Contact Pseudo-MOSFET for in-Situ Characterization of as-Grown Silicon-on-Insulator Wafers. *IEEE Electron Device Lett.* **1992**, *13* (2), 102–104.
(48) Cristoloveanu, S.; Munteanu, D.; Liu, M. S. T. A Review of the Pseudo-MOS Transistor in SOI Wafers: Operation, Parameter Extraction, and Applications. *IEEE Trans. Electron Devices* **2000**, *47* (5), 1018–1027.
(49) Cristoloveanu, S.; Bawedin, M.; Ionica, I. A Review of Electrical Characterization Techniques for Ultrathin FDSOI Materials and Devices. *Solid-State Electronics* **2016**, *117*, 10–36.
(50) Chen, W.-K. *The Electrical Engineering Handbook*; Elsevier Academic Press: Boston, 2005.
(51) Pierret, R. F. Semiconductor Device Fundamentals. Addison-Wesley: 1996.
(52) Neamen, D. A. *Semiconductor Physics and Devices: Basic Principles*, 4. ed.; McGraw-Hill: New York, NY, 2012.
(53) Fruchier, O. Etude du comportement de la charge d'espace dans les structures MOS. Vers une analyse du champ électrique interne par la méthode de l'onde thermique. Thèse Université Montpellier II, **2006**.
(54) Ghibaudo, G. New Method for the Extraction of MOSFET Parameters. *Electron. Lett.* **1988**, *24* (9), 543-545.

(55) Munteanu, D.; Cristoloveanu, S.; Guichard, E. Numerical Simulation of the Pseudo-MOSFET Characterization Technique. *Solid-State Electronics* **1999**, *43* (3), 547–554.
(56) Katayama, K.; Shimura, F. Mechanism of Ultraviolet Irradiation Effect on Si-SiO_2 Interface in Silicon Wafers. *Jpn. J. Appl. Phys.* **1992**, *31* (Part 2, No. 8A), L1001–L1004.
(57) Caplan, P. J.; Poindexter, E. H.; Morrison, S. R. Ultraviolet Bleaching and Regeneration of $\cdot Si{\equiv}Si_3$ Centers at the Si/SiO_2 Interface of Thinly Oxidized Silicon Wafers. *Journal of Applied Physics* **1982**, *53* (1), 541–545.
(58) Katayama, K.; Shimura, F. Mechanism of Ultraviolet Irradiation Effect on Si-SiO_2 Interface in Silicon Wafers. *Jpn. J. Appl. Phys.* **1992**, *31* (Part 2, No. 8A), L1001–L1004.
(59) Saminadayar, K.; Pfister, J. C. Surface-State Generation on MOS Capacitors Irradiated with UV Light and Electrons. *Phys. Stat. Sol. (a)* **1976**, *36* (2), 679–686.
(60) Verhoeven, J. L.; Saminadayar, K.; Pfister, J. C. Illumination with Ultraviolet Light of MOS Capacitors. *Phys. Stat. Sol. (a)* **1974**, *24* (2), 441–448.
(61) Schmid, J.; Hoenes, K.; Rath, M.; Vatter, P.; Hessling, M. UV-C Inactivation of Legionella Rubrilucens. *GMS Hygiene and Infection Control* **2017,** *12*.
(62) deGraaf, G.; Wolffenbuttel, R. F. Illumination Source Identification Using a CMOS Optical Microsystem. *IEEE Trans. Instrum. Meas.* **2004**, *53* (2), 238–242.
(63) He, T.; Lu, M.; Yao, J.; He, J.; Chen, B.; Di Spigna, N. H.; Nackashi, D. P.; Franzon, P. D.; Tour, J. M. Reversible Modulation of Conductance in Silicon Devices via UV/Visible-Light Irradiation. *Adv. Mater.* **2008**, *20* (23), 4541–4546.

Conclusion

This research project has focused on the immobilization of POMs onto Si surfaces for molecular electronics applications. The main goal was to study the redox state of photoreducible POMs once electrostatically immobilized onto functionalized Si surfaces. Following previous studies in our group, a particular attention has been given to the control of the POM deposition and to the understanding of the POM/surface interaction.

$(TBA)_3[PMo_{12}O_{40}]$ POM, (POM(0)), was chosen for its remarkable electron reservoir property and its ability to be reduced chemically in the presence of a reducing agent or by UV irradiation. The electrostatic deposition of this POM onto surfaces requires the presence of positively charged functions on the surface. Accordingly, alkyl GOMs were grafted onto hydrogenated Si surfaces via a fast thermal hydrosilylation reaction. The terminal ester functions were then subjected to post-modifications, leaving at the end a NH_2/NH_3^+-terminated GOM onto Si surface ($SiNH_2$ surface). The efficient grafting was supported by ellipsometry, FTIR spectroscopy and XPS, on Si(111) surfaces and Si(100) surfaces, though the functionalized Si(100) surface was found to be more sensitive to reoxidation. As no improvement could be carried out, the same procedure developed on Si(100) was reproduced on SOI(100) substrates. The functionalization of Si(111) and Si(100) with an alkyl GOM bearing reactive terminal functions thus offers new possibilities (deposition method, choice of the POMs, properties of the final device…) for the immobilization of POMs onto surfaces.

POM(0) and its one- and two-electrons reduced species, POM(I) and POM(II) respectively, were synthesized chemically. The three POMs are distinguishable as bulk powders, and display their own signature in ^{31}P NMR spectroscopy, UV-Vis-NIR spectroscopy and XPS, which was encouraging for the photoreduction study of immobilized POMs.

POM(0) was electrostatically immobilized as submonolayer (thickness of 0.3-0.6 nm) while POM(I) and POM(II) were immobilized as monolayers (thickness of 0.5-0.9 nm and 0.5-1.1 nm respectively) by a dipcoating of a (111)$SiNH_2$ substrate in the corresponding POM solution. However, once immobilized as very thin layers, the differentiation between the three (sub)monolayers was not obviously detected by UV-Vis-NIR spectroscopy and XPS. The instability of these thin layers was suspected thus, the use of characterization tools allowing a real-time surface probing under UV irradiation appeared necessary.

KPFM was thus used to measure the local surface charge of POM-containing surfaces, before and after POM deposition, as well as before and after 15 minutes of UV irradiation with a Hg lamp. A decrease in surface work function was attributed to a POM reduction on the surface, which was found to be irreversible in the case of POM(0) (submonolayer and multilayers) in a ~1h timescale. Doubts remain of the photoreduction of POM(I) layer: results suggest a reversible photoreduction of a POM(I) monolayer, while for the POM(I) multilayer, a partial oxidation is witnessed prior to UV irradiation, such that the UV irradiation leads to an overall reduction to POM(I). In the case of POM(II), no photoreduction is globally observed.

These work function variations were attributed to the molecular surface dipoles of the POMs. From the experiments results, the surface dipole evolves from inward to outward when moving from POM(0) to POM(I) to POM(II) layer. This observation is correlated with an increase of negative charges at the POM/surface interface upon UV light irradiation while the positive charges (TBA cations) tend to lie on the outmost POM surface to ensure the electroneutrality.

To go further in the electrical characterizations, measurements were carried out on a Ψ-MOSFET configuration using POM-functionalized SOI substrates. An effect of the POM multilayer under UV irradiation on the SOI conductance was witnessed, however indivisible from the effect of the bare substrate. The UV irradiation with the Hg lamp induces negative surface charges but most of all surface states at the buried interface which affects the conduction channel, such that the effect of the POM at the top surface is negligible. The Hg lamp was thus found to be too powerful and not adapted for the SOI conductance modulation under UV irradiation. Preliminary tests on KPFM using a LED are found promising in removing the effect of bare SOI under UV irradiation. Investigation is thus required to study the effective reduction of the POM by the LED.

The apparent photoreduction observed on POM monolayer by KPFM could be due to the NH_3^+ groups brought by the organic monolayer. However, in the case of POM(0) multilayers on quartz substrates, a photoreduction is observed even when traces of solvent were removed prior to POM deposition. No electron is apparently provided by the substrate and the photoreduction mechanism remains unclear. More investigations are required to solve the photoreduction mechanism.

In order to have a better control of the POM/surface interaction, the covalent route was also explored with several POM hybrids, on functionalized, hydrogenated, or oxidized Si surfaces. Accordingly, several attempts were carried out. On the activated SiCOOH surface, the POM grafting with $K^{W}_{Si}[(NH_2)_2]$ was more satisfying than $K^{W}_{Sn}[NH_2]$, probably because more NH_2 functions are available for reacting with the surface. Attempts to synthesize $K^{W}_{Si}[(N{=}PPh_3)_2]$ were carried out but doubts still remain on the exact product formed. The grafting of POM-allyl onto hydrogenated Si surface was satisfying but more experimental data are required for a better consistency between the IR and XPS spectra. Finally, the covalent grafting of $K^{W}_{Sn}[COOH]$ and $K^{W}_{Si}[COOH]$ on Si/SiO_2 surface provides insights in the electrical properties of the POM in solid state in relation to the nature of the POM and to the POM/substrate interaction.

Appendices

Appendix 1. Techniques

Appendix 1.1. Ellipsometry

Ellipsometry measurements were carried out using a monowavelength SENTECH SE 400 ellipsometer at an incident angle of 70° and equipped with a 632.8 nm He-Ne laser. The values ns = 3.875 and ks = 0.018 for the optical constants of the silicon substrate were taken. Depending on the layer on the substrate, the optical constants were added to the model and they are listed in the table below:

Optical constants	ns	ks
SiO_2	1.48	0
Organic layer	1.50	0
POM layer	1.48	0

The thickness was measured on five to six area of the surface to check its homogeneity.

Due to a breakdown, few measurements were carried out on a V-VASE spectroscopic ellipsometer from J. A. Woollam Co., Inc. (and are specified in the text). The substrate was positioned thanks to a vacuum system. The scan was performed from 350 to 900 nm (steps of 10 nm) at an incidence angle of 75°. During the measurements, the complex reflectance ratio ρ is measured and is defined as $\rho = \frac{r_p}{r_s} = \tan\Psi e^{i\Delta}$, where r_p and r_s are the reflection coefficients of p and s polarized light, respectively, tanΨ is the amplitude ratio and Δ is the phase difference between the p and s polarizations. Experimental curves Ψ(λ) and Δ(λ) are obtained and fitted by a WVASE32 software with a model of stacked layers defined by the user.

Appendix 1.2. Nuclear Magnetic Resonance (NMR) spectroscopy

^{1}H and ^{31}P NMR spectra were recorded in a 400 MHz Bruker Nanobay spectrometer equipped with a BBFO probe, and using 5 mm diameter NMR tubes.

Appendix 1.3. IR spectroscopy

To follow the Si surface modifications, a Bruker Tensor 27 FTIR spectrometer, equipped with a L-alanine doped triglycine sulfate (DLaTGS) thermodetector and KBr beam splitter, was used. The spectrometer is connected to a dryer (SDAT from Specken Drumag) that dries the compressed air before entering the spectrometer. After the sample positioning, three consecutive spectra of the surface are recorded between 4000 and 800 cm^{-1} at a resolution of 4 cm^{-1} after a waiting time of 13 minutes. The IR absorption spectra are recorded in transmission at an incident angle of 70°, with a number of scans set at 500.

The attenuated total reflection (ATR) FTIR spectroscopy was used to record the IR spectrum of liquid compounds (such as ethylenediamine) using a Bruker Tensor 27 FTIR spectrometer.

For the powder compounds analysis, the IR spectra were recorded on KBr pellets in a JASCO FT/IR – 4100 spectrometer, between 4000 and 250 cm^{-1}, with a resolution of 4 cm^{-1}.

Appendix 1.4. X-ray photoelectron spectroscopy (XPS)

XPS analyses were performed using an Omicron Argus X-ray photoelectron spectrometer, equipped with a monochromated AlKα radiation source (hν = 1486.6 eV) and a 280 W electron beam power. The emission of photoelectrons from the sample was analyzed at a takeoff angle of 45° under ultra-high vacuum conditions ($\leq 10^{-9}$ mBar). Spectra were carried out with a 100 eV pass energy for the survey scan and 20 eV pass energy for the C 1s, O 1s, N 1s, Si 2p, Mo 3d, W 4f, P 2p, P 2s regions. Binding energies were calibrated against the Si 2p binding energy at 99.4 eV for the functionalized Si samples, or against the C 1s (C-C) binding energy at 284.8 eV otherwise, and element peak intensities were corrected by Scofield factors. The peak areas were determined after subtraction of a Shirley background. The spectra were fitted using Casa XPS v.2.3.18PR1.0 software (Casa Software Ltd, U.K.).

Appendix 1.5. UV-Vis-NIR spectroscopy

The modified quartz discs are characterized using a JASCO V-750 spectrophotometer equipped with a film holder accessory. The absorbance spectra are recorded between 190 and 900 nm.

The modified Si substrates are characterized using a JASCO V-750 spectrophotometer equipped with a UV-Vis VeeMAX variable angle specular reflectance accessory. The absorbance spectra are recorded between 190 and 900 nm, at a reflection angle of ~45°.

UV-Vis-NIR spectra of POMs in solution were recorded on an Agilent Cary 5000 series UV-Vis-NIR spectrophotometer from 1200 to 200 nm.

Appendix 1.6. Kelvin Probe Force Microscopy (KPFM)

For the modified Si samples, a Bruker Multimode 8 AFM, equipped with a KPFM module is used. The sample is mounted onto a sample holder: it consists of a magnetic metallic disc where a standard silicon substrate sits on top of it. A small metallic wire (stainless steel) ensures the contact and presses the sample mounted on top of the standard silicon substrate. The tips used for KPFM measurements are SCM-PIT-V2 probes from Bruker (resonance frequency f_0 = 75 kHz, cantilever spring constant k = 3 N/m, tip radius of 25 nm), made of silicon and covered with a Pt-Ir conductive coating. Prior to the measurements, the tip is always calibrated with the reference PFKPFM-SMPL substrate from Bruker. During the POM-containing surface scanning, the lift scan height is set at 60 nm.

For the very last measurements, a Park Systems NX20 AFM was used with PPP-EFM probes from Park Systems (resonance frequency 75 kHz, force constant 2.8 N/m, mean width 28 µm, PtIr5 coating).

Appendix 2. Supplementary information regarding Chapter II

Appendix 2.1. IR and XPS spectra obtained at Dallas

The SiH spectrum was referenced to the SiO_2 spectrum (red), while the Siester (blue), SiCOOH (green) and $SiNH_2$ (orange) spectra were all referenced to the SiH spectrum.

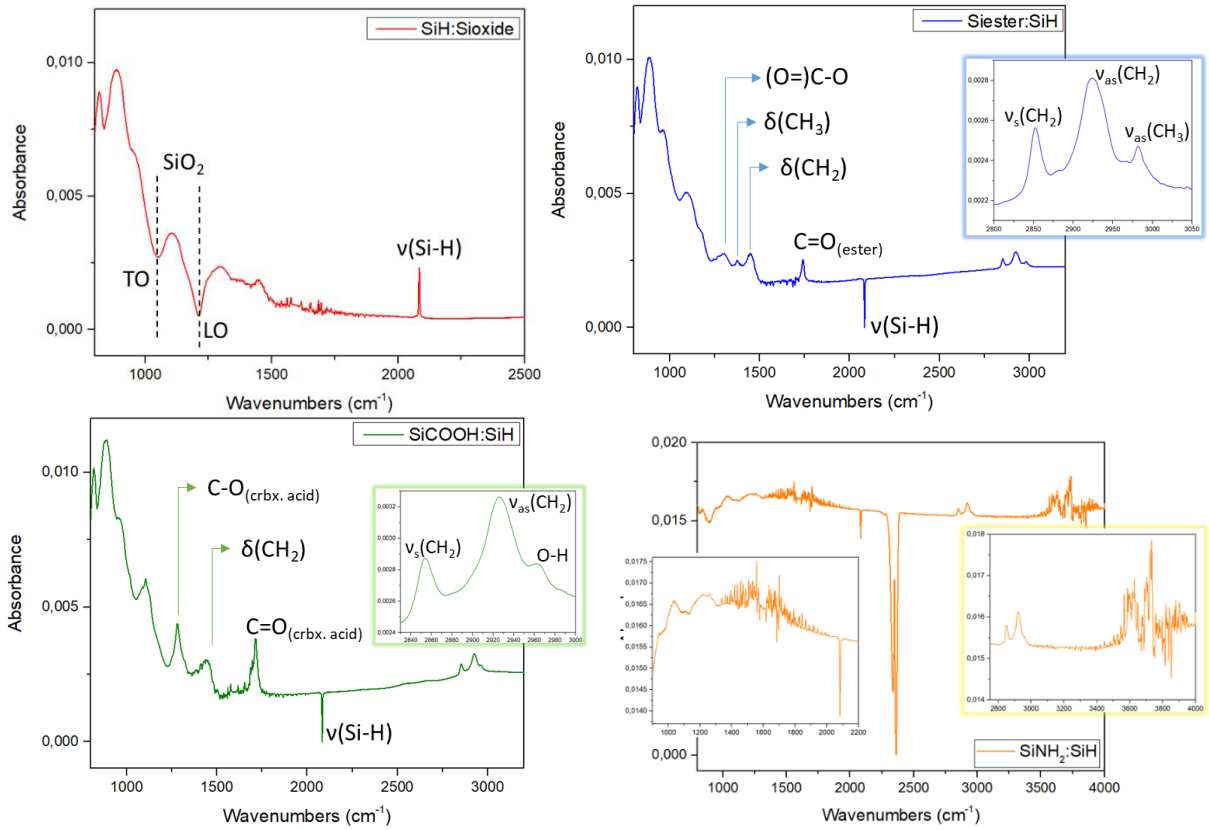

Baselines were not flat due to a different positioning of the substrate between each step. All spectra were recorded inside a N_2-purged glove box, except for the $SiNH_2$ spectrum that was recorded in N_2-purged spectrometer outside the glovebox, which results in a noisy $SiNH_2$/SiH differential spectrum. All the bands for SiH, Siester and SiCOOH were observed.

The XPS spectra (Si 2p, C 1s and O 1s regions) of a SiCOOH surface are shown below. The Si 2p region reveals only a small quantity of oxide (2.5%) as suggested by the component at 103 eV after the peak decomposition.

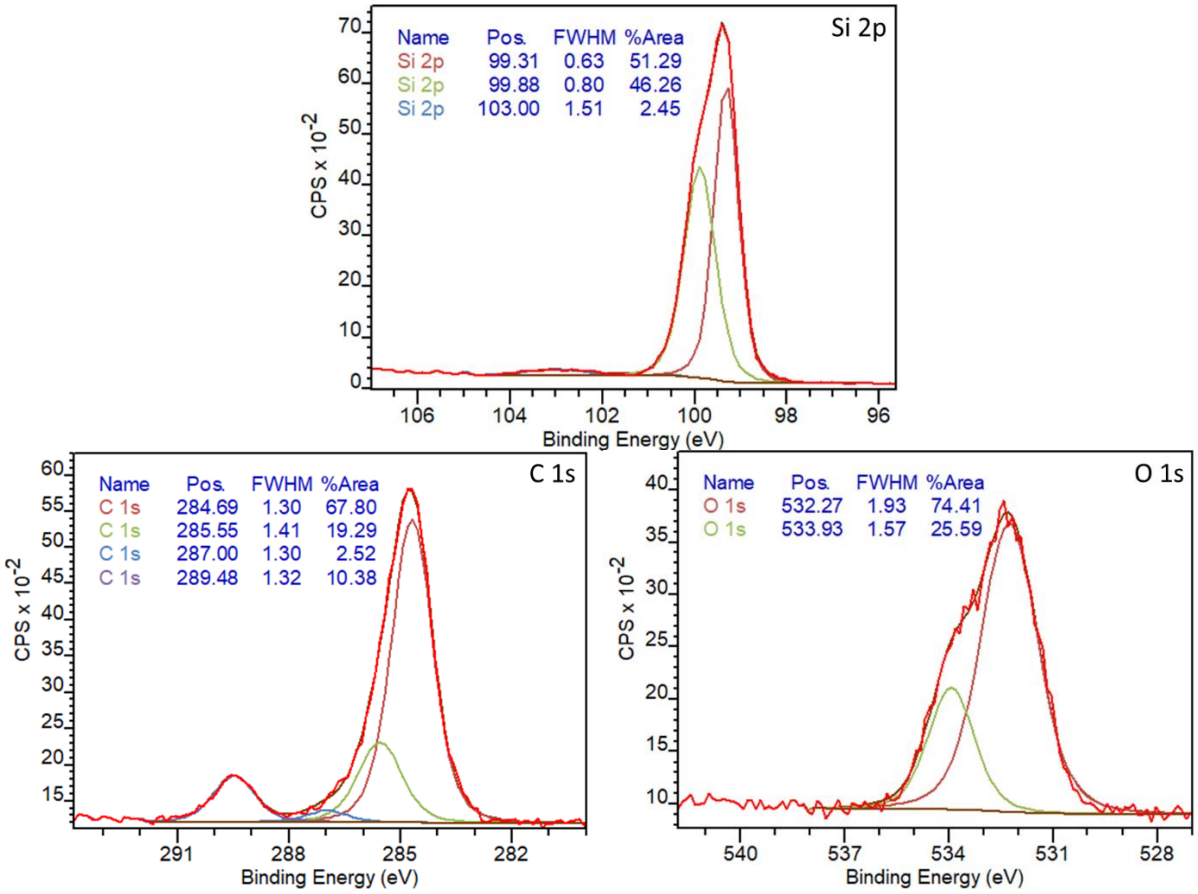
Si 2p
Name Pos. FWHM %Area
Si 2p 99.31 0.63 51.29
Si 2p 99.88 0.80 46.26
Si 2p 103.00 1.51 2.45
CPS x 10-2
Binding Energy (eV)
C 1s
Name Pos. FWHM %Area
C 1s 284.69 1.30 67.80
C 1s 285.55 1.41 19.29
C 1s 287.00 1.30 2.52
C 1s 289.48 1.32 10.38
CPS x 10-2
Binding Energy (eV)
O 1s
Name Pos. FWHM %Area
O 1s 532.27 1.93 74.41
O 1s 533.93 1.57 25.59
CPS x 10-2
Binding Energy (eV)

Appendix 2.2. Raw and corrected IR spectra

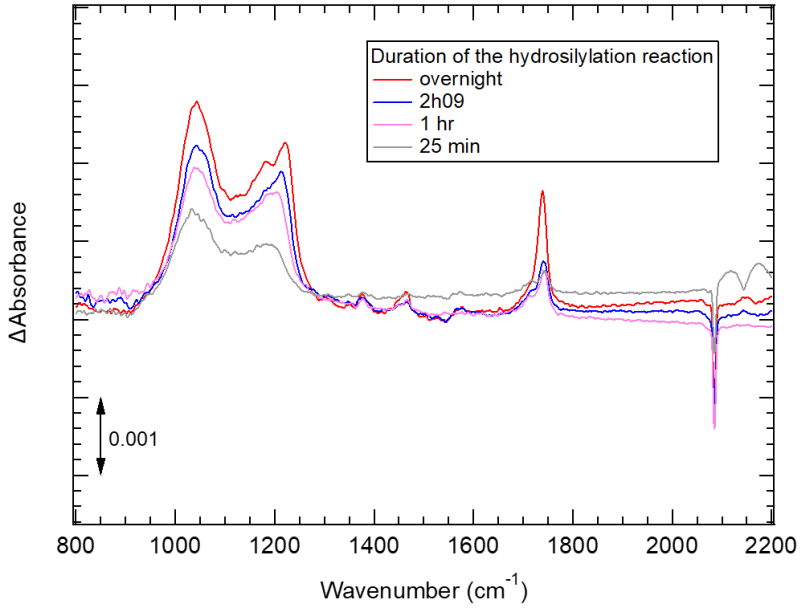

"Raw" Siester/SiH differential spectra obtained on Sil'tronix Si surface after an overnight, 2h09, 1 hour and 25 minutes hydrosilylation in a 1-alkene not distilled before use.

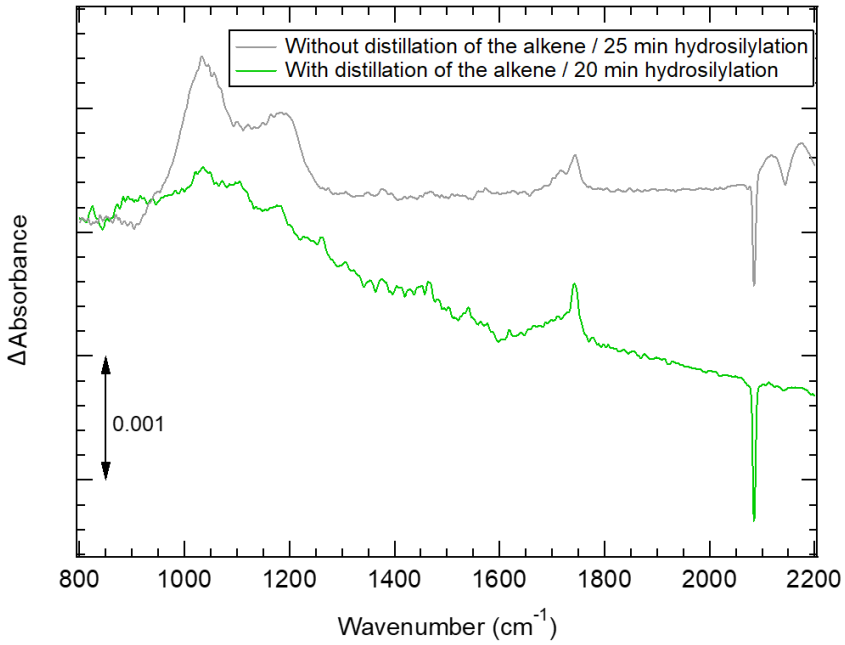

"Raw" Siester/SiH differential spectra obtained after 20-25 minutes hydrosilylation reaction using a 1-alkene used as received in one case, and distilled under vacuum before use in the other case.

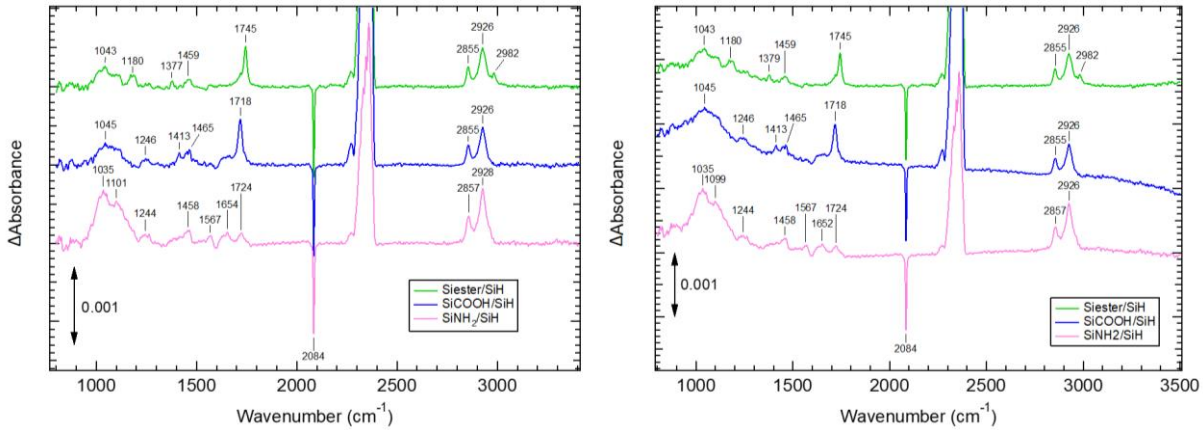

Corrected (left) and raw (right) spectra for the final experiment after choosing the best parameters for each step on Si(111) Sil'tronix substrate

Appendix 2.3. IR spectrum of ethylenediamine

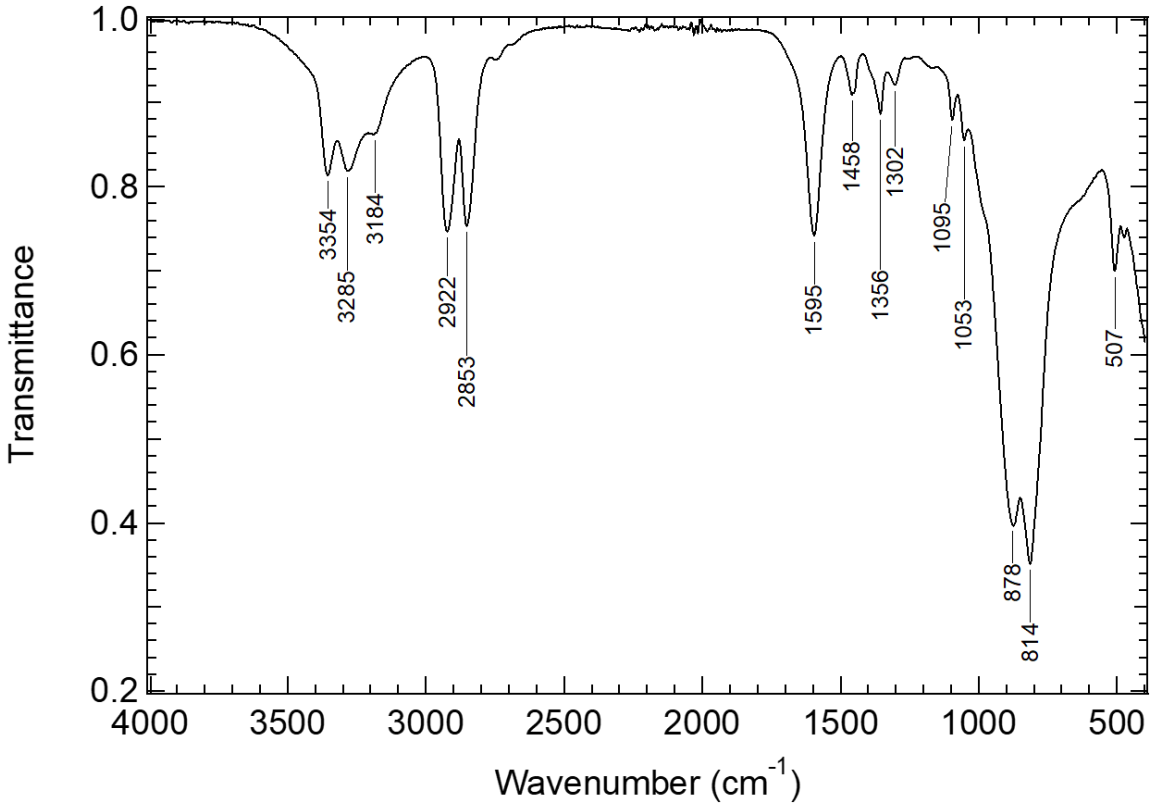

Appendix 3. Supplementary information regarding Chapter III

Appendix 3.1. IR spectrum of $K^{W}_{Sn}[(NH_2)_2]$

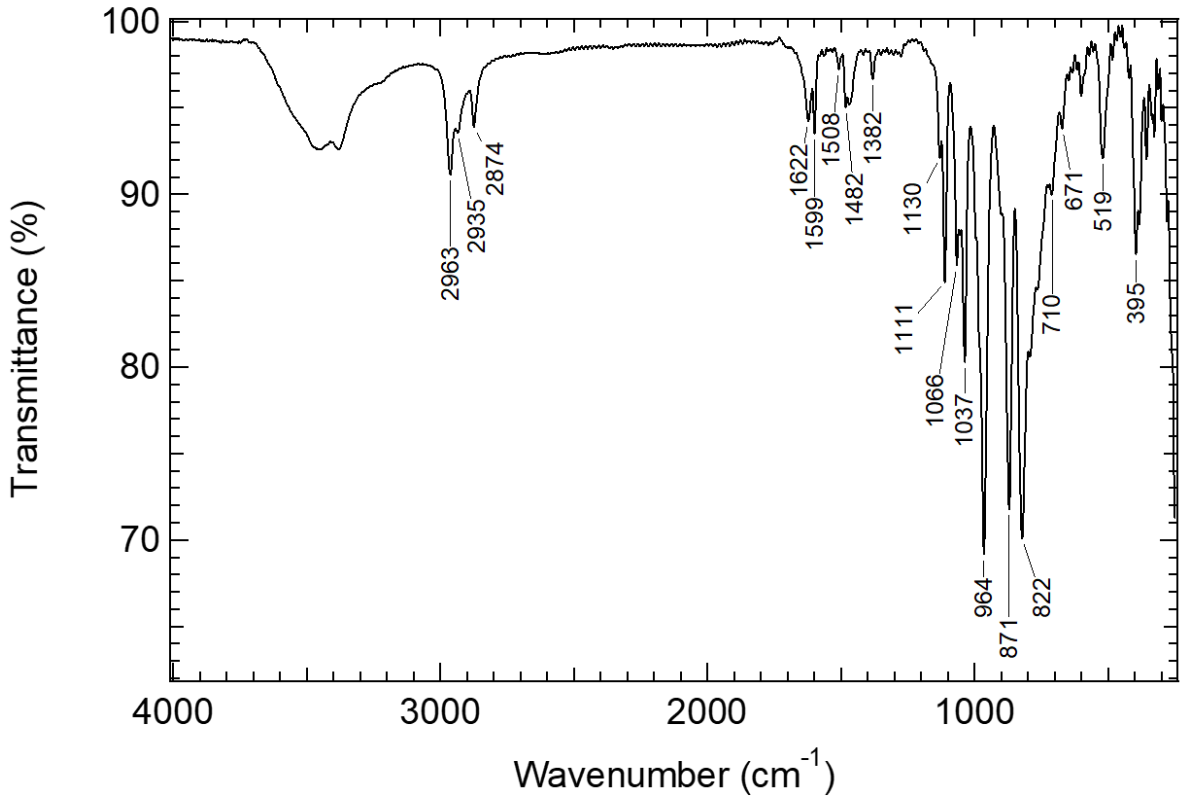

Appendix 3.2. ^{1}H and ^{31}P NMR spectra of PPh_3 in DMSO-d6

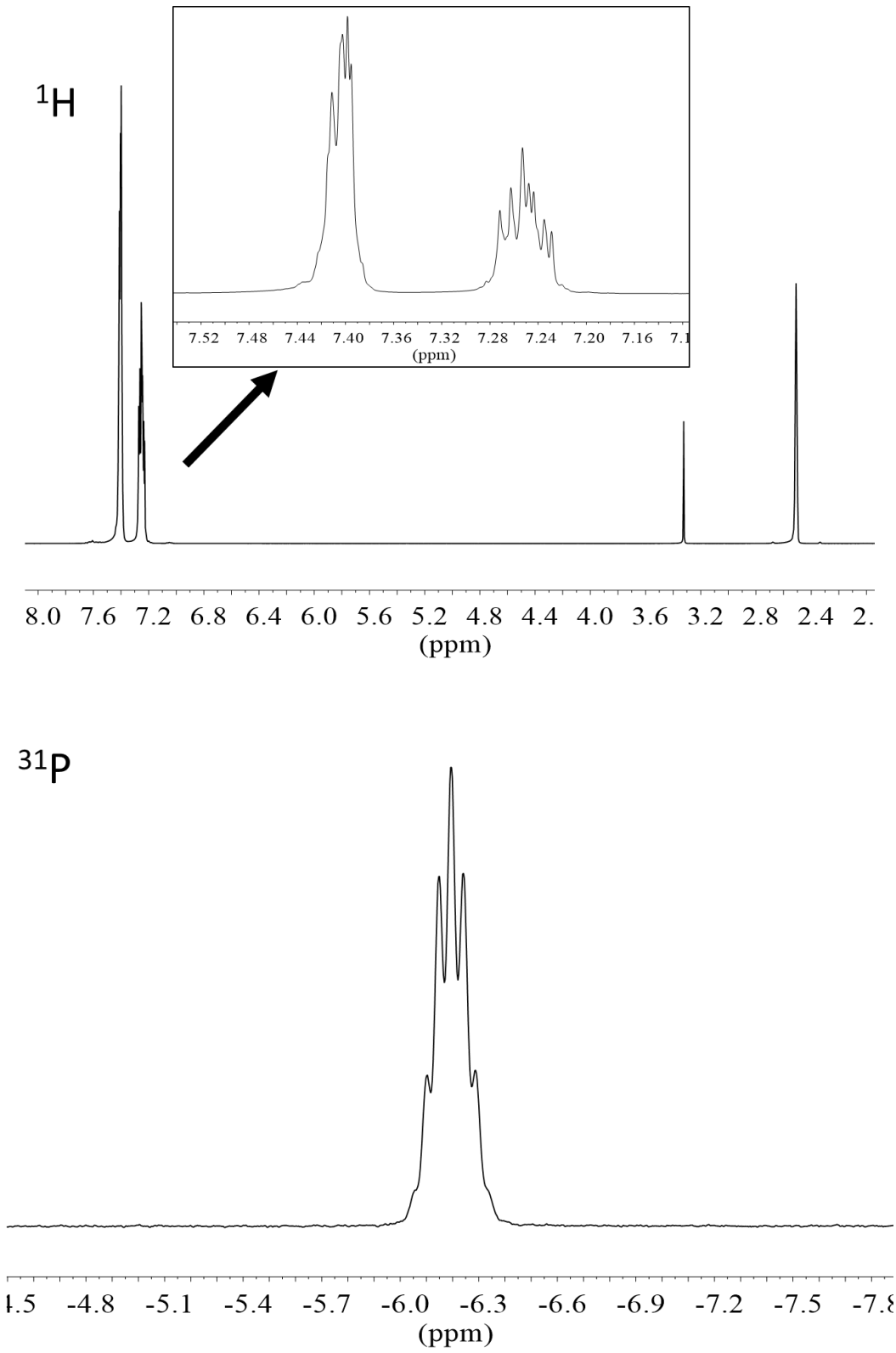

Appendix 3.3. ^{1}H and ^{31}P NMR spectra of $O=PPh_3$ in DMSO-d6

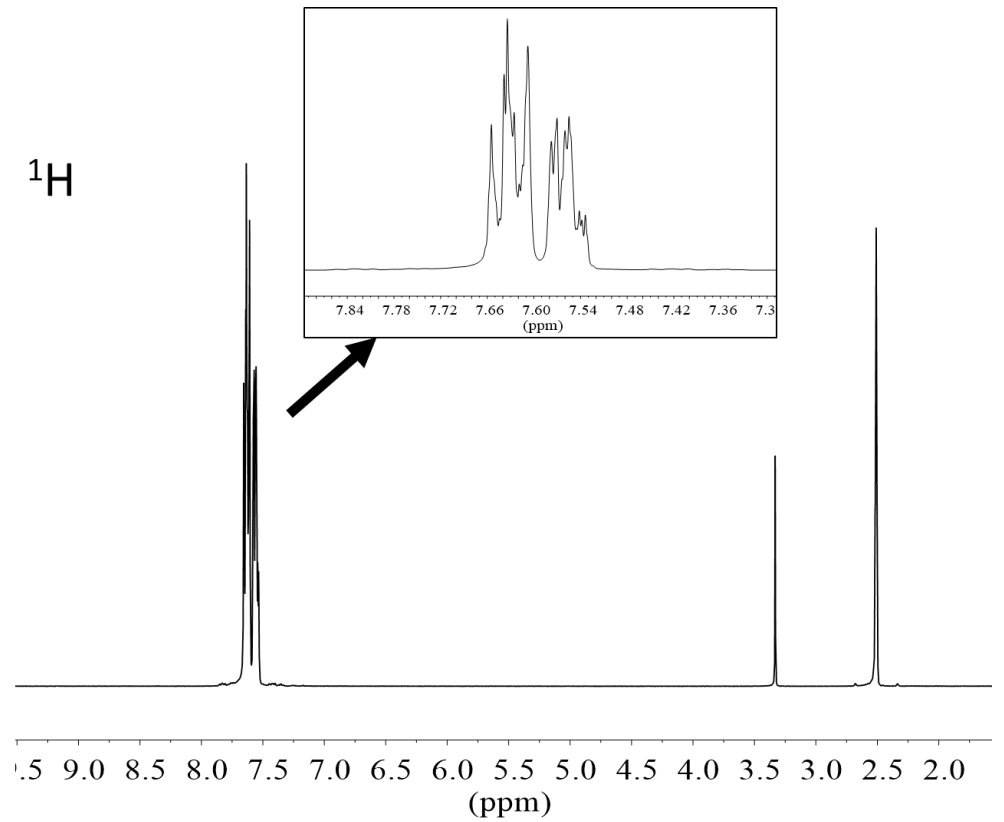

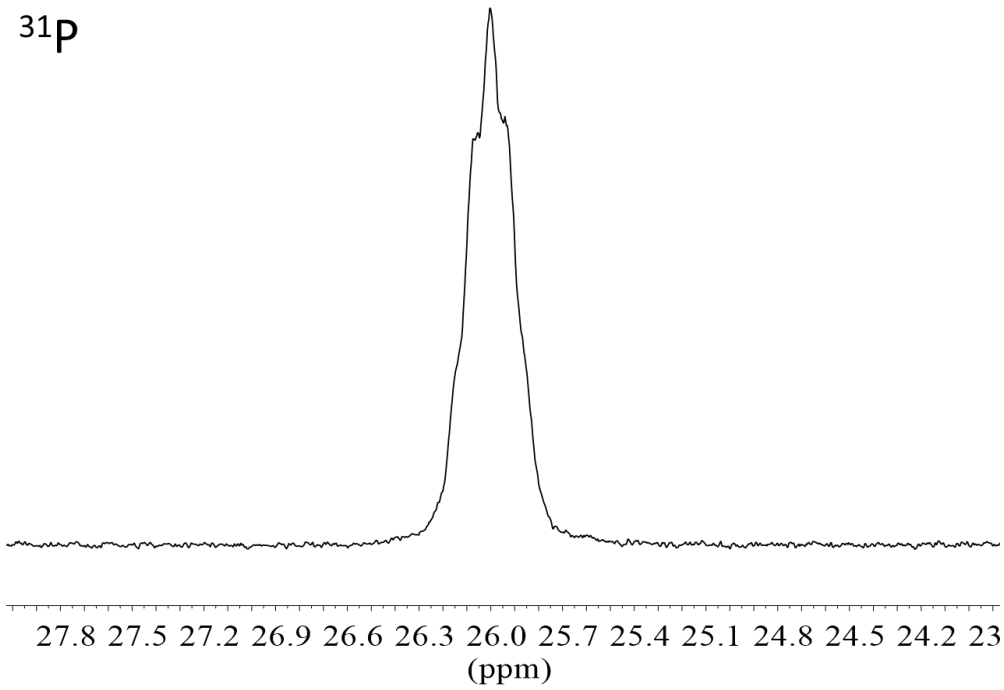

Appendix 3.4. ^{1}H and ^{31}P NMR spectra of PPh_3 in CD_3CN

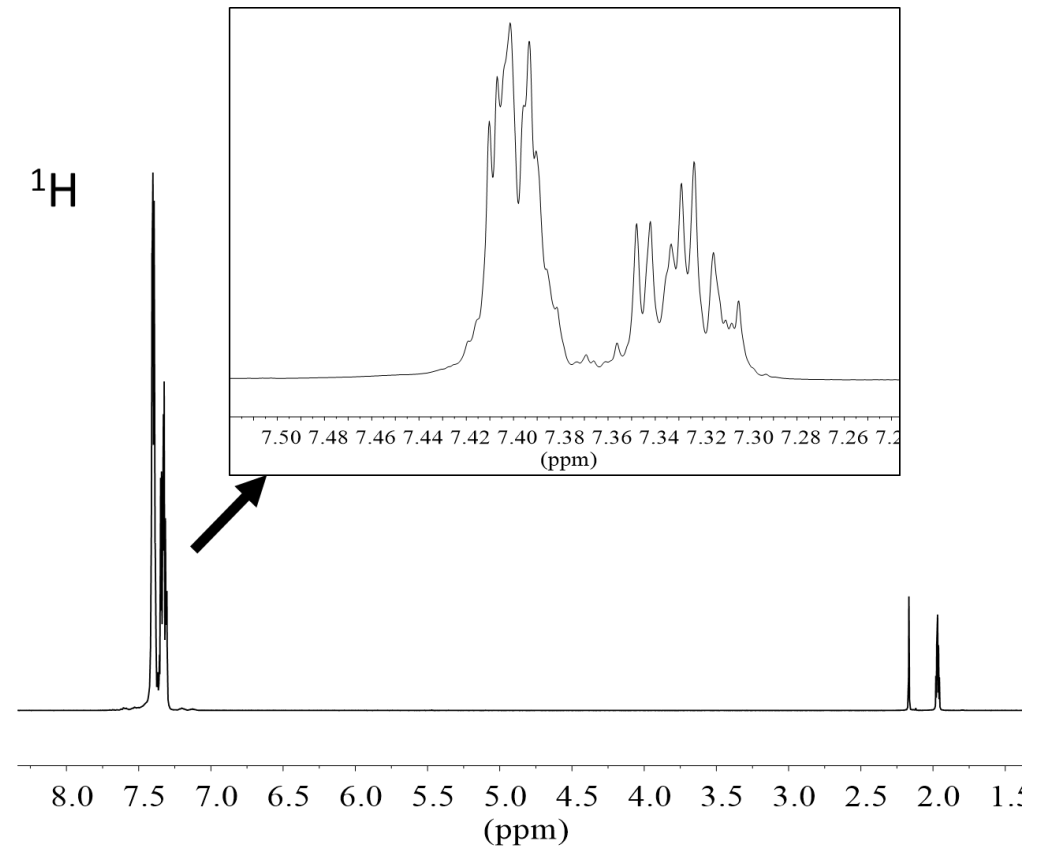

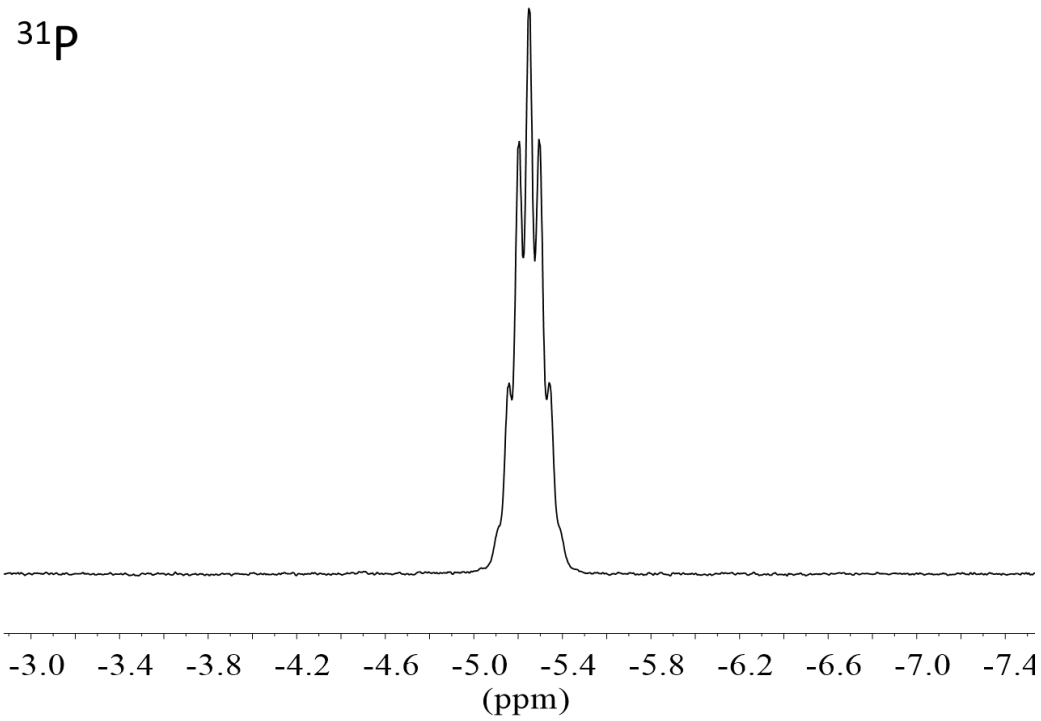

Appendix 3.5. ^{1}H and ^{31}P NMR spectra of $O=PPh_3$ in CD_3CN

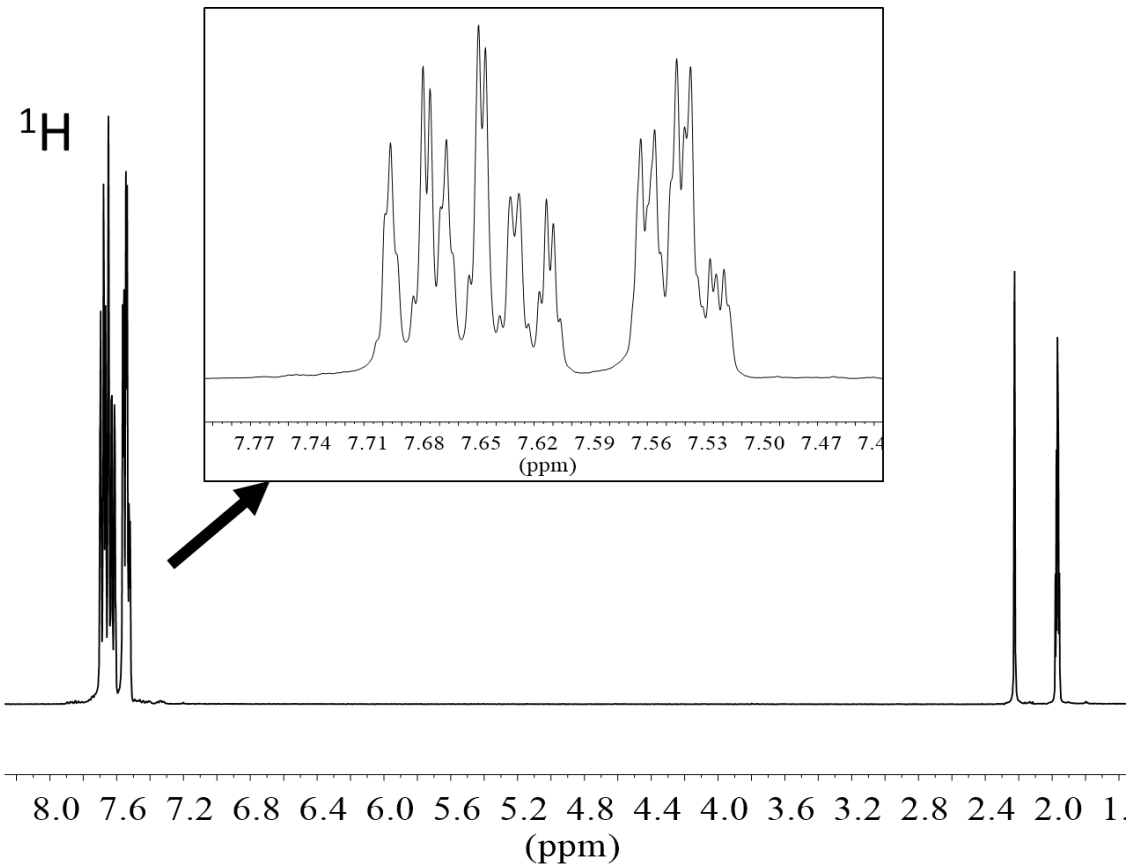

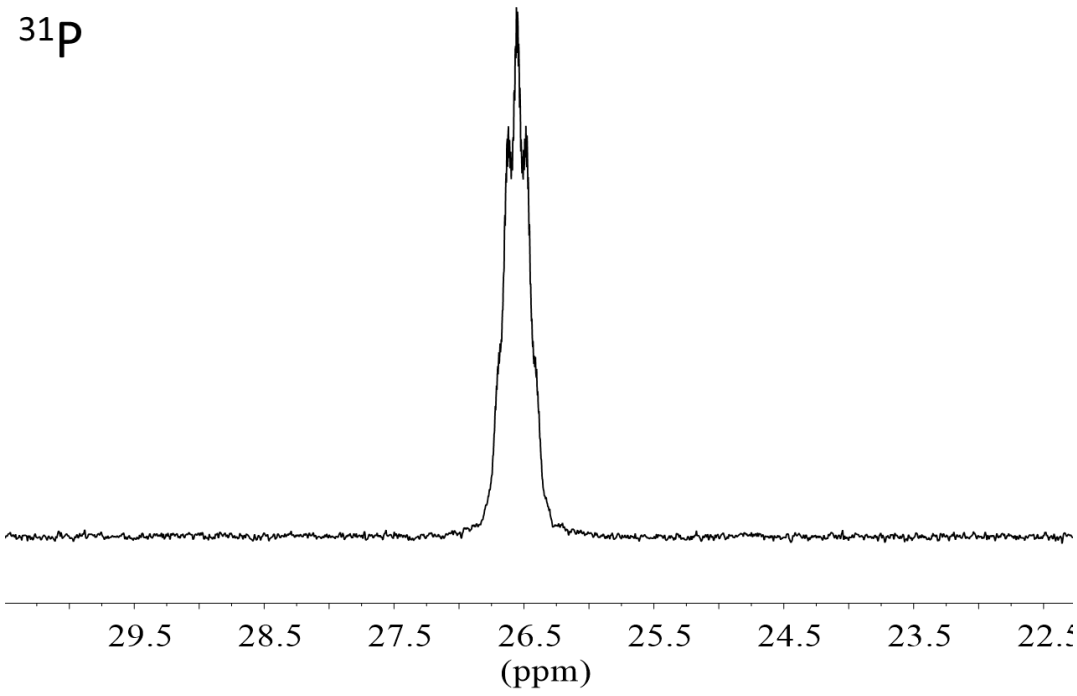

Appendix 4. Supplementary information regarding Chapter IV

Appendix 4.1. Electronic levels in semiconductor materials

The energy diagram of a semiconductor surface with no charge on the surface is shown below.[1]

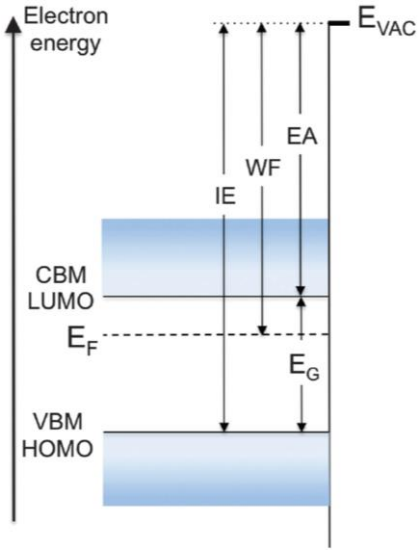

Energy diagram of a semiconductor surface[1]

Conduction and valence bands are represented in blue. The bottom of the conduction band is called conduction band minimum (CBM) in the case of inorganic semiconductor, or lowest unoccupied molecular orbitals (LUMO) in the case of organic semiconductor. On the contrary, the highest level of the valence band is called valence band maximum (VBM) in the case of inorganic semiconductor, or higher occupied molecular orbitals (HOMO) in the case of organic semiconductor. The difference energy between these two levels is called the gap energy E_G. It corresponds to the energy required to generate an electron-hole pair in the semiconductor.

E_{VAC} represents the vacuum level. At this level, the electrons just escaped the semiconductor material surface and are characterized with a null kinetic energy.

In the semiconductor material, electrons are found in the valence band. The ionization energy (IE) is thus defined as the minimum energy required to remove an electron from the material. On the other hand, the electron affinity (EA) can be defined as the energy brought by the electron as it travels from the vacuum level to the CBM/LUMO level.

The work function (WF) is the energy required to remove an electron from the Fermi level (E_F) to a point just outside the material.

Appendix 4.2. Work function (in eV) of POM(0), POM(I) and POM(II) monolayers on $SiNH_2$ surfaces obtained over the KPFM measurements

The work function ϕ (in eV) were calculated from V_{CPD} measured by KPFM after calibration of the tip with a commercial sample. Here, the red values correspond to ϕ measured **right before** UV irradiation. The duration indicated is the time passed after the Hg lamp switched off.

Substrate	**$SiNH_2$-POM(0)**			**$SiNH_2$-POM(II)**	**$SiNH_2$-POM(I)**		**$SiNH_2$**	
Area		**Area #1**	**Area #2**		**Area #1**	**Area #2**	**Area #1**	
	5µm²	5µm²	5µm²	5µm²	5µm²	5µm²	5µm²	**1µm²**
$SiNH_2$	4.07-**4.12**	x	x	4.12-4.07	4.10-**4.14**	x	4.21-**4.28**	**4.28**
$SiNH_2$+UV	x	x	x	x	x	x	4.28	4.32
$SiNH_2$+UV stops	x	x	x	x	x	x	4.28 (~44min)	4.29 eV (~40min)
Si-POM(X)	4.17-4.15 **4.16**	4.16-**4.17**	**4.19**	4.06-**4.12**	4.03-4.07 **4.04**	**4.18**	x	
Si-POM(X)+UV	4.13	4.14	4.15	3.96	3.97	4.11	x	
UV stops	4.13 (~35min)	4.19 (~50min)	4.18 (~35min)	4.14 (~18min)	4.08 (~42min)	4.13	x	
$\Delta\phi_{tip}$, before and after $SiNH_2$ surface scanning	0.13	x	x	0.09	0.08	x	x	
$\Delta\phi_{tip}$, before and after {POM deposition **and** UV irradiation}	0.06	x		0.01	0.08	x	x	
$\Delta\phi_{tip}$, before and after UV irradiation	x	0.04		x	x	0.12	0.01	

Appendix 4.3. Work function (in eV) of POM(0), POM(I) and POM(II) multilayers on Si-SiO_2 surfaces obtained over the KPFM measurements

The work function ϕ (in eV) were calculated from V_{CPD} measured by KPFM after calibration of the tip with a commercial sample. Here, the red values correspond to ϕ measured **right before** UV irradiation. The letters A, B, C represent the different aggregates scanned on one image. The duration indicated is the time passed after the Hg lamp switched off.

Substrate		**Si-SiO_2-POM(0)**		**Si-SiO_2-POM(I)**		**Si-SiO_2-POM(II)**		**Si-SiO_2**	
		$\phi_{surface}$	**ϕ_{agg}**	**$\phi_{surface}$**	**ϕ_{agg}**	**$\phi_{surface}$**	**ϕ_{agg}**	**$\phi_{surface}$** **Cycle #1**	**$\phi_{surface}$** **Cycle #2**
Work function ϕ		**4.36**	x	**4.22**	x	**4.32**	x	4.36-**4.29**	~**4.47**
Si-SiO_2 (5 µm²)		4.46-**4.36**	x	4.18-**4.22**	x	4.37-**4.32**	x	**4.18**	**4.35**
Si-SiO_2 + UV		x	x	x	x	x	x	x	x
Si-SiO_2-POM(X)	Image #1	4.39	4.48	4.14	4.08	4.02	3.77		
	Image #2	**4.43**	**4.52**	**4.20**	**A : 4.18** **B : 4.19** **C : 4.23**	**4.00**	**A : 3.89** **B : 3.93**		
Si-SiO_2-POM(X) + UV		**4.29**	**4.30**	**4.04**	**B : 4.09** **C : 4.09**	x	**B : 3.92**	x	x
UV stops		**4.20** (~1h25)	**4.28**	**3.93** (~2h05)	**A : 4.13** **B : 4.14** **C : 4.20**	**3.80** (~1h20)	**B : 4.15**	**4.16** (~40 min)	**4.32** (~20 min)
$\Delta\phi_{tip}$, before and after Si-SiO_2 surface scanning		0.18		0.07		-0.40		x	x
$\Delta\phi_{tip}$, before and after {POM deposition **and** UV irradiation}		0.32		0.48		0.32		x	x
$\Delta\phi_{tip}$, before and after UV irradiation		x		x		x		-0.22	0.25

Appendix 4.4. I_D-V_{BG} curves on unfunctionalized and functionalized SOI substrates, before, under and after UV irradiation

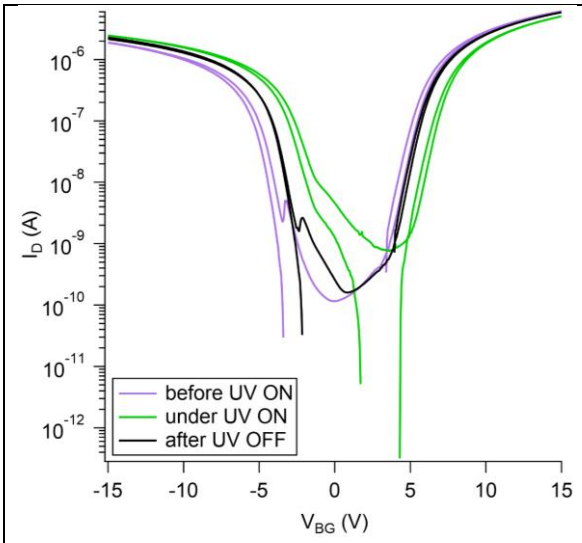

SOI-SiO_2 substrate

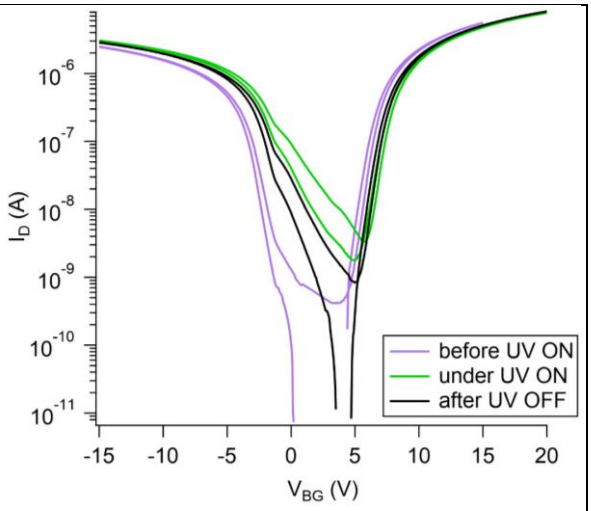

SOI-SiO2-POM(0)

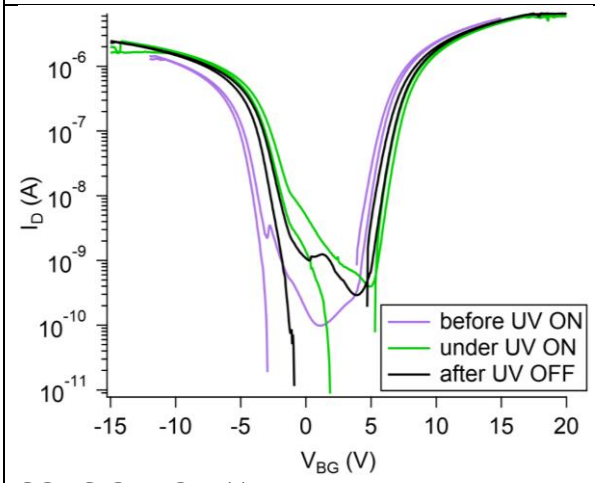

SOI-SiO_2-POM(I)

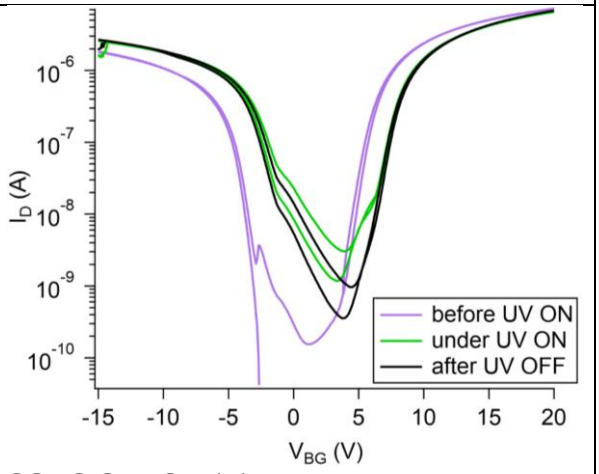

SOI-SiO_2-POM(II)

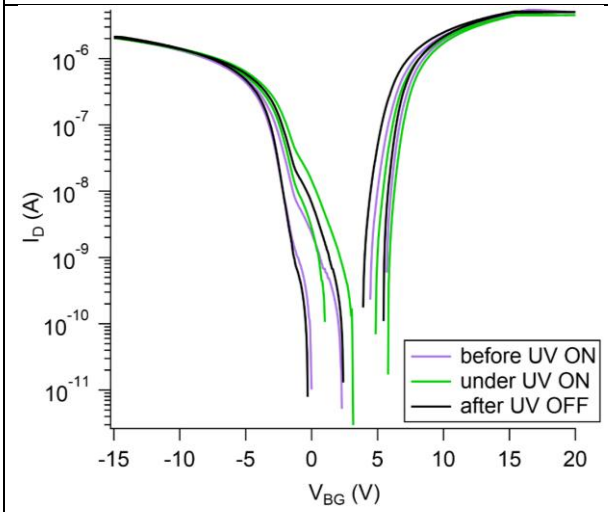

SOI-NH_2-POM(0)

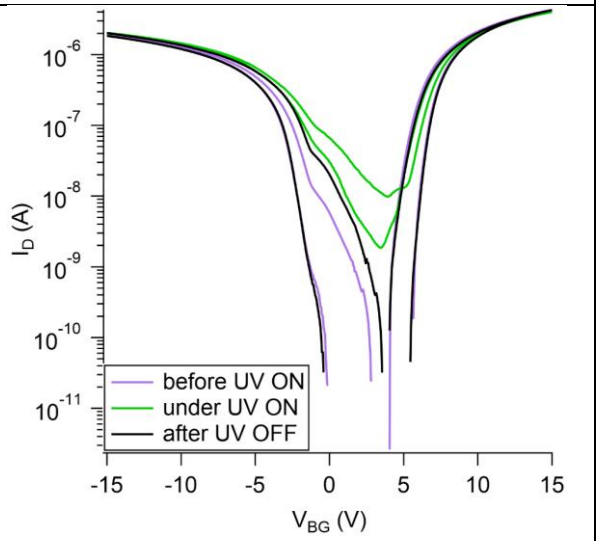

SOI-NH_2-POM(I)

In the case of SOI-ester substrate, the I_D-V_{BG} and g_m-V_{BG} curves are shown below:

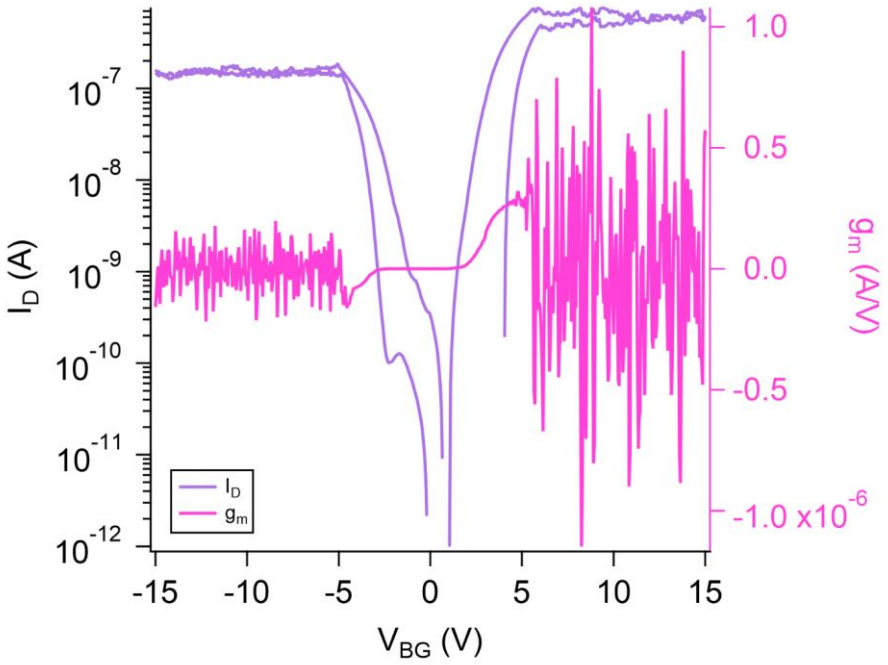

To understand the issue with this substrate, let us compare the drain current (I_D), back gate current (I_{BG}) and source current (I_S) measured at several back gate voltages (V_{BG}) in intervals of 10.0 V (forward bias) on the SOI-SiO_2 sample and on the SOI-ester sample, which are reported in Table 7 and Table 8, respectively. In an ideal case, the induced current in the Ψ-MOSFET only flows between the source and drain, such that the drain current and source current are supposed to be equal but with opposite signs. Also, no current should travel between the source and the back gate nor between the drain and the back gate. However, in practice the back gate current does not equal zero. In the case of the SOI-SiO_2 device (Table 7), for which the I_D-V_{BG} curve is reported above (before UV ON), the drain and source currents are in the same order of magnitude and almost equal. The back gate current is 3 to 4 order of magnitude lower than I_D and I_S, and is thus considered as negligible. On the contrary, in the case of the SOI-ester sample (Table 8), the back gate current is in the same order of magnitude as the drain current. It is even one order of magnitude higher than the source current for the negative back gate voltages, suggesting a current leakage through the BOX. The BOX was probably damaged due to the double baths in HF solution prior to hydrosilylation.

V_{BG}	I_D	I_{BG}	I_S
-15.0	1.88444E-06	-1.73121E-10	-1.88387E-06
-5.0	4.7223E-08	1.3547E-11	-4.72329E-08
5.0	7.39865E-08	8.8433E-11	-7.41096E-08
15.0	6.13229E-06	1.19263E-10	-6.13224E-06

Table 7 : Drain current (I_D), back gate current (I_{BG}) and source current (I_S) measured at several back gate voltages (V_{BG}) in intervals of 10.0 V (forward bias), on the SOI-SiO_2 sample.

V_{BG}	I_D	I_{BG}	I_S
-15.0	1.61407E-07	-1.000012E-07	-6.0957E-08
-5.0	1.36706E-07	-1.000003E-07	-3.47417E-08
5.0	5.58094E-07	7.38703E-08	-6.31728E-07
15.0	5.89367E-07	1.000025E-07	-6.97352E-07

Table 8 : Drain current (I_D), back gate current (I_{BG}) and source current (I_S) measured at several back gate voltages (V_{BG}) in intervals of 10.0 V (forward bias), on the SOI-ester sample.

Appendix 4.5. POM(0) and POM(I) monolayer on SOI-NH_2 surfaces: ΔV_{FB} and ΔV_{Th} variation under UV irradiation

In the case of the POM monolayer devices, ΔV_{FB} and ΔV_{Th} variations are less clear than for the POM multilayer counterparts. Indeed, ΔV_{FB} variation does not follow the variation of ΔV_{Th}.

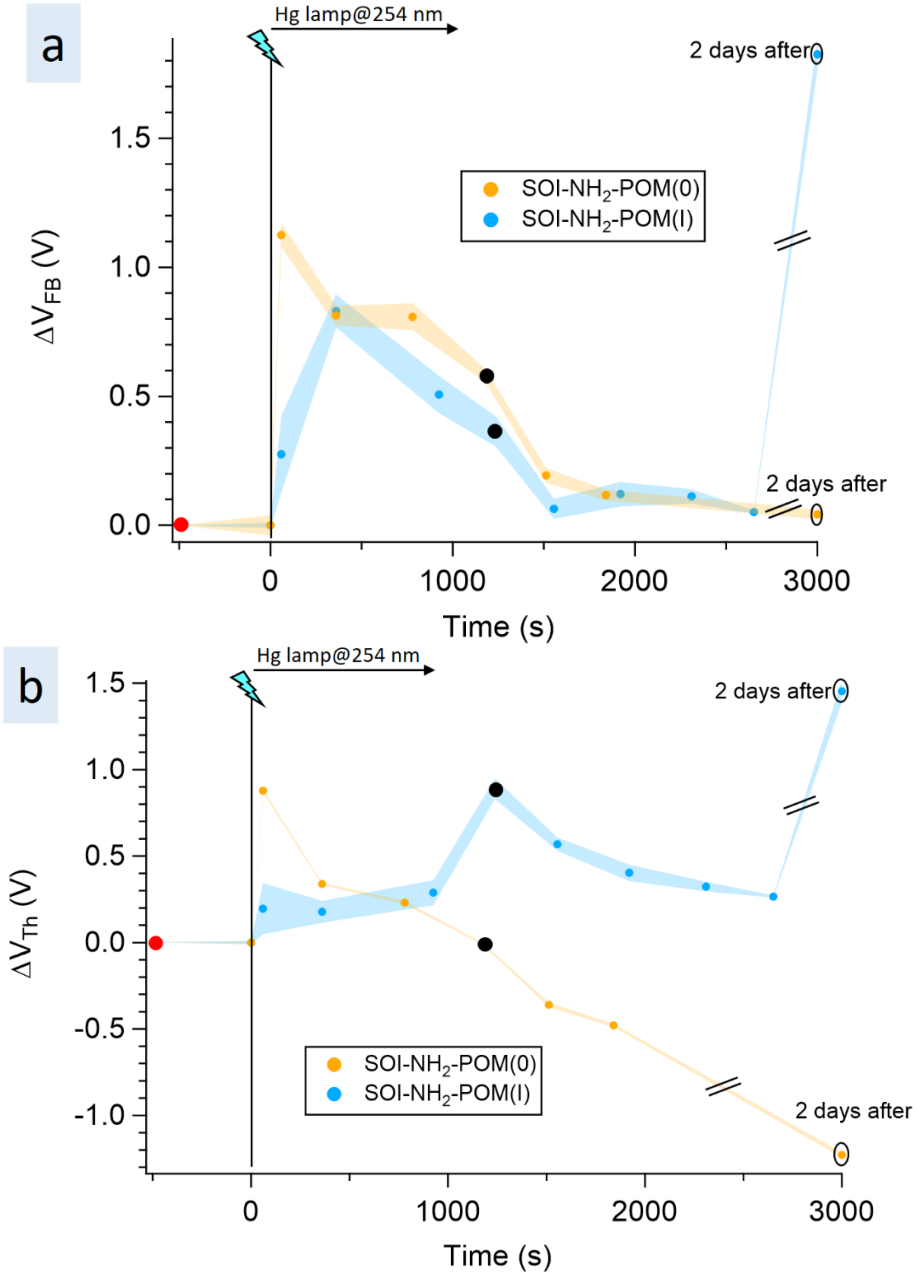

Figure 58 : a) ΔV_{FB} variation and b) ΔV_{Th} variation during the experiment in the case of SOI-NH_2 substrates with POM(0) and POM(I) monolayer. The red closed circle corresponds to the extracted parameters before UV irradiation. The Hg lamp (λ=254 nm) is switched on at t=0 s and several I_D-V_{BG} curves are recorded during 10-15 minutes. The black closed circles correspond to the extracted parameters right after the UV lamp is switched off and last I_D-V_{BG} curves are recorded.

Appendix 4.6. I_D=f(time) obtained on bare SOI, SOI-SiO_2, SOI-NH_2-POM(0) and SOI-NH_2-POM(I) devices in weak and strong inversion regime

The drain current variations at V_{BG} in the weak inversion regime and in the strong inversion regime are shown in Figure 59 and Figure 60, respectively.

The drain current variation at V_{BG} = 11 V can be explained by the photoreduction of the POM. Indeed, if more electrons are present at the surface due to the POM photoreduction, the channel of electrons at the top Si film/BOX interface will be more difficult to induce. To compensate the negative surface charge and to easier create a channel of electrons, the solution is to increase V_{BG}. Here, as V_{BG} is fixed, the more there are electrons on the surface, the more it is difficult to generate an electron channel. Under UV irradiation, a higher decrease in drain current is observed on SOI-NH_2-POM(0) substrate than on SOI-NH_2-POM(I) substrate, meaning that POM(0) is more reduced by UV irradiation than POM(I). When looking at both bare SOI and SOI-SiO_2 reference substrates, UV irradiation on these substrates also decreases their drain current, which supports that the negative surface charging makes the generation of electrons channel more difficult.

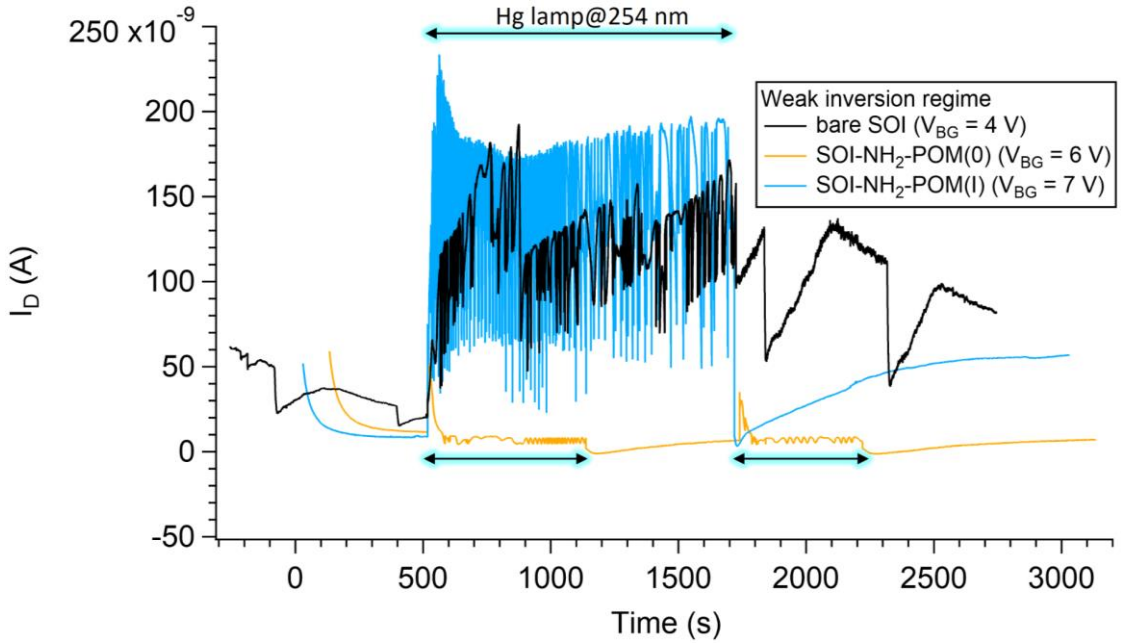

Figure 59 : I_D=f(time) at V_{BG} in the weak inversion regime of the Ψ-MOSFET. For the bare SOI and SOI-NH_2-POM(I) devices, UV lamp was switched on at ~500 s on the figure and switched off at ~1700 s. In the case of SOI-NH_2-POM(0) substrate, UV lamp was switched on at 500 s and off at 1100 s, then switched on again at 1700 s and off again at 2200 s.

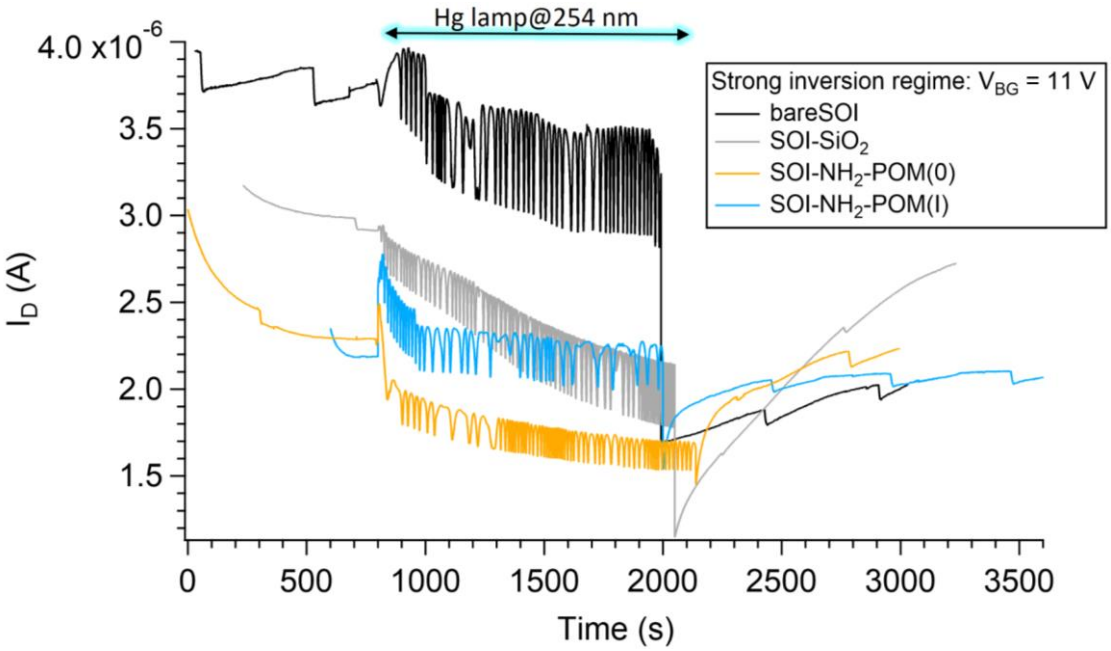

Figure 60 : I_D=f(time) at V_{BG} = 11 V (in the strong inversion regime of the Ψ-MOSFET) for bare SOI, SOI-SiO_2, SOI-NH_2-POM(0) and SOI-NH_2-POM(I) substrates. The UV lamp was switched on at ~800 s on the figure and switched off at ~2000 s.

Appendix 4.7. Effective power of the UV pen lamp and the LED

The effective power was measured by placing the UV pen lamp or the LED at a distance R far from the sensor of the powermeter. The measurements were performed in the dark.

- Effective power of the UV pen lamp (λ = 254 nm)

R (cm)	$1/R^2$ (cm^{-2})	P_{eff} (mW)
2.5	0.16	2.805
3.5	0.082	2.278
5.0	0.040	1.265
5.0	0.040	1.589
5.0	0.040	1.47
5.8	0.030	0.77
7.0	0.020	0.73
10.0	0.010	0.383

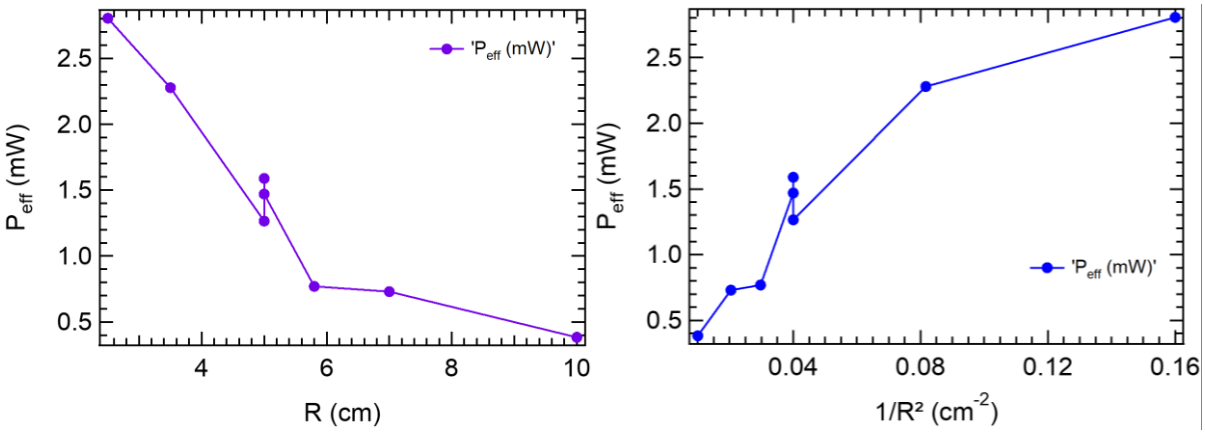

- Effective power of the LED (λ = 285 nm)

R (cm)	$1/R^2$ (cm^{-2})	P_{eff} (µW)
1	1	409.4
2.5	0.16	119.5
4	0.063	45
6	0.028	20

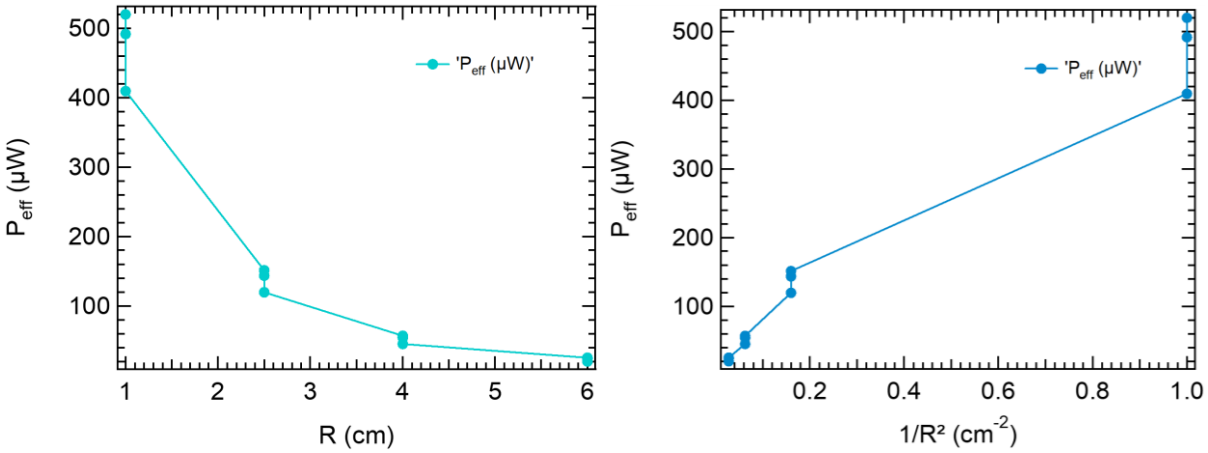

Appendix 5. Surface functionalization procedures

Appendix 5.1. Materials

Dichloromethane, acetone and dimethyl sulfoxide were purchased from VWR. Hydrofluoric acid (HF) 47-51% (TraceMetal™ grade) was purchased from Fisher Chemical. Ammonium fluoride (NH_4F) solution 40% (CMOS™ grade) was purchased from J.T. Baker®. Methanol, Hydrogen peroxide solution 30% (ACS reagent), Ammonium hydroxide solution 28-30% (ACS reagent), Hydrochloric acid 37% (ACS reagent), Ethyl undecylenate 97%, 4-Morpholineethanesulfonic acid (MES) low moisture content ≥99% (titration), potassium tert-butoxide (tBuOK) reagent grade, ≥98%, *N*-(3-Dimethylaminopropyl)-*N′*-ethylcarbodiimide hydrochloride (EDC.HCl), *N*-Hydroxysuccinimide (NHS) were purchased from Sigma Aldrich. Calcium D-gluconate gel was purchased from Alfa Aesar. Ethylene diamine ≥99% extrapure was purchased from Acros Organics.

Si(111) wafers were purchased whether from Neyco (FZ, *n*-type, phosphorus doped, both sides polished, resistivity 0.1-10 Ω.cm, 500 µm thick), or Sil'tronix (Prime FZ, *n*-type, phosphorus doped, both sides polished, resistivity 20-60 Ω.cm, 500 µm thick). Si(100) wafers were purchased from Sil'tronix (Prime FZ, *n*-type, phosphorus doped, both sides polished, resistivity 20-60 Ω.cm, 500 µm thick). The Si(111) and Si(100) wafers are cleaved using a diamond tip scriber, into approximately rectangular substrates of at least 1.5*1.0 cm^2 to fit in the sample holder of the FTIR spectrometer.

Unpatterned SOI(100) wafers are fabricated by SOITEC. For the electrical measurements using the probe station, a supplementary lithography and reactive ion etching steps were performed at IMEP-LAHC to create Si film islands (SOI mesas) with a size of 5 mm^2 x 5 mm^2, prior to surface functionalization. The top Si film and the BOX have a respective thickness of 70 nm and 145 nm. Both the top Si film and the bulk Si substrate are lightly *p*-doped (Bore) with a dopant concentration of ~10^{15} cm^{-3}.

The substrates were handled with Teflon tweezers. For the experiments involving HF and NH_4F solutions, additional Ansell gloves Barrier® 02-100 were used and purchased from VWR.

The water used in all surface experimental procedures (if not specified otherwise) comes from a Millipore Milli-Q® system providing ultrapure water with a resistivity of 18.2 MΩ.cm at 25°C.

A close attention is paid on the glassware and containers used during all the steps of silicon functionalization, which needs to be cleaned with RCA1-RCA2 solutions (see below) and dried in the oven for several hours, generally overnight, prior to use.

Appendix 5.2. Si(111) surface functionalization with an organic alkyl SAM

Step#1 : Oxide layer regrowth

The substrate cleaning begins with a degreasing step to remove grease and residual silicon slivers from the substrate due to handling and cleaving. The substrate is immersed and sonicated consecutively in dichloromethane, acetone and in methanol for 10 minutes each. The substrate is finally rinsed with water and dried under a stream of nitrogen gas.

The substrate is then subjected to the "RCA Standard Clean" procedure developed by Kern and Puotinen[2] at Radio Corporation of America (RCA) laboratories in the late 1960's that was actually slightly modified. It consists of a successive immersion of the substrate in 1) a H_2O : NH_4OH 27% : H_2O_2 30% (4:1:1) solution (called "RCA1 solution") for 15 minutes in a 80°C water bath followed by 2) a H_2O : HCl 27% : H_2O_2 30% (4:1:1) solution (called "RCA2 solution") for 15 minutes in a 80°C water bath. [**Caution is needed as RCA1 and RCA2 solutions are exothermic**.] The substrate is abundantly rinsed with water after each bath and finally dried under a stream of nitrogen gas. The purpose of these solutions is to remove organic contaminants and metal ions from the surface.

After that, the native oxide layer on the surface is removed by immersion of the substrate in a 10% hydrofluoric acid (HF) solution for 30-45 seconds at room temperature followed by a quick water rinse and a drying with nitrogen gas. **[The handling of HF and NH_4F solutions must be carried out with caution: work under hood with the appropriate personal protective equipment is necessary. To protect the skin from exposure to HF or NH_4F solutions, and possibly body tissues damage, another pair of gloves made of a suitable material should be wear additionally. Only Teflon containers are used to prepare those solutions. Calcium gluconate must also be close at hand in case of HF splashes.]** Finally, the hydrophobic substrate is immersed for 15 minutes in RCA1 solution at 80°C to grow the oxide layer on silicon, rinsed with water and dried under nitrogen.

The substrate is kept under an argon atmosphere to the spectrometer where 3 spectra are recorded at the end.

Step#2 : Hydrogenation

Once the cleaned surface is obtained, a hydrogenated surface is obtained by immersing the substrate in a 40% ammonium fluoride (NH_4F) solution for 2min30 followed by a quick rinse with water and finally dried under a stream of N_2 gas. This process was performed near the FTIR spectrometer allowing us to record 3 spectra right after hydrogenation.

Step#3 : Hydrosilylation

Molecular sieves are regenerated inside a Schlenk tube and inserted inside the glove box that has been N_2-purged for at least 1 hour. ~5 mL of neat ethyl 10-undecenoate are collected, poured to the molecular sieves, and degassed with N_2 gas. The solution is finally collected and poured inside a round-bottom flask that contains a magnetic stirrer. The round-bottom flask is capped, exited from the glovebox and quickly connected to the distillation set-up. The solution is heated at 130°C-135°C under vacuum and the distillation head, heart and tail are collected separately.

While cleaning the substrate and performing its oxide regrowth, ~3 mL of the distillation heart (depending on the size of the substrate) are collected with syringe and needle and rapidly poured inside a cleaned and dried Schlenk tube connected to a Schlenk line. 6 freeze-pump-thaw cycles are carried out and 4 more are added while recording the IR spectra of the SiO_2 and SiH surface. The hydrogen-terminated Si surface leaves the FTIR spectrometer after the spectra recording is finished. Back in the Chemistry laboratory, another immersion of the substrate in a 40% solution NH_4F for 1 minute was performed, followed by a quick rinse with water and a drying with nitrogen gas. The freshly prepared SiH surface is then quickly introduced inside the distilled and degassed alkene. The solution is heated at 200°C for 20 min under a continuous flow of Argon. The ester-terminated Si substrate is finally removed from the Schlenk tube, subjected to a rinse with ethyl acetate, an immersion in boiling dichloromethane for a few seconds and a final drying with N_2 gas. The thickness of the layer on both sides is measured and three IR spectra are recorded. The washing is completed with sonication baths in ethyl acetate and in dichloromethane, for 2-5 minutes each if the thicknesses are higher than the expected ones, and three IR spectra are recorded afterwards. Finally, the substrate is stored inside an Ar-purged vial overnight and the post-modifications are conducted the day after.

Step#4 : Ester functions hydrolysis

Three IR spectra of the ester-terminated Si substrate are recorded the day after, right before the post-modifications, otherwise the spectra subtractions between those and the ones recorded the day before are not well defined, the reason being that water molecules concentration inside the sample compartment are too different between the d-day and the day before. The ester functions are then subjected to hydrolysis involving sequential immersion of the substrate in the following solutions: 1) a degassed 0.25M tBuOK/DMSO solution for 2 minutes, 2) a degassed DMSO solution for 30 seconds, 3) a degassed 2M HCl solution for 1

minute. The substrate is finally rinsed with water for 30 seconds to 1 minute and dried under a stream of N_2 gas. The substrate is kept inside an Ar-purged vial to the FTIR spectrometer where 3 IR spectra are recorded.

Step#5 : Carboxylic acid groups activation and reaction with a diamine

At the same time as the recording of the SiCOOH surface IR spectra, a 0.1M MES buffer at pH 6-7 (pH adjusted by adding few drops of a 10mM NaOH solution) is prepared and filtered. The solution is poured inside a Schlenk tube containing EDC to get a final EDC concentration of 4.2 mM. The EDC/MES solution is stirred and degassed a few minutes prior to COOH-terminated substrate immersion for a few minutes. Under Ar bubbling, 0.5 mL of ethylenediamine is added to the solution. The substrate is left for 1h30 under Ar bubbling and the solution is stirred while avoiding contact between the magnetic stirrer and the substrate. After that, the substrate is rinsed with water and dried under a stream of N_2 gas. Three final IR spectra are recorded and the substrate is kept inside an Ar-purged vial.

Appendix 5.3. Si(100) surface functionalization with an organic alkyl SAM

Step#1: Cleaning of the substrate and etching

The substrate is immersed and sonicated consecutively in dichloromethane, acetone and in methanol for 10 minutes each. The substrate is finally rinsed with water and dried under a stream of nitrogen gas. The substrate is then subjected to a successive immersion in 1) H_2O : NH_4OH 27% : H_2O_2 30% (4:1:1) solution (RCA1) for 15 minutes in a 80°C water bath then in 2) H_2O : HCl 27% : H_2O_2 30% (4:1:1) solution (RCA2) for 15 minutes in a 80°C water bath. [**Caution is needed as RCA1 and RCA2 solutions are exothermic**.] The substrate is abundantly rinsed with water after each bath and finally dried under a stream of nitrogen gas. Three IR spectra of the SiO_2 surface are recorded.

The substrate is immersed in a 10% hydrofluoric acid (HF) solution for 10 seconds at room temperature followed by a quick water rinse and a drying with nitrogen gas. Three IR spectra of the SiH surface are recorded.

Step#2 : Hydrosilylation

Molecular sieves are regenerated inside a Schlenk tube and inserted inside the glove box that has been N_2-purged for at least 1 hour. ~5 mL of neat ethyl 10-undecenoate are collected, poured to the molecular sieves, and degassed with N_2 gas.The solution is finally collected and poured inside a round-bottom flask that contains a magnetic stirrer. The round-bottom flask is capped, exited from the glovebox and quickly connected to the distillation set-up. The solution is heated at 130°C-135°C under vacuum and the distillation head, heart and tail are collected separately.

~3 mL of the distillation heart (depending on the size of the substrate) are collected with syringe and needle and rapidly poured inside a cleaned and dried Schlenk tube connected to the Schlenk line. ~5 freeze-pump-thaw cycles are carried out. The freshly prepared SiH surface is then quickly introduced inside the distilled and degassed alkene. The solution is heated at 150°C for 1 hour under a continuous flow of argon. The ester-terminated Si substrate is finally removed from the Schlenk tube, subjected to a rinse with ethyl acetate, an immersion in boiling dichloromethane for a few seconds and a final drying with N_2 gas. The thickness of the layer on both sides is measured and three IR spectra are recorded. The washing is completed with sonication baths in ethyl acetate and in dichloromethane, for ~5 minutes. Finally, the substrate is stored inside an Ar-purged vial overnight and the post-modifications are conducted the day after.

Step#3 : Ester functions hydrolysis

The ester functions are then subjected to hydrolysis involving sequential immersion of the substrate in the following degassed solutions: 1) a degassed 0.25M tBuOK/DMSO solution for 2 minutes, 2) a degassed DMSO solution for 30 seconds, 3) a degassed 2M HCl solution for 1 minute. The substrate is finally rinsed with water for 30 seconds to 1 minute and dried under a stream of N_2 gas. Three IR spectra are recorded.

Step#4 : Carboxylic acid groups activation and reaction with a diamine

An EDC/NHS solution (10^{-2}M / 1.2 mg/mL) is prepared in a small vial. The solution is kept for 20 minutes in a cold bath with a constant Ar bubbling. The cold bath is removed and the SiCOOH surface is immersed in the EDC/NHS solution for 1 hour under a constant Ar bubbling. The treated surface is then rinsed with water and dried under a stream of N_2 gas. The substrate is finally immersed in a degassed ethylenediamine solution for 30 minutes with a continuous Ar bubbling. The substrate is finally rinsed with water and dried under a stream of N_2 gas. Three last IR spectra are recorde.

Appendix 5.4. SOI(100) surface functionalization with an organic alkyl SAM

The functionalization procedure of SOI(100) surfaces is achieved by following the same surface functionalization procedure developed on Si(100) surfaces, without recording any IR spectra.

Appendix 5.5. POM(0), POM(I) and POM(II) (sub)monolayer preparation on $SiNH_2$ and SOI-NH_2 surfaces (dipcoating)

The $SiNH_2$ and SOI-NH_2 surfaces are prepared as described in Appendix 5.2, Appendix 5.3 and Appendix 5.4.

The POM(0), POM(I) and POM(II) deposition is prepared in a N_2-purged glove box. A 1 mM solution of POMs is prepared in dry and degassed acetonitrile in a small vial. The $SiNH_2$ substrate is inserted in another vial. The POM solution is collected and filtered through a syringe filter to the vial containing the substrate. The latter is capped and left in the dark for one hour. The resulting surface is rinsed quickly with a flow of acetonitrile and dried with N_2 gas. Coming out of the glove box, the thickness of the POM layer is measured and the POM containing substrate is purged in a vial with Ar. (Note that in case of XPS characterization, the $SiNH_2$-POM sample is first purged with Ar, followed by XPS analysis and finally thickness measurements. For SOI-NH_2-POM samples, no ellipsometry and XPS measurements were performed.)

Appendix 5.6. POM(0), POM(I), and POM(II) multilayers preparation on SiO_2 surfaces (dropcasting)

The Si or SOI or quartz samples are degreased (dichloromethane, acetone, methanol) and cleaned (with RCA1-RCA2 solutions) as described in the step#1 of the Si(111) and Si(100) surface functionalization procedures (here, no immersion of the substrate in HF bath was performed).

The POM(0), POM(I) and POM(II) deposition is prepared in a N_2-purged glove box. A 1 mM solution of POMs is prepared in dry and degassed acetonitrile in a small vial. After POM dissolution, the latter is collected and filtered through a syringe filter to another vial. For small size samples (5mm², 0.5*1 cm²), only one drop of POM solution is poured on the surface with a pipette, while for bigger size samples (2.5 cm²), 10-15 drops of POM solution are required. After evaporation of the solution in the dark, the substrate is dried with a stream of N_2. Coming out of the glove box, the thickness of the POM layer is measured when it is possible and the POM containing substrate is purged with Ar.

Appendix 5.7. $K^{W}_{Sn}[NH_2]$ and $K^{W}_{Sn}[(NH_2)_2]$ grafting onto activated SiCOOH surface

Note: The grafting attempts were performed with Si(111) substrates, in the first year of the project. The functionalization procedure on Si surfaces was not yet optimized at that time. The procedure of SiCOOH surface differs from the one described in Appendix 5.2 and involved here: i) an immersion in HF 20-25% bath for 1 minute prior to oxide regrowth, ii) the hydrogenation in NH_4F for 15 minutes before IR spectra recording and for 2 minutes right before hydrosilylation, and iii) an overnight hydrosilylation without alkene distillation.

Three IR spectra of the SiCOOH surface are recorded right before the surface activation. The SiCOOH surface is immersed in a solution of EDC/NHS (30/60 mM) in water for 1h15-1h30 in a small Schlenk tube under Ar atmosphere. The surface is rinsed with water and dried with a stream of N_2 gas. The thickness of the resulting layer is measured by ellipsometry. Three IR spectra are recorded (not systematically performed). The substrate is immersed in a 1 mM POM solution in dry acetonitrile under Ar atmosphere and left in the solution for 72 hours in a static Ar atmosphere.

The substrate is rinsed with a flow of dry acetonitrile and dried with N_2. The thickness of the resulting layer is measured by ellipsometry. The substrate is then subjected to ultrasonication baths in dry acetonitrile for 5 minutes followed by a rinse with dry acetonitrile and finally dried with N_2. A second thickness measurements set is performed by ellipsometry. When the thickness measured reaches the one expected or is higher than the one expected, the substrate is subsequently sonicated in a 0.1M $TBAPF_6$ solution in dry acetonitrile for 5 minutes, followed again by a rinse with dry acetonitrile. Finally, the substrate is sonicated for 5 last minutes in dry acetonitrile, rinsed with a flow of dry acetonitrile and dried with N_2. The thickness of the resulting layer is measured by ellipsometry.

Appendix 5.8. Dry hydrosilylation attempts of POM-allyl on (111)SiH surfaces

The freshly prepared (111)SiH substrate is placed in a cleaned and dried flat-bottomed Schlenk tube, under argon atmosphere. Spatulas of POM-allyl powders are added little by little in a way to cover the whole face of the SiH surface facing upwards. The Schlenk tube is then placed in an oil bath at 200°C whether for 20 minutes, 1 hour or 2 hours. After hydrosilylation,

the substrate is rinsed with a flow of acetonitrile and dried with N_2 gas. IR spectra are recorded and thicknesses measured by spectroscopic ellipsometry. The substrate is then rinsed with acetonitrile then sonicated four times in acetonitrile (4*5 minutes). After each sonication bath, the substrate is rinsed with acetonitrile. Finally, the sample is dried under a stream of N_2 gas. IR spectra are recorded and thicknesses measured by spectroscopic ellipsometry.

Appendix 5.9. Photochemical hydrosilylation attempts of POM-allyl on (111)SiH surfaces

Five drops of a 1 mM POM solution in dry and degassed acetonitrile are brought to the freshly prepared (111)SiH surface lying on top of a cleaned quartz disc. The surface is subsequently covered with another cleaned quartz disc. The UV Hg lamp is held horizontally at ~5 cm far from the sample and the experiment is carried out in a dark box as a protection against UV radiation, under a glove box purged with nitrogen. The Hg lamp is switched on for 5 or 15 minutes. The POM-containing Si substrate is removed from the quartz discs and subsequently rinsed with dry and degassed acetonitrile. The substrate is dried with N_2 then with Ar after exiting the glove box. IR spectra are recorded and thicknesses measured by spectroscopic ellipsometry. The substrate is then rinsed with acetonitrile then sonicated four times in acetonitrile (4*5 minutes). After each sonication bath, the substrate is rinsed with acetonitrile. Finally, the sample is dried under a stream of N_2 gas. IR spectra are recorded and thicknesses measured by spectroscopic ellipsometry.

Appendix 5.10. K^{W}_{Sn}[COOH] and K^{W}_{Si}[COOH] grafting onto Si-SiO_2 surface

For the electrical characterization, the Si substrates were purchased from Sil'tronix (n-type Si(100), double-sides polished, highly phosphorus-doped, resistivity < 5.10^{-3} Ω.cm). For the IR spectra recording, the substrates were purchased from Neyco (FZ, *n*-type Si(100), double sides polished, low phosphorus-doped, resistivity 20-30 Ω.cm). The two POMs grafting follow the same procedure.

The substrate is first rinsed with dichloromethane and dried with N_2. It is subsequently immersed in NH_4OH:H_2O_2:H_2O (1:1:2) solution and subjected to sonications for 10 minutes, followed by a copious rinse with distilled water: this procedure (A) is repeated three times. The

substrate is then immersed in distilled water and subjected to sonications for 5 minutes, followed by a rinse with distilled water: this procedure (B) is repeated twice. The thickness of the SiO_2 layer is measured by ellipsometry. When too high, the procedures A and B are repeated.

The substrate is then immersed in a 1 mM POM solution in dry acetonitrile and heated under reflux for 24 hours. The substrate is then rinsed with dry acetonitrile and dried with N_2. It is then subjected to a thorough rinsing treatment. The substrate is immersed in dry acetonitrile and sonicated for 5 minutes and rinsed with a flow of dry acetonitrile. The substrate is then immersed in a 0.1 M $TBAPF_6$ solution in dry acetonitrile, sonicated 5 minutes and rinsed with dry acetonitrile. Finally, a sonication bath of 5 minutes is carried out again in dry acetonitrile followed by a rinse with dry acetonitrile and a drying with a stream of N2. Depending on the thicknesses measured, this thorough rinsing treatment can be repeated.

Appendix 6. POM syntheses

Appendix 6.1. $(TBA)_3[PMo^{VI}_{12}O_{40}]$ synthesis

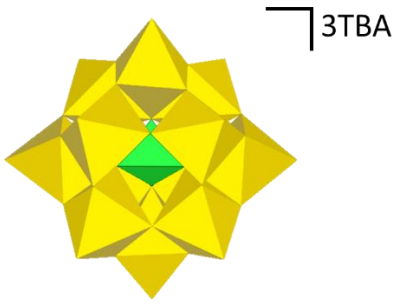

POM(0)

$C_{48}H_{108}N_3PMo_{12}O_{40}$

M = 2549.7 g/mol

The POM(0) was synthesized following a procedure reported by Sanchez *et al.*[3] 60 mL of a 1M solution of sodium molybdate dihydrate $Na_2[MoO_4].2H_2O$ were added to 9 mL of nitric acid HNO_3 and 50 mL of 1,4-dioxane. Under stirring, 5 mL of a 1 M solution of orthophosphoric acid H_3PO_4 and 5g of tetrabutylammonium bromide NBu_4Br are added. After filtration, the yellow heavy solid is immersed in 50 mL of boiling water and stirred, filtered again and washed with 50 mL water, 100 mL ethanol and diethyl ether until obtention of a yellow powder. It is finally recrystallized in acetone while heating: 30 mL of hot acetone are required to recrystallize 1 g of powder. After three days in the refrigerator, the mixture is filtered and yellow crystals are collected, dried under vacuum several days at 60°C. Note that during the experiment, the POM was handled with glass spatula/material to avoid a reduction of the POM.

^{1}H NMR (400 MHz, CD_3CN, ppm): δ = 3.13 (m, 24H, N-*CH*$_2$-CH_2-CH_2-CH_3), δ = 1.65 (m, 24H, N-CH_2-*CH*$_2$-CH_2-CH_3), δ = 1.41 (sex, $^3J_{H-H}$ = 7.4 Hz, 24H, N-CH_2-CH_2-*CH*$_2$-CH_3), δ = 1.01 (t, $^3J_{H-H}$ = 7.3 Hz, 36H, N-CH_2-CH_2-CH_2-*CH*$_3$).

^{31}P NMR (162 MHz, CD_3CN, ppm): δ = -3.29 (s)

IR (KBr, cm^{-1}): 2962 (m), 2933 (m), 2873 (m), 1473 (m), 1381 (w), 1063 (s), 967 (shoulder), 956 (vs), 880 (s), 806 (vs), 739 (w), 619 (w), 504 (m), 465 (w), 387 (s), 342 (m).

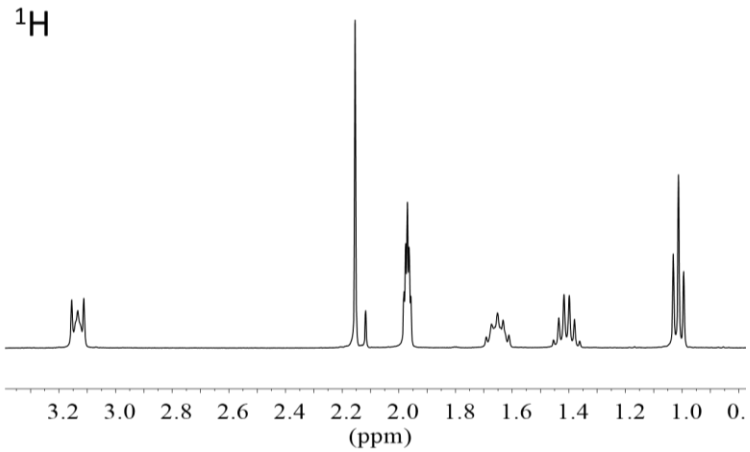

^{1}H of the POM(0) powder recorded in CD_3CN

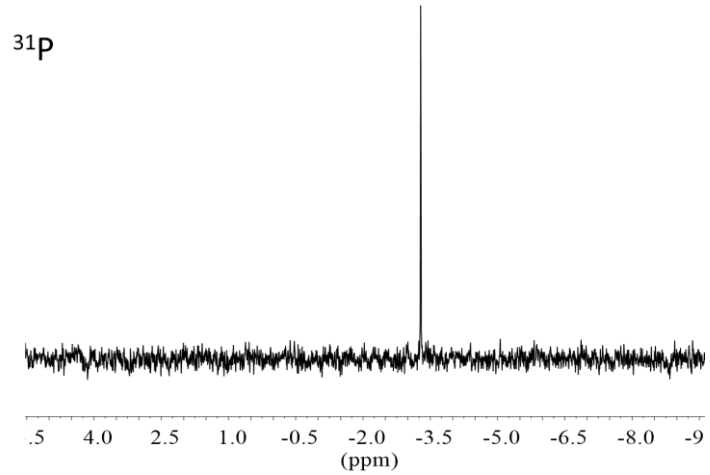

^{31}P of the POM(0) powder recorded in CD_3CN

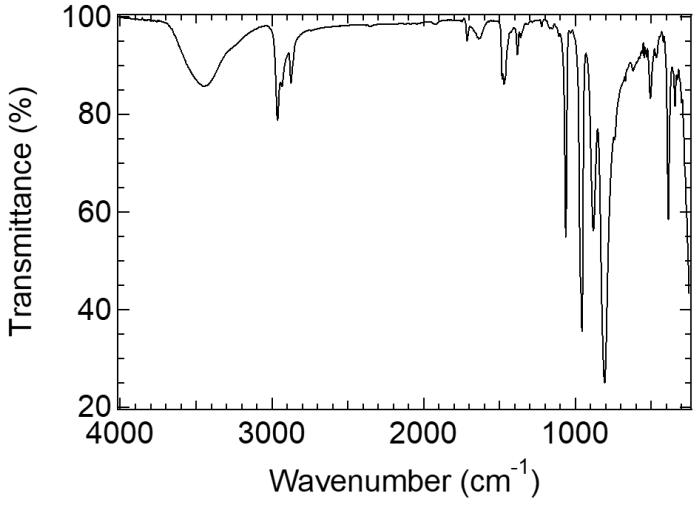

IR spectrum of the POM(0) powder recorded on KBr pellets.

Appendix 6.2. $(TBA)_4[PMo^{VI}_{11}Mo^{V}O_{40}]$ synthesis

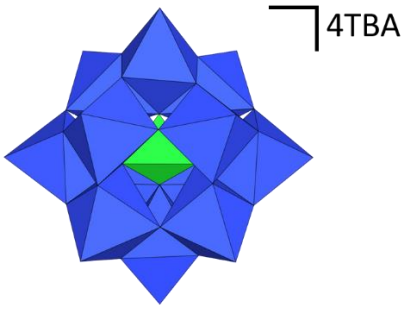

POM(I)

$C_{64}H_{144}N_4PMo_{12}O_{40}$

M = 2792.2 g/mol

100 mg of $(TBA)_3[PMo_{12}O_{40}]$ are dissolved in a minimum volume of dry acetonitrile (~6 mL) in a dry Schlenk tube containing a magnetic stir bar, under Argon. Under stirring, a few drops of phenyllithium is added to the POM(0) solution (color change from yellow to green). The reaction is followed by recording ^{31}P NMR spectra in which the initial singlet at -3.29 ppm of the POM(0) slowly disappears. Drops of phenyllithium is added until the appearance of a signal at 0.49 ppm corresponding to POM(I), and the solution displays a blue color.[4] 15 mg of NBu_4Br are added to the solution followed by the addition of ~15 mL of diethylether, leading to the formation of a blue precipitate. The suspension is filtered on a cellulose membrane. The blue solid is subsequently washed with 10 mL of tetrahydrofuran and 10 mL of methanol. It is finally dried under vacuum, in the dark.

^{1}H NMR (400 MHz, CD_3CN, ppm): δ = 3.17 (m, 32H, N-*CH_2*-CH_2-CH_2-CH_3), δ = 1.67 (m, 32H, N-CH_2-*CH_2*-CH_2-CH_3), δ = 1.43 (m, 32H), δ = 1.01 (t, $^3J_{H-H}$ = 7.3 Hz, 48H, N-CH_2-CH_2-CH_2-*CH_3*).

^{31}P NMR (162 MHz, CD_3CN, ppm): δ = 0.49 (s)

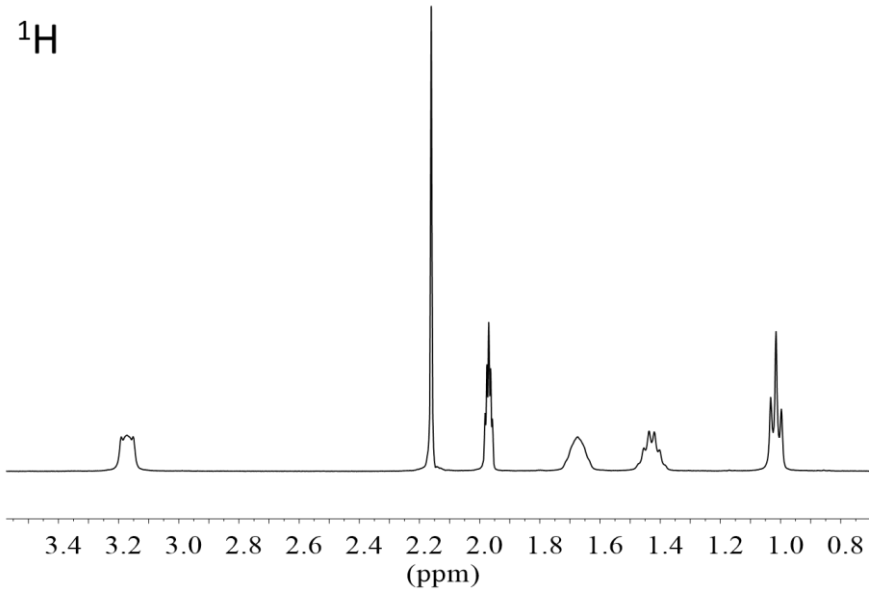

^{1}H of the POM(I) powder recorded in CD_3CN

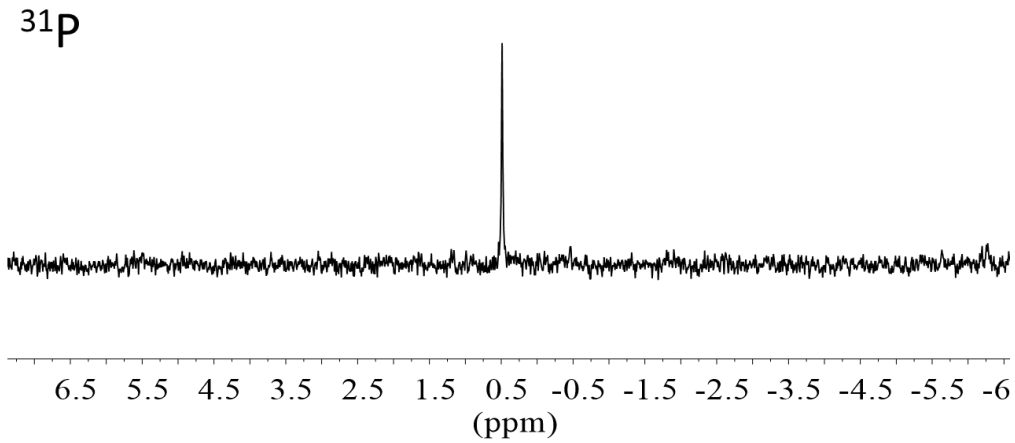

^{31}P of the POM(I) powder recorded in CD_3CN

Appendix 6.3. $Li(TBA)_4[PMo^{VI}_{10}Mo^{V}_{2}O_{40}]$ synthesis

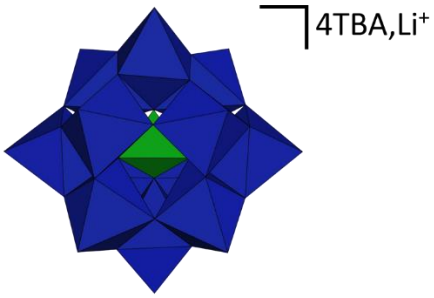

POM(II)

$C_{64}H_{144}N_4LiPMo_{12}O_{40}$

M = 2799.2 g/mol

100 mg of $(TBA)_3[PMo_{12}O_{40}]$ are dissolved in a minimum volume of dry acetonitrile (~6 mL) in a dry Schlenk tube containing a magnetic stir bar, under Argon. Similarly as for the POM(I) synthesis, phenyllithium is added dropwise to the POM(0) solution under stirring, with a larger amount. The reaction is followed by recording ^{31}P NMR spectra: indeed, a unique singlet is seen at -3.29 ppm (POM(0)), then at 0.49 ppm (POM(I)) and finally at -6.27 ppm suggesting the formation of POM(II).[4] 30 mg of NBu_4Br are added to the solution followed by the addition of ~40 mL of diethylether, leading to the formation of a dark blue precipitate. The mixture is filtered on a cellulose membrane. The dark blue solid is subsequently washed with 15 mL of tetrahydrofuran and finally dried under vacuum, in the dark.

^{1}H NMR (400 MHz, CD_3CN, ppm): δ = 3.16 (m, 32H, N-*CH_2*-CH_2-CH_2-CH_3), δ = 1.66 (m, 32H, N-CH_2-*CH_2*-CH_2-CH_3), δ = 1.42 (sex, $^3J_{H-H}$ = 7.4 Hz, 32H, N-CH_2-CH_2-*CH_2*-CH_3), δ = 1.01 (t, $^3J_{H-H}$ = 7.3 Hz, 48H, N-CH_2-CH_2-CH_2-*CH_3*).

^{31}P NMR (162 MHz, CD_3CN, ppm): δ = -6.27 (s)

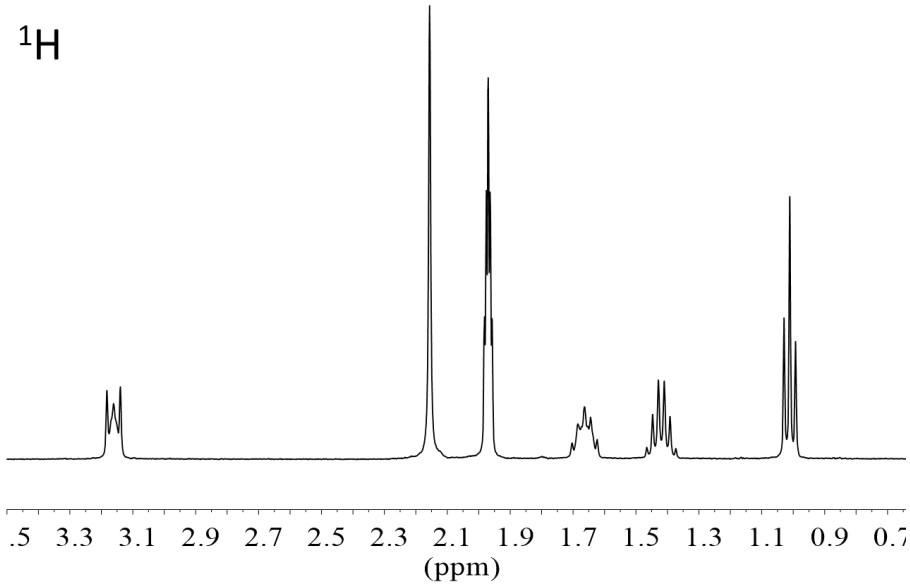

^{1}H of the POM(II) powder recorded in CD_3CN

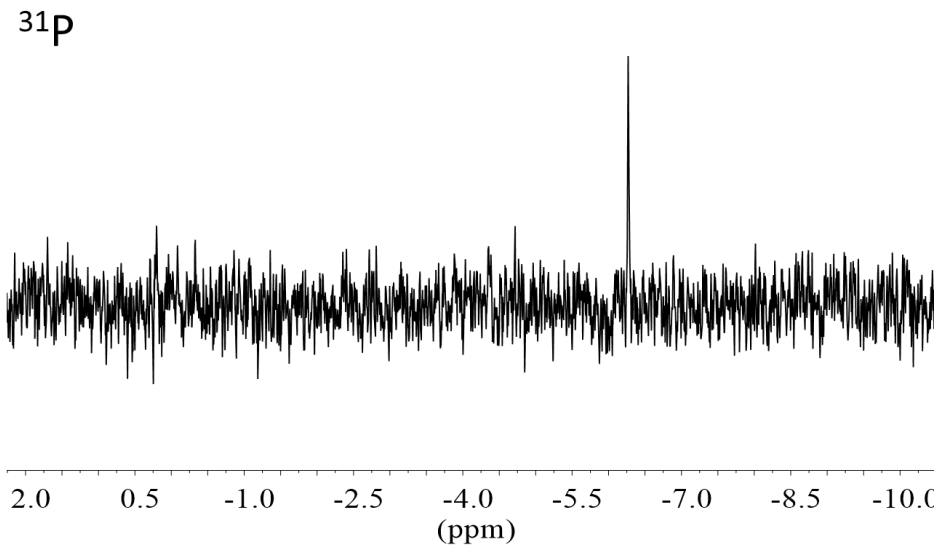

^{31}P of the POM(II) powder recorded in CD_3CN

Appendix 6.4. $TBA_4[PW_{11}O_{39}\{Sn(C_6H_4)I\}]$ synthesis

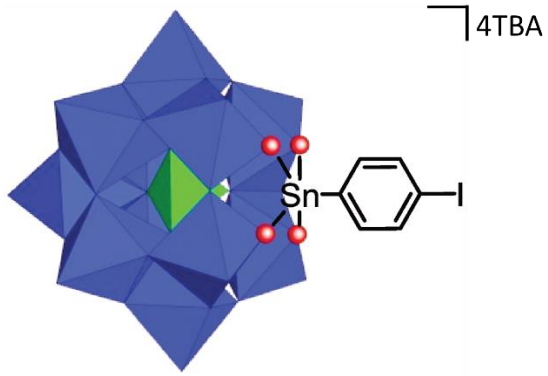

K^{W}_{Sn}[I]

$C_{70}H_{148}N_4O_{39}SnPW_{11}I$

M = 3969.3 g/mol

The synthesis follows procedures reported by the group.[5,6]

2.025 g (0.632 mmol, 1 equivalent) of $K_7[PW_{11}O_{39}].14H_2O$ (kindly provided by S. Renaudineau, chemical technician in the E-POM group) are dissolved in 20 mL of distilled water in a beaker. ~0.46 g of $Cl_3Sn(C_6H_4)I$ (kindly provided by R. Salles, PhD student in the group) are added to the solution and the mixture is stirred for 15 minutes at room temperature. A few drops of a 1.0 M potassium hydroxide solution are added to the solution to stabilize the pH at 3.1-3.2. The solution is centrifuged (15 minutes, 4000 rpm) and filtered on a membrane. A solution of 1.017 g (3.15 mmol, 5 equivalents) of NBu_4Br in 2.5 mL distilled water, is poured to the filtrate. A white solid precipitates. After centrifugation (15 minutes, 4000 rpm), the product is washed three times with 25 mL of ethanol (with intermediate 5 minutes-centrifugations) and dried twice with 20 mL of diethylether. Finally, the white powder is dried under vaccum.

^{1}H NMR (400 MHz, CD_3CN, ppm): δ = 7.88 (d+dd, $^3J_{H-H}$ = 8.2 Hz, 2H, Ar-H), δ = 7.49 (d+dd, $^3J_{H-H}$ = 8.2 Hz, 2H, Ar-H), δ = 3.15 (m, 32H, N-*CH*$_2$-CH_2-CH_2-CH_3), δ = 1.65 (m, 32H, N-CH_2-*CH*$_2$-CH_2-CH_3), δ = 1.41 (sex, $^3J_{H-H}$ = 7.4 Hz, 32H, N-CH_2-CH_2-*CH*$_2$-CH_3), δ = 1.01 (t, $^3J_{H-H}$ = 7.4 Hz, 48H, N-CH_2-CH_2-CH_2-*CH*$_3$).

^{31}P NMR (162 MHz, CD_3CN, ppm): δ = -11.64 (s)

IR (KBr, cm^{-1}): 2961 (m), 2934 (m), 2873 (m), 1483 (m), 1380 (w), 1070 (s), 963 (vs), 886 (s), 815 (vs), 381 (s).

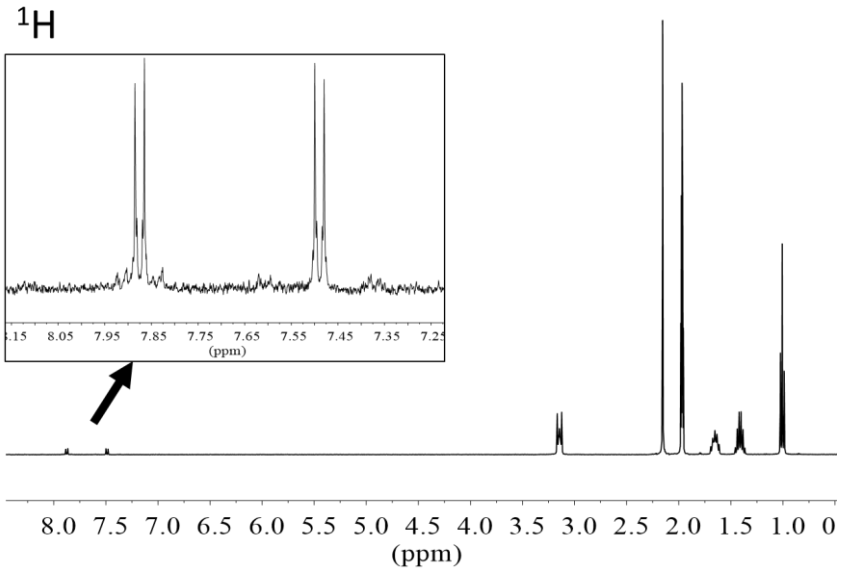

^{1}H of the $K^{W}_{Sn}[I]$ powder recorded in CD_3CN

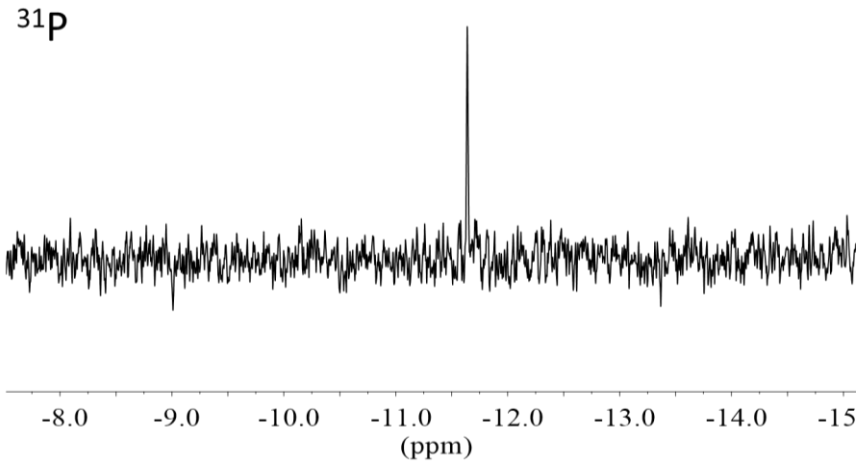

^{31}P of the $K^{W}_{Sn}[I]$ powder recorded in CD_3CN

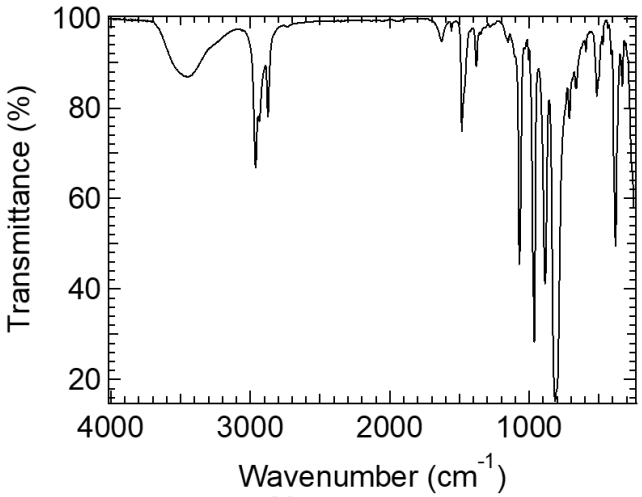

IR spectrum of the $K^{W}_{Sn}[I]$ powder recorded on KBr pellets.

Appendix 6.5. $TBA_4[PW_{11}O_{39}\{Sn(C_6H_4)C{\equiv}C(C_6H_4)NH_2\}]$ synthesis

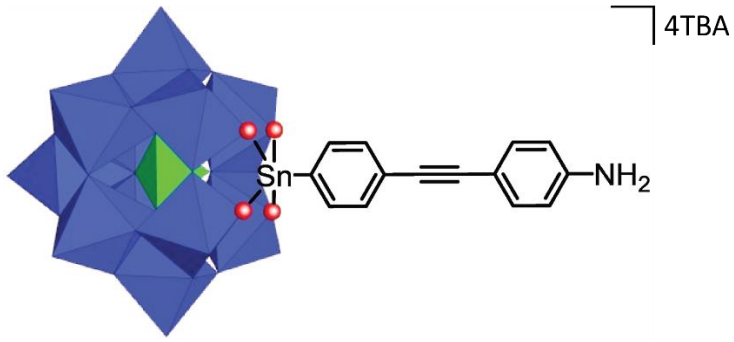

$K^{W}_{Sn}[NH_2]$

$C_{78}H_{154}N_5O_{39}SnPW_{11}$

M = 3958.6 g/mol

The synthesis follows the procedure developed by M. Laurans.[6] $K^{W}_{Sn}[I]$ (390.2 mg, 0.098 mmol), 4-ethynylaniline (30.8 mg, 0.263 mmol), bis(triphenylphosphine)palladium(II) chloride (11.9 mg, 0.017 mmol) and copper iodide (4.3 mg, 0.023 mmol) are introduced inside a dry Schlenk tube containing a magnetic stir bar, under Argon atmosphere. In another dry Schlenk tube, 5 mL of anhydrous DMF are poured and subsequently degassed. 140 µL of freshly distilled triethylamine are collected and added to the Schlenk tube containing DMF. The resulting solution is then transferred to the Schlenk containing the solids through a cannula. The reaction mixture is stirred overnight at room temperature under a static Argon atmosphere. The color of the solution turns from yellow to orange to reddish. After one night, the solution displays a brown color. The addition of an excess of diethyl ether to the reaction mixture leads to the formation of a brown precipitate. After centrifugation, the solid is dissolved in a minimum volume of acetonitrile with NBu_4Br (300 mg, 0.931 mmol). The addition of an excess of ethanol absolute leads to the formation of a precipitate which is subsequently isolated by a centrifugation. The solid is then washed and centrifuged with ethanol absolute and diethyl ether. The solid is dissolved in 3 mL of dry acetonitrile and few spatulas of an ion exchange resin enriched with TBA, for two hours. After filtration on a membrane, the filtrate precipitates by adding an excess of diethyl ether. The brown solid is finally isolated after centrifugation.

^{1}H NMR (400 MHz, CD_3CN, ppm): δ = 7.71 (d+dd, $^{3}J_{H\text{-}H}$ = 8.2 Hz, $^{3}J_{Sn\text{-}H}$ = 94.4 Hz, 2H, Ar-H), δ = 7.58 (d+dd, $^{3}J_{H\text{-}H}$ = 8.1 Hz, $^{4}J_{Sn\text{-}H}$ = 33.6 Hz, 2H, Ar-H), δ = 7.32 (d, $^{3}J_{H\text{-}H}$ = 8.7 Hz, 2H, Ar-H), δ = 6.67 (d, $^{3}J_{H\text{-}H}$ = 8.7 Hz, 2H, Ar-H), δ = 4.49 (s, 2H, Ar-NH_2), δ = 3.15 (m, 32H, N-CH_2-CH_2-CH_2-CH_3), δ = 1.65 (m, 32H, N-CH_2-CH_2-CH_2-CH_3), δ = 1.41 (sex, $^{3}J_{H\text{-}H}$ = 7.3 Hz, 32H, N-CH_2-CH_2-CH_2-CH_3), δ = 1.01 (t, $^{3}J_{H\text{-}H}$ = 7.3 Hz, 48H, N-CH_2-CH_2-CH_2-CH_3).

^{31}P NMR (162 MHz, CD_3CN, ppm): δ = -11.26 (s)

IR (KBr, cm^{-1}): 2961 (m), 2934 (m), 2873 (m), 1620 (w), 1483 (m), 1382 (w), 1069 (s), 962 (vs), 885 (s), 813 (vs), 381 (s).

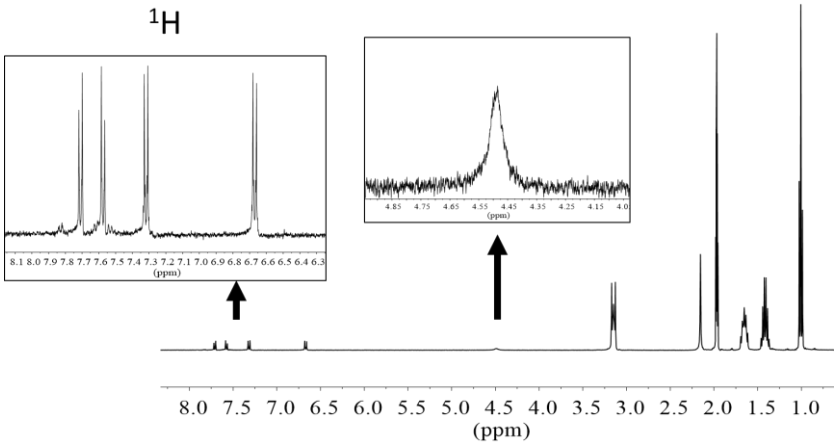

^{1}H of the K$^{W}_{Sn}$[NH$_2$] powder recorded in CD$_3$CN

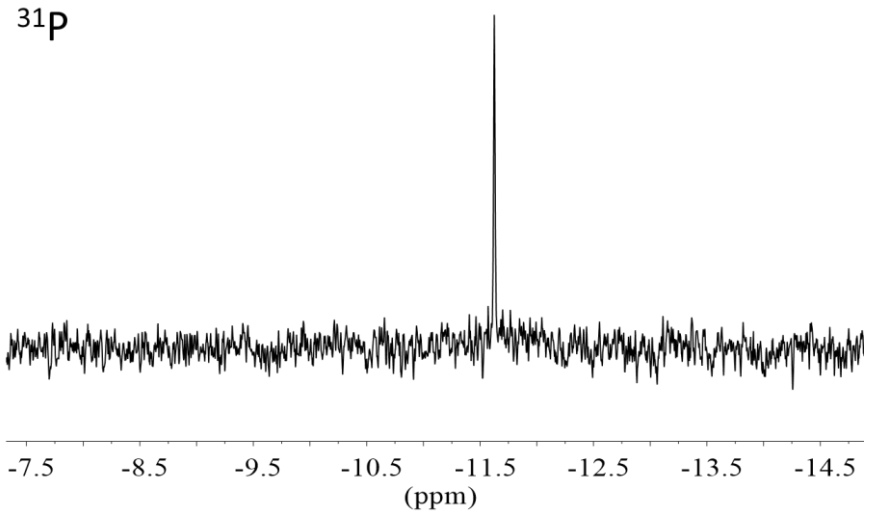

^{31}P of the K$^{W}_{Sn}$[NH$_2$] powder recorded in CD$_3$CN

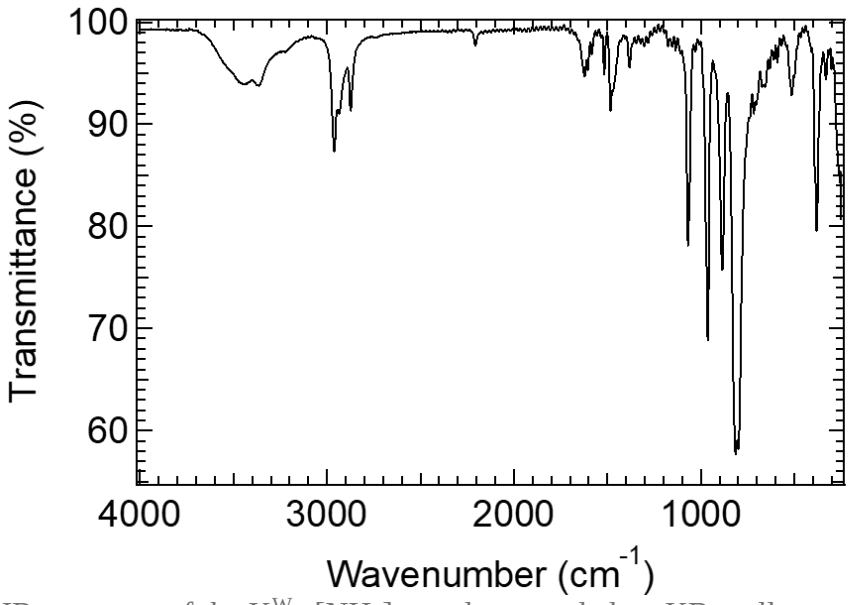

IR spectrum of the $K^{W}_{Sn}[NH_2]$ powder recorded on KBr pellets.

Appendix 6.6. $TBA_3[PW_9O_{34}(OSiCH{=}CH_2)_3(SiCH{=}CH_2)]$ synthesis

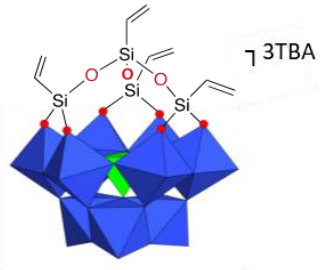

POM-vinyl

$C_{56}H_{120}N_3O_{37}Si_4PW_9$

M = 3225.4 g/mol

The procedure was inspired by the one reported by N. Joo.[7]

α-$K_9PW_9O_{34}.16H_2O$ (2.870 g, 1 mmol) and NBu_4Br (0.968 g, 3 mmol) are suspended in DMF (15 mL). Trichlorovinylsilane ($CH_2{=}CHSiCl_3$) (3.93 mmol) is added **dropwise** under vigorous stirring. The suspension is stirred 3 hours at room temperature followed by a centrifugation. The white solid (NaCl, NaBr, traces of $K_9PW_9O_{34}.16H_2O$) is removed and the supernatant is left two weeks at room temperature in a beaker covered non hermetically with Parafilm® film for a slow evaporation of the solution. After formation of crystals, the latter are filtered, washed with water, ethanol and diethylether. A part of the resulting white powder is recrystallized in acetonitrile: 500 mg of powder are dissolved in a minimum volume of acetonitrile (4.5 mL) in a small beaker, then the latter is covered non hermetically with Parafilm® film and kept in the fridge a few days. After filtration, the crystals are washed with ethanol and dried with diethylether. A white powder is obtained.

^{1}H NMR (400 MHz, CD_3CN, ppm):

δ = 6.00 (m, 12H -CH=CH_2), δ = 3.14 (m, 24H, N-*CH_2*-CH_2-CH_2-CH_3), δ = 1.65 (m, 24H, N-CH_2-*CH_2*-CH_2-CH_3), δ = 1.41 (sex, $^3J_{H\text{-}H}$ = 7.4 Hz, 24H, N-CH_2-CH_2-*CH_2*-CH_3), δ = 1.01 (t, $^3J_{H\text{-}H}$ = 7.4 Hz, 36H, N-CH_2-CH_2-CH_2-*CH_3*).

^{31}P NMR (162 MHz, CD_3CN, ppm): δ = -17.10 (s)

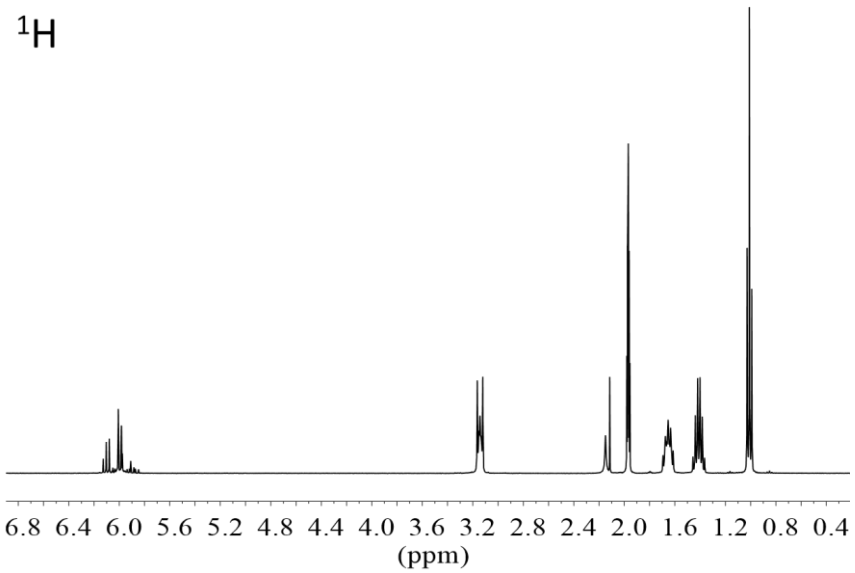

^{1}H of the POM-vinyl powder recorded in CD_3CN

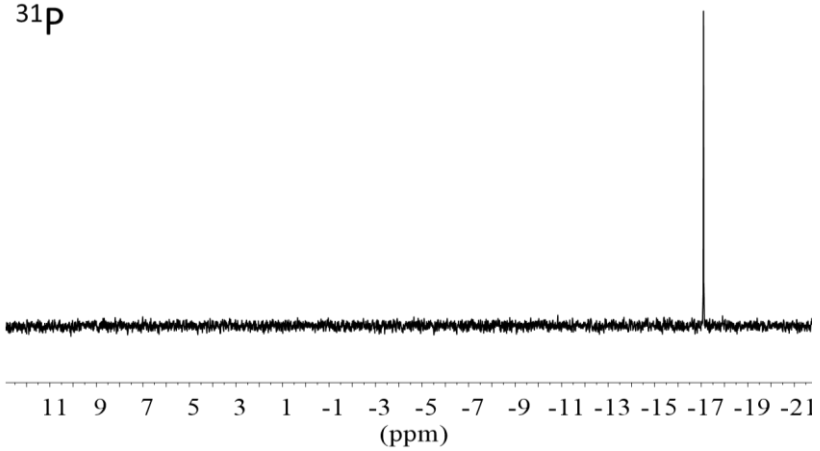

^{31}P of the POM-vinyl powder recorded in CD_3CN

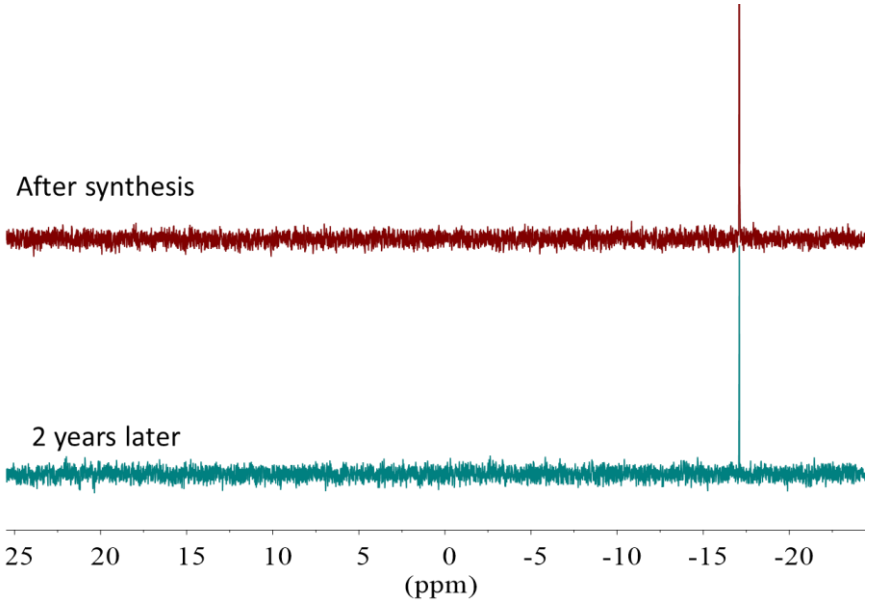

^{31}P of the POM-vinyl powder recorded in CD_3CN, after synthesis vs 2 years later

Appendix 6.7. $TBA_3[PW_9O_{34}(OSiCH_2CH=CH_2)_3(SiCH_2CH=CH_2)]$ synthesis

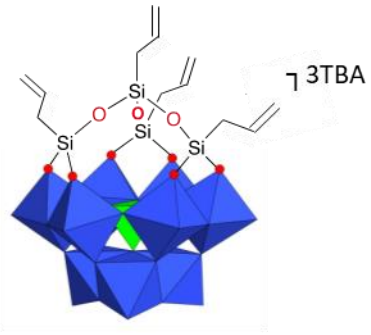

POM-allyl

$C_{60}H_{128}N_3O_{37}Si_4PW_9$

M = 3281.5 g/mol

The procedure was inspired by the one reported by N. Joo.[7]

α-$K_9PW_9O_{34}.16H_2O$ (2.869 g, 1 mmol) and NBu_4Br (0.969 g, 3.01 mmol) are suspended in DMF (15 mL). Allyltrichlorosilane (CH_2=CH-CH_2SiCl_3) (4 mmol) is added **dropwise** under vigorous stirring. The suspension is stirred 3 hours at room temperature followed by a centrifugation. The white solid (NaCl, NaBr, traces of $K_9PW_9O_{34}.16H_2O$) is removed and the supernatant is left one week at room temperature in a beaker covered non hermetically with Parafilm® film for a slow evaporation of the solution. After formation of crystals, the latter are filtered, washed with water, ethanol and diethylether. A white powder is obtained.

^{1}H NMR (400 MHz, CD_3CN, ppm): δ = 5.87 (m, 4H, Si-CH_2-*CH*=CH_2), δ = 4.98 (m, 8H, Si-CH_2-CH=*CH_2*), δ = 3.14 (m, 24H, N-*CH_2*-CH_2-CH_2-CH_3), δ = 1.66 (m, 32H, N-*CH_2*-CH_2-CH_2-CH_3 and Si-*CH_2*-CH=CH_2), δ = 1.41 (sex, $^3J_{H-H}$ = 7.4 Hz, 24H, N-CH_2-CH_2-*CH_2*-CH_3), δ = 1.01 (t, $^3J_{H-H}$ = 7.3 Hz, 36H, N-CH_2-CH_2-CH_2-*CH_3*).

^{31}P NMR (162 MHz, CD_3CN, ppm): δ = -17,24 (s)

IR (KBr, cm^{-1}): 2962 (s), 2934 (s), 2875 (s), 1633 (m), 1484 (s), 1381 (m), 1124 (vs), 1039 (vs), 1001 (sh), 975 (vs), 960 (vs), 870 (vs), 820 (vs), 729 (vs), 391 (vs), 343 (m)

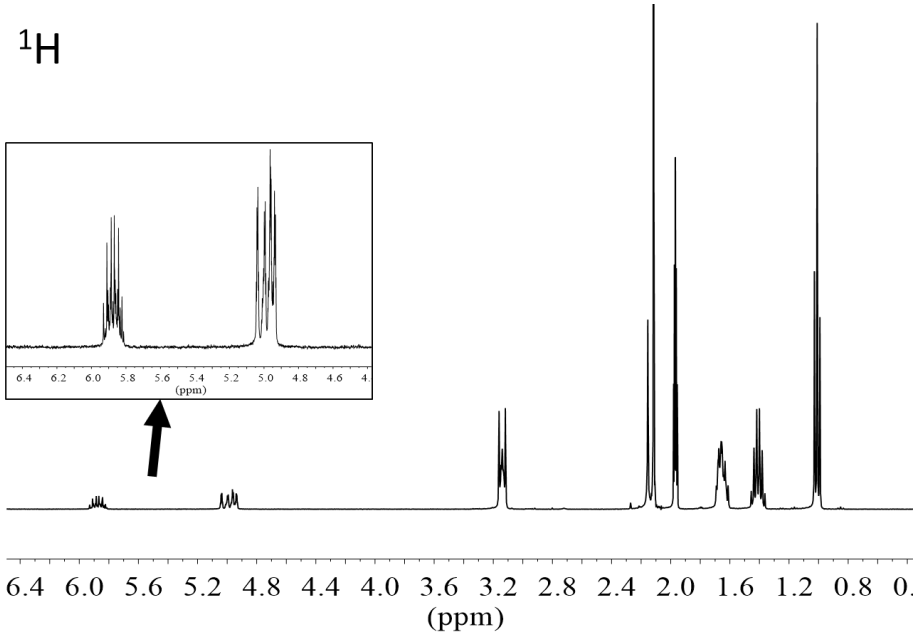

^{1}H of the POM-allyl powder recorded in CD_3CN

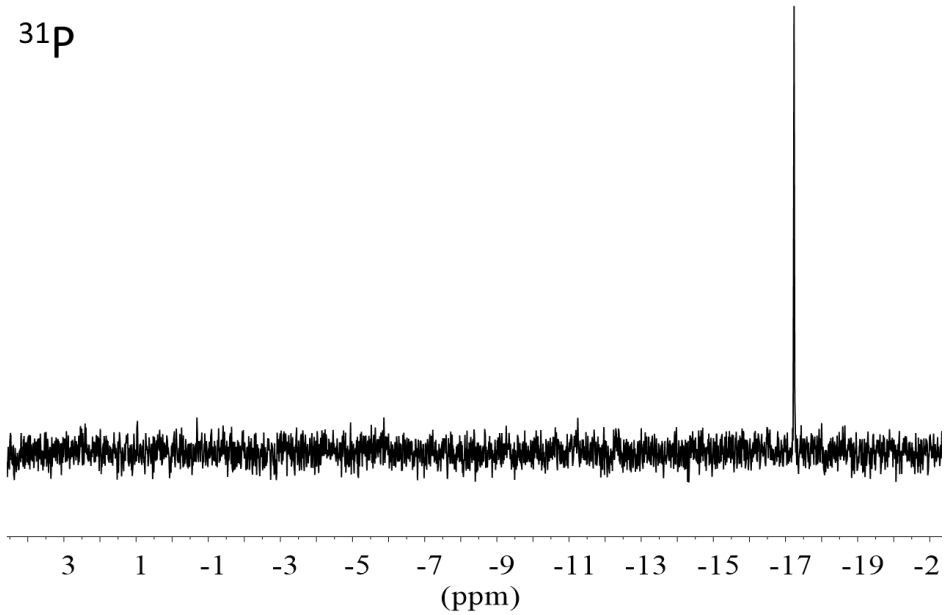

^{31}P of the POM-allyl powder recorded in CD_3CN

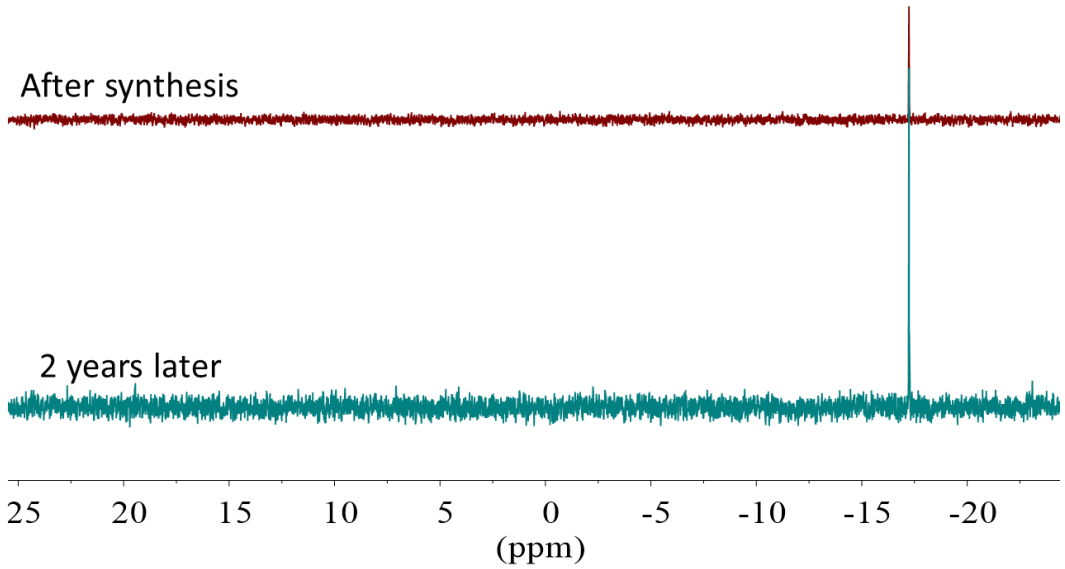

^{31}P of the POM-allyl powder recorded in CD_3CN, after synthesis vs 2 years later

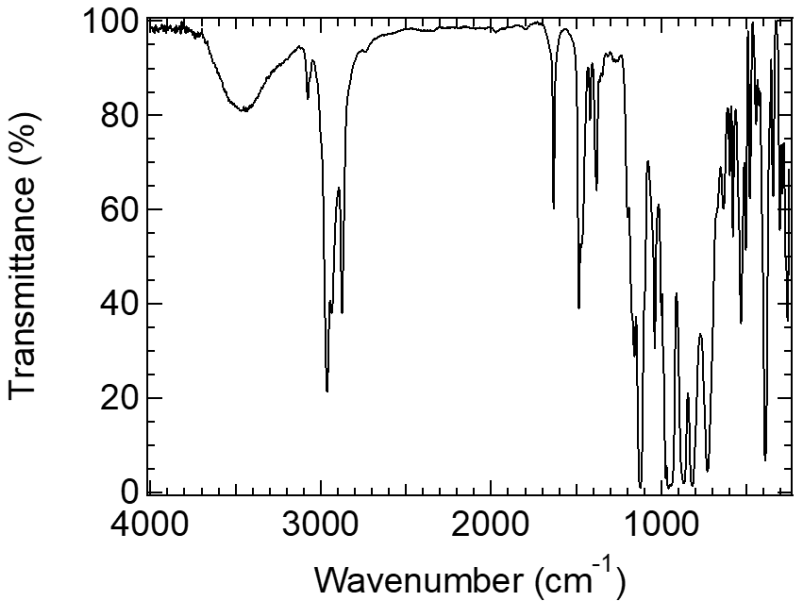

IR spectrum of the $K^{W}_{Sn}[NH_2]$ powder recorded on KBr pellets.

Appendix 7. IR bands assignments

The IR bands positions were systematically compared to the IR bands table of Socrates.[14] Accordingly, the IR bands positions and assignments were extracted from this table (if not specified otherwise) and inventoried hereinafter.

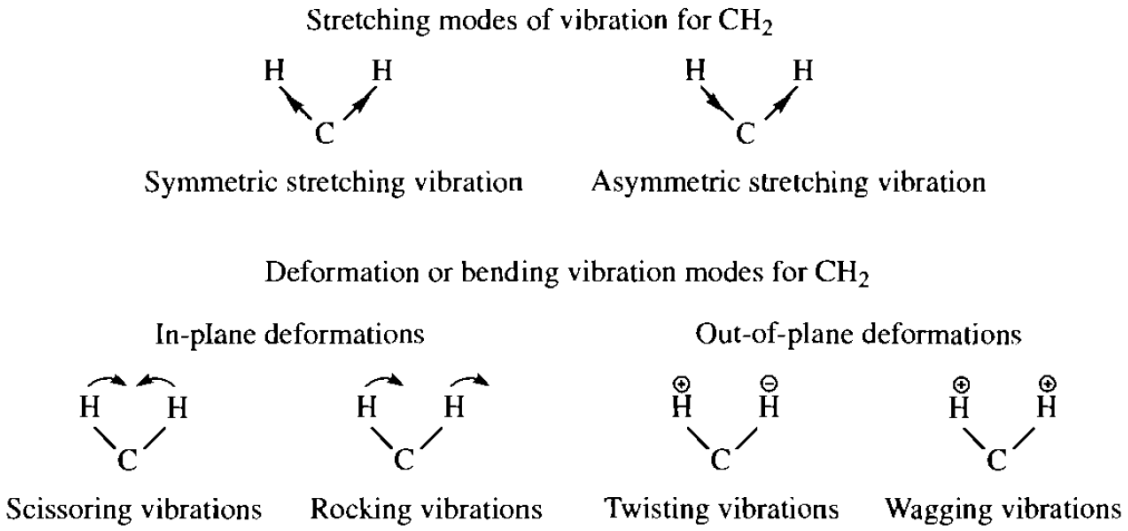

Illustration of the vibrational modes (stretching and deformation) of a CH_2 group.[14]

The symbols used in the table are the following:

asym	asymmetric
def, δ	deformation
m	medium
R	alkyl
sc	scissor
str, ν	stretching
sym	symmetric
v	variable
vib	vibration
vs	very strong
vw	very weak
w	weak

	Wavenumber (cm^{-1})	**Intensity**	**Notation**	**Characteristic bond**
ALKANE / ALIPHATIC CHAIN	1295-1305	-	δ_{twist}^{C-H}	-$(CH_2)_n$- , not usually observed in IR, intensity increases with n
	1370-1390	m-s	δ_{asym}^{C-H}	-CH_3 (aliphatic), characteristic of C-CH_3
	1440-1465	m	δ_{asym}^{C-H}	-CH_3 (aliphatic)
	1440-1480	m	δ_{sc}^{C-H}	-CH_2- scissor vib
	1445-1485	m	δ^{C-H}	-$(CH_2)_n$-
	1450-1480	s	δ_{sym}^{C-H}	N-CH_2-(ethylenediamine complexes), two bands
	2840-2870, 2880[8], 2850[9]	m	ν_{sym}^{C-H}	-CH_2- (acyclic)
	2865-2885	m	ν_{sym}^{C-H}	-CH_3 (aliphatic)
	2915-2940, 2921[10], 2920[8,9]	m-s	ν_{asym}^{C-H}	-CH_2- (acyclic)
	2950-2975	m-s	ν_{asym}^{C-H}	-CH_3 (aliphatic)
ESTER	1050-1160		ν_{sym}^{C-O-C}	R-C(O)-OR’
	1185-1275		ν_{asym}^{C-O-C}	R-C(O)-OR’
	1325-1340	m-w	$\delta_{twist}^{CH_2}$	O-CH_2-CH_3, ethyl ester
	1335-1385	m-w	$\delta_{wagging}^{CH_2}$	O-CH_2-CH_3, ethyl ester
	1360-1390	m-s	$\delta_{sym}^{CH_3}$	O-CH_2-CH_3, ethyl ester
	1435-1480	m	$\delta_{asym}^{CH_3}$	O-CH_2-CH_3, ethyl ester
	1460-1490	m-w	δ^{O-CH_2}	O-CH_2-CH_3, ethyl ester
	1725-1750 (1741[10])	vs	$\nu_{ester}^{C=O}$	Saturated aliphatic ester
	2860-2920	w	ν^{CH_3}	O-CH_2-CH_3, ethyl ester
	2890-2930	w	$\nu_{sym}^{CH_3}$	O-CH_2-CH_3, ethyl ester
	2930-2995, 2981[10]	m	$\nu_{asym}^{CH_3}$ and ν^{CH_2}	O-CH_2-CH_3, ethyl ester

	Wavenumber (cm^{-1})	**Intensity**	**Notation**	**Characteristic bond**
CARBOXYLIC ACID	1210-1320, 1280[8,10]	m-s	ν_{COOH}^{C-O}	Carboxylic acids, -COOH (dimer) Sometimes a doublet
	1395-1440, 1412[10], 1410[8]	w	ν_{COOH}^{C-O} and δ_{COOH}^{O-H}	Carboxylic acids, -COOH (dimer) Combination band due to C-O str and O-H def
	1700-1740, 1712[10], 1713[8]	vs	$\nu_{COOH}^{C=O}$	Saturated aliphatic carboxylic acids
CARBOXYLIC ACID SALTS	1335-1440	m-s	$\nu_{sym}^{CO_2^-}$	Carboxylic acid salts, $-CO_2^-$, usually 2 or 3 peaks
	1540-1695	s	$\nu_{asym}^{CO_2^-}$	Carboxylic acid salts, $-CO_2^-$
PRIMARY AMIDE (AMIDE I)	~1150	w	$\delta_{in-plane\ rocking}^{NH_2}$	Primary amide, not always seen
	1400-1420	m	$\nu_{amide\ I}^{C-N}$	
	1620-1650	w-m	$\delta_{amide\ I}^{N-H}$ and $\nu_{amide\ I}^{C-N}$	Solid phase
	1650-1670	s	$\nu_{amide\ I}^{C=O}$	Usually a doublet involving NH_2 def at ~1620 cm^{-1}
	1540-1650[9]			Amide link

	Wavenumber (cm^{-1})	**Intensity**	**Notation**	**Characteristic bond**
PRIMARY ALIPHATIC AMINE (AMINE I)	1050-1100	m	$\nu_{amine\ I}^{C-N}$	Primary aliphatic amines, -CH_2NH_2 general range
	1020-1240	w-m	$\nu_{amine\ I}^{C-N}$	Primary aliphatic amines, general range
	1145-1295	w	$\delta_{rocking/twisting}^{NH_2}$	Saturated primary amines
	1145-1285	m-w	$\delta_{twisting}^{CH_2/NH_2}$	-CH_2NH_2
	1245-1335	m-w	$\delta_{twisting}^{CH_2}$	-CH_2NH_2
	1335-1385	m-w	$\delta_{wag}^{CH_2}$	-CH_2NH_2
	1430-1470	m	δ^{CH_2}	-CH_2NH_2
	1580-1650, 1570[11,12]	m-s	δ_{sc}^{N-H}	Saturated primary amines
	2850-2890	m	$\nu_{sym}^{CH_2}$	-CH_2NH_2
	2915-2945	m	$\nu_{asym}^{CH_2}$	-CH_2NH_2
	3160-3450	w-m	$\nu_{amine\ I}^{N-H}$	broad, primary amines (condensed phase spectra)

	Wavenumber (cm^{-1})	Intensity	Notation	Characteristic bond
PROTONATED AMINE (NH_3^+)	930-1100	w-m	$\delta_{rocking}^{N^+-H}$/ ν^{C-N}	$-CH_2NH_3^+$
	1005-1135	w-m	$\delta_{rocking}^{N^+-H}$/ ν^{C-N}	$-CH_2NH_3^+$
	1150-1280	w	$\delta_{rocking}^{N^+-H}$	$-CH_2NH_3^+$, NH_3^+ rocking vib
	1480-1520,1490[11], 1484[12]	w	$\delta_{sym}^{N^+-H}$	$-CH_2NH_3^+$, Sym NH_3^+ def vib
	1560-1615	m-s	$\delta_{asym}^{N^+-H}$	$-CH_2NH_3^+$, Asym NH_3^+ def vib
	1585-1635, 1610[11], 1635[12]	m-s	$\delta_{asym}^{N^+-H}$	$-CH_2NH_3^+$, Asym NH_3^+ def vib
	2800-2920	m	$\nu_{sym}^{CH_2}$	$-CH_2NH_3^+$
	2900-2960	m	$\nu_{asym}^{CH_2}$	$-CH_2NH_3^+$
	2910-3010	m	$\nu_{sym}^{N^+-H}$	Sym NH_3 str $-CH_2NH_3^+$
	2985-3115	m, br	$\nu_{asym}^{N^+-H}$	Asym NH_3 str $-CH_2NH_3^+$
	3030-3235	m, br	$\nu_{asym}^{N^+-H}$	Asym NH_3 str $-CH_2NH_3^+$
	3100-3350	m	$\nu_{sym}^{N^+-H}$	$-NH_3^+$
OXIDE	1055[10], 1080[8], ~1050[9], 1050[13]			TO phonon mode of SiO_2
	1093[9]			Si-O-C bonds, distinct from SiO_2 characterized by a pair of modes
	~1090[13]			Si-O-Si bonds (not coupled to LO and TO modes)
	~1160[13]			Si-O-Si bonds (not coupled to LO and TO modes)
	~1190[12]		$\delta_{rocking}^{CH_2}$	$SiO-CH_2-CH_3$
	1224[10], 1240[8], 1100-1250[9], 1260[13]			LO phonon mode of SiO_2

References

(1) Kahn, A. Fermi Level, Work Function and Vacuum Level. *Mater. Horiz.* **2016**, *3* (1), 7–10.

(2) Kern, W. The Evolution of Silicon Wafer Cleaning Technology. *Journal of The Electrochemical Society* **1990**, *137* (6), 1887-1892.

(3) Sanchez, C.; Livage, J.; Launay, J. P.; Fournier, M.; Jeannin, Y. Electron Delocalization in Mixed-Valence Molybdenum Polyanions. *J. Am. Chem. Soc.* **1982**, *104* (11), 3194–3202.

(4) Artero, V.; Proust, A. Reduction of the Phosphododecamolybdate Ion by Phosphonium Ylides and Phosphanes. *European Journal of Inorganic Chemistry* **2000**, No. 11, 2393–2400.

(5) Matt, B.; Moussa, J.; Chamoreau, L.-M.; Afonso, C.; Proust, A.; Amouri, H.; Izzet, G. Elegant Approach to the Synthesis of a Unique Heteroleptic Cyclometalated Iridium(III)-Polyoxometalate Conjugate. *Organometallics* **2012**, *31* (1), 35–38.

(6) Laurans, M. Synthèse d'hybrides de Polyoxométallates: Greffage Contrôlé Sur Électrodes Pour l'étude de Jonctions Moléculaires. Thèse Sorbonne Université 2018.

(7) Joo, N. New functionalized polyoxometalates (POMs) for molecular memory devices compatible with a CMOS processing. Thèse Laboratoire LETI, **2010**.

(8) Caillard, L.; Seitz, O.; Campbell, P. M.; Doherty, R. P.; Lamic-Humblot, A.-F.; Lacaze, E.; Chabal, Y. J.; Pluchery, O. Gold Nanoparticles on Oxide-Free Silicon–Molecule Interface for Single Electron Transport. *Langmuir* **2013**, *29* (16), 5066–5073.

(9) Aureau, D.; Varin, Y.; Roodenko, K.; Seitz, O.; Pluchery, O.; Chabal, Y. J. Controlled Deposition of Gold Nanoparticles on Well-Defined Organic Monolayer Grafted on Silicon Surfaces. *The Journal of Physical Chemistry C* **2010**, *114* (33), 14180–14186.

(10) Seitz, O.; Dai, M.; Aguirre-Tostado, F. S.; Wallace, R. M.; Chabal, Y. J. Copper−Metal Deposition on Self Assembled Monolayer for Making Top Contacts in Molecular Electronic Devices. *Journal of the American Chemical Society* **2009**, *131* (50), 18159–18167.

(11) Pasternack, R. M.; Rivillon Amy, S.; Chabal, Y. J. Attachment of 3-(Aminopropyl)Triethoxysilane on Silicon Oxide Surfaces: Dependence on Solution Temperature. *Langmuir* **2008**, *24* (22), 12963–12971.

(12) Aissaoui, N.; Bergaoui, L.; Landoulsi, J.; Lambert, J.-F.; Boujday, S. Silane Layers on Silicon Surfaces: Mechanism of Interaction, Stability, and Influence on Protein Adsorption. *Langmuir* **2012**, *28* (1), 656–665.

(13) Michalak, D. J.; Amy, S. R.; Estève, A.; Chabal, Y. J. Investigation of the Chemical Purity of Silicon Surfaces Reacted with Liquid Methanol. *The Journal of Physical Chemistry C* **2008**, *112* (31), 11907-11919.

(14) Socrates, G. *Infrared and Raman Characteristic Group Frequencies: Tables and Charts*, 3. ed.; Wiley: Chichester, **2001**.

Résumé

Les polyoxométallates (POMs) sont des oxydes moléculaires des métaux de transition de la gauche de la classification périodique à haut degré d'oxydation. Ils sont notamment caractérisés par des propriétés redox ajustables, c'est-à-dire qu'ils peuvent être réduits successivement et réversiblement à plusieurs électrons, leur permettant ainsi d'être utilisés comme médiateurs redox ou réservoirs d'électrons dans diverses applications telles que l'électro-catalyse, la conversion de l'énergie solaire, les batteries moléculaires ou le stockage de l'information. Des études préliminaires de dépôt de POMs sur surface associé à des mesures de transport à l'état solide ont été encourageantes pour envisager l'incorporation de couches actives de POMs dans des nanodispositifs pour l'électronique moléculaire. Les propriétés électriques d'un tel dispositif étant dépendantes de la qualité de l'assemblage, maîtriser l'immobilisation des POMs sur un substrat et contrôler l'interface POMs/substrat est un sujet qui reste largement à explorer. Nous proposons de l'aborder via une nouvelle voie de fonctionnalisation de surface basée sur des réactions d'hydrosilylation. Avec cette méthode, des monocouches organiques de chaînes alkyles ordonnées portant des fonctions terminales amine/ammonium ont été préparées sur silicium pour permettre le dépôt éléctrostatique de POMs $(n\text{Bu}_4\text{N})_3[\text{PMo}_{12}\text{O}_{40}]$ photoréductibles. La photoréduction de ces POMs immobilisés en surface a été étudiée au moyen de différentes techniques de caractérisation (XPS, spectroscopie UV-Vis-NIR, KPFM). Des mesures électriques dans une configuration pseudo-MOSFET ont été finalement menées afin d'étudier l'influence de l'état de réduction de la couche de POMs sur les propriétés électriques ainsi que la possibilité de photo-commutation des couches oxydées aux couches réduites. En parallèle, le greffage covalent de POMs hybrides sur des surfaces de silicium modifiées a également été exploré durant la thèse dans l'objectif d'augmenter la robustesse du système ou de raccourcir la distance entre la surface du substrat et le POM pour améliorer le transport par effet tunnel.

Abstract

Polyoxometalates (POMs) are metal-oxo clusters formed by early transition metals in their highest oxidation state. More particularly, they exhibit adjustable redox properties, *i.e.* they can be reduced successively and reversibly to one or several electrons, such that they find their applications as redox mediators or electron reservoirs for electrocatalysis, solar energy conversion, molecular batteries or information storage. Previous results of POMs deposition onto surface characterized by electrical transport measurements were encouraging to envision the integration of active layers of POMs into nanodevices for molecular electronics. The electrical properties of the resulting device will depend on the assembly quality. The mastering of POMs immobilization onto substrates and the control of the POM/substrate interface is still required. In this context, NH_2/NH_3^+-terminated organic monolayers grafted on oxide-free silicon substrates were prepared by hydrosilylation and post-modifications. After the electrostatic deposition of photoreducible $(n\text{Bu}_4\text{N})_3[\text{PMo}_{12}\text{O}_{40}]$ POMs, the photoreduction of the immobilized POMs was studied by means of several characterization tools (XPS, UV-Vis-NIR spectroscopy, KPFM). Preliminary electrical characterization of a POM-based pseudo-MOSFET prototype device was carried out to study the influence of the POM redox state on the device conductance and to study the possible photoswitching property. Concurrently, the covalent grafting of POM hybrids onto functionalized, hydrogenated or oxidized Si surfaces was explored during the project, with the prospects of a more stable, controlled and tunable POM/substrate interaction.